ANALYSIS OF SIMULTANEOUS ROTORDYNAMIC FAULTS USING COUPLED MECHANICAL FACE SEAL VIBRATION

A Dissertation
Presented to
The Academic Faculty

by

Philip A. Varney

In Partial Fulfillment
of the Requirements for the Degree
Doctor of Philosophy in the
Woodruff School of Mechanical Engineering

Georgia Institute of Technology
December 2016

ANALYSIS OF SIMULTANEOUS ROTORDYNAMIC FAULTS USING COUPLED MECHANICAL FACE SEAL VIBRATION

Approved by:

Dr. Itzhak Green, Advisor
Woodruff School of Mechanical Engineering
Georgia Institute of Technology

Dr. Aldo Ferri
Woodruff School of Mechanical Engineering
Georgia Institute of Technology

Dr. Michael Leamy
Woodruff School of Mechanical Engineering
Georgia Institute of Technology

Dr. Brad Miller
Department of Engineering and Physics
Harding University

Dr. Jeffrey Streator
Woodruff School of Mechanical Engineering
Georgia Institute of Technology

Date Approved: November 4th 2016

ACKNOWLEDGEMENTS

I first want to thank Dr. Green for his support and advice given throughout this work. His intuition, experience, and enthusiasm has been extraordinarily valuable. I also want to thank him for his readiness to help; at times, we discussed problems, methods, and results on a near-daily basis. This availability is rare amongst faculty members, and has certainly contributed to my academic success. Dr. Green's unique approach for managing graduate students has given me a genuine curiosity for tribology, rotordynamics, and mechanical face seals.

Dr. Brad Miller also deserves special recognition. My academic path has been undeniably influenced by his phenomenal teaching style, subject mastery, and genuine interest in vibrations and dynamics. During my undergraduate studies, he recognized my shared interest in dynamics and went above-and-beyond to create entire courses focused on the subject. Dr. Miller and the engineering faculty at Harding University conclusively and unquestionably prove that quality education comes from quality instruction.

I also thank all of my committee members for their time and advice. Each member has contributed interesting conversations and suggestions while I completed this work. Other students, instructors, and friends deserve recognition for their advice, perspectives, and appreciated diversions, including Patrick and Leigh Anna Smyth, Matt Strasser, Peter Yeh, Eric Smith, Matt Perrella, David MacNair, Tristan and Laurin Vonada, and numerous others. Finally, this work wouldn't be possible without the support of my family, including my wife Julie, all of whom supported me in many different ways while I spent years pursuing my degree.

TABLE OF CONTENTS

LIST OF TABLES

LIST OF FIGURES

NOMENCLATURE

Degrees of Freedom:

ϵ_i	Magnitude of eccentric deflection of element i.
ϵ_{ij}	Eccentric deflection of element i in direction j.
ϵ^*	Relative deflection between the rotating and stationary seal elements.
γ_i	Magnitude of angular deflection of element i.
γ_{ij}	Angular deflection of element i in direction j.
γ^*	Relative angular deflection between the seal elements.
u_{iz}	Axial deflection of element i.
u^*	Relative axial deflection between the seal elements.

Seal Apparatus Parameters:

β	Seal coning angle.
β_r	Phase angle of the rotating seal element imbalance.
$\beta_{r\chi}$	Phase angle of the rotating seal element dynamic angular misalignment.
$\beta_{r\chi_s}$	Phase angle of the rotating seal element static angular misalignment.
ε_{rG}	Rotating seal element imbalance.
$\epsilon_{si,j}$	Stationary seal element static eccentric misalignment about axis j.
$\gamma_{si,j}$	Stationary seal element static angular misalignment about axis j.
$\bar{\lambda}_0$	Inertial maneuver rotation rate.
λ_p, λ_y, λ_{ro}	Pitch, yaw, and roll components of inertial maneuver rotation rate.
ψ_r, ψ_s	Precession angle of the rotating and stationary seal elements.
τ_T	Thermoelastic coning time constant.
χ, χ_s	Rotating seal element dynamic and static angular misalignments.
μ	Lubricant viscosity.

C_o	Set-point centerline axial clearance between the seal elements.
d_r	Axial offset of the rotating seal element.
D_f	Angular damping of the fluid film.
D_r, D_s	Angular damping of the rotating and stationary seal element supports.
$D_{r\epsilon}$, $D_{s\epsilon}$	Eccentric damping of the rotating and stationary seal element supports.
D_{rz}, D_{sz}	Axial damping of the rotating and stationary seal element supports.
F_{spr}	Axial support spring force.
F_{cls}	Closing force acting on the seal elements.
$h(r, \theta, t)$	Fluid film thickness as a function of position and time.
h_i, h_m, h_o	Fluid film thickness evaluated at the inner, mean, and outer radii.
I_{pr}	Polar mass moment of inertia of the rotating seal element.
I_{tr}, I_{ts}	Transverse mass moment of inertia of the rotating and stationary seal elements.
K_f	Angular stiffness of the fluid film.
K_r, K_s	Angular stiffness of the rotating and stationary seal element supports.
$K_{r\epsilon}$, $K_{s\epsilon}$	Eccentric stiffness of the rotating and stationary seal element supports.
K_{rz}, K_{sz}	Axial stiffness of the rotating and stationary seal element support.
m_r, m_s	Mass of the rotating and stationary seal elements.
P_i, P_o	Inner and outer fluid reservoir pressures.
r_b	Seal balance radius.
r_i, r_m, r_o	Sealing dam inner, mean, and outer radii.
r_s	O-ring support spring attachment radius.

Rotor Parameters:

$\alpha(t)$	Shaft rotation angle as a function of time.
β_C	Rotor internal damping coefficient.
$\beta_{\chi b}$	Phase angle of angular component of rotor bow.

β_{rb}	Phase angle of rotor bow.
ε_{RG}	Rotor imbalance.
χ_b	Angular component of rotor bow.
χ_R	Rotor dynamic angular misalignment.
ν	Shaft Poisson ratio.
ω_r	Shaft speed of system.
ζ_ϵ, ζ_γ	External viscous damping ratio of eccentric and angular deflections.
$\bar{a}_O$	Net acceleration of the rotor system caused by maneuver operation.
B_r	Rotor disk width.
c_R	Jeffcott rotor external viscous damping coefficient.
$c_{R\gamma}$	Angular-only rotor external viscous damping coefficient.
d	Rotor shaft diameter.
E_R	Elastic modulus of the rotor shaft.
I	Area moment of inertia of shaft.
I_{pR}, I_{tR}	Polar and transverse rotor mass moment of inertia.
$k_{\epsilon\epsilon}$, $k_{\gamma\gamma}$	Shaft stiffness of eccentric and angular deflections.
$k_{\epsilon\gamma}$	Shaft stiffness coupling eccentric and angular deflections.
$k_{\xi\xi}$, $k_{\eta\eta}$	Jeffcott rotor support stiffness in the ξ and η directions.
$k_{R\gamma}$	Angular-only rotor support stiffness.
L	Overhung shaft length.
m_R	Rotor mass.
r_b	Rotor bow magnitude.
R	Shaft radius.
R_r	Rotor disk radius.

Crack Parameters:

a	Crack depth.
b	Total crack half-width.
b^-, b^+	Lower and upper bounds of the crack half-width.
c_{ij}, $\bar{c}_{ij}$	Dimensional and non-dimensional crack compliance.
c^*_{ij}	Breathing crack compliance reconstruction from the Fourier transform.
$J(y)$	Crack strain energy density function.
K_I	Scalar stress intensity function corresponding to the first mode of crack opening.
L_1	Overhung shaft length from support to crack.

Surface Roughness and Contact Parameters:

δ	Lateral set-point clearance between the rotor and stator.
Ψ	Surface plasticity index.
$\phi(z)$	Asperity height probability density function.
σ, σ_s	Standard deviation of surface and asperity heights.
μ_f	Dry Coulomb friction coefficient.
ν	Material Poisson ratio.
ω	Asperity interference.
ω_c	Critical asperity interference beyond which plastic deformation occurs.
A_n	Nominal contact area.
d	Surface separation distance.
E	Asperity composite elastic modulus.
k_c	Contact stiffness used in the linear elastic contact model.
N	Areal density of asperities.
R_a	Asperity radius of curvature.
S_y	Surface yield strength.

y_s Difference between the mean surface height and the mean asperity height.

z Surface asperity heights.

General Symbols:

λ_f Floquet multiplier.

$\mathbf{\Phi}$ Floquet monodromy transition matrix.

θ Circumferential polar coordinate.

τ Time (non-dimensional).

r Radial polar coordinate.

t Time (dimensional).

Subscripts and Superscripts:

$(\,)^*$ Relative kinematic variables.

$\dot{(\,)}$ First derivative with respect to dimensional time.

$\ddot{(\,)}$ Second derivative with respect to dimensional time.

$(\,)'$ First derivative with respect to non-dimensional time.

$(\,)''$ Second derivative with respect to non-dimensional time.

$\hat{(\,)}$ Unit vector designation.

SUMMARY

Rotating machines are complex systems that are innately vulnerable to different faults. Left unattended, these faults can damage or destroy the machine, both of which are expensive and dangerous. An effective method for detecting incipient rotor faults is real-time vibration monitoring; designing such a system requires a thorough understanding of the system dynamics. Furthermore, the pursuit to increase efficiency has heightened susceptibility to coexisting faults; this scenario must be considered when designing a vibration monitoring system. A fundamental attribute of any vibration monitoring system is the source of the measured vibration. This work hypothesizes that rotor vibration transmitted to associated mechanical face seals could serve as a convenient surrogate for characterizing rotor faults.

The first step in designing a seal-fixed surrogate rotor vibration monitoring system is understanding the coupled rotor-seal dynamics. Towards this end, a comprehensive model is developed to study the dynamics of a mechanical face seal with two flexibly mounted elements, including axial, eccentric, and angular degrees-of-freedom. In addition, and for the first time, this model includes coupled rotordynamics, inertial maneuver loads, and transient operation. Designated the FMSR-ER seal, this model significantly advances the current state-of-the-art in mechanical face seal dynamics. For the first time, this work studies the seal in the context of its actual operating condition: as a constitutive element of a much larger rotordynamic system. A rotor model is also developed accounting for angular misalignment, rotor bow, external viscous damping, and internal structural damping.

The rotor faults considered here include a rotor fatigue crack and intermittent rotor-housing contact. In reality, rotor cracks open and close as the shaft rotates

(i.e., the crack breathes). Here, the breathing mechanism is determined by assuming that the static rotor deflection dominates the breathing behavior. The crack compliances can then be expressed as a function of rotor rotation, thus resulting in a linear time-periodic rotor stiffness matrix. A novel model for intermittent rotor-housing contact is developed using a realistic surface roughness model founded on elastoplastic asperity contact. This new model advances the state-of-the-art by approximating the contact forces using physical principles and measurable surface parameters in lieu of simplifications and heuristics.

The first step in designing the seal-fixed surrogate rotor vibration monitoring system is understanding the undamaged system dynamics. The results presented here indicate that the rotor is unaffected by the seal if the rotor inertia is significantly larger than the seal inertia. Thus, the rotordynamics can be found independently and sent to the seal dynamics as an exogenous input. In addition, this work proves that the seal performance is meaningfully influenced by the rotordynamics. Consequently, the rotordynamics must be considered when designing mechanical face seals. The undamaged system simulation also proves that the most effective seal vibration for observing the rotor response is the stationary seal element tilt (this conclusion is intuitive because the seal is designed to minimize relative angular misalignments between the faces).

Characterizing simultaneous faults is a futile endeavor if each fault is not understood individually. The breathing crack, once initiated, is always present on the rotor. Thus, the fault signatures of the crack are likewise always present in the response. Specifically, these signatures include integer shaft speed harmonics and associated sub-synchronous critical speeds. On the other hand, intermittent rotor-housing contact is (a) fundamentally ephemeral, and (b) defined by phenomena occurring on

vastly different scales (the duration of contact is significantly less than the rotor rotation period, and the scale of contact is comparable to the surface roughness dimension). This piecewise-smooth nonlinearity therefore results in a rich variety of nonlinear dynamics, including periodic, quasiperiodic, and chaotic responses. The multiple fault scenario is then characterized using the system bifurcation behavior. When a crack is present, rotor-housing contact occurs at significantly lower shaft speeds, and particularly so for more severe rotor cracks. In addition, the time-energy-frequency spectrum indicates large increases in instantaneous frequency at each impact along with an increase in energy near the dominant crack-induced shaft speed harmonic.

This work makes several novel contributions to the state-of-the-art regarding mechanical face seals and rotor fault analysis. First, a comprehensive model for a mechanical face seal is developed that accounts for the coupled rotordynamics. This addition is significant because it allows the seal to be designed with regard to complete system performance. Second, this work develops a novel model for rotor-housing contact that appeals to the physics of contact rather than heuristics. Finally, unique multiple fault vibration signatures are discussed relative to a realistic rotor system, where the simultaneous faults are distinguished according to bifurcation behavior and time-energy-frequency signatures. This work concludes by suggesting how the tools presented herein could be used to develop a robust diagnostic algorithm using neural network time-series prediction and machine learning classification methods.

CHAPTER I

INTRODUCTION

On August 16th, 2009, a generator in the Siberian Sanayo hydro-plant failed catastrophically, claiming the lives of 75 workers [1] (see Fig. 1.1, which shows the destroyed generator). Unusual loading conditions induced by the failure of a nearby generator caused the rotor to continually pass through an unstable operating regime, damaging the supporting structure. The resulting loss of stiffness led to unsustainable vibration amplitudes and eventual catastrophic failure. The Sanayo failure was tragic but avoidable, and emphasizes the need for online (i.e., real-time) fault detection.

1.1 Motivation

Rotordynamic machinery is ubiquitous in modern industrial society, playing a central role in power generation, drilling, transportation, and manufacturing. The repercussions of rotor failure in these industries extends beyond safety; failures also result in increased operating cost. In particular, consider the costs incurred by two serious faults: rotor fatigue cracking and rotor-stator rub. Left unattended, rotor cracks can cause catastrophic machine failure, which is not only dangerous but also expensive. Bently and Muszynska [2] document 28 significant rotor failures caused by rotor cracks in the United States power industry between 1976 - 1986, each of which resulted in costly downtime and expensive repairs. In support of this conclusion, the Electric Power Research Institute estimates that the United States power industry has incurred approximately US $1 billion [3] in expenses from rotor cracks alone. Rotor-stator rub is a more common fault that also imparts a significant cost to the operator, and particularly so when sealing components are involved. One study indicates that the cost of worn seals is comparable to 1% of the total per-year fuel cost

Figure 1.1: Sanayo generator failure.

in a single aircraft turbine (approximately $\$100,000.00$ USD, circa 2000) [4]. Chupp et al. [5] indicate that reducing fluid clearances in turbomachines used in a broad array of industries could save 1.554 billion gallons of fossil fuels consumed annually, which amounts to 0.3% of the U.S. energy consumption. In another example, failure caused by rotor-stator rub caused lengthy delays and substantial expenses in the high-pressure fuel turbo-pump of the Space Shuttle Main Engine [6, 7].

Another realistic example of rotor-stator rub is contact between the rotating blades and the stationary housing. A schematic showing possible locations for blade tip rub is shown in Fig. 1.2a, as provided by Batailly et al. [8]. Several adverse effects associated with blade tip rub have been identified, such as modal interaction between the blades and the stator, significant wear of the blade and/or the housing, and undesirable rotor whirl [8]. Adverse wear is often mitigated via abradable coatings, which reduce damage when a blade exceeds the allowable clearance [9]. Severe blade tip rub can propagate fatigue cracks on the blade, eventually resulting in catastrophic blade loss.

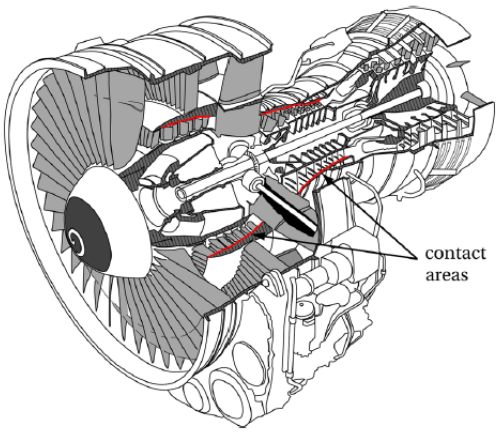

(a) Blade tip rub in a turbofan engine

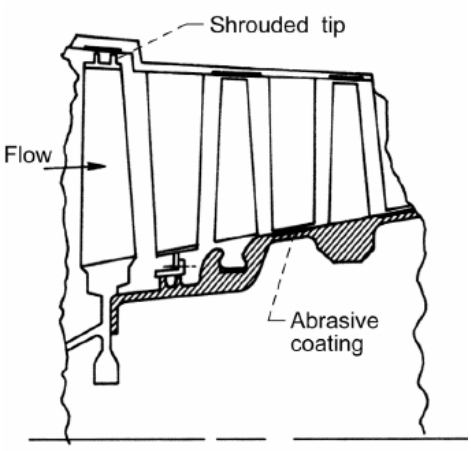

(b) Abradable coating

Figure 1.2: Blade tip rub.

The aforementioned examples reinforce the fact that rotordynamic faults represent a significant financial burden in a wide range of industries. In these industries, improvements in safety and cost can be obtained with accurate real-time fault diagnostics. Currently, many diagnostics are performed when the machine is off-line, and often on a scheduled basis (for example, crack detection using ultrasonic methods); these off-line diagnostics spawn lengthy and expensive downtimes. On the other hand, on-line diagnostics reduce costly scheduled maintenance by permitting repairs on an as-needed basis; the machine is taken off-line only when a fault is detected.

Many industries employ a plethora of monitoring techniques for rotating machines, such as oil analysis, acoustic emission, and ultrasonic methods. Even though these methods are often successful for off-line analyses, they are woefully inadequate for on-line fault characterization. Specifically, this work concerns a method commonly used for real-time analysis: vibration monitoring. Vibration monitoring retains an important advantage in that many industries already measure rotating machine vibration (for example, see ISO-7919 [10]). Rather than requiring expensive modification, existing vibration sensors can be used to characterize rotor faults. Vibration monitoring imparts a second advantage because it is performed in-house, whereas techniques like

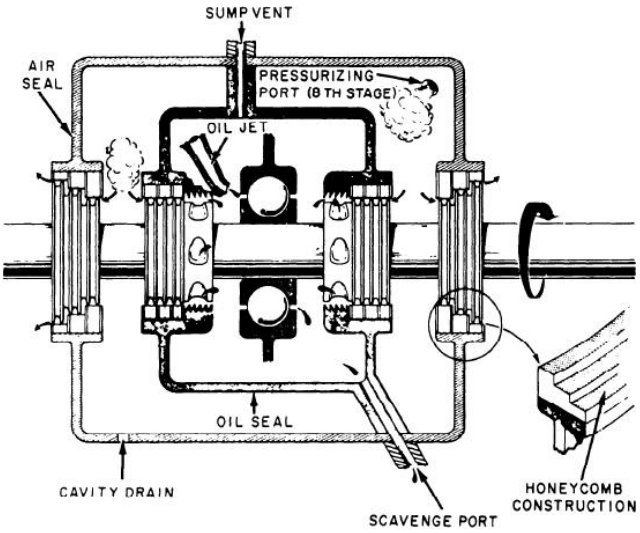

Figure 1.3: Sealing system used to contain bearing lubrication.

oil monitoring often require samples to be sent to outside laboratories, thus incurring lengthy delays. Still, the principal advantage of vibration monitoring is perhaps the relative ease of dynamic modeling. Hallmark vibration signatures are extracted from system-specific models, whereas other methods rely on heuristics, stochastics, and/or an extensive history of data.

The efficiency of rotating machines improves when the power-to-weight ratio is increased; accomplishing this increase requires lighter and more slender shafts, greater rotation rates, and decreased clearances. These enhancements adversely affect reliability by heightening fault susceptibility. Exacerbating this problem is the predilection of rotor systems to faults such as imbalance, misalignment, and looseness. These primary faults are aggravated by mechanical degradation and thermal effects, resulting in greater proclivity for more severe faults such as shaft cracking and rotor-stator rub. In turn, secondary faults can generate or propagate other secondary faults (e.g., rotor-stator rub can increase fatigue stress, which could cause the rotor to crack). Therefore, it is reasonable to assume that multiple simultaneous faults are a realistic operating condition.

Modern turbomachines rely extensively on fluid-film triboelements such as journal bearings and mechanical seals. For example, modern aircraft engines (e.g., turbofans, turbojets, etc.) are often supported using oil-lubricated rolling element bearings, where the lubricant is directly injected into the housing. High pressure air from the compressor is then used in conjunction with a suite of seals to reduce, and preferably eliminate, oil contamination in the primary air flow through the engine (see Fig. 1.3, where a honeycomb seal is used to restrict fluid flow [11]). A plethora of seal designs are used to accomplish fluid sealing throughout the turbomachine, such as labyrinth seals, brush seals, and mechanical face seals [5, 12]. One of the most common seal designs is the labyrinth seal, which employs a consecutive arrangement of circumferential teeth to restrict fluid flow. Leakage rates are typically high in labyrinth seals because the seal operates with a finite clearance between the teeth and the stator. Occasional seal-stator contact eventually causes increased leakage via an increased clearance. Another seal design, the brush seal, uses densely packed brushes to reduce leakage across the seal. This work is primarily concerned with mechanical face seals, which employ either contact or fluid pressure to accomplish sealing across the radial dimension of the seal face. In general, mechanical face seals that use fluid pressure to provide sealing are referred to as non-contacting mechanical face seals (these seals will be described in greater detail in Chapter 2). The advantage of a non-contacting mechanical face seal is the significant reduction of friction, contact, and wear between the seal faces.

Unfortunately, mechanical face seals often fail prematurely and unexpectedly [13, 14]. The design of modern seals could be improved by modeling the complete system dynamics, thus accounting for dynamic interactions between the seal and rotor. One hypothesis explaining premature failure of non-contacting mechanical face seals is unexpected contact between the seal faces, which could be precipitated by a poor seal design, an increased rotordynamic response, or large inertial maneuver loads.

Studying mechanical face seal vibration has utility beyond just improving the seal design. The mechanical seal dynamics are inextricably coupled to those of the rotor via the same mechanisms that permit sealing (i.e., fluid film lubrication). Thus, any vibration generated by the rotor is commensurately transmitted to the seal. Because rotor faults often manifest as aberrant vibrations, this work hypothesizes that the mechanical face seal vibration can be used as convenient surrogate for rotordynamic vibration monitoring.

1.2 Objectives

The objective of this work is to use mechanical seal vibration to identify and characterize complex rotordynamic fault signatures resulting from multiple contemporaneous rotor faults. Completing this task requires the following specific objectives:

1. **System Modeling**: Develop a comprehensive and adaptable model of the seal and rotor that accounts for realistic operating conditions.

2. **Fault Modeling**: Develop realistic models for two severe rotor faults: a breathing fatigue crack and intermittent rotor-housing contact.

3. **Simulation**: Solve the resulting models to ascertain hallmark dynamic signatures of the healthy system and the damaged system. The simulations will be performed over a range of shaft speeds and analyzed using stationary and non-stationary signal processing methods.

As will be shown in the next chapter, each of these objectives represents a novel and substantial contribution to the current state-of-the-art regarding mechanical face seal dynamics and rotor fault analysis. To summarize, current studies regarding mechanical face seal dynamics and rotor faults are entirely disjointed. This work bridges the gap by providing a comprehensive analysis of the complete coupled apparatus (in addition to developing novel and realistic rotor fault models).

1.3 Outline

This work begins in Chapter 2 by outlining previous work relevant to the overall objectives. Past studies concerning mechanical face seal dynamics are discussed in detail and interpreted with regard to using the seal as a possible surrogate rotordynamic condition monitor. The two faults considered herein, a breathing fatigue crack and rotor-housing contact, are discussed in relation to modeling, response characteristics, and experimental results. Previous multiple fault investigations are also summarized. Finally, shortcomings in the existing literature are discussed relative to the novelty and academic contribution of this work.

Chapter 3 presents a comprehensive model of a non-contacting mechanical face seal including angular, axial, and eccentric degrees-of-freedom of both seal elements (rotating and stationary). The model includes a variety of realistic operating conditions such as coupled rotordynamics, inertial maneuver loads, transient operation, face contact, and primary seal faults (e.g., imbalance and misalignment). Chapter 4 continues to develop the system model by presenting a lumped parameter rotordynamic model with angular and eccentric degrees of freedom. The rotor model includes gyroscopic effects, internal damping, viscous external damping, and a generally time-dependent stiffness matrix. Primary rotor faults are also included, such as rotor bow, rotating imbalance, and dynamic angular misalignment. The simplified steady-state equations of motion of the seal-rotor system are given in Chapter 5.

The rotor faults are modeled in Chapters 6 and 7. A model for the breathing fatigue crack is derived in Chapter 6, where the crack opens and closes with rotor rotation. The crack compliance is calculated according to the strain-energy release rate. Several models for rotor-stator contact are presented in Chapter 7, where the contact force is developed using rough surface contact rather than heuristic approximation.

Understanding the undamaged system response is a necessary prerequisite for understanding the dynamic signatures of each fault. Chapter 8 provides the response

of the undamaged seal-rotor system versus shaft speed for several possible system configurations. The results are interpreted with regard to using the mechanical seal as a surrogate rotordynamic condition monitoring system.

The response to each fault is studied in Chapters 9 and 10 for the breathing fatigue crack and rotor-stator contact, respectively. In each case, the steady-state response is simulated versus shaft speed to identify hallmark dynamic signatures of each fault. The results are interpreted using bifurcation diagrams, frequency spectra, rotor/seal orbits, and the Hilbert Huang transform (i.e., the time-energy-frequency spectrum). The multiple fault scenario is investigated in Chapter 11 using similar analysis techniques. The hallmark vibration signatures identified in these chapters are a necessary prerequisite for developing robust diagnostic algorithms in future works.

Finally, the work concludes by summarizing important fault vibration signatures and suggesting avenues for future work. A promising method for predicting the rotor response using only the seal response is demonstrated using a proof-of-concept example involving machine learning.

CHAPTER II

LITERATURE REVIEW

The overall objective of this work is to use mechanical face seal vibration to characterize rotor faults. The faults investigated here include a breathing fatigue crack and rotor-housing contact, and finally, the multiple fault scenario where both faults exist contemporaneously. Characterizing the response to multiple simultaneous faults is a multi-faceted problem. First, the rotor-seal system dynamics must be quantified and interpreted in the undamaged condition. This is important because the design of the seal-fixed condition monitoring system is predicated on how the rotordynamics are transferred to the seal (i.e., the undamaged system dynamics elucidate the best design for the seal-fixed monitoring system). Next, each fault must be studied individually to identify hallmark vibration signatures and suitable signal processing techniques associated with that fault. These prerequisite tasks comprise the framework under which multiple simultaneous faults can be analyzed and characterized. This chapter reviews important contributions made to the literature with regard to the aforementioned tasks. Specifically, the state-of-the-art is summarized regarding mechanical face seal dynamics, signal processing techniques, rotor fatigue cracks, rotor-stator contact, and multiple fault vibration signatures.

2.1 Mechanical Face Seals

The purpose of a mechanical face seal is to separate high and low pressure fluids in rotating machines. These components are categorized according to how fluid sealing is accomplished. Contacting mechanical face seals operate with the seal faces completely closed (i.e., contacting). This design minimizes fluid leakage at the expense of increased friction and wear [15, 16]. Consequently, contacting mechanical

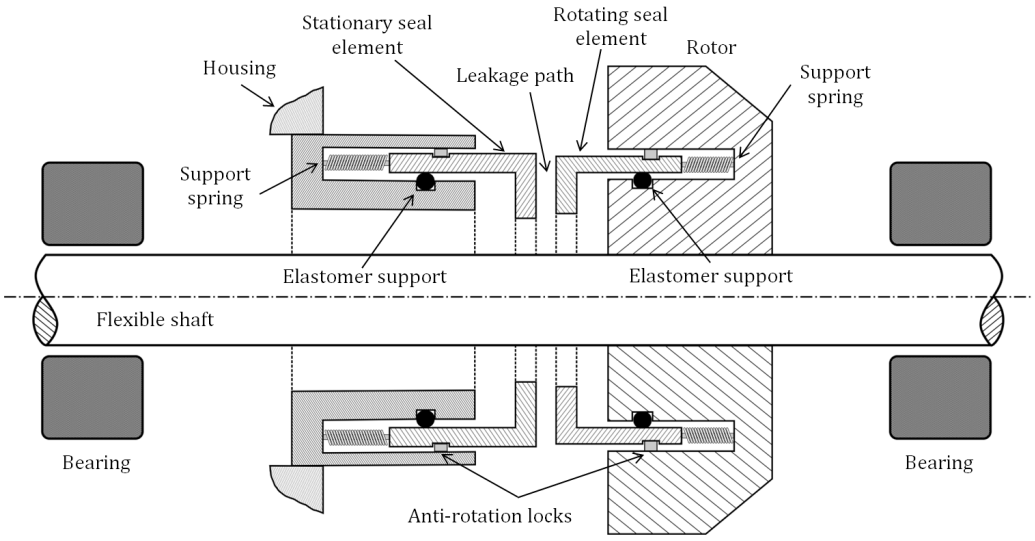

Figure 2.1: FMSR seal showing the coupled external rotor (i.e., the flexible shaft and accompanying disk).

face seals have a finite design life and must be replaced on a continual basis. On the other hand, non-contacting mechanical face seals use hydrostatic and/or hydrodynamic fluid pressure to provide sealing, thus providing a theoretically infinite design life at the expense of increased leakage [17,18]. The advantages of the non-contacting mechanical face seal make it an attractive option for high performance applications where reliability is critical, replacement is difficult, or rotation rates are large enough to preclude a contacting seal design [12]. Non-contacting mechanical seals are also categorized according to how the seal elements are mounted:

1. **Flexibly-mounted stator (FMS)**: The stationary element is flexibly-mounted while the rotating element is rigidly-mounted.

2. **Flexibly-mounted rotor (FMR)**: The rotating element is flexibly-mounted while the stationary element is rigidly-mounted.

3. **Flexibly-mounted stator and rotor (FMSR)**: Each seal element is flexibly-mounted (to the rotor and housing, respectively).

Flexibly-mounting one or both seal elements allows the seal to minimize the relative angular misalignment between the faces (i.e., the seal exhibits dynamic tracking). A non-contacting mechanical face seal is shown schematically in Fig. 2.1, where both the rotating and stationary seal faces (i.e., elements) are flexibly-mounted. The stationary element is attached to the housing via a support spring and a secondary elastomeric seal (a similar arrangement is used to attach the rotating seal element to the rotor). In this work, the term 'rotor' refers to the flexible shaft and accompanying disk(s), whereas prior seal investigations often refer to the rotating seal element as the rotor. Fluid leakage occurs between the seal faces, and flows in the direction of high to low pressure (thus, seals are also described as being either inward or outward pressurized). Anti-rotation locks are used to restrict the seal elements from rotating relative to their attachments in the direction of shaft rotation [19, 20].

2.1.1 Mechanical Seal Dynamics

Seal performance is assessed using the relative angular misalignment between the seal faces; large relative misalignments lead to high leakage rates, thus constituting seal failure. Most seal designs can tolerate only several milliradians of relative misalignment before contact occurs [21–25]. The relative angular misalignment depends on the seal dynamics, which in turn are dictated by component angular misalignments (e.g., installation errors, imperfections, etc.), external rotor excitations, and the specific seal design (fluid pressures, face coning, etc.). Etsion [17] provides a succinct review of early developments regarding mechanical face seal dynamics, and later expands the review to include other relevant studies [26, 27].

A prerequisite for studying mechanical seal dynamics is understanding the applied forces acting on the seal. The most important forces and moments acting on the seal are generated by the fluid pressure between the seal faces, which for small clearances can be calculated using the Reynolds equation [28]. Most mechanical face seals are

narrow in the radial direction; i.e., the inner radius is comparable to the outer radius. Etsion [29] uses this narrow seal assumption to neglect circumferential pressure gradients and seal curvature, thus reducing the Reynolds equation to a more manageable form. The full numeric solution for fluid pressure indicates that the narrow seal approximation is accurate for seals with inner-to-outer radii ratios of 80% or greater. The Reynolds equation for the narrow seal is then solved analytically to obtain the pressures generated by hydrostatic [30], hydrodynamic [31], and squeeze effects [32]. Hydrostatic pressure is typically achieved via face coning, where a radial taper is used to create a converging gap in the direction of fluid flow. Hydrodynamic fluid pressure is generated by relative angular misalignments [19], surface texturing [33–36], or seal face geometry [37]. Other forces and moments are applied to the seal via the elastomeric O-ring secondary seal [38].

The earliest analyses of mechanical face seal dynamics only considered the FMS seal configuration. Etsion [17] simulates the FMS equations of motion using the full nonlinear fluid film forces, and accounts for axial and angular vibration of the stationary seal element. The simulation results are used to draw conclusions regarding seal stability and optimum face coning. Green and Etsion [39] expand the parametric analysis of the FMS seal to further understand seal instability. The FMS equations of motion can also be linearized by reducing the nonlinear fluid film forces and moments to a commensurate set of stiffness and damping coefficients [40]. In general, these investigations regarding FMS seal performance indicate that though the seal is adept at minimizing relative angular misalignments, it also suffers from instability issues.

The transient dynamics of a FMS mechanical face seal have also been studied during start-up and shut-down operation, though not as extensively as the steady-state seal dynamics. In general, the objective of a transient analysis is to find the lift-off speed at which the seal faces separate and contact disappears. Harp and Salant [41] use the influence coefficient method to study mechanical and thermal seal

deformations during transient operation, accounting for fluid and contact forces at the seal interface. Inward pressurized seals are shown to experience high contact pressures prior to lift-off, whereas outward pressurized seals are shown to have high leakage rates. Green [42] treats thermal deformations during transient analysis by reducing the complicated influence coefficient method to an intuitive first-order model obtained via finite element simulation. Asperity contact during transient operation is imposed via the elasto-plastic Chang-Etsion-Bogy rough surface contact model [43]. Importantly, Green's analysis [42] shows that face coning in mechanical seals is often a consequence of thermoelastic deformation, where the thermal deformation time constant is much slower than the seal dynamics (similar results are also shown by Gao et al. [44]). Salant and Cao [45] later perform a similar analysis for a mixed-lubrication seal using influence coefficients. Not surprisingly, their results indicate that thermal deformations are primarily governed by first-order effects.

Instability problems in the FMS seal can be circumvented using a FMR seal configuration. The FMR seal fluid film coefficients are derived by linearizing the fluid film about equilibrium [46]. The FMR fluid film coefficients differ from the FMS coefficients only in the cross-coupling stiffness that appears between the orthogonal seal face tilts. It is important to recognize that these fluid film coefficients are only valid for small tilts about equilibrium in the absence of fluid cavitation. The fluid film coefficients are used in conjunction with the seal kinematics [19] to obtain the complete FMR seal equations of motion [47, 48] for angular and axial degrees-of-freedom. The FMR seal configuration is unequivocally stable if the ratio of transverse to polar mass moments of inertia is less than one (i.e., thin FMR seals are stable for all shaft speeds). In addition, the FMR seal also has better dynamic tracking compared to the FMS configuration, thus resulting in smaller relative angular misalignments. Lee and Green [21] rearrange the FMR equations of motion into a transfer matrix form that accounts for the steady-state coupled rotordynamics. Results from their study

indicate that the rotordynamic response can significantly affect the seal performance. The predicted FMR seal dynamics are verified experimentally by Lee and Green [22, 49, 50] using an overhung rotor with a coupled FMR mechanical face seal. The angular seal dynamics are extracted directly from the rotating seal element using a suite of non-contacting eddy-current proximity probes. Zou et al. [24] improve the condition monitoring system by incorporating real-time data analysis.

The FMS and FMR seal configurations assume that only one element is flexibly-mounted. Wileman [51] generalizes this restriction by considering a seal configuration where both elements are flexibly-mounted to independently rotating shafts (i.e., the FMRR seal). The FMRR fluid film coefficients for angular and axial degrees-of-freedom are derived by Wileman and Green [52]. The FMS and FMR coefficients are shown to be degenerate cases of this more general solution. The fluid film coefficients are then included in the FMRR equations of motion [53], which are solved analytically to obtain the stability threshold shaft speed for different parameter combinations. An extended parametric analysis [54] regarding counter-rotating seals indicates that restoring gyroscopic moments can be transmitted across the film if one of the rotating seal elements is thin.

A complete understanding of the coupled rotor-seal dynamics must consider lateral vibrations (especially for surrogate rotor fault analysis). The aforementioned works only include angular and axial degrees-of-freedom. In reality, the seal elements also experience lateral deflections, which are referred to here as eccentric deflections. Etsion and Sharoni [55] investigate the effect of eccentricity (i.e., fluid shear) on the fluid film forces and moments in an FMS seal. Wileman and Green [56] incorporate the effect of eccentric deflections into the Reynolds equation and provide commensurate fluid film coefficients. These coefficients are later used in the complete FMRR seal equations of motion to show that synchronous rotor whirl prominently affects seal performance [57].

2.1.2 Rub in Non-Contacting Mechanical Face Seals

A possible explanation for premature failure in non-contacting mechanical face seals is unexpected contact between the seal faces. Contact can be precipitated by many effects, including inadequate lubrication, excessive vibration, large misalignments between the faces [49,58], or transient operation [41,42]. Mitigating face contact requires seal redesign and real-time condition monitoring to detect the onset of face contact. Etsion and Constantinescu [58] experimentally observe that dynamic seal face contact in a FMS seal is exacerbated by large relative face misalignment. Lee and Green [21] identify seal face contact in an experimental test rig using integer shaft speed harmonics. Seal face contact has also been detected experimentally using other methods, such as acoustic emission (AE) [59], ultrasonic wave (UW) techniques [60], torque sensor measurements [61], and changes in temperature and leakage [62]. Others have used these same experimental techniques to heuristically identify seal face contact and then actively control the seal to reduce or eliminate contact [63–66].

A better understanding of mechanical face seal contact would improve seal designs and provide assurance that the transmitted rotor vibration is unadulterated by local seal face contact. Though non-contacting face seal dynamics have been thoroughly investigated, little effort has been made to study intermittent contact. Green [42] determines the transition between contacting and non-contacting regimes of operation by simulating the transient seal dynamics; asperity contact forces are included without considering intermittent dynamic contact. Other works have specifically investigated contacting seals using mixed-lubrication rough surface contact [41, 67]; in all of these cases, the contact is perpetual rather than intermittent. Ruan [68] solves the seal dynamics and fluid film simultaneously for a spiral groove gas face seal, where asperity contact is used to calculate contact forces. Though the model seamlessly accounts for the transition between contacting and non-contacting modes of operation, the only cases considered are those where contact briefly occurs during transient operation.

2.1.3 Mechanical Seals: Shortcomings in the Literature

Several shortcomings are identified regarding mechanical face seal dynamics:

1. **Comprehensive Seal Models**: A comprehensive seal model is required that combines angular, axial, and eccentric vibrations with realistic seal operating conditions such as transient operation, primary faults (e.g., imbalance, misalignment), and external inertial maneuver loads.

2. **Coupled Rotordynamics**: The aforementioned works clearly indicate that the rotor prominently influences seal performance [21,57]. The seal model must be expanded to account for realistic coupled rotordynamic effects.

3. **Intermittent Seal Face Contact**: Seal face contact is suggested as a failure mechanism, but only understood with regard to heuristics and experiments. However, using the seal as a surrogate rotor vibration monitor requires that the seal not contaminate the rotor fault signatures via face contact.

These shortcomings are summarized by recognizing that most prior investigations treat the seal as an independent machine element. In reality, mechanical seals are constitutive elements of complicated rotating machines. The performance of the overall rotating machine must be considered when designing the seal and using it as a surrogate rotordynamic condition monitor.

2.2 Signal Processing Tools

Successful fault detection is predicated on appropriately selecting suitable signal processing tools. Here, signal processing techniques are categorized according to the signals they are designed to analyze. Stationary signals result from systems where the underlying dynamics are governed by a time invariant system; i.e., the model is temporally homogeneous. An example of a stationary signal is the synchronous steady-state rotor response to imbalance. On the other hand, non-stationary signals

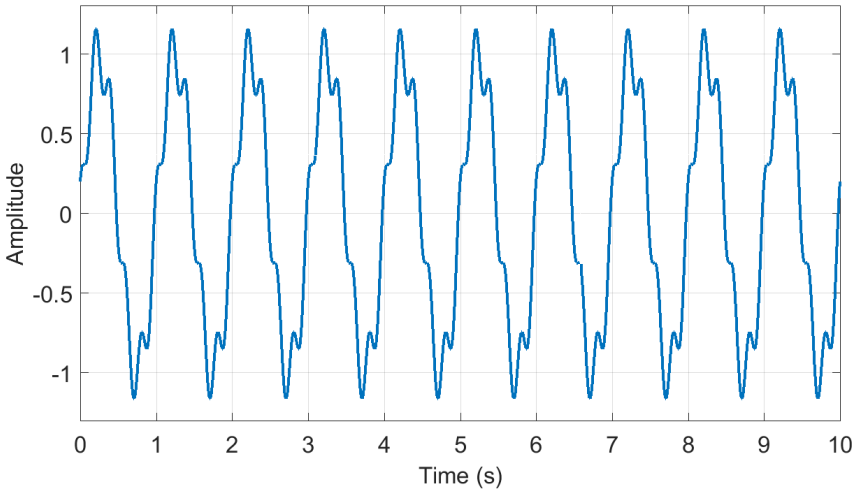

(a) Stationary signal: $y(t) = \sin(2\pi t) + 0.2\cos(10\pi t)$

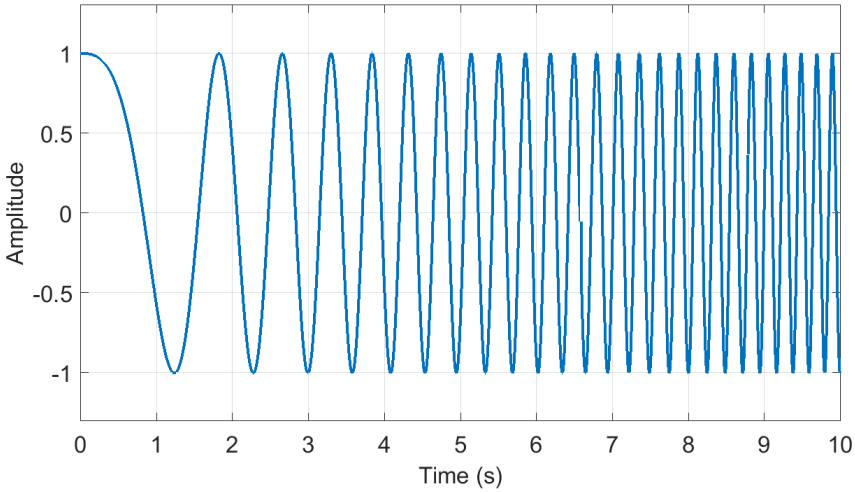

(b) Chirp signal varying between 0.1 Hz and 5 Hz

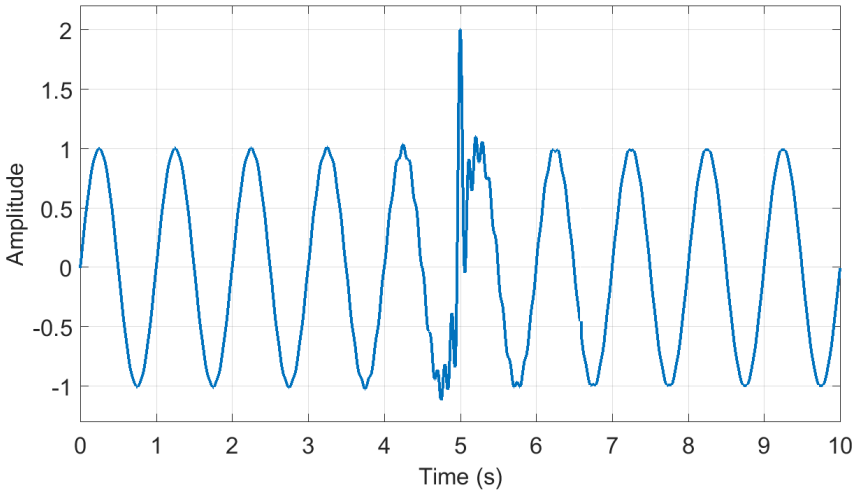

(c) Singular event signal: $y(t) = \sin(2\pi t) + \mathrm{sinc}(2\pi(t-5))$

Figure 2.2: Comparing stationary and non-stationary signals.

originate from systems where the underlying dynamics change with time. For example, intermittent rotor-stator contact is fundamentally non-stationary because the system dynamic models change during impact events. Several non-stationary signals are shown in Fig. 2.2, including a stationary signal for reference. Signal processing tools suitable for stationary and non-stationary analyses are summarized here to motivate later discussion regarding rotordynamic fault signatures.

2.2.1 Stationary Methods

Stationary signal processing methods assume that the same frequencies are represented throughout the signal (i.e., the frequency and amplitude of any given harmonic component are assumed to be constant). The primary signal processing technique for rotordynamic condition monitoring is the fast Fourier transform (FFT), which decomposes a signal into constitutive harmonic components. In rotordynamics, the FFT is typically used to identify harmonics of the shaft speed (1X, 2X etc.). Full-spectrum analysis, developed by Bently-Nevada [69], expands this concept by decomposing each shaft speed harmonic into forward and backward components [69–71]. Full-spectrum analysis can sometimes distinguish faults generating similar frequencies [72–74].

2.2.2 Non-Stationary Methods

Another interpretation is obtained by relaxing the definition of amplitude and frequency. Rather than decomposing a signal into harmonics having constant frequency and amplitude, non-stationary methods decompose a signal into harmonic components whose frequency and amplitude change with time. Non-stationary signals, and the processes that generate them, are then be deciphered by considering how the frequency and amplitude of each component fluctuates with time. These variations are deciphered using the time-frequency-energy spectrum. Several non-stationary signal processing techniques used in rotordynamic analysis are the short-time Fourier transform (STFT), the wavelet transform, and the Hilbert-Huang transform (HHT).

The STFT partitions a signal into overlapping sections and calculates the Fourier transform of each section [75] to study changes in the signal's frequency content. The disadvantage of the STFT is the fundamental compromise between time and frequency resolution. High resolution in the time domain is required to identify when the frequency content changes, whereas high resolution in the frequency domain is desirable to localize specific frequencies. Unfortunately, increasing the frequency resolution decreases the time resolution, and vice versa (i.e., longer partitions are required for greater frequency resolution).

The wavelet transform is another commonly-used non-stationary signal processing tool. The wavelet transform relies on dilated and translated wavelets (i.e., structures with limited time and frequency content) to localize a signal in the time and frequency domains [76]. In general, the wavelet transform has two disadvantages: poor resolution due to energy leakage [77] and a non-adaptive nature [78] (the choice of basis wavelet influences the results). However, a detailed analysis of the wavelet transform is not applicable to this work, and the reader is referred elsewhere for further detail.

The Hilbert-Huang transform (HHT) uses an adaptive algorithm, empirical mode decomposition (EMD), to decompose a signal into a set of nearly-orthogonal components (intrinsic mode functions, or IMFs) [79]. This decomposition conditions each IMF for Hilbert analysis, which is used to determine instantaneous frequency and amplitude. The advantages of this method are its adaptive nature (i.e., the algorithm is not predicated on certain types of signals) and excellent time-frequency resolution. The HHT does suffer from several deficiencies, with the primary issues being mode-mixing and end effects. The problem of mode-mixing is partially rectified by ensemble empirical mode decomposition (EEMD), which adds white noise to the signal before applying EMD, and then averages the IMFs obtained over many trials. This improved method has been used to analyze rotor fault signatures [78, 80]. Other modifications have been suggested to remedy extraneous end effects [78, 81].

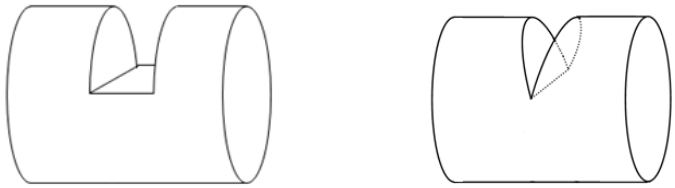

(a) Notch (b) Fatigue crack

Figure 2.3: Comparing a notch and a true fatigue crack.

2.3 Rotor Shaft Cracks

Rotating machines are innately disposed to cyclic bending fatigue stress. Shaft fatigue stress can initiate transverse fatigue cracks when combined with prolonged operation and/or poor design. These transverse shaft cracks represent an uncommon but serious threat to rotating machines and must be detected in an incipient stage to avoid catastrophic failure. In general, rotor cracks are categorized according to how the crack faces behave and how the crack compliance is calculated. The faces of a gaping crack remain open regardless of shaft rotation or loading conditions [82]. On the other hand, the faces of a breathing crack open and close as the crack cross-section varies between tension and compression [83]. It is important to recognize that calculating the crack compliance and expressing the crack breathing behavior are two separate components of crack modeling. In general, most methods for calculating crack compliance are applicable to most methods for determining crack breathing behavior. This section first summarizes common methods for calculating the crack compliance before describing modeling and response characteristics of gaping and breathing cracks.

2.3.1 Crack Compliance

The first step in accurately detecting a crack is precisely modeling the crack compliance. Rotor cracks most fundamentally represent a reduction in rotor stiffness, which is commensurate to an increase in rotor compliance. Thus, the total rotor compliance is found by summing the uncracked rotor compliance and the additional crack

compliance. The most common methods for determining crack compliance are:

1. **Local area moments of inertia**: The crack compliance is calculated using the local area moment of inertia of the crack cross-section [84–90].

2. **Strain energy release rate (SERR)**: Stress intensity factors along the crack edge are used to express the crack strain energy. Castigliano's theorem is then employed to find the local crack compliance [82, 83, 91–93].

3. **Finite element models**: Three dimensional finite element methods are used to obtain crack compliance for general crack shapes [94–97].

Each of these methods for calculating the crack compliance has advantages and disadvantages. The simplest approach is to express the crack compliance using reduced area moments of inertia of the crack cross-section. This method is often used to characterize the compliance of notched shafts where the notch width is finite and measurable [85, 98]. Green and Casey [84] study a globally-asymmetric shaft, and quantify the compliance directly using Euler-Bernoulli beam theory. The analysis is expanded by Varney and Green [85], who use Castligliano's theorem to provide the compliance of an overhung rotor containing a finite-width notch. Al-Shudeifat and Butcher [98] extend the area moment of inertia calculations to find the notch compliance as a function of shaft rotation. Silva and Gomez [99] manufacture a notch of width 0.5 mm using a thin cutting tool in a milling machine, whereas Gomez and Silva [100] compare the compliance of the aforementioned notch to that of a true fatigue crack generated via a three-point bending test. Though convenient, reduced area moments of inertia are invalid for calculating the compliance of a true fatigue crack (see Fig. 2.3).

The most common method for calculating fatigue crack compliance is the SERR. The SERR was first developed by Dimarogonas et al. [82, 101], who emphasize the

appearance of coupled compliances induced by the crack. Dimarogonas and Papadopoulos [92, 102] expand the method to six coupled degrees-of-freedom and apply the result to rotating shafts. A thorough survey of the SERR method is presented by Papadopoulos [83], who summarizes works employing the method, modifications to the method, and avenues for future work.

An alternative method for finding the crack compliance is three-dimensional finite element analysis. One advantage of this approach is that the shape and geometry of the crack can be generalized; Andrieux and Varé [94] develop such a generalized approach and experimentally verify their results versus the global compliance of a cracked rotor. Their results are improved upon by Arem et al. [103, 104], who use the new crack compliances to formulate a novel cracked rotor finite element. Three-dimensional finite element modeling is also used to account for friction at the crack faces during crack closure [95, 97]. Though accurate and applicable to many crack geometries, three-dimensional finite element modeling is time consuming and computationally expensive. In addition, the accuracy gained via such an approach is generally similar to that predicted by the SERR for simple crack geometries [83].

2.3.2 Gaping Cracks

Overview: The faces of a gaping crack always remain open regardless of shaft rotation or loading conditions. This unique situation is usually valid only for finite-width notches or when the rotordynamic response is significantly larger than the static response [92]. In the latter case, the dynamic loads experienced by the crack cross-section tend to open the faces regardless of the shaft's angular position (or, alternatively, can keep the crack entirely closed and essentially undetectable [105]). Gaping cracks are often used as a first step to circumvent complicated crack breathing behavior [85,93,106–110] or to compare with experimental results [84,99,111–113]. Notches are particularly attractive for rotordynamic crack detection experiments because they

are easy to manufacture [3, 114]. For example, Green and Casey [84] manufacture a rectangular notch of width 0.3 mm via electrical discharge machining.

Modeling: The rotor stiffness with a gaping crack is constant in a shaft-fixed reference frame. Consequently, the rotor equations of motion are linear in a shaft-fixed frame, thus permitting the application of conventional modeling approaches and analysis techniques. The transfer matrix method has been used previously to model the steady-state dynamics of a rotor displaying a gaping crack [84, 85, 110, 115–117]. Inagaki [115] uses the transfer matrix to model a rotor that is globally asymmetric. Casey [116] and Green and Casey [84] rearrange the crack compliance matrix obtained via the SERR into an elemental transfer matrix, and use the result to model an overhung rotor. Varney and Green [85, 110] develop a similar transfer matrix for a finite width notch. Another common method for modeling rotor systems with gaping cracks is the finite element method [106, 118–120]. Other researchers include the crack compliance directly in analytic rotor equations of motion [82, 92, 110, 121, 122] or continuous beam theory models [88, 123, 124].

Fault Signatures: The hallmark signature of a rotor containing a gaping crack (or any shaft asymmetry) is the appearance of a 2X shaft speed harmonic in the rotor response when subject to a constant radial load such as gravity. Because the rotor stiffness is constant in a rotating frame, the inertial frame stiffness changes twice per revolution. Thus, a constant inertial force (e.g., gravity) causes the rotor deflection to contain a 2X shaft speed harmonic. The appearance of the 2X harmonic is well-documented and nearly ubiquitous in the literature (for example, see [3, 83, 84, 92, 101, 113–115]). The 2X harmonic induces a sub-critical resonance when the 2X harmonic coincides with a system whirl frequency; this specific sub-critical resonance is denoted the 1/2 critical speed [125]. Green and Casey [84] provide the 1/2 critical speed versus crack depth, and verify the results experimentally in an overhung rotor

test rig. Varney and Green [85] use the 1/2 critical speed to diagnose crack depth and location. Sinou [113] uses the wavelet transform to identify the 1/2 critical speed during transient start-up rotor operation. Another interesting diagnostic signature of a gaping crack is coupling between bending, torsional, and axial modes of vibration [106,117,118,124,126]. In this case, the crack causes vibrations in one mode to appear in another; for example, an axial excitation appears in the lateral rotor vibrations.

2.3.3 Breathing Cracks

Overview: In reality, the faces of a true fatigue crack open and close as the crack cross-section varies between tension and compression [127]. As will be discussed here, this complexity is mirrored in breathing crack models and manifests directly in the rotor response.

Modeling: The stiffness of a rotor containing a breathing crack varies even in a shaft-fixed reference frame. The vast majority of breathing models can be described as either orientation-dependent [86,98,121,128–133] or response-dependent [124,134–137]. Orientation-dependent models only depend on the shaft rotation. This condition is generally met beneath the first rotor critical speed [86], where the bending stress at the crack cross-section is dominated by the static load. Thus, the crack geometry smoothly varies between the fully-opened and fully-closed states. The advantage of modeling an orientation-dependent crack is that the compliance is a known function of shaft rotation, and can be determined before simulating the rotordynamics [83, 87, 90, 97, 134, 138, 139]. Response-dependent crack breathing models assume that the rotordynamic load significantly alters the crack closure. Thus, the crack compliance depends on the rotordynamic response, and must be evaluated at each instant in the numeric simulation (and consequently, the response is nonlinear). Darpe et al. [134] develop the crack-closure line approach, where the instantaneous rotor

loads are used to determine the boundary between the opened and closed crack regions. Another category of crack breathing models is the switching crack, where the crack is either fully-opened or fully-closed [101, 111, 127, 140–142]. The rich dynamic response predicted by this piecewise-smooth nonlinearity is not reflected in reality, where the crack must smoothly vary between the opened and closed states. This conclusion is verified by Patel and Darpe [136], who emphasize the lack of chaotic response in an experimental cracked rotor compared to prediction.

Fault Signatures: A breathing crack causes only integer shaft speed harmonics at pX frequencies that result in $1/p$ sub-critical resonant speeds [111, 127, 134, 140]. These harmonics and their associated critical speeds are excellent crack detection signatures [125, 143, 144]. Bachschmid et al. [145] use a model-based least-squares approach in the frequency domain to diagnose crack depth and location. Saridakis et al. [144] develop an artificial neural network to efficiently compute the crack compliance, and then apply a genetic algorithm to identify the crack location and depth. A stochastic method is developed by Szolc et al. [142] that compares the measured shaft speed harmonics to those calculated from an existing finite element model of the rotor. Their method results in crack depth identification to within 10% of the actual value. Another diagnostic signature is the direction of each shaft speed harmonic (i.e., forward and backward whirl) [73, 74, 146, 147]. Likewise, coupled vibrations between different modes (e.g., lateral and torsional) are also employed to identify breathing shaft cracks [97, 134, 144, 148]. Gasch [140] summarizes many crack breathing signatures and calculates stability using Floquet theory.

A different category of crack signature is obtained from the rotor's transient response. Transient behavior, such as start-up or coast-down responses, are analyzed adeptly using non-stationary signal processing techniques such as wavelets and the Hilbert Huang Transform (HHT). The wavelet transform has been used to monitor transient passage through the sub-critical speeds [109, 113, 148–150]. The

HHT [129, 132] and empirical mode decomposition (EMD) [130, 133, 151] are also used to analyze non-stationary signals from cracked rotors. During transient passage through sub-critical resonances, the HHT identifies crack-induced harmonics with excellent resolution.

2.4 Rotor-Stator Contact

Overview: Another dangerous and expensive rotordynamic fault is rotor-stator contact (i.e., rub). Significant contact forces are generated when the rotating machine components exceed their allowable clearances and contact the stationary components. The nature of rotor-stator contact is fundamentally nonlinear, and specifically, piecewise-smooth [152]. This nonlinearity is cogently described by considering the rotor response to gravity and imbalance when a finite clearance exists between the rotor and stator. Without the clearance, the rotor response is formed as a linear superposition of the synchronous imbalance and the static deflection caused by gravity. A finite clearance, however, could impede this superposition and result in an entirely different response altogether (Varney and Green [153] provide a quantitative method for assessing the importance of gravity in rotor-stator contact situations). The strongly nonlinear nature of rotor-stator contact underscores the importance of accurate contact models. This section summarizes several such contact models along with common rotor-stator contact phenomena.

Modeling: A variety of rotor-stator rub models have been developed to simulate observed contact phenomena. The simplest treatment regards the phenomena as a truncated synchronous response [49, 154]. Though intuitive, the truncation model is incapable of capturing important nonlinear contact phenomena such as intermittent contact and quasiperiodic and/or chaotic responses. To remedy the lack of a true rotordynamic rub model, Beatty [154] introduces the linear-elastic contact model (LECM). Once the rotor exceeds the prescribed clearance, a normal restoring force

is generated at the interface; this force is proportional to the rotor-stator interference by a linear contact stiffness. Most investigations of rotor-stator rub employ some variation of the LECM [155–167], though other rub models have occasionally been considered [168]. Various complications have been incorporated in the LECM, such as torsional degrees of freedom [158,169], stator inertia [164,170–172], nonlinear Hertzian contact forces [173,174], contact damping [170,173], and nonlinear fluid film forces [164, 172, 175]. Smyth, Varney, and Green [176] investigate the influence of a viscoelastically supported stator on the nonlinear rub dynamics, using a fractional calculus approach to model the stator support structure.

Any realistic contact model should precisely emulate the contact physics. In general, a vast majority of simulations still use the LECM to model rotor-stator rub. Yet, the model assumes linear rotor-stator contact using a constant contact stiffness. This contact stiffness is often chosen arbitrarily and in a manner entirely disjointed from the contact physics. Second, the model assumes contact occurs only at the single point of maximum interference. However, it is intuitive to expect a wide circumferential contact arc for strongly conformal curved surfaces with small clearances. Significant advances could be imbued by developing a novel rotor-stator rub model founded on the actual physics of contact. Furthermore, a vast majority of simulations still use a simple Jeffcott rotor in their simulations (though a handful of investigations consider an overhung rotor [161, 177, 178]). The actual system under investigation should be the one considered, and especially when the contact phenomena occur in associated triboelements (e.g., sealing components).

Fault Signatures: The hallmark signature of rotor-stator rub is strongly nonlinear behavior, such as periodic, quasiperiodic, and chaotic responses [153, 175]. As the system parameters are varied, the response bifurcates from one response to another. Bifurcation studies on various system parameters have been performed using shaft speed, imbalance, damping ratio, and friction coefficient as control parameters, and

the results indicate many routes to chaos such as period doubling [153, 163, 170, 175], intermittency [175], quasiperiodicity [175], and direct transition to chaos [153].

Various studies show the possibility of using these strongly nonlinear phenomena to diagnose rub. Yu [179] provides several case studies of real turbomachines experiencing rub, emphasizing the use of shaft speed harmonics and backward whirl to detect rub. Sawicki et al. [157] discuss the use of chaos mapping for rub diagnostics. Rub is also analyzed using full spectrum analysis, which separates each harmonic into its constitutive forward and backward components [69, 71–73, 179]. A powerful approach to rub diagnostics is temporally localizing the phenomena using nonstationary signal processing techniques such as reassigned scalograms, wavelets, and the Hilbert-Huang Transform [162, 180–182]. Abu-Mahfouz and Banerjee [167] identify rotor-stator rub by applying three evolutionary algorithms to the rotor response (particle swarm optimization, differential evolution, and the firefly algorithm).

2.5 Multiple Fault Diagnostics

A need exists to simultaneously detect coexisting faults, because one fault can easily precipitate another. Nonlinearity complicates the issue by precluding superposition; if multiple fault detection is desired, the faults must be considered commensurately. This conclusion is supported by previous investigations. Several authors investigate a cracked rotor with coexisting rotor-stator rub [72, 183, 184] using full spectrum analysis, the wavelet transform, and the HHT. When the faults coexist, the response deviates significantly from that of either fault individually. Huang et al. [185] investigate coexisting misalignment and rotor-stator rub, concluding that the system is complex. Shen et al. [186] investigate rub and rotor bow, demonstrating that with both faults, chaotic behavior is encountered earlier and more often. Similar conclusions are drawn for other combinations, including shaft cracks with rotor bow [146, 187] and shaft cracks with misalignment [73]. Xiang et al. [89] consider an open crack

and lateral contact in the presence of fluid film forces, and generally conclude that the multiple fault scenario is different than either individual fault response. Other works have been marginally successful regarding multiple fault detection. Prabhakar et al. [188] analyze the transient response using the wavelet transform to distinguish misalignment from a crack, with the primary dynamic signature being the subharmonic resonant wavelet coefficients. Patel et al. [74] experimentally compare rotor-stator rub, a breathing crack, and misalignment using full-spectrum analysis at several sub-critical resonance shaft speeds, though the faults are not considered to be coexisting. Markert [189] uses model-based regression to distinguish rub from imbalance. Chen [187] performs a multi-tiered analysis to distinguish rotor bow from a shaft crack, using statistical regression and model simulation. The work by Patel et al. [73] uses steady-state vibration with full spectrum analysis to separate a crack from misalignment. The diagnostic procedure relies on tracking crack growth using changes in the forward components of the 1X and 2X; such an approach is unrealistic considering the lack of rotordynamic crack prognostics.

2.6 Conclusions

Several shortcomings are observed in the previous literature review:

1. Seal performance in real rotordynamic systems is poorly understood. A new seal model is required that treats the seal as constitutive to the rotor.

2. Current rotor-stator contact models are heuristic and insufficient.

3. Multiple fault vibration signatures are poorly understood in complex rotor systems (i.e., coupled rotor-seal systems).

This work seeks to remedy these shortcomings by accomplishing the objectives presented in Chapter 1.

CHAPTER III

SEAL EQUATIONS OF MOTION

Non-contacting mechanical face seals are flexibly-mounted in an effort to minimize relative misalignment between the faces. The relative misalignment depends fundamentally on the seal dynamics, and thus, comprehensive seal dynamic models are required to understand seal behavior, performance, and design. The particular seal configuration considered here is shown in Fig. 3.1, where the primary components of the apparatus are the stationary seal element, the rotating seal element, and the flexible shaft and attached disk (i.e., the rotor). The seal elements are flexibly-mounted using axial springs and circumferential elastomeric O-rings. Rotation of the stationary element about the centerline is constrained using an anti-rotation lock [19]. The seal used here is assumed to be outward-pressurized, i.e., the outer reservoir pressure P_o is greater than the inner reservoir pressure P_i.

A mechanical face seal is one component of a much larger turbomachine, and understanding how the seal interacts with the larger system is important for quantifying seal performance and improving the seal design. Towards this end, the equations of motion for the stationary and rotating seal elements are developed here, including angular, axial, and eccentric degrees of freedom. In addition, the model also includes fluid film forces, contact reactions, misalignments, thermoelastic deformation, and coupled rotordynamics (i.e., interactions with the larger turbomachine). Furthermore, mechanical face seals are often employed on high-performance aircraft engines that experience significant maneuver loads. These maneuver loads are included in the equations of motion developed herein.

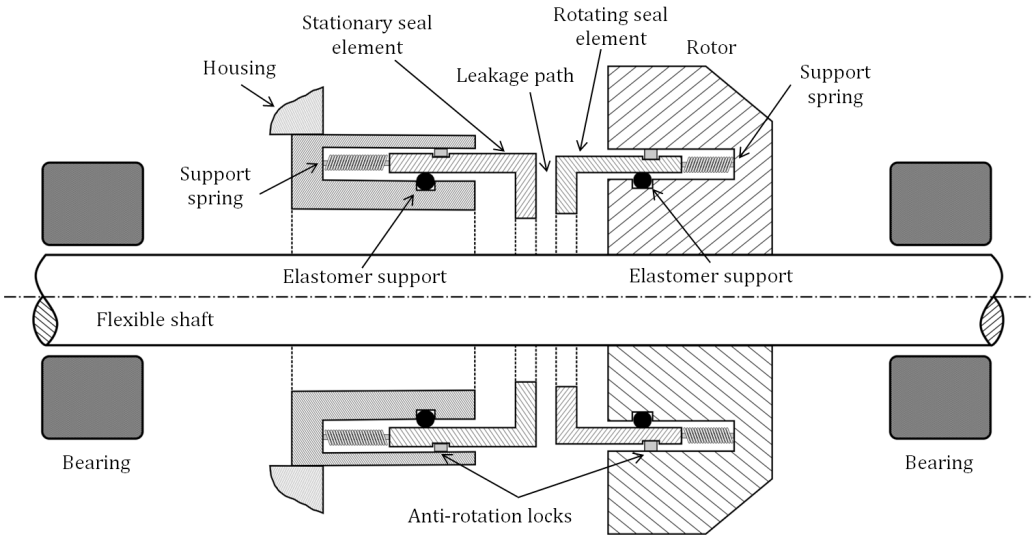

Figure 3.1: FMSR seal showing the coupled external rotor (i.e., the flexible shaft and accompanying disk).

3.1 Seal Element Degrees-of-Freedom

The stationary and rotating seal elements are permitted to translate axially, deflect laterally (i.e., eccentrically), and rotate about axes orthogonal to the axis of rotation. Torsional deflections are not considered in this work because the positive-drive devices employed in the seal constrain torsional rotations. Thus, the dynamics of each seal element are described using five degrees-of-freedom, and the entire seal apparatus (i.e., the FMSR seal) constitutes a ten degree-of-freedom dynamic system. Here, the symbols u, ϵ, and γ are used to denote axial deflection, eccentric deflection, and tilt, respectively. The first subscript on each degree-of-freedom signifies the seal element: 'r' for the rotating element and 's' for the stationary element (later, the coupled rotordynamics will be distinguished with the subscript 'R'). The second subscript signifies direction. The degrees-of-freedom in vector form, including time-dependent thermal coning $\beta(t)$, are:

$$\{q\} = \{\gamma_{s\xi} \;\; \gamma_{s\eta} \;\; u_{sz} \;\; \epsilon_{s\xi} \;\; \epsilon_{s\eta} \;\; : \;\; \gamma_{r\xi} \;\; \gamma_{r\xi} \;\; u_{rz} \;\; \epsilon_{r\xi} \;\; \epsilon_{r\eta} \;\; : \;\; \beta\}^T \tag{3.1}$$

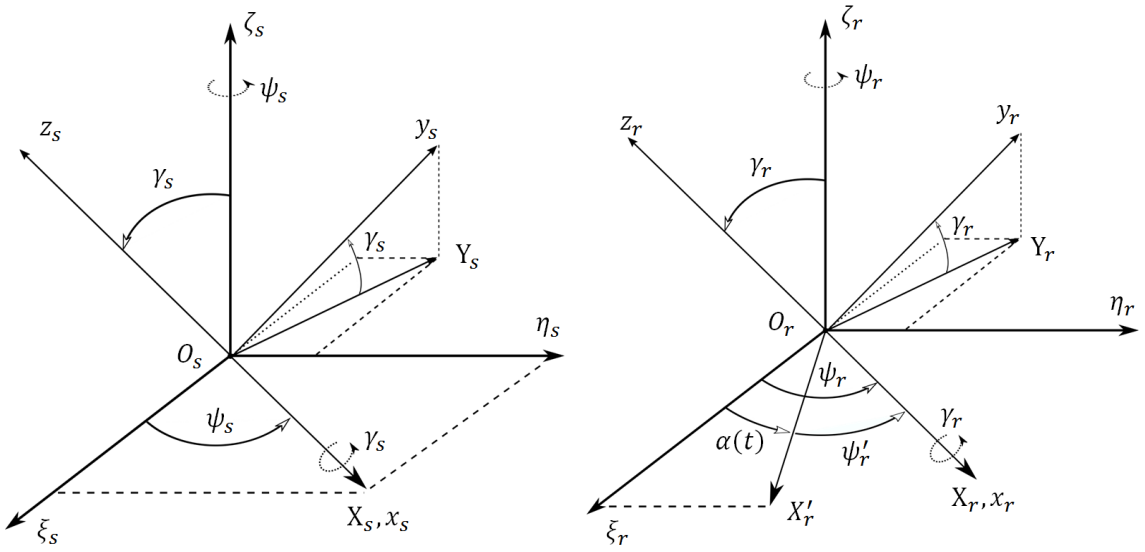

(a) Flexibly-mounted stationary seal element. (b) Flexibly-mounted rotating seal element.

Figure 3.2: Reference frames describing the angular kinematics of the FMSR seal.

This vector can be expanded to include any number of rotor degrees-of-freedom, if the seal dynamics are to be solved commensurately to the rotordynamics. As will be seen, the seal elements are fundamentally coupled by a thin fluid film (and possibly contact) between the seal faces. In addition, the rotating seal element dynamics are inextricably coupled to those of the rotor for practical seal/rotor systems (though the converse depends on the relationship between the seal and rotor inertia).

3.2 Reference Frames

A necessary prerequisite for understanding the system kinematics and dynamics is understanding the reference frames used to describe the dynamics of each seal element. The reference frames are shown graphically in Fig. 3.2 for both seal elements. The reference frames of interest here are:

1. $\xi\eta\zeta$: A system-fixed (e.g., turbomachine-fixed) reference frame attached to the concentric undeflected location of the rotating seal element geometric center, O_r (the stationary element geometric center O_s is axially separated from O_r

by the fixed nominal clearance C_o). The acceleration of this point is $\bar{a}_O$, and the frame rotates with angular velocity $\bar{\lambda}_0$. The acceleration $\bar{a}_O$ and rotation rate $\bar{\lambda}_0$ constitute the inertial maneuver of the overall structure. This frame is inertial if system maneuver is neglected.

2. $\xi_s\eta_s\zeta_s$: A system-fixed reference frame attached to the stationary seal element geometric center, C_s. This frame also experiences the maneuver loads caused by $\bar{a}_O$ and $\bar{\lambda}_0$.

3. $X_sY_sZ_s$: This frame is precessed about ζ_s by the precession ψ_s. X_s defines the axis about which the stationary seal element nutates (i.e., tilts).

4. $x_sy_sz_s$: This principal frame is nutated about X_s by γ_s.

5. $\xi_r\eta_r\zeta_r$: A system-fixed reference frame attached to the rotating seal element geometric center, C_r. This frame also experiences the maneuver loads caused by $\bar{a}_O$ and $\bar{\lambda}_0$. The axis ζ_r defines the direction of shaft rotation.

6. $X_r'Y_r'Z_r'$: This frame is precessed about ζ_r by the shaft rotation angle $\alpha(t)$, which is related to the shaft speed ω_r:

$$\alpha(t) = \int_0^t \omega_r(t)dt \tag{3.2}$$

7. $X_rY_rZ_r$: This frame is precessed about ζ_r by the absolute seal seat precession ψ_r, or alternatively, precessed about Z_r' by the relative seal seat precession ψ' (i.e., $\psi_r = \alpha(t) + \psi'$).

8. $x_ry_rz_r$: This frame is nutated about X_r by γ_r.

9. $1_r2_r3_r$: This body-fixed, but not necessarily principal, frame is obtained by applying spin ϕ about z_r. The spin ϕ is related to the relative precession ψ' by $\dot{\phi} = -\dot{\psi}'$ [19, 20].

10. $x_r^p y_r^p z_r^p$: This frame is rotated about 1_r by the dynamic angular misalignment χ, and represents a body-fixed set of principal axes for the rotating seal element. The dynamic angular misalignment χ defines the angle between the body-fixed spinning reference frame $(123)_r$ and the principal frame.

3.2.1 Inertial Maneuver Profile

The overall system (e.g., turbojet or turbofan engine) accelerates at $\bar{a}_O$ and rotates at $\bar{\lambda}_0$. In component form, the system acceleration is:

$$\bar{a}_O = a_{O\xi}\hat{e}_\xi + a_{O\eta}\hat{e}_\eta + a_{O\zeta}\hat{e}_\zeta \tag{3.3}$$

The system can also experience rotations in addition to translations. The components of the maneuver rotation relative to $\xi\eta\zeta$ are referred to here as pitch, yaw, and roll, respectively. The maneuver angular velocity $\bar{\lambda}_0$ is then written in the following form:

$$\bar{\lambda}_0 = \lambda_p\hat{e}_\xi + \lambda_y\hat{e}_\eta + \lambda_{ro}\hat{e}_\zeta \tag{3.4}$$

where the magnitudes of the pitch, yaw, and roll angular velocities are λ_p, λ_y, and λ_{ro}, respectively, and are functions of time which also may depend on the orientation of the overall structure. To remain consistent with previous seal dynamics literature (e.g., [19]), Eq. 3.4 is transformed into the rotating $x_r y_r z_r$ frame:

$$\begin{aligned}\bar{\lambda}_0 = {} & \big(\lambda_p\cos\psi_r + \lambda_y\sin\psi_r\big)\hat{e}_{x_r} + \big(\gamma_r\lambda_{ro} + \lambda_y\cos\psi_r - \lambda_p\sin\psi_r\big)\hat{e}_{y_r} \\ & + \big(\lambda_{ro} - \gamma_r\lambda_y\cos\psi_r + \lambda_p\sin\psi_r\big)\hat{e}_{z_r}\end{aligned} \tag{3.5}$$

3.3 Kinematic Analysis

A thorough kinematic description of the positions, velocities, and angular velocities of both elements is required to derive the forces acting on the bodies and the equations of motion. The analysis is separated into angular and eccentric components, and uses the reference frames described in Section 3.2.

3.3.1 Angular Kinematics

Non-contacting mechanical face seals can typically only tolerate several milliradians of misalignment before undesirable contact occurs. Consequently, the angular kinematics are simplified by describing the tilt of each element in vector form:

$$\bar{\gamma}_s = \gamma_{s\xi}\hat{e}_\xi + \gamma_{s\eta}\hat{e}_\eta \tag{3.6}$$

$$\bar{\gamma}_r = \gamma_{r\xi}\hat{e}_\xi + \gamma_{r\eta}\hat{e}_\eta \tag{3.7}$$

The absolute angular velocity of each body has been derived in detail in several other works [19, 20, 47, 51]. For brevity, the results of those works are used here without derivation, and the reader is referred to any of the previous references for further detail. Without including inertial maneuver rotation, the absolute angular velocity of the rotating seal element in the rotating $(xyz)_r$ frame is

$$\bar{\lambda}_r = \dot{\gamma}_r\hat{e}_{x_r} + \dot{\psi}_r \sin\gamma_r\hat{e}_{y_r} + \big[\dot{\psi}_r\big(\cos\gamma_r - 1\big) + \omega_r\big]\hat{e}_{z_r} \tag{3.8}$$

The total angular velocity, including inertial maneuver loads, is found by summing Eqs. 3.5 and 3.8:

$$\begin{aligned}\bar{\lambda}_r = \big(\dot{\gamma}_r + \lambda_p\cos\psi_r + \lambda_y\sin\psi_r\big)\hat{e}_{x_r} + \big(\dot{\psi}_r\sin\gamma_r + \gamma_r\lambda_{ro} + \lambda_y\cos\psi_r - \lambda_p\sin\psi_r\big)\hat{e}_{y_r} + \\ \big[\dot{\psi}_r\big(\cos\gamma_r - 1\big) + \omega_r + \lambda_{ro} - \gamma_r\lambda_y\cos\psi_r + \lambda_p\sin\psi_r\big]\hat{e}_{z_r}\end{aligned} \tag{3.9}$$

The dynamic moments will depend on the time rate-of-change of $\bar{\lambda}_r$ within the $x_r y_r z_r$ frame:

$$\begin{aligned}\frac{\partial\bar{\lambda}_r}{\partial t} &= \big[\ddot{\gamma}_r + \dot{\lambda}_p\cos\psi_r - \lambda_p\dot{\psi}_r\sin\psi_r + \dot{\lambda}_y\sin\psi_r + \lambda_y\dot{\psi}_r\cos\psi_r\big]\hat{e}_{x_r} \\ &+ \big[\ddot{\psi}_r\sin\gamma_r + \dot{\psi}_r\dot{\gamma}_r\cos\gamma_r + \dot{\gamma}_r\lambda_{ro} + \gamma_r\dot{\lambda}_{ro} + \dot{\lambda}_y\cos\psi_r - \lambda_y\dot{\psi}_r\sin\psi_r \\ &- \dot{\lambda}_p\sin\psi_r - \lambda_p\dot{\psi}_r\cos\psi_r\big]\hat{e}_{y_r} + \big[\ddot{\psi}_r\big(\cos\gamma_r - 1\big) - \dot{\psi}_r\dot{\gamma}_r\sin\gamma_r + \dot{\omega}_r \\ &+ \dot{\lambda}_{ro} - \dot{\gamma}_r\lambda_y\cos\psi_r - \gamma_r\dot{\lambda}_y\cos\psi_r + \gamma_r\lambda_y\dot{\psi}_r\sin\psi_r + \dot{\lambda}_p\sin\psi_r + \lambda_p\dot{\psi}_r\cos\psi_r\big]\hat{e}_{z_r}\end{aligned} \tag{3.10}$$

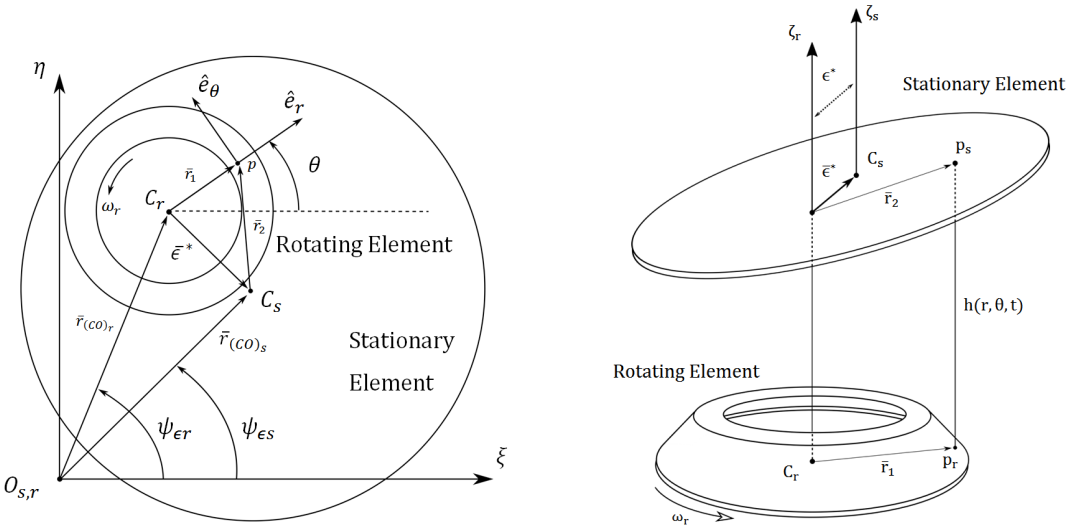

(a) Planar kinematics of seal eccentricity

(b) Film thickness at a corresponding point on each surface

Figure 3.3: Eccentric deflections of the stationary and rotating seal elements.

3.3.2 Eccentric Kinematics

Both seal elements are permitted to deflect laterally (i.e., eccentrically). To remain consistent with prior seal dynamics nomenclature, these lateral deflections will be referred to as eccentricities (not to be confused with lateral imbalance of the center of mass). The eccentric kinematic analysis is performed in the system-fixed $\xi\eta\zeta$ frame because (a) condition monitoring systems usually measure inertial dynamics, and (b) the contact reactions will be easier to intuit in the system-fixed frame. The consequence of choosing a system-fixed versus rotating frame is somewhat arbitrary, since other phenomena (e.g., shaft cracks) are easier to understand in a shaft-fixed rotating frame. Nevertheless, a choice must be made, and the system-fixed frame will be employed herein.

The eccentric kinematics for the stationary and rotating seal elements are shown in Fig. 3.3a. The geometric centers of the stationary and rotating seal elements are denoted C_s and C_r, respectively. The undeflected geometric centers of both elements lie at O_s and O_r along the shaft rotation axis; in this work, these points are assumed

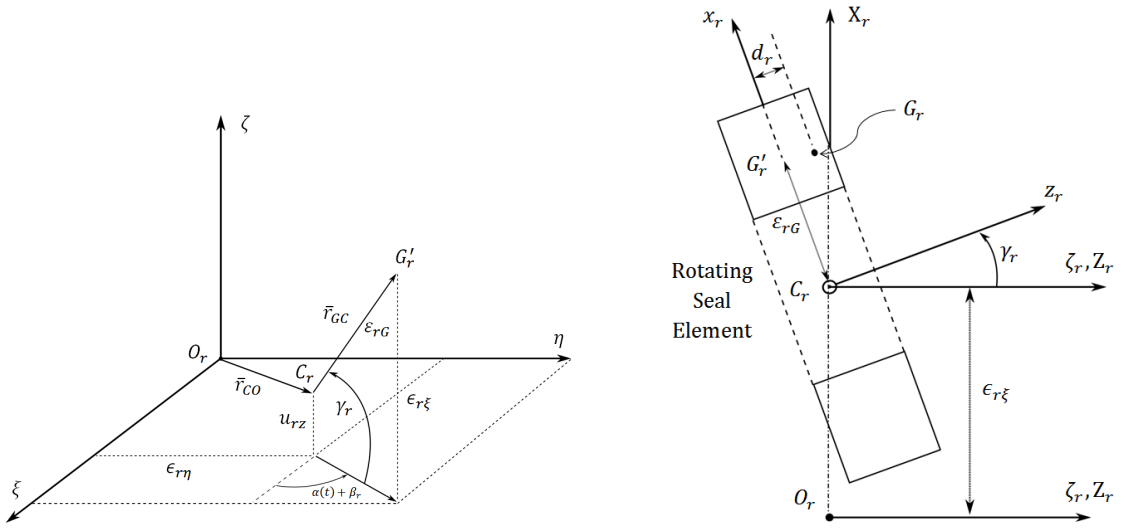

(a) Position analysis of the rotating seal element eccentricities and tilts (d_r not shown for brevity)

(b) Imbalance and offset in the rotating seal element

Figure 3.4: Quantities used to determine the dynamic forces and moments caused by seal eccentricity.

to be co-linear. The eccentric deflection of element j in the i^{th} direction is labeled ϵ_{ji}. Using the inertial $\xi\eta\zeta$ frame, the planar position vectors locating the center of each element with respect to $O_{r,s}$ are

$$\bar{r}_{(CO)_s} = \epsilon_{s\xi}\hat{e}_\xi + \epsilon_{s\eta}\hat{e}_\eta \tag{3.11}$$

$$\bar{r}_{(CO)_r} = \epsilon_{r\xi}\hat{e}_\xi + \epsilon_{r\eta}\hat{e}_\eta \tag{3.12}$$

As will be seen, friction forces and fluid shear forces depend on the relative eccentricity between the elements and the relative eccentric velocity. From Fig. 3.3a, the relative eccentricity vector is

$$\bar{\epsilon}^* = \bar{r}_{(CO)_s} - \bar{r}_{(CO)_r} \tag{3.13}$$

The dynamic forces are functions of the acceleration of each element's center of mass. This work assumes that the stationary seal element is eccentrically balanced; that is, $C_s = G_s$; consequently, the acceleration of the stationary element center of mass relative to C_s is found by differentiating Eq. 3.11:

$$\bar{a}_{G_s} = \bar{a}_{C_s} = \bar{a}_o + \frac{\partial^2 \bar{r}_{(CO)_s}}{\partial t^2} + \dot{\bar{\lambda}}_0 \times \bar{r}_{(CO)_s} + \bar{\lambda}_0 \times \bar{\lambda}_0 \times \bar{r}_{(CO)_s} + 2\bar{\lambda}_0 \times \frac{\partial \bar{r}_{(CO)_s}}{\partial t} \tag{3.14}$$

where $\bar{\lambda}_0$ is the maneuver rotation of the system, and thus, the system-fixed frame rotation rate.

Expressing the rotating seal element center of mass acceleration is complicated by imbalance, axial offset, and shaft rotation; these parameters are shown in Figs. 3.4a and 3.4b. The center of mass G_r is laterally offset from C_r by the eccentric imbalance ε_{rG}, occurring at an angle β_r from the body-fixed spin axis 1_r. Furthermore, G_r is axially offset from C_r by the distance d_r. The following position vector locates the center of mass relative to the geometric center using the body-fixed stationary seal element spin axes $(xyz)_r^p$

$$\bar{r}_{(CG)_r} = \varepsilon_{rG}\cos\beta_r\hat{e}_{x_r^p} + \varepsilon_{rG}\sin\beta_r\hat{e}_{y_r^p} + d_r\hat{e}_{z_r^p} \tag{3.15}$$

where β_r is the static phase angle locating G_r in the $x_r^p y_r^p$ plane (referenced from x_r^p). The body-fixed frame is convenient to use because the imbalance and offset are body-fixed quantities. The position vectors $\bar{r}_{(CG)_r}$ and $\bar{r}_{(CO)_r}$ must be written relative to the same frame before calculating the acceleration of G_r:

$$\bar{r}_{(CG)_r}|^{\xi\eta\zeta} = [R_r]^T\bar{r}_{(CG)_r}|^{(xyz)_r^p} \tag{3.16}$$

where

$$[R_r] = \begin{bmatrix} \cos\big(\alpha(t)+\beta_r\big) & \sin\big(\alpha(t)+\beta_r\big) & \gamma_r\sin\big(\alpha(t)+\beta_r-\psi_r\big) \\ -\sin\big(\alpha(t)+\beta_r\big) & \cos\big(\alpha(t)+\beta_r\big) & \gamma_r\cos\big(\alpha(t)+\beta_r-\psi_r\big) \\ \gamma_r\sin\psi_r & -\gamma_r\cos\psi_r & 1 \end{bmatrix} \tag{3.17}$$

The total position vector locating G_r to the reference point O_r is found by summing Eqs. 3.12 and 3.16:

$$\begin{aligned}\bar{r}_{(OG)_r} = \big[\epsilon_{r\xi} + \varepsilon_{rG}\cos(\alpha(t)+\beta_r) + d_r\gamma_{r\eta}\big]\hat{e}_\xi + \big[\epsilon_{r\eta} + \varepsilon_{rG}\sin(\alpha(t)+\beta_r) - d_r\gamma_{r\xi}\big]\hat{e}_\eta \\ + \big[u_{rz} + d_r + \varepsilon_{rG}\gamma_r\sin(\alpha(t)+\beta_r-\psi_r)\big]\hat{e}_\zeta\end{aligned} \tag{3.18}$$

The absolute acceleration of G_r is evaluated by recognizing that the center of mass G_r translates within a rotating reference frame $(\xi\eta\zeta)$, where the angular velocity and

acceleration of the frame are provided in Section 3.2. Accounting for the acceleration of point O and the rotation of $\xi\eta\zeta$ yields the absolute acceleration of the rotating seal element center of mass:

$$\bar{a}_{G_r} = \bar{a}_O + \frac{\partial^2 \bar{r}_{(OG)_r}}{\partial t^2} + \dot{\bar{\lambda}}_0 \times \bar{r}_{(OG)_r} + \bar{\lambda}_0 \times \bar{\lambda}_0 \times \bar{r}_{(OG)_r} + 2\bar{\lambda}_0 \times \frac{\partial \bar{r}_{(OG)_r}}{\partial t} \tag{3.19}$$

where the partial derivatives signify velocities and accelerations of G_r within the reference frame. Expanding this expression elucidates terms resulting from relative acceleration, maneuver acceleration, centripetal effects, and Coriolis acceleration. Several simplifying assumptions are made for brevity in presenting the expanded results. First, centripetal accelerations resulting from $\bar{\lambda}_0$ are neglected because their overall influence is small compared to centripetal terms resulting from ω_r (that is, $|\bar{\lambda}_0| << \omega_r$). Second, any terms resulting in triple products of the imbalance, maneuver rotation components, or the degrees of freedom are neglected since these terms are at most second-order. The simplified acceleration is then:

$$\begin{aligned}
\bar{a}_{G_r} = &\Big[a_{O\xi} + \ddot{\epsilon}_{r\xi} - \varepsilon_{rG}\big[\omega_r^2 \cos(\alpha+\beta_r) + \dot{\omega}_r \sin(\alpha+\beta_r)\big] + d_r\ddot{\gamma}_{r\eta} + 2\lambda_y\dot{u}_{rz} \\
&\quad - 2\lambda_{ro}\big(\dot{\epsilon}_{r\eta} + \varepsilon_{rG}\omega_r\cos(\alpha+\beta_r)\big) + 2\lambda_y\dot{u}_{rz} + \dot{\lambda}_y d_r - \dot{\lambda}_{ro}\varepsilon_{rG}\sin(\alpha+\beta_r)\Big]\hat{e}_\xi \\
&+\Big[a_{O\eta} + \ddot{\epsilon}_{r\eta} - \varepsilon_{rG}\big[\omega_r^2 \sin(\alpha+\beta_r) - \dot{\omega}_r \cos(\alpha+\beta_r)\big] - d_r\ddot{\gamma}_{r\xi} - 2\lambda_p\dot{u}_{rz} \\
&\quad + 2\lambda_{ro}\big(\dot{\epsilon}_{r\xi} - \varepsilon_{rG}\omega_r\sin(\alpha+\beta_r)\big) - 2\lambda_p\dot{u}_{rz} - \dot{\lambda}_p d_r + \dot{\lambda}_{ro}\varepsilon_{rG}\cos(\alpha+\beta_r)\Big]\hat{e}_\eta \\
&+\Big[a_{O\zeta} + \ddot{u}_{rz} + \lambda_p\big(\dot{\epsilon}_{r\eta} + \varepsilon_{rG}\omega_r\cos(\alpha+\beta_r)\big) + \lambda_y\big(\varepsilon_{rG}\omega_r\cos(\alpha+\beta_r) - \dot{\epsilon}_{r\eta}\big) \\
&\quad + \dot{\lambda}_p\varepsilon_{rG}\sin(\alpha+\beta_r) - \dot{\lambda}_y\varepsilon_{rG}\cos(\alpha+\beta_r)\Big]\hat{e}_\zeta
\end{aligned} \tag{3.20}$$

The acceleration simplifies considerably if inertial maneuver rotations are neglected. Likewise, expanding Eq. 3.14 provides the acceleration of the stationary seal element:

$$\begin{aligned}
\bar{a}_{G_s} = &\Big(a_{O\xi} + \ddot{\epsilon}_{s\xi} - 2\lambda_{ro}\dot{\epsilon}_{s\eta} + 2\lambda_y\dot{u}_{sz}\Big)\hat{e}_\xi + \Big(a_{O\eta} + \ddot{\epsilon}_{s\eta} + 2\lambda_{ro}\dot{\epsilon}_{s\xi} - 2\lambda_p\dot{u}_{sz}\Big)\hat{e}_\eta \\
&+ \Big(a_{O\zeta} + \ddot{u}_{sz} + 2\lambda_p\dot{\epsilon}_{s\eta} - 2\lambda_y\dot{\epsilon}_{s\eta}\Big)\hat{e}_\zeta
\end{aligned} \tag{3.21}$$

This work assumes that the stationary element is balanced (i.e., the center of mass aligns identically with C_s), though this restriction could be removed in future works.

3.3.3 Seal Element Surface Velocities

Fluid pressures exist at every point p within the sealing dam, and contact pressures are generated if the relative clearance and surface roughness dimension are comparable in magnitude. The locations on the seal elements commensurate with point p in the sealing dam are denoted p_s and p_r for the stationary and rotating seal elements. The position and velocity of these points must be found to determine the fluid and contact pressures. For consistent comparison, these quantities must be described using the same coordinate system. The maneuver velocities act with parity on both seal elements, and therefore, do not affect the fluid pressure or shear forces. Furthermore, this work assumes that the rotating element is always contained entirely within the bounds of the stationary element (see Fig. 3.3a).

The geometry of the sealing apparatus lends itself naturally to a polar coordinate description; here, a polar coordinate system (r, θ) will be used referenced relative to the rotating seal element's center. The unit vectors defining the $\xi\eta$ and $r\theta$ frames are related by the following rotation transformation:

$$\begin{Bmatrix} \hat{e}_\xi \\ \hat{e}_\eta \\ \hat{e}_\zeta \end{Bmatrix} = \begin{bmatrix} \cos\theta & -\sin\theta & 0 \\ \sin\theta & \cos\theta & 0 \\ 0 & 0 & 1 \end{bmatrix} \begin{Bmatrix} \hat{e}_r \\ \hat{e}_\theta \\ \hat{e}_\zeta \end{Bmatrix} \tag{3.22}$$

The points p_r and p_s are located relative to the rotating and stationary seal element geometric centers by the vectors $\bar{r}_1$ and $\bar{r}_2$, respectively, as shown in Fig. 3.3a. In the

polar coordinate frame, these vectors are:

$$\bar{r}_1 = r\hat{e}_r \tag{3.23}$$

$$\begin{aligned}\bar{r}_2 &= \bar{r}_1 - \bar{\epsilon}^* \\ &= \Big[r + (\epsilon_{r\xi} - \epsilon_{s\xi})\cos\theta + (\epsilon_{r\eta} - \epsilon_{s\eta})\sin\theta\Big]\hat{e}_r \\ &\qquad + \Big[(\epsilon_{r\eta} - \epsilon_{s\eta})\cos\theta - (\epsilon_{r\xi} - \epsilon_{s\xi})\sin\theta\Big]\hat{e}_\theta\end{aligned} \tag{3.24}$$

Every point p_s on the stationary element has the same velocity in the $\xi\eta$ frame because the element does not rotate about ζ. The velocity $\bar{V}_{ps}$ is then always equal to the velocity of point C_s:

$$\begin{aligned}\bar{V}_{ps} &= \dot{\epsilon}_{s\xi}\hat{e}_\xi + \dot{\epsilon}_{s\eta}\hat{e}_\eta \\ &= (\dot{\epsilon}_{s\xi}\cos\theta + \dot{\epsilon}_{s\eta}\sin\theta)\hat{e}_r + (\dot{\epsilon}_{s\eta}\cos\theta - \dot{\epsilon}_{s\xi}\sin\theta)\hat{e}_\theta\end{aligned} \tag{3.25}$$

The velocity of every point p_r on the rotating element accrues an additional contribution from the element's rotation ω_r:

$$\begin{aligned}\bar{V}_{pr} &= \dot{\epsilon}_{r\xi}\hat{e}_\xi + \dot{\epsilon}_{r\eta}\hat{e}_\eta + \bar{\omega}_r \times \bar{r}_1 \\ &= (\dot{\epsilon}_{r\xi}\cos\theta + \dot{\epsilon}_{r\eta}\sin\theta)\hat{e}_r + (r\omega_r + \dot{\epsilon}_{r\eta}\cos\theta - \dot{\epsilon}_{r\xi}\sin\theta)\hat{e}_\theta\end{aligned} \tag{3.26}$$

As discussed in Appendix A, the fluid pressure depends on the relative radial and tangential velocities between points p_s and p_r. To avoid a confusion in nomenclature, the fluid pressure equations label the rotating and stationary seal elements as elements 1 and 2, respectively. Using this notation, the component velocities are:

$$V_{1r} = \dot{\epsilon}_{r\xi}\cos\theta + \dot{\epsilon}_{r\eta}\sin\theta \tag{3.27}$$

$$V_{2r} = \dot{\epsilon}_{s\xi}\cos\theta + \dot{\epsilon}_{s\eta}\sin\theta \tag{3.28}$$

$$V_{1\theta} = r\omega_r + \dot{\epsilon}_{r\eta}\cos\theta - \dot{\epsilon}_{r\xi}\sin\theta \tag{3.29}$$

$$V_{2\theta} = \dot{\epsilon}_{s\eta}\cos\theta - \dot{\epsilon}_{s\xi}\sin\theta \tag{3.30}$$

3.4 Applied Fluid and Contact Forces

The seal element dynamics are inextricably coupled by fluid and contact forces that exist within the sealing dam. These forces depend on the complex interactions between fluid pressures, fluid shear, surface roughness, and friction, all of which are influenced strongly by the system dynamics (as described using the kinematic expressions provided in earlier sections). The requisite relationship required for deriving the fluid and contact forces is the clearance between the seal elements (i.e., the fluid film thickness), which is discussed first. The fluid and contact forces are then derived as a function of the clearance.

3.4.1 Fluid Film Clearance

The fluid film clearance, shown in Fig. 3.3b, is the axial offset between corresponding points on the stationary and rotating seal elements, and contains contributions from axial and angular deflections in addition to the seal face geometry contributions. To ensure consistency, the film thickness $h(r, \theta)$ is given with respect to the polar coordinate system attached to the rotating seal element center:

$$h(r,\theta) = C_o + (u_{sz} - u_{rz}) + (\bar{\gamma}_s \times \bar{r}_2 - \bar{\gamma}_r \times \bar{r}_1) \cdot \hat{e}_\zeta + \beta(t)(r - r_i) \tag{3.31}$$

where the coning $\beta(t)$ is left as a general function of time since it depends on transient thermo-elastic deformations of the seal faces. Using each element's constitutive tilt components is judicious because it simplifies derivatives of the film thickness and allows any function of the film thickness to be written in terms of the degrees-of-freedom. Thus, the clearance and its derivatives can be evaluated directly during the numeric integration solution process without any additional calculations. Evaluating Eq. 3.31 indicates that film thickness variations caused by relative eccentricity are of order $O(\gamma\epsilon)$ (see Wileman and Green [56] for a more detailed depiction of these

effects). Neglecting these second-order effects gives the total film thickness:

$$h(r,\theta) = C_o + (u_{sz} - u_{rz}) + (\gamma_{s\xi} - \gamma_{r\xi})r\sin\theta - (\gamma_{s\eta} - \gamma_{r\eta})r\cos\theta + \beta(t)(r - r_i) \quad (3.32)$$

Spatial and temporal derivatives of Eq. 3.32 will be useful for calculating the fluid pressure:

$$\frac{\partial h}{\partial r} = (\gamma_{s\xi} - \gamma_{r\xi})\sin\theta - (\gamma_{s\eta} - \gamma_{r\eta})\cos\theta + \beta(t) \quad (3.33)$$

$$\frac{\partial h}{\partial \theta} = (\gamma_{s\xi} - \gamma_{r\xi})r\cos\theta + (\gamma_{s\eta} - \gamma_{r\eta})r\sin\theta \quad (3.34)$$

$$\frac{\partial h}{\partial t} = \dot{u}_{sz} - \dot{u}_{rz} + (\dot{\gamma}_{s\xi} - \dot{\gamma}_{r\xi})r\sin\theta - (\dot{\gamma}_{s\eta} - \dot{\gamma}_{r\eta})r\cos\theta + \dot{\beta}(t)(r - r_i) \quad (3.35)$$

3.4.2 Fluid and Contact Pressure

The fluid film couples the rotating and stationary seal elements, allowing one element to track misalignments in the other. The fluid pressure in the sealing dam is found by solving the Reynolds equation for a narrow seal, as detailed in Appendix A. The resulting fluid pressure profile contains contributions from static and hydrodynamic effects:

$$P_s(r,\theta) = P_o - (P_o - P_i)\frac{h_i^2}{h_o^2 - h_i^2}\left[\left(\frac{h_o}{h}\right)^2 - 1\right] \quad (3.36)$$

$$P_d(r,\theta) = -3\mu\frac{(r_o - r)(r - r_i)}{h_m h^2}\Bigg[2\frac{\partial h}{\partial t} + (V_{1r} - V_{2r})\frac{\partial h}{\partial r} + \frac{(V_{1\theta} - V_{2\theta})}{r}\frac{\partial h}{\partial \theta} + h\frac{\partial}{\partial r}\big(V_{1r} + V_{2r}\big) + \frac{h}{r}\frac{\partial}{\partial \theta}\big(V_{1\theta} + V_{2\theta}\big) + \frac{h}{r}\big(V_{1r} + V_{2r}\big)\Bigg] \quad (3.37)$$

where μ is the fluid viscosity and h_i, h_o, and h_m are the values of the film thickness at the inner, outer, and mean radii of the smaller element, which in this case is the rotating seal element. The relative velocity components and film thickness kinematics are given in Eqs. 3.27 - 3.30 and Eqs. 3.32 - 3.35, respectively.

Contact occurs between the seal faces when the relative film thickness at any point in the sealing dam approaches the same order of magnitude as the surface roughness. The contact pressure $P_c(r,\theta)$ as a function of film thickness is derived in Chapter 7

using the elasto-plastic Jackson-Green rough surface contact model:

$$P_c(r,\theta) = C_1 \exp(C_2 h(r,\theta)) \tag{3.38}$$

where C_1 and C_2 depend on the surface asperity geometry and material properties. Employing a rough surface contact model to approximate the contact pressure is advantageous because the contact pressure depends on real and measurable surface properties rather than implicit assumptions regarding the force-displacement relationship. In addition, an elasto-plastic model is required because one seal surface is typically much harder than the other [42].

The total pressure $P(r,\theta)$ acting at any point in the sealing dam is the sum of the contributions from static fluid pressure (Eq. 3.36), dynamic fluid pressure (Eq. 3.37), and contact pressure (Eq. 3.38). The moments caused by fluid and contact pressure acting on the seal faces are not equal and opposite because of eccentric deflections of both elements (i.e., the moments are evaluated about different points, C_r and C_s). Furthermore, care must be taken when deriving the contact moment acting on the stationary element because the contact and fluid pressures are defined relative to a polar frame fixed to the rotating element. In vector form, the forces and moments caused by normal fluid and contact pressure are

$$\bar{F}_{s\zeta} = \int_{r_i}^{r_o} \int_0^{2\pi} P(r,\theta) r dr d\theta \tag{3.39}$$

$$\bar{M}_r = \int_{r_i}^{r_o} \int_0^{2\pi} -\left[\bar{r}_1 \times P(r,\theta)\hat{e}_\zeta\right] r dr d\theta \tag{3.40}$$

$$\bar{M}_s = \int_{r_i}^{r_o} \int_0^{2\pi} \left[\bar{r}_2 \times P(r,\theta)\hat{e}_\zeta\right] r dr d\theta \tag{3.41}$$

In these expressions, the integral bounds are dictated by the element with smaller radii, which in this work is the rotating element. The net axial force acting on the rotating and stationary elements is equal and opposite; i.e., $\bar{F}_{r\zeta} = -\bar{F}_{s\zeta}$. Since these forces are equal and opposite, the element subscript is dropped ($\bar{F}_{s\zeta} = \bar{F}_\zeta$ and $F_{r\zeta} = -F_\zeta$) while retaining the correct sign in the equation of motion. The moments

acting on the rotating element from axial fluid and contact pressures do not depend on the relative eccentricity because the polar coordinate system $r\theta$ is defined relative to the element's center, O_r. The moments acting about the stationary element's center, however, are more complex since they act about a point that is not the center of the $r\theta$ system.

Evaluating the cross products and expanding the results into component form gives the following forces and moments:

$$M_{r\xi} = -\int_{r_i}^{r_o}\int_{0}^{2\pi} P(r,\theta) r^2 \sin\theta dr d\theta \tag{3.42}$$

$$M_{r\eta} = \int_{r_i}^{r_o}\int_{0}^{2\pi} P(r,\theta) r^2 \cos\theta dr d\theta \tag{3.43}$$

$$M_{s\xi} = \int_{r_i}^{r_o}\int_{0}^{2\pi} P(r,\theta)\big(r\sin\theta - \epsilon_\eta^*\big) r dr d\theta \tag{3.44}$$

$$M_{s\eta} = \int_{r_i}^{r_o}\int_{0}^{2\pi} P(r,\theta)\big(\epsilon_\xi^* - r\cos\theta\big) r dr d\theta \tag{3.45}$$

where the components of relative eccentricity and translation are

$$\epsilon_\xi^* = \epsilon_{s\xi} - \epsilon_{r\xi} \tag{3.46}$$

$$\epsilon_\eta^* = \epsilon_{s\eta} - \epsilon_{r\eta} \tag{3.47}$$

3.4.3 Friction Forces

Friction forces are generated by relative tangential motion between the surfaces at the contact locations, and therefore these forces incur contributions from both relative translation and relative rotation. A dry Coulomb friction law with coefficient μ_f is used here to relate the contact pressure $P_c(r,\theta)$ to the shear stress at each point in the sealing dam. The friction shear stress acts to oppose relative velocity between the surfaces, and varies depending on position $r\theta$ (for the rotating seal element, this direction is labeled $\hat{e}_{fr}(r,\theta)$). The direction is calculated using the relative velocity between corresponding points on the rotating and stationary seal elements:

$$\hat{e}_{fr}(r,\theta) = -\frac{\bar{V}_{pr} - \bar{V}_{ps}}{||\bar{V}_{pr} - \bar{V}_{ps}||} \tag{3.48}$$

The shear stress direction on the stationary seal element is opposite that given in Eq. 3.48. The relative velocity in the $\xi\eta\zeta$ frame is

$$\bar{V}_{pr} - \bar{V}_{ps} = \big(- \dot{\epsilon}^*_\xi - r\omega_r \sin\theta \big)\hat{e}_\xi + \big(- \dot{\epsilon}^*_\eta + r\omega_r \cos\theta \big)\hat{e}_\eta \tag{3.49}$$

and its magnitude, after eliminating second order terms, is:

$$||\bar{V}_{pr} - \bar{V}_{ps}||^2 = r\omega_r \big(r\omega_r + 2\dot{\epsilon}^*_\xi \sin\theta - 2\dot{\epsilon}^*_\eta \cos\theta \big) \approx r^2\omega_r^2 \tag{3.50}$$

Mathematically, the above approximation is reasonable since $r\omega_r >> \dot{\epsilon}^*_{\xi,\eta}$, while intuitively, the approximation implies that the circumferential velocity caused by shaft rotation is much greater than the relative translational velocity. In this manner, the friction shear stress acting on seal element j is:

$$\bar{\tau}_{fj}(r,\theta) = \mu_f P_{cj}(r,\theta)\hat{e}_{fj}(r,\theta) \tag{3.51}$$

The total friction force acting on seal element j is obtained by integrating Eq. 3.51 across the sealing dam:

$$\bar{F}_{fj} = \int_{r_i}^{r_o} \int_0^{2\pi} \mu_f P_{cj}(r,\theta)\hat{e}_{fj}(r,\theta) r dr d\theta \tag{3.52}$$

The contact shear stress also generates a net moment about each element's center because of the element's tilt. In vector form, the moments acting on the stationary and rotating seal elements are

$$\bar{M}_{fs} = \int_{r_i}^{r_o} \int_0^{2\pi} -\Big[\big(\bar{r}_2 + \bar{\gamma}_s \times \bar{r}_2 \big) \times \mu_f P_c(r,\theta)\hat{e}_{fr}(r,\theta) \Big] r dr d\theta \tag{3.53}$$

$$\bar{M}_{fr} = \int_{r_i}^{r_o} \int_0^{2\pi} \Big[\big(\bar{r}_1 + \bar{\gamma}_r \times \bar{r}_1 \big) \times \mu_f P_c(r,\theta)\hat{e}_{fr}(r,\theta) \Big] r dr d\theta \tag{3.54}$$

where $\bar{\gamma}_s$ and $\bar{\gamma}_r$ are provided in Eqs. 3.6 and 3.7, respectively. Expanding Eqs. 3.52 - 3.54, neglecting second-order terms, and ignoring moments about ζ gives the friction

forces and moments caused by eccentricity and rotation:

$$(F_{fr})_\xi = \mu_f \int_{r_i}^{r_o} \int_0^{2\pi} P_c(r,\theta)\left(\frac{-\dot{\epsilon}_\xi^* - r\omega_r \sin\theta}{\omega_r}\right) dr d\theta \tag{3.55}$$

$$(F_{fr})_\eta = \mu_f \int_{r_i}^{r_o} \int_0^{2\pi} P_c(r,\theta)\left(\frac{-\dot{\epsilon}_\eta^* + r\omega_r \cos\theta}{\omega_r}\right) dr d\theta \tag{3.56}$$

$$(F_{fs})_\xi = -(F_{\mu r})_\xi \tag{3.57}$$

$$(F_{fs})_\eta = -(F_{\mu r})_\eta \tag{3.58}$$

$$(M_{fr})_\xi = \mu_f \int_{r_i}^{r_o} \int_0^{2\pi} P_c(r,\theta)\big(\gamma_{r\eta}\cos\theta - \gamma_{r\xi}\sin\theta\big) r^2 \cos\theta dr d\theta \tag{3.59}$$

$$(M_{fr})_\eta = \mu_f \int_{r_i}^{r_o} \int_0^{2\pi} P_c(r,\theta)\big(\gamma_{r\eta}\cos\theta - \gamma_{r\xi}\sin\theta\big) r^2 \sin\theta dr d\theta \tag{3.60}$$

$$(M_{fs})_\xi = -\mu_f \int_{r_i}^{r_o} \int_0^{2\pi} P_c(r,\theta)\big(\gamma_{s\eta}\cos\theta - \gamma_{s\xi}\sin\theta\big) r^2 \cos\theta dr d\theta \tag{3.61}$$

$$(M_{fs})_\eta = -\mu_f \int_{r_i}^{r_o} \int_0^{2\pi} P_c(r,\theta)\big(\gamma_{s\eta}\cos\theta - \gamma_{s\xi}\sin\theta\big) r^2 \sin\theta dr d\theta \tag{3.62}$$

3.4.4 Fluid Shear Forces and Moments

Relative motion between the seal faces induces fluid shear stresses, which are calculated by assuming Couette flow (Etsion and Sharoni [55] demonstrate that the pressure-driven Poiseuille component is negligible in narrow eccentric face seals). The Couette shear stresses $\bar{\tau}_{\mu j}$ acting on body j only depend on the fluid velocities $\bar{v}$ between body j and body i:

$$\bar{\tau}_{\mu j}(r,\theta) = \mu \frac{\partial \bar{v}}{\partial \zeta} \tag{3.63}$$

where $\bar{v}$ denotes the velocity of the fluid between the seal faces. This derivative is approximated by dividing the relative velocity between bodies j and i, $\bar{V}_{pj} - \bar{V}_{pi}$ by the film thickness $h(r,\theta)$. The relative velocity between corresponding points on the seal elements is given in Eq. 3.49. Integrating Eq. 3.63 over the sealing dam provides

the fluid shear forces:

$$\bar{F}_{\mu r}(r,\theta) = \mu \int_{r_i}^{r_o} \int_0^{2\pi} \left[\frac{-\dot{\epsilon}_\xi^* - r\omega_r \sin\theta}{h(r,\theta)} \hat{e}_\xi + \frac{-\dot{\epsilon}_\eta^* + r\omega_r \cos\theta}{h(r,\theta)} \hat{e}_\eta \right] r dr d\theta \tag{3.64}$$

$$\bar{F}_{\mu s}(r,\theta) = -\bar{F}_{\mu r}(r,\theta) \tag{3.65}$$

where the fluid shear force acting on the stationary seal element is obtained by recognizing that an observer fixed to the element sees a relative velocity with opposite sign. The fluid shear stresses also generate moments about each element's geometric center because of relative tilt and eccentricity. These moments are:

$$\bar{M}_{\mu s} = \int_{r_i}^{r_o} \int_0^{2\pi} -\left[\left(\bar{r}_2 + \bar{\gamma}_s \times \bar{r}_2 \right) \times \bar{\tau}_{\mu r}(r,\theta) \right] r dr d\theta \tag{3.66}$$

$$\bar{M}_{\mu r} = \int_{r_i}^{r_o} \int_0^{2\pi} \left[\left(\bar{r}_1 + \bar{\gamma}_r \times \bar{r}_1 \right) \times \bar{\tau}_{\mu r}(r,\theta) \right] r dr d\theta \tag{3.67}$$

The vector expressions for fluid shear moments are expanded to give the component moments acting on each body:

$$(M_{\mu r})_\xi = \mu\omega_r \int_{r_i}^{r_o} \int_0^{2\pi} \frac{\gamma_{r\eta}\cos\theta - \gamma_{r\xi}\sin\theta}{h(r,\theta)} r^3 \cos\theta dr d\theta \tag{3.68}$$

$$(M_{\mu r})_\eta = \mu\omega_r \int_{r_i}^{r_o} \int_0^{2\pi} \frac{\gamma_{r\eta}\cos\theta - \gamma_{r\xi}\sin\theta}{h(r,\theta)} r^3 \sin\theta dr d\theta \tag{3.69}$$

$$(M_{\mu s})_\xi = -\mu\omega_r \int_{r_i}^{r_o} \int_0^{2\pi} \frac{\gamma_{s\eta}\cos\theta - \gamma_{s\xi}\sin\theta}{h(r,\theta)} r^3 \cos\theta dr d\theta \tag{3.70}$$

$$(M_{\mu s})_\eta = -\mu\omega_r \int_{r_i}^{r_o} \int_0^{2\pi} \frac{\gamma_{s\eta}\cos\theta - \gamma_{s\xi}\sin\theta}{h(r,\theta)} r^3 \sin\theta dr d\theta \tag{3.71}$$

Importantly, effects from eccentricity in the fluid shear moments are second-order and therefore eliminated from the analysis.

3.5 Support Forces: Coupled Rotordynamics

The rotating seal element is flexibly attached to the rotor, which also experiences angular, lateral, and/or axial deflections. The effects of coupled rotordynamics have historically been neglected in the analysis of mechanical face seals. Here, the 'rotor'

consists of the flexible shaft and attached rigid disk on which the rotating seal element is affixed (see Fig. 3.1).

The rotating element degrees-of-freedom were judiciously chosen to be absolute in the system-fixed $\xi\eta\zeta$ reference frame to reduce the mathematical and intuitive overhead associated with coupling between the rotor and rotating seal element. Because the degrees-of-freedom are absolute, the coupling between the rotor and the rotating seal element only manifests in the forces induced by support stiffness and damping. These forces depend on the relative deflections between the seal and rotor, where the rotor degrees of freedom are denoted with subscript 'R'. The support force is

$$\begin{aligned}\bar{F}_{s\epsilon,r} = \big[- K_{r\epsilon}(\epsilon_{r\xi} - \epsilon_{R\xi}) - D_{r\epsilon}(\dot{\epsilon}_{r\xi} - \dot{\epsilon}_{R\xi})\big]\hat{e}_\xi + \big[- K_{r\epsilon}(\epsilon_{r\eta} - \epsilon_{R\eta}) - D_{r\epsilon}(\dot{\epsilon}_{r\eta} - \dot{\epsilon}_{R\eta})\big]\hat{e}_\eta \\ + \big[- K_{rz}(u_{rz} - u_{Rz}) - D_{rz}(\dot{u}_{rz} - \dot{u}_{Rz})\big]\hat{e}_\zeta \end{aligned} \tag{3.72}$$

where the eccentric stiffness and damping coefficients are $K_{r\epsilon}$ and $D_{r\epsilon}$, and the axial stiffness and damping coefficients are K_{rz} and D_{rz}. Finally, the support moment is:

$$\begin{aligned}\bar{M}_{sr} = \big[- K_r(\gamma_{r\xi} - \gamma_{R\xi}) - D_r(\dot{\gamma}_{r\xi} - \dot{\gamma}_{R\xi}) - \omega_r D_r(\gamma_{r\eta} - \gamma_{R\eta})\big]\hat{e}_\xi \\ + \big[- K_r(\gamma_{r\eta} - \gamma_{R\eta}) - D_r(\dot{\gamma}_{r\eta} - \dot{\gamma}_{R\eta}) + \omega_r D_r(\gamma_{r\xi} - \gamma_{R\xi})\big]\hat{e}_\eta \end{aligned} \tag{3.73}$$

Equation 3.73 includes the effect of rotating damping caused by the elastomeric O-ring support. The rotating seal element support is typically composed of an axial spring and a circumferential viscoelastic O-ring. Because the O-ring is viscoelastic, the stiffness and damping properties are a function of excitation frequency. However, the stiffness and damping of the fluid film in a liquid-lubricated seal is typically several orders of magnitude greater than the support stiffness and damping [51]. For liquid-lubricated seals such as those considered here, this disparity makes it reasonable to neglect variations in the support properties caused by changes in the excitation frequency.

3.6 Dynamic Moments of the Rotating Seal Element

The dynamic moments acting on the rotating seal element depend on its angular momentum. To remain consistent with earlier works, the angular momentum is derived relative to the geometric center C_r:

$$\bar{h}_{C_r} = [I_{C_r}]\bar{\lambda}_r \tag{3.74}$$

The angular momentum will first be expressed using the rotating (i.e., nutating) $x_r y_r z_r$ reference frame, and then transformed back into the $\xi\eta\zeta$ system-fixed frame prior to evaluating the dynamic moments (i.e., the time rate of change of the angular momentum).

Geometry, installation errors, and/or manufacturing imperfections may cause the principal axes $x_r^p y_r^p z_r^p$ to be misaligned from the spin axes $1_r 2_r 3_r$. This effect is referred to here as dynamic angular misalignment. The misalignment magnitude is χ, and is assumed to occur about the principal 1_r axis without loss of generality. As discussed in Section 3.2, the kinematic constraint between the precession and spin [19, 20] is $\phi = \alpha(t) - \psi_r$, and will be useful for deriving the dynamic misalignment moments. For small misalignments $\chi << 1$, the rotation transformation between the principal axes and the nutating axes $(x_r y_r z_r)$ is:

$$[R] = \begin{bmatrix} \cos\phi & \sin\phi & 0 \\ -\sin\phi & \cos\chi & \chi \\ \chi\sin\phi & -\chi\cos\phi & 1 \end{bmatrix} \tag{3.75}$$

The principal inertia tensor $[I_{C_r}]$ is transformed into the nutating reference frame

$x_r y_r z_r$ using Eq. 3.75:

$$[I_{C_r}]^{x_r y_r x_r} = [R]^T \begin{bmatrix} I_{tr} & 0 & 0 \\ 0 & I_{tr} & 0 \\ 0 & 0 & I_{pr} \end{bmatrix}^{x_r^p y_r^p z_r^p} [R]$$

$$= \begin{bmatrix} I_{tr} + (I_{pr} - I_{tr})\chi^2 \sin^2\phi & -\frac{1}{2}\chi^2(I_{pr} - I_{tr}) \sin 2\phi & (I_{pr} - I_{tr})\chi \sin\phi \\ -\frac{1}{2}\chi^2(I_{pr} - I_{tr}) \sin 2\phi & I_{tr} & -(I_{pr} - I_{tr})\chi \cos\phi \\ (I_{pr} - I_{tr})\chi \sin\phi & -(I_{pr} - I_{tr})\chi \cos\phi & I_{pr} \end{bmatrix} \tag{3.76}$$

For small misalignments, this result reduces to the following:

$$[I_{C_r}] = \begin{bmatrix} I_{tr} & 0 & (I_{pr} - I_{tr})\chi \sin\phi \\ 0 & I_{tr} & -(I_{pr} - I_{tr})\chi \cos\phi \\ (I_{pr} - I_{tr})\chi \sin\phi & -(I_{pr} - I_{tr})\chi \cos\phi & I_{pr} \end{bmatrix} \tag{3.77}$$

Recognizing that C_r is an accelerating reference point that is not the center of mass, the dynamic moment acting on the rotating seal element is:

$$\Sigma \bar{M}_{dyn} = \frac{\partial \bar{h}_{C_r}}{\partial t} + \bar{\omega}_{(xyz)_r} \times \bar{h}_{C_r} + \bar{r}_{(GC)_r} \times m_r \bar{a}_{C_r} \tag{3.78}$$

where

$$\frac{\partial \bar{h}_{C_r}}{\partial t} = [I_{C_r}]\dot{\bar{\lambda}}_r + \frac{\partial([I_{C_r}])}{\partial t}\bar{\lambda}_r \tag{3.79}$$

The angular velocity of the $x_r y_r z_r$ reference frame is denoted $\bar{\omega}_{(xyz)_r}$:

$$\bar{\omega}_{(xyz)_r} = \dot{\gamma}_r \hat{e}_{x_r} + \dot{\psi}_r \sin\gamma_r \hat{e}_{y_r} + \dot{\psi}_r \cos\gamma_r \hat{e}_{z_r} + \bar{\lambda}_0 \tag{3.80}$$

In reality, the inertial maneuver rotations are likely to be much smaller than the shaft rotation rate ω_r. Hence, products of the orthogonal inertial rotations are much smaller than products of any inertial rotation with the shaft speed.

The dynamic moments must now be transformed from the nutating reference frame $x_r y_r z_r$ into the system-fixed reference frame $\xi\eta\zeta$ to maintain consistency with the applied forces derived earlier in the chapter. This task is accomplished using the following rotation transformation, where the subscript indicates the axis about which the rotation occurs and the term in parenthesis indicates the magnitude of the rotation:

$$\left(\bar{M}_{dyn}\right)_{\xi\eta\zeta} = [R_{Z_r}(\psi_r)]^T [R_{x_r}(\gamma_r)]^T \left(\frac{\partial \bar{h}_{C_r}}{\partial t} + \bar{\omega}_{(xyz)_r} \times \bar{h}_{C_r} \right) + \bar{r}_{(GC)_r} \times m_r \bar{a}_{C_r} \quad (3.81)$$

It is important to note that the term $\bar{r}_{(GC)_r} \times m_r \bar{a}_{C_r}$ has already been provided in the system-fixed reference frame $\xi\eta\zeta$. Finally, the inertial degrees-of-freedom are instituted in the equations of motion using the following relationships:

$$\gamma_{r\xi} = \gamma_r \cos\psi_r \quad (3.82)$$

$$\dot{\gamma}_{r\xi} = \dot{\gamma}_r \cos\psi_r - \gamma_r \dot{\psi}_r \sin\psi_r \quad (3.83)$$

$$\ddot{\gamma}_{r\xi} = \ddot{\gamma}_r \cos\psi_r - 2\dot{\gamma}_r \dot{\psi}_r \sin\psi_r - \gamma_r \ddot{\psi}_r \sin\psi_r - \gamma_r \dot{\psi}_r^2 \cos\psi_r \quad (3.84)$$

and

$$\gamma_{r\eta} = \gamma_r \sin\psi_r \quad (3.85)$$

$$\dot{\gamma}_{r\eta} = \dot{\gamma}_r \sin\psi_r + \gamma_r \dot{\psi}_r \cos\psi_r \quad (3.86)$$

$$\ddot{\gamma}_{r\eta} = \ddot{\gamma}_r \sin\psi_r + 2\dot{\gamma}_r \dot{\psi}_r \cos\psi_r + \gamma_r \ddot{\psi}_r \cos\psi_r - \gamma_r \dot{\psi}_r^2 \sin\psi_r \quad (3.87)$$

Evaluating Eq. 3.81 is tedious, and leads to a number of terms involving the rotating seal element degrees-of-freedom and the maneuver rotation rates λ_p, λ_y, and λ_{ro}. In this work, the influence of $\bar{\lambda}_0$ is retained only in terms involving products of either three maneuver rotation rates with the shaft rotation rate. The intermediate operations leading to the dynamic moments amount to algebraic substitutions, and are therefore omitted here for brevity.

3.7 Equations of Motion

The equations of motion governing angular deflections of the rotating seal element, including inertial maneuver loads and coupled rotordynamics, are

$$\Sigma\bar{M}_{C_r}: \quad [R_{Z_r}(\psi_r)]^T[R_{x_r}(\gamma_r)]^T\left(\frac{\partial\bar{h}_{C_r}}{\partial t}+\bar{\omega}_{(xyz)_r}\times\bar{h}_{C_r}\right)+\bar{r}_{(GC)_r}\times m_r\bar{a}_{C_r}= \\ +\bar{r}_{(GC)_r}\times\bar{F}_{gr}+\bar{M}_{sr}+\bar{M}_{fr}+\bar{M}_{\mu r}+\bar{M}_r+\bar{M}_{ri} \tag{3.88}$$

$$\Sigma\bar{F}_{G_r}: \quad m_r\bar{a}_{G_r}=\bar{F}_{gr}+\bar{F}_{zr}+\bar{F}_{\mu r}+\bar{F}_{fr}+\bar{F}_{sr}+\bar{F}_{ri} \tag{3.89}$$

where the applied forces and moments arise from static misalignment ($\bar{M}_{ri}$ and $\bar{F}_{ri}$), gravity $\bar{F}_{gr}$, the flexible supports ($\bar{M}_{sr}$ and $\bar{F}_{sr}$), fluid shear ($\bar{M}_{\mu r}$ and $\bar{F}_{\mu r}$), friction ($\bar{M}_{fr}$ and $\bar{F}_{fr}$), and normal fluid and contact pressure ($\bar{M}_r$ and $\bar{F}_\zeta$). Expanding these equations in component form gives:

$$I_{tr}\ddot{\gamma}_{r\xi}+I_{pr}(\omega_r\dot{\gamma}_{r\eta}+\dot{\omega}_r\gamma_{r\eta})+D_r(\dot{\gamma}_{r\xi}-\dot{\gamma}_{R\xi})+K_r(\gamma_{r\xi}-\gamma_{R\xi})+\omega_rD_r(\gamma_{r\eta}-\gamma_{R\eta})= \\ m_rgd_r+(M_{fr})_\xi+(M_{\mu r})_\xi+M_{r\xi}+K_r\chi_s\cos(\alpha+\beta_{\chi r}) \\ +(I_{tr}-I_{pr})\,\chi\big(\omega_r^2\cos\alpha+\dot{\omega}_r\sin\alpha\big)-I_{tr}(\dot{\lambda}_p-\lambda_y\dot{\psi}_r)-I_{pr}\lambda_y\omega_r \\ -m_r\big\{a_{O\zeta}\big[\varepsilon_{rG}\sin(\alpha+\beta_r)-d_r\gamma_{r\xi}\big]-d_r\big(a_{O\eta}+\ddot{\epsilon}_{r\eta}\big)\big\} \tag{3.90}$$

$$I_{tr}\ddot{\gamma}_{r\eta}-I_{pr}(\omega_r\dot{\gamma}_{r\xi}+\dot{\omega}_r\gamma_{r\xi})+D_r(\dot{\gamma}_{r\eta}-\dot{\gamma}_{R\eta})+K_r(\gamma_{r\eta}-\gamma_{R\eta})-\omega_rD_r(\gamma_{r\xi}-\gamma_{R\xi})= \\ (M_{fr})_\eta+(M_{\mu r})_\eta+M_{r\eta}+K_r\chi_s\sin(\alpha+\beta_{\chi r}) \\ +(I_{tr}-I_{pr})\,\chi\big(\omega_r^2\sin\alpha-\dot{\omega}_r\cos\alpha\big)-I_{tr}(\dot{\lambda}_y+\lambda_p\dot{\psi}_r)+I_{pr}\lambda_p\omega_r \\ +m_r\big\{a_{O\zeta}\big[\varepsilon_{rG}\cos(\alpha+\beta_r)+d_r\gamma_{r\eta}\big]-d_r\big(a_{O\xi}+\ddot{\epsilon}_{r\xi}\big)\big\} \tag{3.91}$$

The static misalignment χ_s is caused by unavoidable imperfections such as improper installation, rotor bow, run-out, etc., and persists even when $\omega_r = 0$. This misalignment is imposed by applying a moment to the rotating seal element that generates χ_s [39]; the line about which χ_s occurs is referenced from axis X_r by the phase angle $\beta_{\chi r}$ (or, alternatively, referenced from ξ_r by the angle $\beta_{\chi r}+\alpha$). The equation of

motion governing axial deflections is

$$m_r\ddot{u}_{rz} + D_{rz}(\dot{u}_{rz} - \dot{u}_{Rz}) + K_{rz}(u_{rz} - u_{Rz}) = -F_\zeta + F_{cls} - m_r\Big[a_{O\zeta} + \dot{\lambda}_p\varepsilon_{rG}\sin(\alpha+\beta_r) - \dot{\lambda}_y\varepsilon_{rG}\cos(\alpha+\beta_r) + 2\lambda_p\big(\dot{\epsilon}_{r\eta} + \varepsilon_{rG}\omega_r\cos(\alpha+\beta_r)\big) + 2\lambda_y\big(\varepsilon_{rG}\omega_r\cos(\alpha+\beta_r) - \dot{\epsilon}_{r\xi}\big)\Big] \tag{3.92}$$

while those for eccentric deflections are:

$$m_r\ddot{\epsilon}_{r\xi} + D_{r\epsilon}(\dot{\epsilon}_{r\xi} - \dot{\epsilon}_{R\xi}) + K_{r\epsilon}(\epsilon_{r\xi} - \epsilon_{R\xi}) = (F_{fr})_\xi + (F_{\mu r})_\xi - m_r(a_{O\xi} - d_r\ddot{\gamma}_{r\eta}) + m_r\varepsilon_{rG}\big[\omega_r^2\cos(\alpha+\beta_r) + \dot{\omega}_r\sin(\alpha+\beta_r)\big] + m_r\Big[2\lambda_{ro}\big(\dot{\epsilon}_{r\eta} + \varepsilon_{rG}\omega_r\cos(\alpha+\beta_r)\big) - 2\lambda_y\dot{u}_{rz} - \dot{\lambda}_y d_r + \dot{\lambda}_{ro}\varepsilon_{rG}\sin(\alpha+\beta_r)\Big] \tag{3.93}$$

$$m_r\ddot{\epsilon}_{r\eta} + D_{r\epsilon}(\dot{\epsilon}_{r\eta} - \dot{\epsilon}_{R\eta}) + K_{r\epsilon}(\epsilon_{r\eta} - \epsilon_{R\eta}) = (F_{fr})_\eta + (F_{\mu r})_\eta - m_r(a_{O\eta} + g + d_r\ddot{\gamma}_{r\xi}) + m_r\varepsilon_{rG}\big[\omega_r^2\sin(\alpha+\beta_r) - \dot{\omega}_r\cos(\alpha+\beta_r)\big] - m_r\Big[2\lambda_{ro}\big(\dot{\epsilon}_{r\xi} - \varepsilon_{rG}\omega_r\sin(\alpha+\beta_r)\big) - 2\lambda_p\dot{u}_{rz} - \dot{\lambda}_p d_r + \dot{\lambda}_{ro}\varepsilon_{rG}\cos(\alpha+\beta_r)\Big] \tag{3.94}$$

where the closing force on the seal is derived in Appendix B:

$$F_{cls} = F_{spr} + \pi\left[P_o(r_o^2 - r_b^2) + P_i(r_b^2 - r_i^2)\right] \tag{3.95}$$

The supporting secondary spring force is F_{spr}, while the radii in the above equation pertain to the rotating seal element (i.e., the smaller element). The equations of motion for the stationary seal element are easily obtained because the degrees-of-freedom are only coupled through fluid and contact forces and moments. These equations of motion, including static angular misalignment γ_{si} and inertial maneuver

loads, are:

$$I_{ts}\ddot{\gamma}_{s\xi}+D_s\dot{\gamma}_{s\xi}+K_s\gamma_{s\xi}=-I_{ts}\dot{\lambda}_p+K_s\gamma_{si,\xi}+M_{s\xi}+(M_{\mu s})_\xi \tag{3.96}$$

$$I_{ts}\ddot{\gamma}_{s\eta}+D_s\dot{\gamma}_{s\eta}+K_s\gamma_{s\eta}=-I_{ts}\dot{\lambda}_y+K_s\gamma_{si,\eta}+M_{s\eta}+(M_{\mu s})_\eta \tag{3.97}$$

$$m_s\ddot{u}_{sz}+D_{sz}\dot{u}_{sz}+K_{sz}u_{sz}=F_\zeta-F_{cls}-m_s\big(a_{O\zeta}+2\lambda_p\dot{\epsilon}_{s\eta}-2\lambda_y\dot{\epsilon}_{s\xi}\big) \tag{3.98}$$

$$m_s\ddot{\epsilon}_{s\xi}+D_{s\epsilon}\dot{\epsilon}_{s\xi}+K_{s\epsilon}\epsilon_{s\xi}=K_{s\epsilon}\epsilon_{si,\xi}+(F_{fs})_\xi+(F_{\mu s})_\xi-m_s\big(a_{O\xi}-2\lambda_{ro}\dot{\epsilon}_{s\eta}+2\lambda_y\dot{u}_{sz}\big) \tag{3.99}$$

$$m_s\ddot{\epsilon}_{s\eta}+D_{s\epsilon}\dot{\epsilon}_{s\eta}+K_{s\epsilon}\epsilon_{s\eta}=K_{s\epsilon}\epsilon_{si,\eta}+(F_{fs})_\eta+(F_{\mu s})_\eta-m_s\big(a_{O\eta}+g+2\lambda_{ro}\dot{\epsilon}_{s\xi}-2\lambda_p\dot{u}_{sz}\big) \tag{3.100}$$

where g is the acceleration due to gravity. The static misalignments $\gamma_{si,\xi}$, $\gamma_{si,\eta}$, $\epsilon_{si,\xi}$, and $\epsilon_{si,\eta}$ are imposed by applying forces and moments that enforce the misalignment. It must be noted once again that these equations of motion for the FMSR seal represent a generalized case of previous works, which considered simpler seal configurations such as the FMR or FMS. The equations of motion given here reduce to the forms derived in previous studies when the appropriate assumptions are instituted in the equations.

3.8 Thermal Deformation: Viscous and Frictional Heating

Face coning in mechanical seals is typically generated by mechanical and thermal deformations. Mechanical deformations are small compared to thermal deformations and occur almost instantaneously [42, 45]. Thermal deformations, on the other hand, are governed by dynamics which occur much slower than the seal dynamics. A complete model for thermo-elastic deformation would require solving the elastic and heat conduction equations simultaneously with the proper boundary conditions. Fortunately, the thermo-elastic dynamics of face coning can be accurately approximated in normal operating conditions by using the first-order model developed by Green [42].

This model relies on parameters obtained from a finite element simulation, and includes the appropriate heat transfer boundary conditions, thermo-elastic deformations, and viscous heat generation:

$$\tau_T \dot{\beta} + \beta = \beta_{ref} \left[\left(\frac{h_{ref}}{h_{mean}} \right) \left(\frac{\omega_r}{\omega_{ref}} \right)^2 + \frac{Q_f}{(Q_v)_{ref}} \right] \tag{3.101}$$

where β is the face coning and h_{mean} is the average film thickness across the sealing dam. The time scale is determined by the time constant τ_T, while the coning magnitude is controlled by the reference parameters β_{ref}, h_{ref}, and ω_{ref} found from the finite element simulation [42]. The frictional heat generation Q_f is normalized by the viscous heat generation at the reference parameters:

$$Q_f = \int_0^{2\pi} \int_{r_i}^{r_o} \mu_f P_c(r,\theta) \omega_r r^2 dr d\theta \tag{3.102}$$

$$(Q_v)_{ref} = \int_0^{2\pi} \int_{r_i}^{r_o} \frac{\mu \omega_{ref}^2}{h_{ref}} r^3 \tag{3.103}$$

Importantly, the frictional heat generation is assumed to occur axisymmetrically even though the asperity contact is usually localized. This assumption is reasonable because of the time-scale discrepancy between the system dynamics and the thermo-elastic deformations [42]. It should be noted that these thermoelastic deformation equations are provided for completeness, especially for future works, and are not simulated in this work.

3.9 System Equations of Motion

In matrix form, the equations of motion for the FMSR-ER system are

$$[M]\{\ddot{q}\} + ([D] + [\Lambda_1] + [G])\{\dot{q}\} + ([K] + [\Lambda_0] + [D_r])\{q\} = F_a(\{q\}, \{\dot{q}\}, t) \tag{3.104}$$

where $[M]$ is the mass matrix, $[D]$ is the damping matrix, $[G]$ is the gyroscopic matrix, $[K]$ is the stiffness matrix, $[\Lambda_{0,1}]$ contains inertial forces due to maneuver rotation, and $[D_r]$ is the rotating damping matrix. The general vector of applied

forces and moments, $F_a(\{q\},\{\dot{q}\},t)$, has been developed in the preceding sections. These matrices are:

$$[M]=\begin{bmatrix}[M_s] & 0_{4\times4}\\ 0_{4\times4} & [M_r]\end{bmatrix},\ [D]+[\Lambda_1]+[G]=\begin{bmatrix}[C_s] & 0_{4\times4}\\ 0_{4\times4} & [C_r]\end{bmatrix},\ [K]+[\Lambda_0]+[D_r]=\begin{bmatrix}[B_s] & 0_{4\times4}\\ 0_{4\times4} & [B_r]\end{bmatrix} \tag{3.105}$$

where

$$[M_s]=\begin{bmatrix} I_{ts} & 0 & 0 & 0 & 0\\ & I_{ts} & 0 & 0 & 0\\ & & m_s & 0 & 0\\ & & & m_s & 0\\ \text{sym.} & & & & m_s\end{bmatrix} \tag{3.106}$$

$$[M_r]=\begin{bmatrix} I_{tr} & 0 & 0 & 0 & -m_r d_r\\ & I_{tr} & 0 & m_r d_r & 0\\ & & m_r & 0 & 0\\ & & & m_r & 0\\ \text{sym.} & & & & m_r\end{bmatrix} \tag{3.107}$$

$$[C_s]=\begin{bmatrix} D_s & 0 & 0 & 0 & 0\\ & D_s & 0 & 0 & 0\\ & & D_{sz} & -2m_s\lambda_y & 2m_s\lambda_p\\ & & & D_{s\epsilon} & -2m_s\lambda_{ro}\\ \text{skew sym.} & & & & D_{s\epsilon}\end{bmatrix} \tag{3.108}$$

$$[C_r] = \begin{bmatrix} D_r & I_{pr}\omega_r & 0 & 0 & 0 \\ & D_r & 0 & 0 & 0 \\ & & D_{rz} & -2m_r\lambda_y & 2m_r\lambda_p \\ & & & D_{r\epsilon} & -2m_r\lambda_{ro} \\ \text{skew sym.} & & & & D_{r\epsilon} \end{bmatrix} \tag{3.109}$$

$$[B_s] = \begin{bmatrix} K_s & 0 & 0 & 0 & 0 \\ & K_s & 0 & 0 & 0 \\ & & K_{sz} & 0 & 0 \\ & & & K_{s\epsilon} & 0 \\ \text{sym.} & & & & K_{s\epsilon} \end{bmatrix} \tag{3.110}$$

$$[B_r] = \begin{bmatrix} K_r - m_r a_{O\zeta} d_r & I_{pr}\dot{\omega}_r + \omega_r D_r & 0 & 0 & 0 \\ & K_r + m_r a_{O\zeta} d_r & 0 & 0 & 0 \\ & & K_{rz} & 0 & 0 \\ & & & K_{r\epsilon} & 0 \\ & \text{skew sym.} & & & K_{r\epsilon} \end{bmatrix} \tag{3.111}$$

Thermoelastic effects, given in Eq. 3.101, can be included in the above equations by appropriately expanding the state vector.

Though the above equations of motion appear to imply linearity, nonlinear effects (and additional couplings) are actually embodied in the forcing function $F_a(\{q\}, \{\dot{q}\}, t)$. The forcing function depends strongly on the clearance between the seal elements, which in turn is intrinsically dependent on all of the system degrees-of-freedom. Specifically, the forcing function contains contributions from inertial effects (both maneuver loads and gravity), misalignments (angular and eccentric), coupled rotor-dynamics, the fluid film (normal pressure and fluid shear), and contact (normal pressure and friction). These forces are provided throughout this chapter, and are not

presented again for brevity. It should also be noted here that the rotor degrees-of-freedom can be included by expanding the state vector.

3.9.1 Seal Performance Metrics

The faces in a mechanical face seal are designed to exhibit dynamic tracking, which minimizes relative deflections between the faces and mitigates the risk of contact (because the clearances are small, contact can occur for even small relative tilts). Consequently, the dynamic performance of a mechanical face seal is best described using the relative motion between the seal faces. Because the element tilts are small, they can be treated as vectors and summarily used to find the relative tilt between the faces:

$$\bar{\gamma}^* = \bar{\gamma}_s - \bar{\gamma}_r \tag{3.112}$$

the magnitude and phase of which are

$$(\gamma^*)^2 = \gamma_s^2 + \gamma_r^2 - 2\gamma_r\gamma_s \cos\left(\psi_s - \psi_r\right) \tag{3.113}$$

$$\psi^* = \tan^{-1}\left(\frac{\gamma_{s\eta} - \gamma_{r\eta}}{\gamma_{s\xi} - \gamma_{r\xi}}\right) \tag{3.114}$$

The relative eccentricity and axial deflection are:

$$(\epsilon^*)^2 = (\epsilon_{s\xi} - \epsilon_{r\xi})^2 + (\epsilon_{s\eta} - \epsilon_{r\eta})^2 \tag{3.115}$$

$$u^* = u_{sz} - u_{rz} \tag{3.116}$$

These expressions will be used to assess the seal apparatus performance.

3.9.2 Numerically Solving the System Equations of Motion

Nonlinear fluid film effects and seal face contact predispose the system equations of motion to numeric solution. Previously, other works linearize the fluid film and reduce the associated forces to those resulting from linearized rotordynamic coefficients; this approach is only valid for small seal face tilts. When the seal faces are in danger of contacting, the tilts are likely large enough to invalidate this assumption. This, in

conjunction with the fundamental nonlinearity of surface asperity contact, establishes numeric solution of the system equations of motion as a robust solution method (and, likely, the only solution method). The degrees-of-freedom are placed in vector form as shown in Eq. 3.1. For the methods used herein, the system equations of motion, Eq. 3.104, must be placed in first-order state space prior to numeric integration. The state vector is defined to be

$$\{x\} = \begin{Bmatrix} \{q\} \\ \{\dot{q}\} \end{Bmatrix} = \begin{Bmatrix} \{x_1\} \\ \{x_2\} \end{Bmatrix} \tag{3.117}$$

Recognizing that $\{\dot{x}_1\} = \{x_2\}$ provides the first-order state-space form of the equations of motion:

$$\{\dot{x}\} = \begin{bmatrix} [0] & [I] \\ -[M]^{-1}([K] + [\Lambda_0] + [D_r]) & -[M]^{-1}([D] + [\Lambda_1] + [G]) \end{bmatrix} \begin{Bmatrix} \{x_1\} \\ \{x_2\} \end{Bmatrix} + \begin{Bmatrix} \{0\} \\ [M]^{-1}\{F(\{x\}, t)\} \end{Bmatrix} \tag{3.118}$$

$$= [A]\{x\} + \{Q(\{x\}, t)\} \tag{3.119}$$

where the state-space forcing function $\{Q\}$ is a general function of the state vector $\{x\}$ and time t, and $[I]$ is the appropriately-sized identify matrix. The sealing dam is then discretized into circumferential and radial nodes, at which the film thickness, fluid pressure, and contact pressure are evaluated. At each time step in the numeric simulation, the fluid and contact pressures are integrated numerically to provide the associated forces and moments.

The equations of motion will later be integrated numerically in MATLAB using ode15s, which is a variable-step adaptive implementation of Gear's Method. This solver is suitable here because of the numeric stiffness induced by small clearances, where minute variations in fluid film thickness can induce dramatic changes in the

system dynamics. The relative and absolute tolerances are carefully selected by considering the magnitude of the state variables and the desired degree of accuracy. Because the film thickness is often measured in microns, suitable values for the relative and absolute tolerances are found to be 10^{-7} and 10^{-9}, respectively. These values are obtained by solving the equations of motion with progressively tighter tolerances until convergence is obtained in the solution.

3.10 Summary

The seal apparatus equations of motion are governed by eleven coupled nonlinear ordinary differential equations, and include the following effects:

1. Angular, axial, and eccentric degrees-of-freedom for both the stationary and rotating seal elements.

2. Transient and steady-state operation allowing for start-up and shut-down regimes.

3. Coupled rotordynamic effects.

4. Static misalignment of both seal elements.

5. Dynamic angular misalignment, eccentric imbalance, and axial imbalance of the rotating seal element.

6. Inertial maneuver loads.

7. Fluid pressure for an isoviscous, isothermal, and incompressible fluid, including both fluid shear and normal pressure effects.

8. Asperity contact pressure and friction obtained from the elasto-plastic Jackson-Green rough surface contact model.

9. Thermo-elastic deformation caused by viscous and frictional heat generation.

This complete model represents a significant step forward in describing and understanding the dynamic performance of non-contacting mechanical face seals. Throughout this work, various simplifications will be made to the system model (e.g., steady-state response, zero inertial maneuver loads, etc.) to emphasize specific phenomena or performance metrics; these simplifications, along with degenerate forms of Eq. 3.104, will be discussed in a later chapter.

CHAPTER IV

ROTOR EQUATIONS OF MOTION

The dynamics of a mechanical face seal are inseparable from those of the rotor. Consequently, the rotordynamics must be thoroughly understood when designing a face seal or using one as a surrogate rotordynamic monitoring system. Moreover, the rotor-seal dynamic interplay is especially important regarding modern high-performance turbomachines, where improvements in efficiency are often achieved by operating flexible rotors at increased rotation rates. These changes result in heightened rotor vibration, and therefore, heightened seal vibration.

This chapter presents several rotordynamic models of varying complexity, with the objective of providing general rotor models applicable for later simulating the response of the coupled rotor-seal system (the FMSR-ER system). First, a four degree-of-freedom rotordynamic model is presented including lateral and angular deflections, viscous damping, and internal damping. The stiffness matrix is given as a general function of time to later permit time-dependent crack compliances. The model reflects realistic operating conditions by incorporating excitations caused by rotating imbalance, rotor bow, and dynamic angular misalignment. Next, two simpler models are provided; the first is the efficacious Jeffcott rotor, which accounts only for cylindrical whirl, and the second is a two degree-of-freedom model accounting only for angular rotor deflections (i.e., conical whirl). These simpler models will later be used to isolate and describe specific rotor fault vibration signatures. Finally, a numeric method for assessing rotor stability, Floquet analysis, is given which is generally applicable to dynamic systems with linear time-periodic (LTP) coefficients.

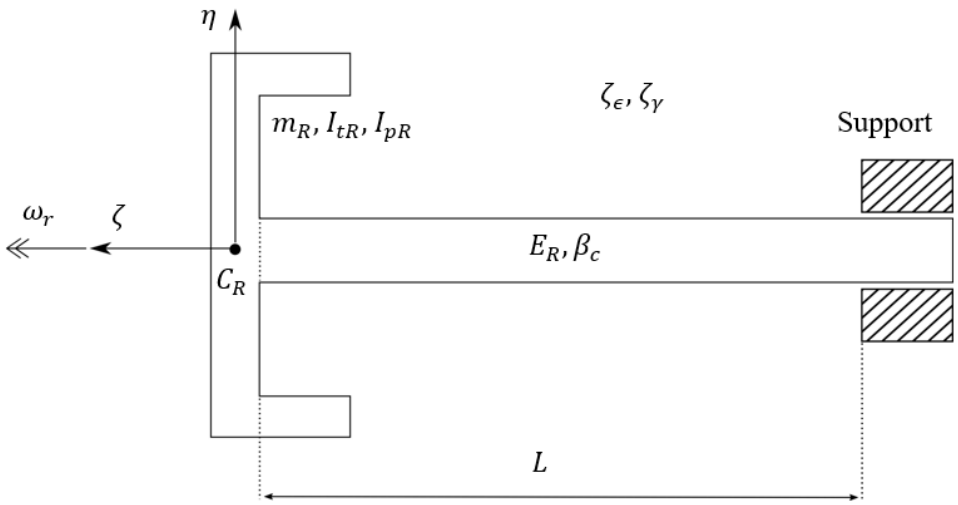

Figure 4.1: Schematic of the four degree-of-freedom rotor with overhung boundary conditions, where C_R is the geometric center of the rotor disk.

4.1 Four Degree-of-Freedom Rotordynamic Model

The four degree-of-freedom rotor model including lateral (i.e., eccentric) and angular deflections is shown schematically in Fig. 4.1. The rotor has mass m_R and transverse and polar mass moments of inertia of I_{tR} and I_{pR}, respectively. The rotor rotates about the system-fixed ζ axis with rotation rate ω_r (the system-fixed frame $\xi\eta\zeta$ is inertial when maneuver loads are ignored). Eccentric and angular deflections in the direction of axis i are denoted ϵ_{Ri} and γ_{Ri}, respectively, where the subscript 'R' distinguishes the rotor degrees-of-freedom from the seal degrees-of-freedom. Torsional and axial rotor degrees-of-freedom are not considered here.

The rotor angular momentum and acceleration are exactly analogous to those of the rotating seal element presented in Chapter 3, because the rotation and translation of both bodies obey the same kinematic constraints [20, 84, 85] (terms resulting from inertial maneuver can also be included analogously, but are omitted here for brevity). Thus, the equations of motion for the rotor only differ from those of the rotating seal element in the relevant system parameters and applied forces. Accounting for these differences, the rotor equations of motion for transient operation are:

$$\begin{bmatrix} m_R & 0 & 0 & 0 \\ 0 & m_R & 0 & 0 \\ 0 & 0 & I_{tR} & 0 \\ 0 & 0 & 0 & I_{tR} \end{bmatrix} \begin{Bmatrix} \ddot{\epsilon}_{R\xi} \\ \ddot{\epsilon}_{R\eta} \\ \ddot{\gamma}_{R\xi} \\ \ddot{\gamma}_{R\eta} \end{Bmatrix} + \left([D_R] + [D_v] + \begin{bmatrix} 0 & 0 & 0 & 0 \\ 0 & 0 & 0 & 0 \\ 0 & 0 & 0 & I_{pR}\omega_r \\ 0 & 0 & -I_{pR}\omega_r & 0 \end{bmatrix} \right) \begin{Bmatrix} \dot{\epsilon}_{R\xi} \\ \dot{\epsilon}_{R\eta} \\ \dot{\gamma}_{R\xi} \\ \dot{\gamma}_{R\eta} \end{Bmatrix}$$

$$+ \left([D_R^*] + [K(t)] + \begin{bmatrix} 0 & 0 & 0 & 0 \\ 0 & 0 & 0 & 0 \\ 0 & 0 & 0 & I_{pR}\dot{\omega}_r \\ 0 & 0 & -I_{pR}\dot{\omega}_r & 0 \end{bmatrix} \right) \begin{Bmatrix} \epsilon_{R\xi} \\ \epsilon_{R\eta} \\ \gamma_{R\xi} \\ \gamma_{R\eta} \end{Bmatrix} = \Big\{ F_R(t) \Big\} \quad (4.1)$$

Expressed in short-hand form, the equations of motion are:

$$[M_R]\{\ddot{q}_R\} + ([D_R] + [D_v] + [G_R])\{\dot{q}_R\} + ([K(t)] + [D_R^*] + [G_R^*])\{q_R\} = \{F_R(t)\} \quad (4.2)$$

The rotor degrees of freedom are likewise placed in vector form:

$$\{q_R\} = \{\epsilon_{R\xi}\ \epsilon_{R\eta}\ \gamma_{R\xi}\ \gamma_{R\eta}\}^T \quad (4.3)$$

The stiffness matrix $[K(t)]$ is left as a general function of time to accommodate the time-variant stiffness coefficients resulting from a shaft with anisotropic stiffness (as will be the case with a rotor crack). If the shaft is undamaged (i.e., isotropic), the stiffness matrix is denoted $[K_R]$, and assumes the following form:

$$[K_R] = \begin{bmatrix} k_{\epsilon\epsilon} & 0 & 0 & -k_{\epsilon\gamma} \\ 0 & k_{\epsilon\epsilon} & k_{\epsilon\gamma} & 0 \\ 0 & k_{\epsilon\gamma} & k_{\gamma\gamma} & 0 \\ -k_{\epsilon\gamma} & 0 & 0 & k_{\gamma\gamma} \end{bmatrix} \quad (4.4)$$

where the coefficients depend on geometry and material properties. The stiffness

coefficients for a symmetric undamaged overhung shaft are [85]:

$$k_{\epsilon\epsilon} = \frac{12E_R I}{L^3} \tag{4.5}$$

$$k_{\epsilon\gamma} = \frac{6E_R I}{L^2} \tag{4.6}$$

$$k_{\gamma\gamma} = \frac{4E_R I}{L} \tag{4.7}$$

where E_R is the elastic modulus, I is the cross-section area moment of inertia, and L is the shaft length. These coefficients can be easily modified to account for other shaft geometries and boundary conditions (e.g., bearing support stiffness), though this work will only consider the overhung case.

External viscous damping is included in the rotor model via the matrix $[D_v]$ to emulate the operating conditions of real turbomachines [190]. For simplicity, external viscous damping effects are assumed to be decoupled such that $[D_v]$ acquires a diagonal form. Taking this into consideration, viscous damping ratios ζ_ϵ and ζ_γ are imposed such that

$$[D_v] = 2\begin{bmatrix} \zeta_\epsilon\sqrt{k_{\epsilon\epsilon}m_R} & 0 & 0 & 0 \\ 0 & \zeta_\epsilon\sqrt{k_{\epsilon\epsilon}m_R} & 0 & 0 \\ 0 & 0 & \zeta_\gamma\sqrt{k_{\gamma\gamma}I_{tR}} & 0 \\ 0 & 0 & 0 & \zeta_\gamma\sqrt{k_{\gamma\gamma}I_{tR}} \end{bmatrix} \tag{4.8}$$

Internal damping caused by material hysteresis is encapsulated in the rotating damping matrix $[D_R]$. Here, the rotating damping matrix is proportional to the undamaged shaft stiffness $[K_R]$ by the equivalent viscous damping coefficient β_C [84, 85]:

$$[D_R] = \frac{1}{2\omega_r}\beta_C[K_R] \tag{4.9}$$

An experimental method for determining the coefficient β_C is presented by Casey and Green [84, 116], who provide an estimate of $\beta_C = 0.01$. Because the internal damping forces rotate with the shaft, the inertial frame equations incur an additional

contribution by transforming the forces to the inertial frame. The matrix $[D_R^*]$ is a consequence of this transformation:

$$[D_R^*] = [R]^T [D_R][\dot{R}] \tag{4.10}$$

where $[R]$ moves a vector from the inertial to shaft-fixed frame according to the shaft rotation angle $\alpha(t)$:

$$[R] = \begin{bmatrix} \cos\alpha & \sin\alpha & 0 & 0 \\ -\sin\alpha & \cos\alpha & 0 & 0 \\ 0 & 0 & \cos\alpha & \sin\alpha \\ 0 & 0 & -\sin\alpha & \cos\alpha \end{bmatrix} \tag{4.11}$$

Rotor excitations arise from natural and unavoidable imbalances and misalignments in the system. Specifically, the rotor center of mass may be displaced from the geometric center C_R by the eccentric imbalance ε_{RG}, while the principal axes are offset by the dynamic angular misalignment χ_R (the physical interpretation of this effect is discussed in Chapter 3). In addition, a fixed rotor bow may result from manufacturing errors, installation imperfections, or residual rotor deformation (e.g., thermoelastic deformation). The forcing function $\{F_R(t)\}$ then includes contributions from each of these effects, along with gravity:

$$\{F_R(t)\} = \begin{Bmatrix} m_R\epsilon_{RG}\big(\omega_r^2\cos\alpha + \dot{\omega}_r\sin\alpha\big) \\ m_R\epsilon_{RG}\big(\omega_r^2\sin\alpha - \dot{\omega}_r\cos\alpha\big) - m_R g \\ (I_{tR} - I_{pR})\chi_R\big(\omega_r^2\cos\alpha + \dot{\omega}_r\sin\alpha\big) \\ (I_{tR} - I_{pR})\chi_R\big(\omega_r^2\sin\alpha - \dot{\omega}_r\cos\alpha\big) \end{Bmatrix} + \{F_{rb}\} \tag{4.12}$$

The excitation caused by rotor bow is obtained by finding the inertial forces $\{F_{rb}\}$ required to induce the prescribed rotor bow. The force required to institute rotor

bow in the shaft-fixed rotating frame, assuming isotropic shaft stiffness, is:

$$\{F_{rb}\}^{rot} = [K_R] \begin{Bmatrix} r_b \cos\beta_{rb} \\ r_b \sin\beta_{rb} \\ \chi_b \cos\beta_{\chi b} \\ \chi_b \sin\beta_{\chi b} \end{Bmatrix} \tag{4.13}$$

where r_b and χ_b are the eccentric and angular magnitudes of rotor bow, with static phase orientations of β_{rb} and $\beta_{\chi b}$, respectively. The rotor bow excitation force is then transformed into the inertial $\xi\eta\zeta$ frame using Eq. 6.31:

$$\{F_{rb}\} = [R]^T \begin{bmatrix} k_{\epsilon\epsilon} & 0 & 0 & -k_{\epsilon\gamma} \\ 0 & k_{\epsilon\epsilon} & k_{\epsilon\gamma} & 0 \\ 0 & k_{\epsilon\gamma} & k_{\gamma\gamma} & 0 \\ -k_{\epsilon\gamma} & 0 & 0 & k_{\gamma\gamma} \end{bmatrix} \begin{Bmatrix} r_b \cos\beta_{rb} \\ r_b \sin\beta_{rb} \\ \chi_b \cos\beta_{\chi b} \\ \chi_b \sin\beta_{\chi b} \end{Bmatrix} \tag{4.14}$$

For the case where $\beta_{rb} = \beta_{\chi b} = 0$, the rotor bow force reduces to:

$$\{F_{rb}\} = \begin{Bmatrix} r_b k_{\epsilon\epsilon} \cos\alpha - k_{\epsilon\gamma}\chi_b \sin\alpha \\ r_b k_{\epsilon\epsilon} \sin\alpha + k_{\epsilon\gamma}\chi_b \cos\alpha \\ \chi_b k_{\gamma\gamma} \cos\alpha + k_{\epsilon\gamma} r_b \sin\alpha \\ \chi_b k_{\gamma\gamma} \sin\alpha - k_{\epsilon\gamma} r_b \cos\alpha \end{Bmatrix} \tag{4.15}$$

These equations can also be modified to account for a time-variant stiffness matrix by replacing $[K_R]$ with $[K(t)]$.

4.1.1 Free Response

The free response eigenvalue problem for the isotropic rotor (i.e., $[K(t)] = [K_R]$) is solved by inserting the following solution into the steady-state homogeneous equations of motion:

$$\bar{q}_{R0}(t) = \bar{Q}_{R0} \exp(\lambda t) \tag{4.16}$$

Performing the pertinent substitutions gives the characteristic equation for rotor free vibration:

$$|\lambda^2 M_R + \lambda(D_R + D_v + G_R) + K_R + D_R^*| = 0 \tag{4.17}$$

where the bracket notation for matrices is henceforth omitted for simplicity. Solving this equation for λ provides the generally non-synchronous whirl frequencies of the undamaged overhung rotor. It should be emphasized that this conventional procedure is only valid for the undamaged rotor.

4.1.2 Synchronous Steady-State Solution

The equations of motion for the isotropic rotor are now solved exactly for the steady-state synchronous response. At steady-state, the shaft rotation angle $\alpha(t)$ is identically equal to $\omega_r t$, which allows the following solution to be assumed:

$$\bar{q}_R(t) = \mathrm{Re}\left[\bar{Q}_R \exp\left(i\,\omega_r t\right)\right] \tag{4.18}$$

where

$$\cos(\omega_r t) = \mathrm{Re}\left[\exp\left(i\,\omega_r t\right)\right] \tag{4.19}$$

$$\sin(\omega_r t) = \mathrm{Re}\left[-i\,\exp\left(i\,\omega_r t\right)\right] \tag{4.20}$$

Inserting this solution and its derivatives into Eq. 4.2 provides the complex frequency response of the rotor:

$$\left[-\omega_r^2 M_R + i\,\omega_r\big(D_R + D_v + G_R\big) + K_R + D_R^*\right]\bar{Q}_R = \bar{F}_R(\omega_r) \tag{4.21}$$

In complex notation, the synchronous excitation magnitude is:

$$\bar{F}_R(\omega_r) = \left\{\begin{array}{c} m_R\epsilon_{RG}\omega_r^2 + r_b k_{\epsilon\epsilon} + i\,k_{\epsilon\gamma}\chi_b \\ -i\left(m_R\epsilon_{RG}\omega_r^2 + r_b k_{\epsilon\epsilon}\right) + k_{\epsilon\gamma}\chi_b \\ \left[\chi_b k_{\gamma\gamma} + (I_{tR} - I_{pR})\chi_R\omega_r^2\right] - i\,k_{\epsilon\gamma} r_b \\ -i\left[\chi_b k_{\gamma\gamma} + (I_{tR} - I_{pR})\chi_R\omega_r^2\right] - k_{\epsilon\gamma} r_b \end{array}\right\} \tag{4.22}$$

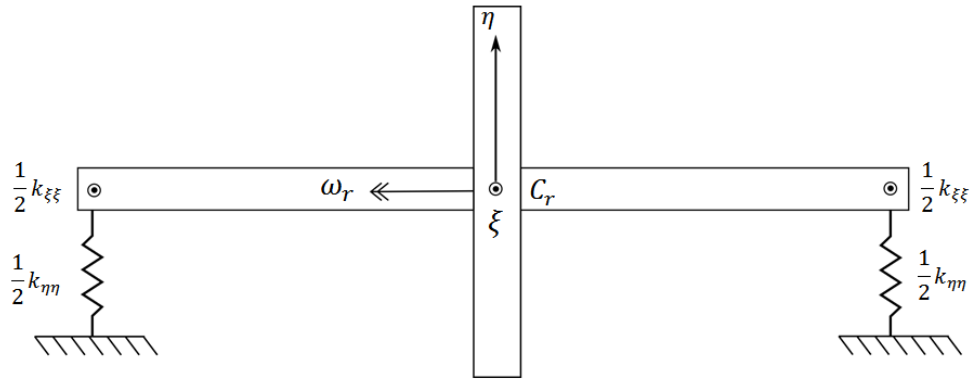

(a) Undeflected Jeffcott rotor

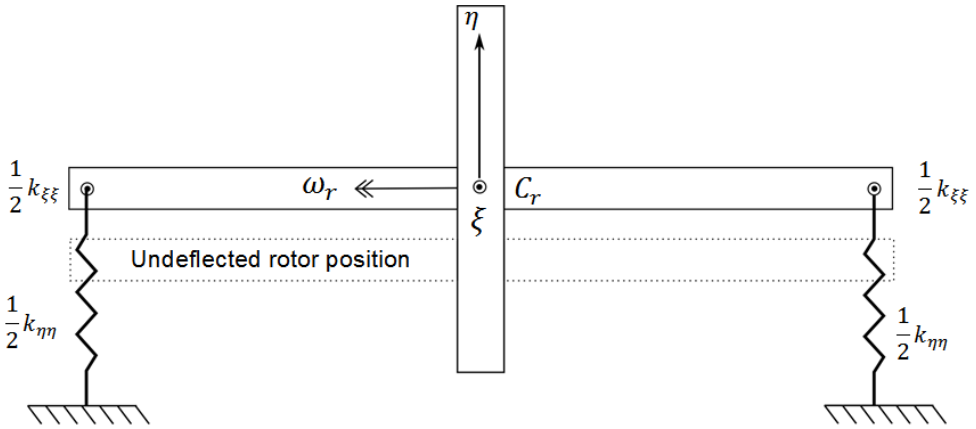

(b) Deflected Jeffcott rotor

Figure 4.2: Jeffcott rotor considering only lateral deflections.

Thus, the synchronous steady-state response magnitude is found by rearranging Eq. 4.21:

$$\bar{Q}_R = \Big[-\omega_r^2 M_R + i\,\omega_r \big(D_R + D_v + G_R\big) + K_R + D_R^* \Big]^{-1} \bar{F}_R(\omega_r) \tag{4.23}$$

This steady-state solution will later be used to efficiently study the performance of the FMSR-ER system with an undamaged rotor.

4.2 Jeffcott Rotor: Cylindrical Vibration

The Jeffcott rotor only considers lateral (i.e., eccentric) rotor deflections, which results in purely cylindrical vibration [190, 191]. A schematic of the Jeffcott rotor is

shown in Fig. 4.2. Though simple, the model allows fault-specific vibration signatures to be investigated independently from potentially complex rotordynamic interactions. In the model, the rotor and shaft mass m_R are lumped at the shaft midpoint. In this work, the shaft is assumed to be rigid and supported on flexible bearings with generally asymmetric stiffness. The direct stiffness coefficients are $k_{\xi\xi}$ and $k_{\eta\eta}$, while the coupling stiffness coefficient is denoted $k_{\xi\eta}$. The inertial frame Jeffcott rotor equations of motion, including eccentric imbalance ε_{RG}, transient operation, and gravity are [190]:

$$m_R\ddot{\epsilon}_{R\xi} + c_R\dot{\epsilon}_{R\xi} + k_{\xi\xi}\epsilon_{R\xi} + k_{\xi\eta}\epsilon_{R\eta} = m_R\varepsilon_{RG}(\omega_r^2\cos\alpha + \dot{\omega}_r\sin\alpha) \tag{4.24}$$

$$m_R\ddot{\epsilon}_{R\eta} + c_R\dot{\epsilon}_{R\eta} + k_{\eta\eta}\epsilon_{R\eta} + k_{\xi\eta}\epsilon_{R\xi} = m_R\varepsilon_{RG}(\omega_r^2\sin\alpha - \dot{\omega}_r\cos\alpha) - m_Rg \tag{4.25}$$

The damping coefficient c_R is assumed to arise from external viscous dissipation and/or support damping. In the symmetric case, it is assumed that $k_{\xi\eta} = 0$ and $k_{\xi\xi} = k_{\eta\eta} = k_R$.

4.3 Lumped Parameter Gyroscopic Rotor: Conical Vibration

The equations of motion for a rotor where only conical vibration is considered are derived by Genta [190] in a manner analogous to the methods discussed in Chapter 3:

$$I_{tR}\ddot{\gamma}_{R\xi} + I_{pR}\omega_r\dot{\gamma}_{R\eta} + c_{R\gamma}\dot{\gamma}_{R\xi} + k_{R\gamma}\gamma_{R\xi} = (I_{tR} - I_{pR})\chi_R\big(\omega_r^2\cos\alpha + \dot{\omega}_r\sin\alpha\big) \tag{4.26}$$

$$I_{tR}\ddot{\gamma}_{R\eta} - I_{pR}\omega_r\dot{\gamma}_{R\xi} + c_{R\gamma}\dot{\gamma}_{R\eta} + k_{R\gamma}\gamma_{R\eta} = (I_{tR} - I_{pR})\chi_R\big(\omega_r^2\sin\alpha - \dot{\omega}_r\cos\alpha\big) \tag{4.27}$$

The transverse and polar mass moments of inertia of the rotor are I_{tR} and I_{pR}, respectively. The external viscous damping coefficient is $c_{R\gamma}$, while the support and/or shaft stiffness is $k_{R\gamma}$. The dynamic angular misalignment of the rotor is χ_R. It is important to note that the gyroscopic terms distinguish these equations from those of the Jeffcott rotor (otherwise, the physics of cylindrical and conical whirl would

be exactly analogous, but with different parameter values). As will be seen, these equations of motion will be particularly useful for studying the effect of rotor tilt on the performance of various seal systems.

4.4 Floquet Stability

Floquet analysis is a powerful tool for determining the stability of dynamic systems with linear time-periodic coefficients. The objective here is to provide a practical method for performing Floquet stability analysis numerically; a thorough mathematical treatment of Floquet theory is provided elsewhere [192, 193]. The premise of Floquet theory is that a first-order system of linear time-periodic (LTP) differential equations with fundamental period T can be rewritten such that

$$\bar{X}(t+T) = \mathbf{\Phi}\bar{X}(t) \tag{4.28}$$

where the matrix $\mathbf{\Phi}$ is called the monodromy matrix, and represents a Poincaré map that updates the solution $\bar{X}$ at time t to the solution at time $t+T$. The objective is to determine if this mapping indicates convergence or divergence of the solution following a perturbation from the steady-state limit cycle. In general, however, the matrix $\mathbf{\Phi}$ is not directly (i.e., analytically) obtainable. To obtain $\mathbf{\Phi}$, assume that a periodic solution $\bar{q}_0(t)$ exists with fundamental period T, and then introduce a perturbation $\Delta\bar{q}$:

$$\bar{q}(t) = \bar{q}_0(t) + \Delta\bar{q}(t) \tag{4.29}$$

Inserting this disturbance and its derivatives into Eq. 4.2 results in the autonomous perturbation equations for the overhung rotor:

$$M_R\Delta\ddot{\bar{q}}_R + (D_R + D_v + G_R)\Delta\dot{\bar{q}}_R + (K(t) + D_R^*)\Delta\bar{q}_R = 0 \tag{4.30}$$

where matrix notation has been dropped for brevity. In first-order state space, the perturbation equations of motion are:

$$\dot{\bar{x}} = \mathbf{A}(t)\bar{x} \tag{4.31}$$

where the state vector is

$$\bar{x} = [\Delta\bar{q} \quad \Delta\dot{\bar{q}}]^T \tag{4.32}$$

The perturbation state space equations are now used to find the monodromy matrix $\mathbf{\Phi}$. The fundamental period T is divided into N intervals with length Δt, such that $T = N\Delta t$. Thus, if the number of intervals is large, the state matrix $\mathbf{A}(t)$ can be assumed constant over Δt, which then allows the equations to be integrated numerically over each finite interval. The initial conditions are assumed to be unity without loss of generality [192]. The numeric integration transfers the state at time t_i to the state at time $t_{i+1} = t_i + \Delta t$:

$$\bar{x}(t_{i+1}) = \mathbf{T}_i\bar{x}(t_i) \tag{4.33}$$

Thus, the monodromy matrix is the successive product of all the interval transfer matrices:

$$\mathbf{\Phi} = \mathbf{T}_N \ldots \mathbf{T}_{i+1}\mathbf{T}_i\mathbf{T}_{i-1} \ldots \mathbf{T}_1\mathbf{T}_0 \tag{4.34}$$

Here, the specific form of the transfer matrix $\mathbf{T}_i$ is found by integrating the state-space equations of motion using the Newmark-Beta method, according to the procedure established by Guilhen et al. [194]:

$$\mathbf{T}_i = \begin{bmatrix} \mathbf{B}_0 & \mathbf{B}_1 \\ 2(\mathbf{B}_0 - \mathbf{I})/\Delta t & 2\mathbf{B}_1/\Delta t - \mathbf{I} \end{bmatrix} \tag{4.35}$$

where $\mathbf{I}$ is the identity matrix and

$$\begin{aligned} \mathbf{B}_0 &= 4\mathbf{D}_0^{-1}M_R/\Delta t \\ \mathbf{B}_1 &= \mathbf{D}_0^{-1}\left(4M_R/\Delta t^2 + 2C/\Delta t - K_i\right) \\ \mathbf{D}_0 &= 4M_R/\Delta t^2 + 2C/\Delta t + K_{i+1} \end{aligned} \tag{4.36}$$

Damping and gyroscopic effects are described using a single matrix:

$$C = D_R + D_v + G_R \tag{4.37}$$

These matrices can be modified if the damping matrix is also linear time-periodic (such a condition is not encountered in this work). Stability is then determined by finding the eigenvalues of $\mathbf{\Phi}$, which in this context are the Floquet multipliers λ_f:

$$|\mathbf{\Phi} - \lambda_f \mathbf{I}| = 0 \tag{4.38}$$

These multipliers determine the local orbital convergence or divergence of the solution following one iteration of the minimal period T. The solution $\bar{x}(t)$ is asymptotically stable if the modulus of every λ_f is less than unity, which guarantees the existence of a stable limit cycle (i.e., periodic attractor). That is, any perturbation from the limit cycle results in the solution returning to the limit cycle. On the other hand, the solution is divergent (i.e., unstable) if the modulus of any Floquet multiplier is greater than unity.

Floquet analysis is essential for determining the stability of linear time-periodic systems where the coordinate transformation resulting in constant-coefficient equations is unknown. Earlier works show that a gaping crack results in rotor equations of motion with constant-coefficient equations in the shaft-fixed reference frame. Consequently, stability can also be assessed in the rotating frame using a classical eigenvalue analysis. In other cases, however, such as a breathing shaft crack, the stiffness matrix is periodic even in the shaft-fixed frame, thus precluding a conventional stability analysis.

CHAPTER V

DEGENERATE FORMS OF THE SYSTEM EQUATIONS OF MOTION

The inertial frame equations of motion for the FMSR seal were derived in Chapter 3, and include axial, angular, and eccentric degrees-of-freedom for both seal elements. In addition, the model permits coupled rotordynamics, transient operation, and inertial maneuver loads. Several accompanying rotordynamic models were then presented in Chapter 4. As a reminder, the seal system including eccentric deflections and coupled rotordynamics is referred to as the FMSR-ER seal.

The FMSR-ER equations of motion presented earlier represent a powerful tool for analyzing many different aspects of seal performance. However, the objective of this work is to employ mechanical seal vibration to identify hallmark vibration signatures for several rotor faults. To this end, it will be advantageous to reduce the previously-given equations of motion to several simpler forms. These simpler models can then be used to isolate and investigate specific phenomena associated with certain faults and/or operating conditions. Specifically, this chapter considers the following simpler conditions and systems:

1. **Simplified fluid and contact reactions**: Simplified expressions for healthy seal operation (i.e., small relative misalignments) will reduce computation time.

2. **FMS seal equations of motion**: The reduced FMS seal models will be advantageous for investigating seal face contact and seal-rotor interactions.

3. **Reduced FMSR-ER equations of motion**: The steady-state FMSR-ER equations will later be used to study surrogate rotor fault detection.

5.1 Simplifying the Applied Forces and Moments

The total applied forces and moments on the FMSR-ER seal caused by contact, friction, fluid pressure, and fluid shear are found by combining the integrands in Eqs. 3.39 - 3.41, Eqs. 3.52 - 3.54, and Eqs. 3.64 - 3.67:

$$M^A_{s\xi} = \int_{r_i}^{r_o}\int_0^{2\pi}\Big\{(P_f+P_c)\big(r\sin\theta-\epsilon^*_\eta\big) - \left(\mu_f P_c + \frac{\mu\omega_r r}{h}\right)\big(\gamma_{s\eta}\cos\theta-\gamma_{s\xi}\sin\theta\big)r\cos\theta\Big\}rdrd\theta \tag{5.1}$$

$$M^A_{s\eta} = \int_{r_i}^{r_o}\int_0^{2\pi}\Big\{(P_f+P_c)\big(\epsilon^*_\xi-r\cos\theta\big) - \left(\mu_f P_c + \frac{\mu\omega_r r}{h}\right)\big(\gamma_{s\eta}\cos\theta-\gamma_{s\xi}\sin\theta\big)r\sin\theta\Big\}rdrd\theta \tag{5.2}$$

$$F^A_{s\zeta} = \int_{r_i}^{r_o}\int_0^{2\pi}\big(P_f+Pc\big)rdrd\theta \tag{5.3}$$

$$F^A_{s\xi} = \int_{r_i}^{r_o}\int_0^{2\pi}\left(\frac{\mu_f P_c}{\omega_r}+\frac{\mu r}{h}\right)\big(\dot\epsilon^*_\xi+r\omega_r\sin\theta\big)drd\theta \tag{5.4}$$

$$F^A_{s\eta} = \int_{r_i}^{r_o}\int_0^{2\pi}\left(\frac{\mu_f P_c}{\omega_r}+\frac{\mu r}{h}\right)\big(\dot\epsilon^*_\eta-r\omega_r\cos\theta\big)drd\theta \tag{5.5}$$

$$M^A_{r\xi} = \int_{r_i}^{r_o}\int_0^{2\pi}\Big\{\left(\mu_f P_c + \frac{\mu\omega_r r}{h}\right)\big(\gamma_{r\eta}\cos\theta-\gamma_{r\xi}\sin\theta\big)r\cos\theta - (P_f+P_c)r\sin\theta\Big\}rdrd\theta \tag{5.6}$$

$$M^A_{r\eta} = \int_{r_i}^{r_o}\int_0^{2\pi}\Big\{\left(\mu_f P_c + \frac{\mu\omega_r r}{h}\right)\big(\gamma_{r\eta}\cos\theta-\gamma_{r\xi}\sin\theta\big)r\sin\theta + (P_f+P_c)r\cos\theta\Big\}rdrd\theta \tag{5.7}$$

$$\tag{5.8}$$

where

$$F^A_{r\zeta} = -F^A_{s\zeta} \tag{5.9}$$

$$F^A_{r\xi} = -F^A_{s\xi} \tag{5.10}$$

$$F^A_{r\eta} = -F^A_{s\eta} \tag{5.11}$$

The superscript 'A' signifies that these are the total applied forces caused by fluid effects and seal face contact.

Seal face contact is unlikely except in unusual situations (e.g., poor seal design) because the seal is designed to minimize relative tilt between the faces. Therefore, it is reasonable to neglect seal face contact when simulating the FMSR-ER system to identify rotor fault signatures (i.e., proper seal design is a prerequisite for using the seal as a surrogate rotor vibration monitor). The applied forces without seal face contact are:

$$M_{s\xi}^A = \int_{r_i}^{r_o} \int_0^{2\pi} \left\{ P_f\big(r\sin\theta - \epsilon_\eta^*\big) - \frac{\mu\omega_r r}{h}\big(\gamma_{s\eta}\cos\theta - \gamma_{s\xi}\sin\theta\big) r\cos\theta \right\} r\,dr\,d\theta \tag{5.12}$$

$$M_{s\eta}^A = \int_{r_i}^{r_o} \int_0^{2\pi} \left\{ P_f\big(\epsilon_\xi^* - r\cos\theta\big) - \frac{\mu\omega_r r}{h}\big(\gamma_{s\eta}\cos\theta - \gamma_{s\xi}\sin\theta\big) r\sin\theta \right\} r\,dr\,d\theta \tag{5.13}$$

$$F_{s\zeta}^A = \int_{r_i}^{r_o} \int_0^{2\pi} P_f r\,dr\,d\theta \tag{5.14}$$

$$F_{s\xi}^A = \int_{r_i}^{r_o} \int_0^{2\pi} \frac{\mu r}{h}\big(\dot\epsilon_\xi^* + r\omega_r\sin\theta\big)\,dr\,d\theta \tag{5.15}$$

$$F_{s\eta}^A = \int_{r_i}^{r_o} \int_0^{2\pi} \frac{\mu r}{h}\big(\dot\epsilon_\eta^* - r\omega_r\cos\theta\big)\,dr\,d\theta \tag{5.16}$$

$$M_{r\xi}^A = \int_{r_i}^{r_o} \int_0^{2\pi} \left\{ \frac{\mu\omega_r r}{h}\big(\gamma_{r\eta}\cos\theta - \gamma_{r\xi}\sin\theta\big) r\cos\theta - P_f r\sin\theta \right\} r\,dr\,d\theta \tag{5.17}$$

$$M_{r\eta}^A = \int_{r_i}^{r_o} \int_0^{2\pi} \left\{ \frac{\mu\omega_r r}{h}\big(\gamma_{r\eta}\cos\theta - \gamma_{r\xi}\sin\theta\big) r\sin\theta + P_f r\cos\theta \right\} r\,dr\,d\theta \tag{5.18}$$

$$F_{r\zeta}^A = -F_{s\zeta}^A \tag{5.19}$$

$$F_{r\xi}^A = -F_{s\xi}^A \tag{5.20}$$

$$F_{r\eta}^A = -F_{s\eta}^A \tag{5.21}$$

5.1.1 Simplifying the Fluid Shear Moments

The general form for the moment caused by fluid shear is

$$M_\mu = \int_{r_i}^{r_o} \int_0^{2\pi} \frac{\mu\omega_r}{h}\big(\gamma_{s\eta}\cos\theta - \gamma_{s\xi}\sin\theta\big)\cos\theta \Big\} r^3\,dr\,d\theta \tag{5.22}$$

where the subscript 'μ' denotes that only fluid shear is considered. Imposing the narrow seal assumption, i.e., assuming that $r = r_m$, gives:

$$M_\mu = \mu\omega_r r_m^3 \int_{r_i}^{r_o} \int_0^{2\pi} \frac{\gamma_{s\eta}\cos\theta - \gamma_{s\xi}\sin\theta}{h}\cos\theta dr d\theta \tag{5.23}$$

In general, the film thickness can be written:

$$h(r,\theta) = C + \gamma^* r\sin(\theta - \psi^*) + \beta(r - r_i) \tag{5.24}$$

where the asterisk denotes relative seal face deflections, as given in Eqs. 3.113 and 3.114. The effects of coning and tilt will be considered separately to address their phenomenological effect on the fluid shear moments. The objective of considering these effects separately is not to obtain separate contributions whose sum comprises the total fluid shear moment, but rather to identify the effects that do not meaningfully contribute to the fluid shear moments.

The contribution from only relative tilt to the fluid shear moments is derived here. In this case, recognizing that $dh = \gamma^*\sin(\theta - \psi^*)dr$, the integral is posed in the following form:

$$M_\mu = \mu\omega_r r_m^3 \int_0^{2\pi} \frac{\gamma_{s\eta}\cos\theta - \gamma_{s\xi}\sin\theta}{\gamma^*\sin(\theta - \psi^*)}\cos\theta\left(\int_{h_i}^{h_o}\frac{dh}{h}\right)d\theta \tag{5.25}$$

Peforming the integration on h and substituting in the general form of Eq. 5.24 gives:

$$M_\mu = \mu\omega_r r_m^3 \int_0^{2\pi} \frac{\gamma_{s\eta}\cos\theta - \gamma_{s\xi}\sin\theta}{\gamma^*\sin(\theta - \psi^*)}\ln\left(\frac{C + \gamma^* r_o\sin(\theta - \psi^*)}{C + \gamma^* r_i\sin(\theta - \psi^*)}\right)\cos\theta d\theta \tag{5.26}$$

Now, the logarithm quotient is expanded into a subtraction and replaced by its Taylor series about $\gamma^* = 0$, which assumes that the relative tilt γ^* is small (this assumption is reasonable, since contact typically occurs if the relative tilt exceeds several milliradians). The result is:

$$M_\mu = \mu\omega_r r_m^3 \int_0^{2\pi} \frac{\gamma_{s\eta}\cos\theta - \gamma_{s\xi}\sin\theta}{\gamma^*\sin(\theta - \psi^*)}\left\{\frac{\gamma^* r_o\sin(\theta - \psi^*)}{C} - \frac{(\gamma^* r_o\sin(\theta - \psi^*))^2}{2C^2} - \frac{\gamma^* r_i\sin(\theta - \psi^*)}{C} + \frac{(\gamma^* r_i\sin(\theta - \psi^*))^2}{2C^2}\right\}\cos\theta d\theta \tag{5.27}$$

Expanding terms and simplifying gives:

$$M_\mu = \mu\omega_r r_m^3 (r_o - r_i) \int_0^{2\pi} \left(\gamma_{s\eta}\cos\theta - \gamma_{s\xi}\sin\theta\right)\left\{\frac{1}{C} - \frac{\gamma^*(r_o - r_i)\sin(\theta - \psi^*)}{2C^2}\right\}\cos\theta d\theta \tag{5.28}$$

The first term integrates to zero because of 2π periodicity over the circumferential integral. The second term in the bracket is proportional to $\gamma^*\gamma_i$, and therefore only contributes second-order effects. It can easily be shown that when considering only coning, the integral is once again zero because of 2π-periodicity. This analysis indicates that neglecting fluid shear moments is a reasonable assumption when simulating the undamaged seal dynamics for normal operating conditions.

5.2 FMS Equations of Motion

The FMS and FMR seal configurations have been studied extensively in the literature, which therefore makes the FMS seal a useful benchmark for studying seal face contact apart from the complexity imposed by the FMSR-ER seal. The equations of motion of the FMS seal are obtained from the FMSR-ER equations of motion given in Chapter 3 by eliminating the rotating seal element deflections and ignoring inertial maneuver loads. The FMS equations of motion, without considering eccentric deflections, are:

$$I_{ts}\ddot{\gamma}_{s\xi} + D_s\dot{\gamma}_{s\xi} + K_s\gamma_{s\xi} = K_s\gamma_{si,\xi} + M^A_{s\xi} \tag{5.29}$$

$$I_{ts}\ddot{\gamma}_{s\eta} + D_s\dot{\gamma}_{s\eta} + K_s\gamma_{s\eta} = K_s\gamma_{si,\eta} + M^A_{s\eta} \tag{5.30}$$

$$m_s\ddot{u}_{sz} + D_{sz}\dot{u}_{sz} + K_{sz}u_{sz} = F_\zeta - F_{cls} \tag{5.31}$$

where the applied forces and moments are given in Section 5.1. The rotating seal element tilt γ_r is assumed to be constant, and thus, the film thickness expression becomes

$$h(r,\theta) = C_o + u_{sz} + \gamma_s r\sin(\theta - \psi_s) - \gamma_r r\sin\left(\theta - \alpha(t)\right) + \beta(r - r_i) \tag{5.32}$$

where

$$\gamma_s^2 = \gamma_{s\xi}^2 + \gamma_{s\eta}^2 \tag{5.33}$$

$$\psi_s = \tan^{-1}\left(\frac{\gamma_{s\eta}}{\gamma_{s\xi}}\right) \tag{5.34}$$

These FMS equations of motion will later be used to investigate fundamental aspects of seal face contact. Also, the FMSR-ER equations of motion can also be used to provide the equations of motion for the FMR seal configuration, though this configuration is not studied in this work.

5.3 FMS-R Steady-State Equations of Motion

The nature of the dynamic coupling between the seal and rotor has important implications for studying seal-rotor interactions. If the rotor influences the seal dynamics but not vice versa, then the rotordynamics can be solved separately and sent to the seal dynamic analyses as an external input. This aspect of rotor-seal coupling will be investigated later for the case where the FMS seal is coupled to the conical (angular) rotordynamics; this simplified situation permits an exact solution of the equations of motion following linearization of the fluid film forces. To reiterate, the FMS and rotor are designated with subscripts 's' and 'R', respectively. Retaining previous nomenclature, this coupled rotor-seal system will be referred to as the FMS-R seal.

The equations of motion of the FMS are given above in Eqs. 5.29 - 5.31. The rotor equations of motion, accounting only for conical vibration, are given in Chapter 4 and repeated here:

$$I_{tR}\ddot{\gamma}_{R\xi} + I_{pR}\omega_r\dot{\gamma}_{R\eta} + c_{R\gamma}\dot{\gamma}_{R\xi} + k_{R\gamma}\gamma_{R\xi} = M_\xi + (I_{tR} - I_{pR})\chi_R\big(\omega_r^2\cos\alpha + \dot{\omega}_r\sin\alpha\big) \tag{5.35}$$

$$I_{tR}\ddot{\gamma}_{R\eta} - I_{pR}\omega_r\dot{\gamma}_{R\xi} + c_{R\gamma}\dot{\gamma}_{R\eta} + k_{R\gamma}\gamma_{R\eta} = M_\eta + (I_{tR} - I_{pR})\chi_R\big(\omega_r^2\sin\alpha - \dot{\omega}_r\cos\alpha\big) \tag{5.36}$$

where the fluid film moments are:

$$M_\xi = \int_0^{2\pi} \int_{r_i}^{r_o} P_f r^2 \sin\theta \, dr \, d\theta \tag{5.37}$$

$$M_\eta = -\int_0^{2\pi} \int_{r_i}^{r_o} P_f r^2 \cos\theta \, dr \, d\theta \tag{5.38}$$

These fluid moments appear directly in the rotor equations of motion because the rotating seal element is commensurate with the rotor in this simplified case.

5.3.1 Linearized Equations of Motion

Solving the equations of motion for the FMS-R requires multiple integrations of the fluid pressure at each simulation time step. Though valid over a wide range of parameters, these numeric integrations are tedious and inhibit a comprehensive parametric investigation of seal-rotor coupling. Several assumptions can be applied to reduce the fluid film forces and moments to stiffness and damping coefficients. The first is that the seal is narrow, which is true for most practical face seals [19]. The second assumption is that the seal experiences only small deflections (angular and axial) about a steady operational state. This assumption is reasonable here because (a) the seal is balanced, and (b) only parameters avoiding seal face contact are considered. The final assumption is that the hydrostatic pressure is sufficient to suppress cavitation.

The fluid film stiffness and damping coefficients, K_f and D_f, are found analytically by Wileman and Green [52]. An important conclusion from their work is that linearizing about a stable operating mode decouples the angular and axial degrees of freedom. Since the shaft axial stiffness is typically large, and the seal is assumed to be balanced, the axial linearized equation of motion will not be considered here. These linearized fluid film stiffness and damping coefficients are

$$K_f = \pi(P_o - P_i)(\tilde{\beta} R_i - 1) E_o^2 \frac{r_o^4}{C_o} \tag{5.39}$$

$$D_f = 2\pi R_m^3 G_o \frac{S r_o^4}{C_o \omega_r} \tag{5.40}$$

where

$$S = 6\mu\omega_r \left(\frac{r_o}{C_o}\right)^2 (1 - R_i^2) \tag{5.41}$$

$$E_o = \frac{(1 - R_i)R_m}{2 + \tilde{\beta}(1 - R_i)} \tag{5.42}$$

$$G_o = \frac{\ln(1 + \tilde{\beta}(1 - R_i)) - \dfrac{2\tilde{\beta}(1 - R_i)}{2 + \tilde{\beta}(1 - R_i)}}{\tilde{\beta}^3(1 - R_i)^2} \tag{5.43}$$

Normalized terms in the above expressions are given by $R = r/r_o$ and $\tilde{\beta} = \beta r_o/C_o$. These fluid film coefficients are then used to express the fluid forces and moments [52]. In matrix form, the steady-state linearized equations of motion for the FMS-R seal are:

$$\begin{bmatrix} I_{ts} & 0 & 0 & 0 \\ 0 & I_{ts} & 0 & 0 \\ 0 & 0 & I_{tR} & 0 \\ 0 & 0 & 0 & I_{tR} \end{bmatrix} \begin{Bmatrix} \ddot{\gamma}_{s\xi} \\ \ddot{\gamma}_{s\eta} \\ \ddot{\gamma}_{R\xi} \\ \ddot{\gamma}_{R\eta} \end{Bmatrix} + \begin{bmatrix} D_s + D_f & 0 & -D_f & 0 \\ 0 & D_s + D_f & 0 & -D_f \\ -D_f & 0 & D_R + D_f & I_{pR}\omega_r \\ 0 & -D_f & -I_{pR}\omega_r & D_R + D_f \end{bmatrix} \begin{Bmatrix} \dot{\gamma}_{s\xi} \\ \dot{\gamma}_{s\eta} \\ \dot{\gamma}_{R\xi} \\ \dot{\gamma}_{R\eta} \end{Bmatrix}$$

$$+ \begin{bmatrix} K_s + K_f & \frac{1}{2}D_f\omega_r & -K_f & -\frac{1}{2}D_f\omega_r \\ -\frac{1}{2}D_f\omega_r & K_s + K_f & \frac{1}{2}D_f\omega_r & -K_f \\ -K_f & -\frac{1}{2}D_f\omega_r & k_R + K_f & \frac{1}{2}D_f\omega_r \\ \frac{1}{2}D_f\omega_r & -K_f & -\frac{1}{2}D_f\omega_r & k_R + K_f \end{bmatrix} \begin{Bmatrix} \gamma_{s\xi} \\ \gamma_{s\eta} \\ \gamma_{R\xi} \\ \gamma_{R\eta} \end{Bmatrix}$$

$$= \begin{Bmatrix} K_s\gamma_{si,\xi} \\ K_s\gamma_{si,\eta} \\ \left[(I_{tR} - I_{pR})\chi_R\omega_r^2 + k_R\chi_b\right]\cos\omega_r t \\ \left[(I_{tR} - I_{pR})\chi_R\omega_r^2 + k_R\chi_b\right]\sin\omega_r t \end{Bmatrix} \tag{5.44}$$

where the rotor forcing function includes dynamic angular misalignment χ_R and static angular misalignment χ_b (i.e., angular deflection from rotor bow). In short-hand matrix form, these equations are:

$$[M_{sr}]\{\ddot{q}\} + [D_{sr}]\{\dot{q}\} + [K_{sr}]\{q\} = \{F_{sr}(t)\} \tag{5.45}$$

where

$$\{q_{sr}\} = \{\gamma_{s\xi} \quad \gamma_{s\eta} \quad \gamma_{R\xi} \quad \gamma_{R\eta}\}^T \tag{5.46}$$

These linear ordinary differential equations are solved analytically to provide a closed-form steady-state solution from which general trends in seal behavior can be expediently extracted. The system's whirl frequencies λ are found from the linearized equations of motion by setting the forcing terms equal to zero and inserting a solution $\bar{A}\exp(\lambda t)$. This procedure yields the characteristic equation whose roots are the generally non-synchronous whirl frequencies:

$$\Delta(\lambda, \omega_r) = \det\left(\lambda^2[M_{sr}] + \lambda[D_{sr}] + [K_{sr}]\right) = 0 \tag{5.47}$$

Likewise, the steady-state synchronous response is found by assuming a solution $\bar{\Gamma}\exp(i\omega_r t)$ and inserting the solution into Eq. 5.45. The steady-state solution will later be used to expediently extract the system response for a range of parameters.

5.4 FMSR-E: Reduced Steady State Equations of Motion

The mechanisms that transmit vibration between the rotating and stationary seal elements elements are vital for determining the efficacy of using mechanical face seal monitoring systems as surrogate rotordynamic vibration monitoring systems. Consequently, the steady-state performance of the undamaged FMSR-ER seal will provide a framework for interpreting transmitted rotordynamic vibration signatures. Ignoring inertial maneuver loads, moments caused by fluid shear, and seal face contact, the steady-state equations of motion for the FMSR-ER system are:

$$I_{ts}\ddot{\gamma}_{s\xi} + D_s\dot{\gamma}_{s\xi} + K_s\gamma_{s\xi} = K_s\gamma_{si,\xi} + M^A_{s\xi} \tag{5.48}$$

$$I_{ts}\ddot{\gamma}_{s\eta} + D_s\dot{\gamma}_{s\eta} + K_s\gamma_{s\eta} = K_s\gamma_{si,\eta} + M^A_{s\eta} \tag{5.49}$$

$$m_s\ddot{u}_{sz} + D_{sz}\dot{u}_{sz} + K_{sz}u_{sz} = F^A_{s\zeta} - F_{cls} \tag{5.50}$$

$$m_s\ddot{\epsilon}_{s\xi} + D_{s\epsilon}\dot{\epsilon}_{s\xi} + K_{s\epsilon}\epsilon_{s\xi} = F^A_{s\xi} \tag{5.51}$$

$$m_s\ddot{\epsilon}_{s\eta} + D_{s\epsilon}\dot{\epsilon}_{s\eta} + K_{s\epsilon}\epsilon_{s\eta} = F^A_{s\eta} - m_s g \tag{5.52}$$

and

$$I_{tr}\ddot{\gamma}_{r\xi} + I_{pr}\omega_r\dot{\gamma}_{r\eta} + D_r(\dot{\gamma}_{r\xi} - \dot{\gamma}_{R\xi}) + K_r(\gamma_{r\xi} - \gamma_{R\xi}) + \omega_r D_r(\gamma_{r\eta} - \gamma_{R\eta}) = M^A_{r\xi}$$
$$+ (I_{tr} - I_{pr})\,\chi\omega_r^2\cos(\omega_r t + \beta_{r\chi}) + K_r\chi_s\cos(\omega_r t + \beta_{r\chi_s}) \quad (5.53)$$

$$I_{tr}\ddot{\gamma}_{r\eta} - I_{pr}\omega_r\dot{\gamma}_{r\xi} + D_r(\dot{\gamma}_{r\eta} - \dot{\gamma}_{R\eta}) + K_r(\gamma_{r\eta} - \gamma_{R\eta}) - \omega_r D_r(\gamma_{r\xi} - \gamma_{R\xi}) = M^A_{r\eta}$$
$$+ (I_{tr} - I_{pr})\,\chi\omega_r^2\sin(\omega_r t + \beta_{r\chi}) + K_r\chi_s\sin(\omega_r t + \beta_{r\chi_s}) \quad (5.54)$$

$$m_r\ddot{u}_{rz} + D_{rz}(\dot{u}_{rz} - \dot{u}_{Rz}) + K_{rz}(u_{rz} - u_{Rz}) = F^A_{r\zeta} + F_{cls} \quad (5.55)$$

$$m_r\ddot{\epsilon}_{r\xi} + D_{r\epsilon}(\dot{\epsilon}_{r\xi} - \dot{\epsilon}_{R\xi}) + K_{r\epsilon}(\epsilon_{r\xi} - \epsilon_{R\xi}) = F^A_{r\xi} + m_r\varepsilon_{rG}\omega_r^2\cos(\omega_r t + \beta_r) \quad (5.56)$$

$$m_r\ddot{\epsilon}_{r\eta} + D_{r\epsilon}(\dot{\epsilon}_{r\eta} - \dot{\epsilon}_{R\eta}) + K_{r\epsilon}(\epsilon_{r\eta} - \epsilon_{R\eta}) = F^A_{r\eta} + m_r\varepsilon_{rG}\omega_r^2\sin(\omega_r t + \beta_r) - m_r g \quad (5.57)$$

where the applied forces due to fluid pressure, fluid shear, contact pressure, and friction are provided in Eqs. 5.12 - 5.21. The rotor equations of motion are provided in Chapter 3. Furthermore, the seal coning at steady-state is assumed to be constant; i.e., thermoelastic deformations of the seal can be neglected.

CHAPTER VI

DEVELOPING THE CRACK MODEL

The first step in developing a condition monitoring system capable of identifying incipient rotor cracks is understanding the physical nature of the crack. Towards this end, a rotor crack most fundamentally represents a reduction in rotor stiffness (or, equivalently, an increase in compliance). This chapter first presents a method for quantifying the additional compliance contributed by a fully-open shaft crack using the strain energy release rate. Then, the method is expanded to incorporate rotation-dependent crack breathing behavior. Finally, an expedient approach is presented for incorporating the time-dependent crack compliance into the global FMSR-ER numeric simulation.

6.1 Gaping Cracks

The simplest approach for modeling rotordynamic cracks is to assume that the crack faces always remain open. In this case, the cracked shaft compliance is constant in a shaft-fixed reference frame [140]. As discussed in Chapter 2, open cracks are typically modeled as either finite-width notches or true fatigue cracks. This work primarily concerns true fatigue cracks, whereas earlier works [85, 93, 110] provide a method for calculating the compliance of a finite-width notch.

The overhung rotor displaying a transverse fatigue crack is shown in Fig. 6.1, where the crack is located a distance L_1 from the support (and thus, the rotor is located a distance L_2 from the crack, where $L = L_1 + L_2$). The depth of the crack is a, and the crack half-width is b (see Fig. 6.2b). Because the crack remains open, the crack compliance and shaft stiffness are constant relative to the shaft-fixed $X_R Y_R Z_R$ reference frame, where Z_R signifies the shaft rotation direction. The crack compliance

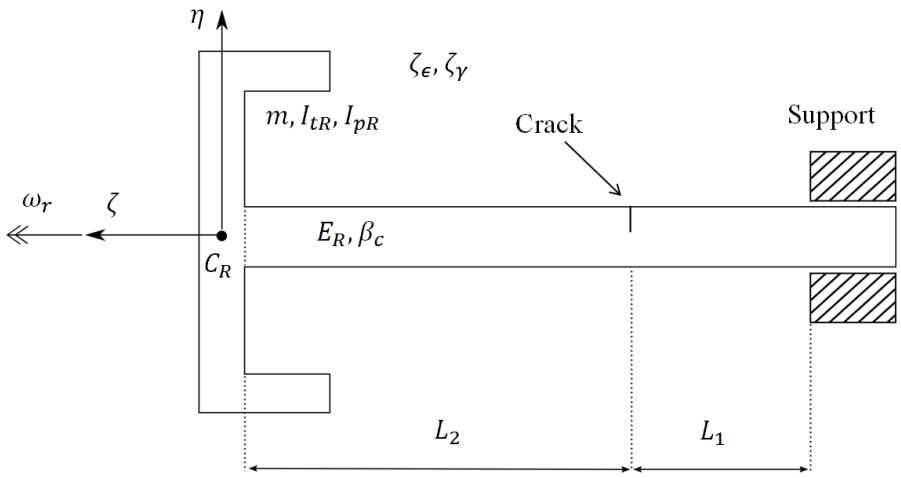

Figure 6.1: Schematic of the overhung rotor showing a gaping fatigue crack and the inertial reference frame $\xi\eta\zeta$.

is often found using the strain energy release rate (SERR) [92]. The SERR is a scalar quantity that depends on several factors, including the rotor material properties, the crack geometry, and the loading conditions imposed on the crack. In general, the strain energy release rate $J(A)$ is [82]:

$$J(A) = \frac{1-\nu^2}{E_R}\left[\left(\sum_{i=1}^{6} K_{Ii}\right)^2 + \left(\sum_{i=1}^{6} K_{IIi}\right)^2 + \left(\sum_{i=1}^{6} K_{IIIi}\right)^2\right] \tag{6.1}$$

where A denotes the crack area. The strain energy of the crack u_c is then found by integrating Eq. 6.1 over the total crack area:

$$u_c = \int_A J(A)dA \tag{6.2}$$

The stress intensity factors K_{ni} define the stress amplitude at the crack tip singularity [101,195]. The subscript i denotes the direction of the applied load, while the subscript n indicates the mode of crack formation. In general, for mode n, the stress intensity factor is given by

$$K_{ni} = \sigma_i\sqrt{\pi\alpha}F_n\left(\frac{\alpha}{h}\right) \quad \text{n = I, II, or III} \tag{6.3}$$

where F_n is a general intensity function that depends on the mode of crack formation, and σ_i represents the stress at the crack (the stresses are given in detail by Darpe et

al. [134]). The quantities α and h are shown in Fig. 6.2b. Solutions for these stress intensity factors are only available for rectangular regions; to find the compliance introduced by a cracked shaft with circular cross-section, the crack area must be divided into many narrow rectangular regions over which the stress intensity factors are known. The strain energy u_c^{dx} incurred over one such narrow rectangular region is

$$u_c^{dx} = \frac{\partial}{\partial P_i} \int_0^a J(y) dy \tag{6.4}$$

where the SERR is only a function of y because the rectangular region is narrow. Now, Eq. 6.4 is integrated across the crack width to obtain the complete crack strain energy u_c. Castigliano's theorem then gives the compliance in the i^{th} direction due to a force in the j^{th} direction:

$$c_{ij} = \frac{\partial^2 u_c}{\partial P_i \partial P_j} = \frac{\partial^2}{\partial P_i \partial P_j} \int_{-b}^{b} \int_0^a J(y) dy dx \tag{6.5}$$

The crack compliances are now arranged into a local compliance matrix [82] that relates the additional deflections caused by the crack to the applied loads:

$$\begin{Bmatrix} \epsilon_{X_R} \\ \epsilon_{Y_R} \\ \gamma_{X_R} \\ \gamma_{Y_R} \end{Bmatrix} = \begin{bmatrix} c_{22} & 0 & 0 & 0 \\ 0 & c_{33} & 0 & 0 \\ 0 & 0 & c_{55} & c_{45} \\ 0 & 0 & c_{45} & c_{44} \end{bmatrix} \begin{Bmatrix} F_{X_R} \\ F_{Y_R} \\ M_{X_R} \\ M_{Y_R} \end{Bmatrix} \tag{6.6}$$

where F and M are forces and moments relative to the specified direction. Though the crack also influences the axial and torsional deflections, these compliances are not considered here because axial and torsional deflections have previously been neglected in the FMSR-ER system dynamics. Performing the integrations results in the

following crack compliances [92]:

$$c_{22} = \frac{2\left(1-\nu^2\right)}{\pi E_R R} \int_{-\bar{b}}^{\bar{b}} \int_{0}^{\bar{\alpha}} \bar{y} F_{III}^2 \left(\frac{y}{h}\right) d\bar{y} d\bar{x} \tag{6.7}$$

$$c_{33} = \frac{2\left(1-\nu^2\right)}{\pi E_R R} \int_{-\bar{b}}^{\bar{b}} \int_{0}^{\bar{\alpha}} \bar{y} F_{II}^2 \left(\frac{y}{h}\right) d\bar{y} d\bar{x} \tag{6.8}$$

$$c_{44} = \frac{16\left(1-\nu^2\right)}{\pi E_R R^3} \int_{-\bar{b}}^{\bar{b}} \int_{0}^{\bar{\alpha}} \bar{x}^2 \bar{y} F_{IY}^2 \left(\frac{y}{h}\right) d\bar{y} d\bar{x} \tag{6.9}$$

$$c_{45} = \frac{16\left(1-\nu^2\right)}{\pi E_R R^3} \int_{-\bar{b}}^{\bar{b}} \int_{0}^{\bar{\alpha}} \bar{x} \bar{y} \sqrt{1-\bar{x}^2} F_{IX} \left(\frac{y}{h}\right) F_{IY} \left(\frac{y}{h}\right) d\bar{y} d\bar{x} \tag{6.10}$$

$$c_{55} = \frac{32\left(1-\nu^2\right)}{\pi E_R R^3} \int_{-\bar{b}}^{\bar{b}} \int_{0}^{\bar{\alpha}} \bar{y} \left(1-\bar{x}^2\right) F_{IX}^2 \left(\frac{y}{h}\right) d\bar{y} d\bar{x} \tag{6.11}$$

where

$$F_{IX}\left(\frac{y}{h}\right) = \left[\frac{\tan\beta_0}{\beta_0}\right]^{1/2} \left[0.932 + 0.199(1-\sin\beta_0)^4\right] / \cos\beta_0 \tag{6.12}$$

$$F_{IY}\left(\frac{y}{h}\right) = \left[\frac{\tan\beta_0}{\beta_0}\right]^{1/2} \left[0.752 + 2.02\left(\frac{y}{h}\right) + 0.37(1-\sin\beta_0)^3\right] / \cos\beta_0 \tag{6.13}$$

$$F_{II}\left(\frac{y}{h}\right) = \left[1.122 - 0.561\left(\frac{y}{h}\right) + 0.085\left(\frac{y}{h}\right)^2 + 0.18\left(\frac{y}{h}\right)^3\right] / \left(1-\frac{y}{h}\right)^{1/2} \tag{6.14}$$

$$F_{III}\left(\frac{y}{h}\right) = \left[\frac{\tan\beta_0}{\beta_0}\right]^{1/2} \tag{6.15}$$

and

$$\beta_0 = \frac{\pi y}{2h} \tag{6.16}$$

An overbar indicates variables that have been normalized by the shaft radius R. The subscripts on the crack compliances are retained relative to previous works [84,85,92] to maintain consistency. The crack compliance terms are then normalized according

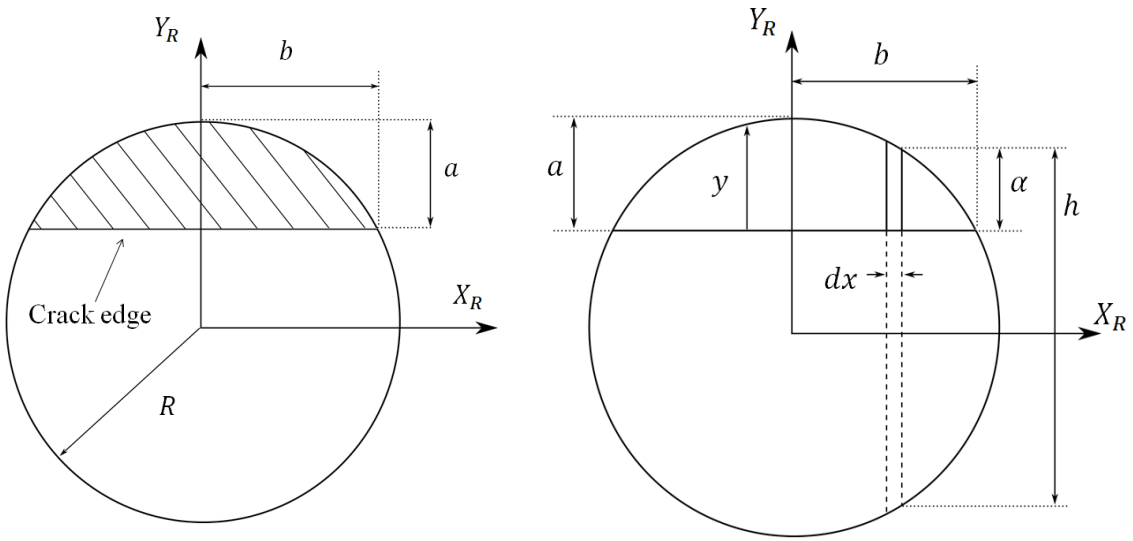

(a) Crack half-width b and depth a

(b) Quantities used to calculate the compliance using the strain energy release rate.

Figure 6.2: Crack cross-section schematic relative to the shaft-fixed $X_R Y_R Z_R$ reference frame.

to the following relations:

$$\bar{c}_{22} = \frac{\pi E_R R}{(1-\nu^2)} c_{22} \tag{6.17}$$

$$\bar{c}_{33} = \frac{\pi E_R R}{(1-\nu^2)} c_{33} \tag{6.18}$$

$$\bar{c}_{44} = \frac{\pi E_R R^3}{(1-\nu^2)} c_{44} \tag{6.19}$$

$$\bar{c}_{45} = \frac{\pi E_R R^3}{(1-\nu^2)} c_{45} \tag{6.20}$$

$$\bar{c}_{55} = \frac{\pi E_R R^3}{(1-\nu^2)} c_{55} \tag{6.21}$$

The crack compliances are typically accurate for crack depths up to 80% of the shaft diameter [92]. Previous works have calculated the cross-coupling coefficient c_{45} by integrating over half of the crack width (i.e., 0 to b) and doubling the result [84, 85]. However, integrating over the full crack width, $-b$ to b, indicates that c_{45} is zero when the crack is fully open. This conclusion has also been validated by other researchers [83, 134].

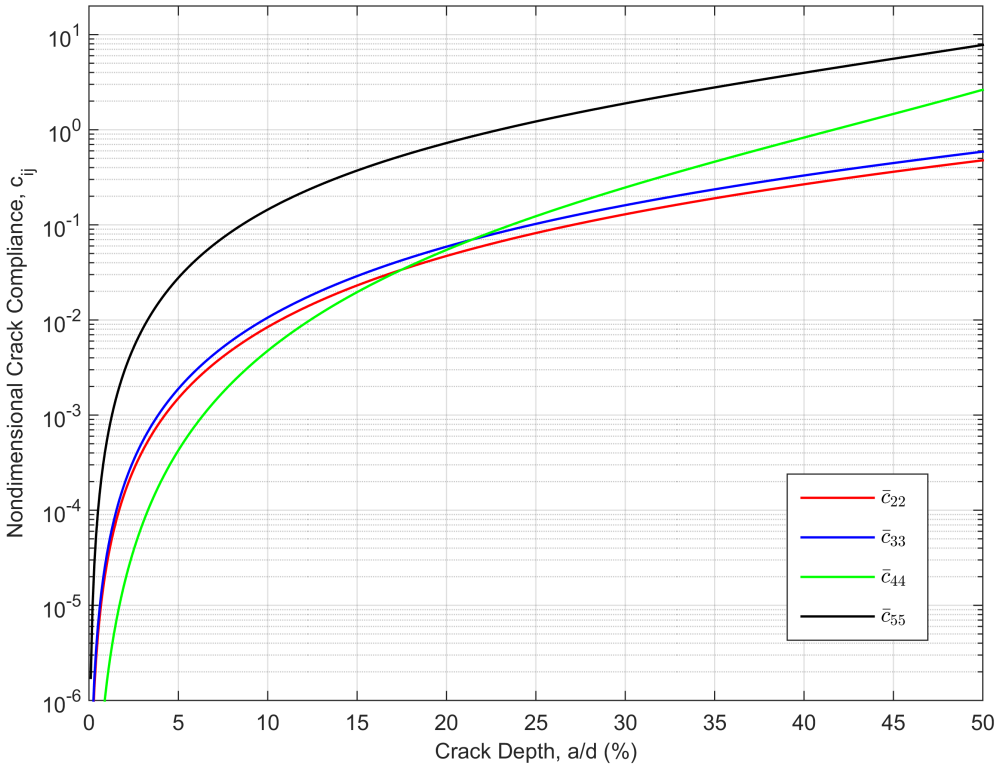

Figure 6.3: Non-dimensional crack compliances for a gaping fatigue crack ($E_R = 210$ GPa, $\nu = 0.3$, d = 35 mm).

The non-dimensional crack compliances (Eqs. 6.17 - 6.21) are found via numeric integration and shown in Fig. 6.3. The results are corroborated versus the representative values provided in reference [196]. Note that singularities are present in Eqs. 6.12 - 6.15, as discussed by Papadopolous [196]. These singularities are avoided by ending the numeric integration prior to the singularity (i.e., before y is equal to h).

The global compliance matrix of the cracked shaft relative to the shaft-fixed frame has previously been obtained using the transfer matrix [93, 110]:

$$[C]_{rot} = \begin{bmatrix} C_{11} & -c_{45}L_2^2 & c_{45}L_2 & C_{14} \\ -c_{45}L_2^2 & C_{22} & C_{23} & -c_{45}L_2 \\ c_{45}L_2 & C_{32} & C_{33} & c_{45} \\ C_{41} & -c_{45}L_2 & c_{45} & C_{44} \end{bmatrix} \tag{6.22}$$

where

$$C_{11} = c_{22} + c_{44}L_2^2 + \frac{(L_1+L_2)^3}{3E_RI} \tag{6.23}$$

$$C_{22} = c_{33} + c_{55}L_2^2 + \frac{(L_1+L_2)^3}{3E_RI} \tag{6.24}$$

$$C_{33} = c_{55} + \frac{(L_1+L_2)}{E_RI} \tag{6.25}$$

$$C_{44} = c_{44} + \frac{(L_1+L_2)}{E_RI} \tag{6.26}$$

and

$$C_{14} = C_{41} = c_{44}L_2 + \frac{(L_1+L_2)^2}{2E_RI} \tag{6.27}$$

$$C_{23} = C_{32} = -c_{55}L_2 - \frac{(L_1+L_2)^2}{2E_RI} \tag{6.28}$$

Recalling that the coupling compliance coefficient c_{45} is zero for an open crack, the local compliance matrix reduces to the following form:

$$[C]_{\text{rot}} = \begin{bmatrix} C_{11} & 0 & 0 & C_{14} \\ 0 & C_{22} & C_{23} & 0 \\ 0 & C_{32} & C_{33} & 0 \\ C_{41} & 0 & 0 & C_{44} \end{bmatrix} \tag{6.29}$$

Importantly, and necessarily, removing the crack compliances reduces the global compliance matrix to that of an Euler-Bernoulli beam of length $L_1 + L_2$, as expected. The stiffness matrix of the overall cracked shaft in the shaft-fixed reference frame is obtained by inverting Eq. 6.22:

$$[K]_{\text{rot}} = [C]_{\text{rot}}^{-1} \tag{6.30}$$

For the general case of transient operation ($\omega_r = \omega_r(t)$), the shaft rotation angle is $\alpha(t)$. Thus, a vector in the $\xi\eta\zeta$ frame is expressed in the shaft-fixed $X_RY_RZ_R$ frame

via the following rotation transformation:

$$[R] = \begin{bmatrix} \cos\alpha & \sin\alpha & 0 & 0 \\ -\sin\alpha & \cos\alpha & 0 & 0 \\ 0 & 0 & \cos\alpha & \sin\alpha \\ 0 & 0 & -\sin\alpha & \cos\alpha \end{bmatrix} \tag{6.31}$$

Using this coordinate transformation, the stiffness matrix in the inertial (or, system-fixed) reference frame $\xi\eta\zeta$ is:

$$[K(t)] = [R]^T [C]^{-1}_{\text{rot}} [R] \tag{6.32}$$

Expanding this expression is tedious, and thus, the details are omitted here. Still, the general form of the inertial stiffness matrix arising from the gaping fatigue crack is

$$[K(t)] = [K_0] + [K_c]\cos(2\alpha) + [K_s]\sin(2\alpha) \tag{6.33}$$

The inertial frame stiffness thus varies twice per revolution. To understand this conclusion intuitively, consider the cases where the crack is oriented upward (i.e., $Y_R = \eta$) and downward (i.e., $Y_R = -\eta$). Both orientations result in identical cracked shaft stiffness coefficients; thus, the stiffness of any coefficient varies twice per revolution. In the presence of gravity, or any other fixed-direction inertial force, the deflection also varies twice per revolution because the crack orientation changes with respect to the excitation direction. However, in the case of only synchronous excitation, though, such as imbalance, the excitation is fixed relative to the crack orientation, and therefore does not induce a twice-per-revolution frequency.

The direct stiffness coefficients (i.e., the diagonal elements of $[K(t)]$) are calculated for representative parameters to emphasize the innate observation that a gaping crack constitutes strictly 2X higher harmonics of the shaft speed. In both cases, the direct stiffness coefficients are normalized by those of the undamaged shaft, and displayed in Fig. 6.4. Importantly, it is clear that the stiffness varies twice per revolution; this

is corroborated by examining the frequency content of the direct stiffness coefficients, which once again indicates the exclusive presence of a 2X harmonic. Furthermore, the normalized maximum value of any cracked shaft stiffness coefficient never reaches or eclipses unity because the crack always remains open.

6.2 Breathing Cracks

In reality, the faces of a fatigue crack open and close as portions of the crack alternate between tension and compression. Previous approaches for modeling crack breathing behavior have been discussed in Chapter 2, and can be categorized into three groups: switching cracks, shaft-weight dominant cracks, and response-dependent cracks. Crack breathing is inherently smooth because the crack cannot instantly transition between the fully closed and fully open states; modeling such a behavior results in rotordynamic responses that are not observed in practice. For example, the switching crack model predicts chaotic rotor vibration, which has not observed been observed in real cracked rotors [136]. The other approaches are qualitatively similar because they predict only integer shaft speed harmonics (pX) at steady-state. The response-dependent crack model requires a significant investment of computational resources because the compliances must be found via numeric integration at each simulation time step. In addition, the model assumes that the crack edge is straight, homogeneous, and measurable. These assumptions likely mitigate improvements in accuracy realized via response-dependent crack models. Consequently, this work uses a crack breathing model where the crack compliances vary harmonically with shaft rotation according to a known function (i.e., the rotor static response dictates the breathing behavior). This simplification is acceptable here because the objective is to demonstrate that mechanical seals can be used to characterize rotor faults.

Two methods for implementing crack breathing are discussed here. The first method is simpler, and assumes that each crack compliance given in Eqs. 6.7 - 6.11

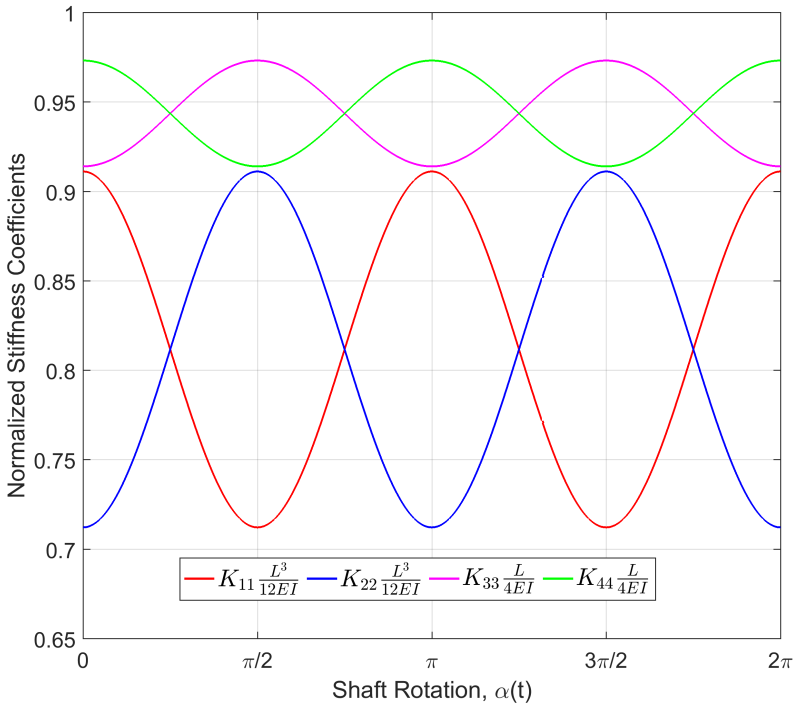

(a) Direct stiffness coefficients versus shaft rotation angle $\alpha(t)$

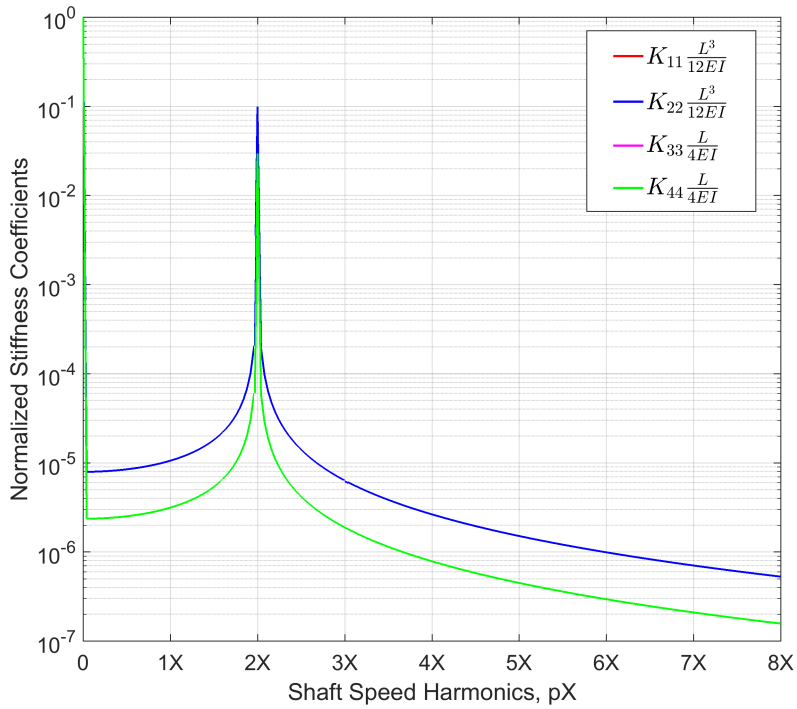

(b) Frequency content of the direct stiffness coefficients (note that the content is identical in the pairs $K_{11,22}$ and $K_{33,44}$)

Figure 6.4: Observations regarding the time-variant stiffness of an overhung shaft displaying a gaping fatigue crack ($a/d = 40\%$, $E_R = 210$ GPa, $\nu = 0.3$, $d = 35$ mm, $L = 250$ mm, $L_1 = 0.05\ L$).

varies according to a single harmonic function. In the second case, the crack compliances are found via the crack closure line (CCL) approach [134], where the bounds over which the crack is open are determined by the respective stress intensity functions. Then, the compliances are found by integrating only over the open crack region. Both methods assume that the static response dominates the breathing so that the compliances can be entirely expressed over one shaft rotation.

6.2.1 Breathing Crack Method 1: Single Sinusoid Approach

This simple approach assumes that the compliances vary according to a single harmonic function. The crack is completely open when $\alpha(t) = 0$, and completely closed when $\alpha(t) = \pi$. It is assumed that the crack does not contribute compliance when it is fully-closed. Because the crack initially faces upwards (i.e., in the η direction), each compliance in the shaft-fixed rotating frame $X_R Y_R Z_R$ is:

$$c_{ij} = \frac{1}{2}\big[1 + \cos\alpha(t)\big](c_{ij})_o \tag{6.34}$$

where the subscript o denotes the compliance for the completely-opened scenario.

This approach is problematic for two reasons. The first issue is that the method only scales the coefficients generated by the open crack according to a function that is assigned independently from the crack strain energy. Specifically, the coupling coefficient c_{45} is zero only when the crack is fully open (or fully closed) because the integrand in Eq. 6.10 is anti-symmetric across the integral domain. Once the crack begins to close, the integrand is no longer anti-symmetric, and the resultant integral is no longer zero. However, scaling the coefficients sinusoidally provides no mechanism for quantifying c_{45}. The second problem with this approach is that it assumes the crack is fully open or fully closed for only a single value of $\alpha(t)$ (0 and π for the open and closed states, respectively). In reality, however, the crack remains fully open or fully closed for a finite interval of rotation in which the crack is entirely contained within a region of complete tension or compression, respectively.

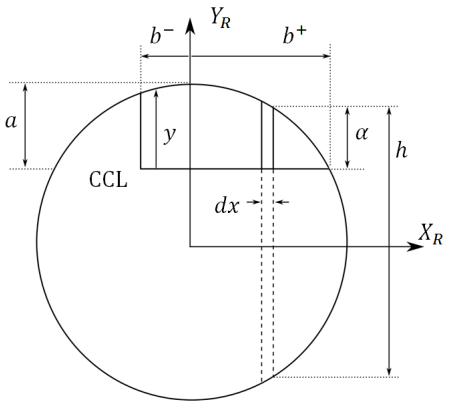

Figure 6.5: Crack cross-section showing the CCL and the crack boundaries.

6.2.2 Breathing Crack Method 2: Modified Crack Closure Line

The aforementioned inconsistencies are rectified by using a breathing model that depends on fracture mechanics in lieu of heuristics. The method presented here is derived from the crack closure line (CCL) approach presented by Darpe et al. [134]. The CCL signifies the boundary between the open and closed regions of the crack; the crack compliances are then obtained by integrating across only the open region:

$$c_{22} = \frac{2\left(1-\nu^2\right)}{\pi E_R R} \int_{-\bar{b}^-}^{\bar{b}^+} \int_{0}^{\bar{\alpha}} \bar{y} F_{III}^2 \left(\frac{y}{h}\right) d\bar{y} d\bar{x} \tag{6.35}$$

$$c_{33} = \frac{2\left(1-\nu^2\right)}{\pi E_R R} \int_{-\bar{b}^-}^{\bar{b}^+} \int_{0}^{\bar{\alpha}} \bar{y} F_{II}^2 \left(\frac{y}{h}\right) d\bar{y} d\bar{x} \tag{6.36}$$

$$c_{44} = \frac{16\left(1-\nu^2\right)}{\pi E_R R^3} \int_{-\bar{b}^-}^{\bar{b}^+} \int_{0}^{\bar{\alpha}} \bar{x}^2 \bar{y} F_{IY}^2 \left(\frac{y}{h}\right) d\bar{y} d\bar{x} \tag{6.37}$$

$$c_{45} = \frac{16\left(1-\nu^2\right)}{\pi E_R R^3} \int_{-\bar{b}^-}^{\bar{b}^+} \int_{0}^{\bar{\alpha}} \bar{x} \bar{y} \sqrt{1-\bar{x}^2} F_{IX} \left(\frac{y}{h}\right) F_{IY} \left(\frac{y}{h}\right) d\bar{y} d\bar{x} \tag{6.38}$$

$$c_{55} = \frac{32\left(1-\nu^2\right)}{\pi E_R R^3} \int_{-\bar{b}^-}^{\bar{b}^+} \int_{0}^{\bar{\alpha}} \bar{y} \left(1-\bar{x}^2\right) F_{IX}^2 \left(\frac{y}{h}\right) d\bar{y} d\bar{x} \tag{6.39}$$

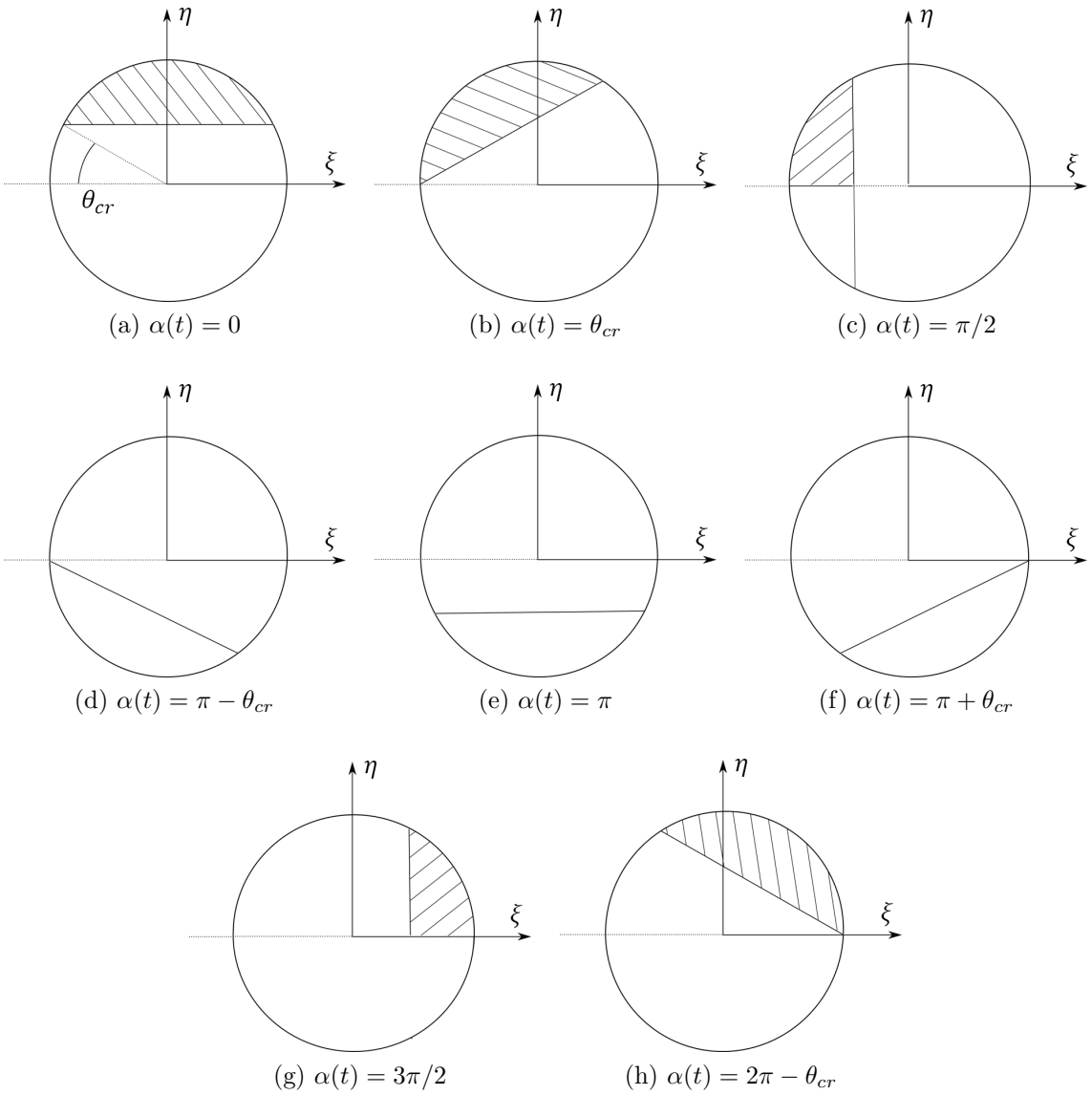

(a) $\alpha(t) = 0$ (b) $\alpha(t) = \theta_{cr}$ (c) $\alpha(t) = \pi/2$

(d) $\alpha(t) = \pi - \theta_{cr}$ (e) $\alpha(t) = \pi$ (f) $\alpha(t) = \pi + \theta_{cr}$

(g) $\alpha(t) = 3\pi/2$ (h) $\alpha(t) = 2\pi - \theta_{cr}$

Figure 6.6: Crack breathing behavior for various orientations, where gravity acts in the negative η direction. Shading indicates open regions of the crack.

where $\bar{b}^-$ and $\bar{b}^+$ signify the normalized lower and upper bounds of the open region. These terms, along with the CCL, are shown in Fig. 6.5. The CCL position is specified by the bounds b^- and b^+, which are determined by evaluating the stress intensity function for the first mode of crack opening, K_I, at every point along the outer crack edge (modes II and III do not meaningfully contribute to crack breathing [134]). Here, only the rotor weight is assumed to contribute significantly to the crack breathing behavior (i.e., the rotor speed is beneath the first critical speed), though this assumption could be relaxed in future works at the expense of computational expediency. The stress intensity functions depend on the local axial stresses σ_i at the crack, the shape functions given in Eqs. 6.12 and 6.13, and the crack geometry. The stresses, in turn, depend on the internal bending moments generated by the rotor weight. The total stress intensity function K_I at location x along the outer crack edge, where x is a local coordinate that extends along the crack edge, is found by summing the stress intensity functions caused by moments about X_R and Y_R:

$$K_I = K_{I,\,X_R} + K_{I,\,Y_R} \tag{6.40}$$

This approach is permissible because the stress intensity functions are scalar quantities. Using the expressions for stress provided by previous researchers [92, 134] and evaluating the moments at the crack cross section caused by the rotor weight in the rotating frame gives the following forms for $K_{I,\,X_R}$ and $K_{I,\,Y_R}$:

$$K_{I,\,X_R} = \frac{4(m_R g \cos\alpha) L_2}{\pi R^4} \sqrt{R^2 - x^2} \sqrt{\pi y} F_{IX}(y/h) \tag{6.41}$$

$$K_{I,\,Y_R} = -\frac{4(m_R g \sin\alpha) L_2}{\pi R^4} x \sqrt{\pi y} F_{IY}(y/h) \tag{6.42}$$

The location where K_I changes from negative to positive denotes the location where the crack cross-section changes from closed to open. This location is a function of angular position $\alpha(t)$ because gravity is a rotating force in the rotor-fixed $X_R Y_R Z_R$ frame.

This approach rectifies the conceptual problems associated with the pure-sinusoidal breathing approach because it permits c_{45} to be calculated and accounts for the finite range of rotation over which the crack remains fully-open or fully-closed. These regions are shown in Fig. 6.6 for several representative values of shaft rotation $\alpha(t)$. The region over which the crack remains fully-open or fully-closed is defined by the angle θ_{cr}:

$$\theta_{cr} = \tan^{-1}\left(\frac{R-a}{b}\right) \tag{6.43}$$

where b is the half-width of the fully-open crack (see Fig. 6.2b). Thus, the crack remains fully-open for $-\theta_{cr} < \alpha(t) < \theta_{cr}$ and fully-closed for $\pi - \theta_{cr} < \alpha(t) < \pi + \theta_{cr}$.

The breathing crack compliances are calculated over a range of crack depths for representative parameters and provided in Figs. 6.7 - 6.9. The direct compliances increase monotonically with crack depth for a given rotor orientation, while the coupling coefficient c_{45} switches sign once $\alpha = \pi$ is reached. In all cases, the crack compliances are equal to the gaping crack compliances when the crack is fully-open and are zero when the crack is fully closed.

The objective for calculating the crack compliances is to simulate the cracked rotordynamics in the time domain. Evaluating the integrals contained in Eqs. 6.35 - 6.39 is computationally expensive. Moreover, integrating the compliances over a single rotation $\alpha = 0 \rightarrow 2\pi$ and interpolating at each time instant is not only computationally expensive, but also introduces small but non-negligible error into the compliance calculations (and thus, the numeric simulation). Because the compliance calculations are 2π-periodic, they can be expressed as a sum of complex exponentials with fundamental period 2π. Recognizing this, the fast Fourier transform is calculated for each compliance

$$c_{ij}(t) \xrightarrow{\mathscr{F}} C_{ij}(\omega) \tag{6.44}$$

and then used to reconstruct an expedient analytic expression that can be used in

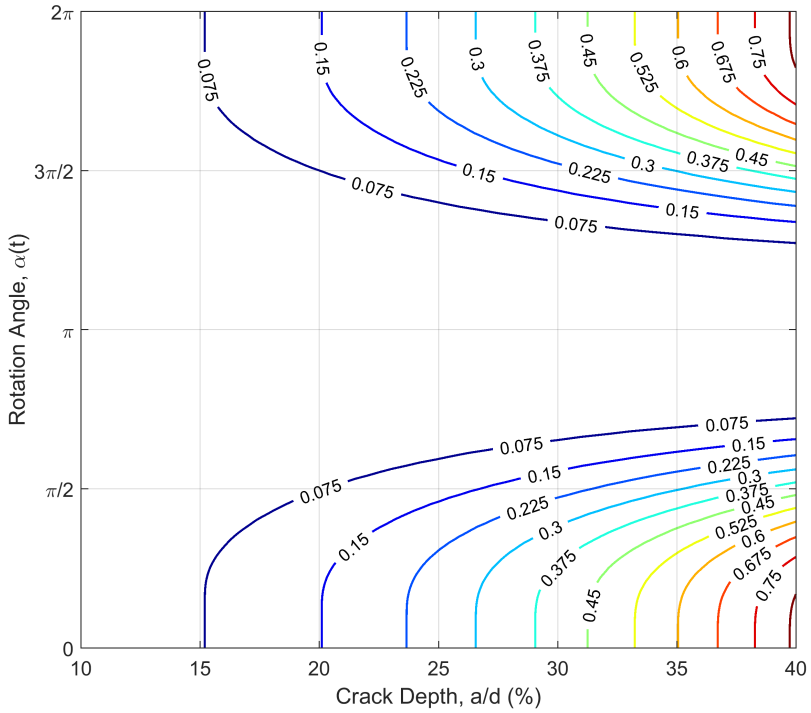

(a) $\bar{c}_{22}$

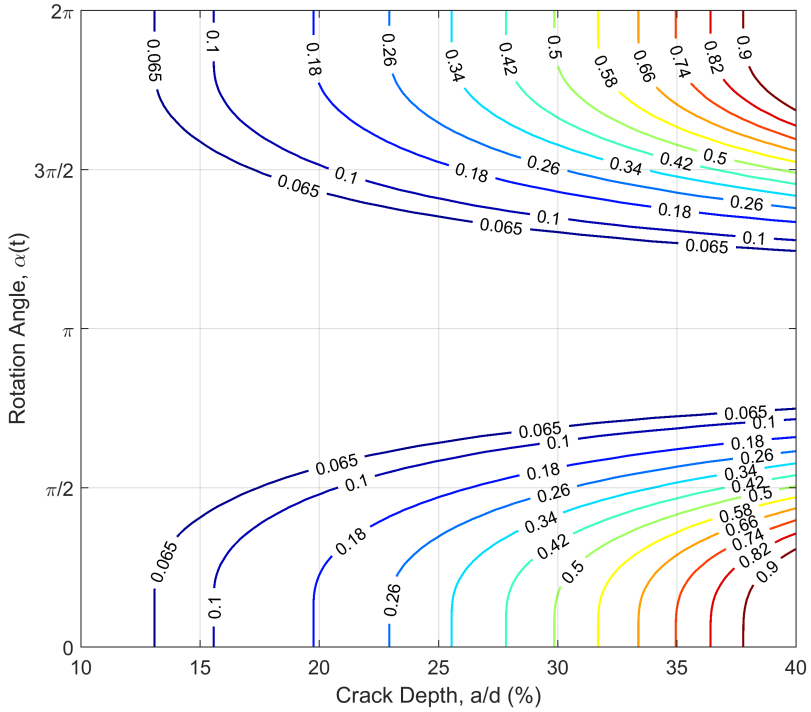

(b) $\bar{c}_{33}$

Figure 6.7: Non-dimensional eccentric crack compliances versus crack depth and shaft rotation ($E_R = 210$ GPa, $\nu = 0.3$, $d = 35$ mm, $L = 250$ mm, $L_1 = 0.05\ L$).

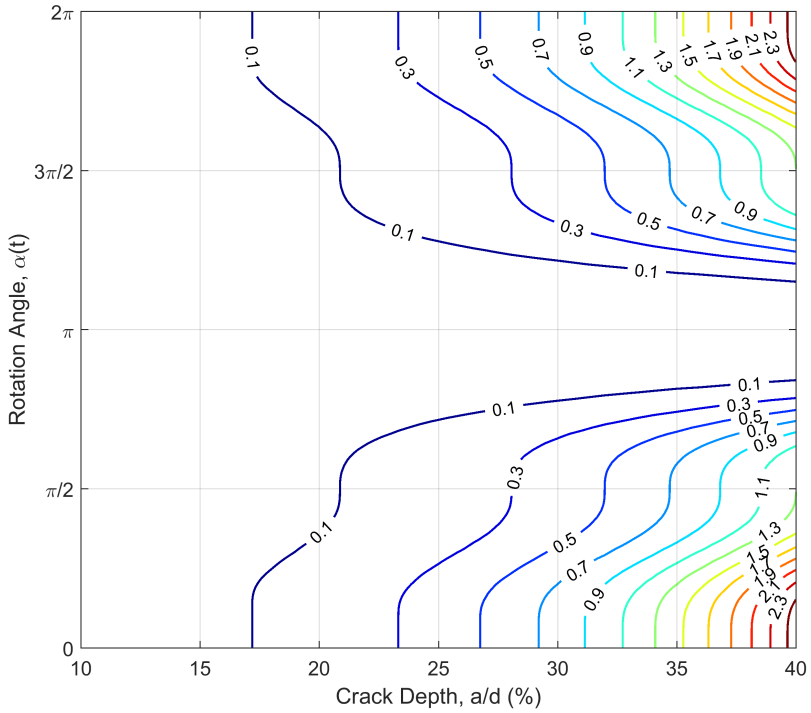

(a) $\bar{c}_{44}$

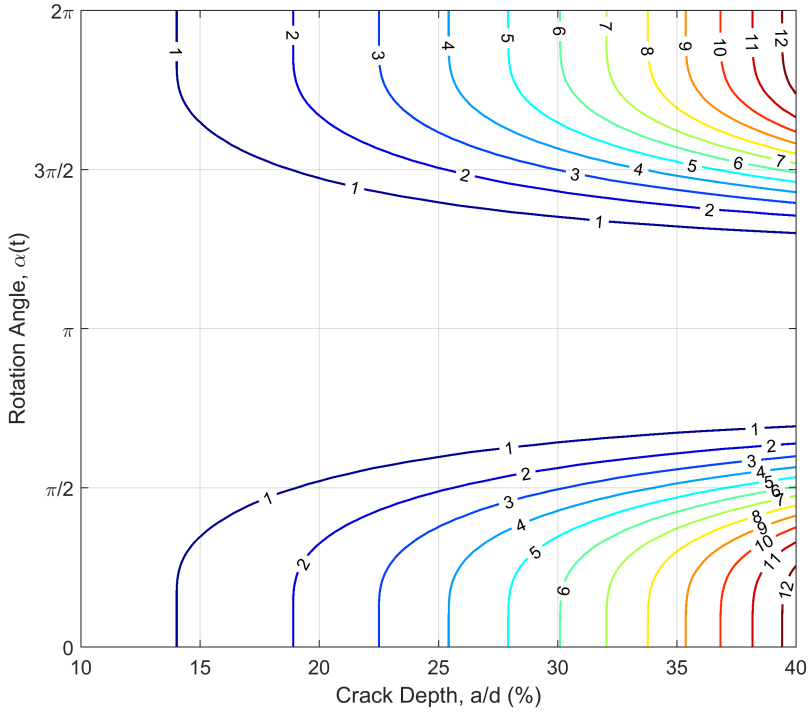

(b) $\bar{c}_{55}$

Figure 6.8: Non-dimensional angular crack compliances versus crack depth and shaft rotation ($E_R = 210$ GPa, $\nu = 0.3$, $d = 35$ mm, $L = 250$ mm, $L_1 = 0.05\ L$).

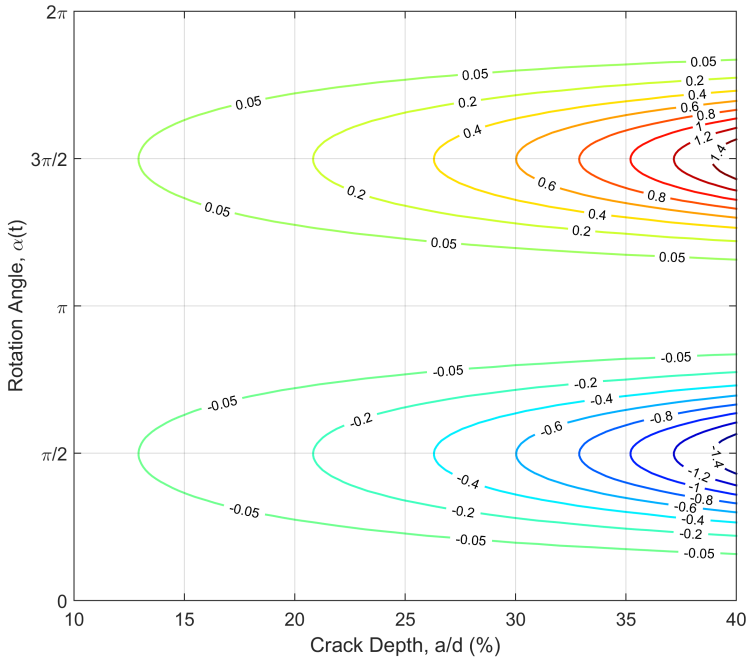

Figure 6.9: Non-dimensional coupling coefficient c_{45} ($E_R = 210$ GPa, $\nu = 0.3$, $d = 35$ mm, $L = 250$ mm, $L_1 = 0.05\ L$).

the later numeric integration routines:

$$c_{ij}^{*} = \Re\left\{\frac{1}{2}C_{ij}^{0} + \sum_{k=1}^{N} |C_{ij}^{k}| \exp\left[i(k\omega_r t + \phi^{k})\right]\right\} \tag{6.45}$$

where $\Re(\bullet)$ denotes the real part of the expression, C_{ij}^{0} is the mean value over one period, N is the desired number of harmonics, $|C_{ij}^{k}|$ is the modulus of $C_{ij}(\omega)$ evaluated at the k^{th} harmonic, and ϕ_k is the phase of $C_{ij}(\omega)$ at the k^{th} harmonic. This expression is analytic with respect to time, and only relies on the crack compliances calculated over a single revolution.

The compliances are calculated over one period for a crack depth of 40%, and shown along with their Fourier reconstruction in Fig. 6.10 (the frequency content of each compliance is shown in Fig. 6.11 for reference). Each compliance is successfully reconstructed from the Fourier transform using $N = 25$ harmonics. Importantly, the compliance calculations validate the angular bound θ_{cr}.

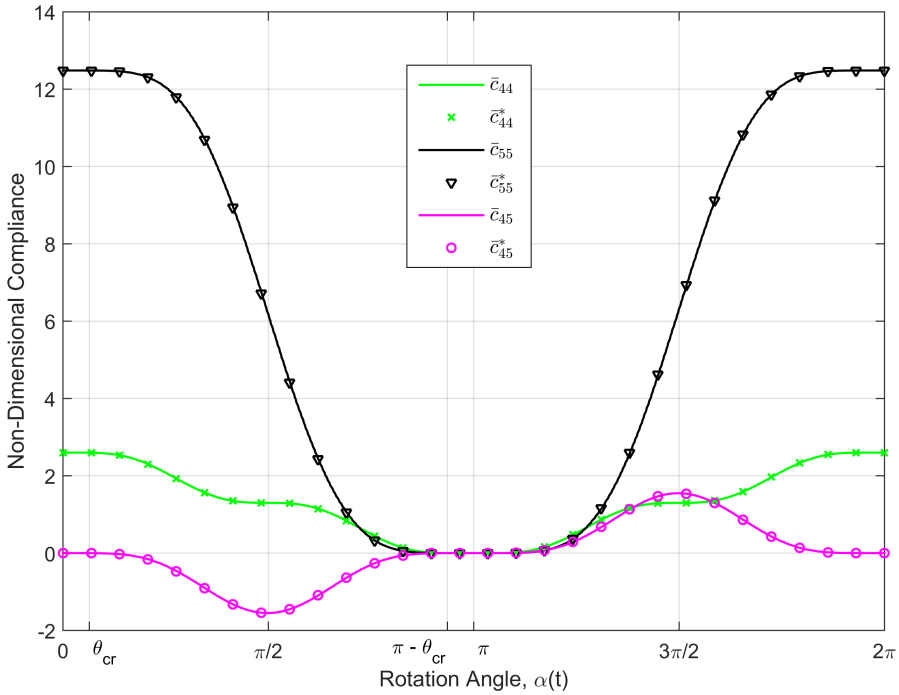

(a) Angular crack compliances

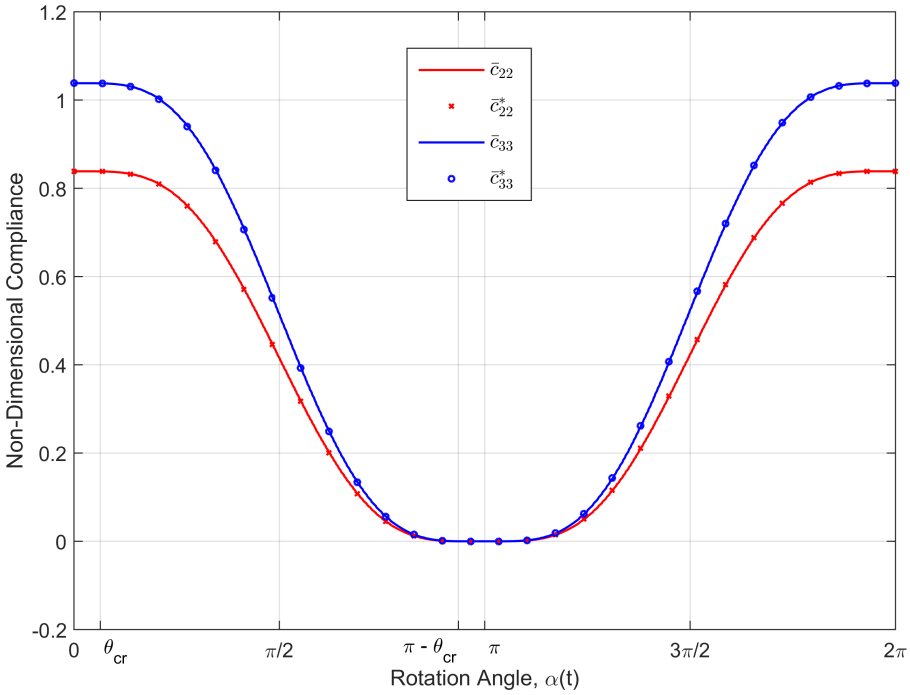

(b) Eccentric crack compliances

Figure 6.10: CCL Breathing Crack: Non-dimensional crack compliances versus shaft rotation, showing a comparison between direct calculation and a Fourier transform approximation ($a/d = 40\%$, $E_R = 210$ GPa, $\nu = 0.3$, $d = 35$ mm, $L = 250$ mm, $L_1 = 0.05\ L$).

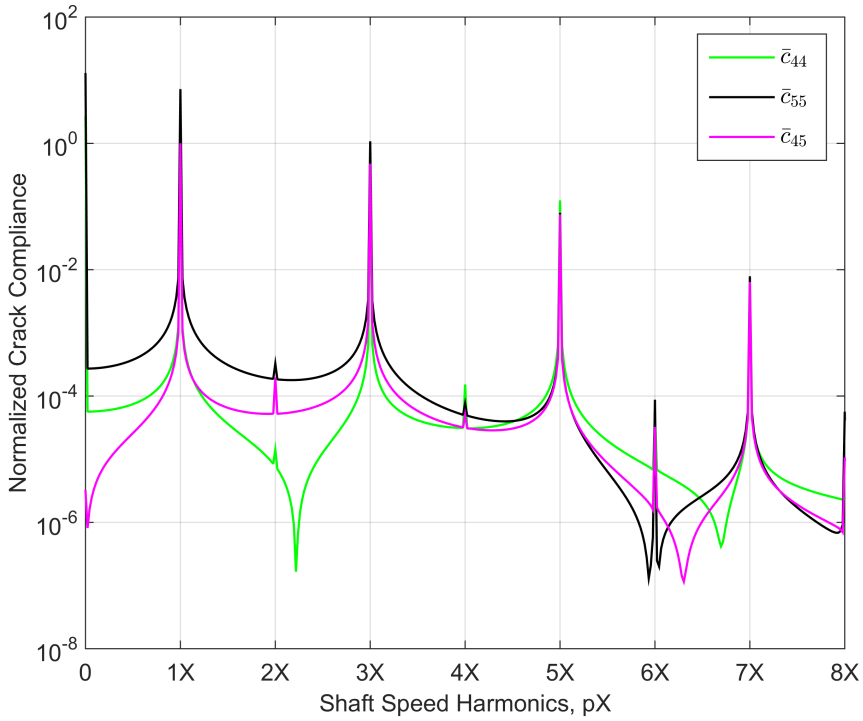

(a) Angular crack compliances

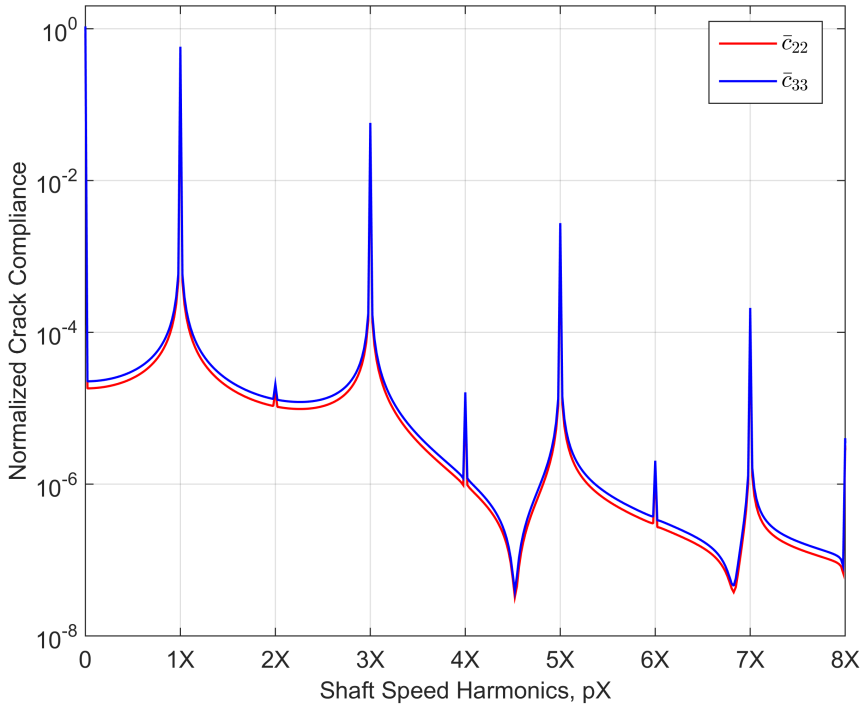

(b) Eccentric crack compliances

Figure 6.11: CCL Breathing Crack: Frequency content of each compliance used to compile the frequency-domain reconstruction ($a/d = 40\%$, $E_R = 210$ GPa, $\nu = 0.3$, $d = 35$ mm, $L = 250$ mm, $L_1 = 0.05\ L$).

The compliance matrix of the cracked overhung shaft (Eq. 6.22) using the new time-dependent compliances is inverted into the stiffness matrix and then transformed from the shaft-fixed reference into the inertial $\xi\eta\zeta$ frame (see Eq. 6.32). The direct (i.e., diagonal) stiffness coefficients are provided in Fig. 6.12. The stiffness coefficients are identical to the gaping crack for rotation values between $-\theta_{cr}$ and θ_{cr}. When the crack is completely closed, the rotor stiffness returns to that of the undamaged shaft. Importantly, the frequency content of the direct stiffness coefficients elucidates the expected frequency content in the rotordynamic response: integer harmonics of the shaft speed (e.g., 1X, 2X, 3X, etc.).

6.3 Summary

Several methods for obtaining the compliances and stiffness matrix for a gaping crack and breathing crack have been presented herein using the strain energy release rate approach. In both cases, the resultant stiffness matrix for the overhung cracked shaft is linear time-periodic in the inertial reference frame (in the shaft-fixed frame, the gaping crack compliance is constant while the breathing crack compliance is still linear time-periodic). The gaping crack stiffness coefficients include only a 2X shaft speed harmonic, whereas the breathing crack model predicts many shaft speed harmonics. The time-dependent stiffness matrix for the cracked shaft, $[K(t)]$, can now be inserted directly into Eq. 4.1 to simulate the rotor response to the crack.

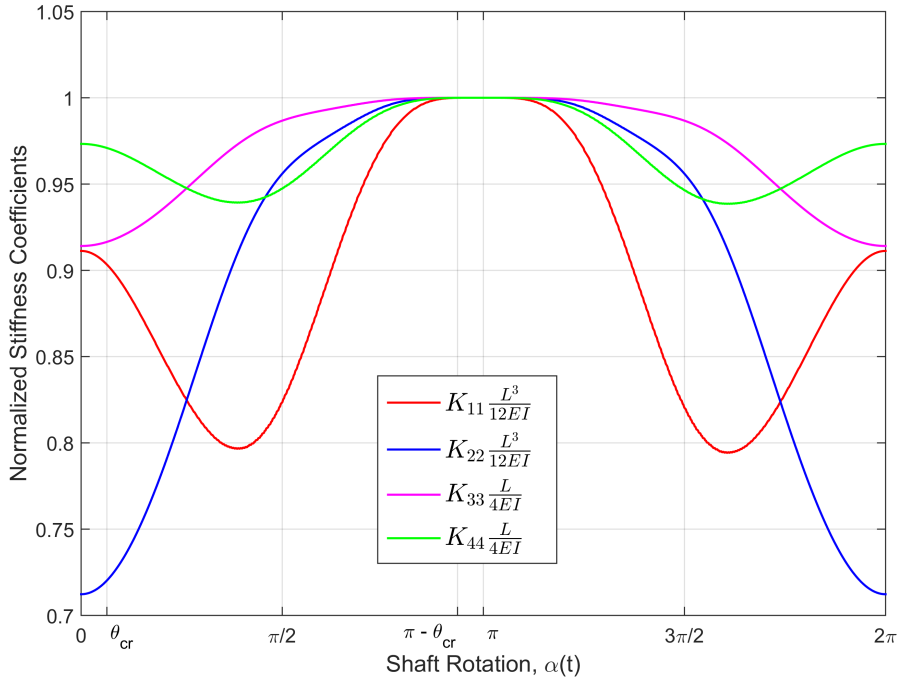

(a) Direct stiffness coefficients

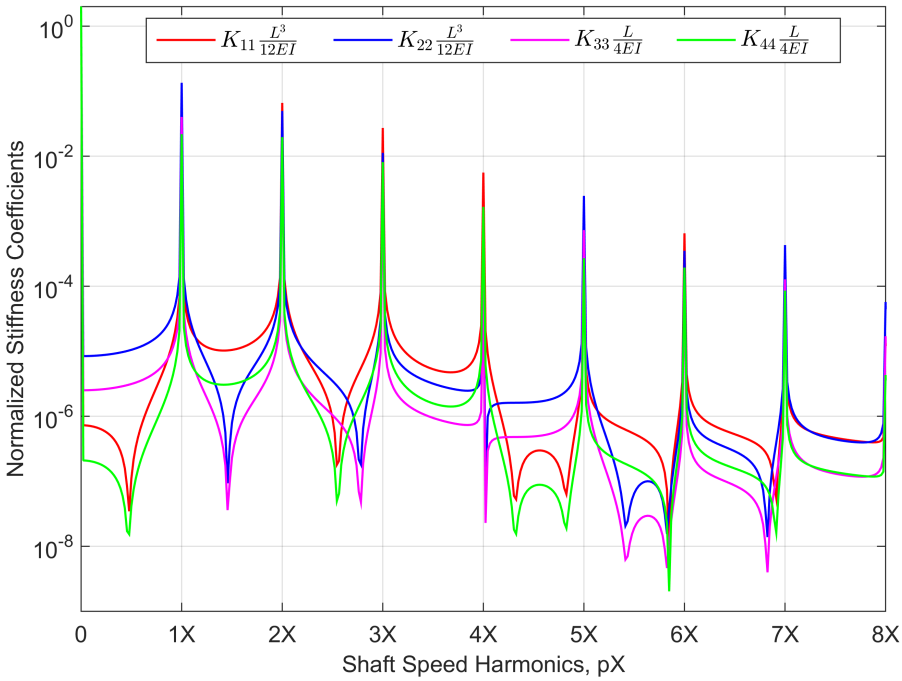

(b) Frequency content

Figure 6.12: CCL Breathing Crack: Inertial frame direct stiffness coefficients showing magnitude in the time and frequency domains. ($a/d = 40\%$, $E_R = 210$ GPa, $\nu = 0.3$, $d = 35$ mm, $L = 250$ mm, $L_1 = 0.05\ L$).

CHAPTER VII

MODELING ROTOR-STATOR RUB

One method for increasing turbomachine efficiency is to reduce clearances between the rotating and stationary machine elements [5, 8]. Unfortunately, reducing these clearances increases the likelihood of undesirable contact (i.e., rub) between the rotating and stationary components (e.g., the rotor and housing, or the seal faces). Prolonged or severe rub can result in decreased machine life via increased wear, heightened susceptibility to fatigue, and adverse thermal effects. Detecting rub requires detailed knowledge of the conditions precipitating and following the onset of contact.

Significant contact forces are developed when the rotor vibration exceeds the allowable system clearances. Thus, this fault is characterized by piecewise-smooth nonlinearity, where the rotor alternates between contacting and non-contacting operation states. As will be seen in later results, this piecewise nonlinearity causes the rotor response to exhibit rich complexity [152, 197] and even chaotic behavior; consequently, realistic rub models are required to simulate the system.

This chapter presents two approaches for modeling rotor-stator contact: the linear-elastic contact model (LECM) and the rough surface contact model (RSCM). The LECM is a simpler approach, and is only presented here in relation to the Jeffcott rotor. On the other hand, the RSCM constitutes a more general approach correlating the contact pressure to the rotor-stator clearance (or, the seal face clearance). Qualitative differences between the models are discussed, along with advantages and disadvantages of each approach. The chapter concludes by using the RSCM to derive the contact forces generated between the four degree-of-freedom overhung rotor and associated housing.

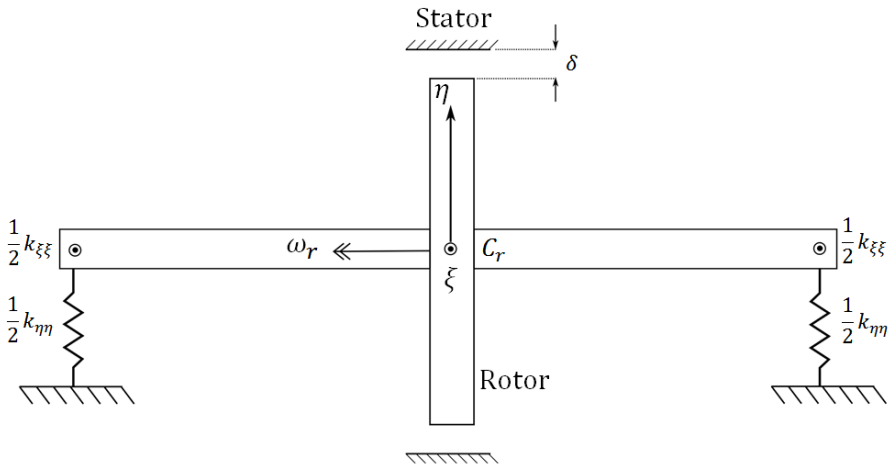

Figure 7.1: Jeffcott rotor schematic indicating the fixed clearance δ between the rotor and the housing (i.e., the stator).

7.1 The Linear-Elastic Contact Model

The linear-elastic contact model (LECM) is perhaps the most widely-used model for predicting contact forces generated by lateral (i.e., eccentric) rotor-stator rub. The LECM is only discussed in relation to the Jeffcott rotor shown in Figs. 7.1 and 7.2. The rotor is constrained within a stationary housing (i.e., the stator) with fixed clearance δ. Contact occurs when the rotor deflection ϵ_R exceeds the allowable clearance. When contact occurs (that is, when $\epsilon_R > \delta$), an elastic normal restoring force F_n and tangential friction force F_f are generated at the interface, as indicated in Fig. 7.2. The elastic restoring force is linearly proportional to the interference between the rotor and stator by the contact stiffness k_c, while the tangential friction force is proportional to the normal force by the dry friction coefficient μ_f. The magnitudes of these forces are

$$F_n = \begin{cases} 0 & \epsilon_R < \delta \\ k_c(\epsilon_R - \delta)\mathcal{H}(\epsilon_R - \delta) & \epsilon_R > \delta \end{cases} \tag{7.1}$$

$$F_f = \mu_f F_n \tag{7.2}$$

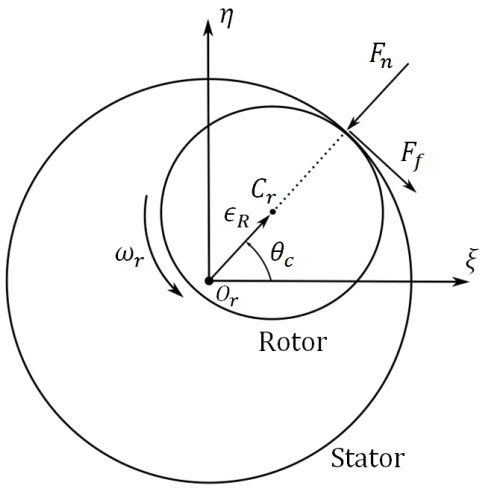

Figure 7.2: Contact forces between the rotor and housing.

The Heaviside function $\mathcal{H}(\epsilon_R - \delta)$ ensures that contact forces are only developed when the rotor deflection exactly exceeds the clearance. The friction force opposes the relative surface velocity of the contact point, and can switch directions for certain shaft speeds and/or parameter ranges. This direction reversal is not considered here due to the chosen system parameters and high shaft speeds (i.e., the tangential velocity from shaft rotation is much greater than the translational velocity). Thus, the friction force direction corresponds to that shown in Fig. 7.2. The contact force acts normal to the interface at the angle of maximum interference θ_c, which is related to the rotor degrees-of-freedom by the following expressions:

$$\cos\theta_c = \frac{\epsilon_{R\xi}}{\epsilon_R} \quad , \quad \sin\theta_c = \frac{\epsilon_{R\eta}}{\epsilon_R}, \tag{7.3}$$

Using these expressions, the contact forces are decomposed into the inertial ξ and η directions:

$$F_{c\xi} = \quad F_f \sin\theta_c - F_n \cos\theta_c \tag{7.4}$$

$$F_{c\eta} = -F_f \cos\theta_c - F_n \sin\theta_c \tag{7.5}$$

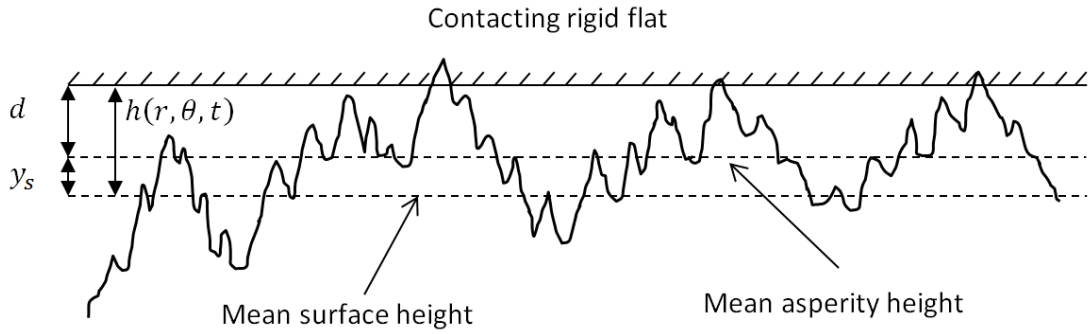

Figure 7.3: Contact between a rigid flat and a composite rough surface.

Taking into account Eqs. 7.1 - 7.5, the Jeffcott rotor contact forces resulting from linear-elastic deformation and dry Coulomb friction are:

$$F_{c\xi} = k_c \frac{\epsilon_R - \delta}{\epsilon_R}(\mu_f \epsilon_{R\eta} - \epsilon_{R\xi})\mathcal{H}(\epsilon_R - \delta) \tag{7.6}$$

$$F_{c\eta} = k_c \frac{\epsilon_R - \delta}{\epsilon_R}(-\epsilon_{R\eta} - \mu_f \epsilon_{R\xi})\mathcal{H}(\epsilon_R - \delta) \tag{7.7}$$

These contact force expressions represent a hybrid piecewise smooth nonlinearity in the rotor equations of motion.

The principle advantage of the LECM is that it emulates the most fundamental aspect of rotor-stator rub in the simplest manner possible (i.e., rub occurs on a finer spatial scale and faster temporal scale when compared to the rotordynamic response without rub). Nonetheless, the model is dissociated from the true nature of contacting surfaces. Estimating the contact stiffness k_c is an inextricable complication and principle disadvantage of the LECM. In addition, the LECM assumes that rotor-stator rub occurs only at the point of maximum interference. However, rotor-stator rub constitutes strongly conformal contact because the rotor-stator clearance is significantly smaller than the radii of either component; thus, the point contact assumption is likely invalid for many real cases of rotor-stator rub.

7.2 Rough Surface Contact Model

Though useful as a first step, the LECM is predicated on an arcane description of contact stiffness, and consequently does not emulate the actual physics of contact at the interface. Thus, the LECM fails to elucidate how real surface parameters influence contact severity and surface durability. In addition, the contact forces given in Eqs. 7.6 and 7.7 are only valid for annular rotor-stator contact, and the associated presence of negative interferences prohibits the calculation of possible fluid film forces. These deficiencies are addressed by considering the actual nature of the contacting surfaces. Real engineering surfaces are not smooth, but instead are composed of asperities of varying height (i.e., real surfaces are rough). Rather than assuming a contact stiffness, the contact pressure can be found using underlying physical principles and measurable surface properties instead of simplifying assumptions. Furthermore, the developments presented here are equally valid for both annular rotor-housing contact and axial seal face contact.

In the same manner as the elastic Greenwood-Williamson model [198], the contact of two opposing rough surfaces is reduced to that of one rigid flat contacting a single composite rough surface (see Fig. 7.3). The asperity heights z are defined from the mean asperity height, where y_s is the distance between the mean surface height and the mean asperity height [199]. The standard deviation of surface heights and asperity heights are σ and σ_s, respectively, the composite areal asperity density is N, and R_a is the composite average asperity radius of curvature [198]. Here, the asperity heights obey a Gaussian distribution $\phi(z)$ without loss of generality:

$$\phi(z/\sigma) = \frac{1}{\sqrt{2\pi}} \left(\frac{\sigma}{\sigma_s}\right) \exp\left[-0.5 \left(\frac{\sigma}{\sigma_s}\right)^2 \left(\frac{z}{\sigma}\right)^2\right] \tag{7.8}$$

Jackson and Green [200] extend a finite element study of flattening elastoplastic hemispherical contact to rough surface contact, and show that hardness is a function of geometry and material properties [201]. The interference between each asperity and

the contacting rigid flat is $\omega = z - d$, where d is the general surface separation distance (if $h(r, \theta, t)$ is the clearance between two elements expressed in polar coordinates, then $d = h(r, \theta) - y_s$). The critical interference ω_c denotes the interference where yielding first occurs, and is calculated using the von Mises yield criterion:

$$\omega_c = \left(\frac{\pi C S_y}{2E}\right)^2 R_a \tag{7.9}$$

Using this critical interference, the contact force at the point of initial yielding is

$$\bar{F}_{cy} = \frac{4}{3}\left(\frac{R_a}{E}\right)^2 \left(\frac{1}{2}\pi C S_y\right)^3 \tag{7.10}$$

where the over-bar denotes quantities provided for single-asperity contact. The material Poisson ratio is ν and the yield strength is S_y. Specifically, the product CS_y is chosen as $CS_y = \min\left(C(\nu_1)S_{y1}, C(\nu_2)S_{y2}\right)$ [202] for surfaces 1 and 2. The yield strength S_y is found from the plasticity index Ψ [201], while C is calculated according to Green [202]. Here, E is the composite elastic modulus for the contacting surfaces [198]. The plasticity index quantifies the contribution of plasticity to surface asperity deformation, where larger plasticity indices indicate greater plastic deformation. The relationship between plasticity index, material properties, and surface asperity geometry is:

$$\Psi = \frac{2E\sqrt{\sigma_s / R_a}}{1.639\pi S_y} \tag{7.11}$$

Thus, plasticity is most prominent for soft, rough surfaces.

As shown by Jackson and Green [200], the contact force is commensurate to the Hertzian model for deformations beneath the critical yield point, i.e., $0 \leq \omega/\omega_c \leq 1.9\omega_c$. For $\omega > 1.9\omega_c$, the contact force acting on a single asperity is

$$\begin{aligned}\bar{F} = \bar{F}_{cy}\Bigg\{ &\left[\exp\left(-\frac{1}{4}\left(\frac{\omega}{\omega_c}\right)^{5/12}\right)\right]\left(\frac{\omega}{\omega_c}\right)^{3/2} \\ &+ \frac{4H_G}{CS_y}\left[1 - \exp\left(-\frac{1}{25}\left(\frac{\omega}{\omega_c}\right)^{5/9}\right)\right]\left(\frac{\omega}{\omega_c}\right)\Bigg\}\end{aligned} \tag{7.12}$$

where

$$H_G = 2.84CS_y \left[1 - \exp\left(-0.82\left(\sqrt{\frac{\omega}{R_a}}\left(\frac{\omega}{1.9\omega_c}\right)^{\frac{B}{2}}\right)^{-0.7}\right)\right] \tag{7.13}$$

and

$$B = 0.14\exp(23S_y/E) \tag{7.14}$$

Equation 7.13 indicates that surface hardness H_G depends on both material and surface properties along with deformation magnitudes.

When the rigid flat and composite rough surface are separated by a distance $d = h(r,\theta) - y_s$, any asperity whose height exceeds d contacts the rigid flat. Thus, the contribution of all asperities of height z towards the contact force at (r, θ) is

$$\tilde{F}(z,r,\theta) = NA_n\bar{F}(z-d)\phi(z) \tag{7.15}$$

where A_n is the nominal contact area. Thus, the total contact force at a prescribed surface separation distance is found by summing the contribution of all asperities whose height exceeds the surface separation distance. This summation is achieved by integrating Eq. 7.15 over the entire vertical contact range (i.e., all asperity heights above d):

$$F(r,\theta) = NA_n\int_d^\infty \bar{F}(z-d)\phi(z)\,dz \tag{7.16}$$

Rather than evaluate the nominal contact area A_n at every time step in the subsequent simulations, Eq. 7.16 is redefined to calculate the average contact pressure, $P_c(r,\theta) = F(r,\theta)/A_n$:

$$P_c(r,\theta) = N\int_d^\infty \bar{F}(z-d)\phi(z)\,dz \tag{7.17}$$

Note that the resulting contact pressure is quasi-static because asperity inertial effects and hysteresis from loading-unloading are neglected. Thus, the contact force only depends on the instantaneous clearance between the approaching surfaces.

In general, the clearance $h(r,\theta)$ between the approaching surfaces is a function of both surface location and time because the clearance depends on the degrees-of-freedom. Assuming a quasi-static contact law permits the contact pressure to be

curve-fit versus local surface clearance $h(r, \theta)$. This approach significantly reduces computation time when solving the system equations of motion, because the numeric integration in Eq. 7.17 is performed once rather than at every nodal point (r, θ) at every time step in the simulation. Here, an exponential curve fit is performed on the contact pressure P_c versus clearance h [199]:

$$P_c(r, \theta) = C_1 \exp(C_2 h) \tag{7.18}$$

where C_1 and C_2 are constants. This expression depends only on the surface and material parameters, and is valid for both annular rotor-housing contact and axial seal face contact. The contact pressure versus clearance relationship is shown in Fig. 7.4 for two nominally flat approaching surfaces, where the result from Eq. 7.17 is compared to the curve fit expression given in Eq. 7.18. The surface and material properties employed in the calculation are representative of real mechanical seals [42], and are given in Table 7.1. The figure clearly indicates agreement between the numeric integration and the exponential curve-fit.

The exponential contact pressure expression given in Eq. 7.18 is then used to study the influence of plasticity in Fig. 7.5, where the plasticity index is varied by changing the yield strength according to Eq. 7.11. Several general observations are made from the comparison. First, the contact pressure increases exponentially as the surfaces draw closer because more asperities interact. For the asperity height distribution considered here, the contact pressure decreases by almost an entire order of magnitude for each additional σ of surface separation distance. The second observation evident from Fig. 7.5 is that the contact pressure decreases significantly as the plasticity index increases. This conclusion is intuitive, as higher plasticity indexes indicate that more asperities are fully plastically deformed, and are therefore unable to support increases in contact pressure.

The RSCM fundamentally assumes that the bulk substrate does not significantly contribute to the contact force (i.e., only the asperities on each surface deform).

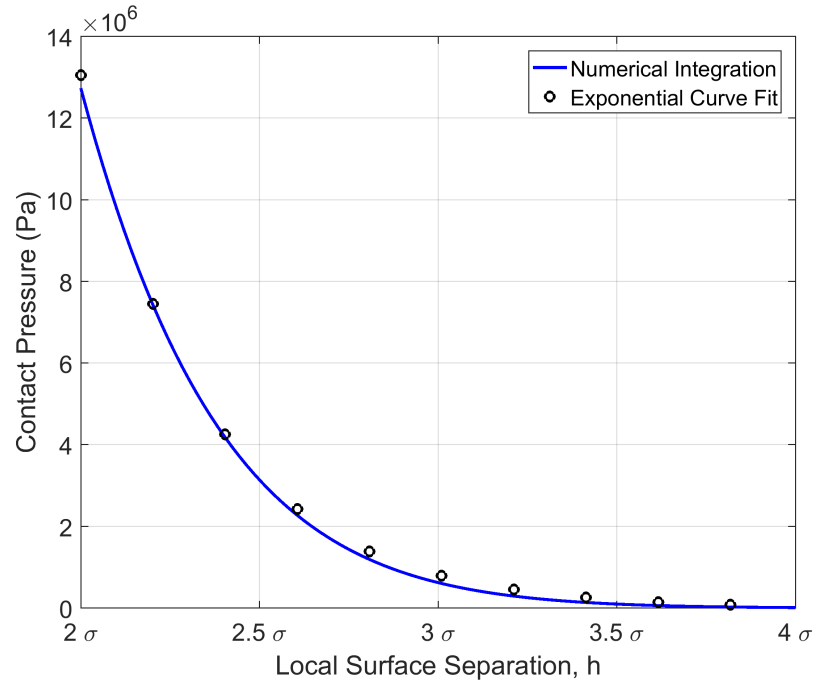

Figure 7.4: Comparing the numeric and approximated contact pressures for the RSCM (see Table 7.1 for surface parameters).

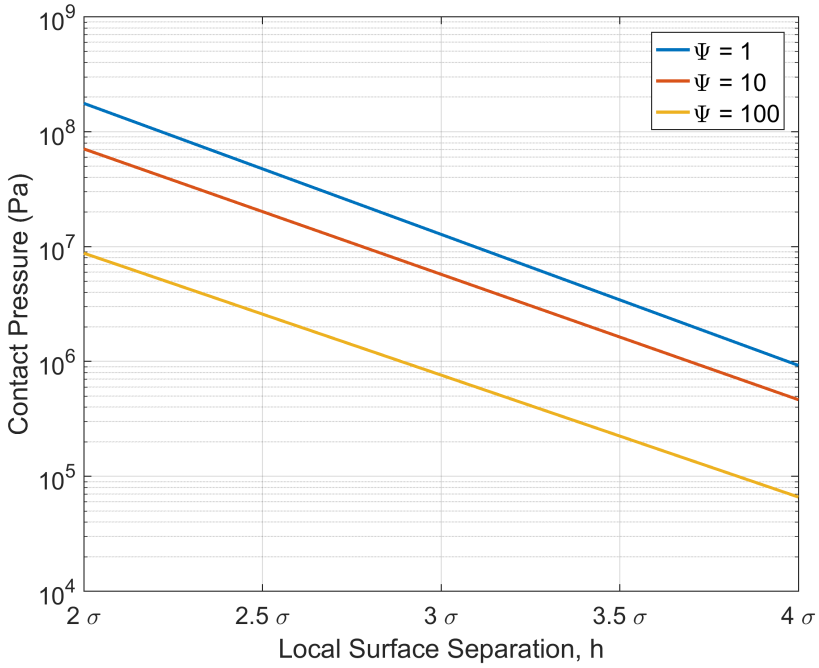

Figure 7.5: Contact pressure versus surface separation distance for various plasticity indices, calculated using the elastoplastic Jackson-Green rough surface contact model.

In reality, it is likely that both substrate and asperity deformation contribute to the overall contact force developed between the interacting surfaces. However, the purpose here is to develop an approach to rotordynamic contact modeling that is based on the geometry and physics of real surfaces. For specific applications in future work, the contact force relationships provided here could be modified to account for substrate deformation by recognizing that the asperities and bulk substrate behave as springs in series. It should also be noted that some of the rough surface parameters are difficult to precisely measure due to scale-dependent effects (e.g., the average asperity radius of curvature R_a). These differences are minimized by the integration processes used to obtain the overall contact reaction (i.e., the dynamic response is not sensitive to individual parameter variations [199]).

For later comparison to the LECM, the steady-state equations of motion for the Jeffcott rotor including RSCM forces are:

$$m_R\ddot{\epsilon}_\xi + c_R\dot{\epsilon}_{R\xi} + k_R\epsilon_{R\xi} = m_R\varepsilon_{RG}\omega_r^2\cos(\omega_r t) - F_{c\xi} + F_{f\xi} \tag{7.19}$$

$$m_R\ddot{\epsilon}_\eta + c_R\dot{\epsilon}_{R\eta} + k_R\epsilon_{R\eta} = m_R\varepsilon_{RG}\omega_r^2\sin(\omega_r t) - F_{c\eta} - F_{f\eta} - m_R g \tag{7.20}$$

where the contact forces are generated by progressive asperity interaction at the rotor-stator interface. These forces are found by integrating the contact pressure across the nominal contact area:

$$F_{c\xi} = R_r B_r \int_0^{2\pi} P_c(\theta)\cos\theta\, d\theta \tag{7.21}$$

$$F_{c\eta} = R_r B_r \int_0^{2\pi} P_c(\theta)\sin\theta\, d\theta \tag{7.22}$$

where the rotor's radius and length are R_r and B_r, respectively. Here, a Coulomb model is used to correlate the friction force to the normal contact force, where the dry friction coefficient is μ_f. Hence, the resultant friction forces in the ξ and η directions

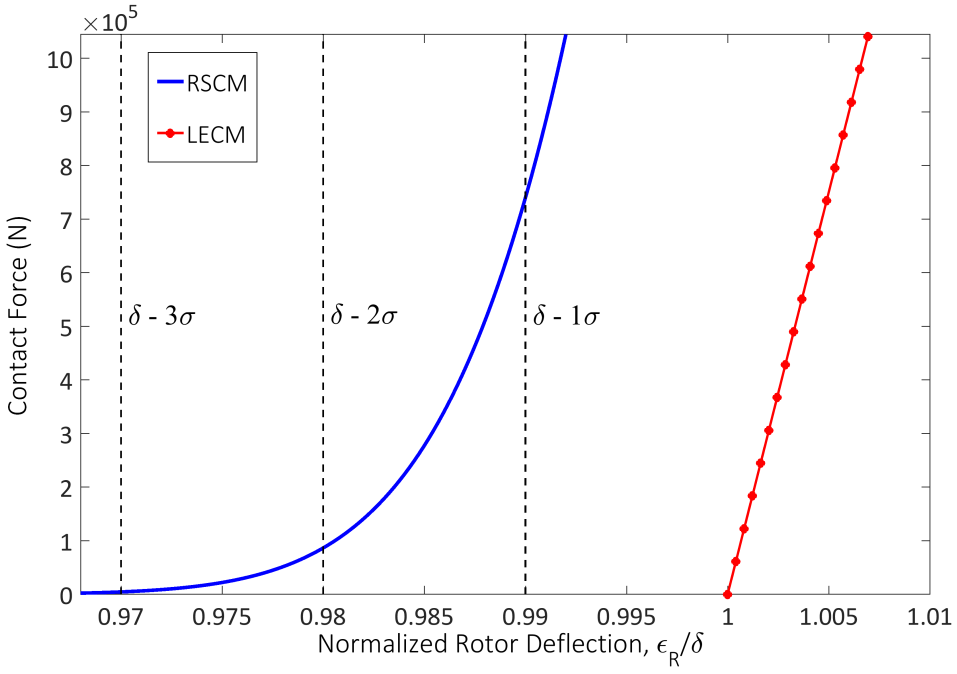

Figure 7.6: Comparing the Jeffcott rotor contact force between the elastoplastic RSCM and the LECM as a function of rotor deflection.

are

$$F_{f\xi} = \mu_f F_{c\eta} \tag{7.23}$$

$$F_{f\eta} = \mu_f F_{c\xi} \tag{7.24}$$

Since only lateral deflections are considered, the contact pressure is homogeneous along the rotor's length and does not depend on axial position.

7.3 Comparing the LECM and RSCM

The LECM and RSCM are distinct approaches to contact modeling that differ both qualitatively and quantitatively. Comparison between these models is facilitated here by considering annular contact between the rotor and an encompassing housing (i.e., the rotor and stator). A necessary prerequisite for calculating the contact force is an expression relating the rotor-stator circumferential clearance $h(\theta)$ to circumferential position θ (see Fig. 7.2). This circumferential clearance expression is obtained here

by modifying the well-known journal bearing film thickness equation; this approach is valid when the clearance δ is much smaller than the rotor and stator radii. Once more, consider a rotor whose deflection ϵ_R is oriented from the inertial ξ axis by θ_c. The clearance between the rotor and stator is then a function of only circumferential position:

$$h(\theta) = \delta[1 - (\epsilon_R/\delta)\cos(\theta - \theta_c)] \tag{7.25}$$

where θ is defined from the inertial ξ axis. As the circumferential clearance approaches the surface roughness dimension, the asperities on each surface begin to interact and deform, generating contact pressure between the surfaces. The clearance given in Eq. 7.25 is then inserted into Eq. 7.18 to find the contact pressure at any circumferential location. The requisite contact force is subsequently found by integrating the pressure profile around the circumference (assuming homogeneity in pressure along the rotor's length B_r).

The contact force versus rotor deflection (i.e., separation distance) for both contact models is shown in Fig. 7.6 using the representative surface parameters provided in Table 7.1. Here, a linear contact stiffness of $k_c = 1.5(10)^8$ N/m is used to calculate the LECM contact force (the necessity of arbitrarily selecting a contact stiffness reinforces previous discussion regarding the LECM's shortcomings); this value is chosen for aesthetic comparison with the RSCM. Several crucial differences between the RSCM and LECM are gleaned from Fig. 7.6:

1. The LECM predicts a contact force only when the rotor deflection ϵ_R identically exceeds the clearance δ. On the other hand, the RSCM indicates that the contact force exponentially increases as more asperities interact.

2. The RSCM predicts a nonlinear force-displacement relationship, whereas the LECM is linear once contact occurs (this switching behavior causes nonlinearity

Table 7.1: Rotor and surface parameters used to facilitate comparison between the LECM and RSCM.

Parameter	**Value**
Equivalent modulus, E	$25(10)^9$ Pa
Surface height standard deviation, σ	$1(10)^{-6}$ m
Areal density of asperities, N	$5(10)^{11}$ asp/m^2
Asperity radius, R_a	$2(10)^{-6}$ m
Yield strength, S_y	$0.1(10)^9$ Pa
Set-point clearance, δ	$1.6(10)^{-4}$ m
Rotor radius, R_r	0.1 m
Rotor length, B_r	0.01 m

in the system even though the LECM force-displacement relationship is by itself linear following the onset of contact).

3. The slope of the LECM contact force is controlled by arbitrarily selecting a desired contact stiffness k_c, whereas the character of the RSCM force-displacement relationship is dictated by real and measurable surface parameters.

In either case, the system dynamics engendered by rotor-stator rub are fundamentally defined by temporal and spatial phenomena occurring on vastly disparate scales. Many times, chaotic behavior is a hallmark signature of this piecewise-smooth nonlinearity; thus, the system response is likely sensitive to even small differences in contact force. Consequently, it is important to correctly model the actual physics of contact occurring at the rotor-stator interface (or, the seal face interface).

7.4 Overhung Rotor Contact Forces

A lumped-parameter rotordynamic model with four degrees-of-freedom (two eccentric deflections and two angular tilts) was presented in Chapter 4. The overhung rotor is constrained in some housing (i.e., stator); when the lateral deflection of any point

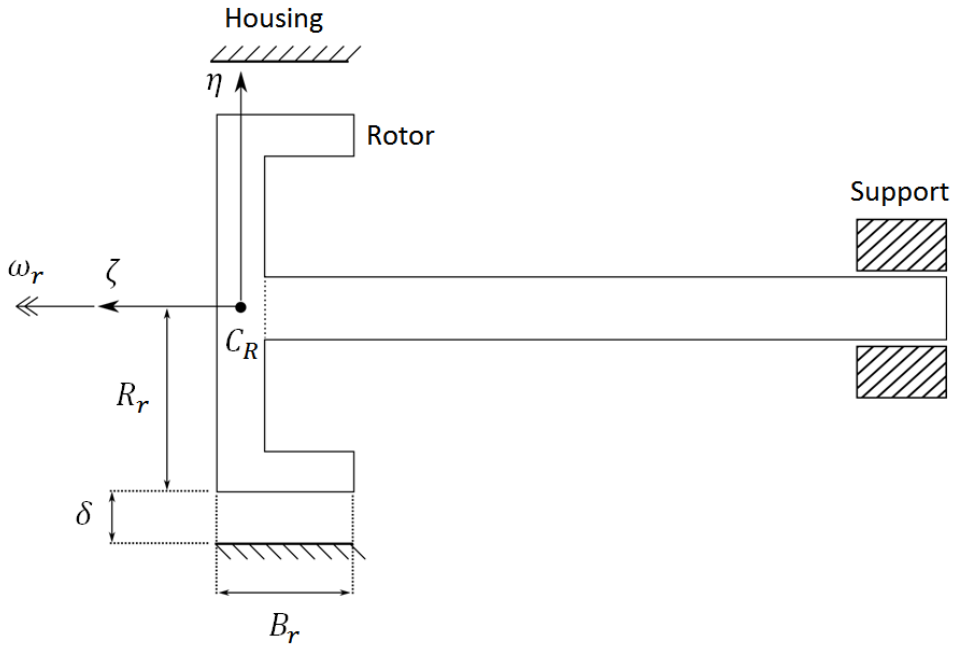

Figure 7.7: Overhung rotordynamic system showing finite clearance δ between the rotor and the housing (i.e., the stator).

on the rotor approaches the annular clearance δ, the rotor and housing interact to generate contact reactions. The clearance is shown in Fig. 7.7, where the rotor is shown undeflected in the figure for reference. The axial width of the rotor is designated B_r, while the rotor radius is designated R_r.

Depending on the system parameters, both eccentric and angular vibrations may contribute to lateral deflections of the rotor surface. If this is the case, the contact pressure developed between the rotor and housing is a function of both axial and circumferential location (i.e., the contact pressure is not homogeneous in the axial direction). On the other hand, the contact pressure is essentially constant in the axial direction if lateral deflections caused by tilt are much smaller than the rotor eccentric response. Understanding whether or not this condition is met is important with regard to computational efficiency. If the contact pressure is constant along the rotor width B_r, then the contact forces are found via a single numeric integration along the circumference (otherwise, an additional numeric integration in the axial

direction is required at every simulation time step). This work considers clearances on the order of 10^{-4} m; as will be seen later, the rotor tilts are typically on the order of fractions of milliradians. Thus, if the rotor width B_r is relatively small (e.g., 0.01 m), lateral deflections caused by tilt can be neglected in comparison to the rotor eccentric deflection. Furthermore, assuming constant contact pressure in the axial direction allows contact moments to be neglected in the analysis.

The eccentric contact forces have components arising from asperity contact pressure and dry friction, according to Fig. 7.2. The asperity contact pressure is once again found using the elastoplastic Jackson-Green rough surface contact model. Because rotor tilts are neglected, the contact pressure adheres to the same approximation described in Eq. 7.18. Thus, the reactions caused by rotor-housing contact are:

$$F_{n\xi} = -R_r B_r \int_0^{2\pi} P_c(\theta) \cos\theta d\theta \tag{7.26}$$

$$F_{n\eta} = -R_r B_r \int_0^{2\pi} P_c(\theta) \sin\theta d\theta \tag{7.27}$$

$$M_{n\xi} = 0 \tag{7.28}$$

$$M_{n\eta} = 0 \tag{7.29}$$

The eccentric forces caused by dry friction are then related to the normal forces:

$$F_{f\xi} = \quad \mu_f |F_{c\eta}| \tag{7.30}$$

$$F_{f\eta} = -\mu_f |F_{c\xi}| \tag{7.31}$$

Once again, the friction force direction is assumed to be invariant, i.e., it always opposes the relative surface velocity induced by rotor rotation. The parameters and shaft speeds considered here do not result in surface velocities that cause friction reversal. These forces can now be included in Eq. 4.12 to study the dynamics of rotor-housing contact in the overall FMSR-ER system.

CHAPTER VIII

RESULTS: HEALTHY FMSR-ER PERFORMANCE

Mechanical face seals are constitutive components of a much larger turbomachine, and successfully designing a face seal requires a thorough understanding of the complete system dynamics. Furthermore, understanding the dynamic performance of the healthy (i.e., undamaged) sealing system is a fundamental prerequisite for studying fault signatures in coupled rotor-seal systems. This chapter discusses the dynamic performance of the healthy seal apparatus, with specific regard to:

1. FMSR-E performance (i.e., seal performance without coupled rotordynamics).
2. Basic principles of rotor-seal dynamic interaction using the FMS-R seal system.
3. FMSR-ER performance.

The objective of this chapter is to provide a fundamental understanding of how the rotordynamics are transferred to the seal dynamics. This issue is centrally important to this work because these mechanisms establish the efficacy and manner by which a seal vibration monitoring system can be used as a surrogate rotordynamic condition monitor. It is also important here to emphasize that the objective of this work is, after all, to use the FMSR-ER dynamic response to detect coexisting faults in a coupled rotor system. Consequently, a thorough parametric study of the FMSR-E seal with regard to sealing performance is tangential to this objective, and has been discussed elsewhere by Wileman and Green [51, 54, 57]. Such an analysis is therefore reserved for future investigations.

Table 8.1: Seal dynamic parameters ($d_r = 0$ in all cases considered here). Imbalance and misalignment magnitudes are specified where applicable.

Parameter	**Rotating Element**	**Stationary Element**
Transverse moment of inertia	$I_{tr} = 4(10)^{-4}$ kg·m^2	$I_{ts} = 4(10)^{-4}$ kg·m^2
Polar moment of inertia	(variable)	–
Element mass	$m_r = 0.5$ kg	$m_s = 0.5$ kg
Axial support stiffness	$K_{rz} = 5(10)^5$ N/m	$K_{sz} = K_{rz}$
Angular support stiffness	$K_r = 363.9$ N·m/rad	$K_s = K_r$
Eccentric support stiffness	$K_{r\epsilon} = 1(10)^5$ N/m	$K_{s\epsilon} = K_{r\epsilon}$
Axial support damping	$D_{rz} = 100$ N·s/m	$D_{sz} = D_{rz}$
Angular support damping	$D_r = 0.0728$ N·m·s/rad	$D_s = D_r$
Eccentric support damping	$D_{r\epsilon} = 75$ N·s/m	$D_{s\epsilon} = D_{r\epsilon}$

Table 8.2: Seal geometry and fluid properties.

Parameter	
Viscosity	1.2 mPa·s
Pressure differential, $P_o - P_i$	400 kPa
Set-point clearance, C_o	5 μm
Coning, β	1 mrad
Inner radius, r_i	0.0355 m
Outer radius, r_o	0.0408 m
Closing force, F_{cls}	20 N

8.1 FMSR-E Performance

The steady-state equations of motion of the FMSR-E seal (i.e., without coupled rotordynamics) are solved to obtain the seal response to static angular misalignment, dynamic angular misalignment, and mass imbalance (the solution procedure is discussed in Section 3.9.2). The parameters used herein are provided in Tables 8.1 and 8.2, and are indicative of parameters used in previous works [49, 203]. The eccentric stiffness and damping, $K_{r\epsilon}$ and $D_{r\epsilon}$, are found using the procedure discussed by English [204]. Gravity, inertial maneuver loads, and stationary seal element angular misalignment are neglected in the following analysis without loss of generality. The steady-state response of the FMSR seal (i.e., no eccentric deflections or external rotordynamic effects) has been validated via comparison with the work by Wileman and Green [54] using the parameters specified therein. Importantly, both the critical speed and the speed at which the minimum relative misalignment occurs are corroborated by the current solution method (the magnitude differs slightly due to ambiguity in the parameters provided by Wileman and Green [54]).

Different seal responses (e.g., relative versus absolute) are presented here for specific reasons. On one hand, the seal performance is best summarized using the relative dynamic variables γ^* and ϵ^*, since these quantities concisely encapsulate the ability of one seal element to track the other (thus mitigating leakage and face contact). On the other hand, the utility of using a seal-fixed seal dynamic vibration monitoring system to detect rotor faults depends on the absolute dynamic response of the stationary seal element. Therefore, both responses are presented here to quantify both the seal performance and its utility as a surrogate rotor condition monitoring system.

Each type of seal excitation (ε_{rG}, χ_s, and χ) is studied here for both a thin ($I_{tr}/I_{pr} = 0.5$) and thick ($I_{tr}/I_{pr} = 2$) seal. Specifically, angular and eccentric excitations are studied independently, in addition to the total excitation case (i.e., all eccentric and angular excitations are included). As a reminder, the angular excitations refer to

static and dynamic angular misalignments, while the eccentric excitation consists of rotating seal element mass imbalance. The relative and absolute dynamic responses for the thick seal are shown in Figs. 8.1 and 8.2, respectively, while analogous responses are given for a thin seal in Figs. 8.3 and 8.4. For the parameters considered here, the critical speeds associated with eccentric and angular modes for the thick seal are approximately 450 rad/s and 1100 rad/s, respectively, and are distinguished by comparing Figs. 8.1a and 8.1b. Several observations regarding seal performance for a thick seal seal ($I_{tr}/I_{pr} = 0.5$) are immediately evident:

1. The relative tilt (Fig. 8.1a) is primarily influenced by angular excitations, while the relative eccentricity (Fig. 8.1b) is almost exclusively influenced by the eccentric imbalance ε_{rG} over all considered shaft speeds.

2. The relative eccentricity between the seal elements is increased by at least an order of magnitude in the presence of imbalance (i.e., the relative eccentricity depends primarily on eccentric excitations).

3. The relative tilt is dominated by static angular misalignment χ_s when the shaft speed is beneath the first critical speed, and dominated by dynamic angular misalignment χ above this speed. This conclusion is intuitive, since the dynamic angular misalignment excitation is proportional to ω_r^2.

The efficacy of using the stationary seal element as a surrogate rotordynamic condition monitoring system depends on whether or not excitations on the rotating element are sufficiently transmitted to the stationary element (i.e., the element on which the monitoring system is affixed). Ideally, the seal system should be designed independently from its use as a rotordynamic condition monitoring system, as its primary function is dissociated from diagnostics.

In addition, it would be advantageous to the operator if only one regime of seal response (e.g., either eccentric or angular) was required for rotor fault detection.

Addressing this issue requires an analysis of the absolute dynamic response of the stationary seal element. To this end, the absolute dynamic response of the stationary seal element is provided in Fig. 8.2. Interestingly, the absolute eccentric response of the stationary seal element seen in Fig. 8.2b is significantly less than the rotating seal element imbalance. The minuscule response magnitude demonstrates that the seal is not useful for minimizing relative eccentric deflections between the seal faces. Consequently, the eccentric vibration of the stationary seal element is a poor target signal for surrogate fault detection. On the other hand, the stationary seal element tilt in Fig. 8.2a is measurable according to standards used in previous works [49]. This conclusion is not surprising because the purpose of the seal is to minimize the relative tilt between the faces; thus, the stationary and rotating seal elements experience nearly the same angular response.

The dynamic signatures generated by each type of fault for a thin seal are qualitatively similar to those for the thick seal, with several key differences. First, the relative and absolute stationary seal element tilts provided in Figs. 8.3a and 8.4a contain only one critical speed; this is because the gyroscopic effect in a thin rotor tends to stabilize the angular vibration of the rotating seal element [47]. Secondly, in the absence of imbalance, the angular vibration contains a local minimum (in this case, near 410 rad/s) because, for a thin rotor, the dynamic and static angular misalignment excitations are exactly out of phase for a certain shaft speed.

The influence of angular and eccentric misalignment magnitude is investigated by considering the relative and absolute seal responses versus shaft speed and excitation magnitude. The influence of static angular misalignment χ_s on the relative and absolute seal dynamic response is provided in Figs. 8.5 and 8.6 for a thick rotating seal element. Dynamic angular misalignment is neglected to isolate the effect of static angular misalignment. As expected from previous results, the static angular misalignment primarily affects the relative tilt beneath the first critical speed (i.e., the

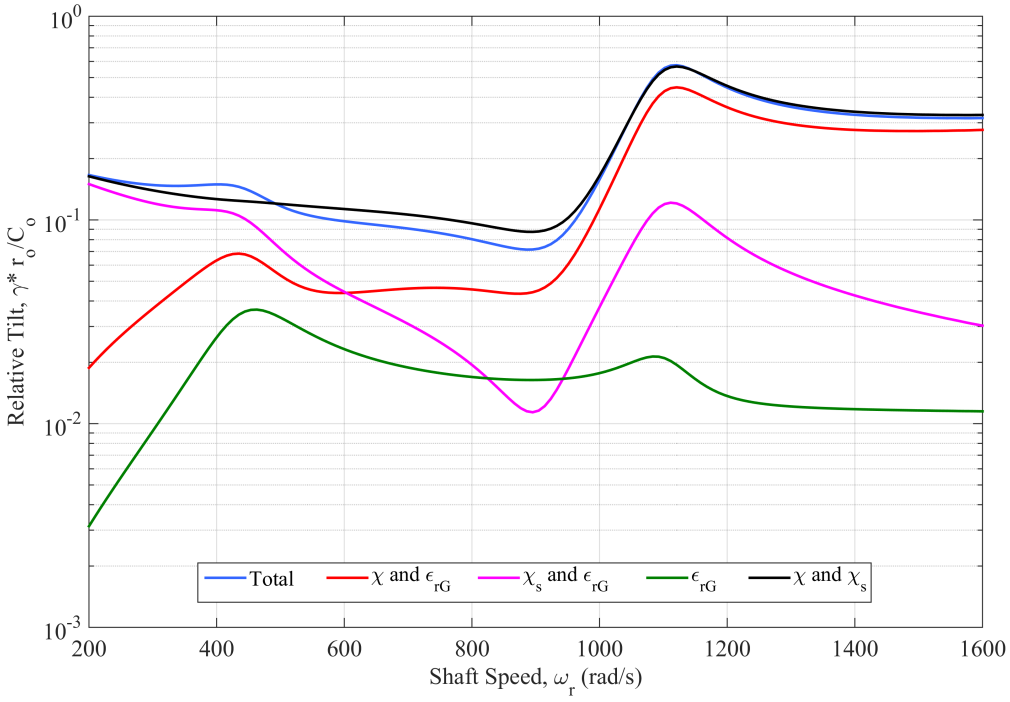

(a) Normalized relative tilt, $\gamma^* r_o/C_o$

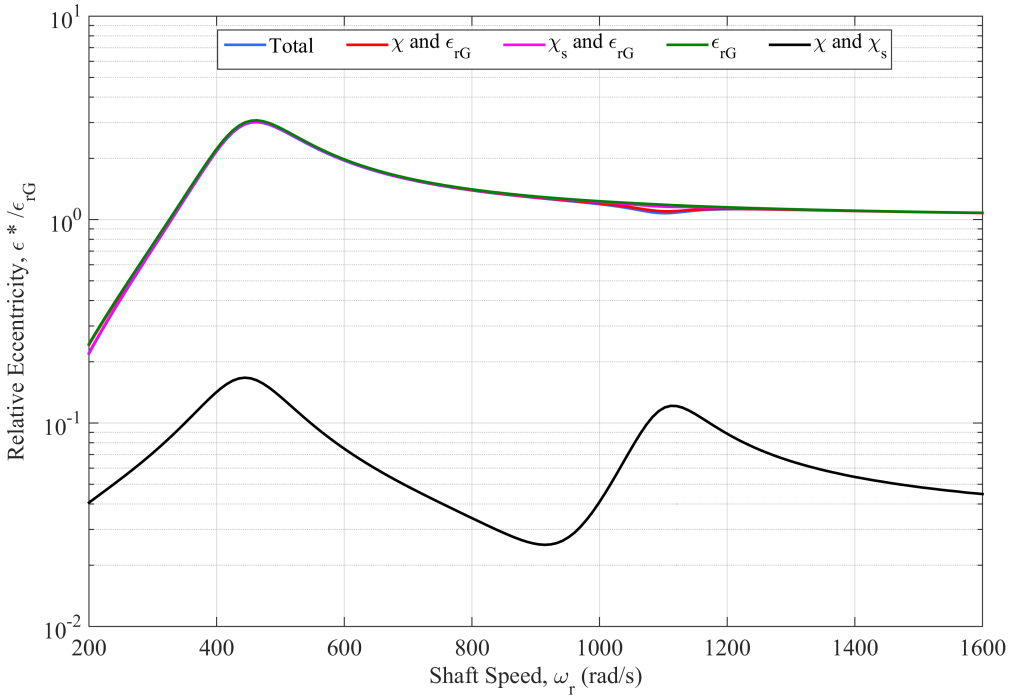

(b) Normalized relative eccentricity, $\epsilon^*/\varepsilon_{rG}$

Figure 8.1: FMSR-E: Comparing the effects of different forcing functions on the seal performance (thick seal: $I_{tr}/I_{pr} = 2$, $\varepsilon_{rG} = 5(10)^{-5}$ m, $\chi = 5$ mrad, $\chi_s = 1$ mrad).

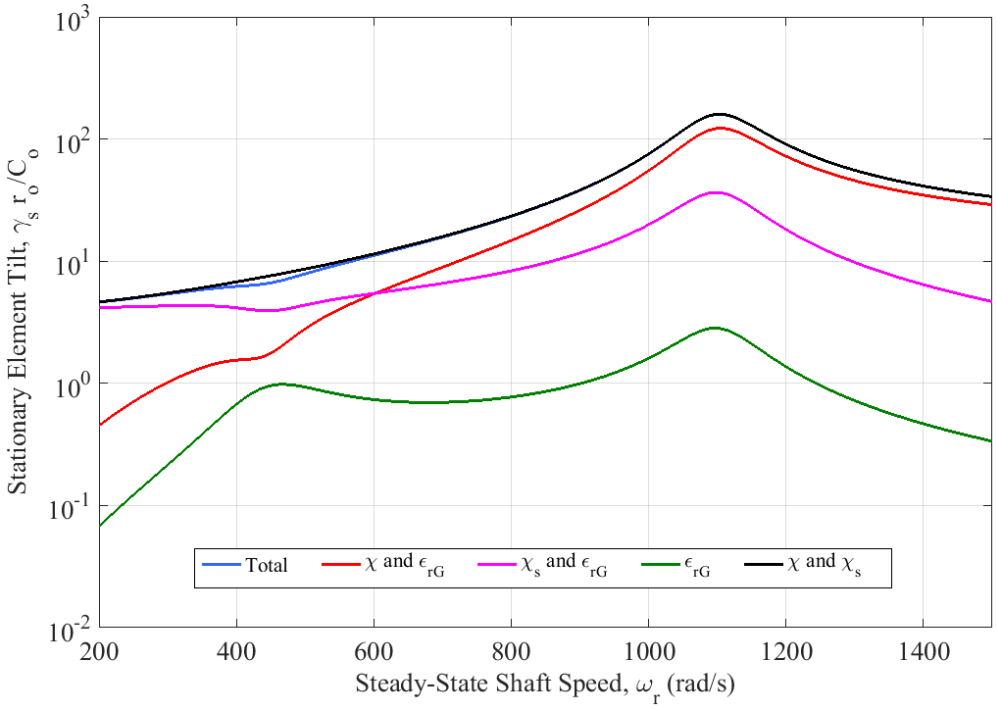

(a) Normalized stationary seal element tilt, $\gamma_s r_o/C_o$

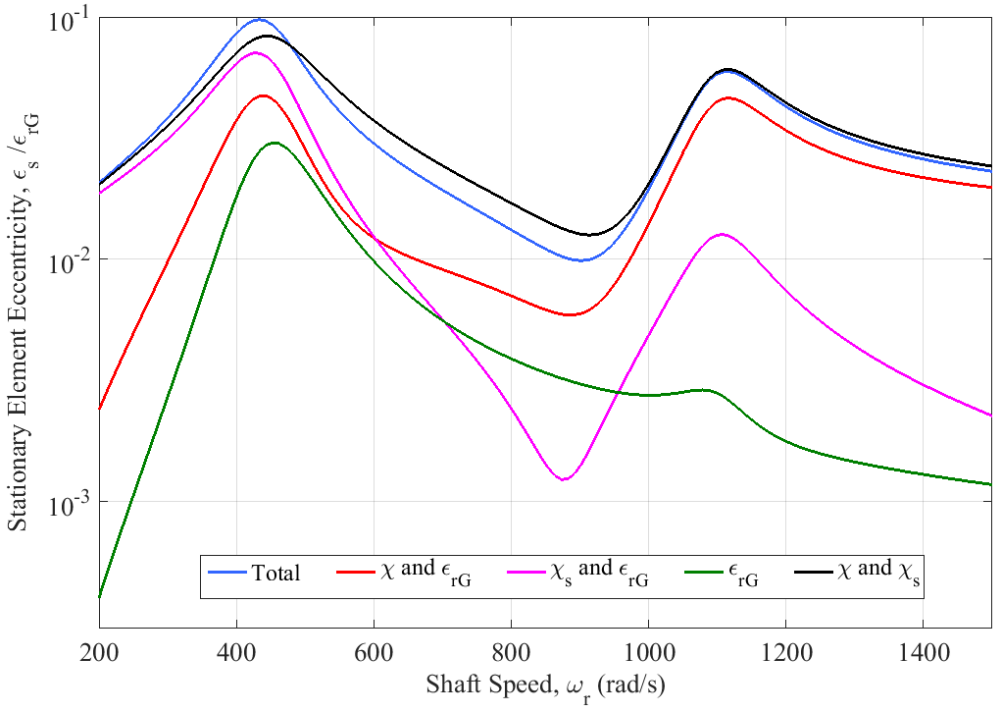

(b) Normalized stationary seal element eccentricity, $\epsilon_s/\varepsilon_{rG}$

Figure 8.2: FMSR-E: Comparing the effects of different forcing functions on the stationary seal element response (thick seal: $I_{tr}/I_{pr} = 2$, $\varepsilon_{rG} = 5(10)^{-5}$ m, $\chi = 5$ mrad, $\chi_s = 1$ mrad).

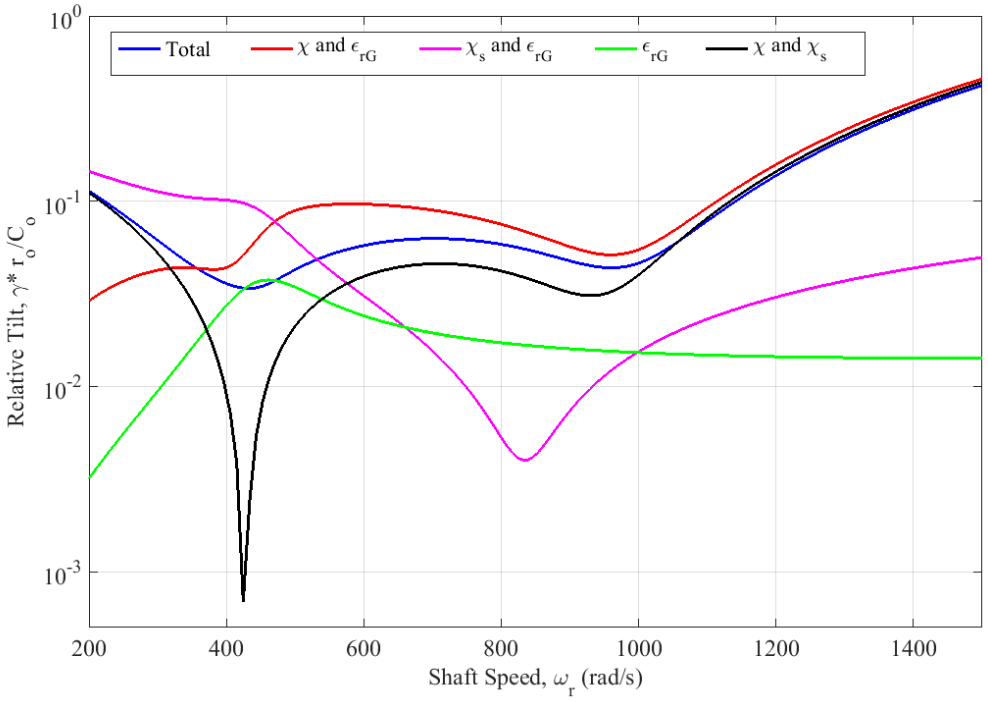

(a) Normalized relative tilt, $\gamma^* r_o/C_o$

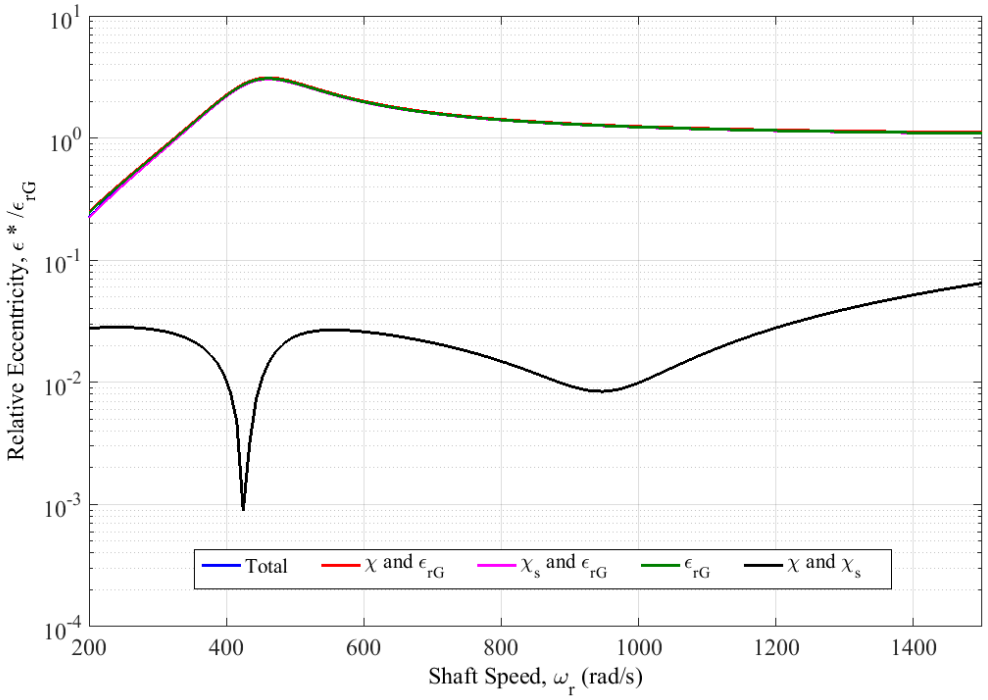

(b) Normalized relative eccentricity, $\epsilon^*/\varepsilon_{rG}$

Figure 8.3: FMSR-E: Comparing the effects of different forcing functions on seal performance (thin seal: $I_{tr}/I_{pr} = 0.5$, $\varepsilon_{rG} = 5(10)^{-5}$ m, $\chi = 5$ mrad, $\chi_s = 1$ mrad).

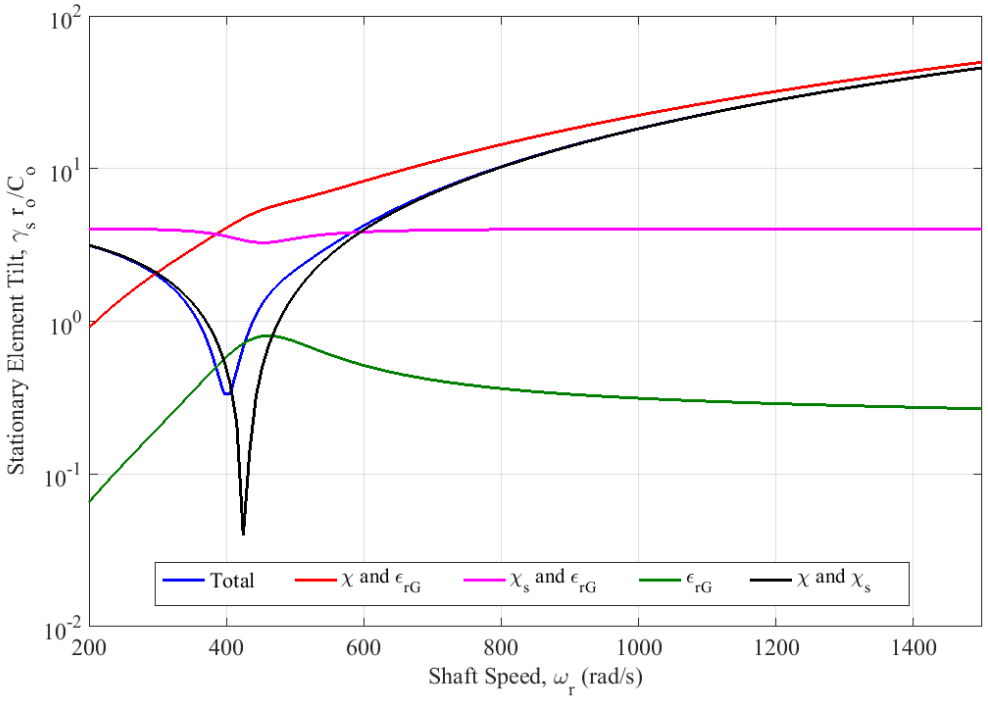

(a) Normalized stationary seal element tilt, $\gamma_s r_o/C_o$

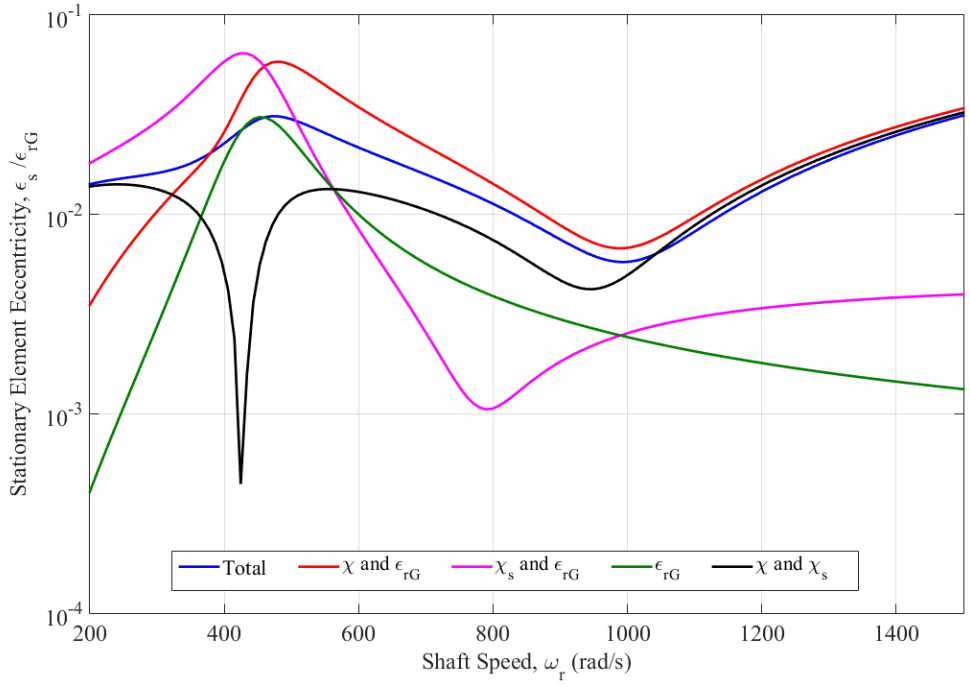

(b) Normalized stationary seal element eccentricity, $\epsilon_s/\varepsilon_{rG}$

Figure 8.4: FMSR-E: Comparing the effects of different forcing functions on the stationary seal element response (thin seal: $I_{tr}/I_{pr} = 0.5$, $\varepsilon_{rG} = 5(10)^{-5}$ m, $\chi = 5$ mrad, $\chi_s = 1$ mrad).

response is more sensitive to changes in χ_s beneath the first critical speed). As shown in Fig. 8.5b, the relative eccentricity remains virtually unchanged with variations in χ_s, though the absolute stationary seal element eccentricity (Fig. 8.6b) is influenced by static angular misalignment. Analogous results are seen for the thin rotor, and are not given here for brevity.

The seal performance versus dynamic angular misalignment χ is provided in Figs. 8.7 and 8.8 for relative and absolute performance, respectively. The dynamic angular misalignment primarily impacts the seal response at shaft speeds above the first critical speed (this conclusion is intuitive because the dynamic angular misalignment excitation is proportional to ω_r^2). The relative seal tilt (Fig. 8.7a) is especially sensitive to χ in the vicinity of the second critical speed. The relative eccentricity is not strongly influenced by dynamic angular misalignment. On the other hand, the absolute seal tilt and eccentricity (Fig. 8.8) increase with increasing dynamic angular misalignment, where the effect is particularly pronounced for shaft speeds above the first critical speed.

The effect of rotating seal element eccentric imbalance ε_{rG} is shown in Figs. 8.9 and 8.10 for a thick rotating seal element. The relative tilt (Fig. 8.9a) depends strongly on eccentric imbalance, where the response magnitude increases for larger imbalances. However, the absolute tilt of the stationary element (Fig. 8.10a) is dominated by static and dynamic angular misalignment, and shows little discernible influence of imbalance magnitude. The imbalance magnitude mostly affects the absolute stationary seal element eccentricity near the first critical speed.

The relative and absolute dynamic seal responses versus rotating seal element inertia ratio I_{tr}/I_{pr} are provided in Figs. 8.11 and 8.12, respectively. The relative eccentric response (Fig. 8.11b) does not significantly depend on the inertia ratio. However, the relative tilt, absolute tilt, and absolute eccentricity all show a qualitative change in dynamic behavior when the rotating seal element is sufficiently thin

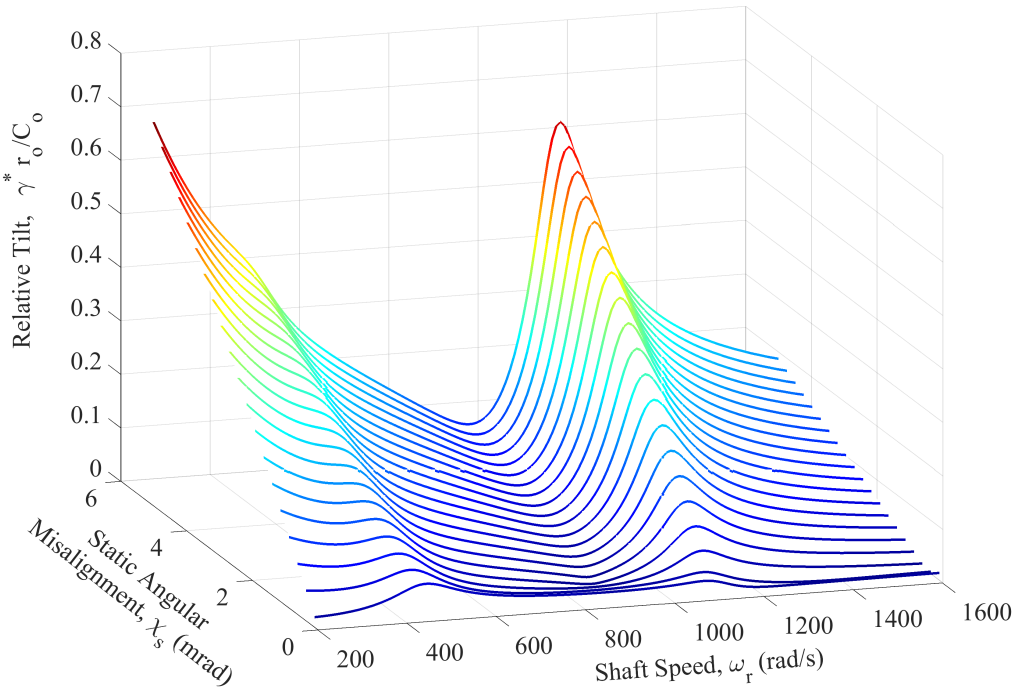

(a) Normalized relative tilt, $\gamma^* r_o/C_o$

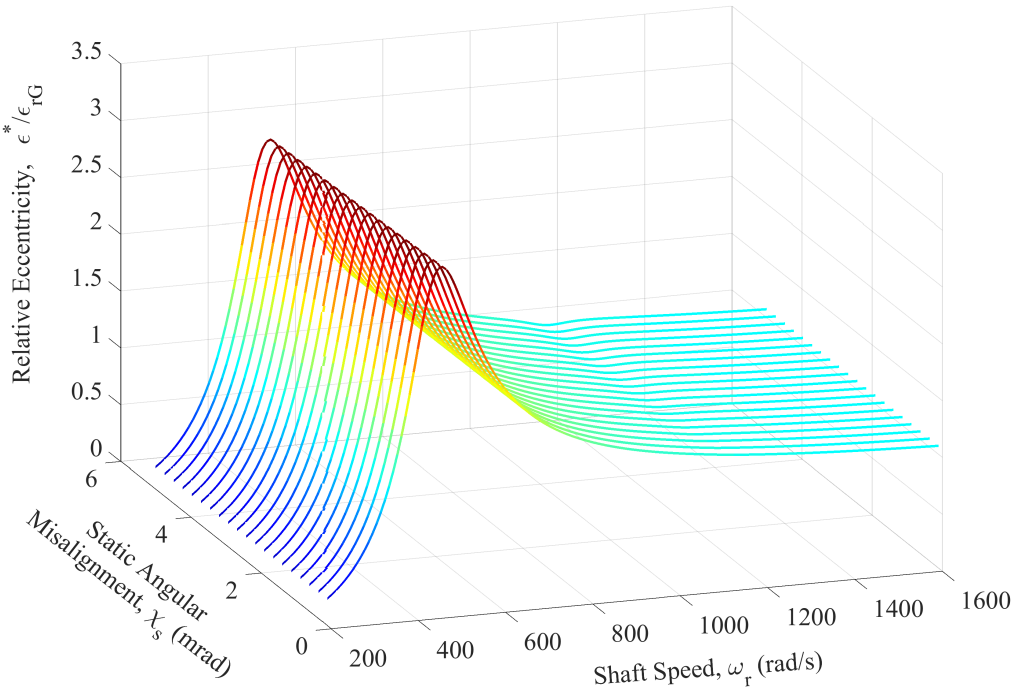

(b) Normalized relative eccentricity, $\epsilon^*/\varepsilon_{rG}$

Figure 8.5: FMSR-E: Influence of rotating seal element static angular misalignment on the relative dynamic response (thick seal: $I_{tr}/I_{pr} = 2$, $\varepsilon_{rG} = 1(10)^{-4}$ m, $\chi = 0$).

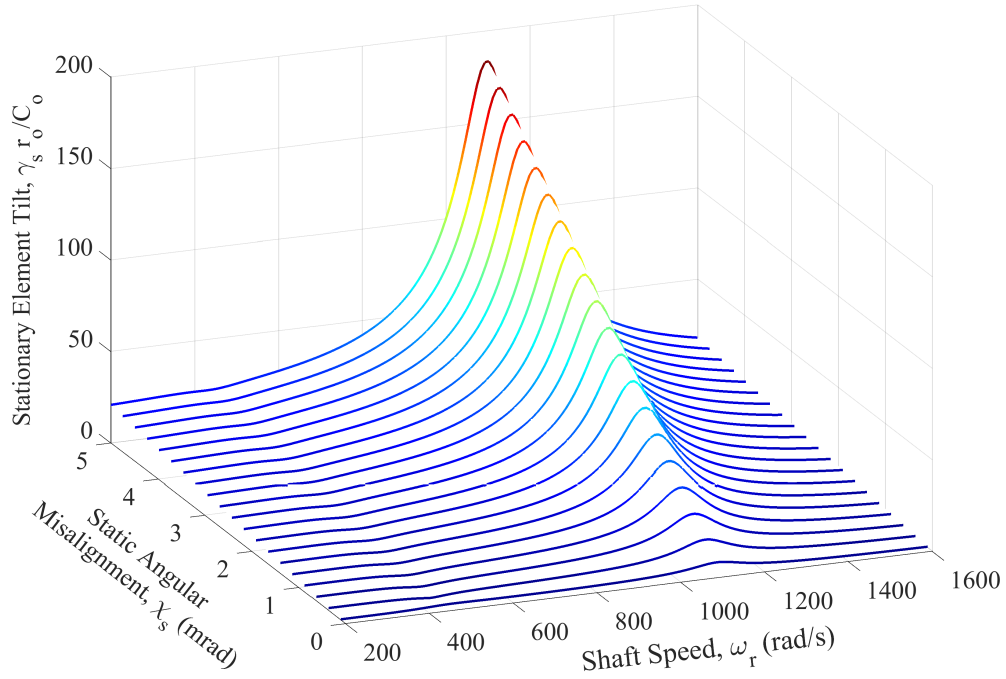

(a) Normalized stationary seal element tilt, $\gamma_s r_o/C_o$

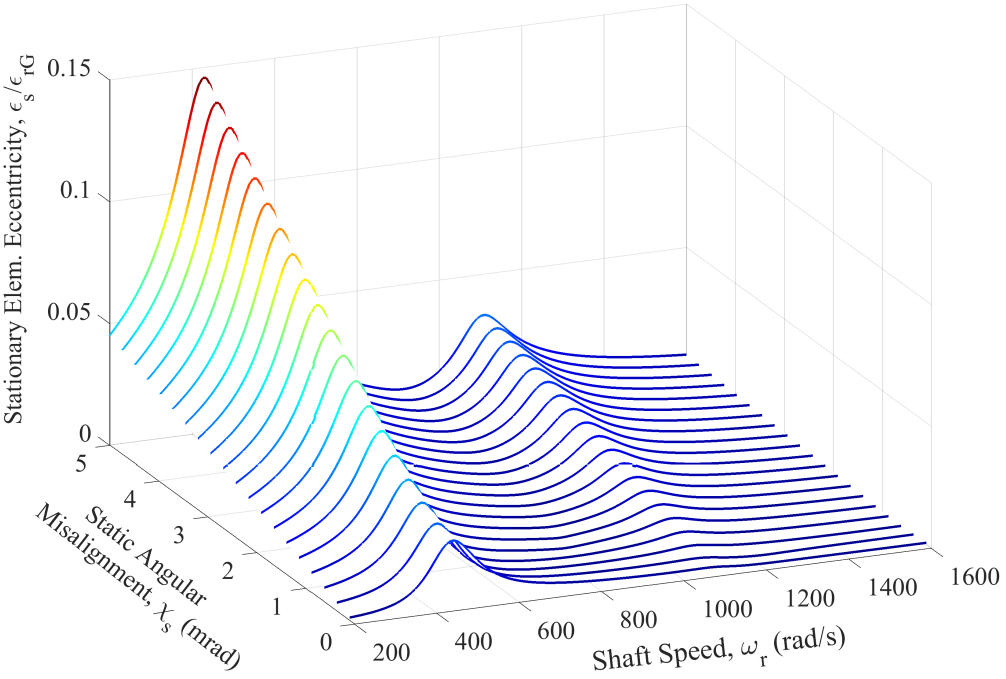

(b) Normalized stationary seal element eccentricity, $\epsilon_s/\varepsilon_{rG}$

Figure 8.6: FMSR-E: Influence of rotating seal element static angular misalignment on the absolute dynamic response (thick seal: $I_{tr}/I_{pr} = 2$, $\varepsilon_{rG} = 1(10)^{-4}$ m, $\chi = 0$).

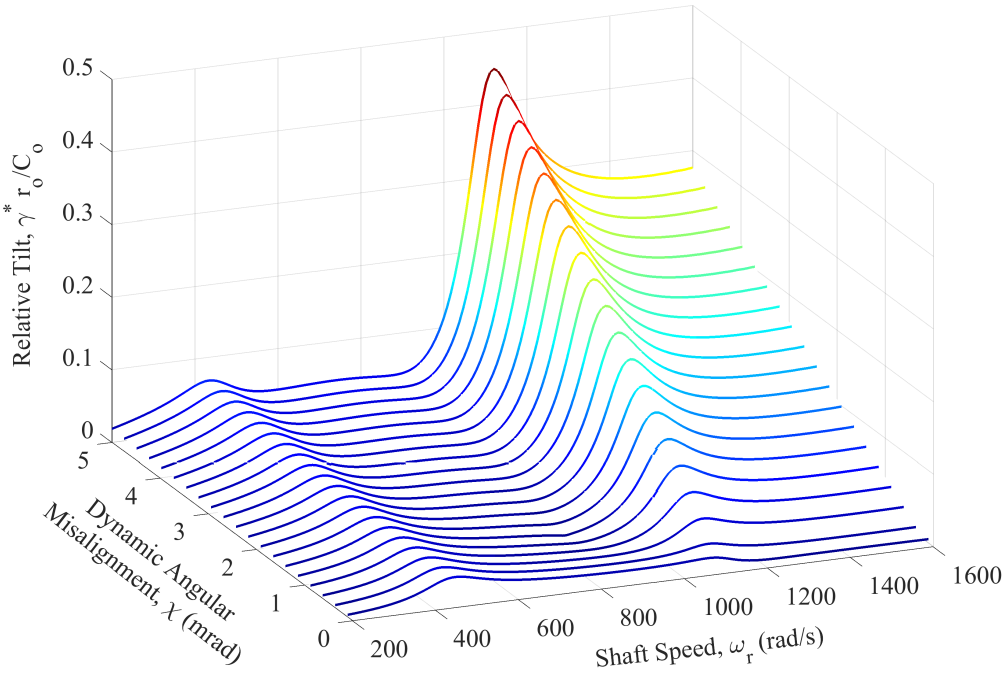

(a) Normalized relative tilt, $\gamma^* r_o/C_o$

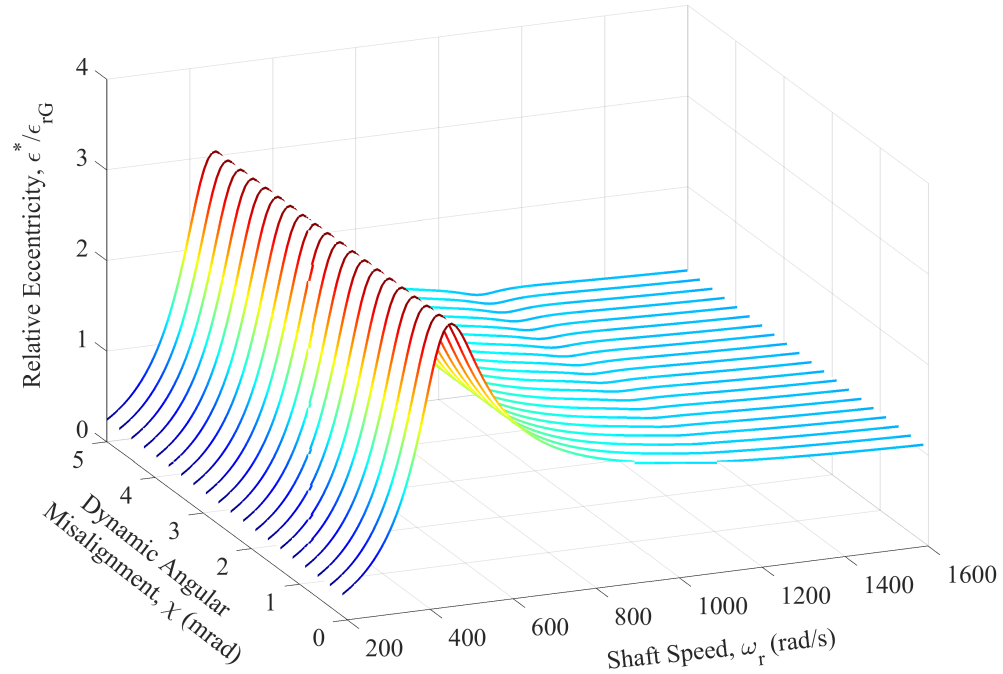

(b) Normalized relative eccentricity, $\epsilon^*/\varepsilon_{rG}$

Figure 8.7: FMSR-E: Influence of rotating seal element dynamic angular misalignment on the relative dynamic response (thick seal : $I_{tr}/I_{pr} = 0.5$, $\varepsilon_{rG} = 5(10)^{-5}$ m, $\chi_s = 0$).

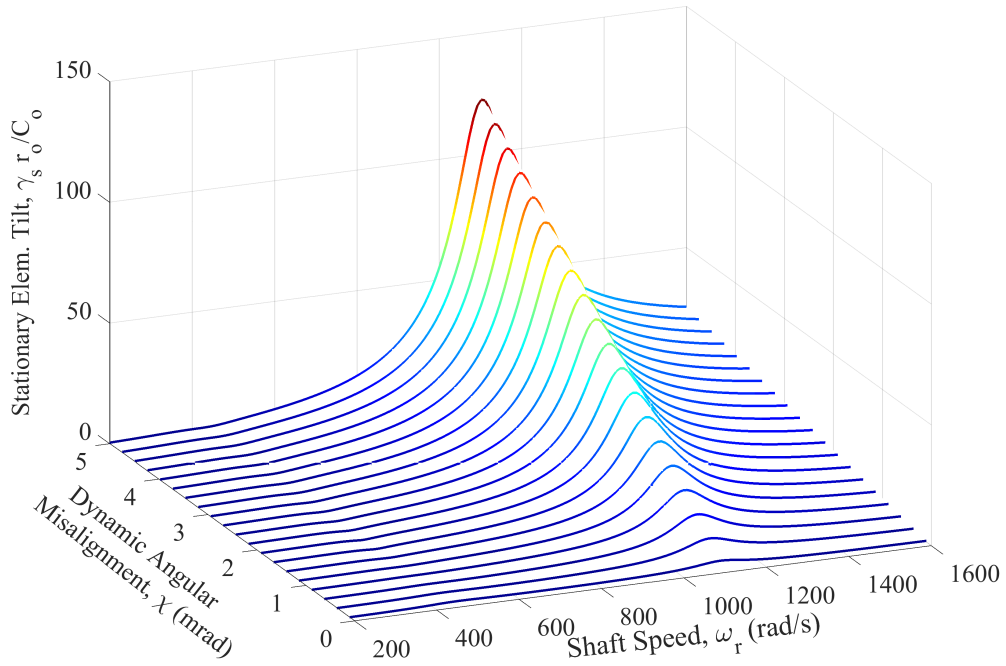

(a) Normalized stationary seal element tilt, $\gamma_s r_o/C_o$

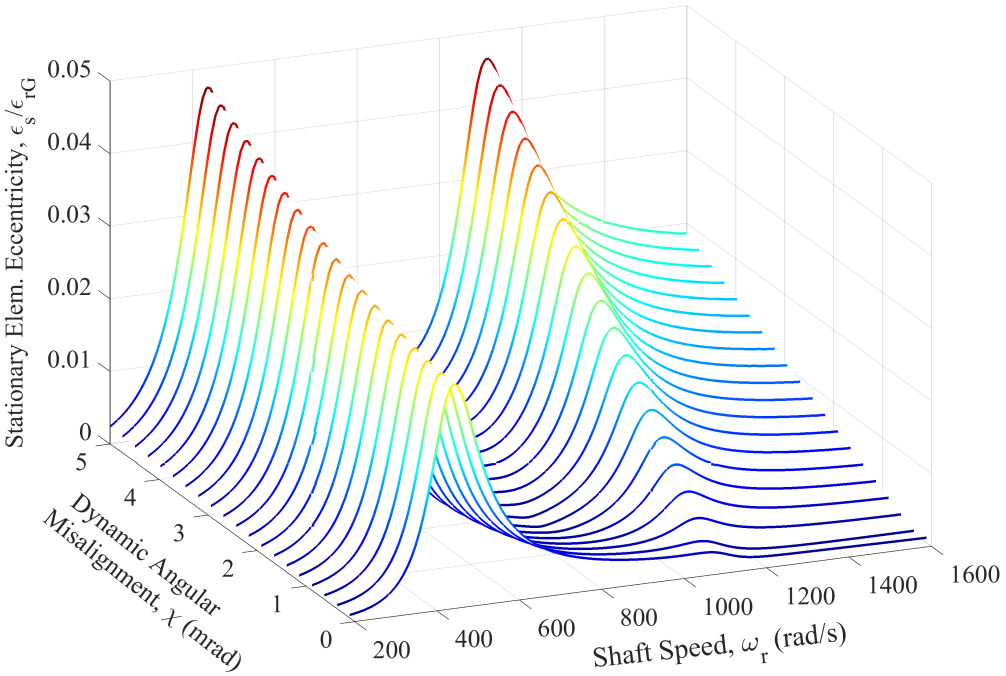

(b) Normalized stationary seal element eccentricity, $\epsilon_s/\varepsilon_{rG}$

Figure 8.8: FMSR-E: Influence of rotating seal element dynamic angular misalignment on the absolute dynamic response (thick seal: $I_{tr}/I_{pr} = 0.5$, $\varepsilon_{rG} = 5(10)^{-5}$ m, $\chi_s = 0$).

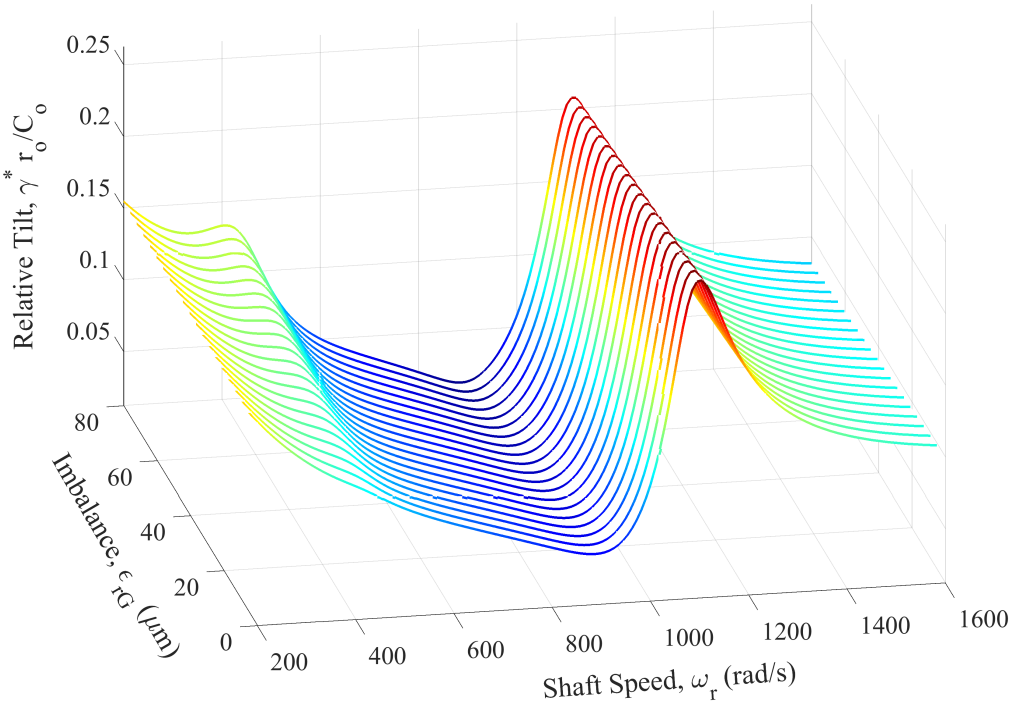

(a) Normalized relative tilt, $\gamma^* r_o/C_o$

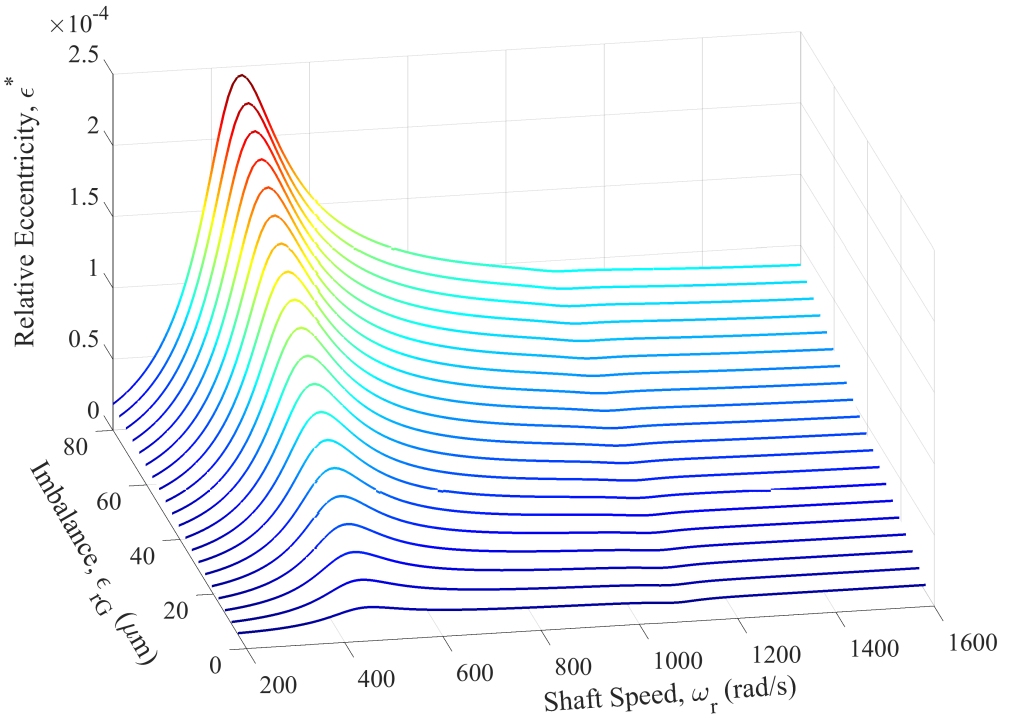

(b) Relative eccentricity, ϵ^*

Figure 8.9: FMSR-E: Influence of rotating seal element eccentric imbalance on the relative dynamic response (thick seal: $I_{tr}/I_{pr} = 0.5$, $\chi_s = 1$ mrad, $\chi_s = 1$ mrad).

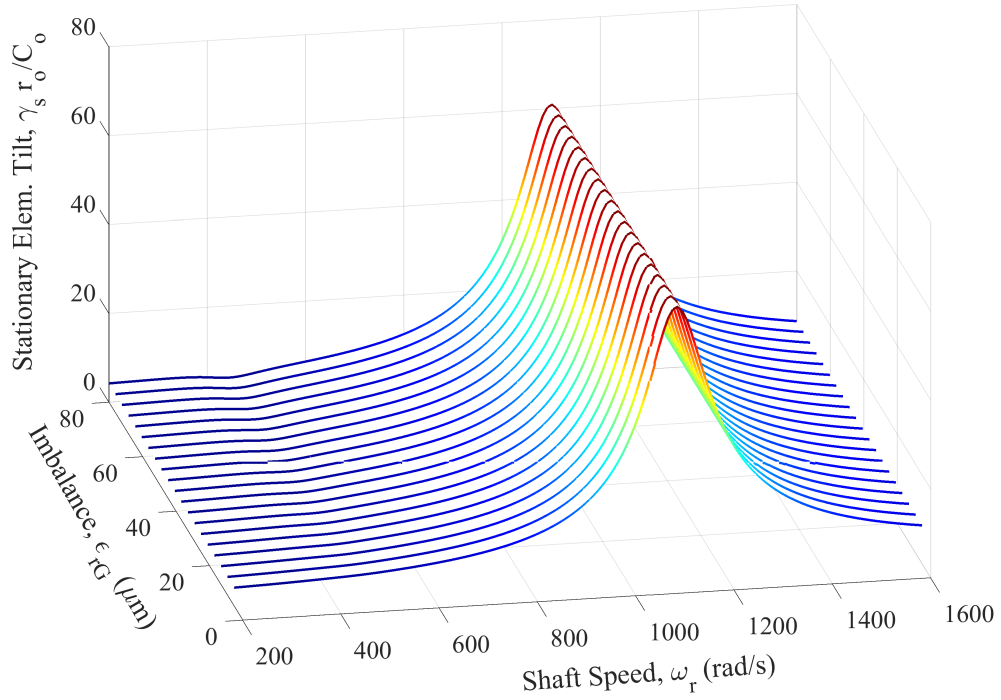

(a) Normalized stationary seal element tilt, $\gamma_s r_o/C_o$

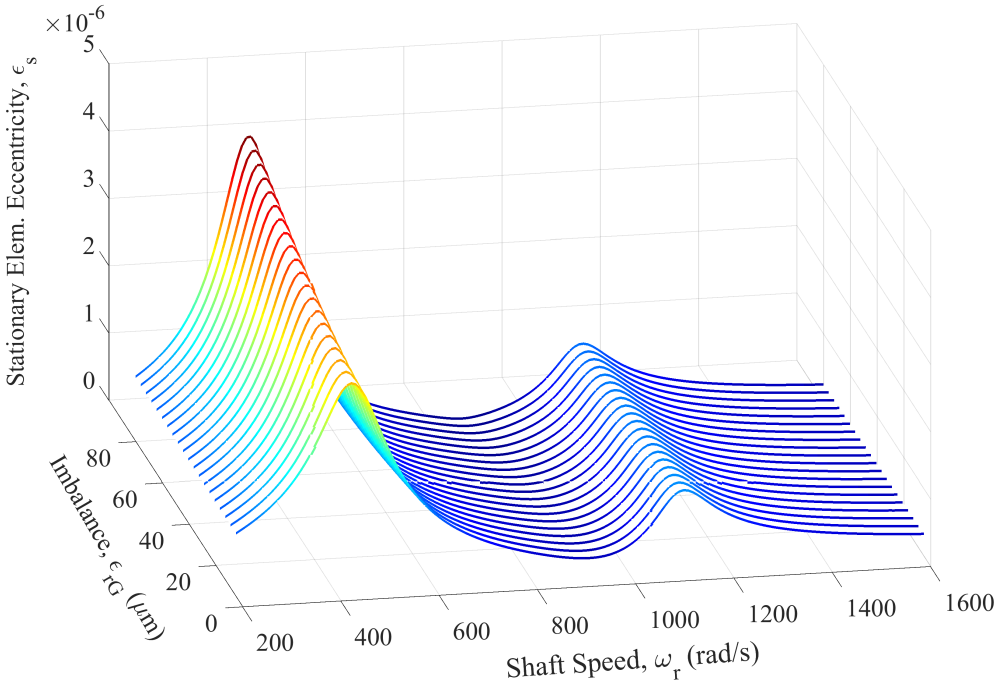

(b) Stationary seal element eccentricity, $\epsilon_s/\varepsilon_{rG}$

Figure 8.10: FMSR-E: Influence of rotating seal element eccentric imbalance on the absolute dynamic response (thick seal: $I_{tr}/I_{pr} = 0.5$, $\chi_s = 1$ mrad, $\chi_s = 1$ mrad).

($I_{tr}/I_{pr} < 1$). In this case, the gyroscopic term minimizes the relative tilt at large shaft speeds. A local minimum in the response appears when $I_{pr} > I_{tr}$ because the static and dynamic angular misalignments destructively interfere at this shaft speed (i.e., $K_r\chi_s - (I_{tr} - I_{pr})\chi\omega_r^2 = 0$).

Several conclusions regarding the use of a FMSR seal as a surrogate rotordynamic condition monitoring system are drawn from the previous results. First, the fluid film minimizes relative tilts but not relative eccentricities. Thus, the stationary element tilt is identified as a target for surrogate rotordynamic monitoring. This conclusion does not depend on whether the rotating seal element is thick or thin, and thus, the seal can be designed with exclusive regard for seal performance. These conclusions are important because the rotordynamic response is inextricable from the rotating seal element dynamic response (as a consequence of joining the two elements via an elastomeric O-ring). Then, because of the fluid film, the dynamic response of the rotating seal element is transferred to the stationary element. Thus, the mechanisms that transmit excitations between the elements are also indicative of how rotor vibrations are transmitted between the seal elements.

8.2 Fundamental Aspects of Rotor-Seal Coupling

The objective of this section is to investigate how the rotordynamics influence the seal dynamics, and specifically, to establish criteria for which the rotor influences the seal but not vice-versa. Fundamental aspects of rotor-seal coupling are studied here using the FMS-R seal to avoid undue complexity (recall that the FMS-R seal consists of a stationary seal element and the angular rotor dynamics). The equations of motion have been previously provided in Section 5.3, where the fluid film forces are linearized into commensurate stiffness and damping coefficients. Thus, the analytic solution provided therein is used here to study rotor-seal interactions.

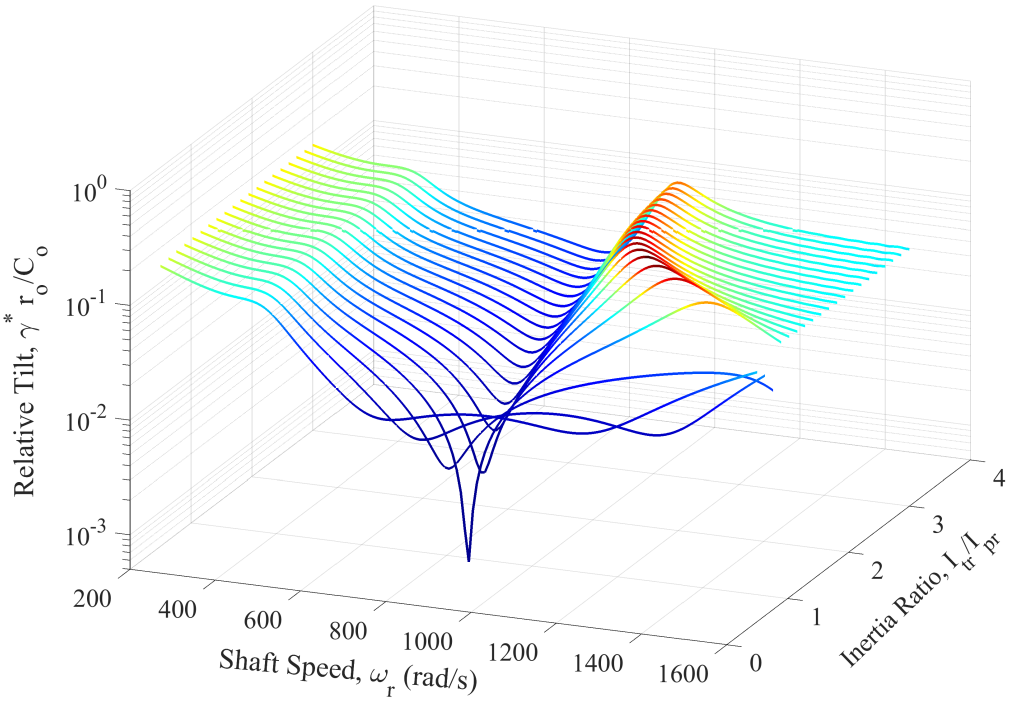

(a) Normalized relative tilt, $\gamma^* r_o/C_o$

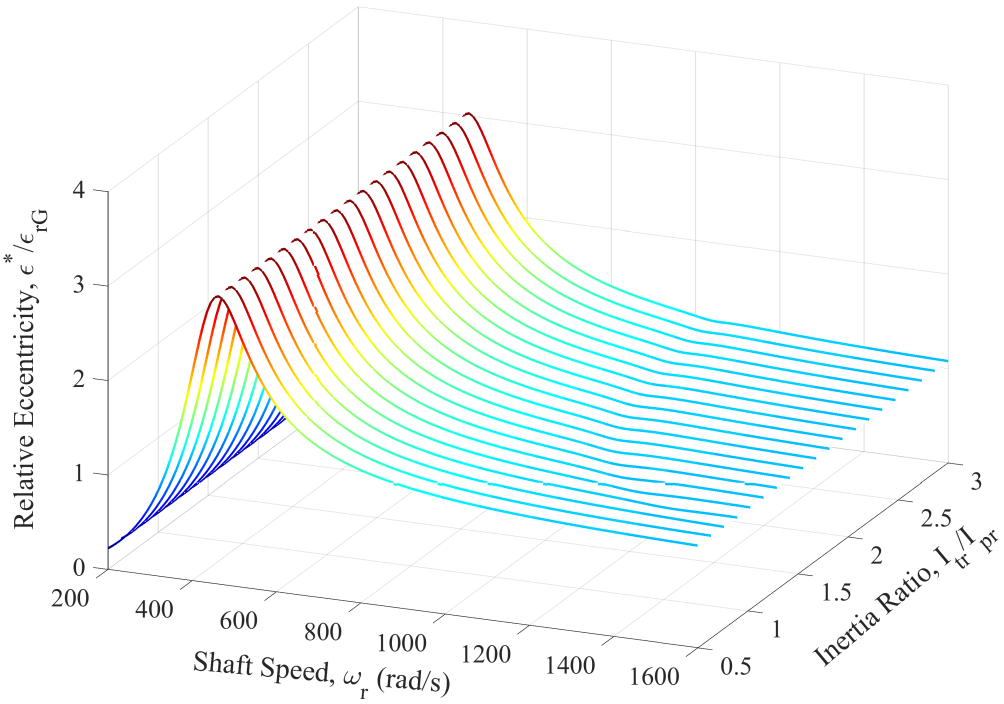

(b) Normalized relative eccentricity, $\epsilon^*/\varepsilon_{rG}$

Figure 8.11: FMSR-E: Influence of rotating seal element inertia ratio on the relative dynamic response ($\varepsilon_{rG} = 5(10)^{-5}m$, $\chi_s = 1$ mrad, $\chi_s = 1$ mrad).

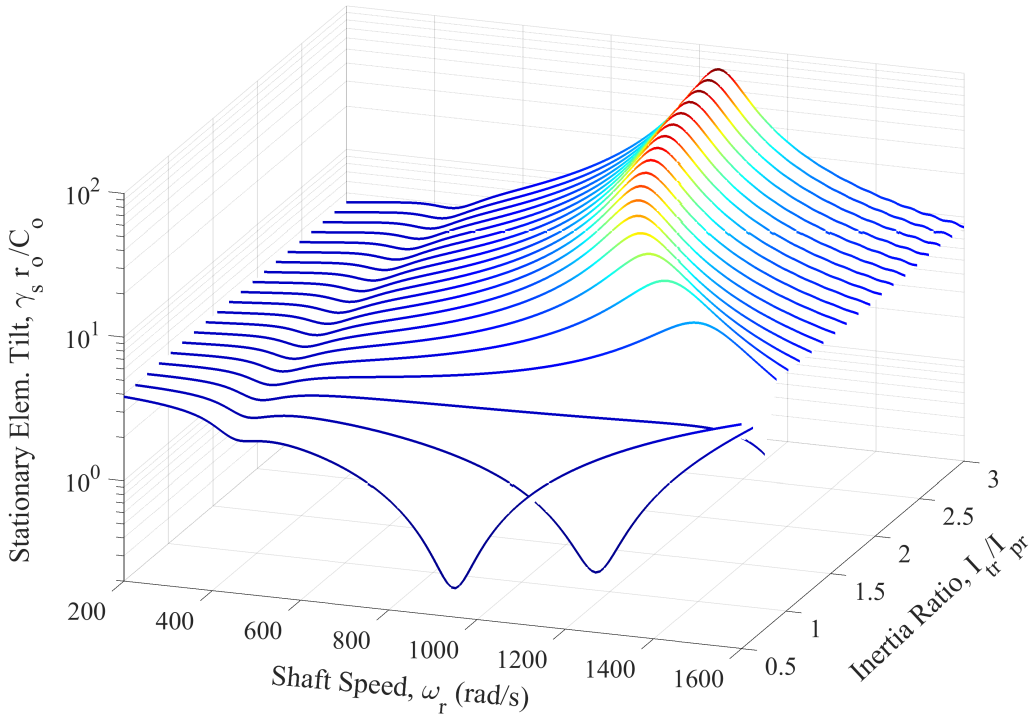

(a) Normalized stationary seal element tilt, $\gamma_s r_o/C_o$

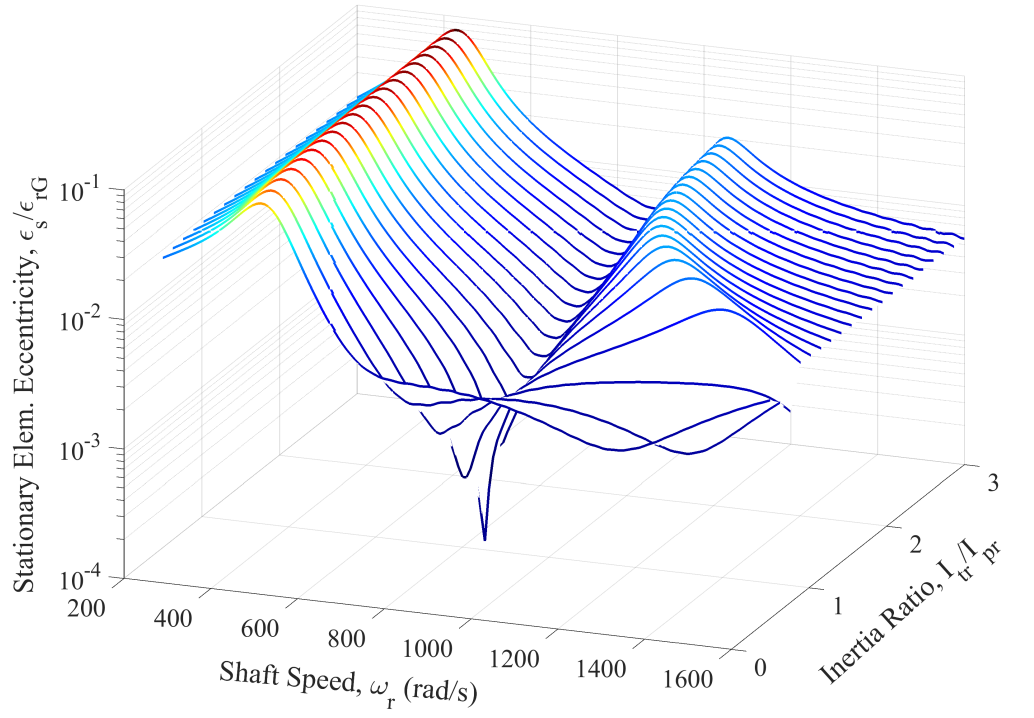

(b) Normalized stationary seal element eccentricity, $\epsilon_s/\varepsilon_{rG}$

Figure 8.12: FMSR-E: Influence of rotating seal element inertia ratio on the absolute dynamic response ($\varepsilon_{rG} = 5(10)^{-5}m$, $\chi_s = 1$ mrad, $\chi_s = 1$ mrad).

Table 8.3: FMS-R: Rotor and seal dynamic and support properties.

Parameter	**Rotor**	**FMS**
Polar moment of inertia	$I_{pR} = I_{tR}/C$ kg·m^2	–
Transverse moment of inertia	$I_{tR} = 0.2$ kg·m^2	$I_{ts} = 1.7(10)^{-3}$ kg·m^2
Angular support stiffness	$k_{R\gamma} = 5(10)^5$ N·m/rad	$K_s = 363.9$ N·m/rad
Angular external/support damping	$c_{R\gamma} = 20$ N·m·s/rad	$D_s = 0.22$ N·m·s/rad

8.2.1 Steady-State Response

The parameters used here are given in Tables 8.2 and 8.3. The FMS stiffness and damping values used here, K_s and D_s, are representative of values obtained from an existing experimental FMS seal test rig [22]. Likewise, the rotor parameters $k_{R\gamma}$ and $c_{R\gamma}$ are representative of the rotor found in an associated experimental test rig [84,85]. Other parameters, such as inertia ratio $C = I_{tR}/I_{pR}$, dynamic angular misalignment χ, and shaft speed ω_r will be provided where applicable. Static misalignments of the seal and rotor are not considered here because superposition applies to the linearized equations of motion; the system response to these terms can be found independently and added to the response to dynamic rotor misalignment.

The efficacy of the linearized steady-state analytic solution is established by comparing to a numeric simulation of the full nonlinear equations of motion. The relative tilt versus shaft speed is shown in Fig. 8.13 for several values of dynamic angular misalignment. Several observations are gleaned from the comparison. First, the relative tilt reaches a local maximum near 1000 rad/s; this peak occurs identically at the rotor's first 1X forward critical speed. The critical speed is verified from the Campbell diagram shown in Fig. 8.14. For the parameters considered here, the analytic steady-state solution is accurate for shaft speeds below the critical speed. These conclusions are reasonable because the linearized fluid film coefficients are found by assuming that the relative tilt is small.

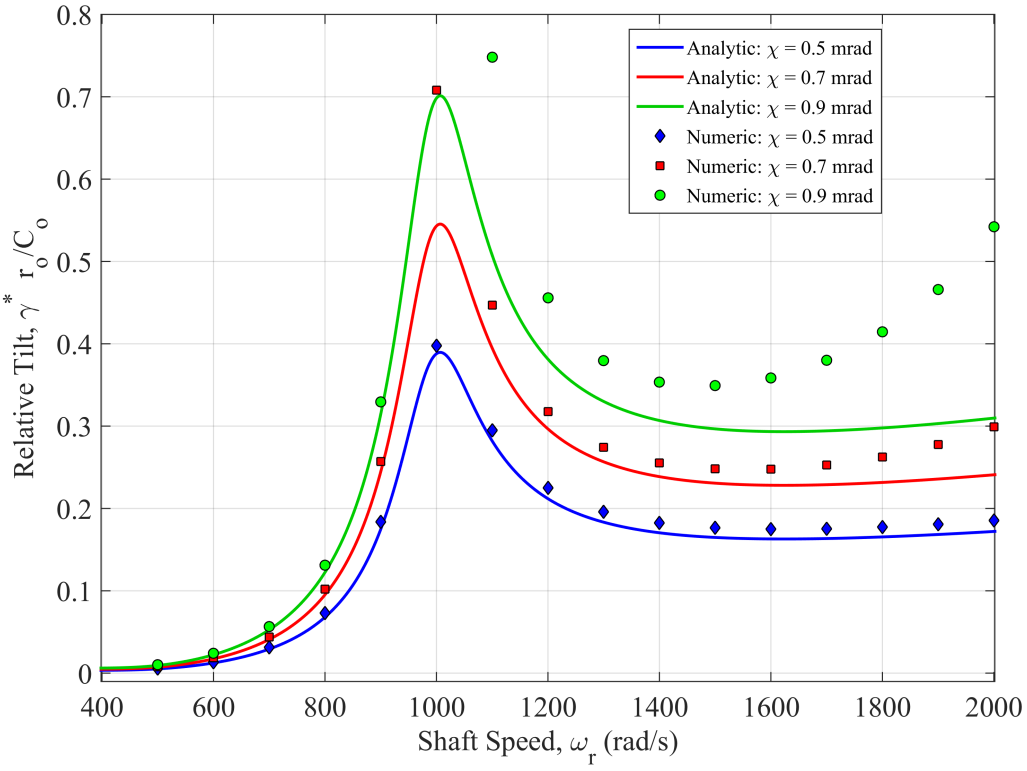

Figure 8.13: Comparing the numeric solution of the full nonlinear equations of motion to the analytic solution of the linearized equations of motion (thick rotor: $C = 2$).

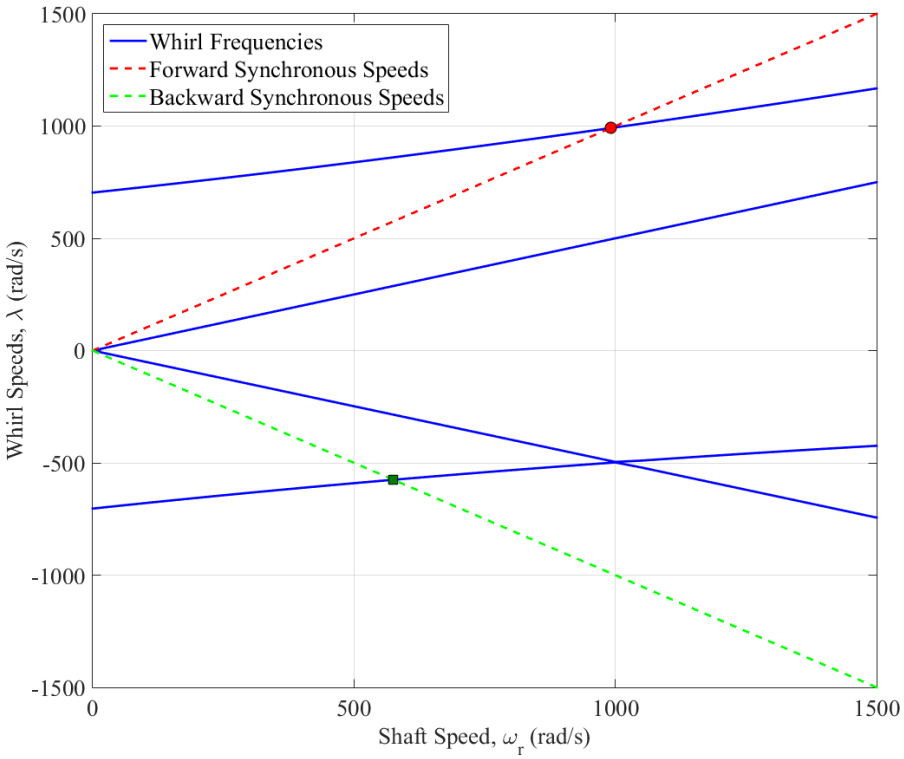

Figure 8.14: Campbell diagram indicating the forward ($\lambda^+ = 990$ rad/s) and backward ($\lambda^- = 575$ rad/s) synchronous critical speeds.

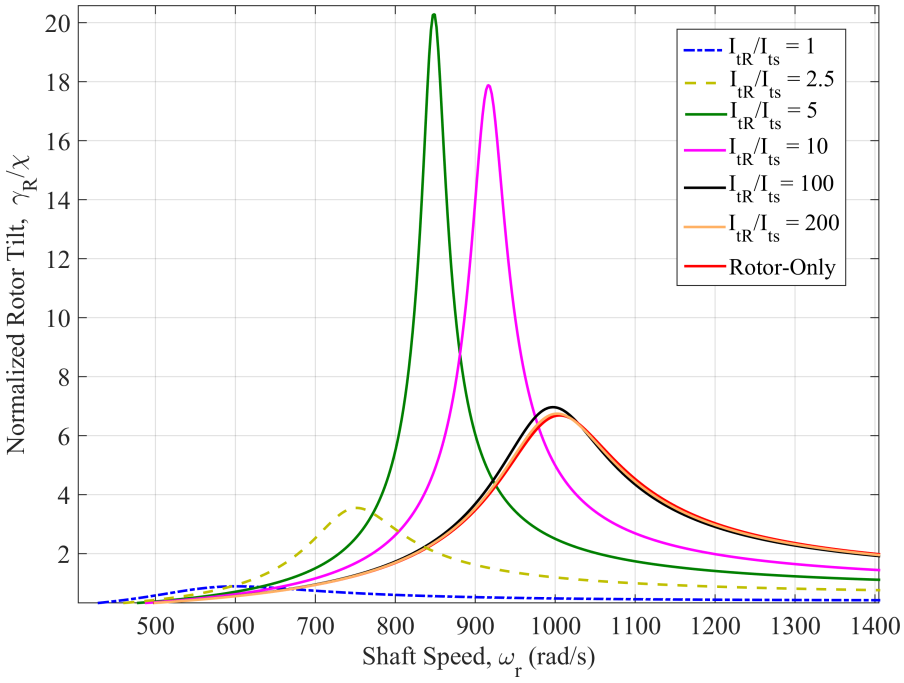

Figure 8.15: Investigating the influence of the seal dynamics on the rotor response ($\chi = 0.5$ mrad, $C = 2$).

Dynamic coupling between the rotor and seal is investigated by varying the ratio between the rotor and seal transverse mass moments of inertia. The dynamic response of a thick rotor to an angular misalignment of $\chi = 0.5$ mrad is given in Fig. 8.15, which shows relative tilt γ^* versus shaft speed ω_r for several inertia ratios. The dynamic response of only the rotor (i.e., no seal) is provided for comparison. As expected, the seal dynamics do not meaningfully influence the rotordynamics for inertia ratios I_{tR}/I_{ts} above 100. The importance of this conclusion cannot be understated, because it implies that for massive rotors ($I_{tR} >> I_{ts}$), the rotordynamics influence the seal dynamics but not vice versa. Thus, the rotordynamics can be solved independently and sent as a known exogenous input to a separate seal dynamic simulation. Importantly, this conclusion does not depend on whether or not the rotor is thick or thin.

8.2.2 Summary

The most salient conclusion drawn from the FMS-R analysis is that the rotordynamics are uninfluenced by the seal dynamics when the rotor is much larger than the seal. In this case, the rotordynamics can be solved separately from the seal dynamics. This conclusion is also important with regard to fault diagnostics because it implies that the seal is an unbiased observer of the rotor. Thus, the character of any fault-induced rotordynamic signature is dictated exclusively by the rotor (i.e., the rotordynamics are unadulterated by the seal dynamics when the seal is operating as-intended).

8.3 FMSR-ER Performance

The steady-state equations of motion for the FMSR-ER system are simulated here to study the influence of the rotordynamic response on the seal dynamic performance. The equations of motion for the rotor are provided in Eq. 4.1, while those for the FMSR-E seal are given in Eqs. 5.48 - 5.57. The seal properties are provided in Tables 8.1 and 8.2, and are representative of mechanical seals investigated in previous

Table 8.4: Overhung rotor parameters.

Parameter	**Value**
Rotor mass, m_R	20 kg
Rotor transverse mass moment of inertia, I_{tR}	0.2 kg·m^2
Rotor polar mass moment of inertia, I_{pR}	(variable)
Shaft diameter, d	0.035 m
Shaft length, L	0.4 m
Shaft elastic modulus, E	210 GPa
Proportional damping coefficient, β_c	0.01
External viscous damping coefficient, $\zeta_\epsilon = \zeta_\gamma$	0.01

Table 8.5: Rotor and seal excitation parameters (rotor bow is not considered here; i.e., $r_b = \chi_b = 0$).

Parameter	**Value**
Rotor imbalance, ε_{RG}	$1(10)^{-5}$ m
Rotating seal element imbalance, ε_{rG}	$5(10)^{-5}$ m
Rotor dynamic angular misalignment, χ_R	1 mrad
Rotating seal element dynamic angular misalignment, χ	1 mrad
Rotating seal element static angular misalignment, χ_s	0.5 mrad

works [42]. The rotor parameters are selected to emulate a realistic rotor-seal system where the rotor inertia is much larger than that of the seal (see Table 8.4). In this case, as the results of Section 8.2 indicate, the rotor influences the seal dynamics but not vice versa. Excitation parameters (i.e., imbalance, dynamic angular misalignment, rotor bow, etc.) are provided in Table 8.5.

The first objective is to again verify that the rotordynamics are not influenced by the seal dynamics for the parameters given in Tables 8.1, 8.2, and 8.4. The rotor tilt γ_R and eccentric response ϵ_R are provided in Figs. 8.16a and 8.16b, respectively, for simulations that both include and neglect the seal dynamics. The simulation is performed for the case where both the rotor and the rotating seal element are thick ($I_{tr}/I_{pr} = I_{tR}/I_{pR} = 2$). The rotor tilt and eccentricity indicate that the rotordynamics are decoupled from the seal dynamics (though later results will show that the converse is not true; the seal dynamics are inextricable from the rotordynamics). Identical conclusions are reached for other cases (e.g., thin rotor, thin seal, etc.).

The FMSR-ER equations of motion are solved numerically according the methods presented in Section 3.9.2. Because the rotor is undamaged, the synchronous steady-state solution given in Eqs. 4.18 and 4.23 is used to explicitly evaluate the rotor response at every time step in the numeric integration. The resulting seal and rotor steady-state response is provided in Figs. 8.17 - 8.20 for various combinations of thick and thin rotor and seal elements. For each combination of seal and rotor elements, the seal performance is assessed by considering the relative performance metrics (relative tilts and eccentricities). In addition, transmittance of rotor vibration to the stationary seal element is studied using the stationary seal element absolute dynamic response (i.e., tilt and eccentricity). The absolute vibration of the stationary seal element is important for determining the efficacy of using the seal as a surrogate rotordynamic vibration monitoring system. If the rotordynamics significantly alter the stationary seal element response, it is reasonable to conclude that fault-induced rotor vibrations

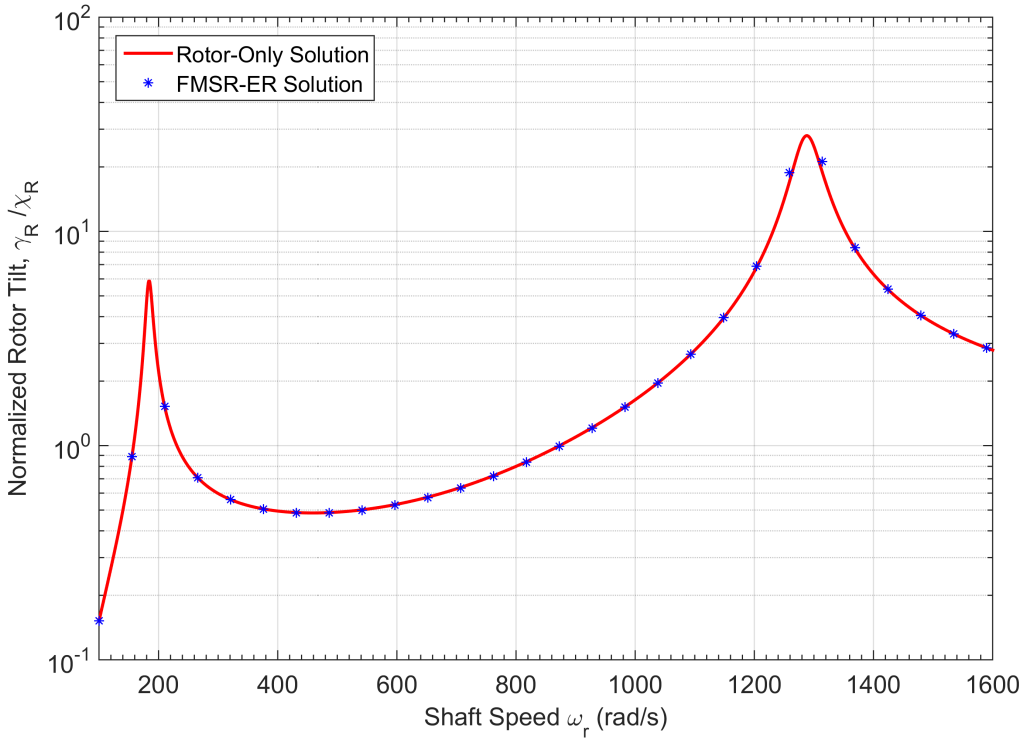

(a) Rotor tilt response, γ_R

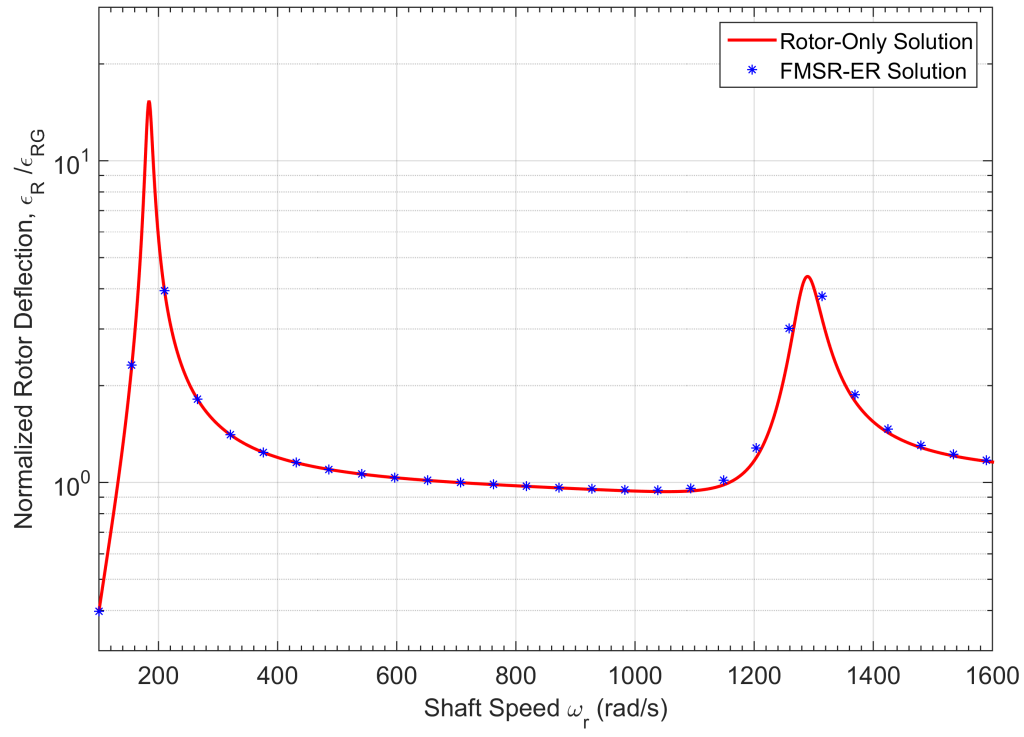

(b) Rotor eccentric response, ϵ_R

Figure 8.16: Rotor response with and without the seal (solution is performed for the thick rotor-thick seal case).

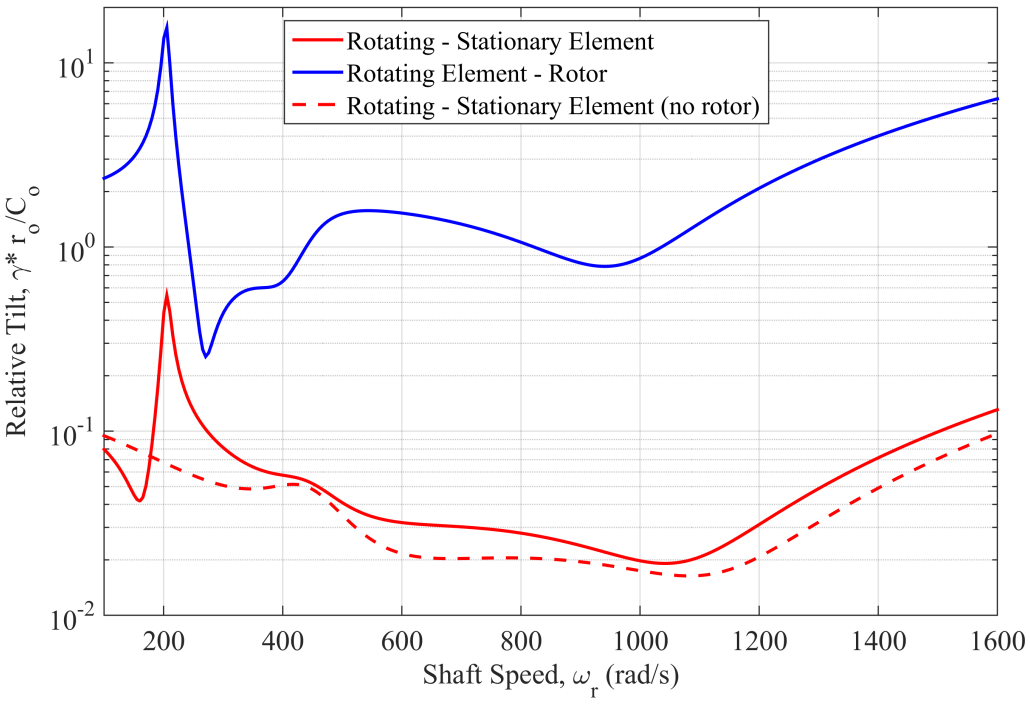

(a) Normalized relative tilt

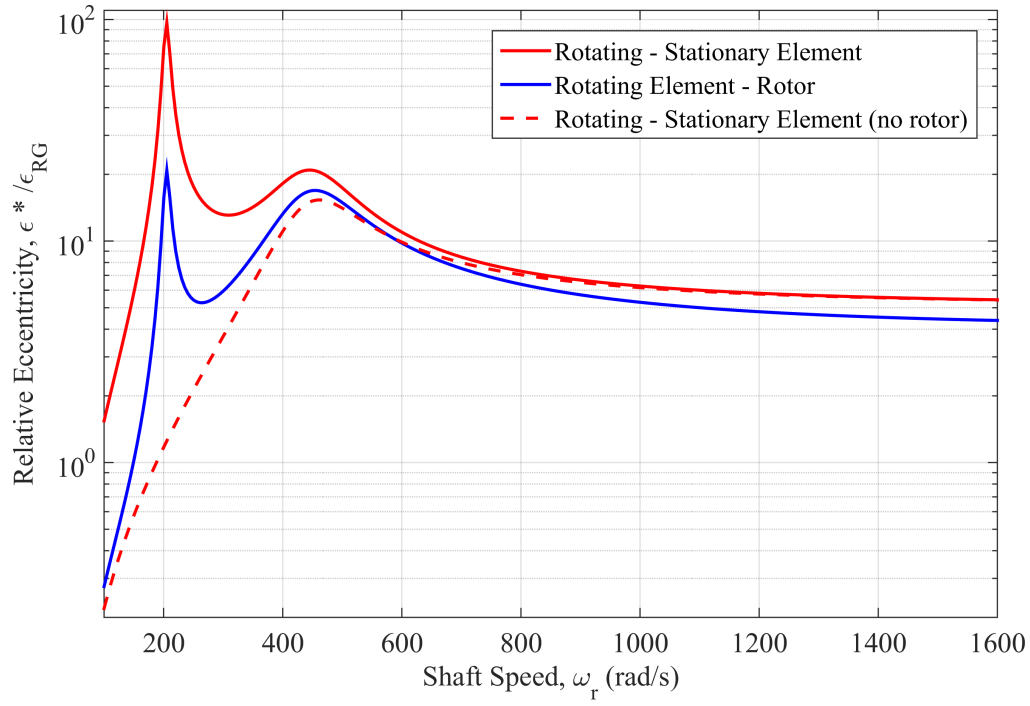

(b) Normalized relative eccentricity

Figure 8.17: Thin Rotor - Thin Seal: Seal dynamic performance versus shaft speed for the undamaged FMSR-ER system.

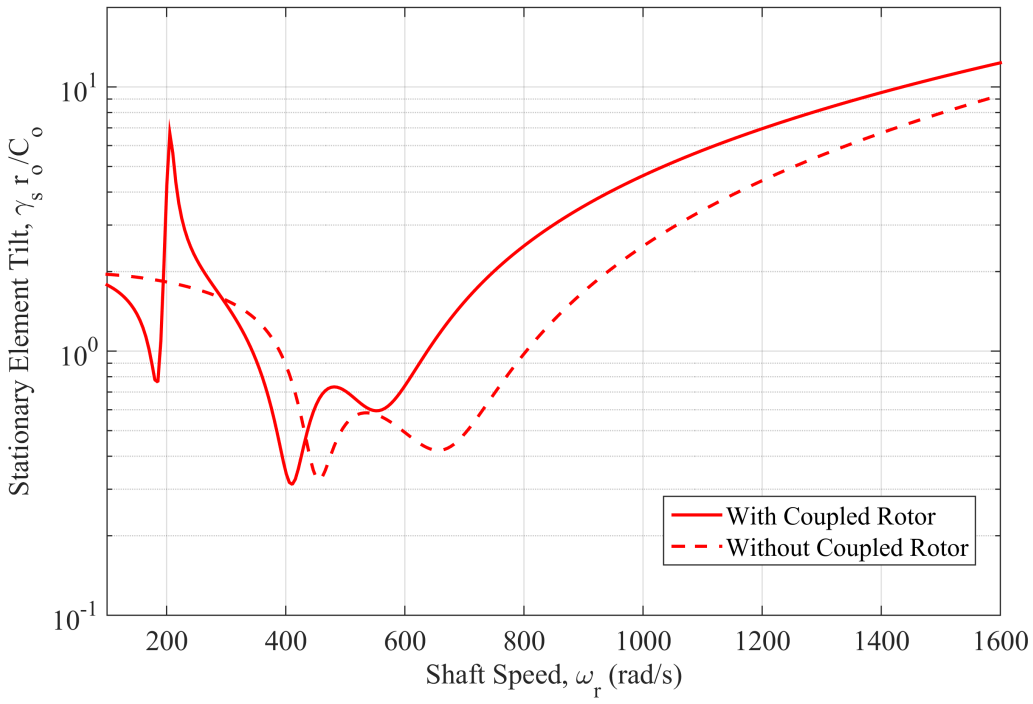

(a) Normalized stationary element tilt

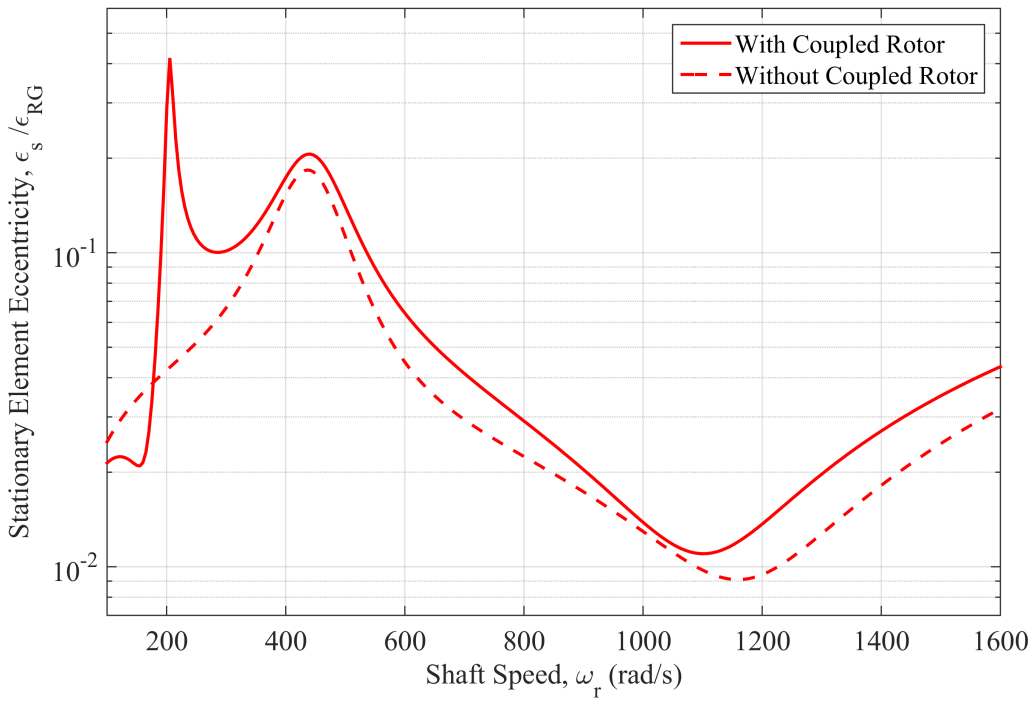

(b) Normalized stationary element eccentricity

Figure 8.18: Thin Rotor - Thin Seal: Absolute stationary seal element response versus shaft speed for the undamaged FMSR-ER system.

will also manifest in the stationary element response.

The FMSR-ER response for a thin rotor and thin seal is provided in Figs. 8.17 and 8.18, where the seal response without the rotor is shown for comparison. Because both rotating bodies are thin, each element contributes only a single resonance (200 rad/s for the rotor, and 440 rad/s for the seal). Similar results are observed for the thick rotor - thick seal scenario shown in Figs. 8.19 and 8.20 for the relative and absolute responses, respectively. In this case, the inertia properties of both elements cause the response to incur additional resonances. The rotor contributes resonances near 190 and 1300 rad/s, respectively, while the seal induces resonances near 450 and 1100 rad/s, respectively.

Several important conclusions are drawn from the results:

1. The seal is adept at minimizing relative tilt between the seal faces.

2. The seal does not minimize relative eccentricities between the seal faces.

3. The rotordynamic response manifests prominently in the stationary seal element response (and, by association, the rotating seal element response).

The importance of these conclusions extends beyond assessing the seal performance. Because the rotordynamics distinctly appear in the seal response, it is reasonable to assume that fault-induced rotordynamic signatures will also appear in the seal response. Furthermore, considering points (1) and (2) above, it is clear that the stationary element mounted monitoring system should rely on tilt measurements rather than eccentric deflection measurements. Interestingly, the same mechanism that allows the seal to function properly, fluid lubrication, also ensures that the element can function as a surrogate rotordynamic monitor.

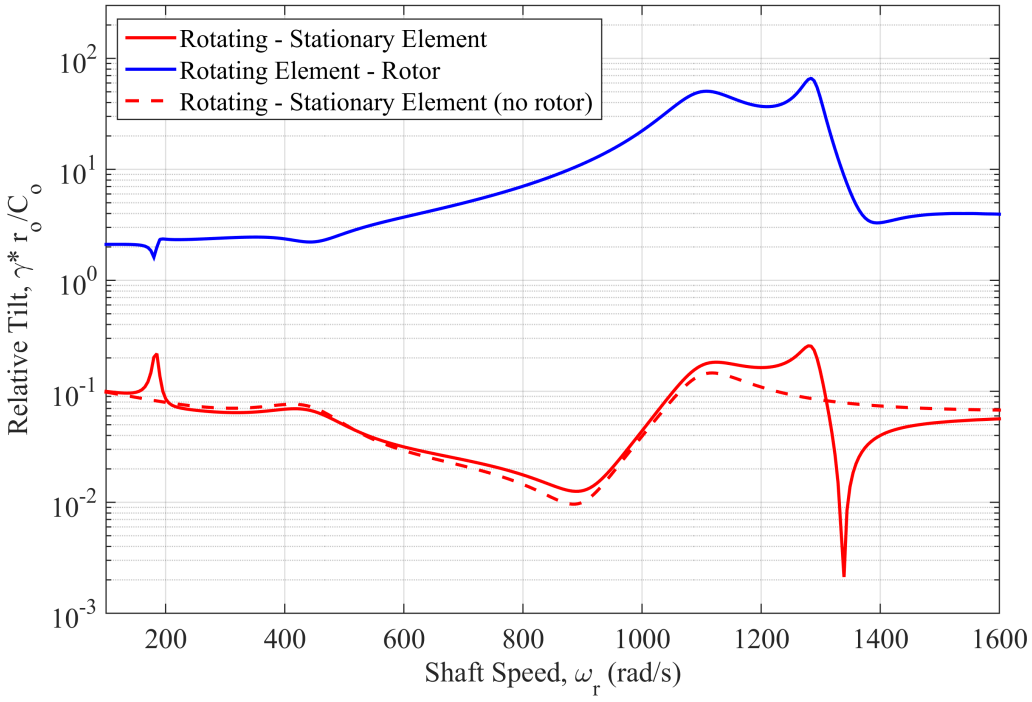

(a) Normalized relative tilt

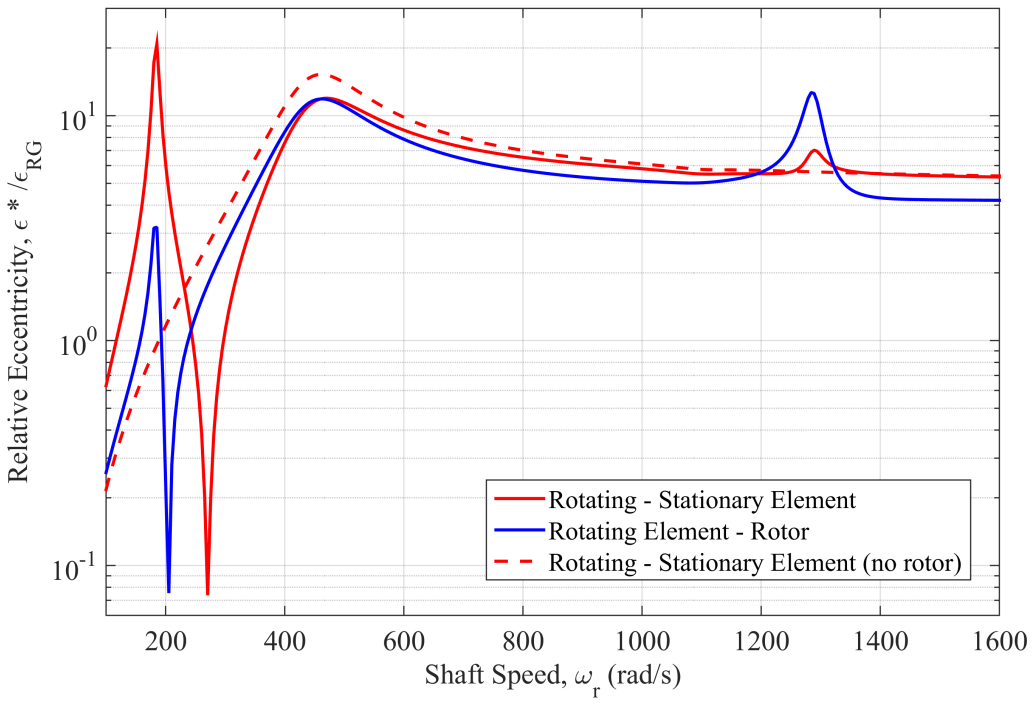

(b) Normalized relative eccentricity

Figure 8.19: Thick Rotor - Thick Seal: Seal dynamic performance versus shaft speed for the undamaged FMSR-ER system ($\chi_R = 0.1$ mrad).

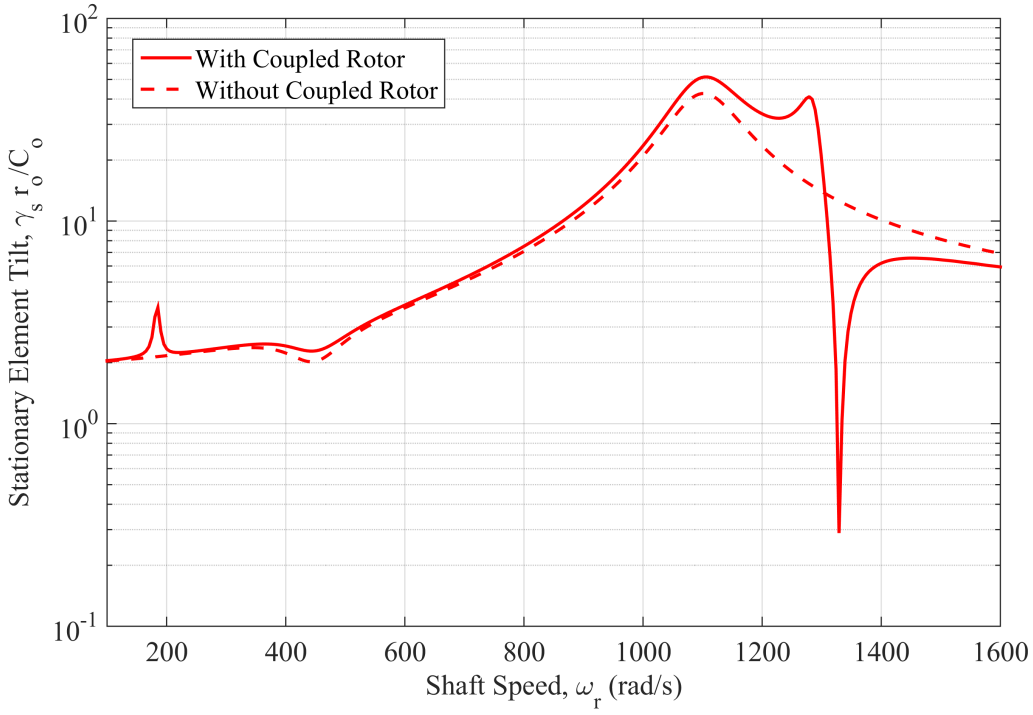

(a) Normalized stationary element tilt

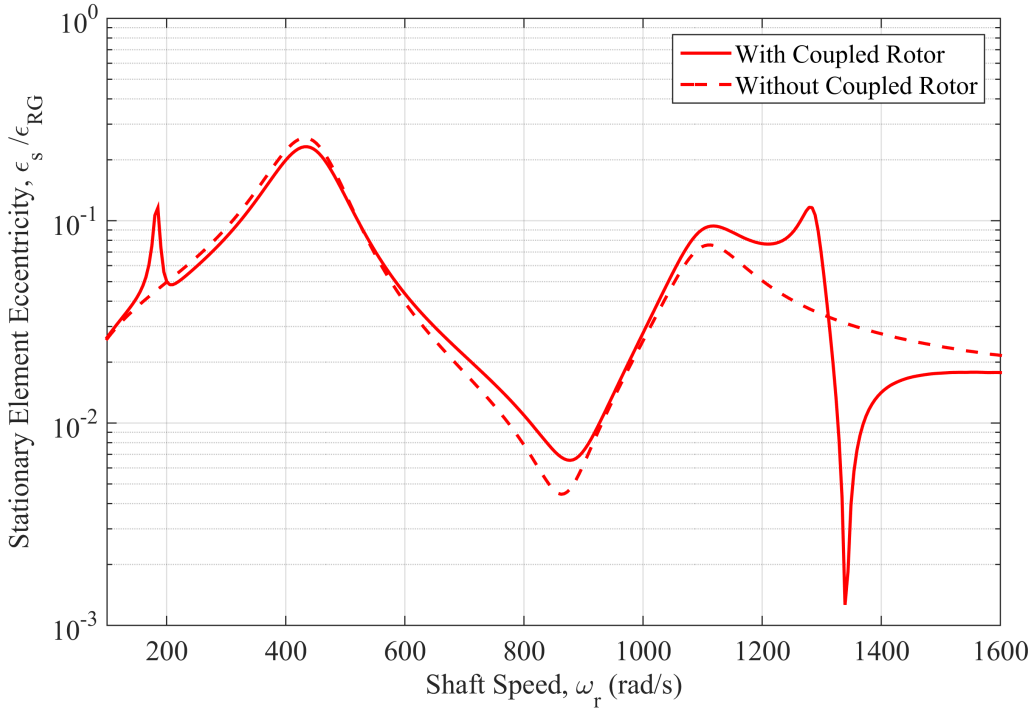

(b) Normalized stationary element eccentricity

Figure 8.20: Thick Rotor - Thick Seal: Absolute stationary seal element response versus shaft speed for the undamaged FMSR-ER system ($\chi_R = 0.1$ mrad).

8.4 Summary

The results presented in this chapter show that the rotor and stationary seal element are inextricably coupled. The rotordynamic response is first transmitted to the rotating seal element via the elastomeric support, and then transferred to the stationary seal element via the fluid film. If the rotor is much larger than the seal, which is assuredly the case in real turbomachines, the rotordynamics are entirely estranged from the seal dynamics. Consequently, simulations considering the efficacy of using a seal as a surrogate rotordynamic monitor can reasonably consider the rotor separately from the seal. In such a case, the rotor response can be sent directly to the seal equations of motion as an exogenous input.

In addition, the results presented here affirm the superiority of using stationary seal element tilts instead of eccentric deflections as a target response regime for surrogate diagnostics. The FMSR-ER seal adeptly minimizes relative tilts between the seal faces, but fails to minimize relative eccentricities. Consequently, the stationary seal element nearly identically emulates the dynamics of the rotating seal element (which in turn is inseparable from the rotordynamics). Considering these observations, results presented in later chapters regarding each fault will focus on two regimes of vibration: (1) the unadulterated rotor eccentric response, where the faults most prominently manifest, and (2) the stationary seal element tilt, which is the target signal of the seal-fixed surrogate rotordynamic condition monitor.

CHAPTER IX

RESULTS: CRACKED ROTORDYNAMIC RESPONSE

Though rare, shaft fatigue cracks in rotordynamic systems are exceptionally dangerous and can result in catastrophic machine failure. Consequently, turbomachine operators should employ state-of-the-art online crack detection schemes such as vibration monitoring to mitigate the risk associated with propagating fatigue cracks. A necessary prerequisite to such a monitoring system is a thorough understanding of how rotor cracks manifest in the machine vibration. Towards this end, this chapter presents the FMSR-ER response to a single shaft crack in the absence of other rotor faults (i.e., rub). Two types of rotor cracks, gaping and breathing, are simulated here to provide the free and forced response of both the rotor and seal.

9.1 Solution Method

The FMSR-ER equations of motion incorporating the cracked rotor are numerically integrated using MATLAB's ode15s. Even though the rotordynamics are not influenced by the seal dynamics, the equations of motion are placed into a consistent state-space formulation and solved simultaneously to ensure that the variable-step solver evaluates both the seal and rotor response at the same instances in time. Furthermore, time is normalized by the shaft speed such that $\tau = \omega_r t$; this ensures homogeneity in the subsequent frequency domain analysis. The steady-state solution is extracted for an integer number of periods, where the number of periods required to attain steady-state depends on the external viscous damping ratio and system parameters (typically, between 200 and 500 shaft revolutions are simulated). The relative and absolute tolerances are selected to be $1(10)^{-7}$ and $1(10)^{-9}$, respectively.

Table 9.1: Overhung rotor parameters.

Parameter	
Rotor mass, m_R	20 kg
Rotor transverse mass moment of inertia, I_{tR}	0.2 kg·m^2
Rotor polar mass moment of inertia, I_{pR}	(variable)
Shaft diameter, d	35 mm
Shaft length, L	250 mm
Shaft elastic modulus, E_R	210 GPa
Proportional damping coefficient, β_c	0.01

The rotor parameters for the results presented here are provided in Table 9.1, while those for the seal are given in Tables 8.1 and 8.2.

9.2 Gaping Crack Results

In certain cases, such as when the imbalance is large and out-of-phase with the crack, the crack remains open and does not open and close as the shaft rotates [92] (i.e., a gaping crack). Understanding how a gaping crack influences the rotordynamic response can provide insight for analyzing the more complicated scenario of a breathing rotor crack. Towards this end, this section presents the FMSR-ER response where the shaft contains a gaping fatigue crack. In all cases considered here, the crack is located a distance $L_1 = 0.05L$ from the support.

9.2.1 Floquet Stability

The rotor stability considering a gaping crack can be calculated in the rotating frame using a conventional eigenvalue analysis [84] or in the inertial frame using the Floquet analysis described in Chapter 4. In this work, the stability analysis is performed using Floquet theory. This choice is made to facilitate comparison with the stability of the

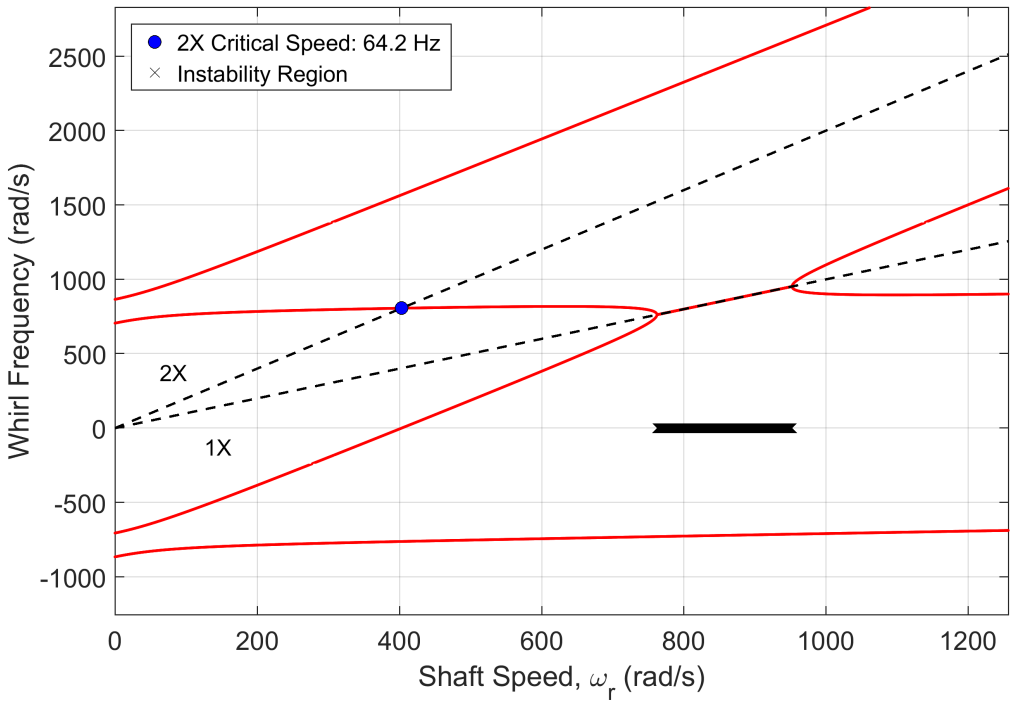

(a) Stability calculated using a conventional eigenvalue analysis

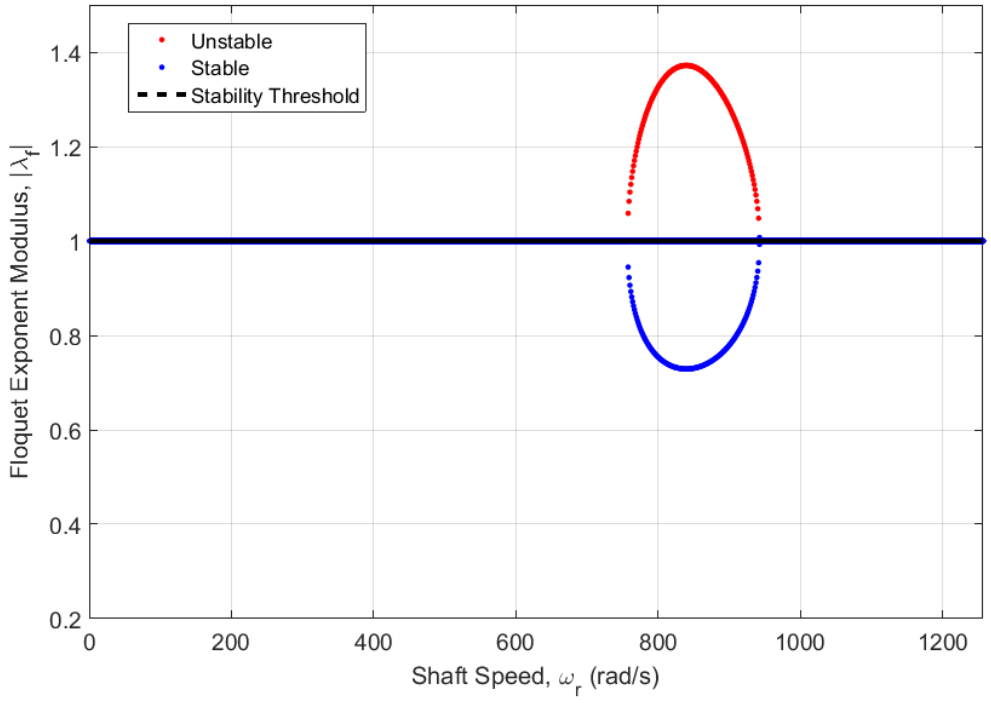

(b) Stability calculated using Floquet analysis

Figure 9.1: Validating the rotor stability analysis for an undamped rotor (i.e., $\beta_c = \zeta_\epsilon = \zeta_\gamma = 0$).

rotor displaying a breathing crack, which cannot be analyzed with a routine eigenvalue analysis.

The Floquet stability analysis method is first verified by comparing the resulting instability bounds to those provided by Casey and Green [84], where instability was determined using a classical eigenvalue analysis in the rotating frame. For comparison with the results given therein, the analysis is performed for the undamped overhung rotor using the test rig parameters provided by Casey [116]. The resulting Campbell diagram (i.e., the locus of eigenvalues versus shaft speed) is shown in Fig 9.1a for a gaping fatigue crack of depth 40%. The coefficient c_{45} is included in the analysis to facilitate comparison, though this work has shown that c_{45} is actually zero for an open crack. In the classical eigenvalue analysis, the instability region is identified by an eigenvalue with a positive real component (i.e., ω_r = 758 rad/s - 942 rad/s). The Floquet analysis gives lower and upper instability bounds of 763 rad/s and 952 rad/s, respectively. These estimates are sufficiently close, especially considering that the Floquet analysis is predicated on solving the equations of motion numerically using the Newmark-Beta method.

The stability analysis is now performed for the parameters specified herein using only the cracked rotor equations of motion rather than the full FMSR-ER equations of motion; this approach implicitly assumes that the seal dynamics are stable. The Floquet exponents λ_f are obtained across a range of shaft speeds for a 40% depth gaping crack, and the moduli $|\lambda_f|$ are shown in Figs. 9.2 and 9.3 for a thin and thick rotor, respectively. For each case, two scenarios are investigated: no external viscous damping ($\zeta_\epsilon = \zeta_\gamma = 0$) and small external viscous damping ($\zeta_\epsilon = \zeta_\gamma = 0.01$). In both cases, an external viscous damping ratio of 1% prominently improves rotor stability. Without external viscous damping, the rotor response remains unstable with increasing shaft speed once the first local region of instability is encountered. This broad range of instability is a consequence of internal damping β_C, and occurs

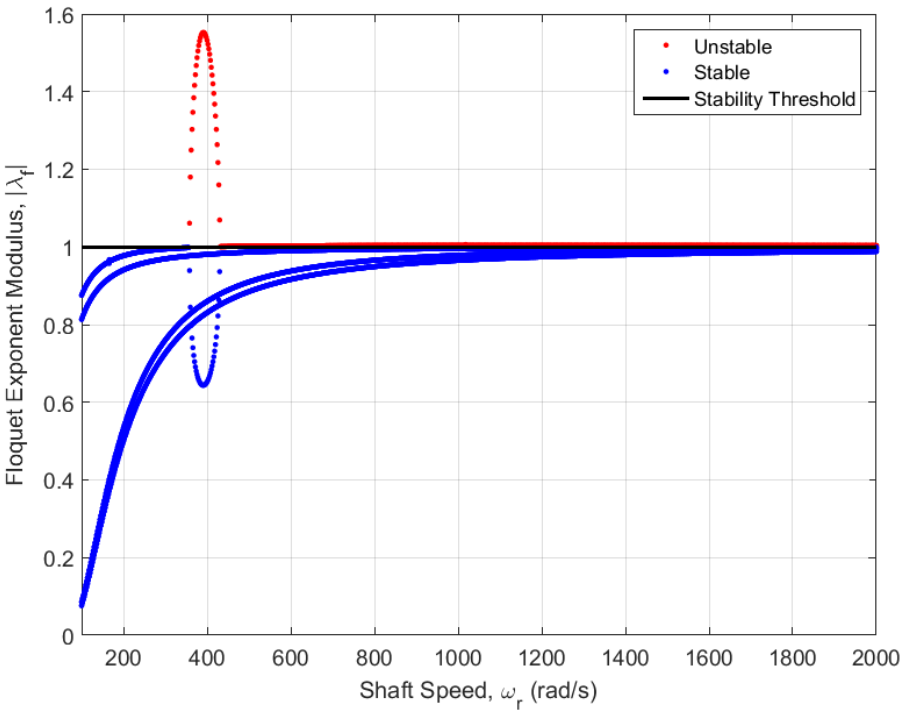

(a) External viscous damping: $\zeta_\epsilon = \zeta_\gamma = 0$

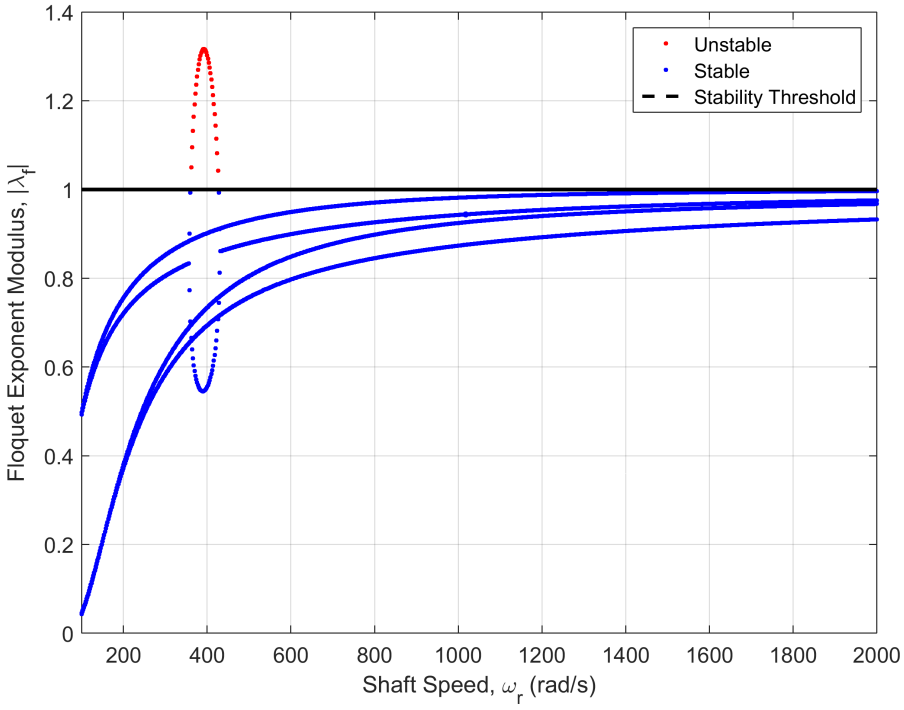

(b) External viscous damping: $\zeta_\epsilon = \zeta_\gamma = 0.01$

Figure 9.2: Stability of a thin rotor with a 40% depth gaping crack ($I_{pR} = 0.4$ kg·m^2).

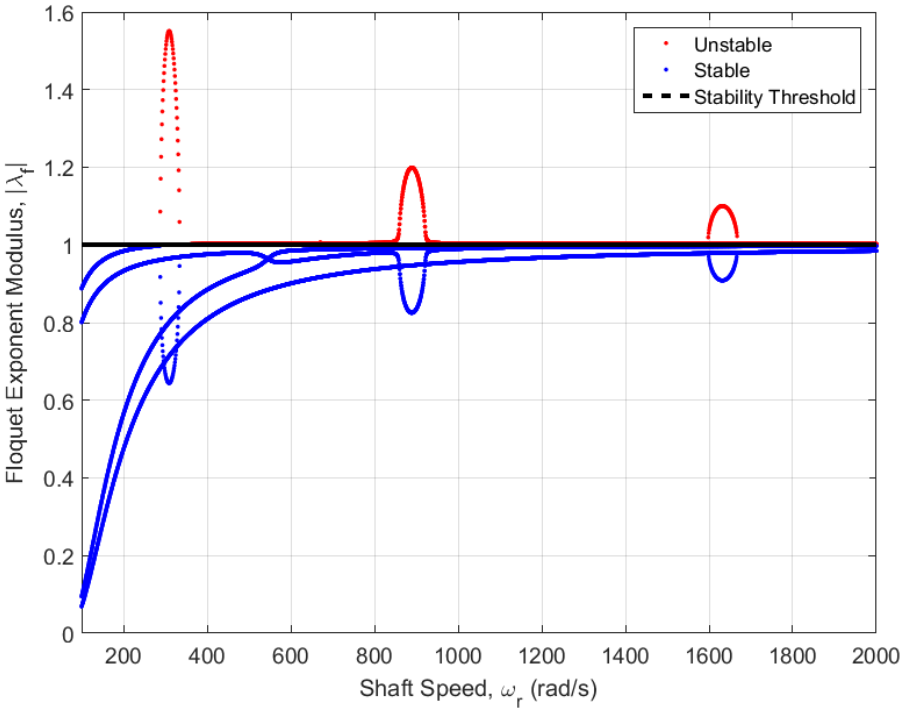

(a) External viscous damping: $\zeta_\epsilon = \zeta_\gamma = 0$

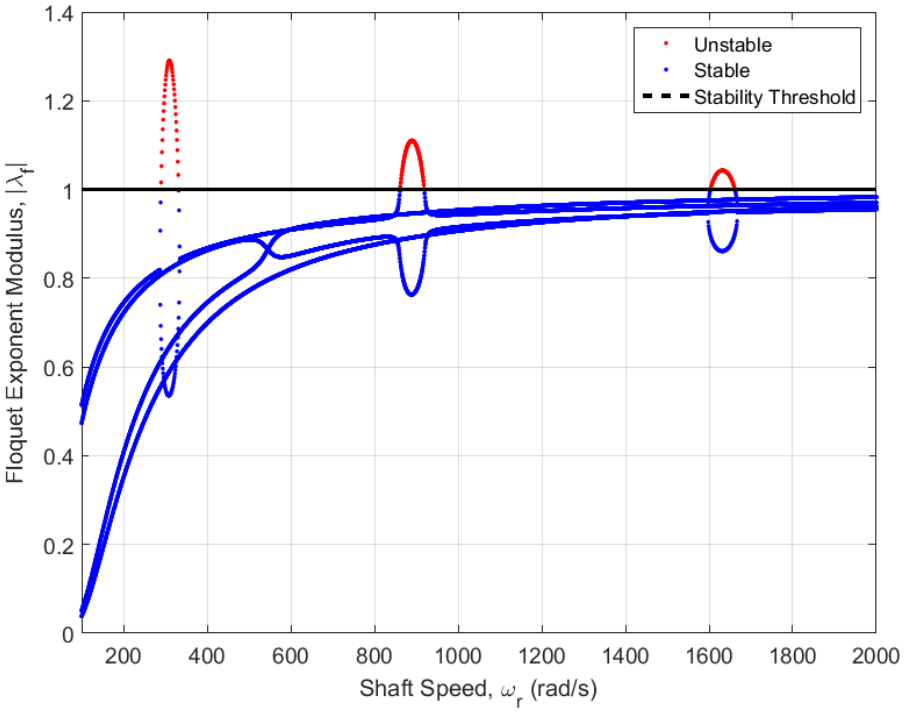

(b) External viscous damping: $\zeta_\epsilon = \zeta_\gamma = 0.01$

Figure 9.3: Stability of a thick rotor with a 40% depth gaping crack ($I_{pR} = 0.1$ kg·m^2).

in a similar fashion even when $a = 0\%$. In general, the gyroscopic effect stabilizes the thin rotor over a wider range of shaft speeds than the thick rotor. Additionally, the thin rotor response over the considered shaft speed range shows only a single region of instability, whereas the thick rotor displays recurring regions of local instability.

The cracked rotor equations of motion are solved numerically to validate the stability predictions. Specifically, the validation is performed for the thick rotor with 1% external viscous damping and a gaping crack of 40% depth. The normalized rotor eccentric response is shown in Fig. 9.4 for both a stable ($\omega_r = 280$ rad/s) and unstable ($\omega_r = 320$ rad/s) shaft speed near the first region of instability. The calculated responses are commensurate with the stability predictions gleaned from the Floquet analysis. Simulations at other shaft speeds likewise verify the stability analysis, and are not provided here for brevity.

The stability analysis is repeated over a wide range of crack depths, as shown in Figs. 9.5 - 9.8 for external viscous damping ratios of 0%, 0.5%, 1%, and 2%, respectively (in the figures, the dark regions represent regions of instability). As observed previously, internal damping in the absence of external viscous damping results in an expansive region of rotor instability (see Fig. 9.5). This wide range of instability disappears when external viscous damping is included, as shown in Fig. 9.6. The figures indicate that once again, the thin rotor exhibits improved stability compared to the thick rotor. For all cases presented here with external viscous damping, the thin rotor has only a single region of instability, whereas the thick rotor has multiple recurring instability regions.

These instability regions are influenced by crack depth, a conclusion that has also been reached by previous researchers [84, 140]. In all cases considered here, the shaft speed range over which the rotor response is unstable increases with increasing crack depth. If a crack is suspected, operating in (or even near, due to crack propagation) these instability regions can quickly result in catastrophic machine failure. This

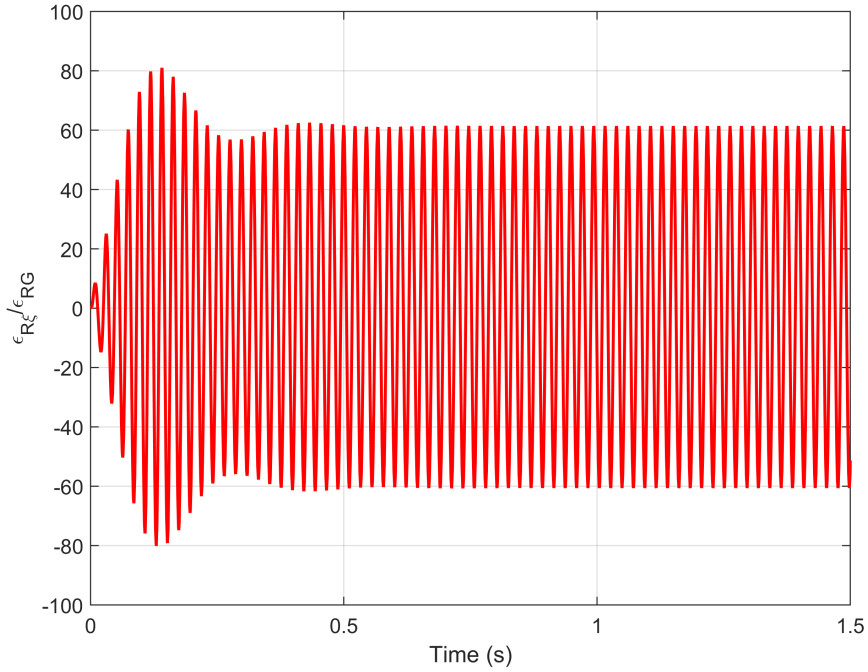

(a) Stable: $\omega_r = 280$ rad/s

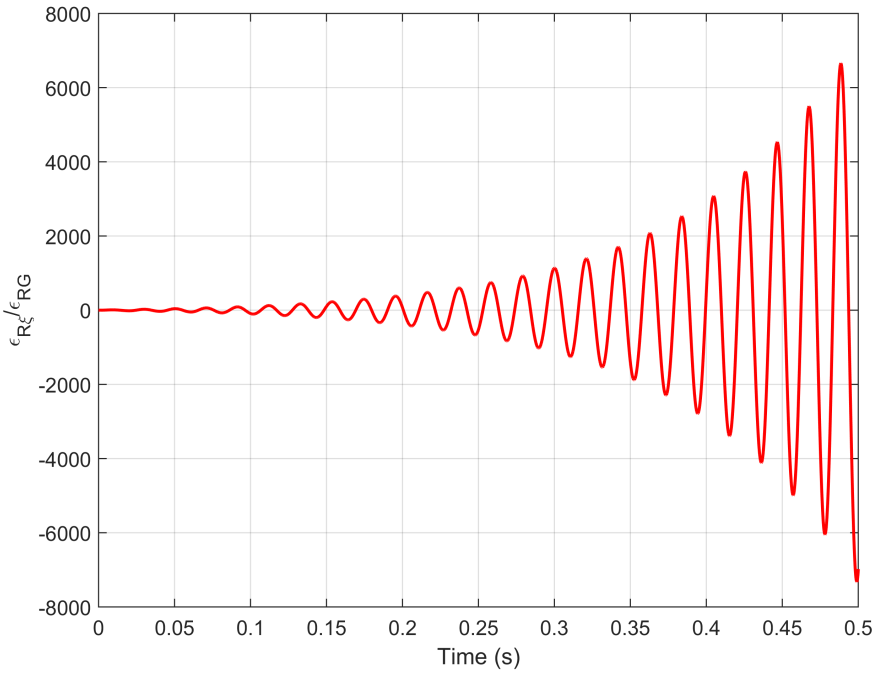

(b) Unstable: $\omega_r = 320$ rad/s

Figure 9.4: Waveforms demonstrating selected unstable and stable shaft speeds, as predicted by Floquet analysis for the thick rotor with a gaping fatigue crack ($\zeta_\epsilon = \zeta_\gamma = 0.01$, a = 40%).

observation underscores the need to detect and rectify incipient rotor cracks.

9.2.2 Steady-State Response

The FMSR-ER steady-state response to eccentric imbalance, angular misalignment, gravity, and a gaping fatigue crack is obtained by integrating the corresponding equations of motion according to the procedure discussed in Section 9.1. The rotating seal element is assumed to have a static angular misalignment of $\chi_s = 0.5$ mrad, a dynamic angular misalignment of $\chi = 0.1$ mrad, and an eccentric imbalance of $\varepsilon_{rG} = 5$ μm. Gravity must be included in the analysis because it is responsible for generating the 2X harmonic (as discussed in Chapter 2). Consequently, static deflections caused by gravity must be appropriately considered in the initial conditions and misalignments of the stationary seal element. Failing to consider gravity exacerbates the misalignment between the stationary and rotating seal faces, which in turn amplifies the synchronous 1X vibration component of both seal elements. Thus, it is assumed here that the stationary seal element is installed to mirror the rotor static deflection caused by gravity:

$$\bar{q}_s = \left\{\epsilon_{s\xi,i} \;\; \epsilon_{s\eta,i} \;\; \gamma_{s\xi,i} \;\; \gamma_{s\eta,i}\right\}^T \tag{9.1}$$

where $\bar{q}_s$ is the misalignment and the subscript i denotes that these terms are initial static deflections. Eccentric and angular deflections must both be considered due to coupling terms in the rotor stiffness matrix (i.e., eccentric forces causes both eccentric and angular deflections). These initial static misalignments are found directly from the rotor's static deflection:

$$\bar{q}_s = [K_R]^{-1}(\bar{F}_g)_R \tag{9.2}$$

where $[K_R]$ is the stiffness matrix of the undamaged rotor and $(\bar{F}_g)_R$ is the gravity force acting on the rotor. These static misalignments, tilt and eccentric, are imposed in the stationary seal element equations of motion by applying the forces and moments required to generate them (see Chapter 3). Inertial maneuver loads of the overall

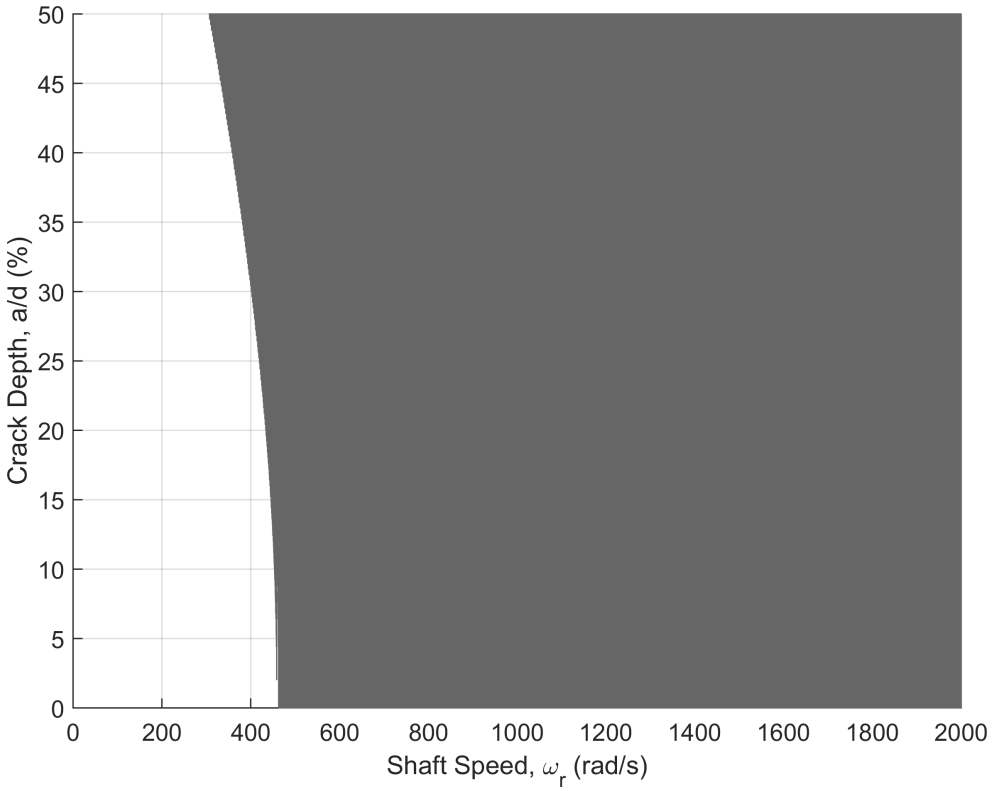

(a) Thin rotor ($I_{pR} = 0.4$ kg·m^2)

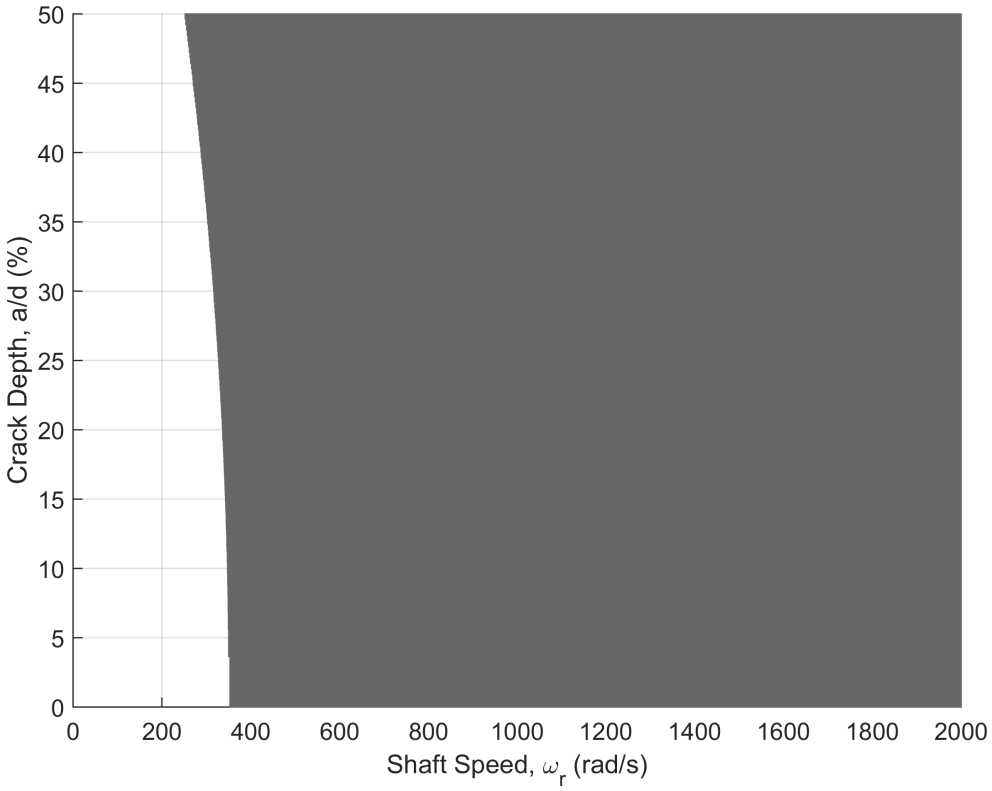

(b) Thick rotor ($I_{pR} = 0.1$ kg·m^2)

Figure 9.5: Gaping Fatigue Crack: Floquet stability with no external viscous damping ($\zeta_\epsilon = \zeta_\gamma = 0$).

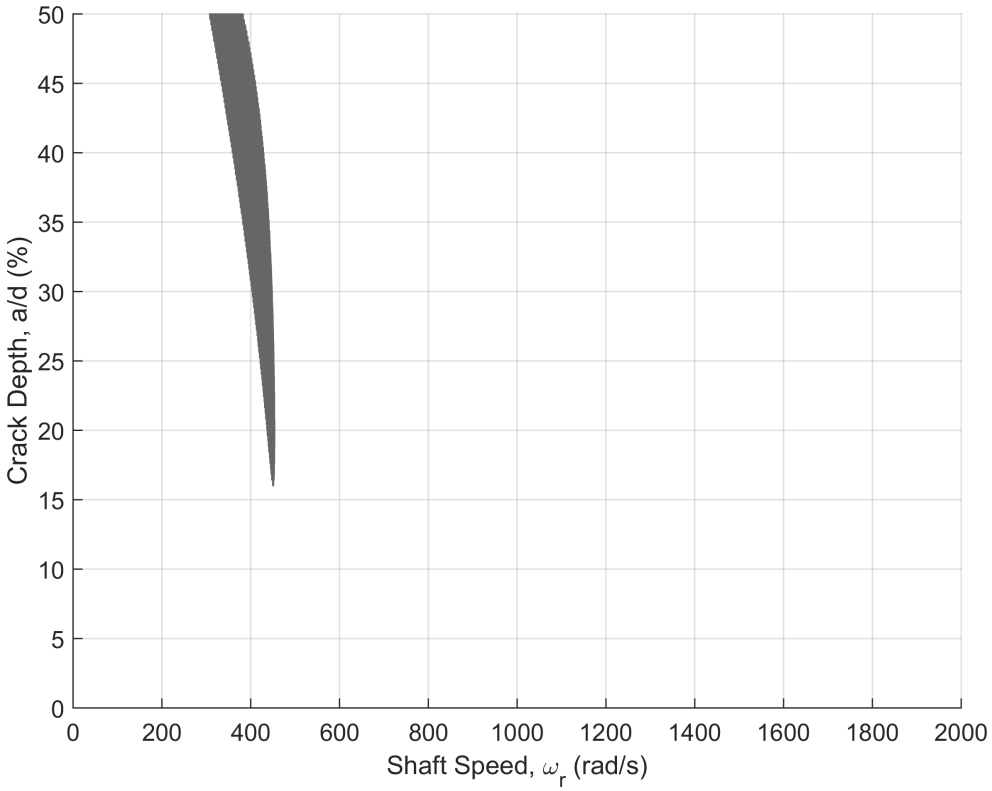

(a) Thin rotor ($I_{pR} = 0.4$ kg·m^2)

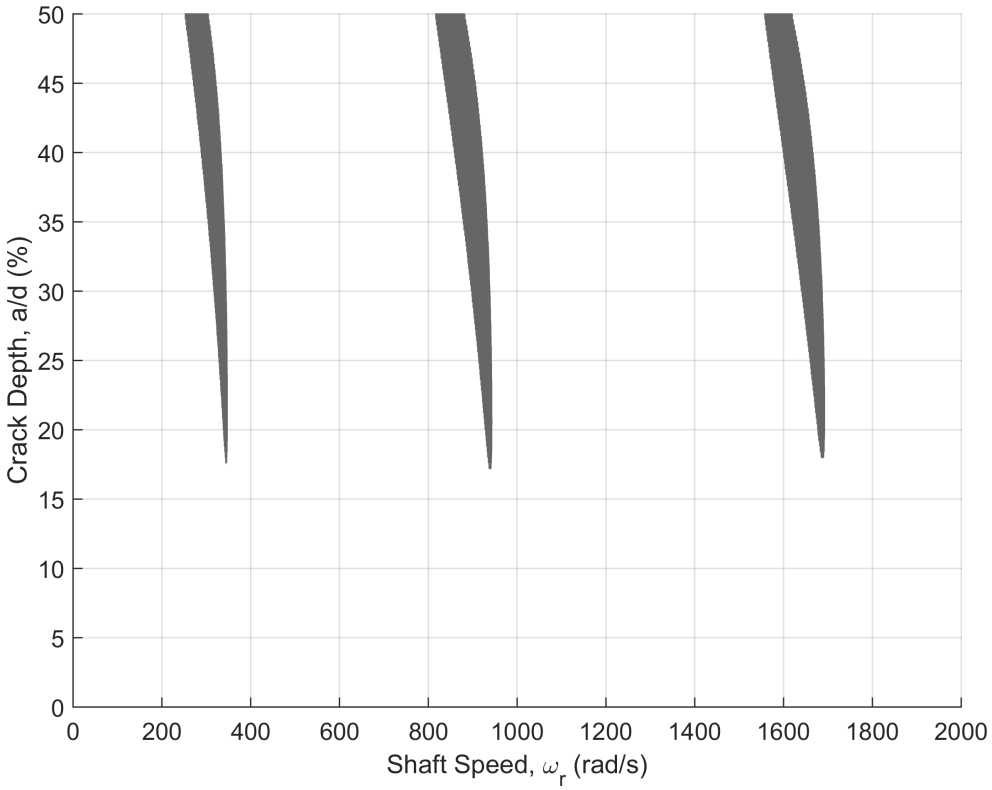

(b) Thick rotor ($I_{pR} = 0.1$ kg·m^2)

Figure 9.6: Gaping Fatigue Crack: Floquet stability with no external viscous damping ($\zeta_\epsilon = \zeta_\gamma = 0.005$).

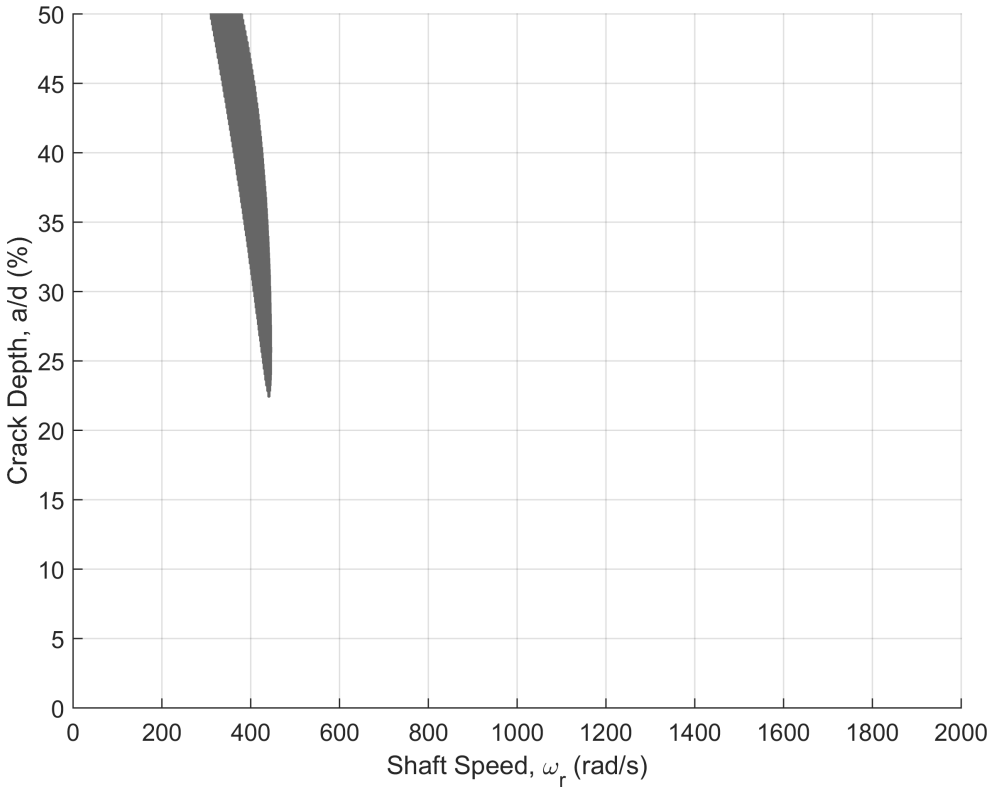

(a) Thin rotor ($I_{pR} = 0.4$ kg·m^2)

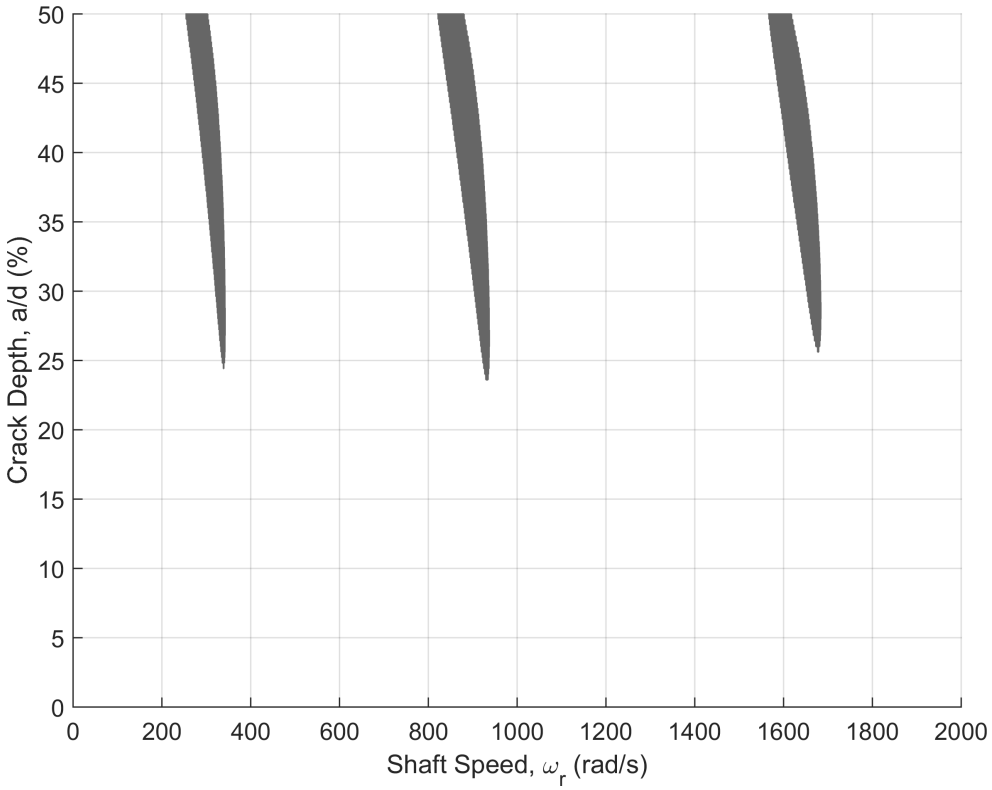

(b) Thick rotor ($I_{pR} = 0.1$ kg·m^2)

Figure 9.7: Gaping Fatigue Crack: Floquet stability with small external viscous damping ($\zeta_\epsilon = \zeta_\gamma = 0.01$).

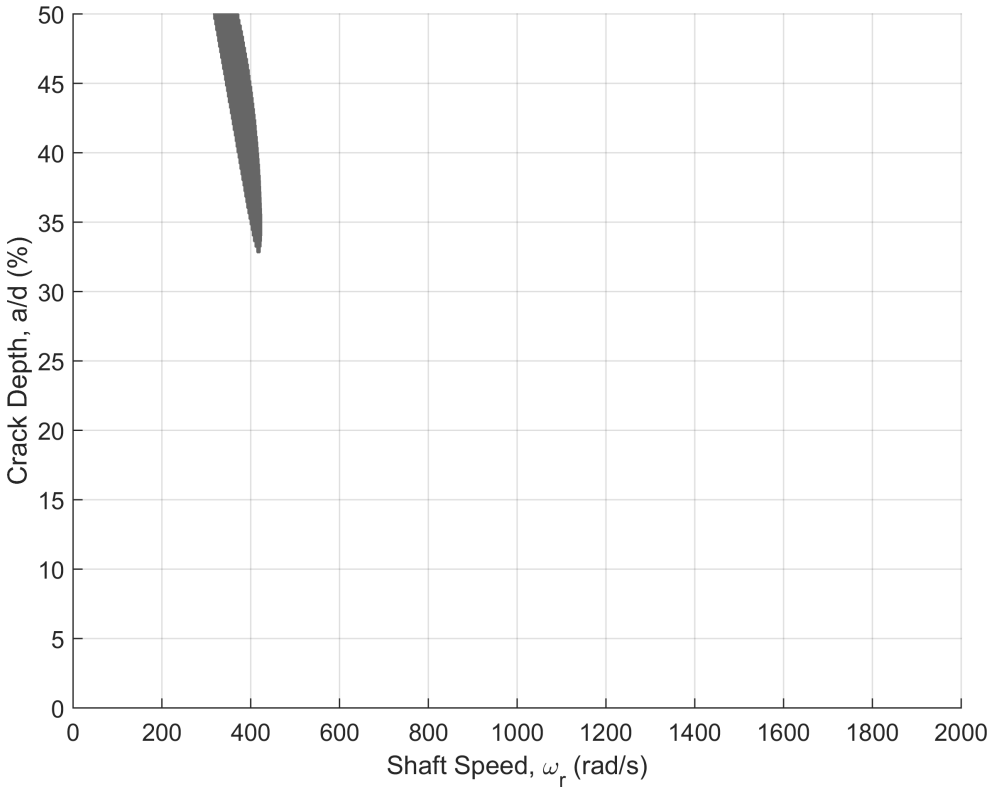

(a) Thin rotor ($I_{pR} = 0.4$ kg·m^2)

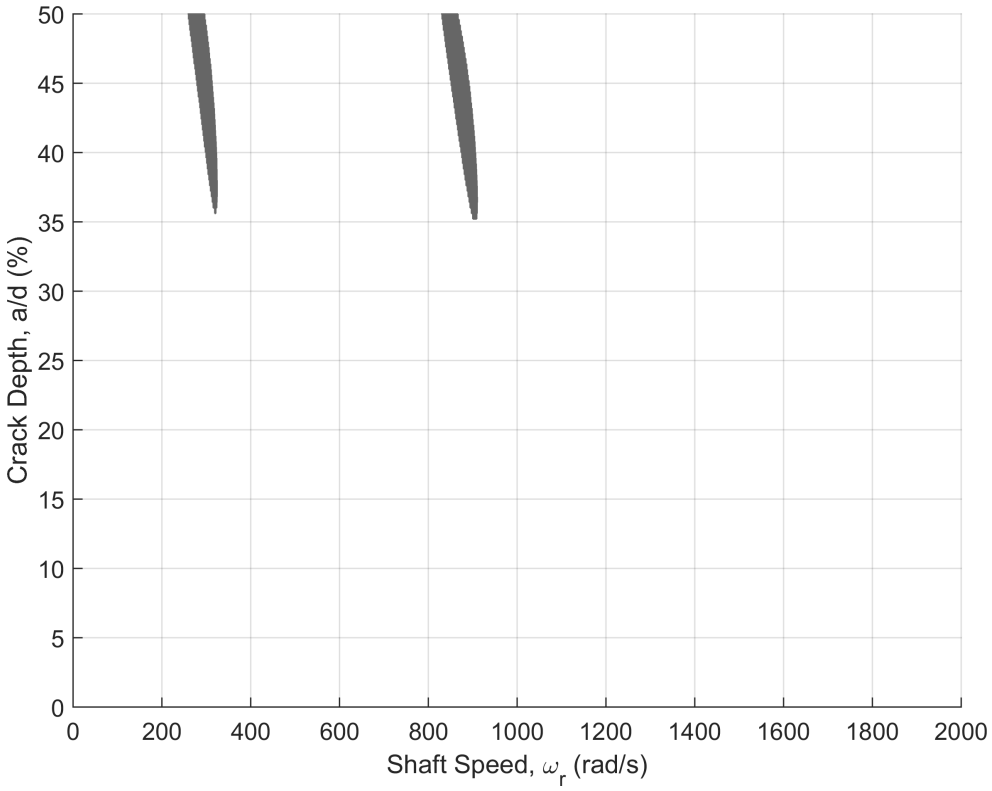

(b) Thick rotor ($I_{pR} = 0.1$ kg·m^2)

Figure 9.8: Gaping Fatigue Crack: Floquet stability with small external viscous damping ($\zeta_\epsilon = \zeta_\gamma = 0.02$).

system are neglected (i.e., the reference frame $\xi\eta\zeta$ is inertial). The rotor's dynamic angular misalignment is $\chi_R = 1$ mrad and the eccentric rotating imbalance is $\varepsilon_{RG} = 5$ μm. The static axial offset d_r and rotor bow (r_b and χ_b) are assumed to be zero. All static phase misalignments are also assumed to be zero, without loss of generality.

Appropriately choosing the initial conditions minimizes the time required for numeric transients to decay in the solution. The initial conditions for the rotor are found by solving the undamaged rotor equations of motion analytically at steady-state:

$$\bar{Q}_{Ro} = \Re\left\{ \left[-\omega_r^2 M_R + i\,\omega_r\big(D_R + D_v + G_R\big) + K_R + D_R^* \right]^{-1} \bar{F}_R \right\} \tag{9.3}$$

where matrix notation has been dropped for brevity and $\bar{F}_R$ includes the forces and moments caused by imbalance, misalignment, and gravity. The rotating seal element initial conditions, both positions and velocities, are then assumed to be commensurate to those of the rotor. The stationary seal element initial conditions are assumed to be the static misalignments for each degree of freedom, as provided in Eq. 9.2.

The steady-state solution for a single shaft speed of 165 rad/s is given in Fig. 9.9 for a thin rotor ($I_{pR} = 0.1$ kg·m^2) where the crack depth is 40% (all the results shown herein assume that $L_1 = 0.05L$). As will be shown later, this shaft speed is near the 1/2 critical speed of the cracked rotor. The relative tilt between the seal elements is shown in the time domain in Fig. 9.9a, while the frequency content contained in the tilt of all three elements is shown in Fig. 9.9b. The frequency content displayed by all three elements clearly highlights the 2X shaft speed harmonic induced by the gaping fatigue crack. This conclusion is expected because both seal elements are inextricably coupled to the rotordynamics via the elastic support (rotating seal element) and fluid film (stationary seal element). In addition, the response also displays prominent components due to synchronous excitation and static offset. The seal element response also contains a minuscule 3X harmonic, where the small magnitude indicates that this component can be attributed to numeric error in the simulation (i.e., the magnitude is beneath the error tolerances specified in the solution process).

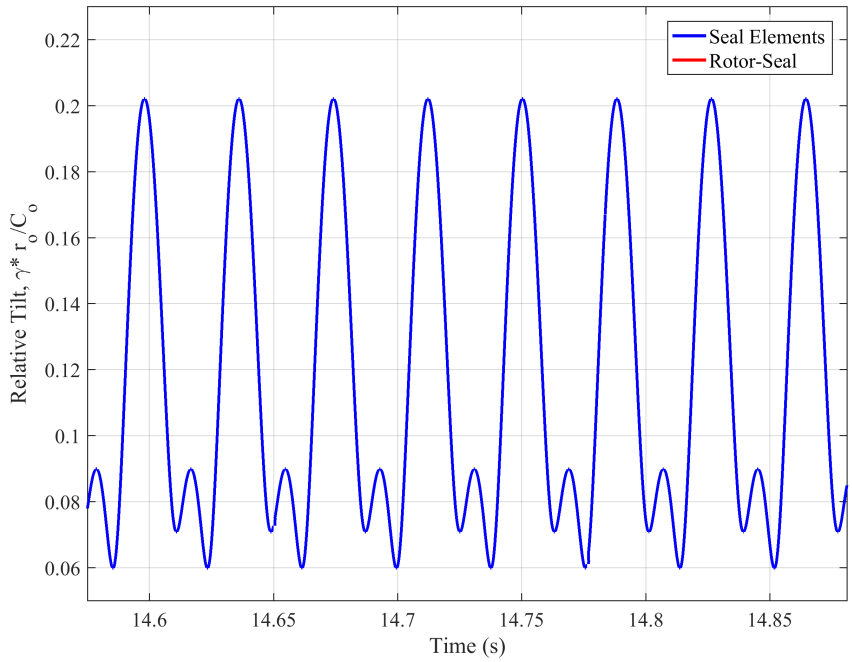

(a) Normalized relative tilt between the seal elements

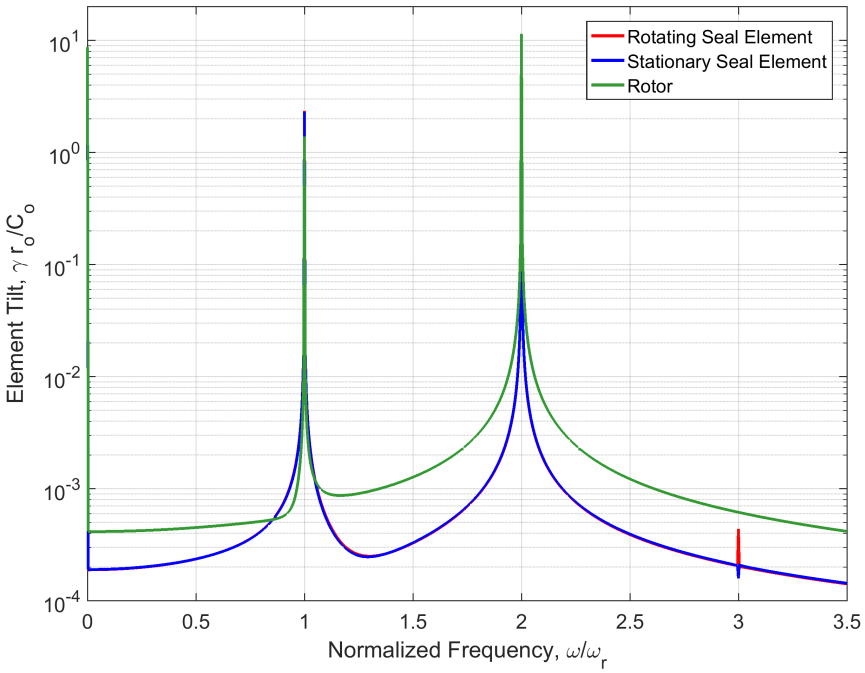

(b) Frequency content contained in the tilt of all three elements

Figure 9.9: Rotor and seal response to gravity, misalignment, and imbalance for a thin rotor ($I_{pR} = 0.1$ kg·m^2) with a gaping fatigue crack depth of 40%.

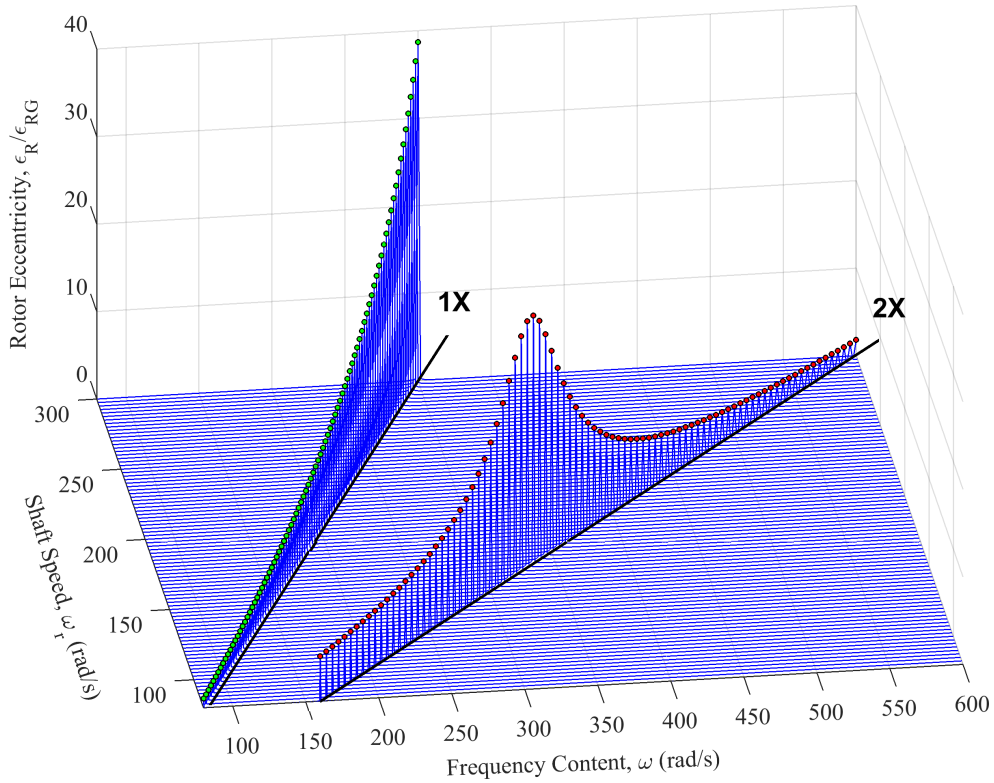

(a) Normalized rotor eccentric magnitude, $\epsilon_R/\varepsilon_{RG}$

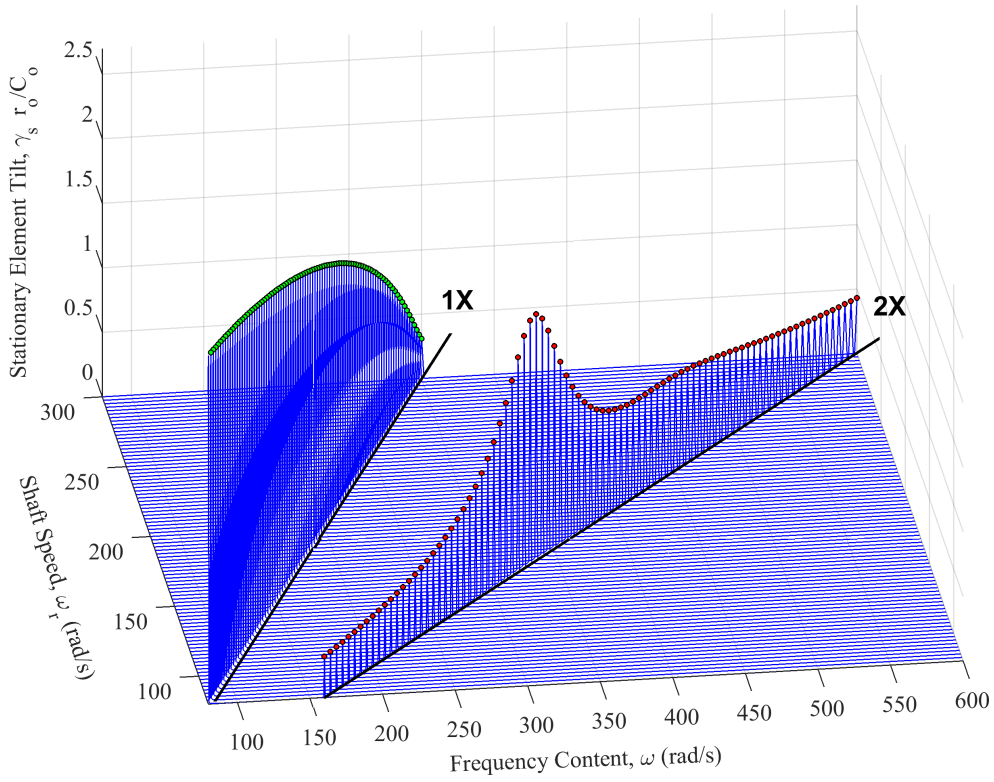

(b) Normalized stationary seal element tilt, $\gamma_s r_o/C_o$

Figure 9.10: Rotor and seal response to a gaping fatigue crack of 40% depth ($\zeta_\epsilon = \zeta_\gamma = 0.02$).

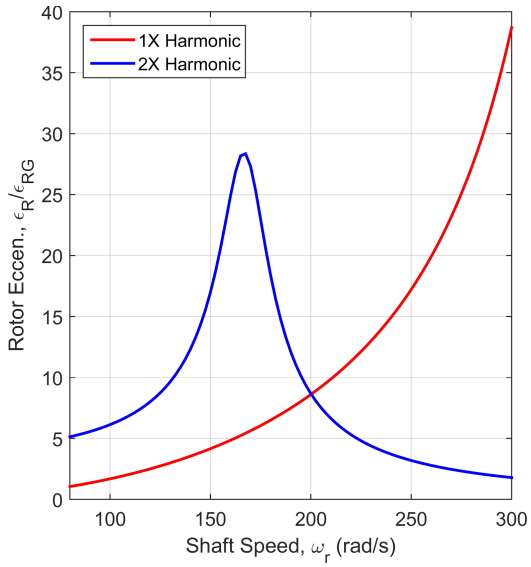

(a) 1X and 2X components of the rotor eccentric response

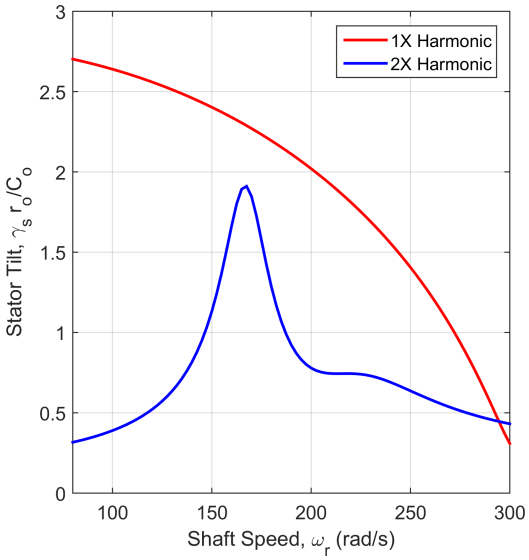

(b) 1X and 2X components of the stationary seal element tilt

Figure 9.11: Magnitudes of the 1X and 2X harmonic components of the rotor and stationary seal element response for a 40% depth gaping crack ($\zeta_\epsilon = \zeta_\gamma = 0.02$).

Rotors containing gaping cracks are well-known to exhibit a 1/2 critical speed when the shaft speed reaches one-half of a system whirl frequency [85]. To demonstrate this phenomenon, the system is simulated over a wide range of shaft speeds, and the frequency content of each resulting steady-state waveform is shown versus shaft speed in Figs. 9.10a and 9.10b for the rotor deflection and stationary seal element tilt, respectively (the rotor tilt and stationary seal element eccentric response are omitted according to the discussion given in the previous chapter). The rotor and rotating seal element are thin ($I_p = 2I_t$), and the external viscous damping ratio is 2% for both eccentric and angular deflections. The response of the rotating seal element is omitted because it is nearly identical to the stationary seal element, as a consequence of the fluid film.

As expected, the response of both elements indicates only 1X and 2X shaft speed harmonics. These harmonics are extracted and displayed in Fig. 9.11. The considered shaft speed range was chosen to highlight the 1/2 critical speed, which occurs at

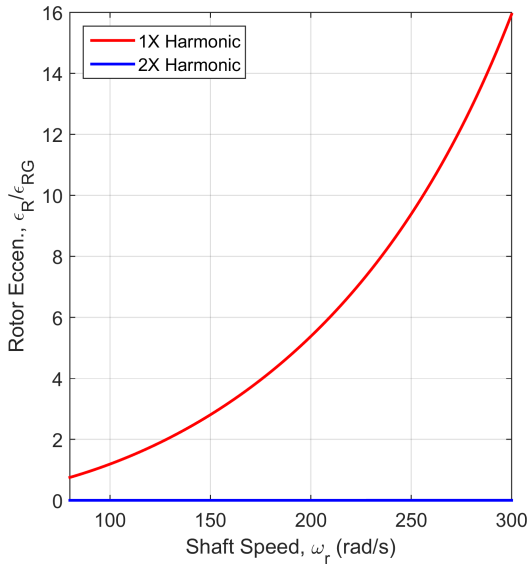

(a) 1X and 2X components of the rotor eccentric response

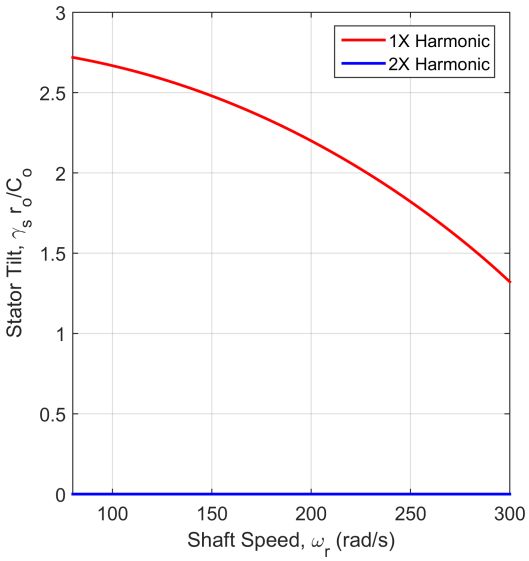

(b) 1X and 2X components of the stationary seal element tilt

Figure 9.12: Magnitudes of the 1X and 2X harmonic components of the rotor and stationary seal element response without a crack ($\zeta_\epsilon = \zeta_\gamma = 0.02$).

approximately 167.5 rad/s for the parameters considered here (the reference case with no crack is shown in Fig. 9.12). The 1/2 critical speed, an important crack diagnostic tool, displays prominently in both the tilt and eccentric response of the stationary seal element. The 2X component in the stationary seal element response is also amplified near shaft speeds of approximately 220 rad/s. This is expected because the seal response without a crack (see Fig. 8.4b) shows a natural frequency of approximately 450 rad/s.

The 1X and 2X harmonics are also provided for a shallower crack of depth 20%. In this case, the magnitude of the 2X harmonic is reduced and the 1/2 critical speed occurs at a higher shaft speed (190 rad/s). The increase in 1/2 critical speed for the shallower crack is intuitive because the stiffness of the overhung rotor is increased compared to the 40% crack scenario. Similar responses for the 1X and 2X harmonic can be found for gaping cracks with different depths, and have been addressed in other studies [85].

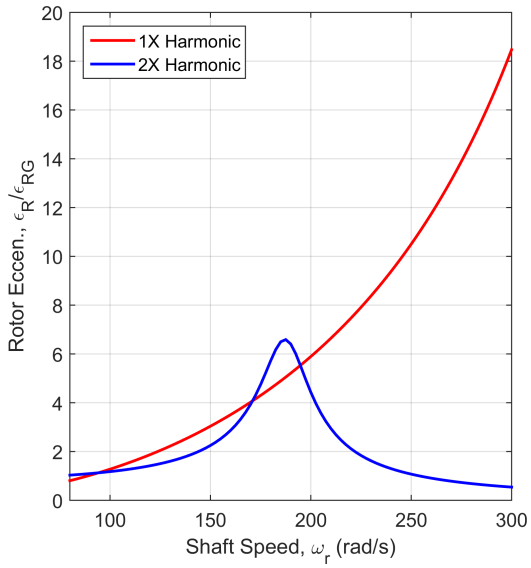

(a) 1X and 2X components of the rotor eccentric response

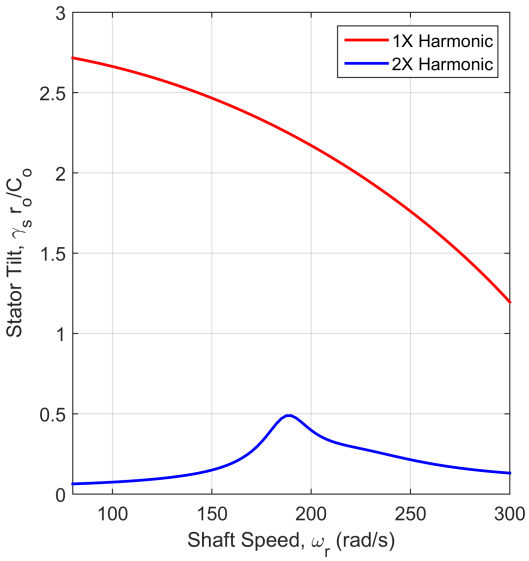

(b) 1X and 2X components of the stationary seal element tilt

Figure 9.13: Magnitudes of the 1X and 2X harmonic components of the rotor and stationary seal element response for a 20% depth gaping crack ($\zeta_\epsilon = \zeta_\gamma = 0.02$).

The angular and eccentric orbits for the seal and rotor also provide useful knowledge regarding the nature of the cracked rotor-seal system. The orbits obtained during passage through the 1/2 critical speed for the above-provided parameters are shown in Figs. 9.14 and 9.15 for the rotor eccentric response and stationary seal element tilt, respectively. In both cases, the orbit is primarily circular with a subsidiary inner loop caused by the 2X harmonic. Once again, it is important to note that the crack vibration signatures directly manifest in the stationary seal element angular orbit, which is easily measurable. The orbit character is validated by previous experimental work; an example angular orbit is shown in Fig. 9.16 (normalized by the maximum deflection observed in either degree-of-freedom), where the test rig parameters are provided by Varney and Green [85] and the crack depth is approximately 40%. The simulated orbits for both elements are shown over a wider range of shaft speeds in Fig. 9.17 for a crack of 40%. Once again, the rotor and stationary seal element vibration are prominently amplified near the 1/2 critical speed.

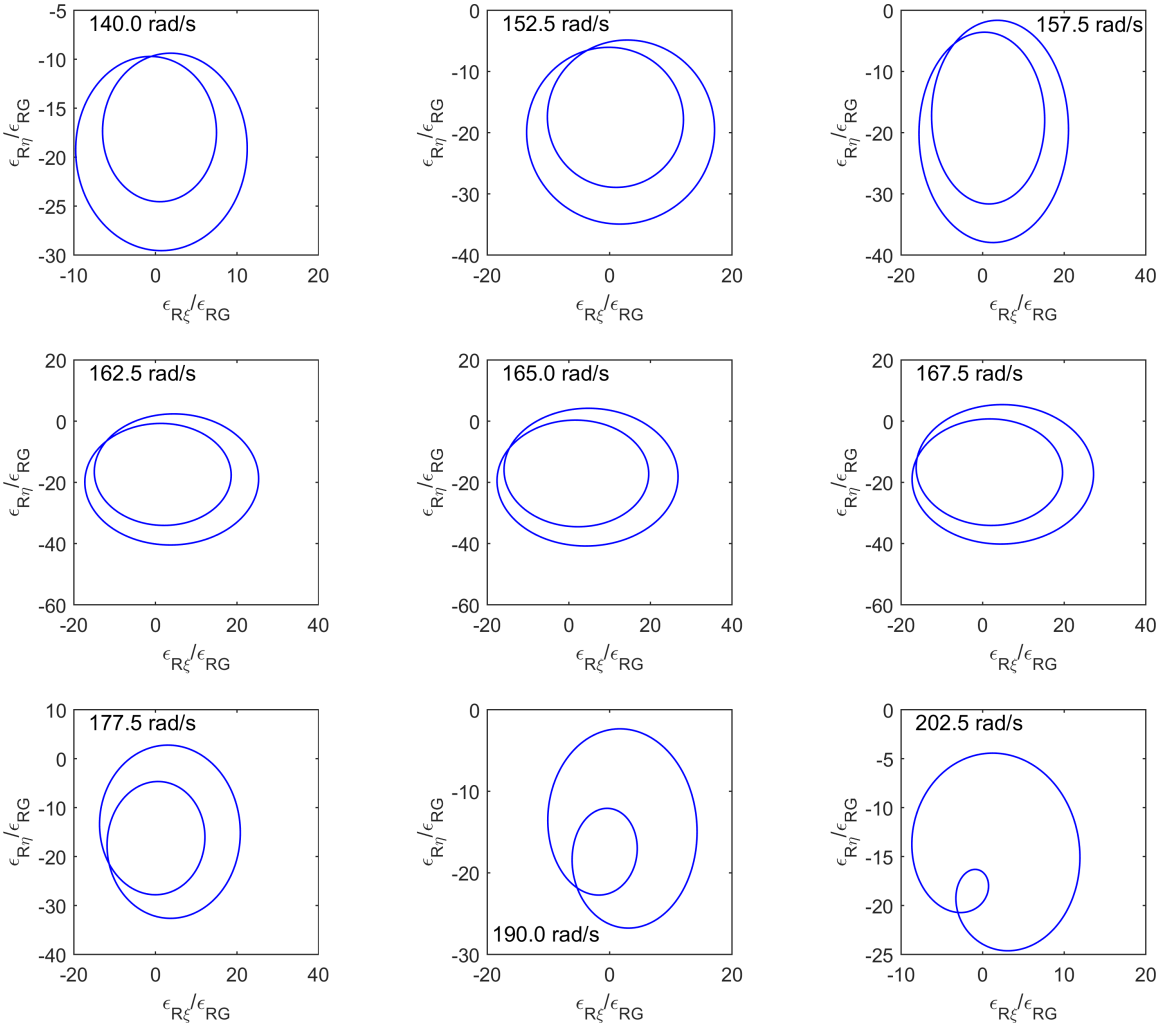

Figure 9.14: Eccentric orbits of the rotor observed during passage through the 1/2 critical speed of $\omega_r = 167.5$ rad/s for a 40% gaping fatigue crack.

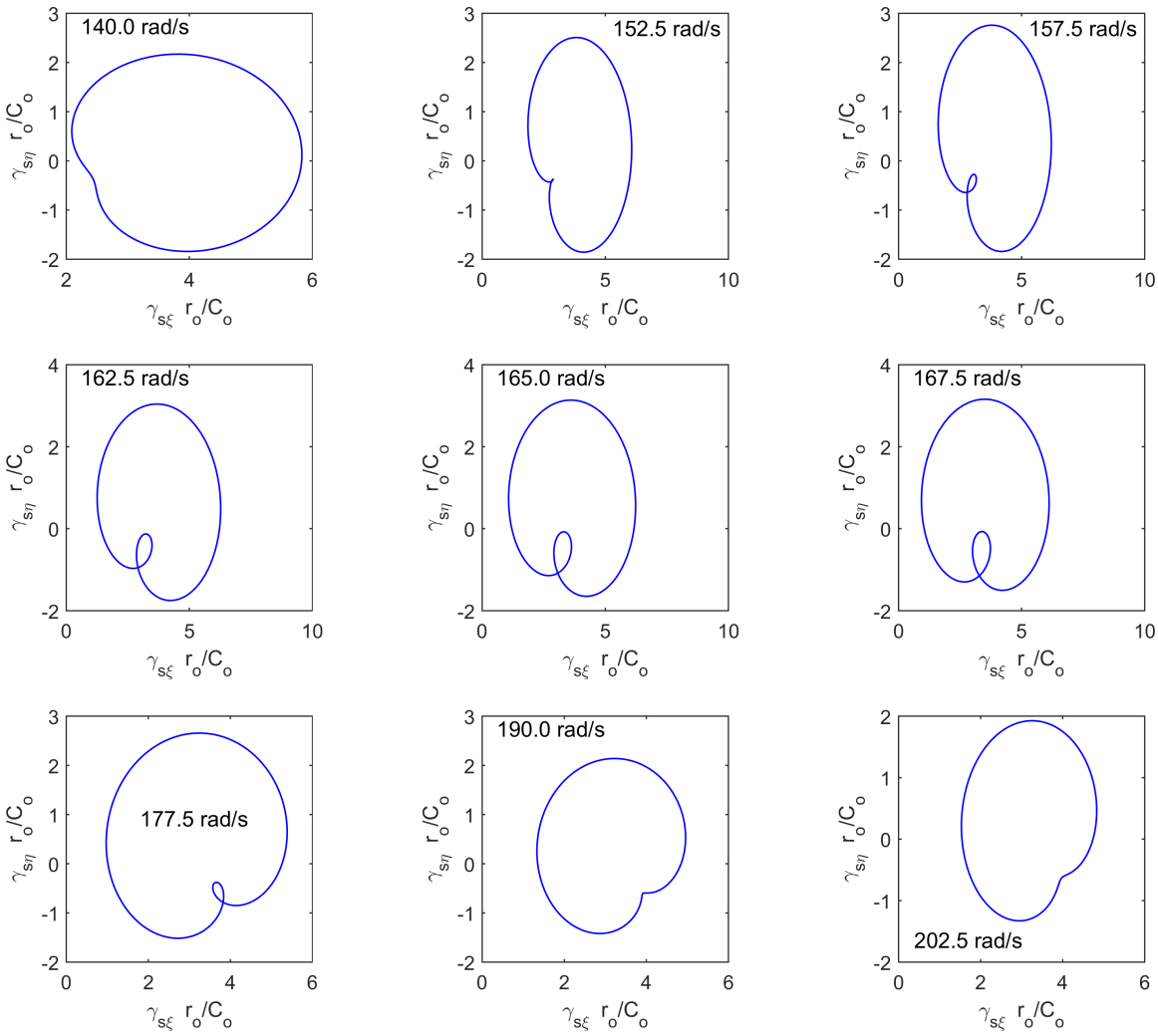

Figure 9.15: Angular orbits of the stationary seal element observed during passage through the 1/2 critical speed of $\omega_r = 167.5$ rad/s for a 40% gaping fatigue crack.

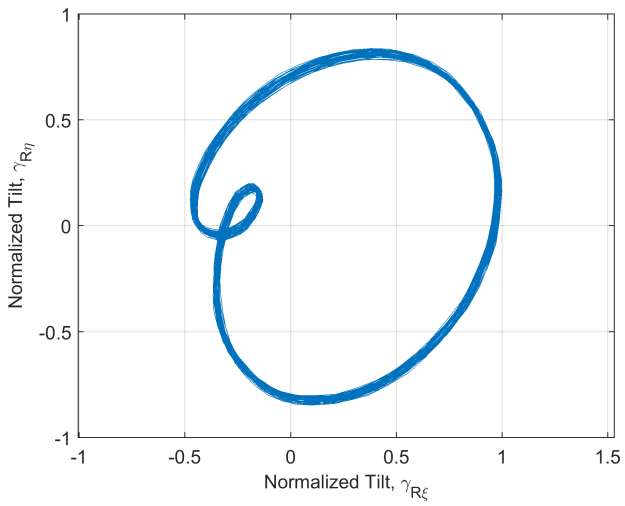

Figure 9.16: Experimental angular orbit measured from an overhung rotor test rig.

9.3 Breathing Crack Results

In reality, the crack opens and closes as the shaft rotates. This breathing behavior modifies the crack compliance, and consequently, changes the dynamic response of the FMSR-ER system. The FMSR-ER equations of motion are solved here using the crack-closure line shaft-weight dependent compliance method discussed in Chapter 6. The compliance coefficients are approximated using the Fourier transform method shown in Eq. 6.45 (see Fig. 6.10). The numeric approach used to solve the equations of motion is identical to the approach used for the gaping fatigue crack solution.

9.3.1 Floquet Stability

The rotor stability incorporating a breathing crack is calculated using Floquet analysis and shown in Figs. 9.18 - 9.20 for external viscous damping ratios of 0.5%, 1%, and 2%, respectively. These results have been corroborated by simulating the FMSR-ER equations of motion at the instability boundary (the results are analogous to those

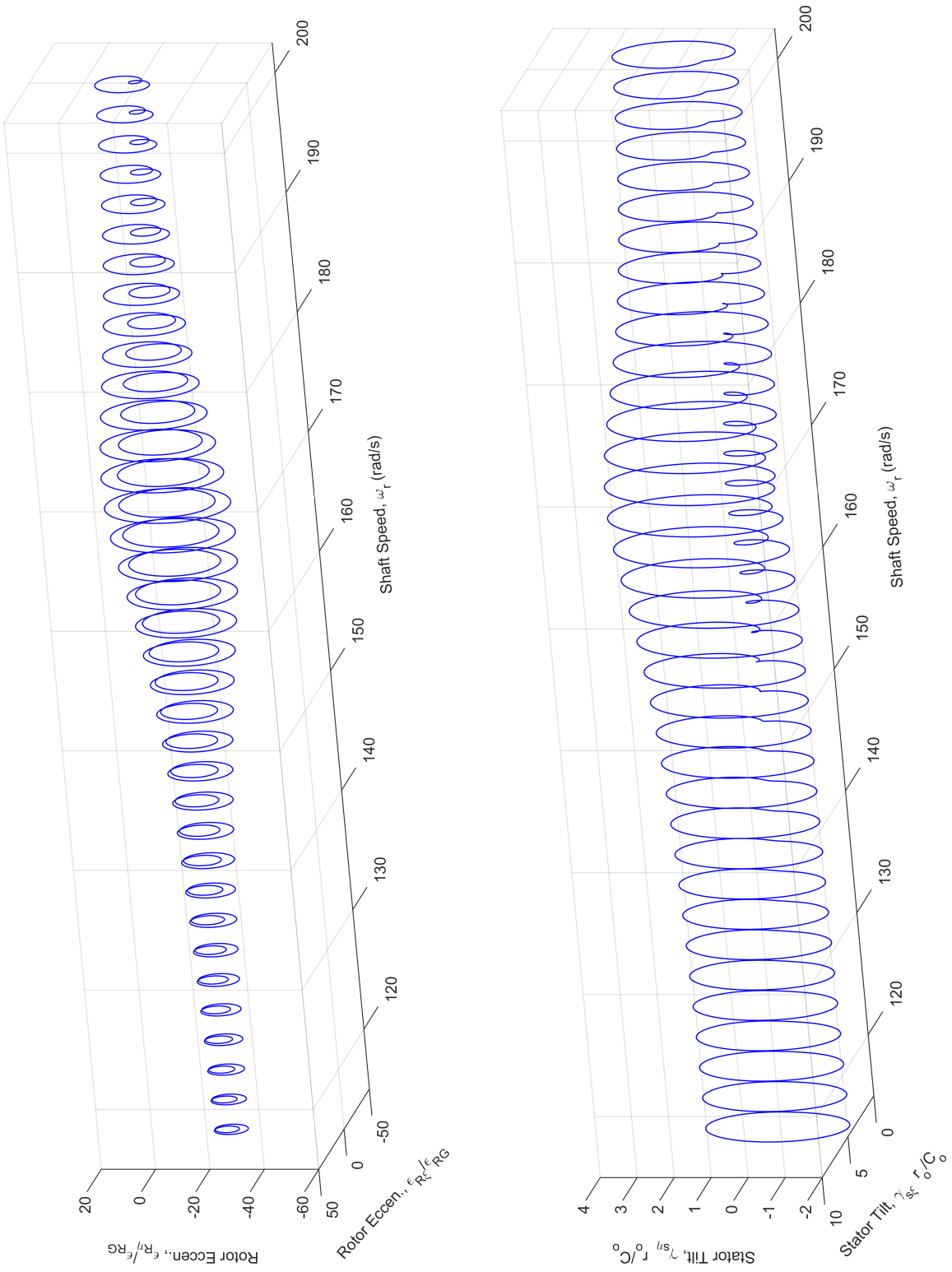

(a) Rotor eccentric response

(b) Stationary seal element tilt

Figure 9.17: Rotor and seal orbits during passage through the 1/2 critical speed of $\omega_r = 167.5$ rad/s (gaping fatigue crack of 40%).

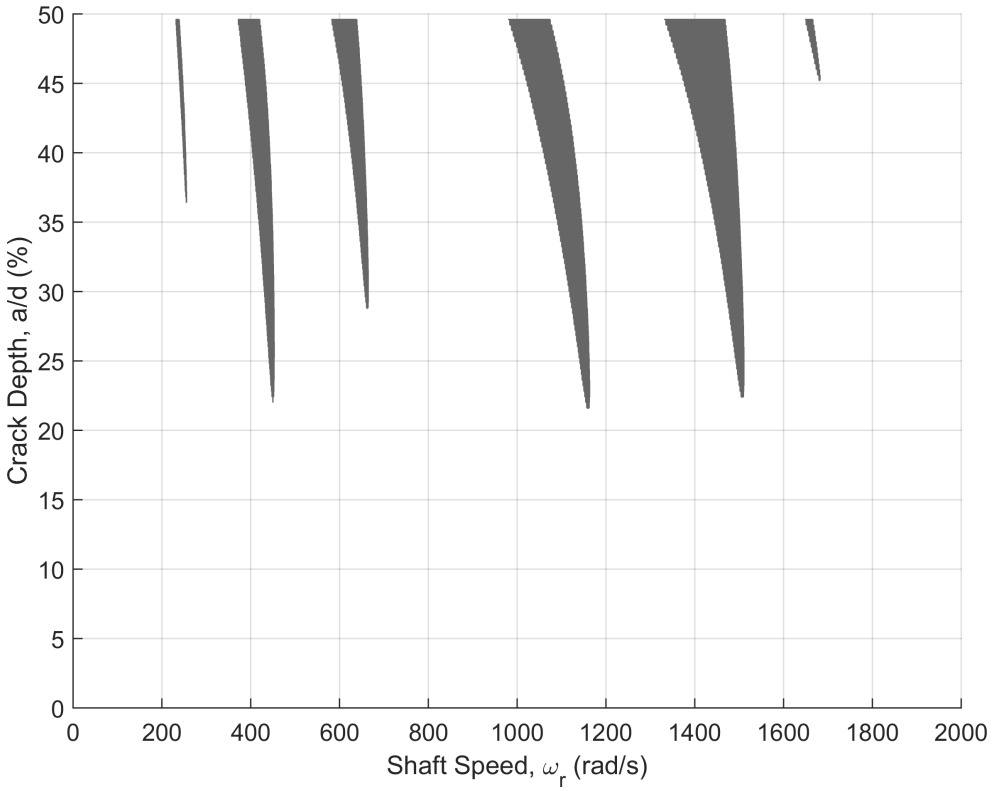

(a) Thin rotor ($I_{pR} = 0.4$ kg·m^2)

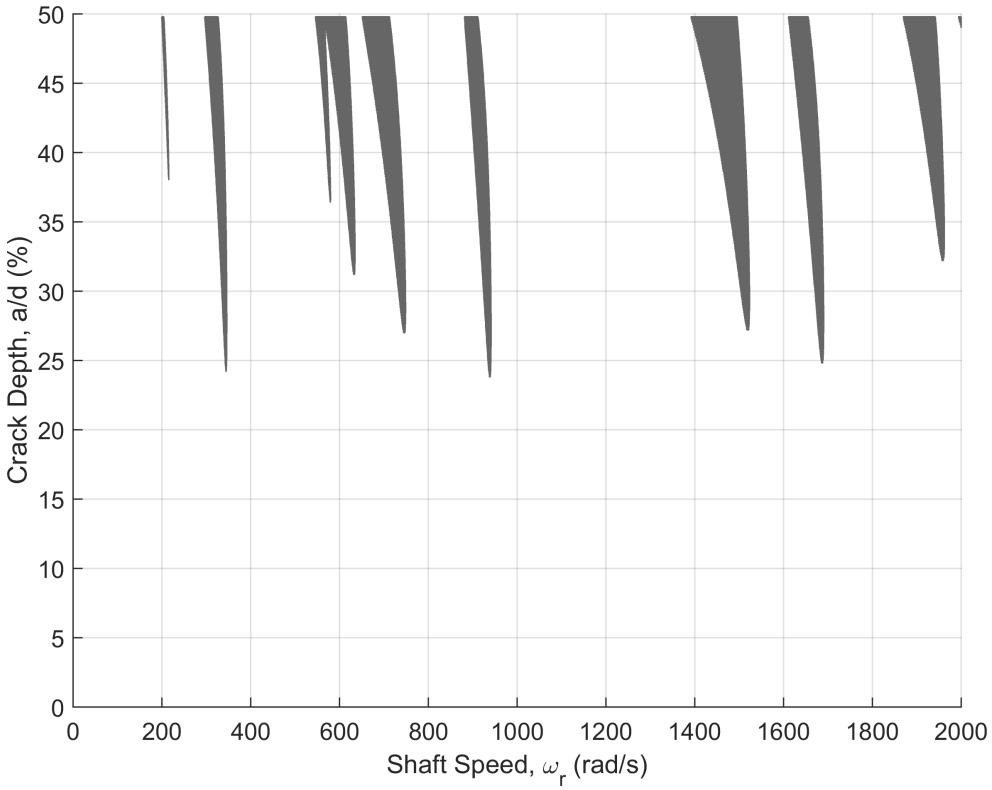

(b) Thick rotor ($I_{pR} = 0.1$ kg·m^2)

Figure 9.18: Breathing Crack: Floquet stability ($\zeta_\epsilon = \zeta_\gamma = 0.005$).

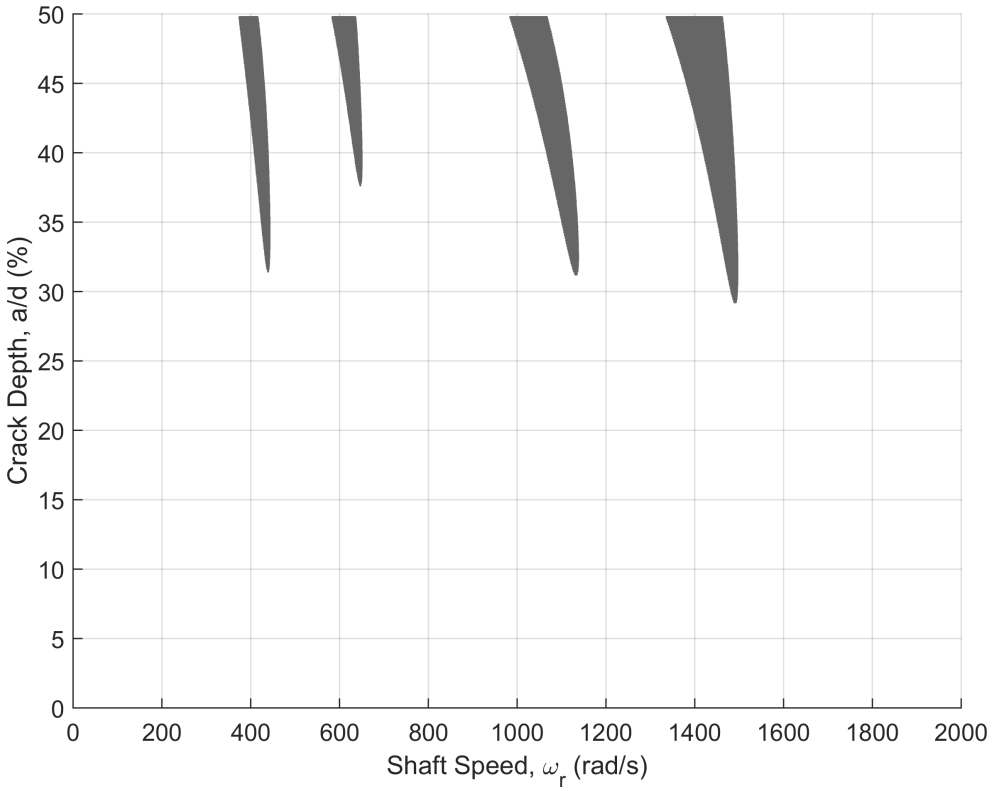

(a) Thin rotor ($I_{pR} = 0.4$ kg·m^2)

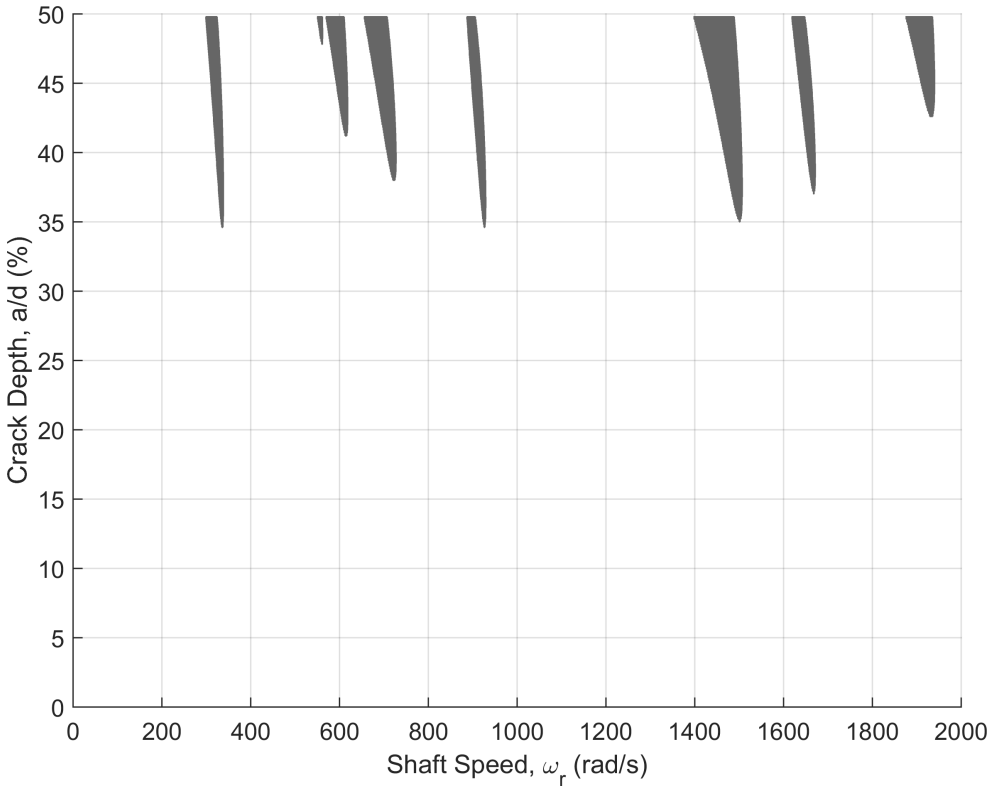

(b) Thick rotor ($I_{pR} = 0.1$ kg·m^2)

Figure 9.19: Breathing Crack: Floquet stability ($\zeta_\epsilon = \zeta_\gamma = 0.01$).

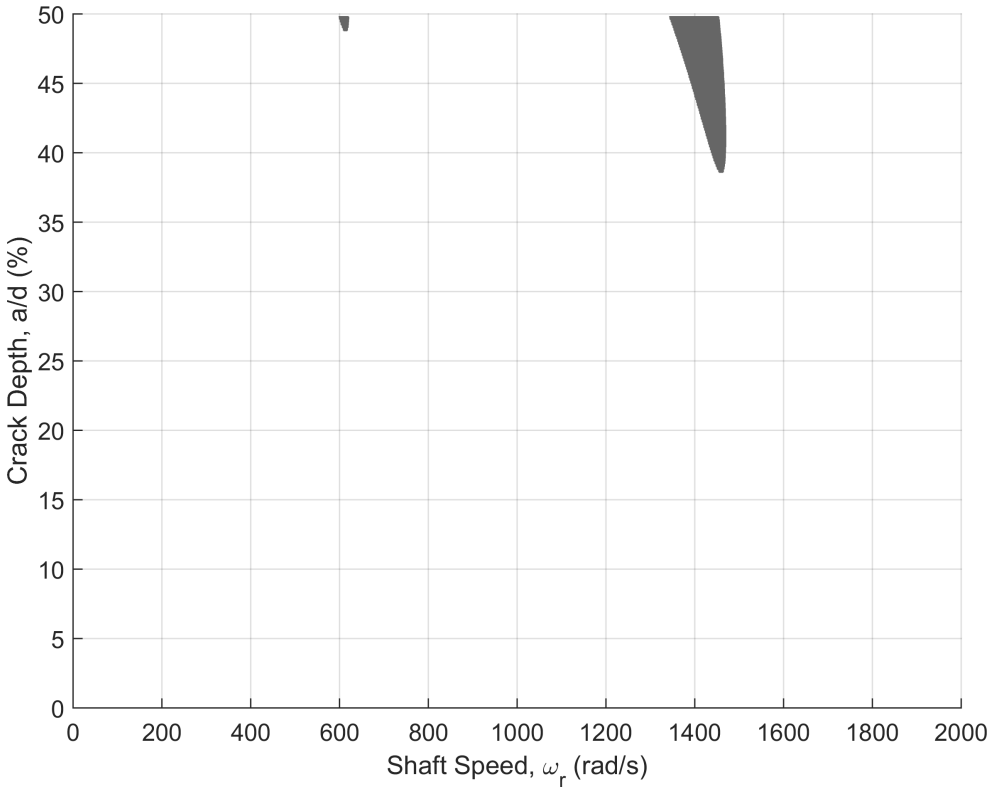

(a) Thin rotor ($I_{pR} = 0.4$ kg·m^2)

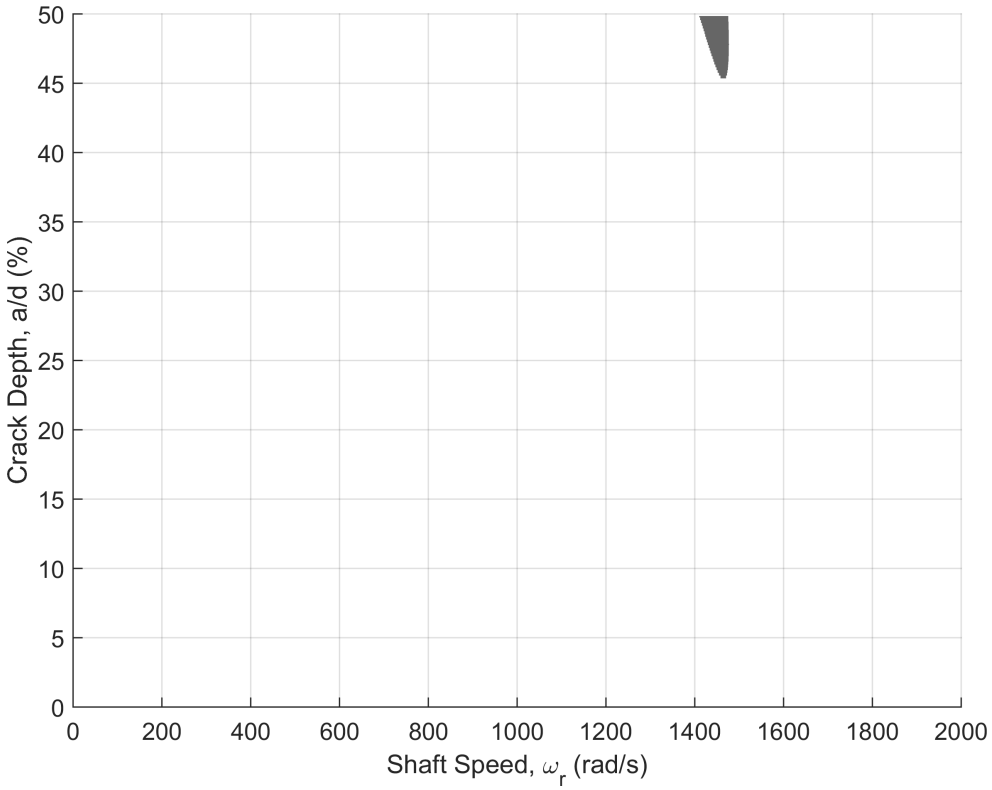

(b) Thick rotor ($I_{pR} = 0.1$ kg·m^2)

Figure 9.20: Breathing Crack: Floquet stability ($\zeta_\epsilon = \zeta_\gamma = 0.02$).

presented earlier for the gaping crack in Fig. 9.4). Similar to the gaping crack, the rotor stability with a breathing crack depends strongly on the external damping ratio, the rotor thickness, and the crack depth. Several important conclusions are drawn from the stability analysis, and are similar in nature to observations made for the gaping fatigue crack:

1. The rotor instability shaft speed range increases with increasing crack depth.

2. Increasing the external viscous damping ratio decreases the extent and prevalence of localized crack-induced instability regions.

3. The breathing crack generates more localized instability regions for a thick rotor than a thin rotor, except for the case of high external viscous damping.

Still, there are several important differences between the rotor stability with a gaping versus breathing fatigue crack. These differences are most prominently observed regarding the prevalence of instability regions (i.e., the number of branches on the instability plots) and the approximate lower threshold of crack depth abetting instability (i.e., the shallowest crack over the considered shaft speed range that causes instability):

1. For small external viscous damping ratios, the breathing crack causes more regions of rotor instability than the commensurate gaping fatigue crack.

2. For a given external damping ratio, the gaping fatigue crack model predicts instability for shallower cracks than the breathing model predicts. For example, comparing Figs. 9.6b and 9.18b, the lower threshold of crack depth causing instability is approximately 17% for the gaping fatigue crack and 24% for the breathing crack. This observation is valid for both thin and thick rotors.

Accurately predicting rotor instability therefore hinges on accurately identifying an appropriate crack model. To reiterate, the stability predictions are important because

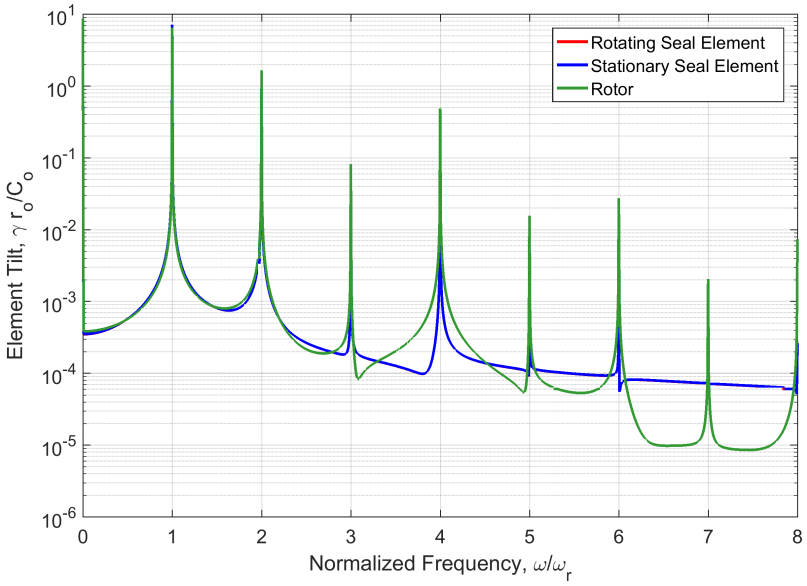

Figure 9.21: Rotor and seal response to gravity, misalignment, and imbalance for a thin rotor ($I_{pR} = 0.4$ kg·m^2) with a breathing crack of 40% ($\omega_r = 500$ rad/s).

they provide an upper limit on crack depth beyond which catastrophic failure occurs via the onset of instability. The crack must be detected before its propagation causes rotor failure.

9.3.2 Steady-State Response

The FMSR-ER equations of motion with the breathing crack are simulated using the same method and initial conditions discussed in Section 9.2.2. For the cases shown here, the rotating seal element is assumed to have a static angular misalignment of $\chi_s = 0.5$ mrad, a dynamic angular misalignment of $\chi = 0.1$ mrad, and an imbalance of $\varepsilon_{rG} = 5$ μm, while the rotor dynamic angular misalignment is $\chi_R = 1$ mrad and the imbalance is $\varepsilon_{RG} = 5$ μm. The static axial offset d_r and rotor bow (r_b and χ_b) are assumed to be zero. All static phase misalignments are also assumed to be zero, without loss of generality.

The frequency content at a single shaft of $\omega_r = 500$ rad/s is found by extracting the steady-state response and performing the fast Fourier transform (FFT). As expected

from the frequency content of the crack inertial stiffness coefficients (Fig. 6.12b), the rotor and seal response both contain integer harmonics of the shaft speed at pX frequencies, where p = 1, 2, 3, .., etc. The frequency content contained in the rotating and stationary seal element angular responses are nearly identical because the seal is designed to minimize relative misalignments. It is apparent, even at a single shaft speed, that the dynamic response to a breathing crack differs dramatically from that of a gaping crack, which induced only a 2X shaft speed harmonic. This difference in frequency content between the gaping and breathing cracks underscores the importance of correctly modeling the actual nature of the crack.

The appearance of additional integer shaft speed harmonics in the breathing crack response implies the commensurate appearance of additional sub-synchronous critical speeds (e.g., the 1/2 critical speed, the 1/3 critical speed, etc.). These sub-synchronous resonances are found by simulating the FMSR-ER equations of motion over a wide range of shaft speeds beneath the synchronous critical speed of the undamaged system. The results for a thin rotor with a breathing crack of 20% depth are given in Figs. 9.22a and 9.22b for the rotor eccentric response and stationary seal element tilt, respectively. The external viscous damping ratio is assumed to be 1%. Only the response of a thin rotor is considered here for simplicity in displaying results; analogous simulations of the thick rotor would contain additional sub-synchronous resonances.

The magnitudes of the higher harmonic frequencies are extracted from Fig. 9.22 and plotted versus shaft speed in Fig. 9.23. As hypothesized, additional sub-synchronous resonances appear in the response. For the parameters considered here, the 1/2 and 1/3 critical speeds are approximately 190 rad/s and 120 rad/s, respectively. Other sub-synchronous resonances also appear (e.g., 1/5 critical speed), though the amplitude is significantly diminished when compared to the 1/2 and 1/3 critical speed

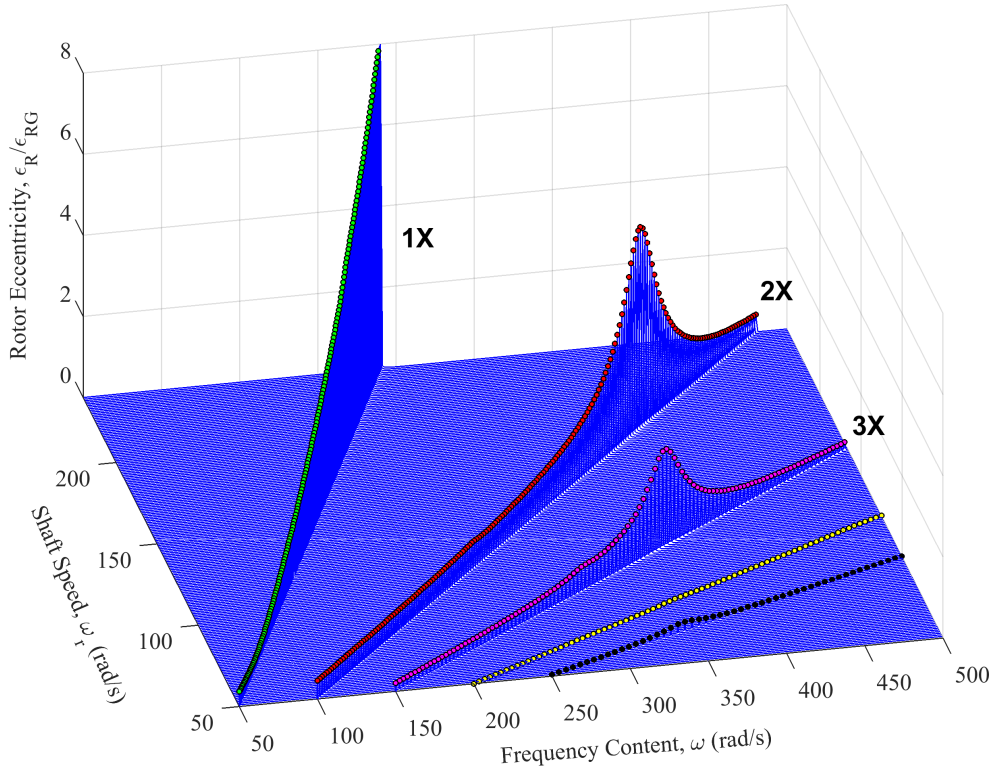

(a) Normalized rotor eccentric magnitude, $\epsilon_R/\varepsilon_{RG}$

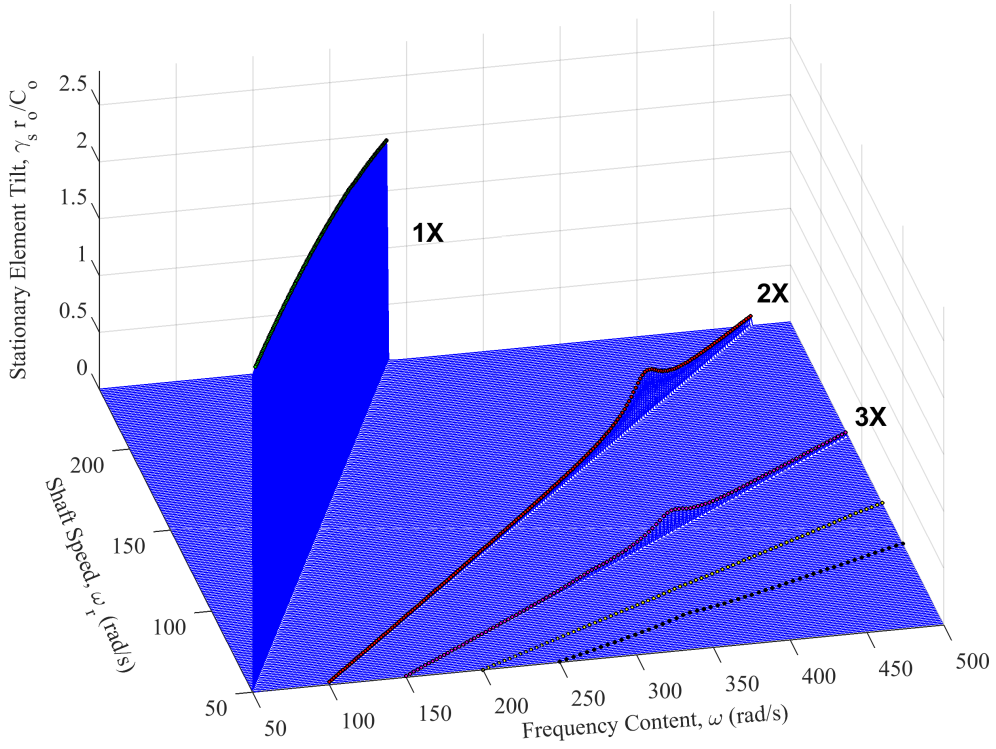

(b) Normalized stationary element tilt magnitude, $\gamma_s r_o/C_o$

Figure 9.22: Rotor and seal response to a breathing crack of 20% depth ($\zeta_\epsilon = \zeta_\gamma = 0.01$).

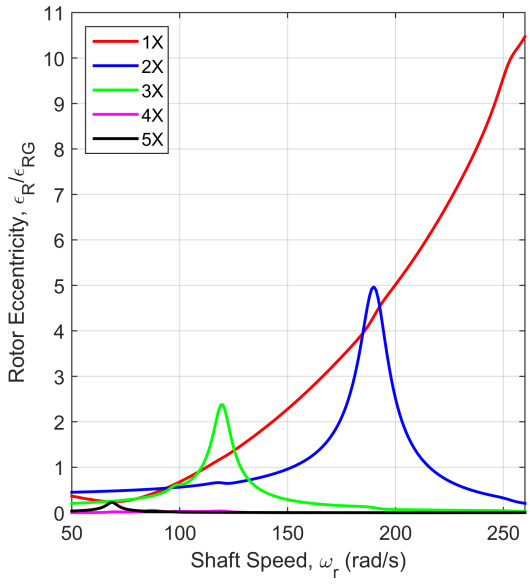

(a) 1X and 2X components of the rotor eccentric response.

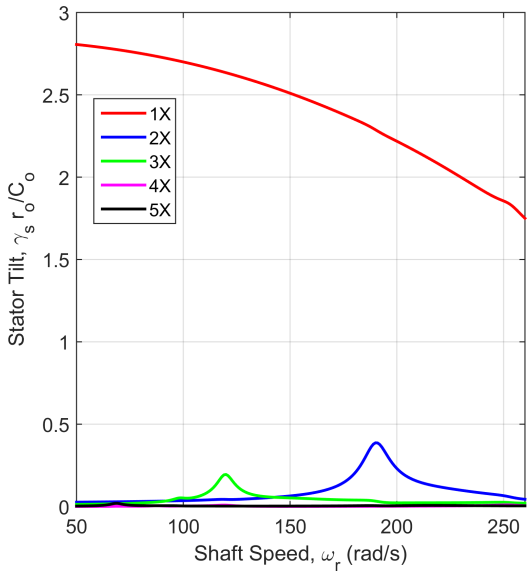

(b) 1X and 2X components of the stationary seal element tilt

Figure 9.23: Magnitudes of the 1X and 2X harmonic components of the rotor and stationary seal element response for a 20% depth breathing crack ($\zeta_\epsilon = \zeta_\gamma = 0.01$).

response. The response of the cracked rotor is transmitted directly to the stationary seal element via the rotating seal element and the fluid film. The seal response, however, is still dominated by the 1X harmonic because of additional synchronous excitations in the seal response caused by the seal angular misalignment and eccentric imbalance.

The angular and eccentric orbits of the rotor and stationary seal element at steady-state are given in Figs. 9.24 and 9.25 for shaft speeds in the vicinity of the 1/3 critical speed and in Figs. 9.26 and 9.27 for shaft speeds in the vicinity of the 1/2 critical speed. The qualitative nature of the orbit shape is dictated by the prominence of the higher harmonics relative to the synchronous 1X component. In the vicinity of the 1/3 critical speed, the rotor eccentric orbits in Fig. 9.24 contain three prominent lobes caused by interactions between the 3X and 1X harmonics. Importantly for diagnostics, the orbit differs significantly from an elliptical shape because the 3X harmonic is comparable in magnitude to the synchronous 1X components (see Fig. 9.23a). The

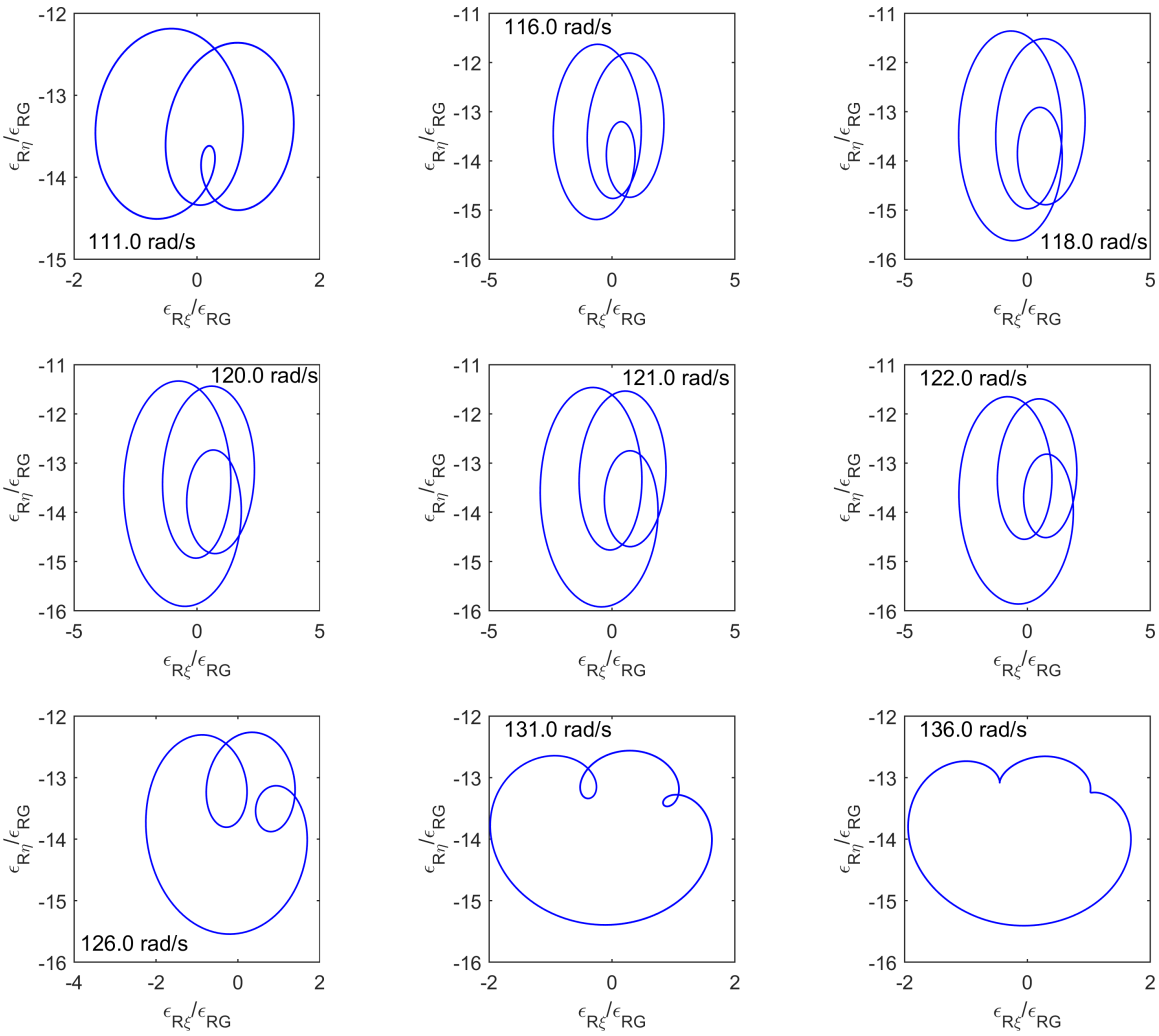

Figure 9.24: Eccentric orbits of the rotor observed during passage through the 1/3 critical speed for a 20% breathing crack.

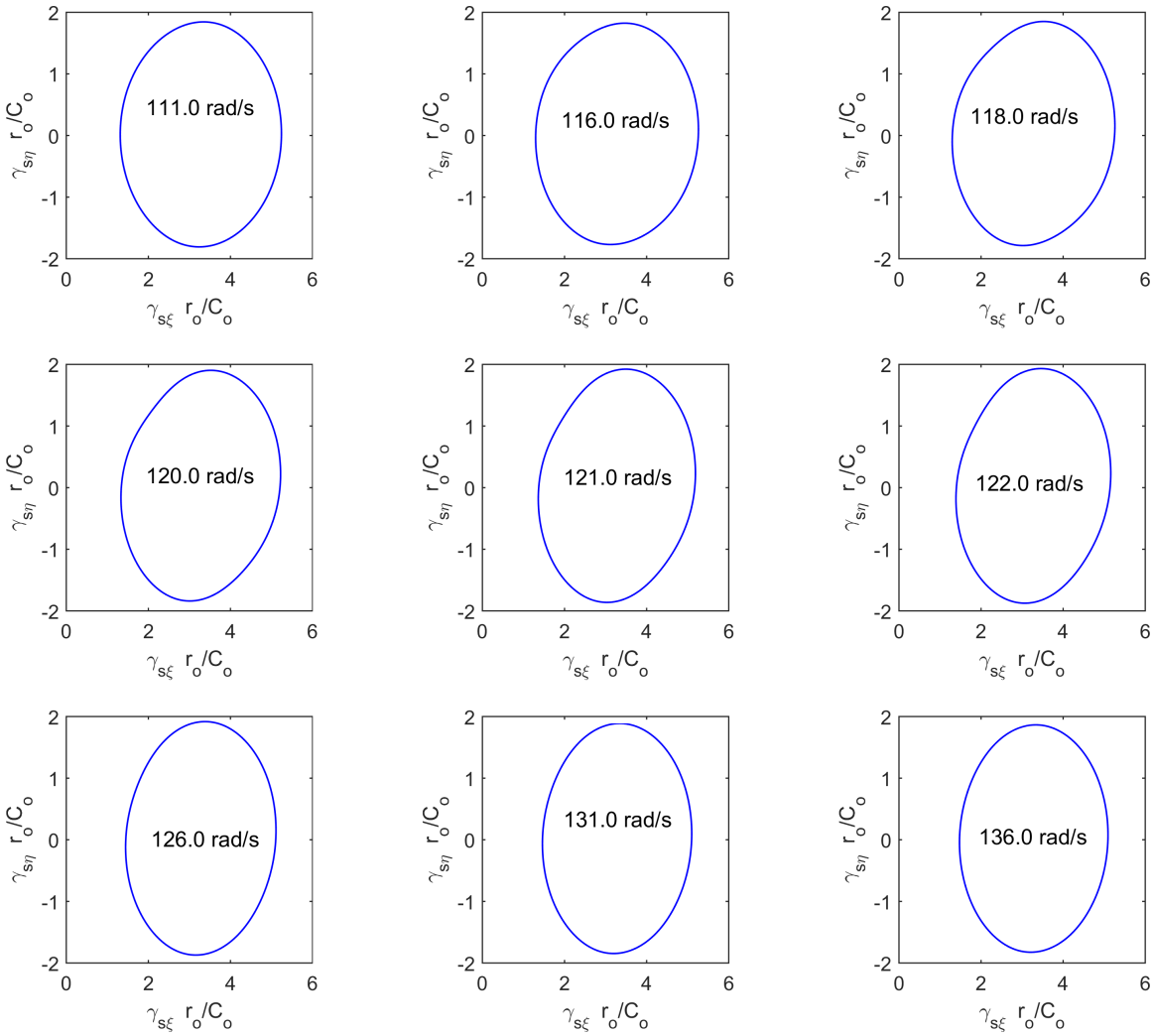

Figure 9.25: Angular orbits of the stationary seal element observed during passage through the 1/3 critical speed for a 20% breathing crack.

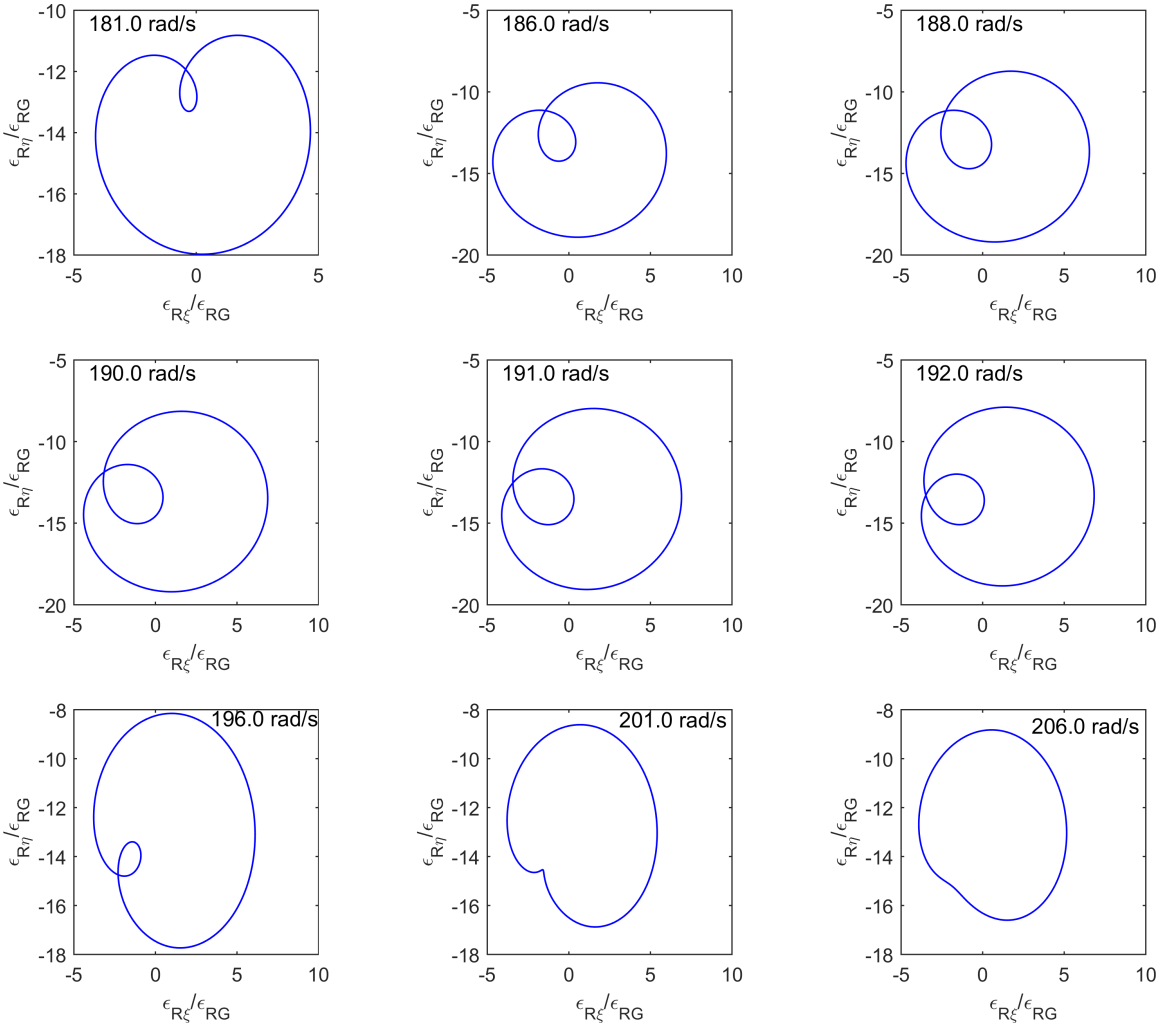

Figure 9.26: Eccentric orbits of the rotor observed during passage through the 1/2 critical speed for a 20% breathing crack.

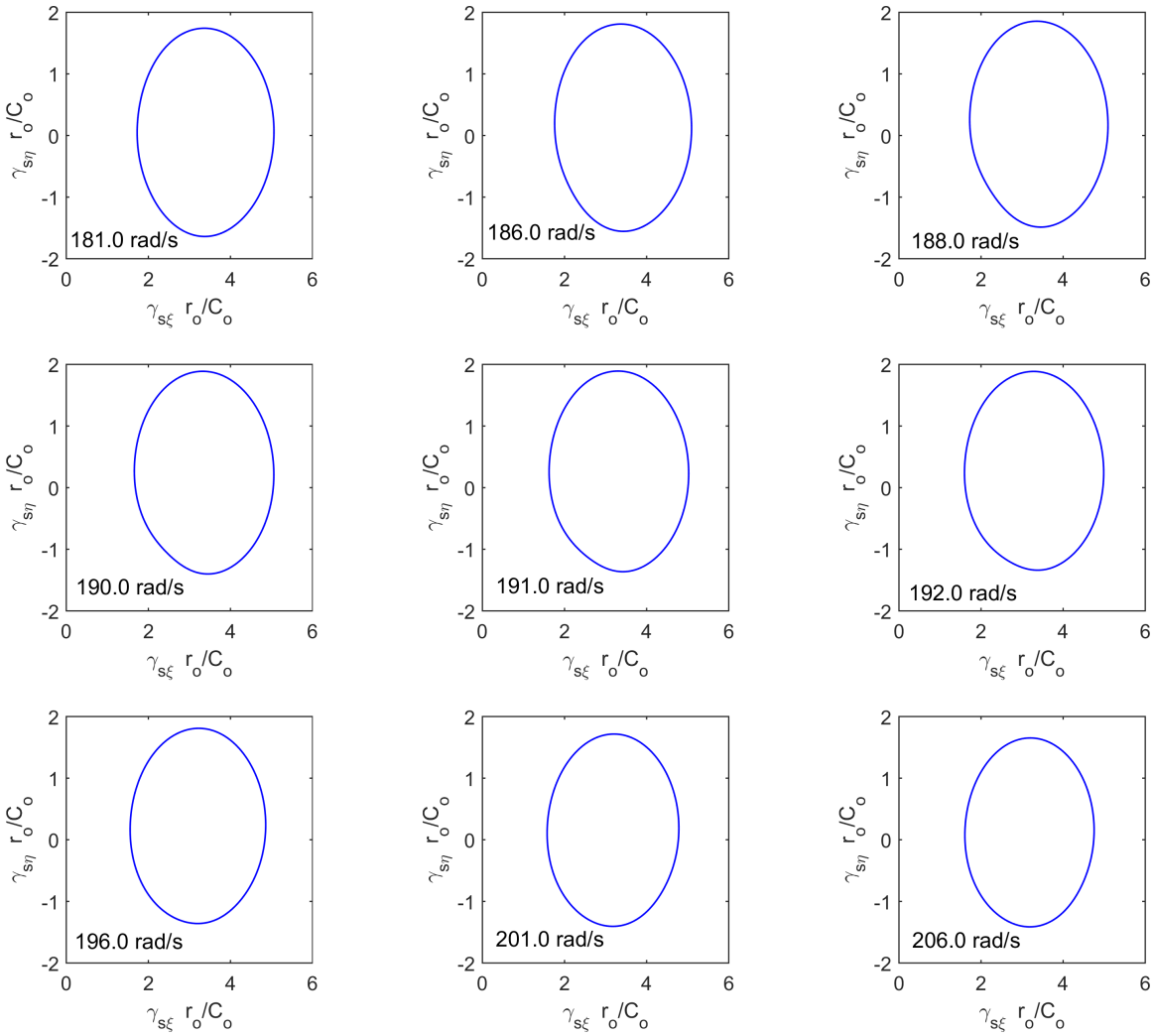

Figure 9.27: Angular orbits of the stationary seal element observed during passage through the 1/2 critical speed for a 20% breathing crack.

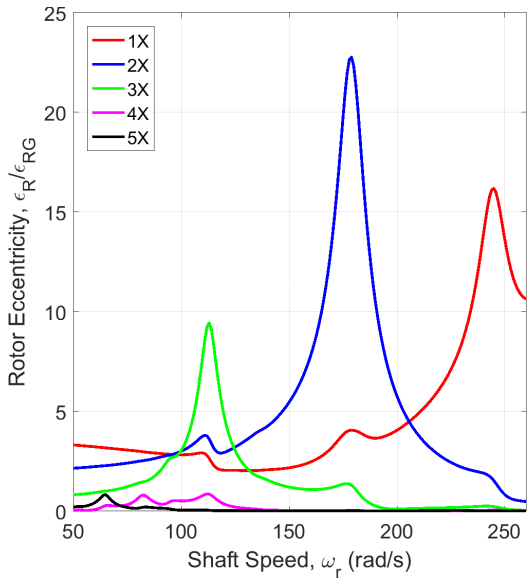

(a) 1X and 2X components of the rotor eccentric response

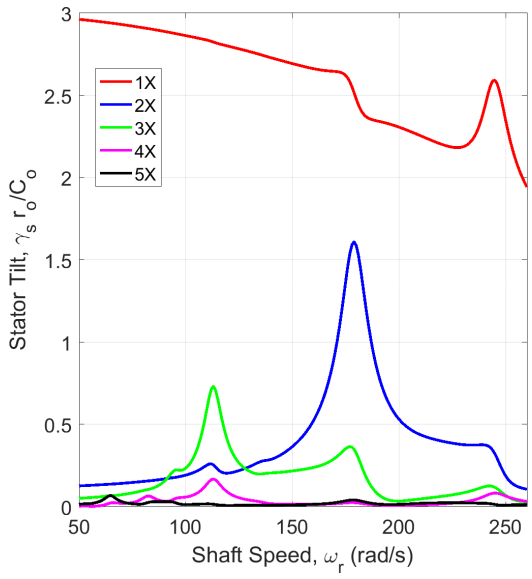

(b) 1X and 2X components of the stationary seal element tilt

Figure 9.28: Magnitudes of the 1X and 2X harmonic components of the rotor and stationary seal element response for a 40% depth breathing crack ($\zeta_\epsilon = \zeta_\gamma = 0.01$).

orbits of the stationary seal element, however, are primarily elliptical because the response is monopolized by the 1X harmonic. Analogous conclusions are also drawn for orbits in the vicinity of the 1/2 critical speed (Figs. 9.26 and 9.27). In this case, the rotor orbits contain only two distinguishable lobes induced by interactions between the 1X and 2X harmonics. The angular orbits of the stationary seal element are still nearly elliptical.

The prominence of the integer shaft speed harmonics increases as the crack depth increases. This is shown in Fig. 9.28, where the magnitudes of the first five shaft speed harmonics are given versus shaft speed. For the deeper crack, the 3X harmonic manifests prominently in the rotor response near the 1/3 critical speed of approximately 113 rad/s. Likewise, the magnitude of the 2X harmonic eclipses that of the synchronous component in the vicinity of the 1/2 critical speed of 179 rad/s in every case except the tilt of the stationary seal element. Several other interesting observations can be made from Fig. 9.28. First, the magnitude and nature of the synchronous

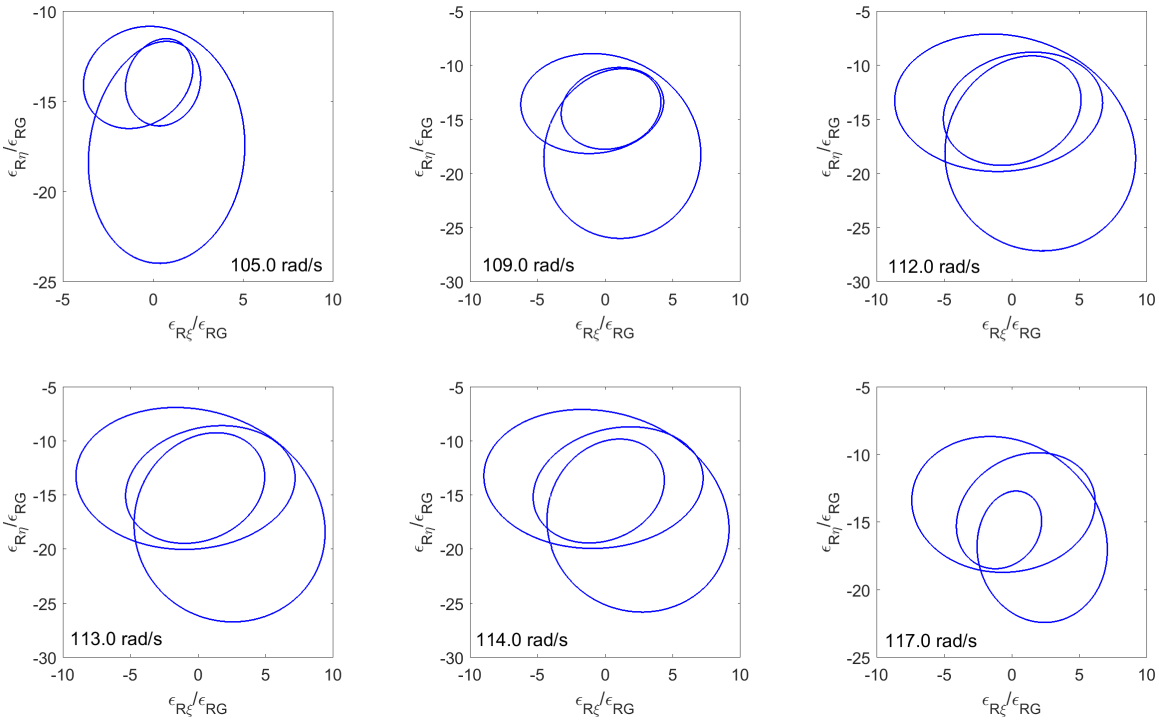

Figure 9.29: Eccentric orbits of the rotor observed during passage through the 1/3 critical speed for a 40% breathing crack.

1X harmonic is influenced by the breathing crack; this conclusion is intuitive since the 1X harmonic is a principal constitutive component of the breathing crack compliance. This behavior was not present in the gaping crack response, where the 1X harmonic was only marginally influenced by the crack because of the associated shift in the synchronous critical speed. The second observation is that the breathing crack harmonics are coupled for deep cracks; the response of other harmonics is amplified by a sub-synchronous resonance in another (e.g., the 1X harmonic is amplified near the 1/2 critical speed, and vice versa). This coupling is particularly pronounced for harmonics higher than the 3X, where the coupling is often comparable in magnitude to the sub-synchronous resonance itself.

The angular and eccentric orbits of the rotor and stationary seal element are given in Figs. 9.29 and 9.30 for shaft speeds near the 1/3 critical speed, and in Figs. 9.31 and 9.32 for shaft speeds near the 1/2 critical speed. The conclusions regarding the

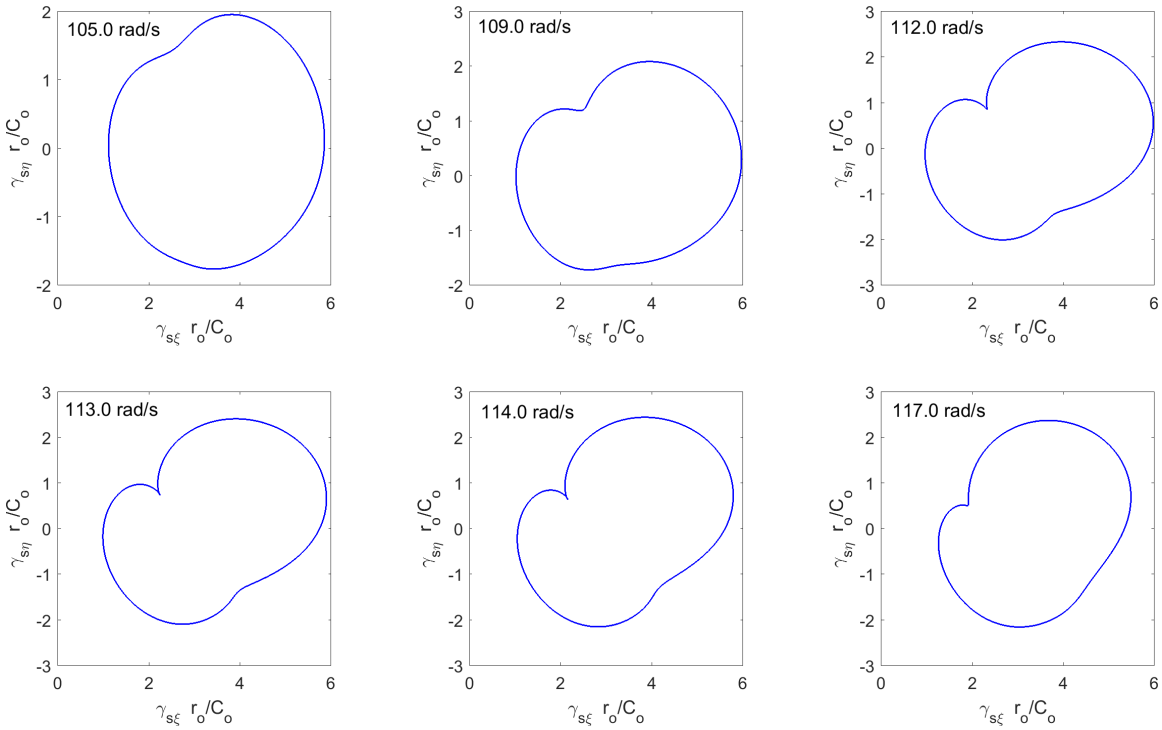

Figure 9.30: Angular orbits of the stationary seal element observed during passage through the 1/3 critical speed for a 40% breathing crack.

number of lobes in relation to the dominant shaft speed harmonic are unchanged in relation to crack depth (e.g., 20% versus 40%), and have previously been discussed. Here, the orbits of the stationary seal element indicate a significant contribution from the crack-induced higher harmonic oscillations. Thus, as the crack becomes deeper, orbital plots of the stationary seal element dynamics become a more feasible diagnostic tool if the shaft speed is near a sub-synchronous critical speed.

9.3.3 Time-Energy-Frequency Analysis

The FMSR-ER response to a breathing crack is now analyzed using the Hilbert-Huang Transform (HHT). As discussed in Appendix C, the HHT is an algorithmic approach that first decomposes a signal into nearly-orthogonal intrinsic mode functions (IMFs) and then extracts the instantaneous frequency and amplitude of each IMF using the Hilbert transform (see Appendix C for a discussion of instantaneous frequency

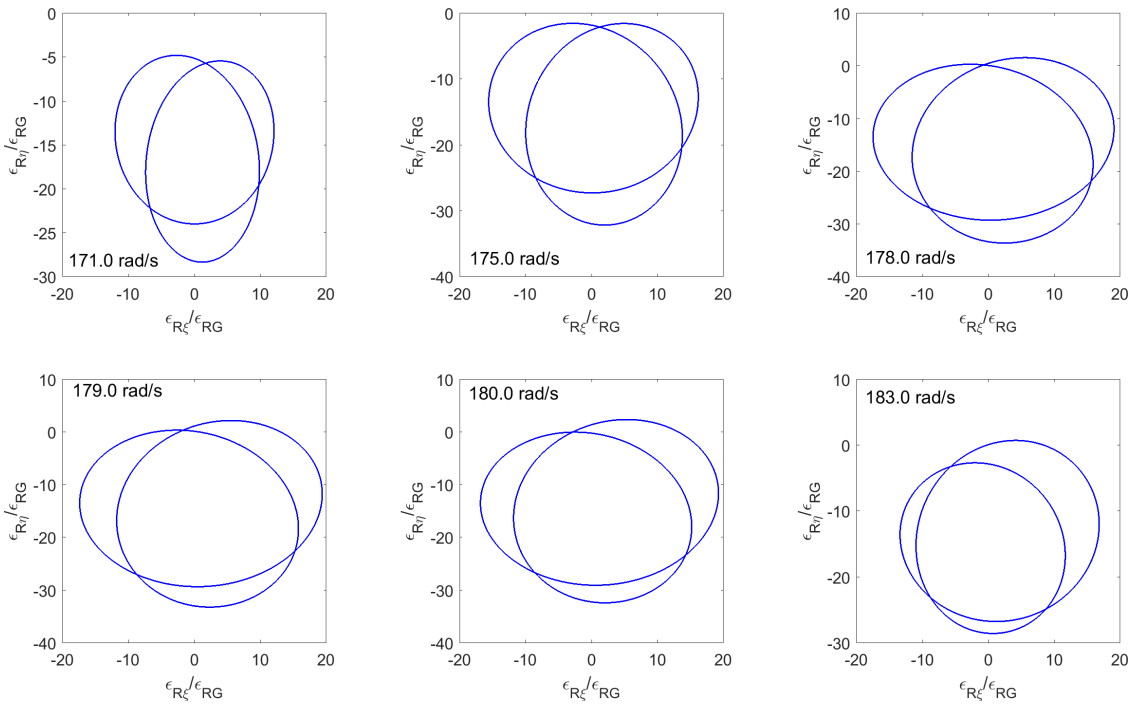

Figure 9.31: Eccentric orbits of the rotor observed during passage through the 1/2 critical speed for a 40% breathing crack.

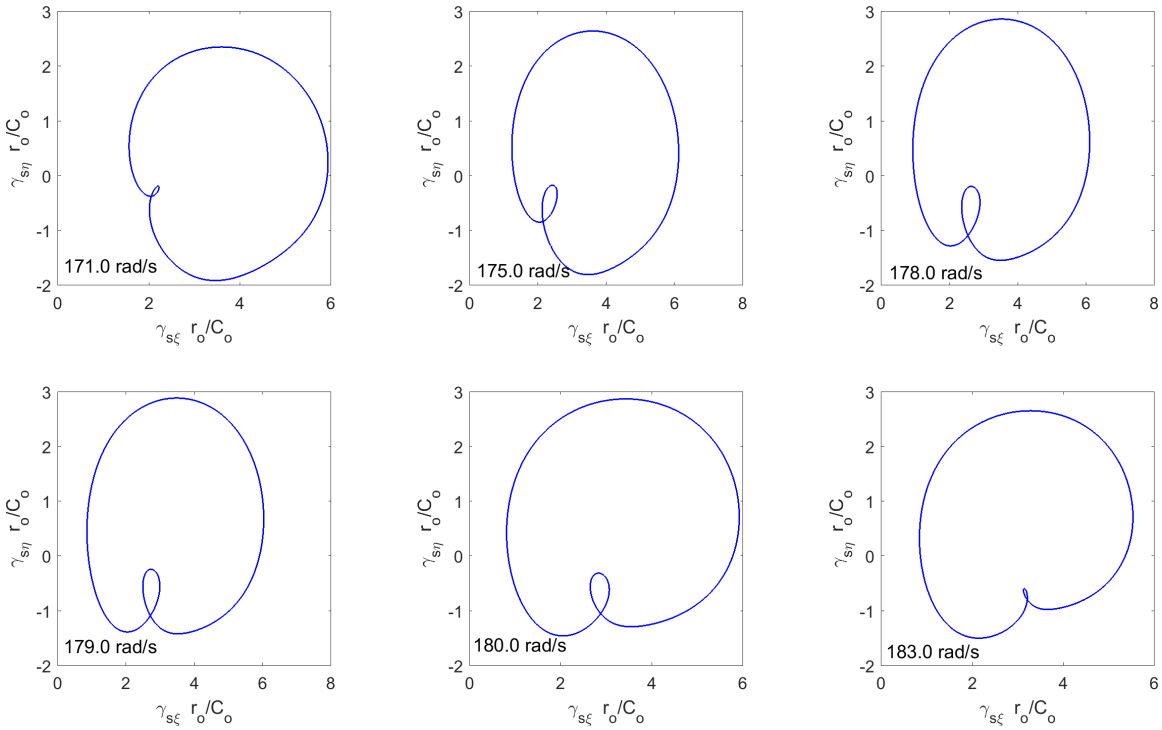

Figure 9.32: Angular orbits of the stationary seal element (stator) observed during passage through the 1/2 critical speed for a 40% breathing crack.

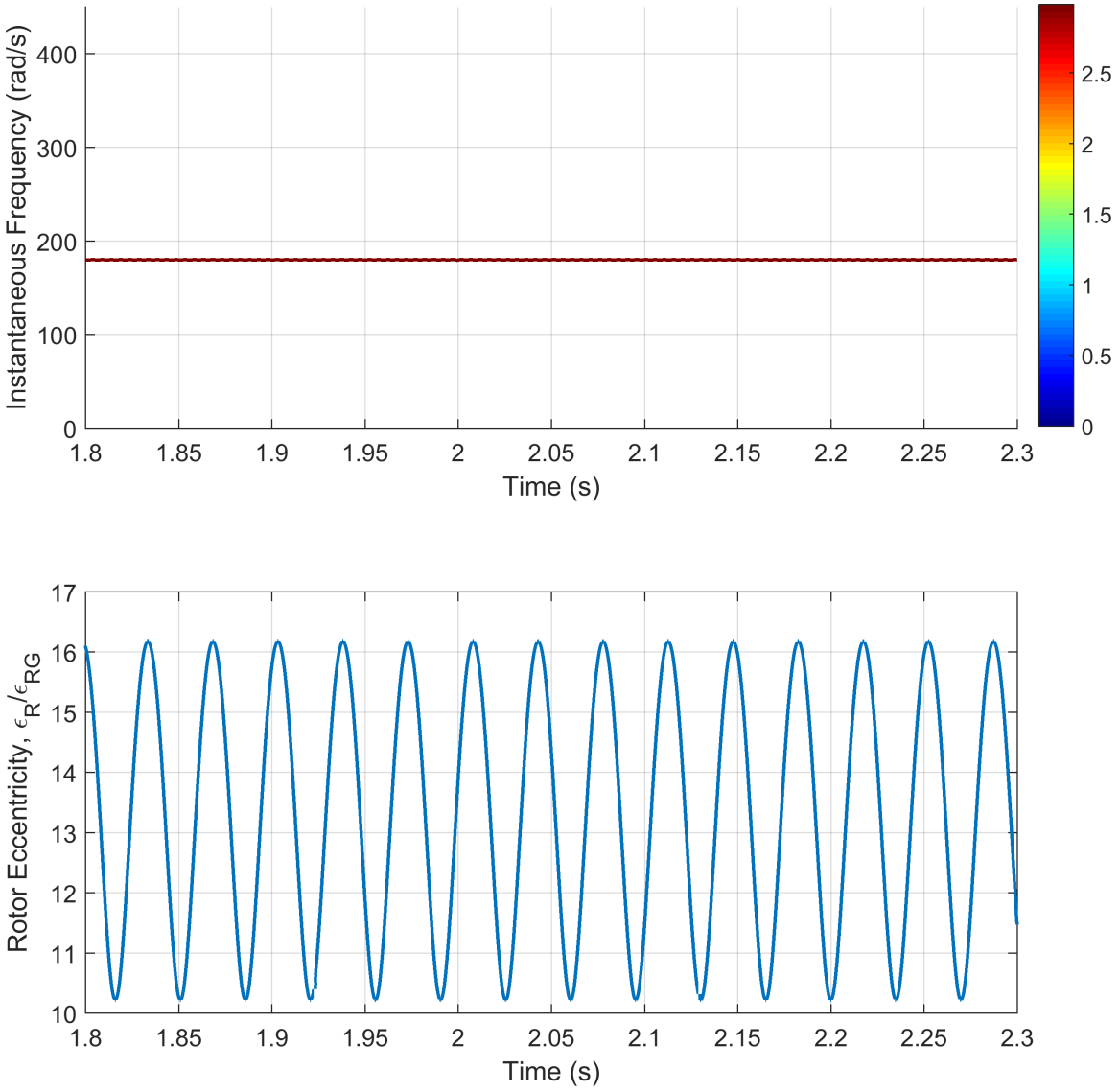

Figure 9.33: Time-energy-frequency content in the undamaged rotor eccentric response $\epsilon_{R\xi}$ ($\omega_r = 180$ rad/s, a = 0%, $\zeta_\epsilon = \zeta_\gamma = 0.01$).

and amplitude). The HHT is a valuable tool for elucidating rotor fault signatures because each IMF typically has physical significance; thus, the dynamic response can be separated into components related to the undamaged system and components related to the fault. This capability is profoundly useful for characterizing the nature of different rotor faults, including breathing shaft cracks.

The FMSR-ER steady-state response to a breathing crack is simulated using the parameters and procedures discussed in Section 9.3.2. The steady-state waveforms and time-energy-frequency spectra (calculated using the HHT) are provided in Figs. 9.33 - 9.37 for shaft speeds in the vicinity of the 1/3 and 1/2 critical speeds (115 rad/s and 180 rad/s, respectively). Only the rotor eccentricity and stationary seal element tilt are analyzed here; these cases are representative of phenomena observed in other degrees-of-freedom. The color bar in each time-energy-frequency spectrum indicates the magnitude of the instantaneous amplitude.

The time-energy-frequency spectrum for an undamaged rotor is given in Fig. 9.33 to establish a baseline for the undamaged system response. Importantly, the steady-state response for each FMSR-ER degree-of-freedom satisfies the criteria for an IMF (see Appendix C). Consequently, the response can be decomposed into a single oscillatory IMF and a single monotonic residue that correspond to the synchronous response and the static response, respectively. The time-energy-frequency spectrum in Fig. 9.33 indicates that the instantaneous frequency is constant and equal to the shaft speed (180 rad/s). The instantaneous amplitude is also constant throughout the response.

The time-energy-frequency spectrum is fundamentally altered when the rotor contains a breathing crack. As discussed in Section 9.3.2, the steady-state response in the vicinity of the 1/3 critical speed is dominated by the 1X and 3X shaft speed harmonics. The steady-state waveforms (see Figs. 9.34 and 9.35) are analyzed using the HHT, thus indicating the prevalence of two distinct IMFs; one is centered

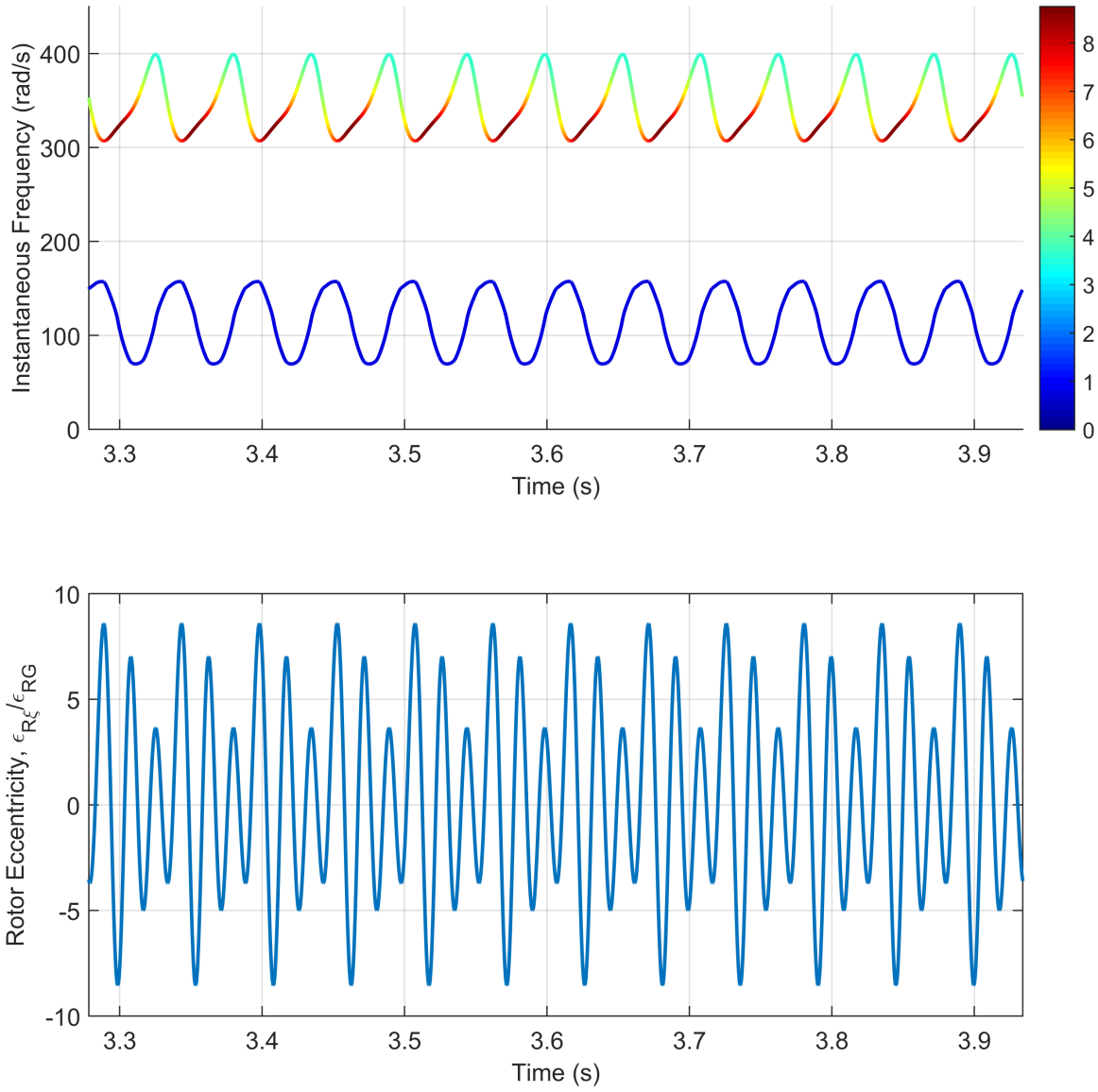

Figure 9.34: Time-energy-frequency content in the rotor eccentricity $\epsilon_{R\xi}$ caused by a breathing crack, calculated in the vicinity of the 1/3 critical speed ($\omega_r = 115$ rad/s, a = 40%, $\zeta_\epsilon = \zeta_\gamma = 0.01$).

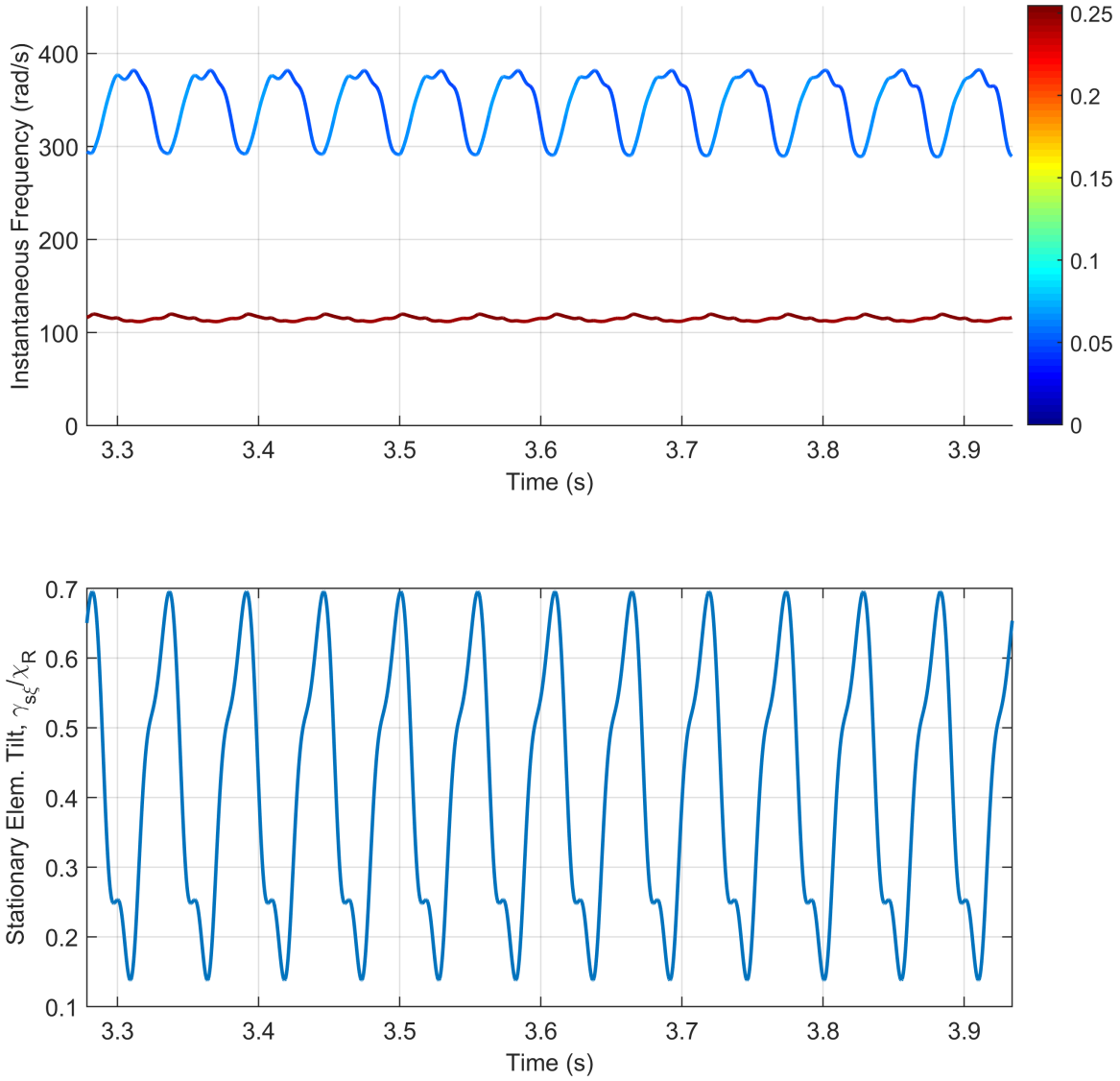

Figure 9.35: Time-energy-frequency content in the stationary seal element tilt $\gamma_{s\xi}$ caused by a breathing crack, calculated in the vicinity of the 1/3 critical speed (ω_r = 115 rad/s, a = 40%, $\zeta_\epsilon = \zeta_\gamma = 0.01$).

near the shaft speed, while the other is centered near the 3X shaft speed frequency. These IMFs are observed in both the rotor response and the stationary seal element response. In each case, the instantaneous frequency of both IMFs vary smoothly and periodically. The instantaneous amplitude is nearly constant in the synchronous IMF, but varies significantly for the IMF associated with the 3X harmonic. This periodic and consistent variation is expected because the crack is not an intermittent phenomenon; once the shaft develops a crack, the crack is always present and always influences the rotor vibration.

One distinct difference emerges between the time-energy-frequency spectra for the rotor and stationary seal element responses. The time-energy-frequency spectrum for the rotor eccentricity, shown in Fig. 9.34, indicates that the response is primarily composed of the IMF associated with the 3X harmonic; the total response is modulated by a subsidiary synchronous component centered near the shaft speed frequency. On the other hand, the time-energy-frequency spectrum for the stationary seal element tilt is dominated by the IMF associated with synchronous vibration; this conclusion was also observed in the stationary seal element orbits near the 1/3 critical speed (see Figs. 9.27 and 9.30), where the orbit shape was primarily circular.

Similar conclusions are also drawn regarding the time-energy-frequency spectrum in the vicinity of the 1/2 critical speed, as shown in Figs. 9.36 and 9.37. The response is again composed of two periodic and smoothly varying IMFs, centered near instantaneous frequencies corresponding to the 1X and 2X shaft speed harmonics. The energy of both components is nearly constant, and especially so for the synchronous IMF. Comparing the rotor and stationary seal element results, the primary IMF in the rotor eccentricity is centered near the 2X harmonic, while in the stationary seal element tilt the 1X and 2X IMFs are comparable in magnitude.

The time-energy-frequency spectrum is now calculated for the same parameters but with a shallower crack (a = 20%), in the vicinity of the 1/2 critical speed (190

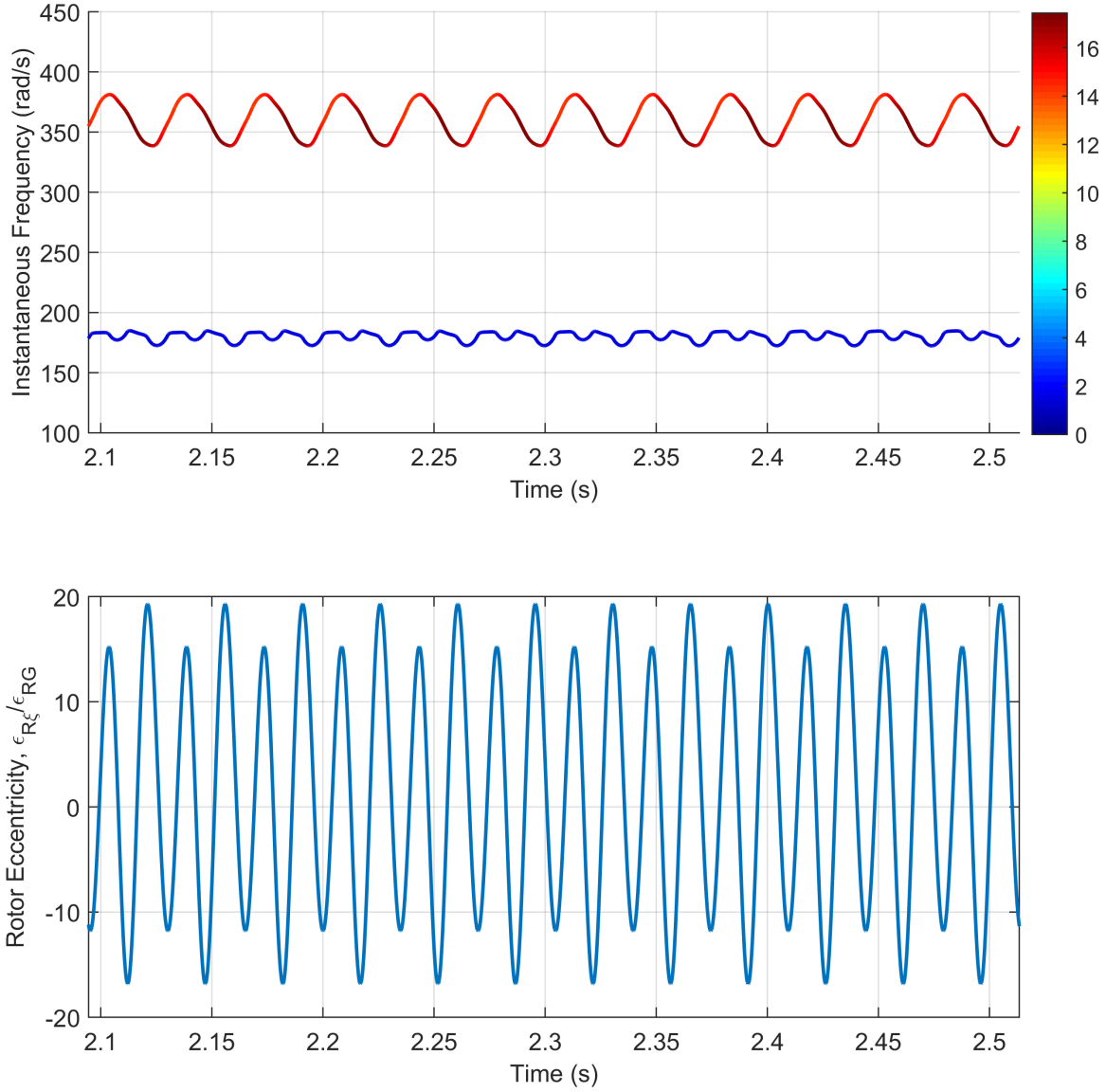

Figure 9.36: Time-energy-frequency content in the rotor eccentricity $\epsilon_{R\xi}$ caused by a breathing crack, calculated in the vicinity of the 1/2 critical speed ($\omega_r = 180$ rad/s, a = 40%, $\zeta_\epsilon = \zeta_\gamma = 0.01$).

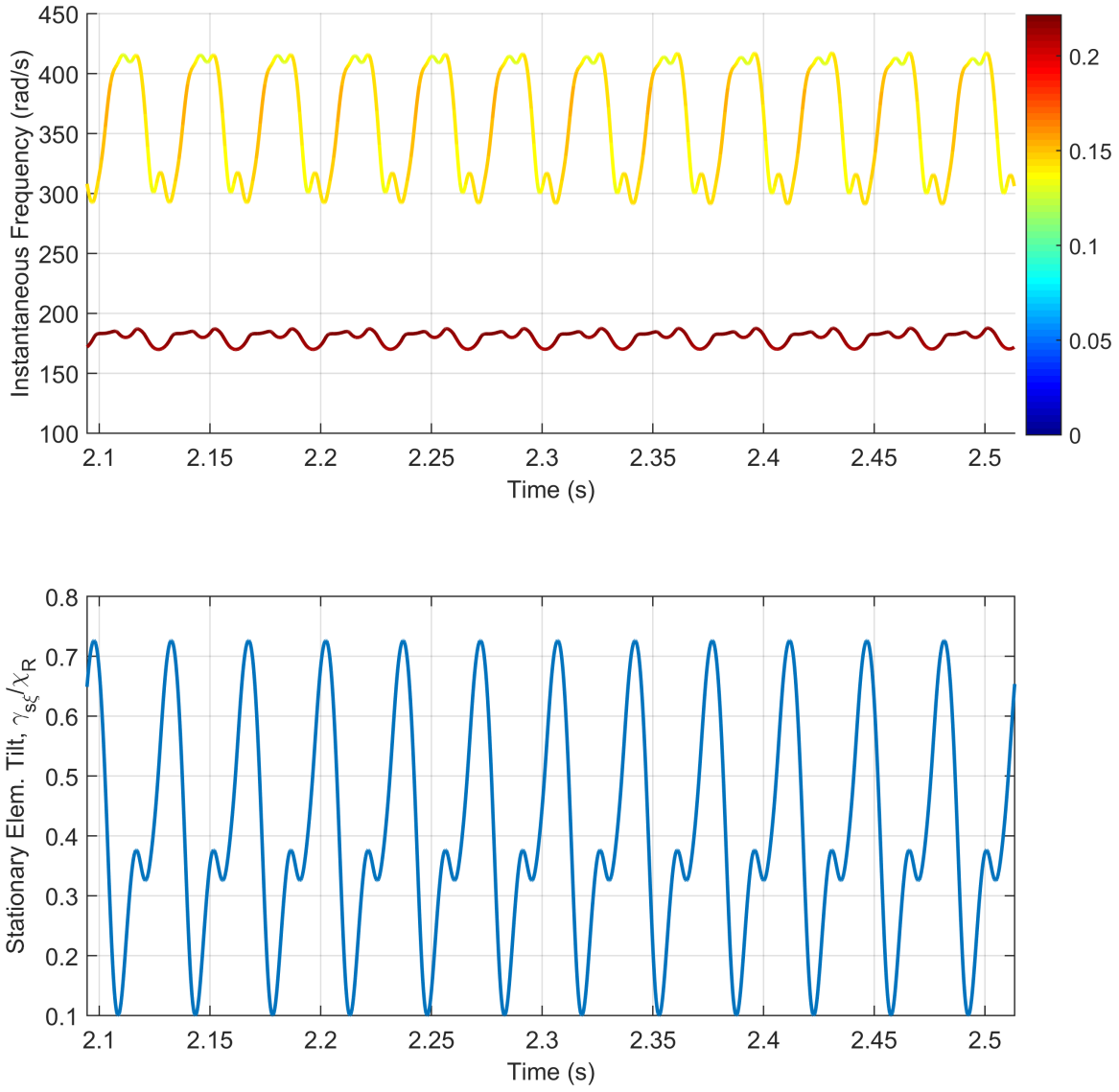

Figure 9.37: Time-energy-frequency content in the stationary seal element tilt $\gamma_{s\xi}$ caused by a breathing crack, calculated in the vicinity of the 1/2 critical speed (ω_r = 180 rad/s, a = 40%, $\zeta_\epsilon = \zeta_\gamma = 0.01$).

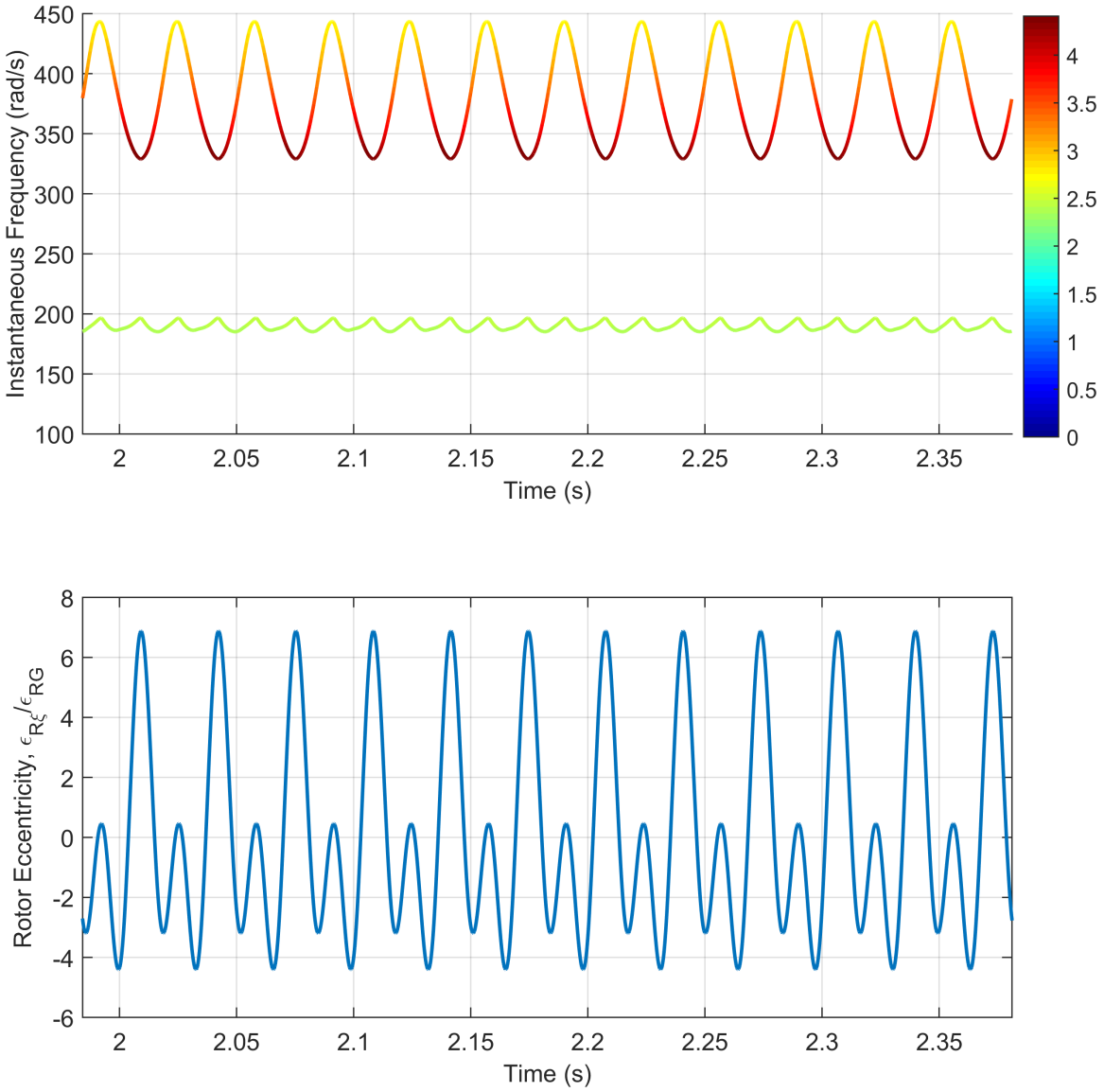

Figure 9.38: Time-energy-frequency content in the rotor eccentricity $\epsilon_{R\xi}$ caused by a breathing crack, calculated in the vicinity of the 1/2 critical speed ($\omega_r = 190$ rad/s, a = 20%, $\zeta_\epsilon = \zeta_\gamma = 0.01$).

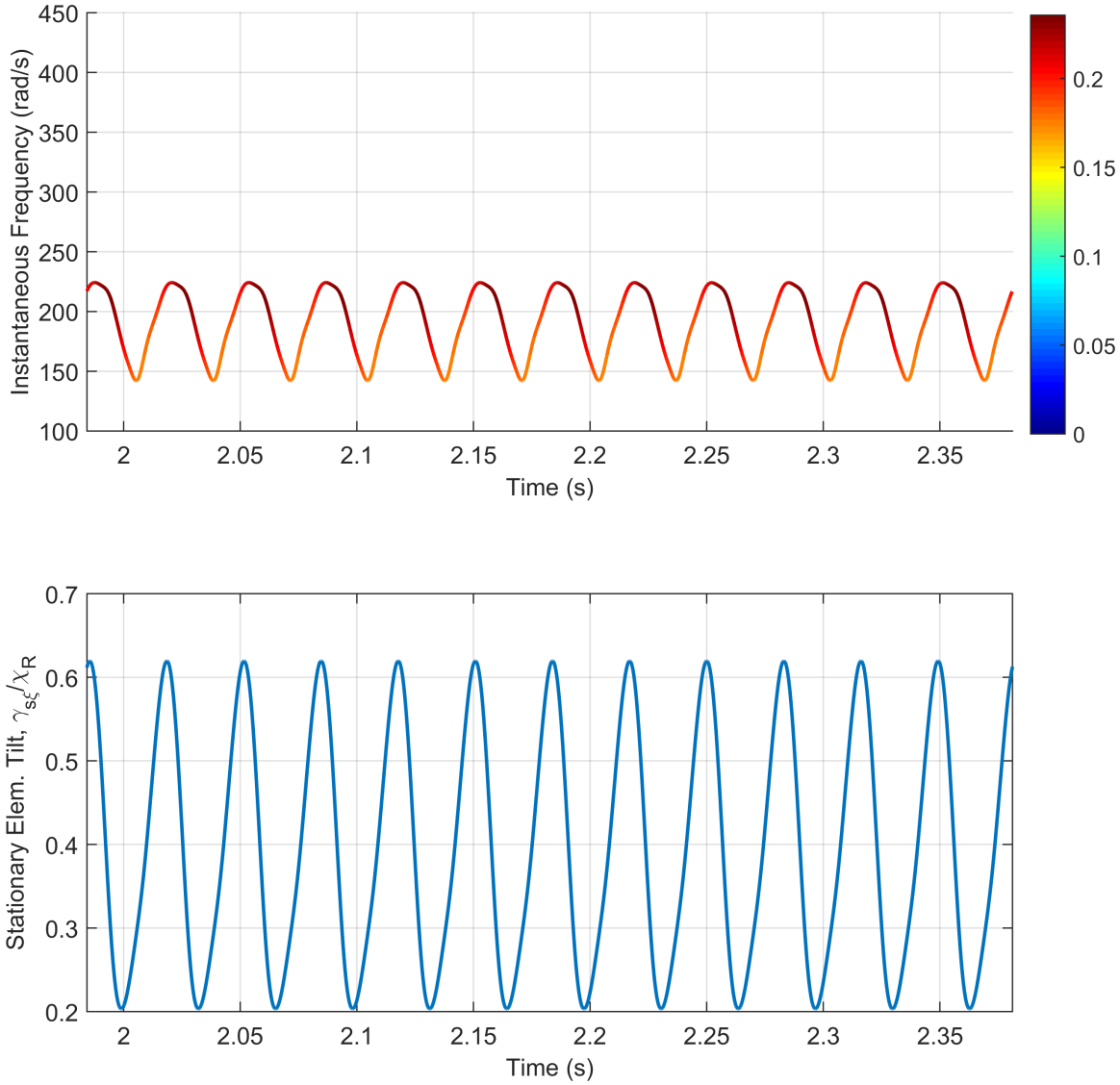

Figure 9.39: Time-energy-frequency content in the stationary seal element tilt $\gamma_{s\xi}$ caused by a breathing crack, calculated using the HHT in the vicinity of the 1/2 critical speed ($\omega_r = 190$ rad/s, a = 20%, $\zeta_\epsilon = \zeta_\gamma = 0.01$).

rad/s). The time-energy-frequency spectra, along with the corresponding steady-state waveforms, are given in Figs. 9.38 and 9.39. The rotor eccentricity still contains two constitutive IMFs related to the 1X and 2X shaft speed harmonics. The stationary seal element tilt, however, is composed of only a single IMF. Still, in contrast to the undamaged rotor time-energy-frequency spectrum presented earlier, this single IMF displays variations in both instantaneous frequency and amplitude.

The FMSR-ER response to a crack is described by several key features in the time-energy-frequency spectra, as calculated via the HHT:

1. The IMFs of the FMSR-ER system containing a breathing crack are periodic and smoothly-varying.

2. Near the sub-synchronous critical speeds, and for relatively deep cracks, the steady-state response is decomposed into two IMFs: one centered near the synchronous frequency, and one centered near the higher harmonic corresponding to the particular sub-synchronous critical speed. This conclusion is valid for both the rotor and the stationary seal element.

3. For shallower cracks, the rotor response is still composed of two distinct IMFs, while the stationary seal response can be described by a single IMF. Still, this single IMF contains significant periodic variation in both instantaneous frequency and amplitude.

The breathing crack manifests prominently in the HHT for both the rotor and the seal for a variety of shaft speeds and crack depths, and differs substantially from that of the undamaged rotor. Therefore, it is reasonable to assert that the HHT is a valuable tool for crack detection, and can be implemented using a condition monitoring system affixed to the stationary seal element.

9.4 Summary

The equations of motion for the FMSR-ER system with a cracked shaft have been solved here for two cases: a gaping crack and a breathing crack. In both cases, the principle vibration signatures corresponding to the cracked rotor are higher harmonic oscillations of the shaft speed; the gaping crack produces only a 2X harmonic, whereas the breathing crack produces pX harmonics, where p is an integer. For both cases, the rotor and seal responses indicate sub-synchronous critical speeds corresponding to each integer shaft speed harmonic. These sub-synchronous resonances manifest in both the rotor and seal dynamics. The appearance of crack-induced vibrations in the stationary seal element dynamics is an important observation. Because the hallmark crack vibration signatures appear in the seal dynamics, the stationary seal element can serve as a cost-effective and practical surrogate crack monitoring system for the rotor. The time-energy-frequency spectrum, obtained via the HHT, is also prominently influenced by a breathing crack. In general, the vibration signals obtained from the FMSR-ER elements can be decomposed into IMFs that, in contrast to the undamaged case, show smooth and periodic variation in instantaneous frequency for both shallow and deep cracks. This oscillatory variation in instantaneous frequency is also a fundamental crack vibration signature.

CHAPTER X

RESULTS: INTERMITTENT RUB

10.1 Overview

Intermittent contact (i.e., rub) in rotordynamic systems is a complex nonlinear response defined by phenomena occurring on vastly different spatial and temporal scales. The objective of this chapter is to identify the hallmark dynamic signatures of intermittent rotor rub. Several scenarios are analyzed here to isolate specific attributes of rub in different rotor and/or sealing systems. These scenarios, and the purpose for including them here, are the following:

1. **System**: Rotor-stator rub using the Jeffcott rotor and the LECM.

   Objective: Establish nonlinear analysis tools and study the rich nonlinear response induced by intermittent rotor-stator contact.

2. **System**: Rotor-stator rub using the Jeffcott rotor and the RSCM.

   Objective: Elucidate differences between the LECM and RSCM.

3. **System**: Seal face impact in a FMS mechanical face seal system.

   Objective: Establish dynamic signatures of seal face contact and assess their practical implications.

4. **System**: Lateral rotor-housing in the FMSR-ER system.

   Objective: Find seal vibration signatures caused by rotor-housing contact.

This chapter will show that even though the considered systems are different, the principal dynamic signatures of rub remain similar in every case. A general discussion of rotordynamic nonlinear responses and associated analysis tools is provided first to motivate later results and discussion.

10.2 Nonlinear Response Analysis Tools

Rotor and seal responses to nonlinear excitations are presented in this chapter using waveforms, orbits, frequency spectra, and Poincaré sections. In conventional nonlinear dynamics, an orbit is a projection of the entire solution $\mathbf{x}(t) \in \mathbb{R}^n \times \mathbb{S}^1$ unto the n-dimensional phase space. This approach removes the time-evolution of the response but retains the nature of the solution. Here, as is typical in rotordynamics, the orbit is the trace of the rotor geometric center rather than the full solution $\mathbf{x}(t)$. The waveforms are time responses of a specified degree-of-freedom demonstrating the evolution of one state variable versus time. However, it is difficult to ascertain the nature of the solution from only the waveform (particularly so for other dynamic responses such as quasiperiodic and chaotic responses). The frequency spectra further elucidates the character of each state variable, and provides additional utility because rotordynamic condition monitoring systems often rely on shaft speed harmonics for detecting faults.

Poincaré sections qualitatively assess the system dynamics; specifically, the Poincaré section Σ is a surface in the state-space transverse to the dynamic evolution of the system. In a non-autonomous system with excitation period T, 'transverse to the flow' implies that the solution $\mathbf{x}(t)$ is sampled every T seconds. If time is normalized by the shaft speed ω_r, the Poincaré section is obtained by sampling the response every 2π non-dimensional units of time (i.e., once per rotor revolution), which supplies a stroboscopic picture of the dynamic evolution. These sampled points are referred to as Poincaré return points, and a plot of the Poincaré return points versus a specified control parameter gives the bifurcation diagram. Thus, because the Poincaré section qualitatively characterizes the response, the bifurcation diagram exposes qualitative changes in system behavior versus changes in some control parameter (e.g., shaft speed, imbalance magnitude, etc.).

10.2.1 Categories of Nonlinear Responses

The qualitative nature of the nonlinear rotordynamic response is categorized as either periodic, quasiperiodic, or chaotic. Each case leads to distinct vibration patterns:

Periodic Response: Nayfeh and Balachandran [193] define a periodic solution of least-period T as a solution for which if $\mathbf{x} = \mathbf{x}_0$ at $t = t_0$, then $\mathbf{x}(\mathbf{x}_0; t_0) = \mathbf{x}(\mathbf{x}_0; t_0+T)$. The number of the periodic response is determined by the number of unique Poincaré return points; e.g., a period-k response has k unique return points. The waveform repeats over time at the lowest period of the system, while the orbit commensurately traces an identically-repeated closed loop. In the frequency domain, a period-k response contains frequencies at p/k harmonics of the shaft speed, where p is an integer (p = 1, 2, 3, ...). For example, a period-3 response has harmonics 1/3, 2/3, 1, 4/3, 5/3, 2, etc., while a period-2 response has harmonics 1/2, 3/2, etc.

Quasiperiodic Response: Quasiperiodic solutions are recognized by (a) incommensurate frequency content (i.e., the ratio of peaks is irrational) and (b) closed loops in the Poincaré section [193, 205, 206]. A convenient description of quasiperiodic motion is toroidal motion. The solution travels along the inside perimeter of the torus, and the Poincaré section records the rotor position as it passes a certain cross-section of the torus. In a period-k response, the solution passes only through k locations on the torus cross-section perimeter; for a quasiperiodic response, the solution traces out the interior perimeter.

Chaotic Response: Whereas periodic and quasiperiodic responses have defined peaks in the frequency domain and a clear structure in the Poincaré section, chaotic responses display broad-band frequency content and complicated and/or fractal Poincaré sections. Nayfeh and Balachandran [193] give a detailed discussion of chaos; here, chaotic and/or aperiodic responses are identified by broadband frequency content and complex Poincaré sections.

10.3 Fundamental Aspects of Rotor-Stator Rub

Rotor-stator rub is first studied using the Jeffcott rotor model and the LECM. From this simpler case, the general character and rich nonlinear response caused by rotor-stator rub can be isolated and investigated, and later extended to more complex systems (i.e., the FMSR-ER). Thus, the objective of this section is to describe and visualize nonlinear rotor responses and their associated bifurcation structure.

10.3.1 Solution Procedure

The equations of motion for the Jeffcott rotor are provided in Chapter 4, while the contact forces obtained via the LECM are given in Eqs. 7.6 and 7.7. As a reminder, the steady-state equations of motion are:

$$m\ddot{\epsilon}_{R\xi} + c\dot{\epsilon}_{R\xi} + k\epsilon_{R\xi} + k_c\frac{\epsilon_R - \delta}{\epsilon_R}(\epsilon_{R\xi} - \mu_f\epsilon_{R\eta})\mathcal{H}(\epsilon_R - \delta) = m\varepsilon_{RG}\omega_r^2\cos(\omega_r t) \quad (10.1)$$

$$m\ddot{\epsilon}_{R\eta} + c\dot{\epsilon}_{R\eta} + k\epsilon_{R\eta} + k_c\frac{\epsilon_R - \delta}{\epsilon_R}(\epsilon_{R\eta} + \mu_f\epsilon_{R\xi})\mathcal{H}(\epsilon_R - \delta) = m\varepsilon_{RG}\omega_r^2\sin(\omega_r t) - mg \quad (10.2)$$

where the subscript 'R' on the rotor parameters is omitted for brevity by recognizing that the support considered here is symmetric ($k_{\xi\xi} = k_{\eta\eta} = k$). The equations of motion describe a nonlinear non-autonomous system of second-order differential equations where the dominant frequency is the shaft speed ω_r. This piecewise-smooth hybrid dynamical system [152, 207, 208] alternates between the linear non-contacting state and the nonlinear contacting state, where the switching behavior is a strong nonlinearity that precludes closed-form analytic solutions.

Time is normalized by the shaft speed (such that $\tau = \omega_r t$) to reduce computation time and allow direct comparison between responses at different shaft speeds. This process commensurately normalizes the frequency domain such that the synchronous component always occurs at unity. Defining derivatives with respect to τ by $(\bullet)'$ and

Table 10.1: Rotor parameters used to study the Jeffcott rotor - LECM system.

Parameter	**Value**
Rotor mass, m	2 kg
Rotor stiffness, k	$1.0(10)^6$ N/m
Damping Coefficient, c	280 N·s/m
Imbalance, ε_{RG}	40 μm
Clearance, δ	50 μm
Friction Coefficient, μ_f	0.1
Contact Stiffness, k_c	500 k

dividing by $m\omega_r^2$ yields the following mass-normalized form of Eqs. (10.1) and (10.2):

$$\epsilon_{R\xi}'' + \frac{2\zeta\omega_n}{\omega_r}\epsilon_{R\xi}' + \frac{\omega_n^2}{\omega_r^2}\epsilon_{R\xi} + \frac{\omega_c^2}{\omega_r^2}\frac{\epsilon_R - \delta}{\epsilon_R}(\epsilon_{R\xi} - \mu_f\epsilon_{R\eta})\mathcal{H}(\epsilon_R - \delta) = \varepsilon_{RG}\cos\tau \tag{10.3}$$

$$\epsilon_{R\eta}'' + \frac{2\zeta\omega_n}{\omega_r}\epsilon_{R\eta}' + \frac{\omega_n^2}{\omega_r^2}\epsilon_{R\eta} + \frac{\omega_c^2}{\omega_r^2}\frac{\epsilon_R - \delta}{\epsilon_R}(\epsilon_{R\eta} + \mu_f\epsilon_{R\xi})\mathcal{H}(\epsilon_R - \delta) = \varepsilon_{RG}\sin\tau - \frac{g}{\omega_r^2} \tag{10.4}$$

where $\omega_n^2 = k/m$ and $\omega_c^2 = k_c/m$. The damping terms are normalized such that $c/m = 2\zeta\omega_n$, where ζ is the damping ratio.

The equations of motion are integrated numerically using MATLAB®'s hybrid 4th/5th order variable-step Runge-Kutta solver, ode45. To extract only the steady-state response, the solution is carried out to 750 periods of the non-dimensional forcing frequency (i.e., 1500π non-dimensional units of time). The time ranges of the waveforms presented in the following sections all reside in the steady-state regime. The relative tolerance was set to 10^{-9} while the absolute tolerance was set to 10^{-12}. These values were selected by progressively increasing the tolerance until convergence was obtained in the steady-state solution (e.g., increasing the tolerance resulted in the same solution). The rotor static deflection caused by gravity is used as the initial condition with zero initial velocity; the system is then set into motion via the non-autonomous terms in Eqs. 10.3 and 10.4.

10.3.2 Nonlinear Responses

A variety of periodic responses are observed in the rotor response to intermittent lateral contact for the parameters given in Table 10.1. An example period-3 response is shown in Fig. 10.1, including the waveform, frequency spectrum, orbit, and Poincaré section. The dashed line in the waveform (Fig. 10.1a) represents the threshold deflection above which contact occurs (i.e., $\epsilon_R/\delta = 1$); this clearance is indicated in the rotor orbit as circle with a radius of unity. The Poincaré section is duplicated in the orbit plot for clarity. The waveform indicates a dynamic response where the rotor rebounds from the stator in such a manner that the trajectory repeats every three rotor revolutions; the distinct trajectories per every third revolution are clearly seen in the orbit plot provided in Fig. 10.1c. As expected, the period-3 response induces $p/3$ shaft speed harmonics ($p = 1, 2, 3, ...,$ etc.). Likewise, the Poincaré section displays three unique return points. Additional periodic responses (period-1, period-3, and period-6) are provided in Figs. 10.2 and 10.3, which show the the rotor orbits and frequency spectra, respectively. In each case, the number of Poincaré return points indicates the order of the periodic response, where each periodic response is defined in the frequency domain by fractional shaft speed harmonics.

An example chaotic response is displayed in Fig. 10.4, where the defining features of chaotic rotor-stator impact are observed in the response (broadband frequency content and scattering of the Poincaré return points). The example chaotic waveform is modulated only by integer shaft speed harmonics. Other chaotic responses often include frequency modulation from fractional shaft speed harmonics; several frequency-modulated chaotic responses are shown in Figs. 10.5 and 10.6 in the time and frequency domains, respectively. In general, the frequency modulation can be heuristically correlated to the structure contained in the Poincaré section. In Fig. 10.6c, frequency modulation is seen at normalized frequencies of $p/3$ (where $p = 1, 2, 3, ...$). Correspondingly, the Poincaré section contains three unique components

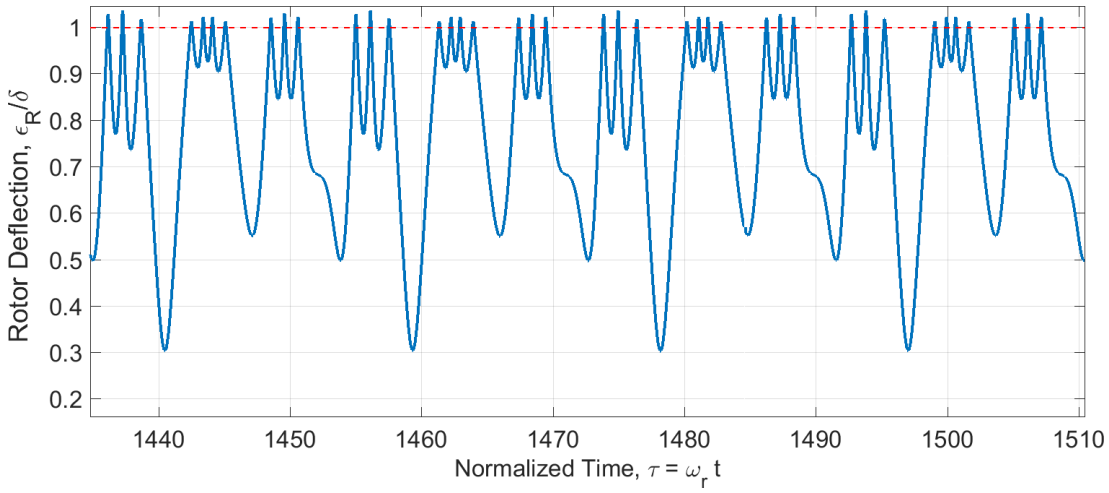

(a) Steady-state waveform

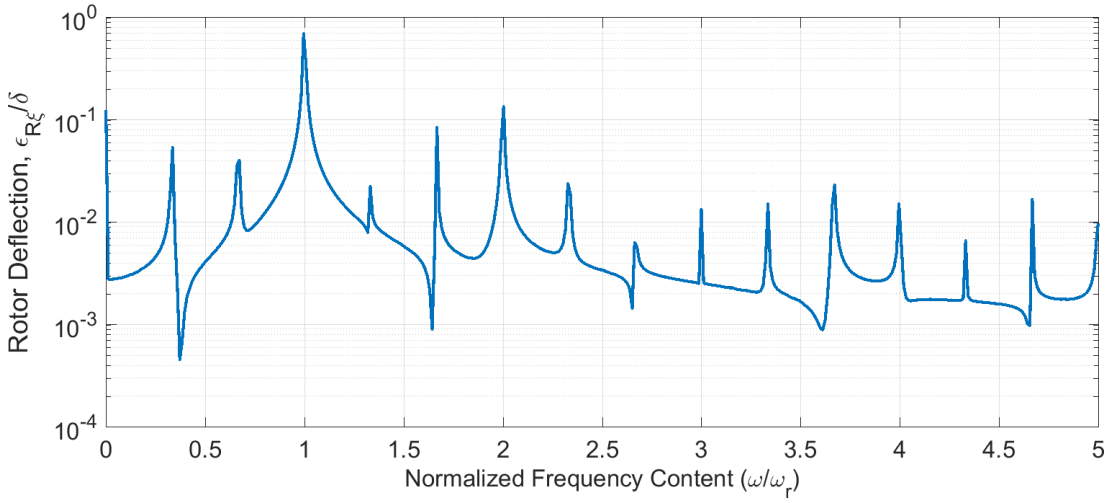

(b) Frequency spectrum

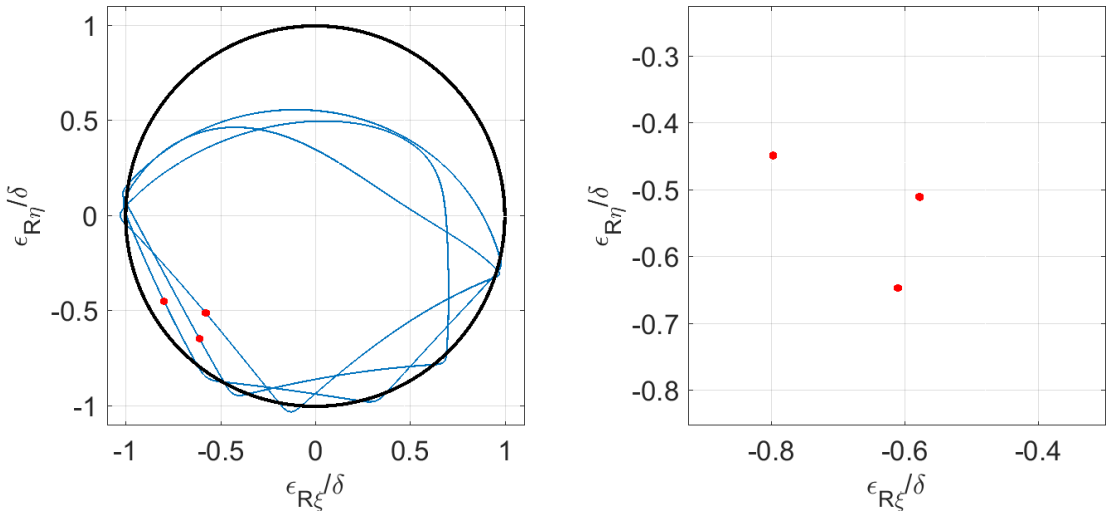

(c) Orbit

(d) Poincaré section

Figure 10.1: Example periodic response showing a period-3 motion ($\omega_r/\omega_n = 0.915$).

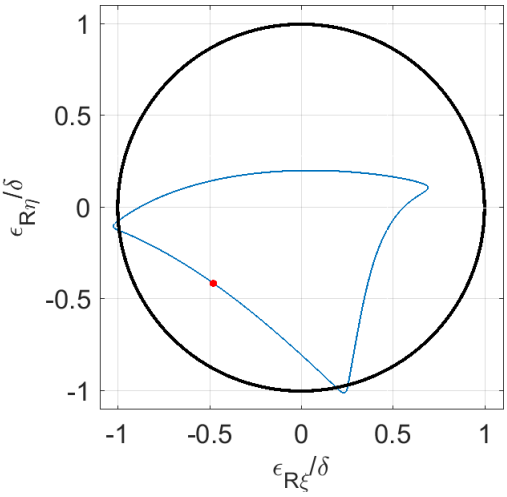

(a) Period-1 Orbit: $\omega_r/\omega_n = 0.85$

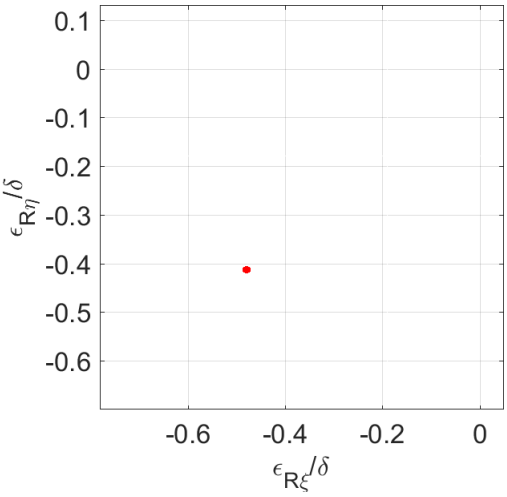

(b) Poincaré section

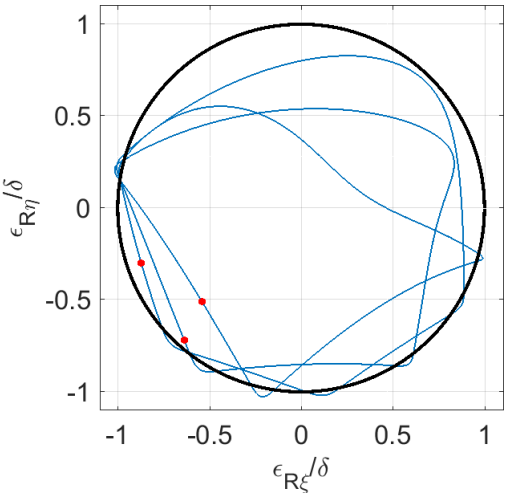

(c) Period-3 Orbit: $\omega_r/\omega_n = 0.99$

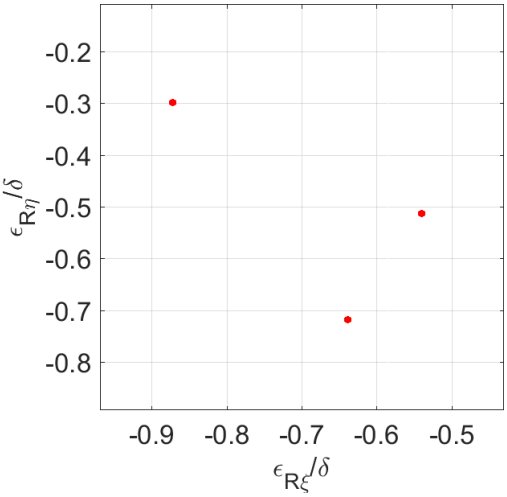

(d) Poincaré section

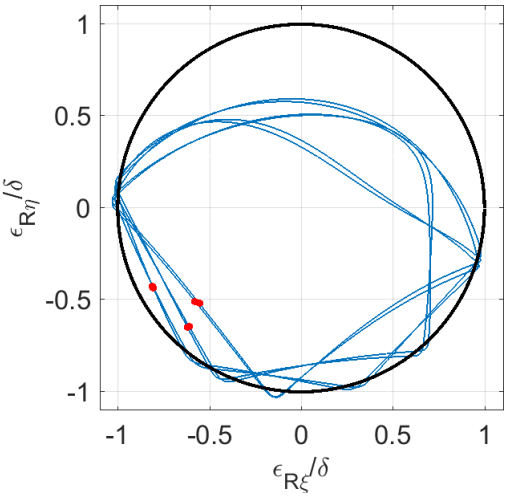

(e) Period-6 Orbit: $\omega_r/\omega_n = 0.923$

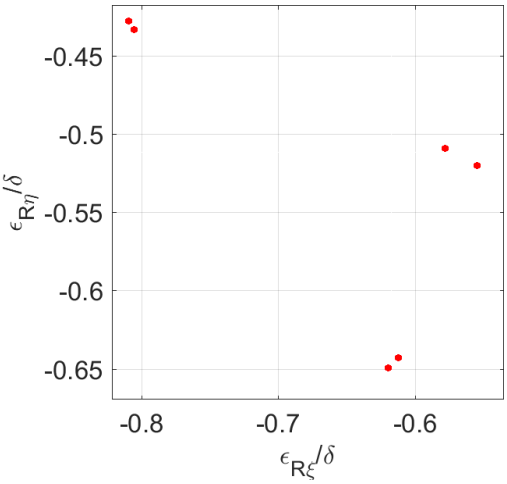

(f) Poincaré section

Figure 10.2: Periodic Responses: Orbits and Poincaré sections.

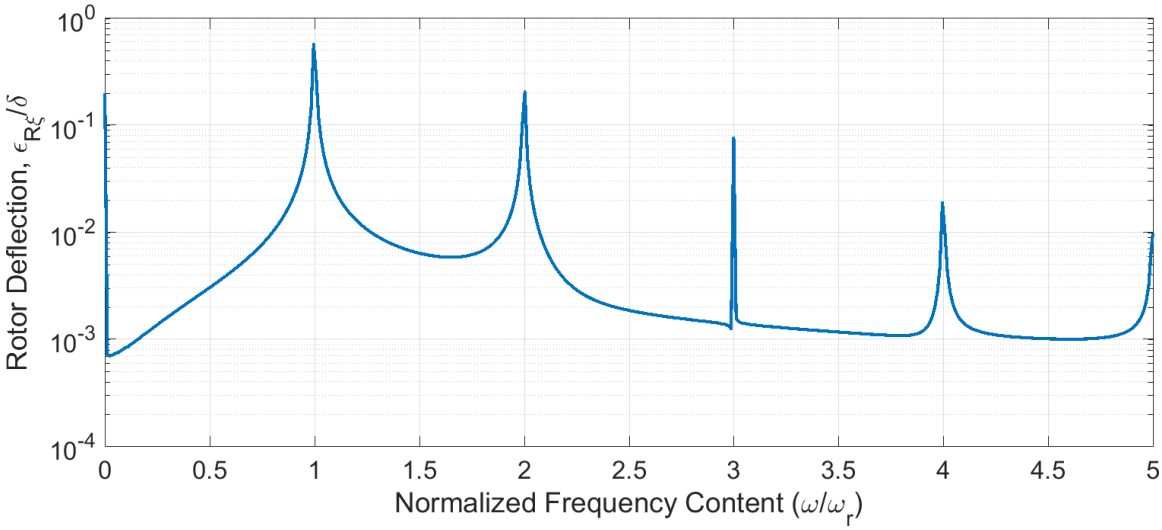

(a) Period-1: $\omega_r/\omega_n = 0.85$

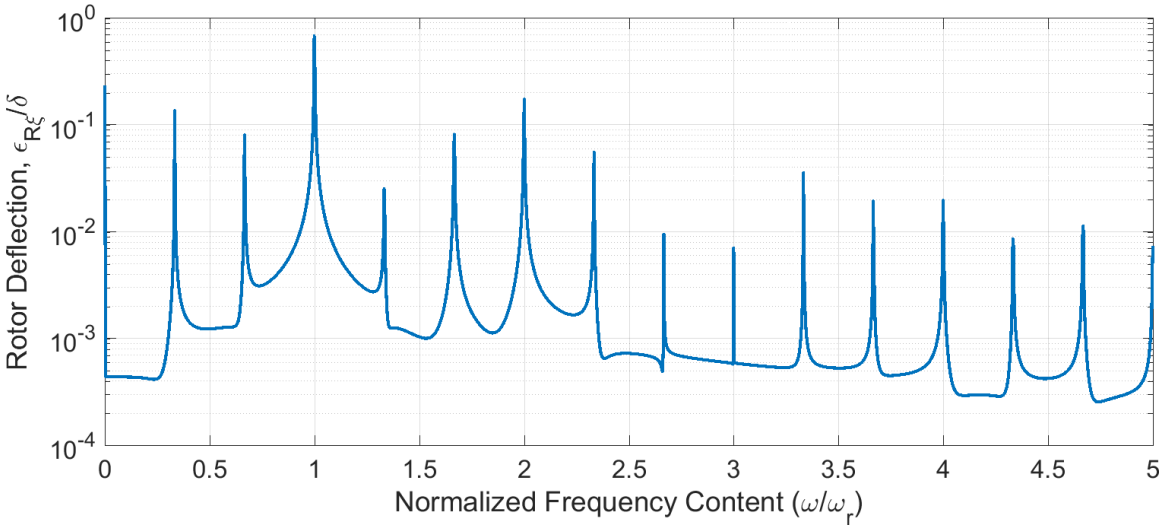

(b) Period-3: $\omega_r/\omega_n = 0.99$

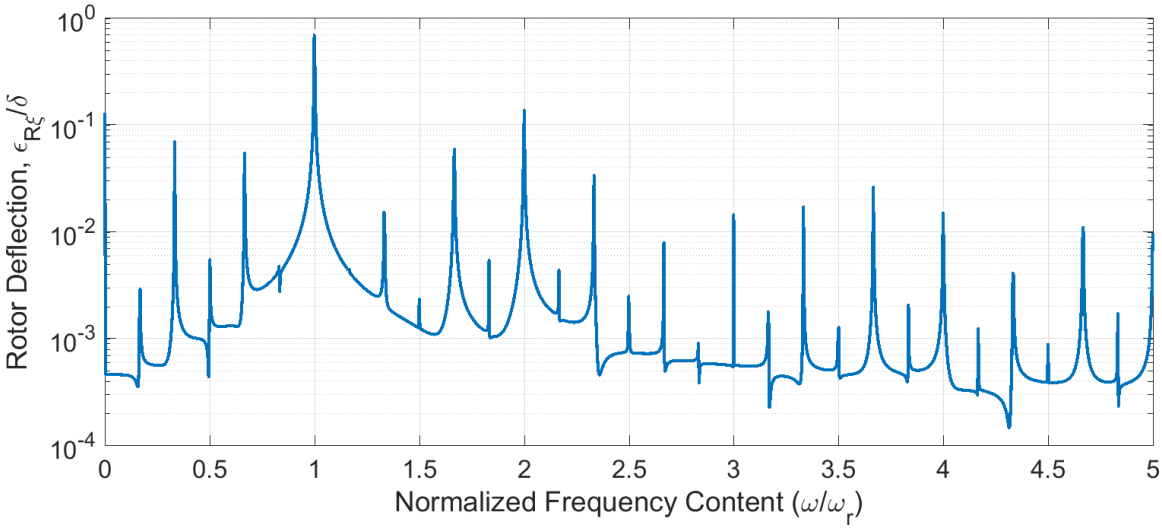

(c) Period-6: $\omega_r/\omega_n = 0.923$

Figure 10.3: Periodic Responses: Frequency domain indicating integer and fractional shaft speed harmonics.

signifying the presence of a period-3 unstable ghost attractor.

Quasiperiodic responses can also be caused by rotor-stator contact; an example quasiperiodic response is provided in Fig. 10.7. The response is generated using the parameters given in Table 10.1 (with the exception of $\varepsilon_{RG} = 60$ μm). The quasiperiodic motion is identified by (a) incommensurate frequencies, and (b) a closed loop of Poincaré return points. Similar quasiperiodic responses could be found for other parameters, but are not provided here for brevity. A lengthier discussion of quasiperiodicity, including additional examples, is provided by Varney and Green [209].

10.3.3 Bifurcations and Routes to Chaos

Bifurcations in the rotor response are studied using shaft speed as a control parameter. The bifurcation diagrams are shown in Fig. 10.8 for the parameters given in Table 10.1. Large regions of periodic response are visible, and particularly so below a shaft speed ratio of 0.75. From the figure, it is clear that even small changes in shaft speed cause qualitatively different rotor responses, indicating the richness evident in the system dynamics. A prominent sequence of period-doubling bifurcations leads to chaos near a shaft speed ratio of 0.9; this region is shown in greater detail in Fig. 10.9a. Another possible route to chaos is a sudden transition from periodic motion to chaotic behavior (i.e., a grazing bifurcation). This type of bifurcation is seen here in Fig. 10.9b (where the response is calculated with $\varepsilon_{RG} = 60$ μm). These grazing motions occur when a portion of the rotor orbit reaches and then exceeds the allowable clearance; the new point of contact causes a qualitative change in the dynamic response. Finally, a quasiperiodic route to chaos is also observed, and shown in Fig. 10.9c (once again, with $\varepsilon_{RG} = 60$ μm). The response begins as periodic and gradually transitions into chaos via quasiperiodic motion.

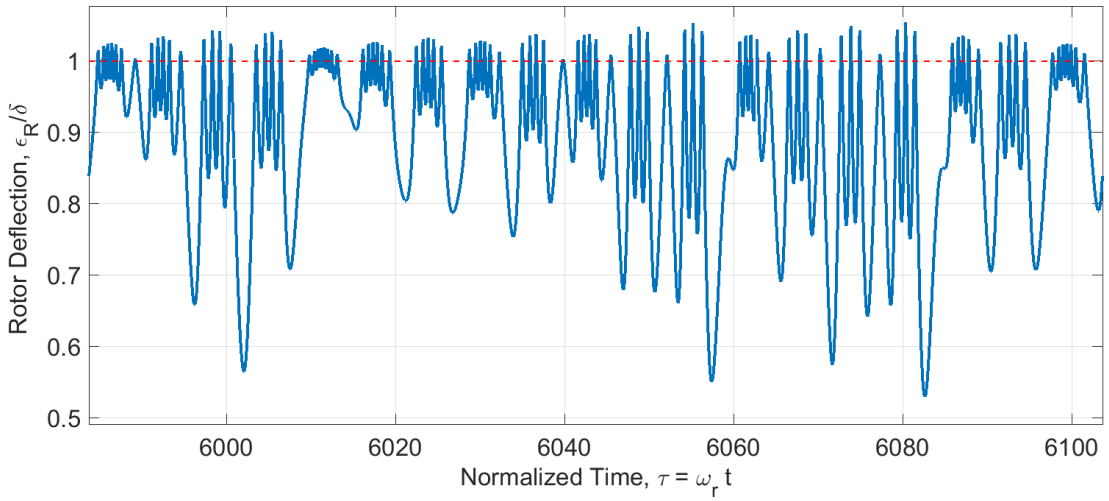

(a) Steady-state waveform

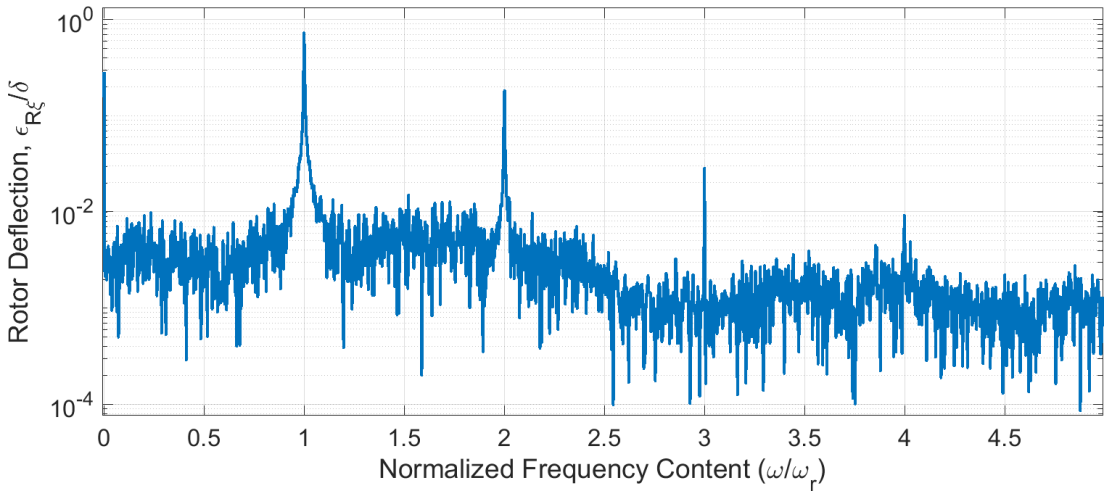

(b) Frequency spectrum

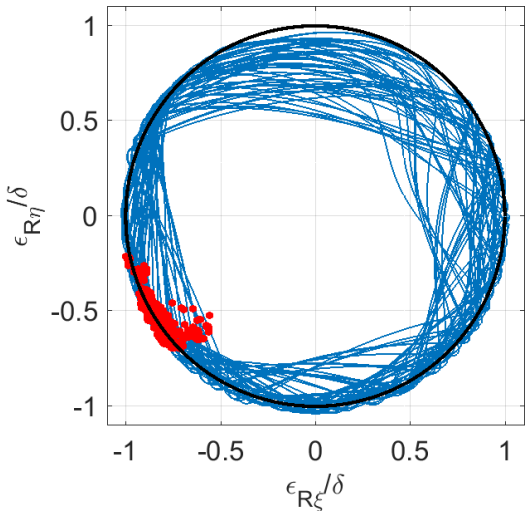

(c) Orbit

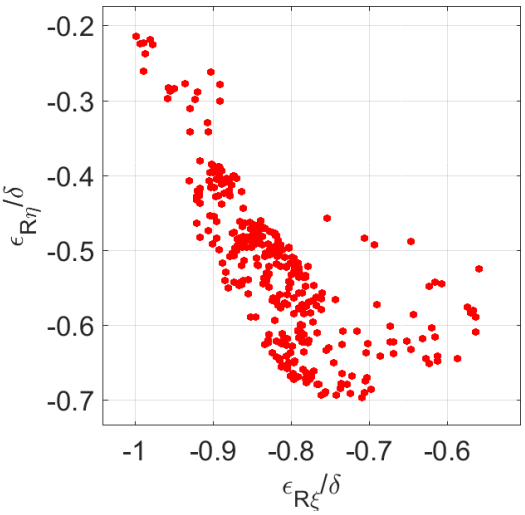

(d) Poincaré section

Figure 10.4: Example chaotic response ($\omega_r/\omega_n = 1.1$).

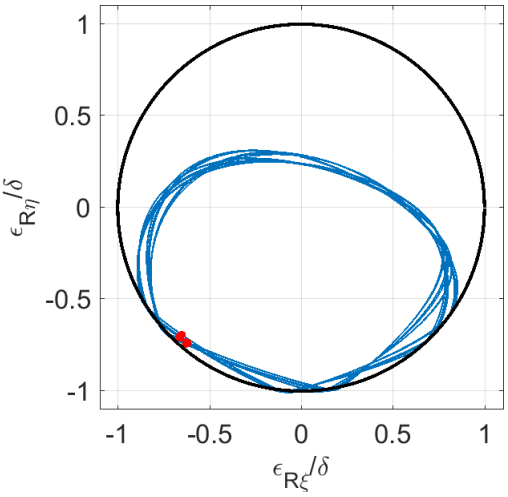

(a) Orbit: $\omega_r/\omega_n = 0.75$

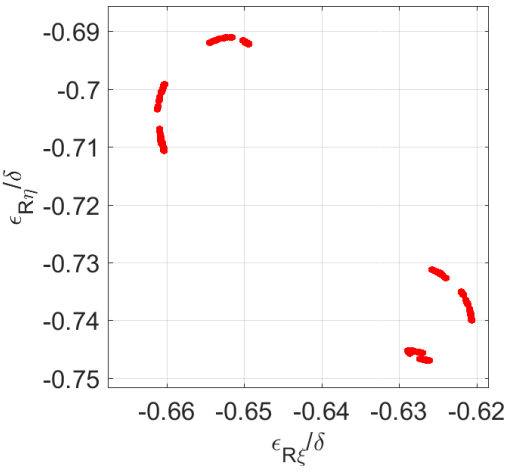

(b) Poincaré section

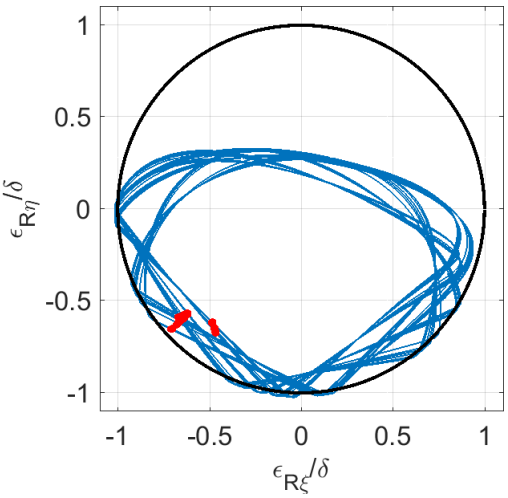

(c) Orbit: $\omega_r/\omega_n = 0.7942$

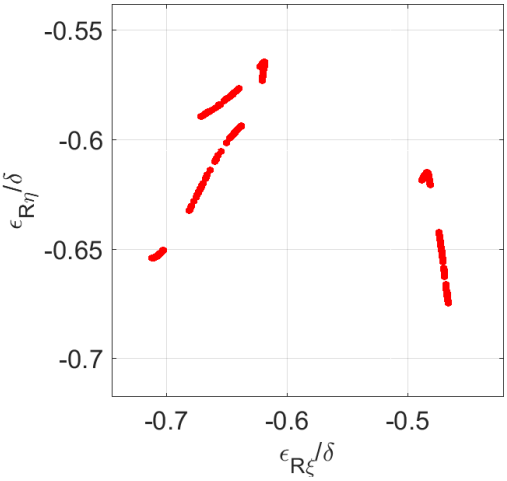

(d) Poincaré section

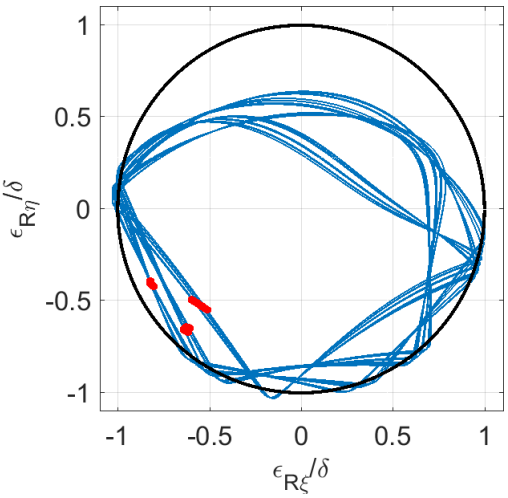

(e) Orbit: $\omega_r/\omega_n = 0.9346$

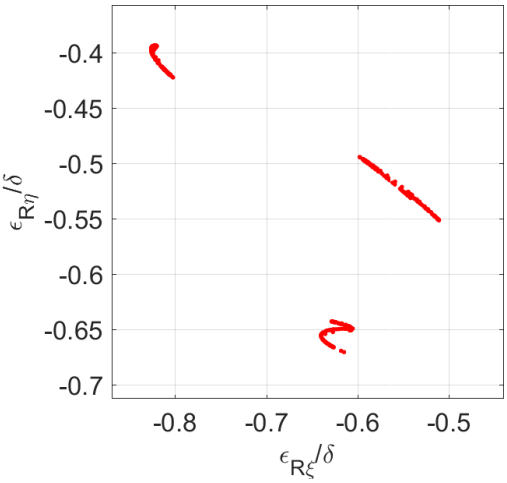

(f) Poincaré section

Figure 10.5: Chaotic Responses: Orbits and Poincaré sections.

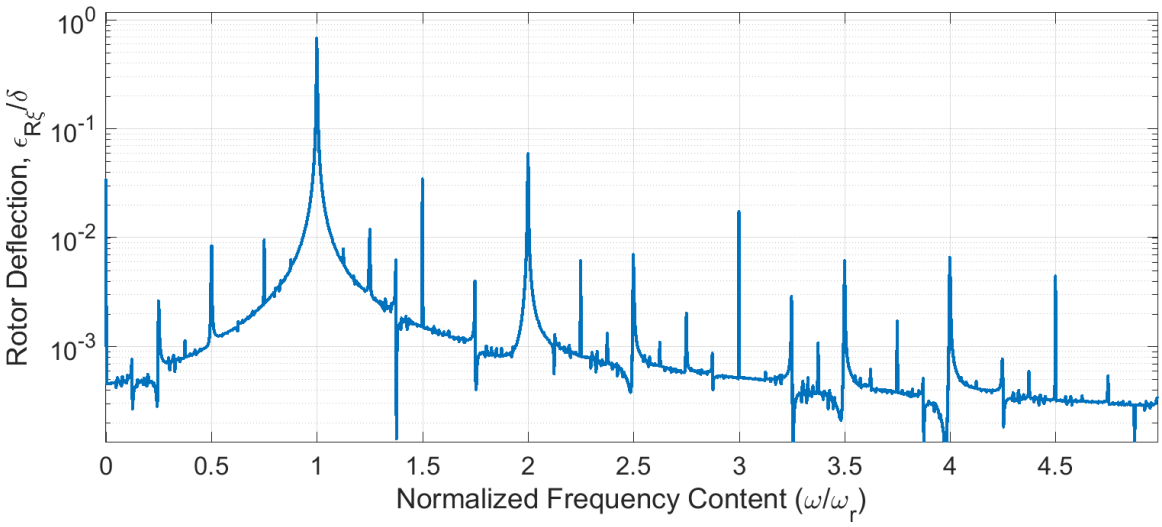

(a) $\omega_r/\omega_n = 0.75$

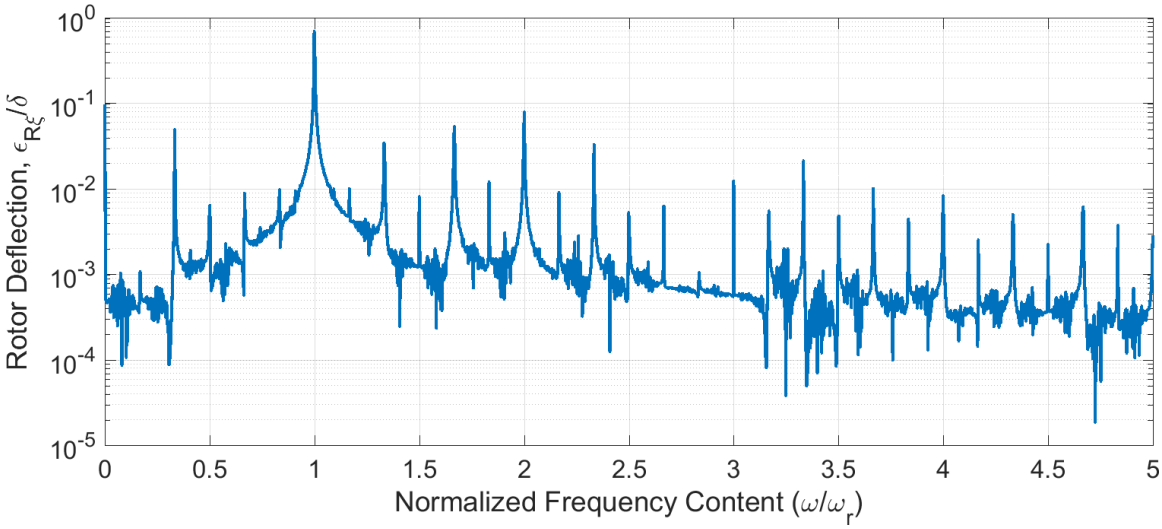

(b) $\omega_r/\omega_n = 0.7942$

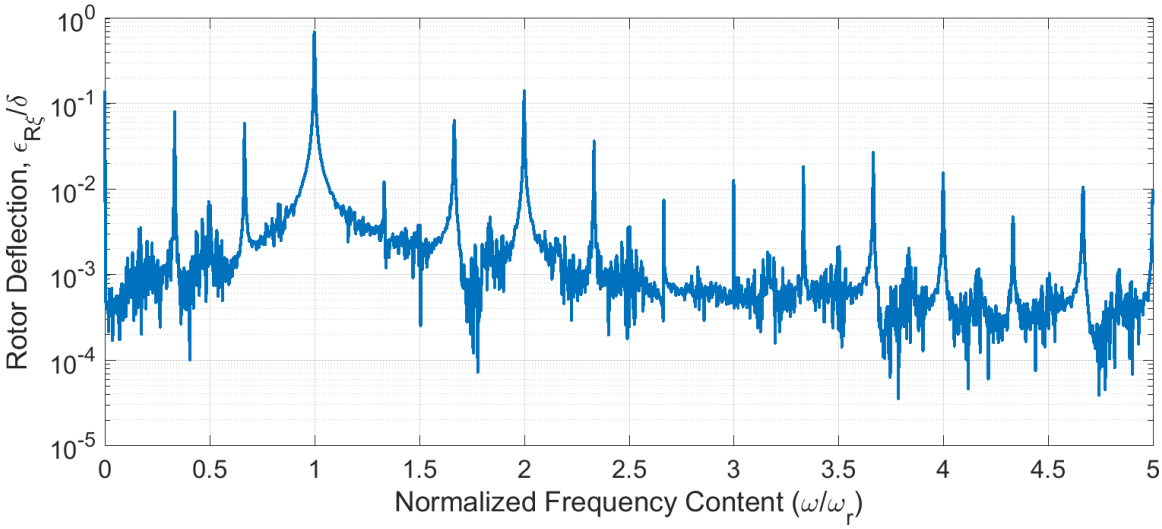

(c) $\omega_r/\omega_n = 0.9346$

Figure 10.6: Chaotic Responses: Frequency domain showing broadband character.

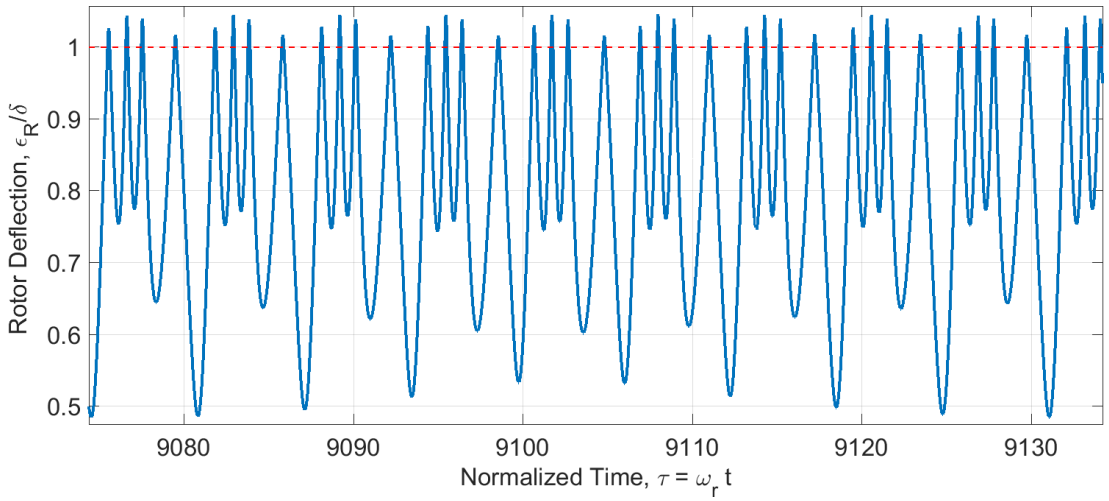

(a) Steady-state waveform

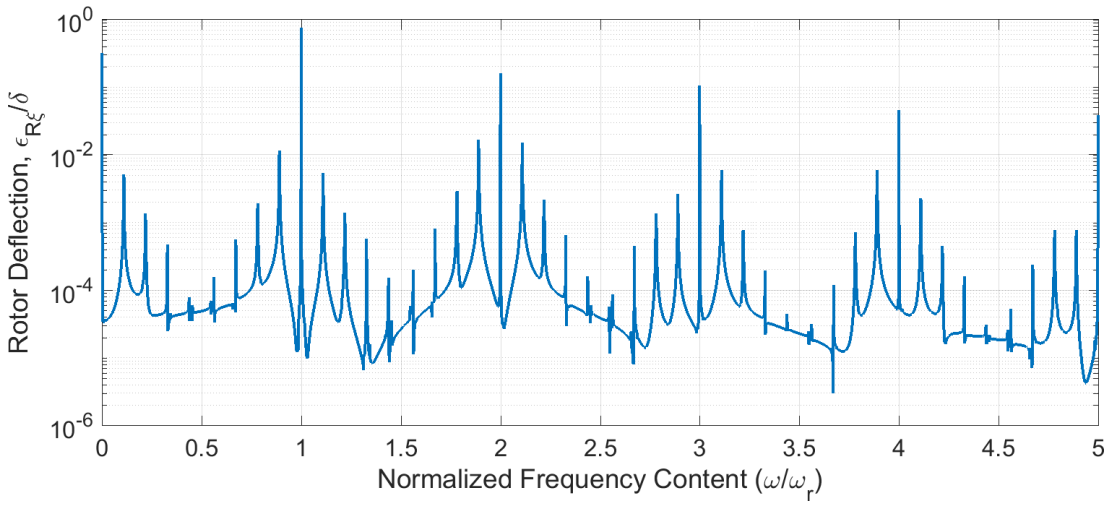

(b) Frequency spectrum

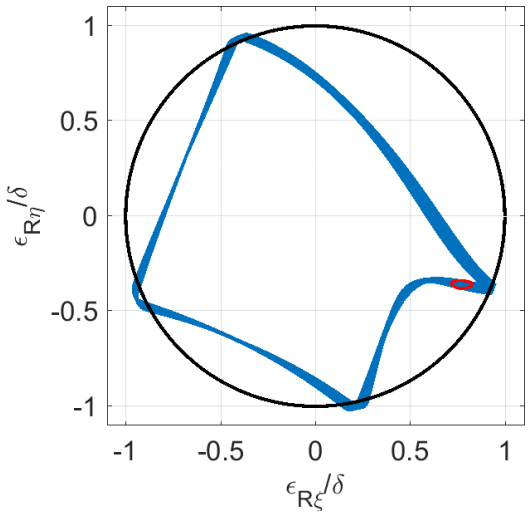

(c) Orbit

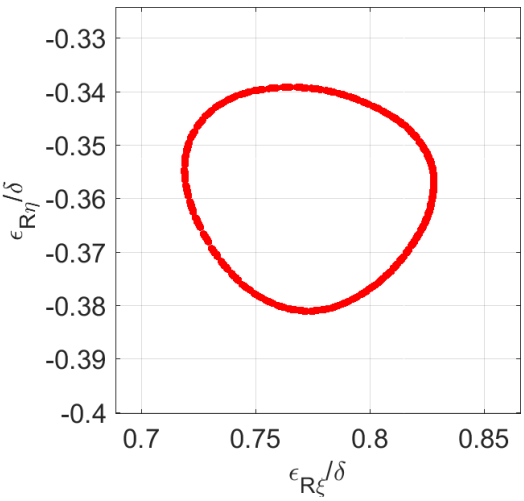

(d) Poincaré section

Figure 10.7: Example quasiperiodic response ($\omega_r/\omega_n = 0.8884$, $\varepsilon_{RG} = 60$ μm).

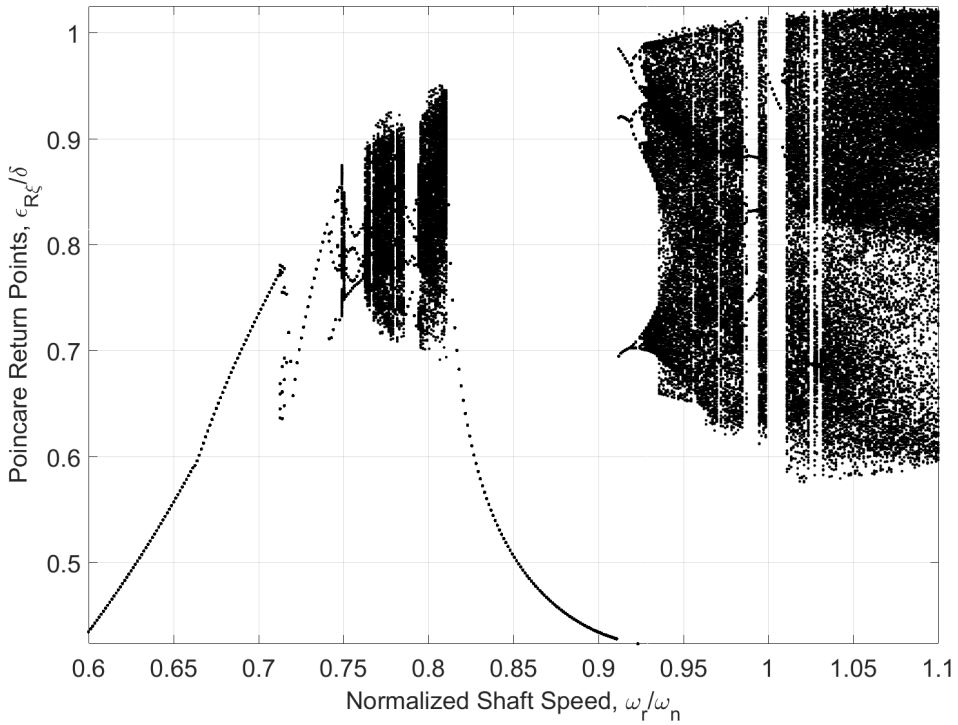

(a) $\varepsilon_{RG} = 40$ μm

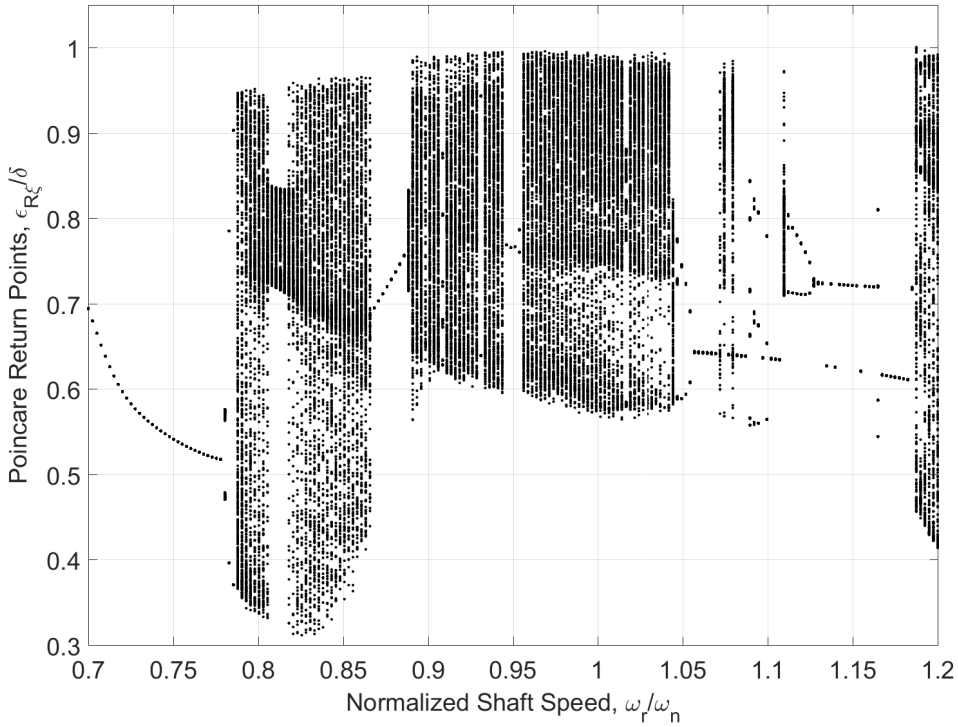

(b) $\varepsilon_{RG} = 60$ μm

Figure 10.8: Bifurcation using shaft speed as control parameter.

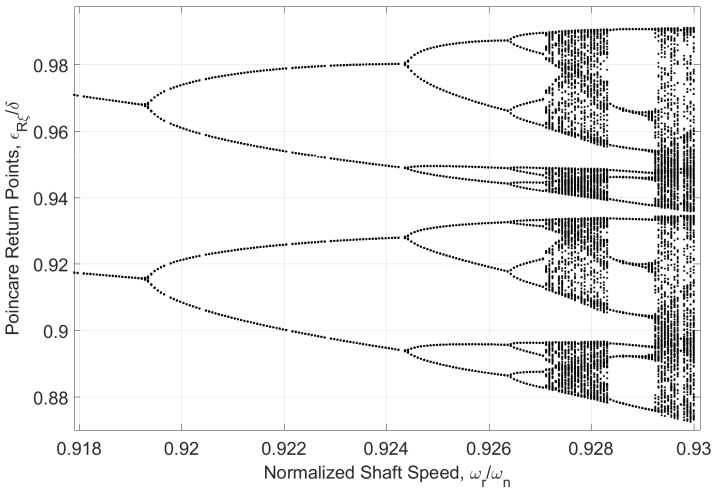

(a) Period doubling as a route to chaos ($\varepsilon_{RG} = 40$ μm)

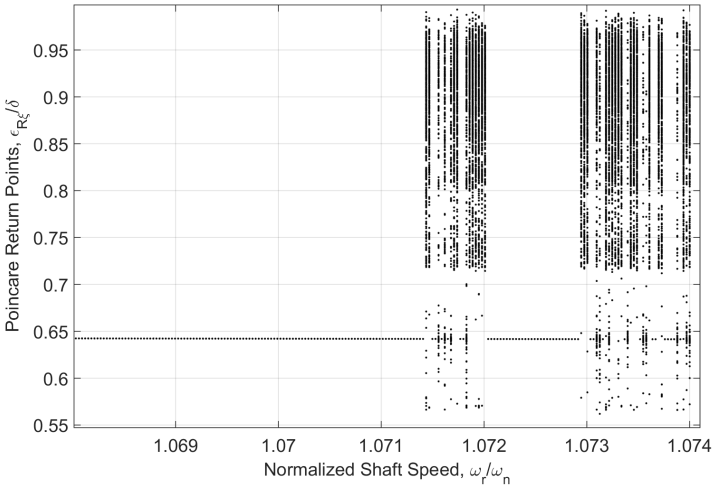

(b) Grazing bifurcation as a route to chaos ($\varepsilon_{RG} = 60$ μm)

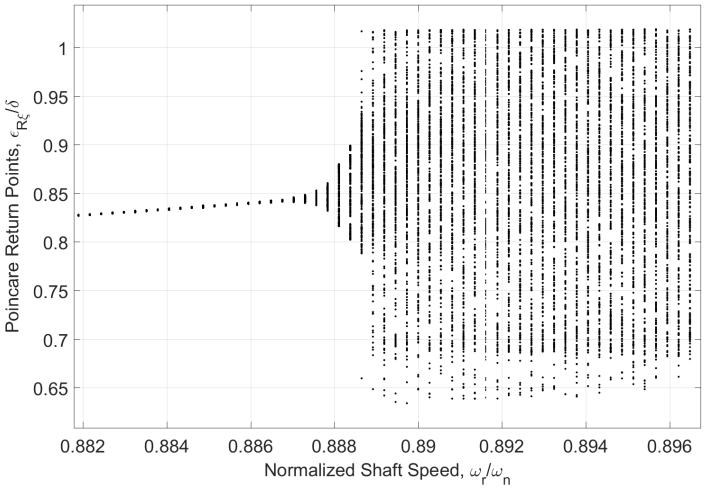

(c) Quasiperiodic route to chaos ($\varepsilon_{RG} = 60$ μm)

Figure 10.9: Routes to chaos using shaft speed ω_r as a control parameter.

Table 10.2: Rotor parameters used to compare the LECM and RSCM.

Parameter	**Value**
Rotor Mass, m	1 kg
Damping Coefficient, c	250 N·s/m
Stiffness, k	$1(10)^5$ N/m
Imbalance, ϵ_{RG}	$0.8(10)^{-4}$ m
Clearance, δ	$1.6(10)^{-4}$ m
Friction Coefficient, μ_f	0.15
Rotor Radius, R_r	0.1 m
Rotor Length, B_r	0.1 m

Table 10.3: Surface parameters.

Parameter	**Value**
Equivalent Modulus, E	25 GPa
Surface Height Stand. Dev., σ	1 μm
Asperity Density, N	$5(10)^{11}$ asp/m^2
Asperity Radius, R	2 μm
Yield Strength, S_y	0.1 GPa

10.4 Comparing the LECM and RSCM

The objective of this section is to delineate differences in the rotor response caused by the LECM and RSCM; this comparison is performed here using the Jeffcott rotor model with lateral contact. The equations of motion including the RSCM forces, Eqs. 7.19 and 7.20, are integrated numerically according to the procedure discussed in Section 10.3.1. The rotor and surface parameters used here are tabulated in Tables 10.2 and 10.3, respectively. The rough surface parameters are calculated from real surface measurements [42].

Rotor orbits comparing the LECM and RSCM are provided in Figs. 10.10 and 10.11. As shown in Fig. 10.11, an important observation is that the exponential pressure curve fit provides excellent agreement with the full numeric contact pressure calculation, as the resulting rotor orbits are nearly identical, even for a chaotic response comprising many rotor-stator impacts. Intuitively, similar responses are gleaned from the LECM and RSCM when the number of contacts per revolution is small, as shown in Fig. 10.10 for a period-2 orbit at $\omega_r = 1.45\omega_n$. The reduced radius of $\epsilon_R = \delta - 3\sigma$ is normalized by the clearance and shown with a dashed line to accentuate the importance of surface roughness dimension in the rotordynamics. As the number of contacts per revolution increases, the cumulative influence of different contact models generates qualitatively different responses. For example, consider the rotor response shown in Fig. 10.11 using each contact model at $\omega_r = 1.7\omega_n$; the LECM predicts a period-4 response, while the RSCM predicts chaotic motion.

Still, the qualitative differences between the models are best elucidated by observing displacements on the scale of the contact phenomena. A small portion of the full rotor orbits originally given in Fig. 10.11 are provided in Fig. 10.12, showing the rotor-stator impact on a much finer scale. In both figures, the set-point clearance δ is shown along with a chosen representation of surface roughness; i.e., a radial line at $\epsilon_R = \delta - 3\sigma$. The LECM rotor-stator contact force is immediately activated when

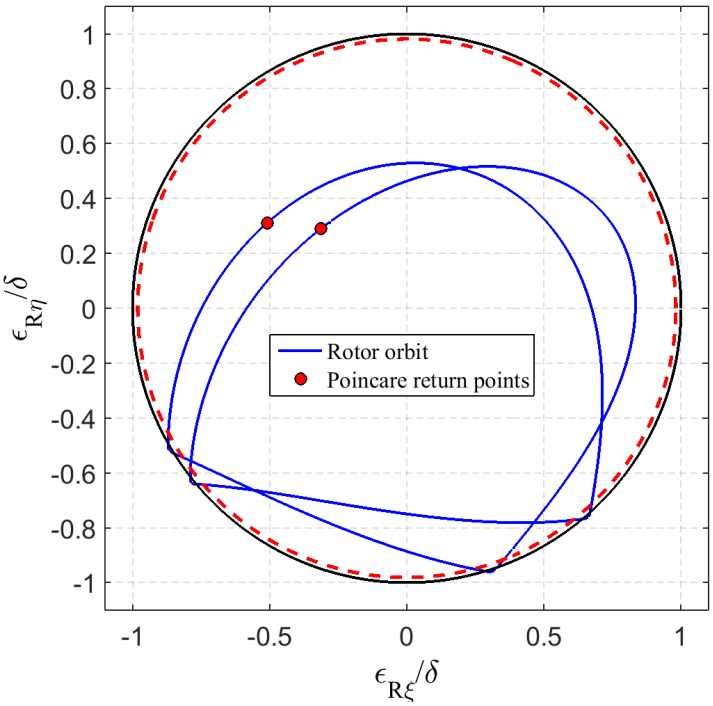

(a) LECM ($k_c = 5(10)^8$ N/m)

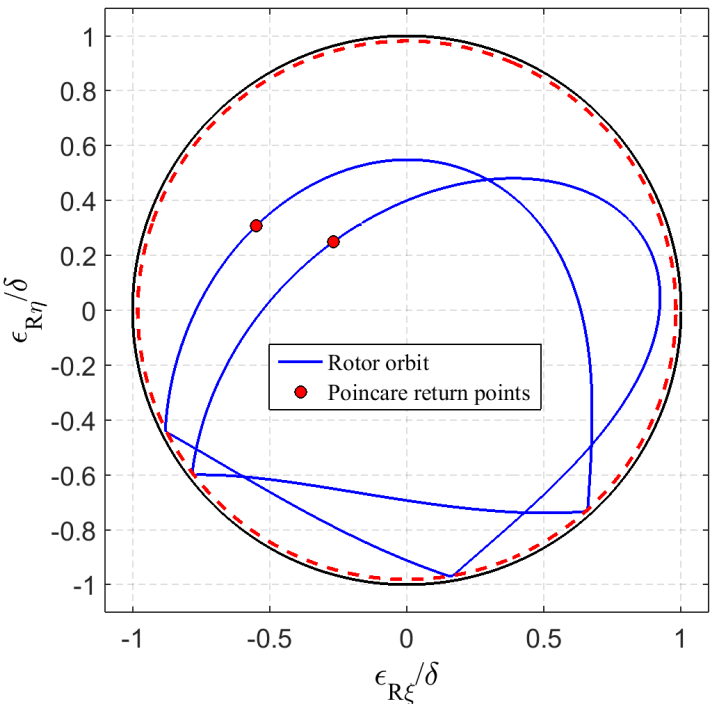

(b) RSCM

Figure 10.10: Comparing the rotor orbits using the LECM and RSCM at a shaft speed of $\omega_r = 1.45\omega_n$.

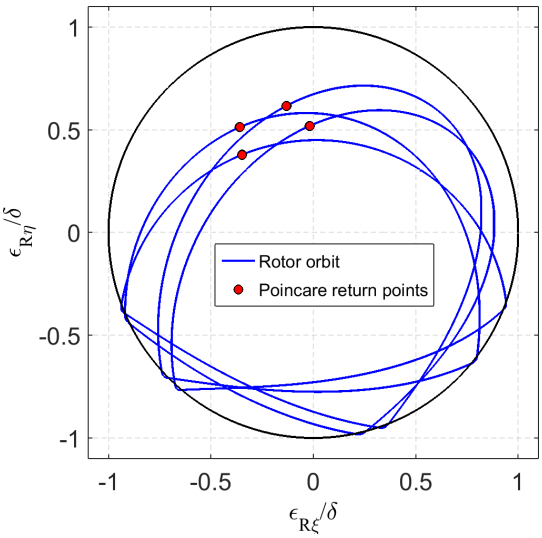

(a) LECM ($k_c = 5(10)^8$ N/m)

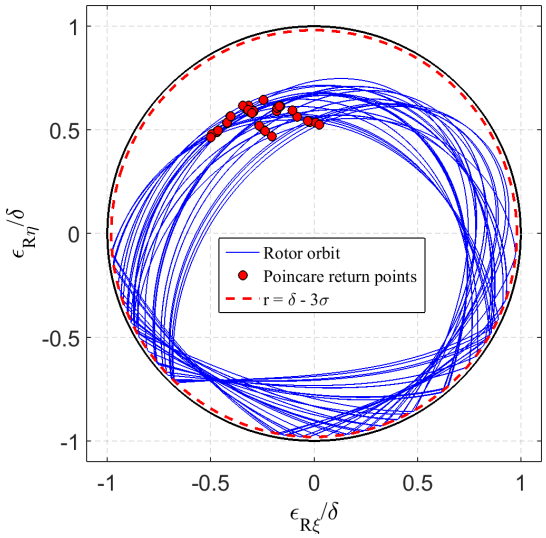

(b) RSCM: Full simulation

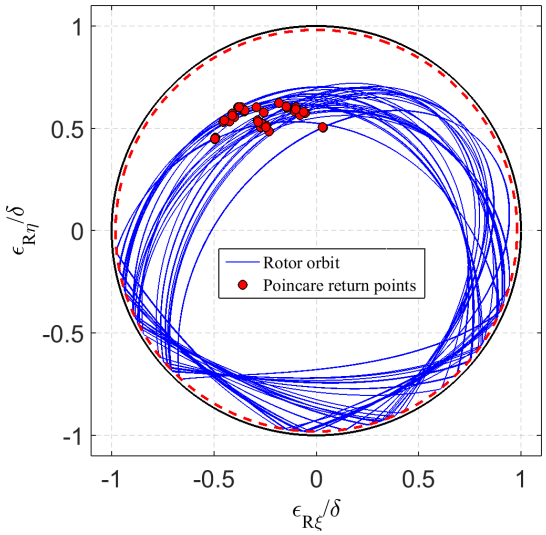

(c) RSCM: Contact pressure curve fit

Figure 10.11: Comparing the rotor orbits using the LECM and RSCM at $\omega_r = 1.7\omega_n$.

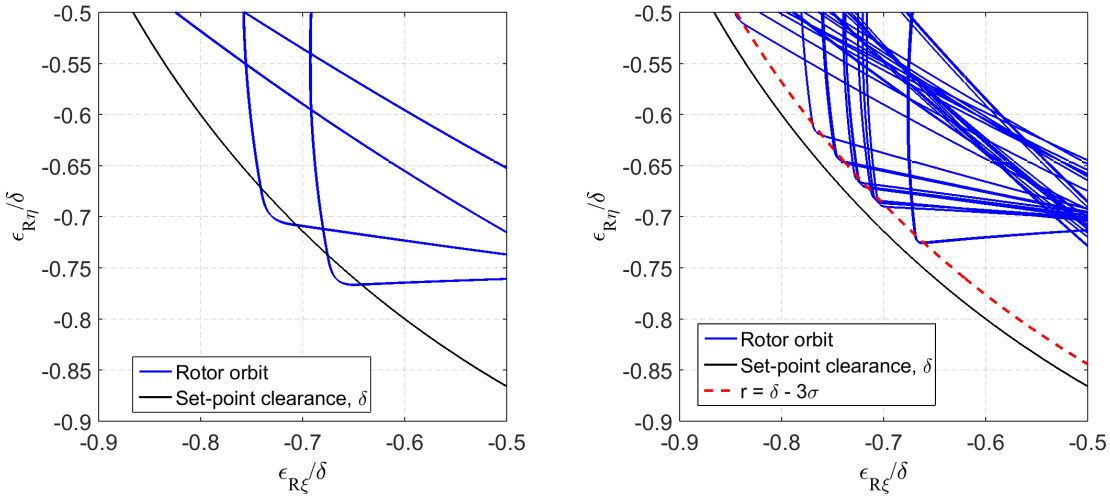

(a) LECM ($k_c = 5(10)^8$ N/m) (b) RSCM

Figure 10.12: Comparing the LECM and RSCM on the scale of impact ($\omega_r = 1.7\omega_n$).

the rotor deflection exceeds the set-point clearance, and henceforth the contact force depends only on the contact stiffness k_c and the rotor-stator interference $\epsilon_R - \delta$. The RSCM instead predicts a gradual increase in the contact force as the local rotor-stator clearance approaches the surface roughness dimension. In fact, Fig. 10.12b shows that the rotor rebounds from the stator when only a small percentage of the asperities interact. This effective reduced clearance is likely important for rotor-stator systems with clearances near the surface roughness dimension. Interestingly, these results show that rotor rebound occurs when the local clearance is on the order of 3σ, implying that asperity deformation is a principal mechanism for rotor-stator rub.

Shaft speed bifurcations are a useful tool for ascertaining broad differences in rotor-dynamic responses obtained from the LECM and RSCM. Representative shaft speed bifurcation diagrams are shown in Figs. 10.13a and 10.13b for the LECM and RSCM, respectively. Each model begins by predicting a period-1 response until approximately $\omega_r = 1.42\omega_n$, where a period-doubling bifurcation results in a transition to period-2 motion. Beyond this point, the models begin to predict different responses. For the

Table 10.4: Surface parameters used to study seal face contact.

Parameter	**Set 1**	**Set 2**
Plasticity index, Ψ	5	5
Equivalent Modulus, E	24 GPa	24 GPa
Surface Stand. Dev., σ	0.7 μm	0.9 μm
Asperity Density, N	$4.2(10)^{11}$ asp./m^2	$4.2(10)^{11}$ asp./m^2
Asperity Radius, R	1.7 μm	1.7 μm

parameters considered here, the RSCM indicates a greater proclivity for chaotic motion (note the expanded shaft speed ranges over which chaos is observed). Though the bifurcations indicate some generic similarities between the models, it is clear that the RSCM predicts different responses than the LECM. Thus, an appropriate (i.e., accurate) contact model must be carefully selected when studying rotor-stator rub.

10.5 Impact Phenomena in a FMS Seal

Seal face contact is important to study in this work because surrogate rotor fault detection is predicated on healthy seal operation. Seal face contact could adulterate the transmitted rotor fault signatures, thereby precluding accurate fault identification. Thus, the specific goal of this section is to (a) investigate the conditions precipitating seal face contact, and (b) identify vibration signatures induced by the undesired contact.

The particular scenario investigated here is face contact in a FMS seal designed to operate in the non-contacting regime. The FMS configuration is used because of its (relative) simplicity. Several cases are investigated here, including the non-contacting condition for comparison, light contact along the inner radius, heavy contact, and failure of a flat-faced seal via instability-induced severe contact. The FMS equations of motion are provided in Eqs. 5.29 - 5.31 and integrated numerically using MATLAB®'s implicit variable-step ordinary differential equation solver, ode15s. A stiff solver is

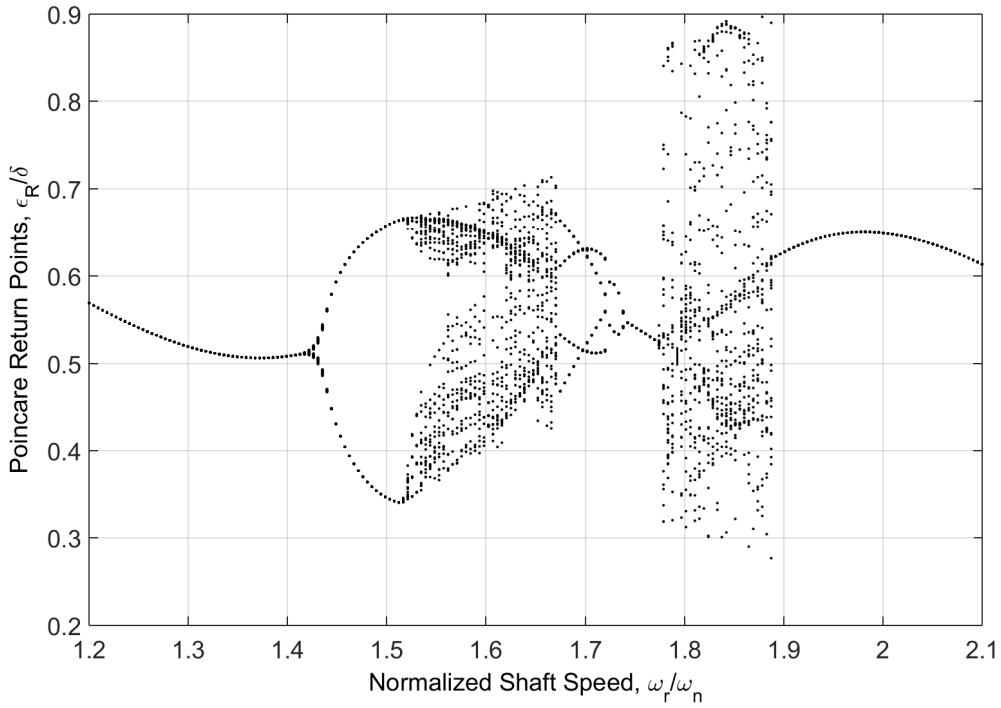

(a) LECM ($k_c = 5(10)^8$ N/m)

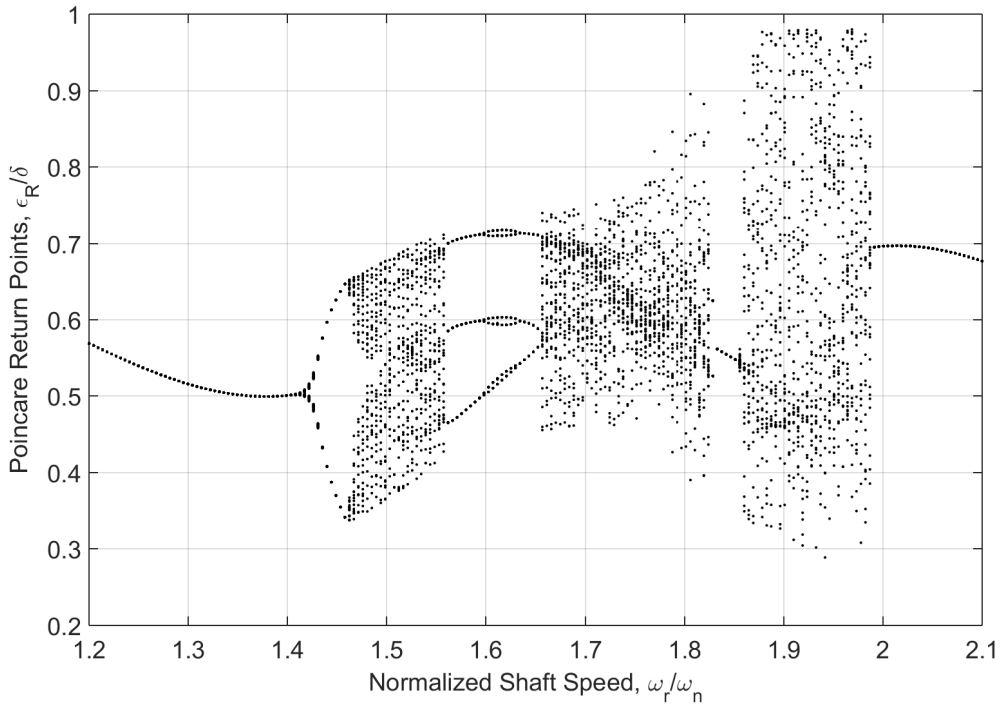

(b) RSCM

Figure 10.13: Shaft speed bifurcation study comparing the LECM and RSCM.

Table 10.5: Seal parameters used to study seal face contact.

Parameter	**Set 1**	**Set 2**
Seal mass, m_s	1.5 kg	1.5 kg
Axial Stiffness, K_{sz}	$1(10)^5$ N/m	$5(10)^5$ N/m
Axial Damping, D_{sz}	300 N $\cdot$ s/m	300 N·s/m
Radius of Gyration, r_g	0.04 m	0.04 m
Inner Radius, r_i	0.03 m	0.03 m
Outer Radius, r_o	0.04 m	0.04 m
Spring Force, F_{spr}	20 N	20 N
Inner Pressure, P_i	100 kPa	100 kPa
Outer Pressure, P_o	500 kPa	400 kPa
Face Coning, β	0.1 mrad	0.8 mrad
Clearance, C_o	5 μm	5 μm
Viscosity, μ	0.5 mPa·s	0.8 mPa·s

required because small variations in film thickness result in large changes in the system dynamics. The initial conditions are selected to be $\gamma_{s\xi}(t = 0) = \gamma_r$ while setting all other initial conditions to zero (the rotor operates with a constant angular misalignment γ_r). Once again, time is normalized by the shaft speed such that the non-dimensional time is given by $\tau = \omega_r t$. The seal and surface parameters used here are tabulated in Tables 10.4 and 10.5 unless otherwise noted. The rough surface model parameters are calculated from real surface measurements [200].

The numeric solution procedure is validated by comparing to previous results given by Green and Etsion [39] for a non-contacting FMS seal (the parameters used in the validation are provided therein). The validation results are shown in Fig. 10.14, where the normalized relative tilt is given versus rotor tilt γ_r for several representative shaft speeds (recall that the rotor tilt is assumed to be constant in a FMS seal). The calculated results follow the trends given by Green and Etsion [39], with some

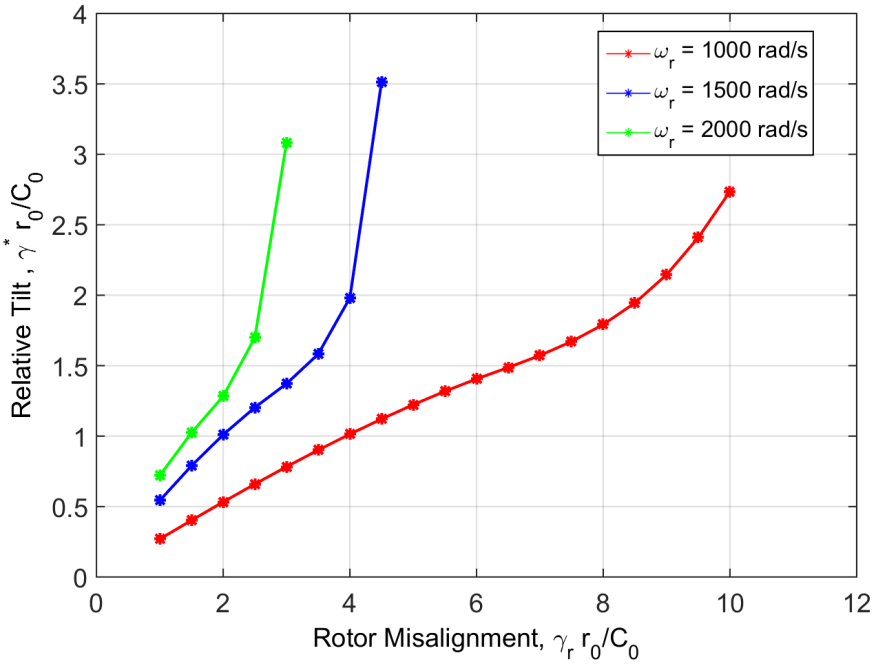

Figure 10.14: Validation results for a non-contacting FMS seal.

allowance made for parameters not provided in the original work (see Fig. 4(b) in reference [39] for comparison).

An example of light contact between the seal faces is shown in Figs. 10.15 and 10.16 using the minimum film thickness and pressure profiles. For comparison, the commensurate case without contact is displayed in Fig. 10.15 (it is merely coincidental that the lower envelope of the non-contacting scenario appears to intersect the 3σ boundary). The minimum film thickness waveforms are qualitatively similar even when face contact occurs, and only differ in amplitude and offset. This similarity is explained by the seal geometry and the primary function of a FMS seal. First, as shown in Fig. 10.16a, contact between the seal faces is geographically limited by the coning-induced face taper. Even though large contact pressures are generated, the small contact area results in small contact forces and moments when compared to those resulting from the fluid film (see Fig. 10.16b). A second explanation for the qualitative similarity in waveform shape is gleaned from the primary function

of a flexibly-mounted seal element. In a FMS seal, the lubrication couples the seal elements, and the support elasticity allows the flexibly-mounted element to track the misaligned element [23, 38, 210]; this tracking continuously minimizes the relative tilt between the seal faces. These two effects, localized contact regions and seal face misalignment tracking, serve to minimize the rich nonlinear responses often observed in other contacting rotor-stator systems. Furthermore, this implies that detecting seal face contact via conventional methods, such as acoustic emission or vibration monitoring, may be very difficult for light contact conditions. Thus, light contact can persist for some time in such a situation, and the locally-high contact pressures could cause significant surface wear prior to detection.

An example of heavy contact between the seal faces is shown in Fig. 10.17, where the minimum film thickness and frequency spectra are used to indicate contact. In this case, the response is characterized by rich nonlinear phenomena in the frequency domain, angular tilt orbit, and Poincaré section. The frequency domain contains many shaft speed harmonics, which, along with scattering in the Poincaré section, indicates aperiodic seal motion. The appearance of these symptoms during seal operation should immediately lead to shut-down to preclude catastrophic failure. Prolonged operation with these conditions would lead to significant seal face wear.

Severe contact between the seal faces has long been suggested as a primary mechanism for seal failure. Still, previous evidence for attributing seal failure to adverse face contact has been intuitive or experimental. For the first time, Fig. 10.18 provides analytic evidence that contact can cause failure in a flat-faced FMS seal. In this case, the lack of face coning generates an instability that eventually results in severe contact (which is exacerbated by the large contact area between the seal faces). This flat-face ($\beta = 0$) condition is reasonable considering that face coning is often generated via thermal deformation, which in turn is induced by viscous heat generation [42]. The thermal deformation time constant has been shown [42] to be several orders of

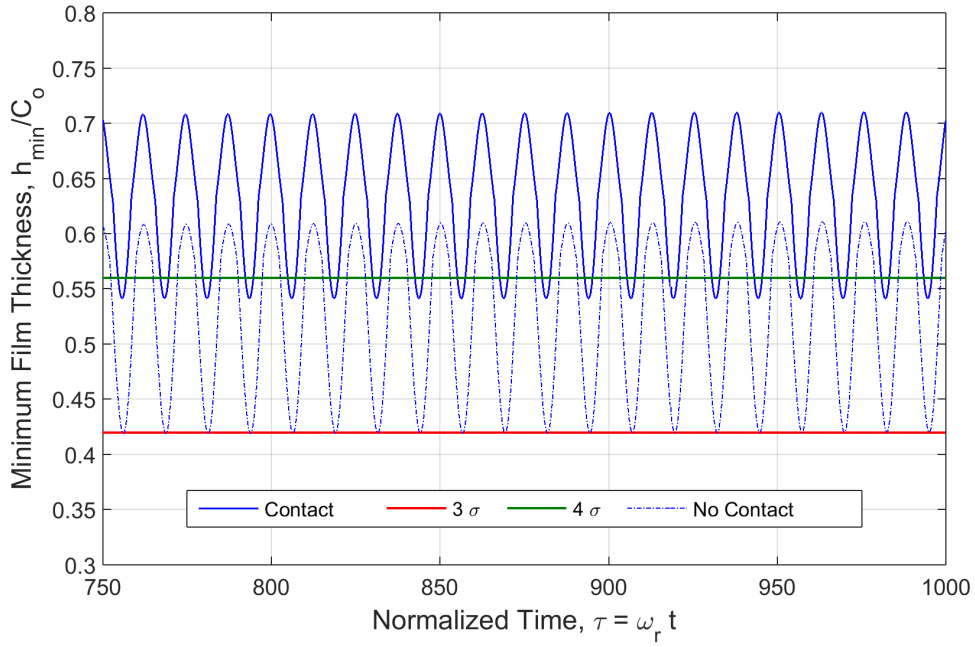

Figure 10.15: Comparison of coned-face FMS minimum film thickness with and without contact using the Jackson-Green rough surface contact model (Parameter Set 1: $\gamma_r = 2$ mrad, $\gamma_{si} = 5$ mrad, $\omega_r = 1000$ rad/s).

magnitude higher than the period of seal rotation during lift-off or shut-down. Thus, FMS seals often operate for many revolutions prior to the generation of significant face coning.

The minimum film thickness of the flat-faced seal during unstable operation is shown in Fig. 10.18a, where contact is generated primarily when the minimum film thickness is reduced beneath 4σ (the results are generated from parameter set 2 in Tables 10.4 and 10.5). Once the instability generates a sufficiently large dynamic response, the seal transitions into a violent impact-rebound cycle, where the minimum film thickness becomes temporarily much larger than the desired set-point clearance C_o. Failure can then be attributed to either excessive leakage or seal damage via large contact forces (as shown in Fig. 10.18c). The aperiodic behavior of the seal motion at the onset of failure is evident in the frequency spectra, Fig. 10.18b. Interestingly, no significant contact indicators were present in the seal motion prior to failure ($\tau < 850$).

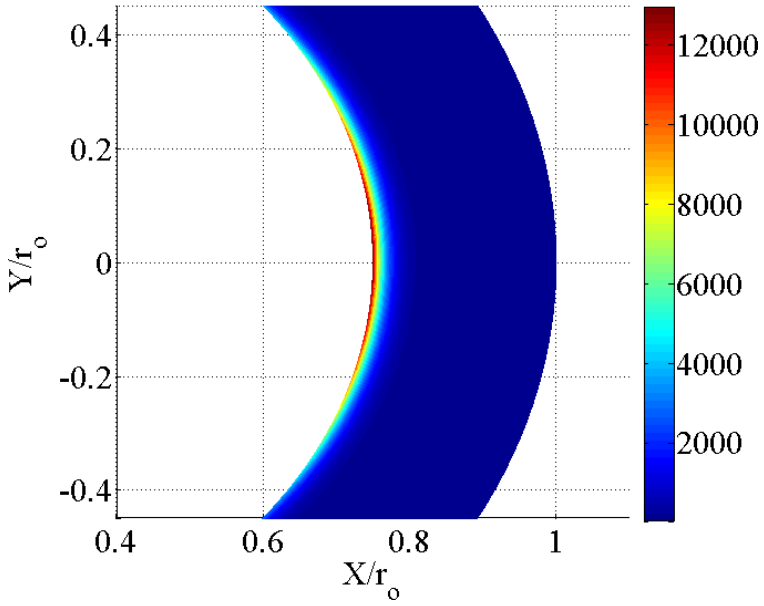

(a) Contact pressure (Pa)

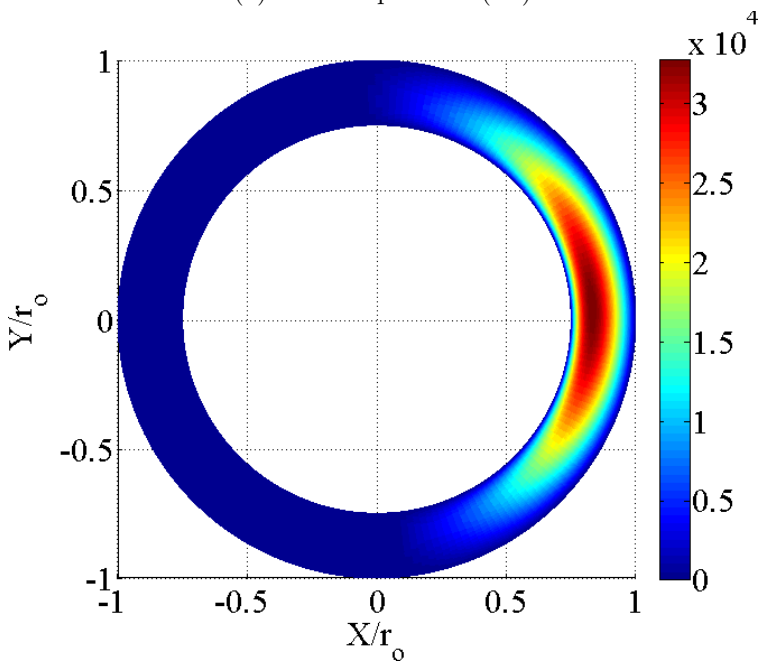

(b) Fluid film pressure (MPa)

Figure 10.16: Example contact and fluid pressure profiles ($\omega_r = 1000$ rad/s).

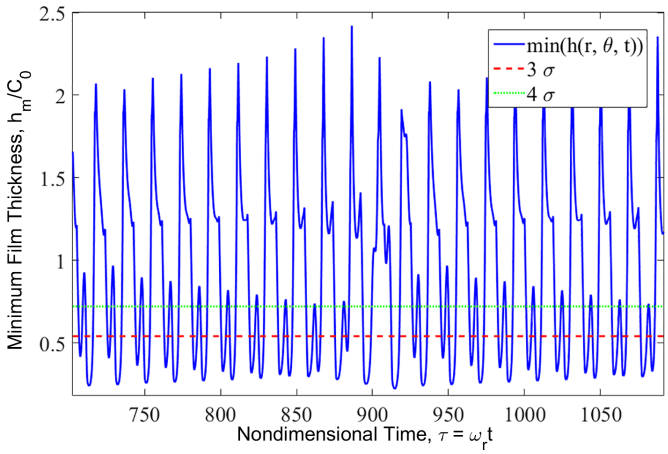

(a) Normalized minimum film thickness

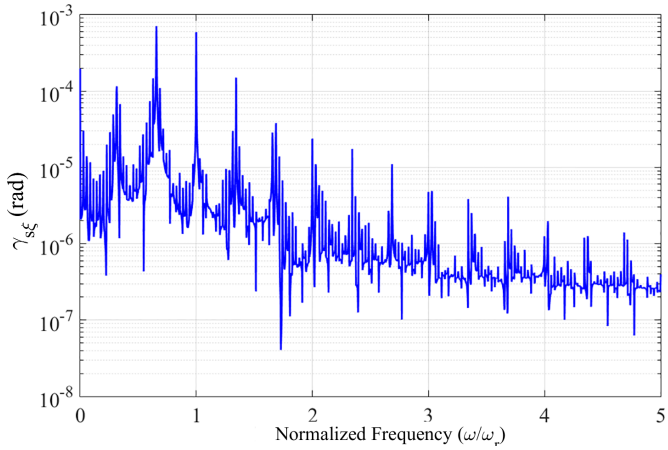

(b) Frequency spectrum of $\gamma_{s\xi}$

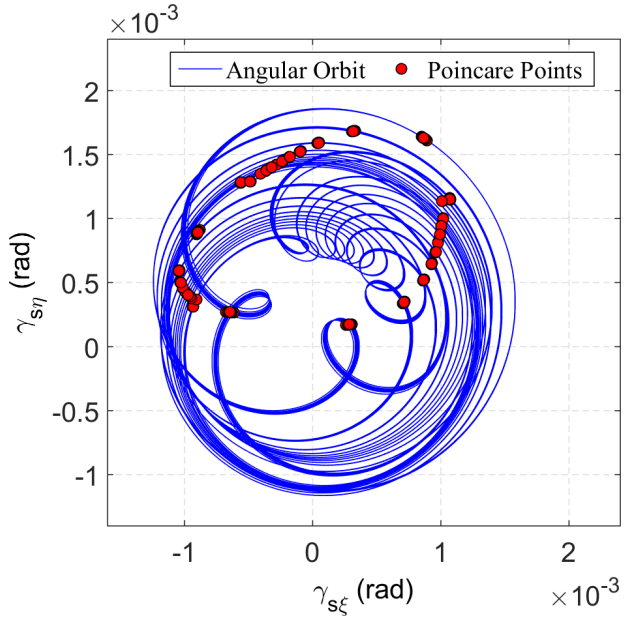

(c) Angular orbit and Poincaré section

Figure 10.17: FMS response to heavy contact using the Jackson-Green rough surface contact model (Parameter Set 2: $\gamma_r = 1$ mrad, $\gamma_{si} = 5$ mrad, $\omega_r = 2000$ rad/s).

Table 10.6: Overhung rotor parameters.

Parameter	
Rotor dynamic angular misalignment, χ_R	1 mrad
Rotor imbalance, ε_{RG}	7 μm
Rotor disk radius, R_r	100 mm
Rotor disk width, B_r	10 mm
Annular clearance, δ	0.13 μm
External viscous damping ratios, ζ_ϵ and ζ_γ	0.1

These results should serve as an additional motivator for always including coning in a mechanical face seal, as the taper caused by coning limits the contact pressure to a localized region of the seal faces (and thus, the contact forces are small even if the local contact pressures are large).

These results have several important conclusions for surrogate rotor fault detection using a mechanical face seal. The first conclusion is that light contact between the faces causes a dynamic response that is mostly synchronous. Thus, it is hypothesized that the rotor fault signal is unadulterated even in the presence of some seal face contact. Another important conclusion that can be drawn from these results is that severe contact is only prevalent for damaged or poorly-designed seals. It is clear upon comparing parameter sets 1 and 2 in Tables 10.4 and 10.5 that the parameters generating severe contact (set 2) are defined by a reduced pressure differential, increased axial stiffness, and increased roughness, all of which predilect the seal to experience contact. Thus, the seal should be designed *a priori* to (a) maximize fluid stiffness, and (b) ensure that the set-point axial clearance C_o is much greater than the surface roughness σ.

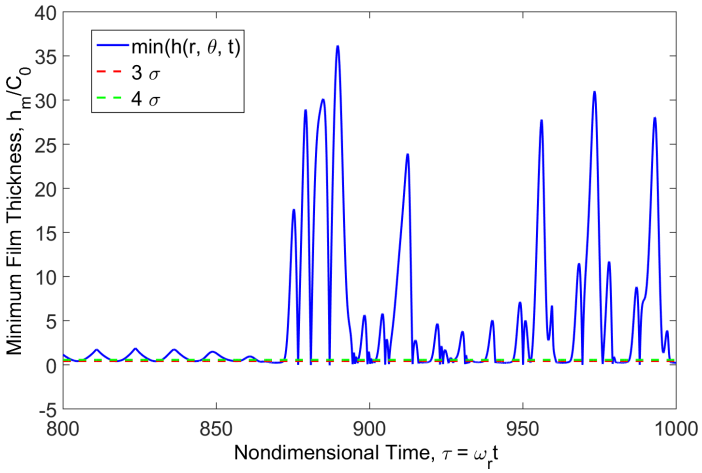

(a) Normalized minimum film thickness

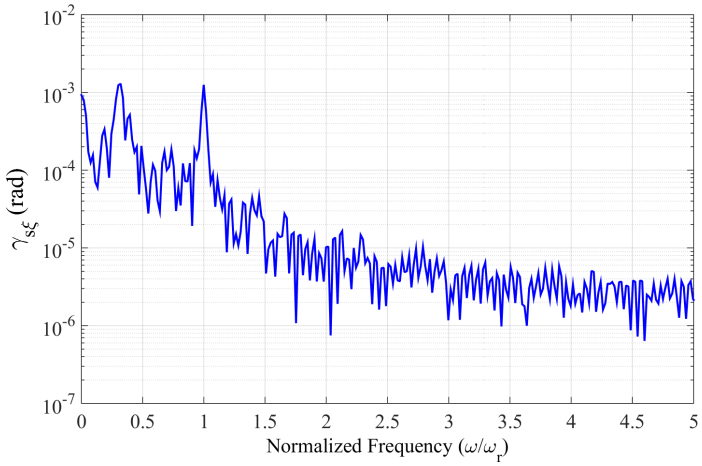

(b) Frequency spectrum of $\gamma_{s\xi}$

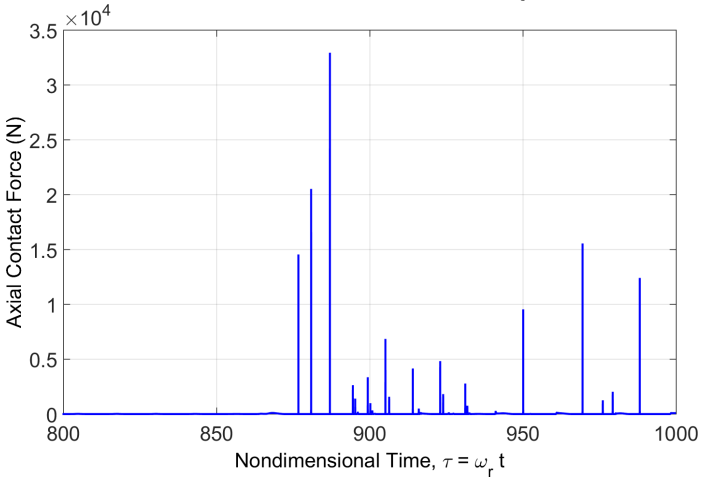

(c) Axial contact force

Figure 10.18: Severe contact condition in a flat-faced seal with no coning (Parameter Set 2: $\gamma_r = 2$ mrad, $\gamma_{si} = 5$ mrad, $\omega_r = 1000$ rad/s, $\beta = 0$).

10.6 Lateral Contact in the FMSR-ER System

The objective here is to validate the use of seal vibration signatures to detect rotor-housing contact (here, the term 'housing' is used to avoid confusion with the stationary seal element). The FMSR-ER equations of motion are solved numerically using the methods presented for the cracked rotor in Section 9.3.2. The eccentric rub forces between the rotor and the annular casing (i.e., the housing) are generated via rough surface contact between the surfaces according to the methods presented in Chapter 7 (see Eqs. 7.26 - 7.31). For the results shown here, the rotating seal element has a dynamic angular misalignment of $\chi = 0.1$ mrad, a static angular misalignment of $\chi_s = 0.5$ mrad, and an eccentric imbalance of $\varepsilon_{rG} = 5$ μm. Additional parameters for the seal are given in Tables 8.1 and 8.2, while the rotor parameters are given in Tables 9.1 and 10.6 (rotor bow and inertial maneuver loads are neglected in this analysis). The rotor is assumed to be thin, where the polar mass moment of inertia is $I_{pR} = 0.4$ kg·m^2. Furthermore, the rotor and housing are assumed to be rough with a composite surface height standard deviation of $\sigma = 0.8$ μm, an average radius of $R_a = 1.7$ μm, an asperity density of $N = 4.2(10)^{11}$ asp./m^2, and a composite elastic modulus of $E = 24$ GPa.

The equations of motion are simulated over a range of shaft speeds, and the steady-state response is extracted and sampled once per-period to obtain the associated Poincaré return points. The corresponding bifurcation diagrams are provided in Figs. 10.19 and 10.20 for the rotor and stationary seal element, respectively, where the rotor-housing coefficient of friction is $\mu_f = 0.1$. Specifically, the bifurcation diagrams correspond to eccentric and angular degrees of freedom for both the rotor and stationary seal element (the rotating seal element results are omitted due to similarity with the stationary element results). The bifurcation diagrams without friction are given in Fig. 10.21. In both cases, with and without friction, contact between the rotor and housing occurs at a shaft speed of approximately $\omega_r = 305$ rad/s. The

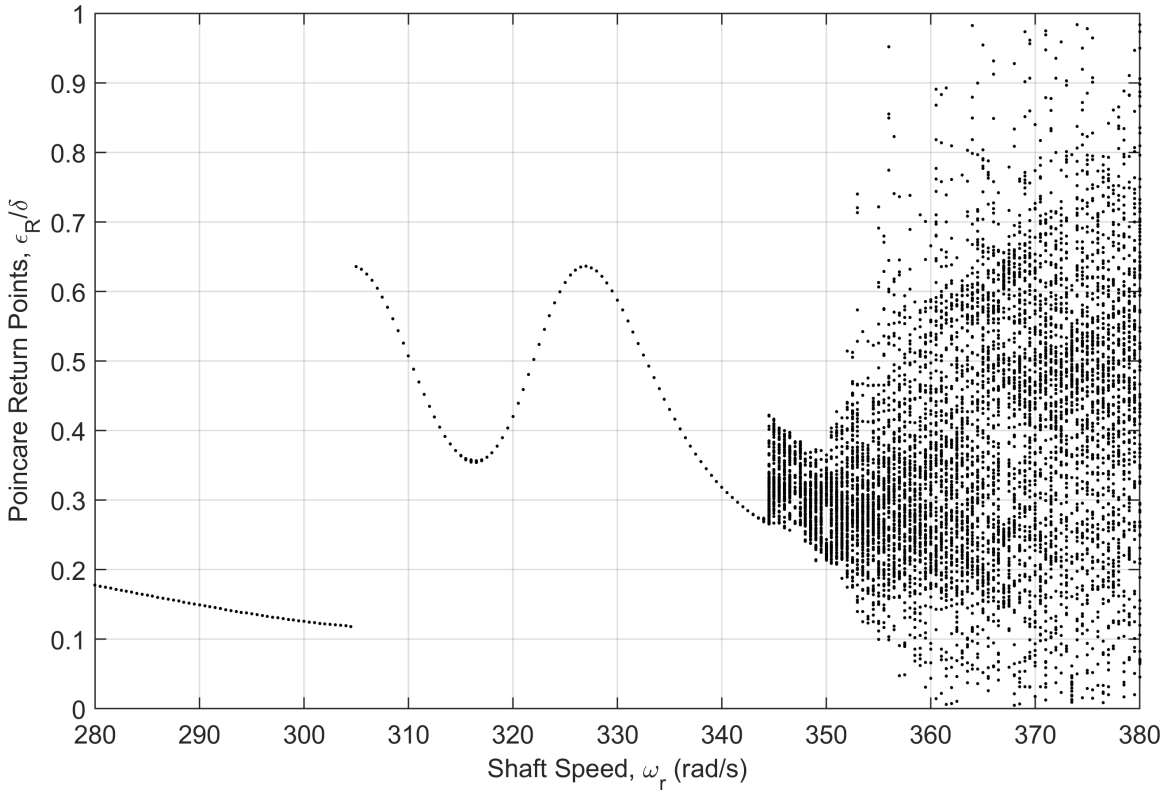

(a) Rotor eccentricity

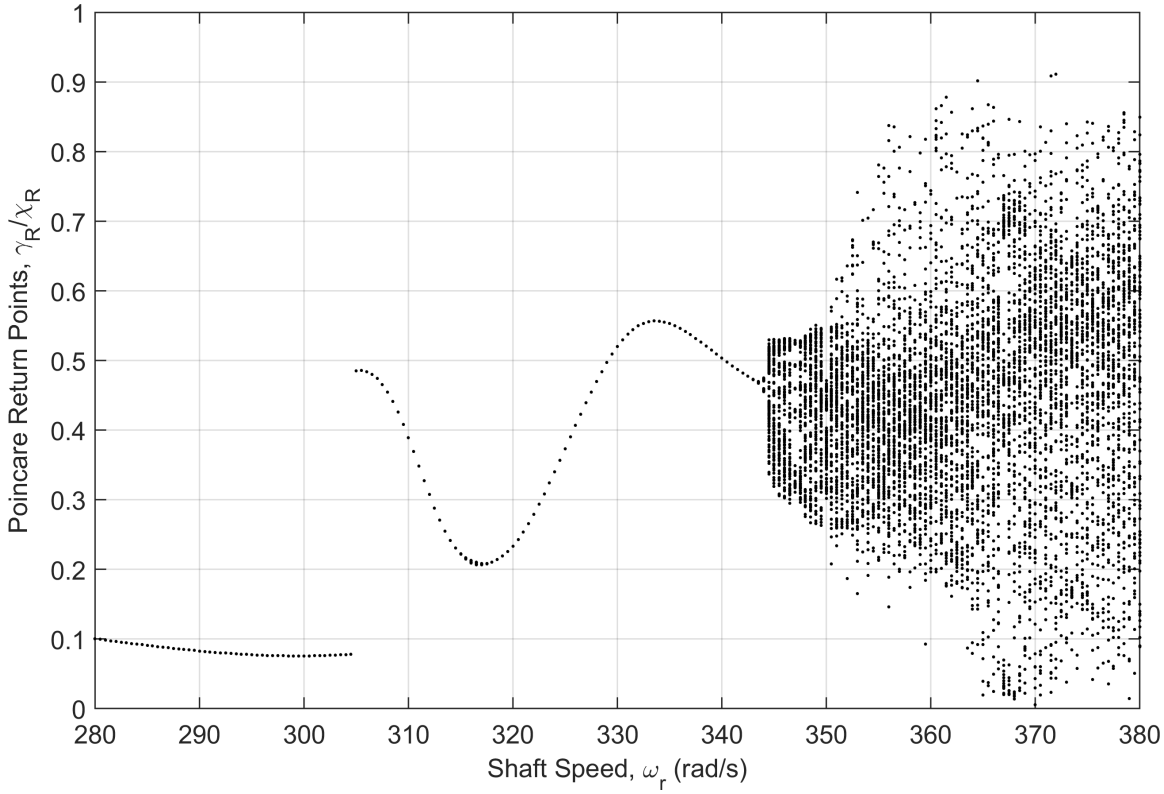

(b) Rotor tilt

Figure 10.19: Shaft speed bifurcations of the rotor ($\mu_f = 0.1$).

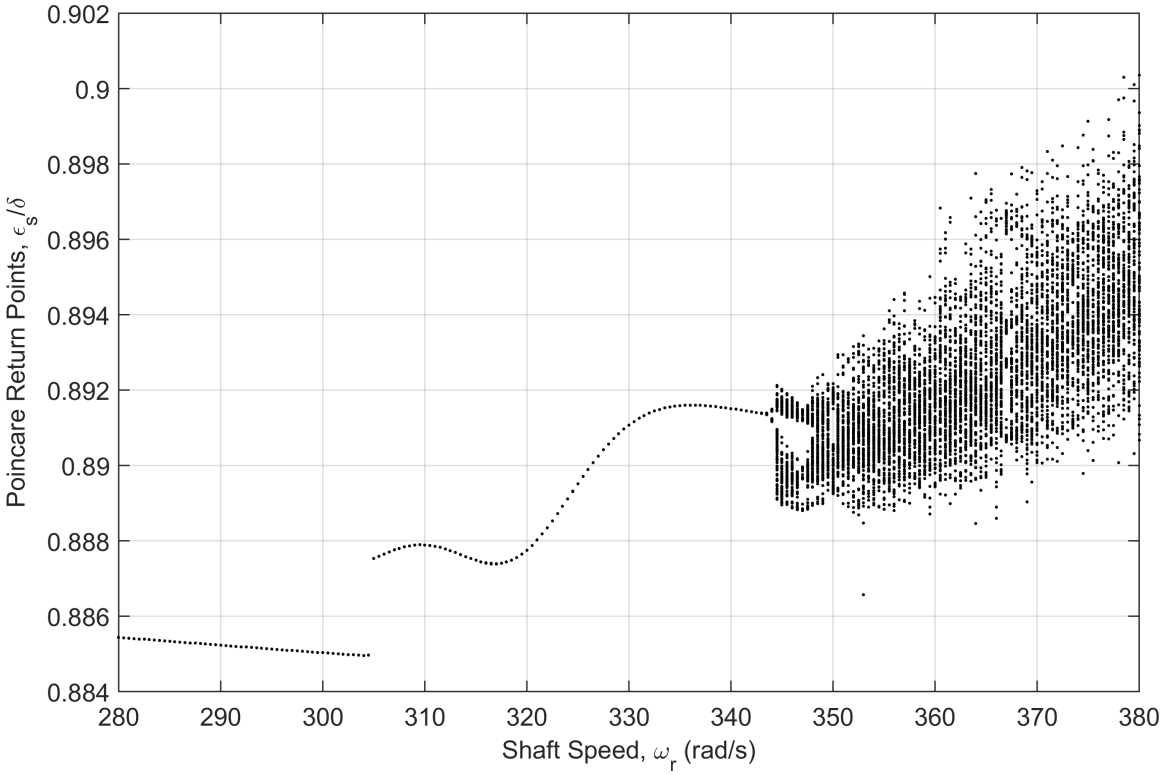

(a) Stationary seal element eccentricity

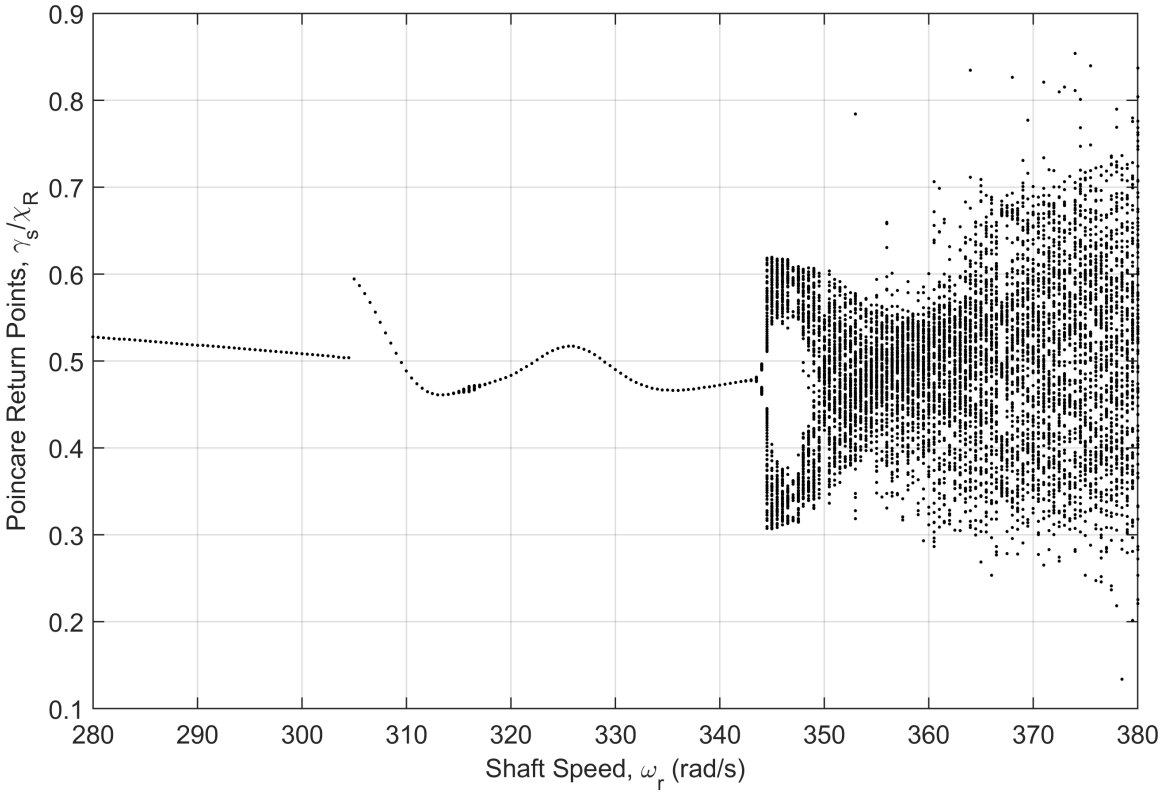

(b) Stationary seal element tilt

Figure 10.20: Shaft speed bifurcations of the stationary seal element ($\mu_f = 0.1$).

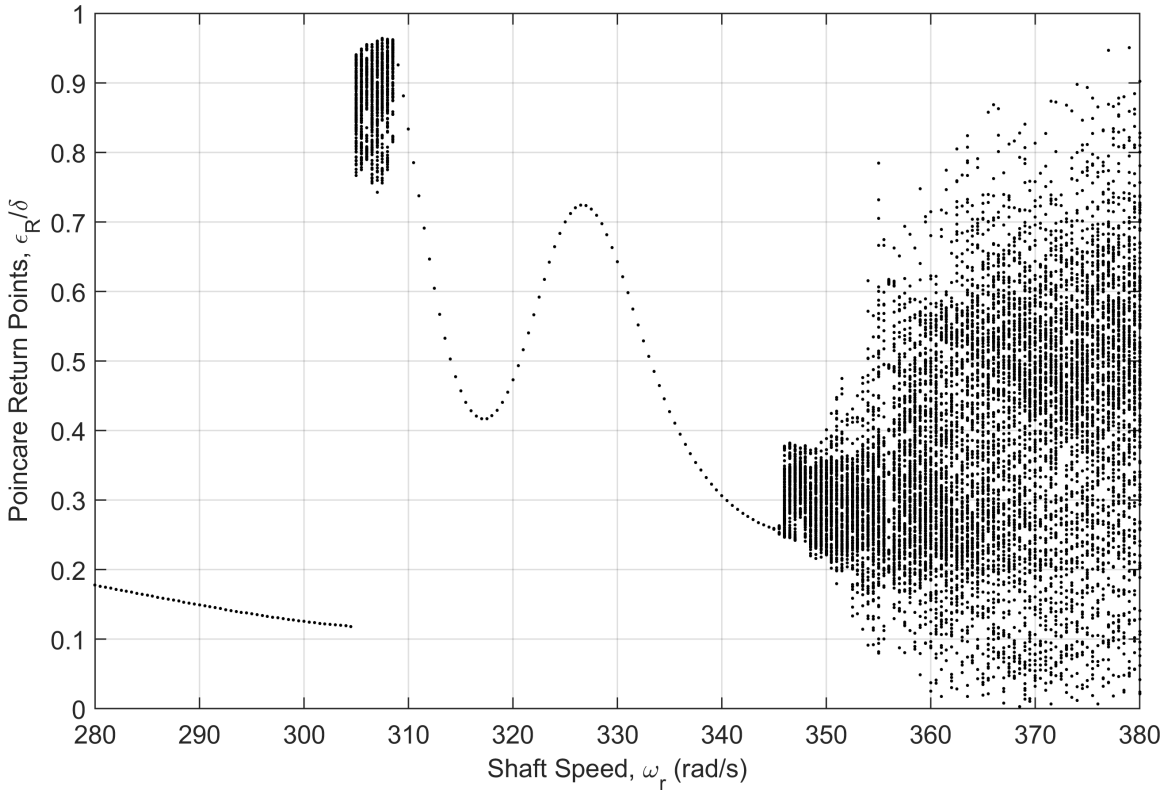

(a) Rotor eccentricity

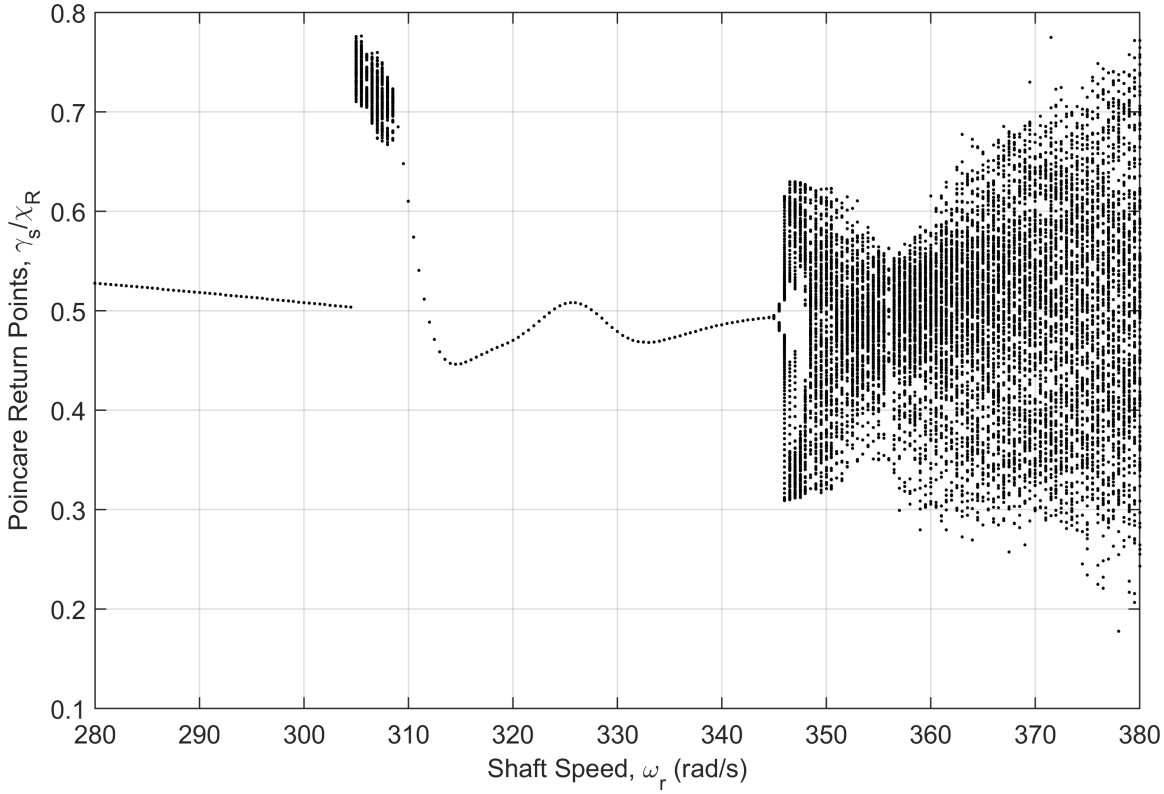

(b) Stationary seal element tilt

Figure 10.21: Shaft speed bifurcations of the stationary seal element ($\mu_f = 0$).

steady-state rotor eccentric and angular responses beneath the onset of contact are strictly synchronous, as shown in Fig. 10.22. The annular clearance is denoted with a solid line, while the 3σ surface height boundary is indicated with a dashed line.

As the rotor eccentric deflection increases, the local clearance between the rotor and housing approaches the same order of magnitude as the surface roughness. Once this occurs, a sufficient number of asperities on both surfaces interact and the rotor-dynamics (and by association, the seal dynamics) bifurcate into a different response. The rotor response with and without friction differs following this bifurcation. When friction is included, the rotor immediately transitions into a period-1 motion with one impact per period (see Figs. 10.23 and 10.24). Without friction, the rotor bifurcates into a chaotic motion, which then persists for a small range of shaft speeds.

The period-1 motion occurring at $\omega_r = 320$ rad/s causes the rotor to impact the housing once per revolution, as shown in Fig. 10.23a. The rotor tilt (shown in Fig. 10.23b) is fundamentally coupled to the rotor eccentric deflection, and therefore also demonstrates the signatures of rotor-housing contact. The rotor response is then transmitted to the stationary seal element, where the contact signatures again manifest in both the eccentric and angular responses (Figs. 10.23c and 10.23d). Interestingly, the stationary seal element eccentric vibrations are small (several orders of magnitude smaller than the lateral rotor-housing clearance), and likely indistinguishable from noise in a realistic operating environment. Even if the stationary seal element eccentricities were large, the orbit is primarily circular, thus indicating the dominance of the synchronous 1X harmonic. On the other hand, the stationary seal element tilt prominently indicates rotor-housing contact signatures, thus further reinforcing the use of the stationary element angular response for surrogate rotor fault detection.

Two representative examples of chaotic response are shown in Figs. 10.25 and 10.27 for shaft speeds of 345 rad/s and 370 rad/s, respectively. The associated frequency

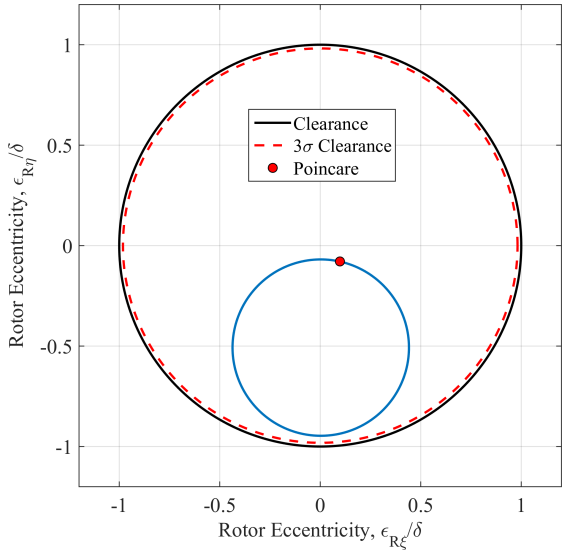

(a) Rotor eccentric orbit

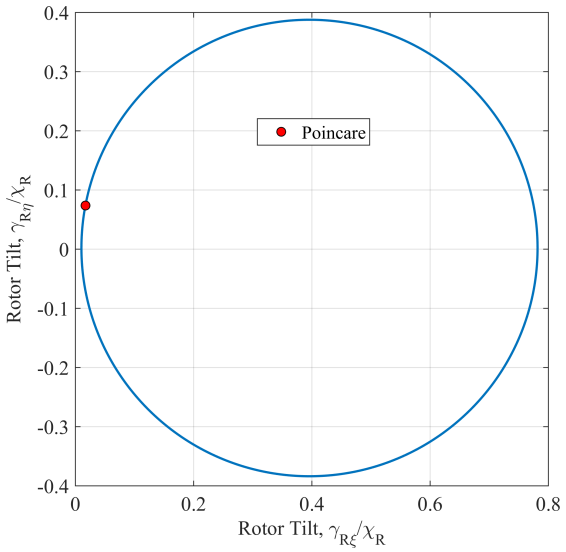

(b) Rotor tilt orbit

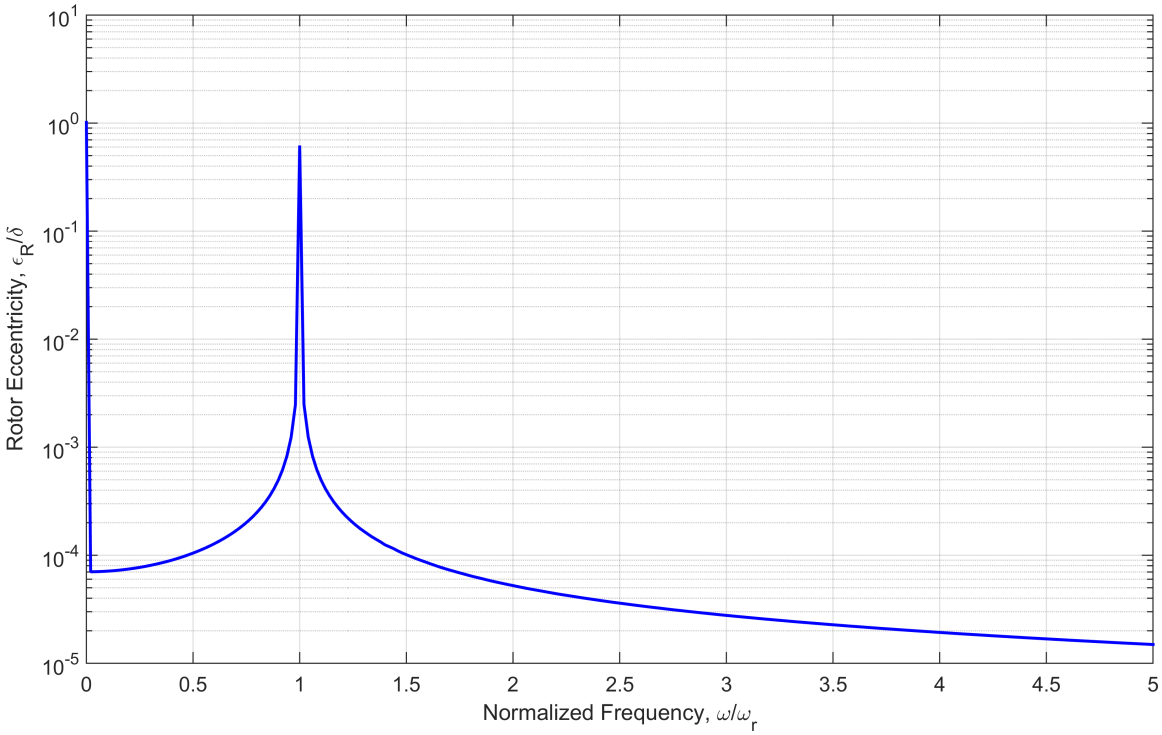

(c) Rotor eccentricity frequency content

Figure 10.22: Rotor response at $\omega_r = 300$ rad/s prior to the onset of contact ($\mu_f = 0.1$).

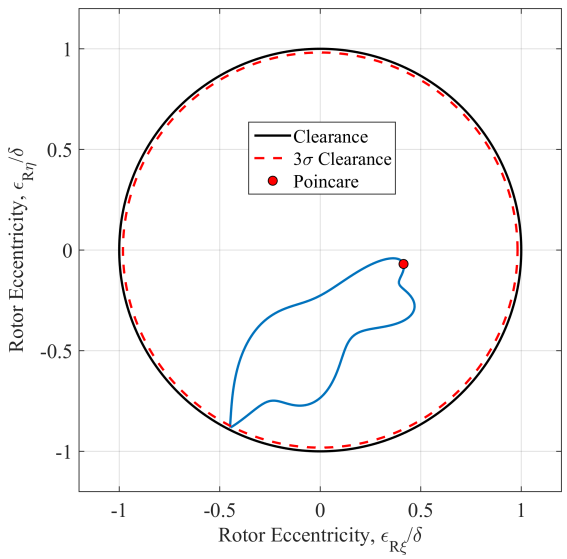

(a) Rotor eccentric orbit

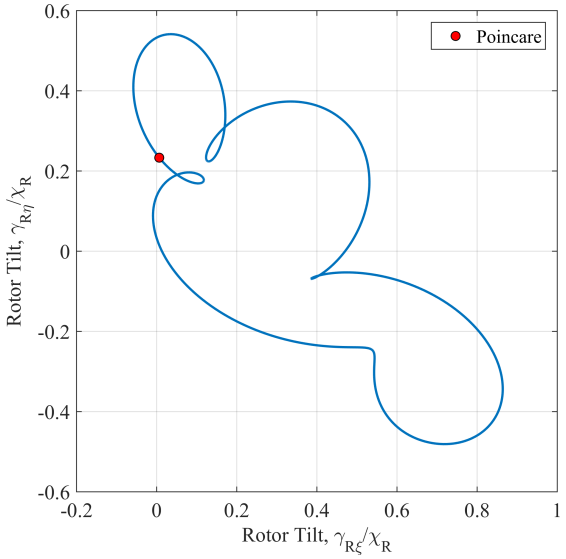

(b) Rotor tilt orbit

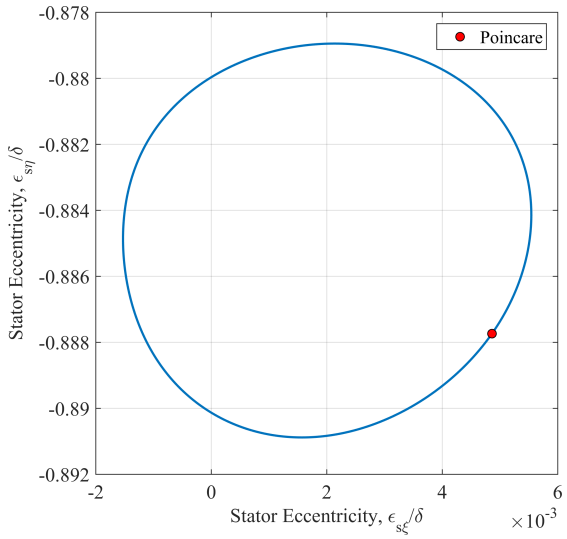

(c) Stationary seal element eccentric orbit

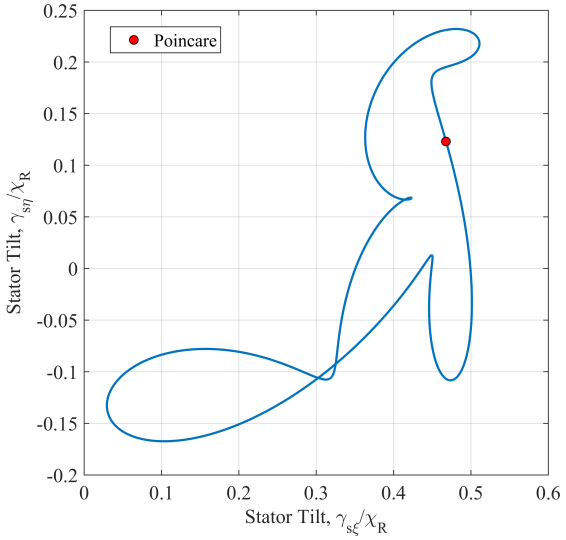

(d) Stationary seal element tilt orbit

Figure 10.23: FMSR-ER Response: Period-1 motion at $\omega_r = 320$ rad/s ($\mu_f = 0.1$).

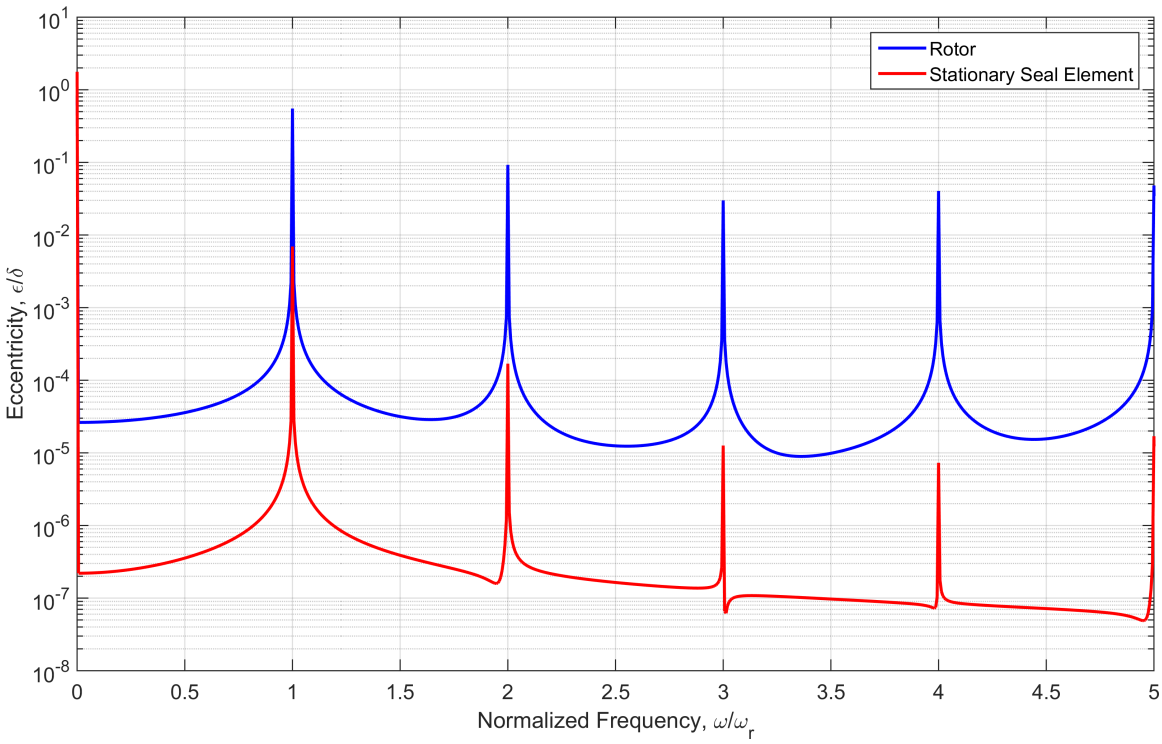

(a) Eccentric degrees of freedom

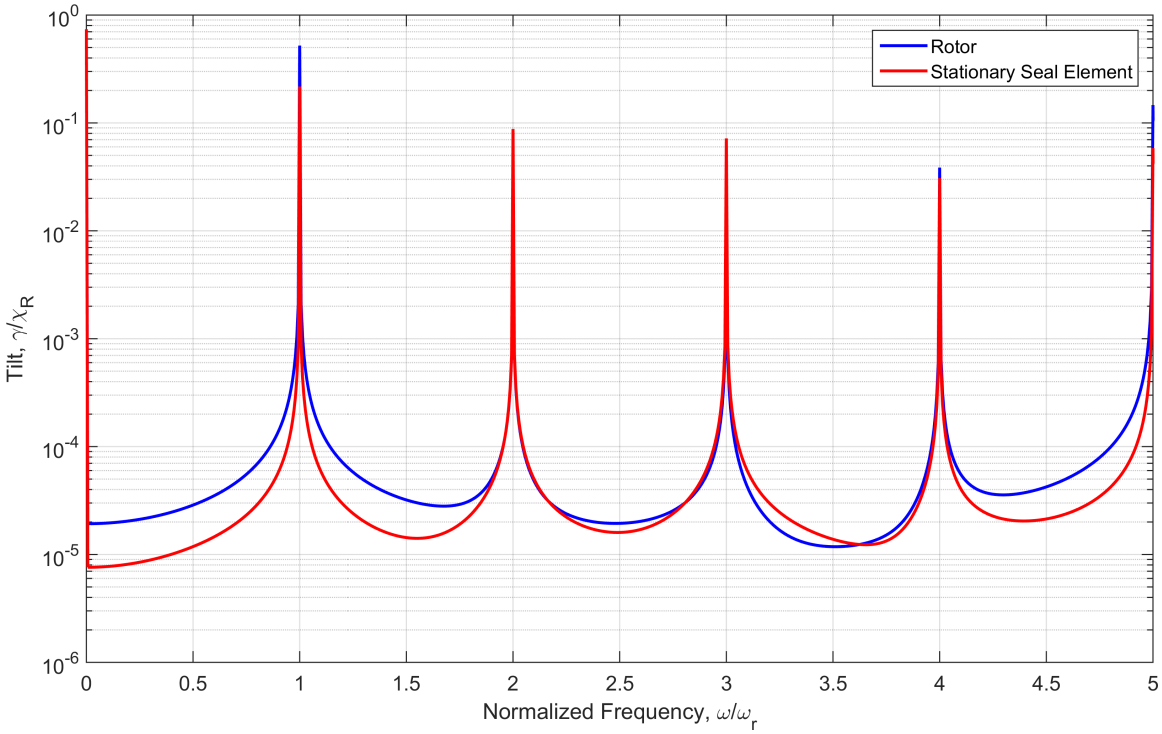

(b) Angular degrees of freedom

Figure 10.24: FMSR-ER Response: Frequency content contained in the period-1 motion at $\omega_r = 320$ rad/s ($\mu_f = 0.1$).

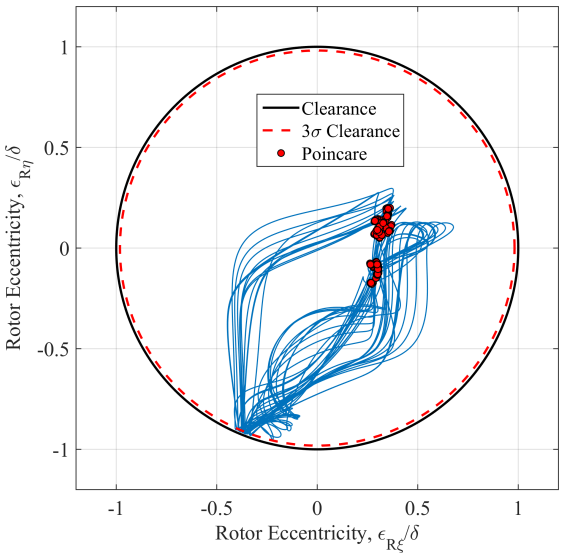

(a) Rotor eccentric orbit

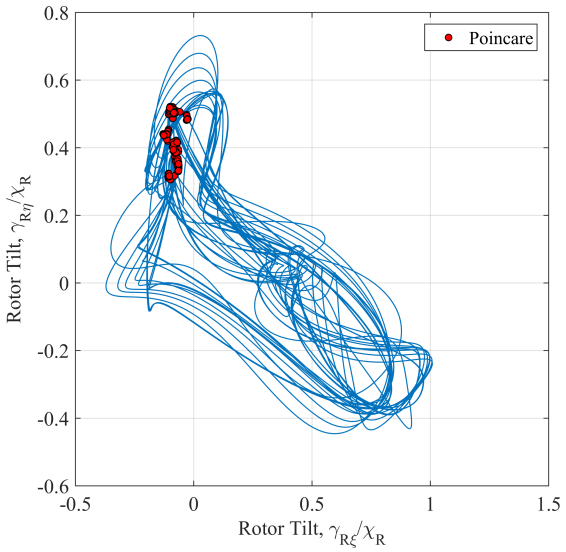

(b) Rotor tilt orbit

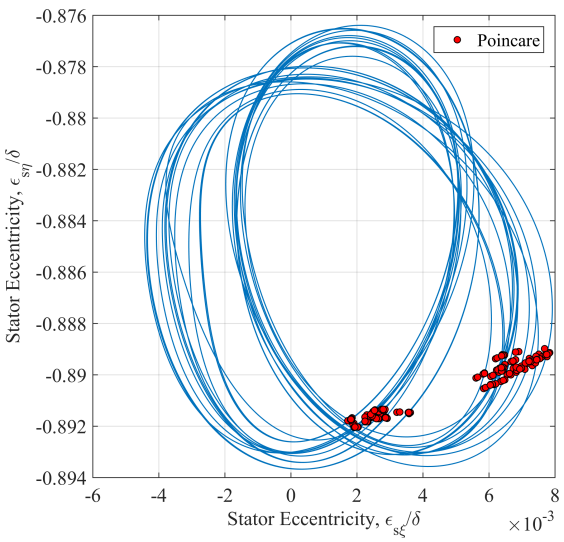

(c) Stationary seal element eccentric orbit

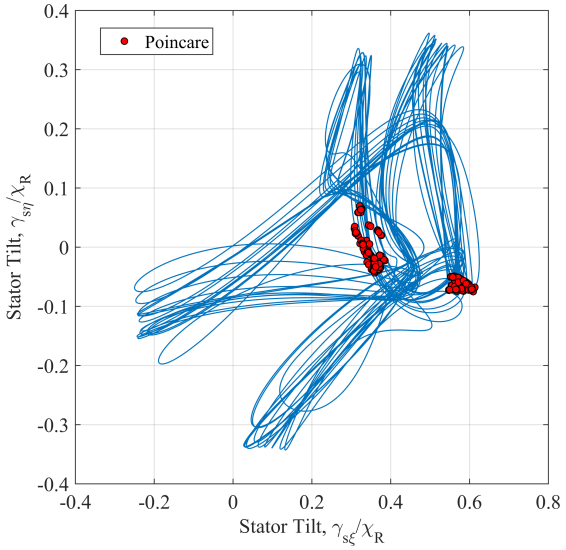

(d) Stationary seal element tilt orbit

Figure 10.25: FMSR-ER Response: Chaotic motion at $\omega_r = 345$ rad/s ($\mu_f = 0.1$).

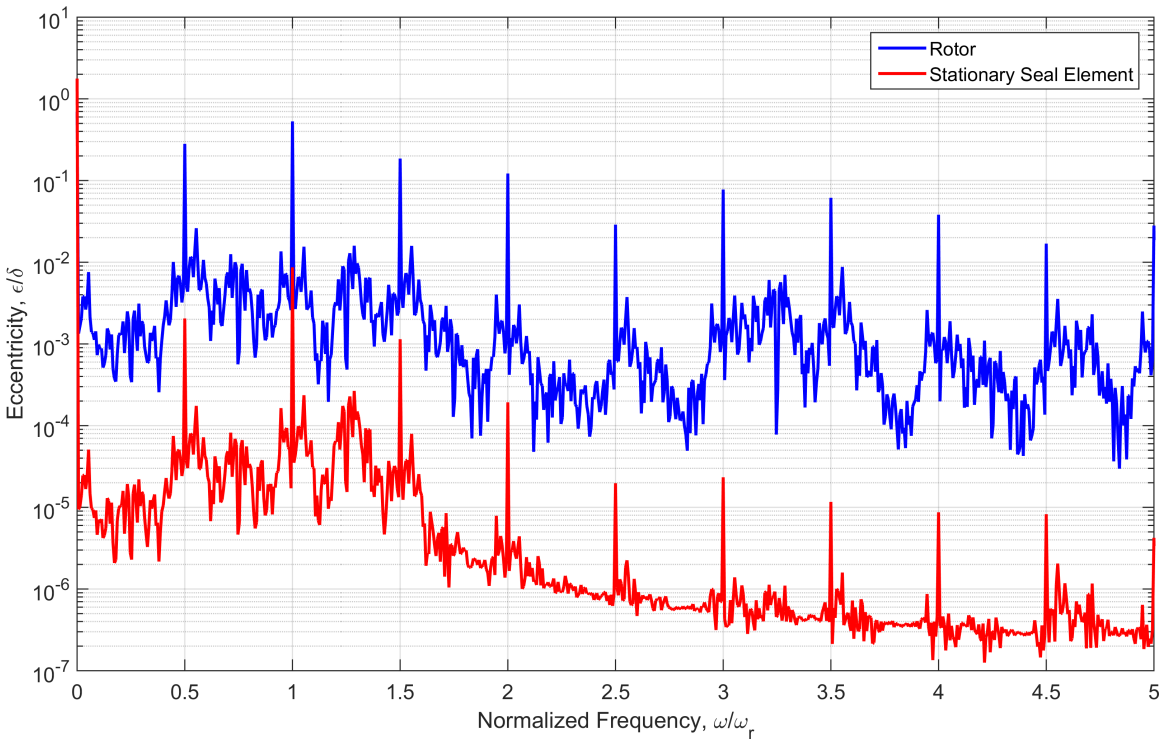

(a) Eccentric degrees of freedom

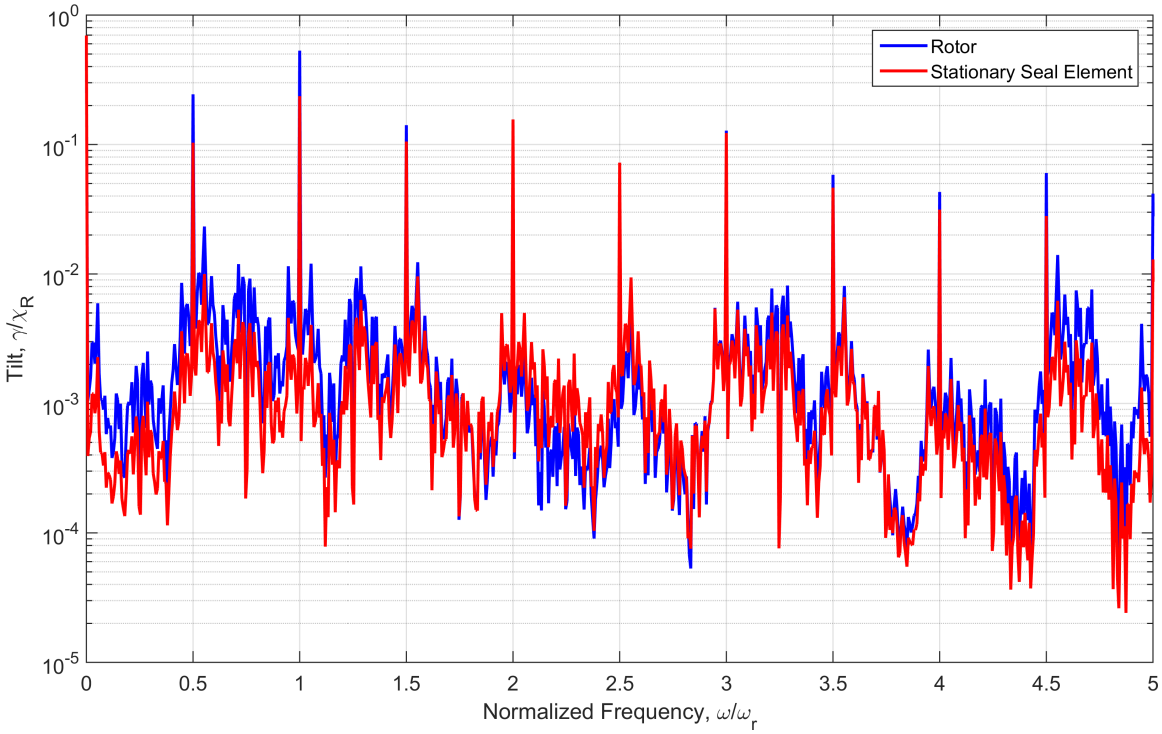

(b) Angular degrees of freedom

Figure 10.26: FMSR-ER Response: Frequency content contained in the chaotic motion at $\omega_r = 345$ rad/s ($\mu_f = 0.1$).

content is provided in Figs. 10.26 and 10.28. Both responses are defined by a scattering in the Poincaré return points and broad-band frequency content. The lower shaft speed (345 rad/s) causes a chaotic motion that is modulated by integer and fractional shaft speed harmonics (and consequently, the Poincaré section shows two distinct groups of return points). The higher shaft speed (370 rad/s) generates a chaotic response where the Poincaré return points are generally scattered and do not display any discernible groupings. Likewise, the frequency content indicates that the response is modulated by only integer shaft speed harmonics.

10.6.1 Time-Energy-Frequency Signatures Using the HHT

Intermittent rotor-stator rub is fundamentally nonlinear and resembles a piecewise-smooth hybrid dynamical system. Because of this, the rotor response is dictated by phenomena that occur on vastly different scales: contact occurs on the dimension of the surface roughness, while the rotor deflection occurs on the dimension of the clearance. Consequently, the system dynamics fundamentally change when contact occurs: the response during contact is governed by different dynamic processes than the response between contact events (i.e., the response is non-stationary). A useful technique for analyzing non-stationary signals is the Hilbert Huang transform (HHT), which is used here to obtain the time-energy-frequency spectrum of FMSR-ER response (see Appendix C for a discussion of the HHT).

The HHT is used to analyze the period-1 response shown in Fig. 10.23, and the resulting time-energy-frequency spectra are given in Figs. 10.29 and 10.30 for the rotor eccentricity and stationary seal element tilt, respectively. The steady-state waveforms are normalized and provided in the figures for reference (the clearance δ and surface roughness $\delta - 3\sigma$ are shown in the rotor eccentricity to demonstrate scale). The waveform clearly indicates that the rotor eccentric response suddenly changes when the local clearance is comparable to the surface roughness (i.e., the rotor rebounds

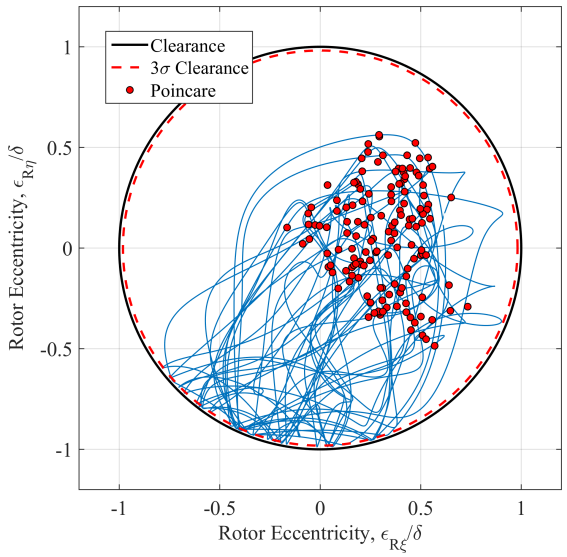

(a) Rotor eccentric orbit

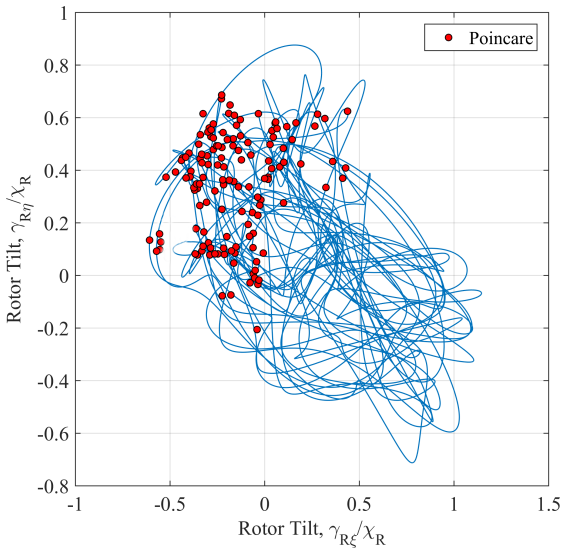

(b) Rotor tilt orbit

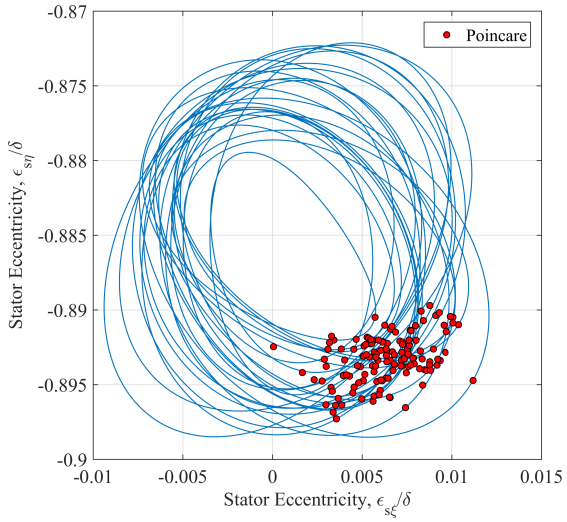

(c) Stationary seal element eccentric orbit

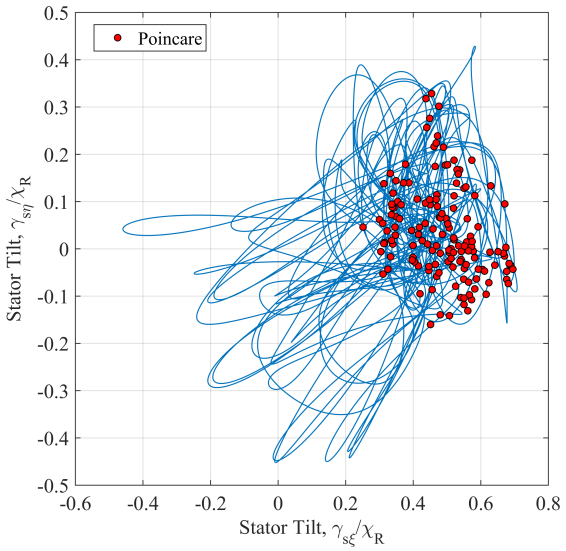

(d) Stationary seal element tilt orbit

Figure 10.27: FMSR-ER Response: Chaotic motion at $\omega_r = 370$ rad/s ($\mu_f = 0.1$).

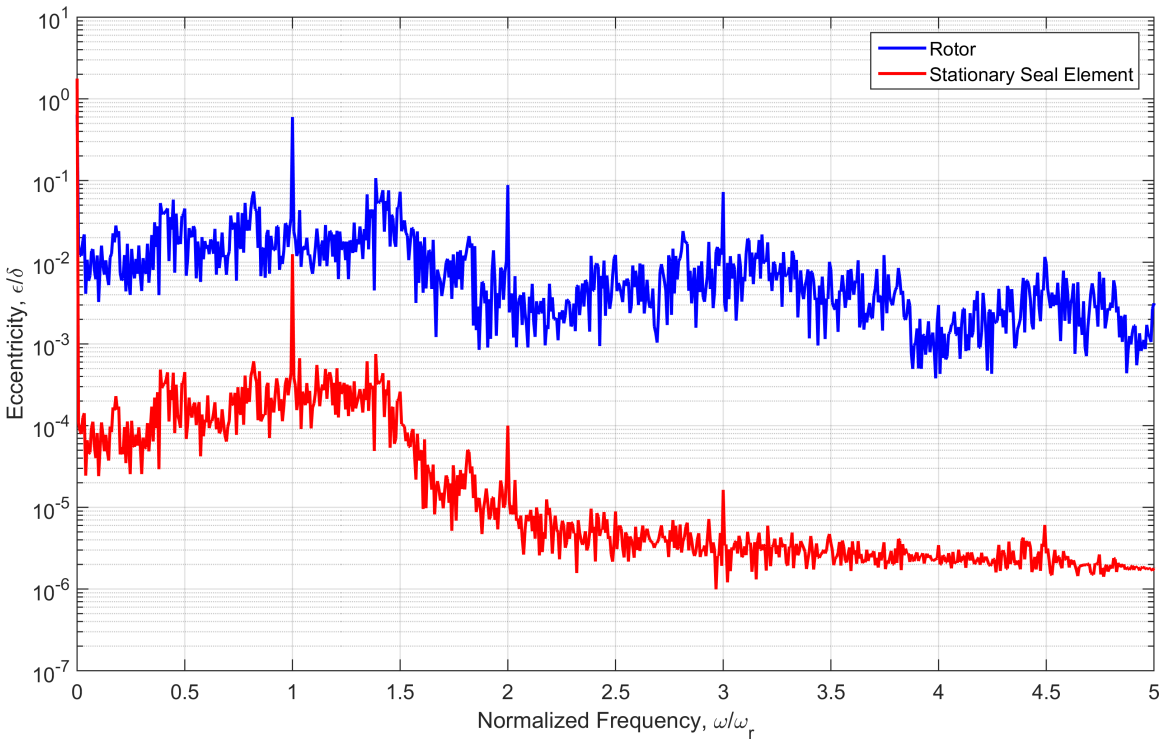

(a) Eccentric degrees of freedom

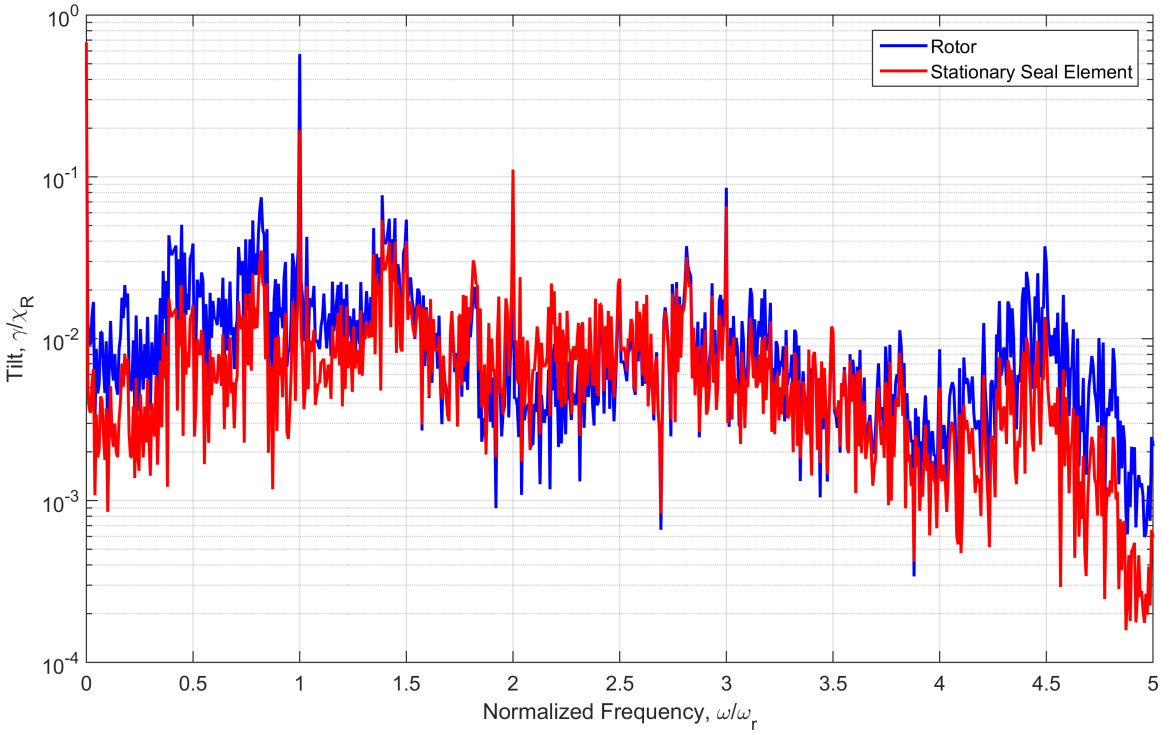

(b) Angular degrees of freedom

Figure 10.28: FMSR-ER Response: Frequency content contained in the chaotic motion at $\omega_r = 370$ rad/s ($\mu_f = 0.1$).

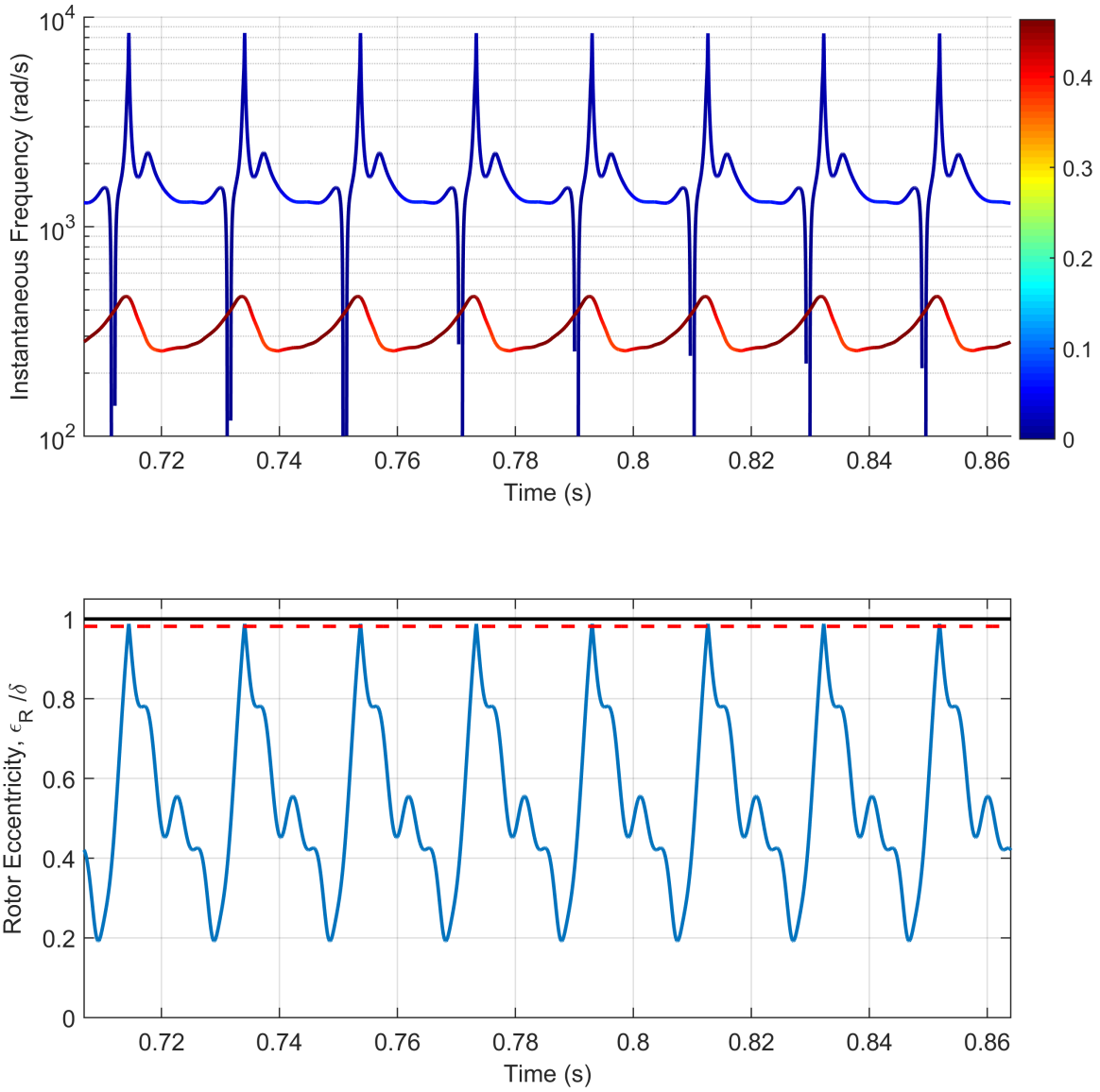

Figure 10.29: HHT: Rotor eccentric response ϵ_R corresponding to a period-1 response ($\omega_r = 320$ rad/s).

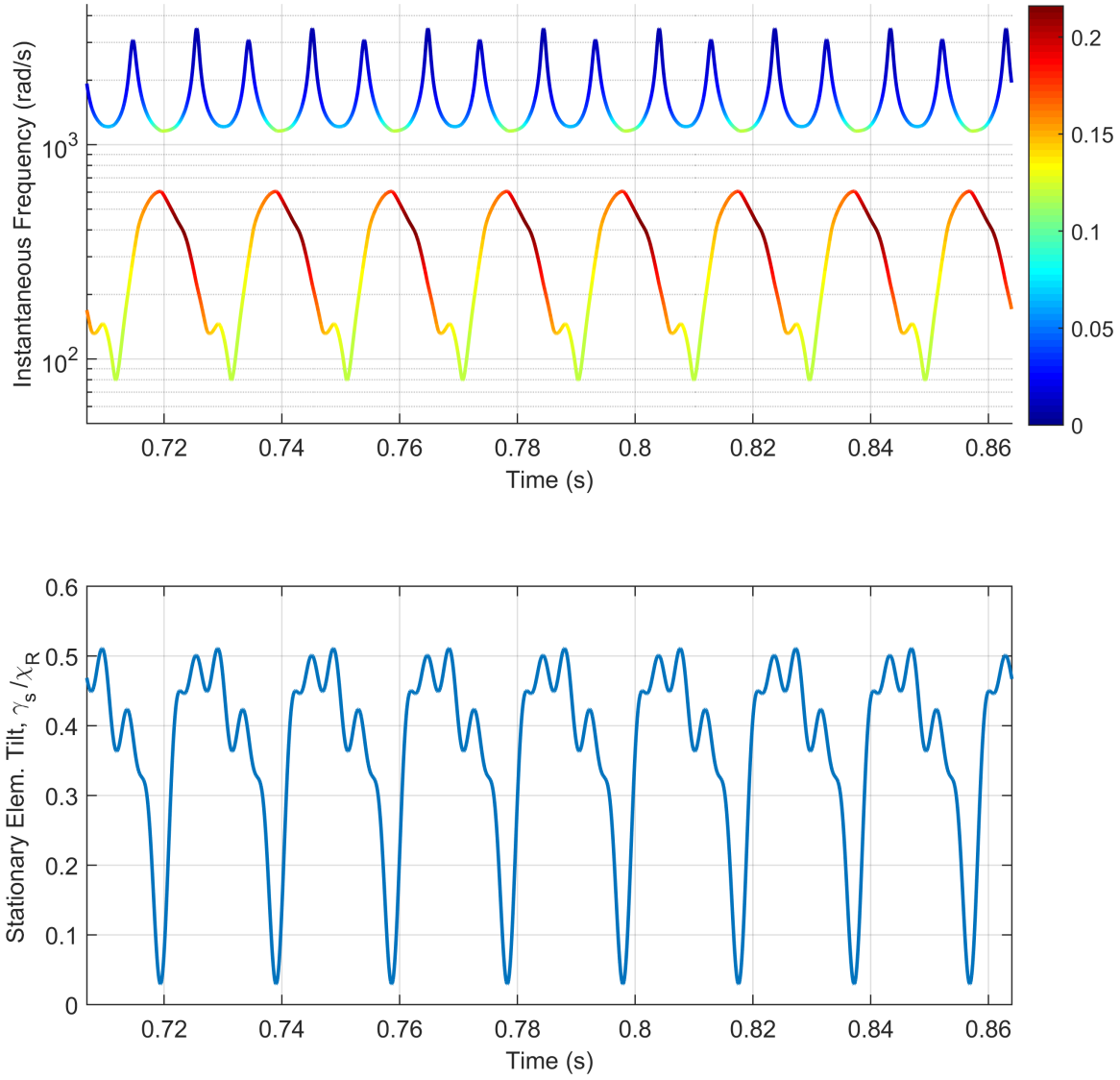

Figure 10.30: HHT: Stationary seal element tilt response γ_s corresponding to a period-1 response ($\omega_r = 320$ rad/s).

from the housing). In the classical frequency domain, this period-1 motion is reconstructed using integer shaft speed harmonics comprised of constant magnitude and frequency. However, the time-energy-frequency spectrum shows that the period-1 response is composed of two intrinsic mode functions (IMFs, as discussed in Appendix C); this is observed for both the rotor eccentricity and stationary seal element tilt. The first IMF contains most of the signal energy and is centered near the shaft speed; this IMF primarily represents the synchronous response. On the other hand, the second IMF originates from the intermittent rotor-housing contact. At each contact, the time-energy-frequency spectrum displays a sudden increase in instantaneous frequency, where the maximum instantaneous frequency observed is much larger than the shaft speed. Thus, rotor-housing contact is defined in the time-energy-frequency spectrum by high-frequency, short-duration increases in instantaneous frequency. It is important to recognize that these phenomena are more evident in the rotor eccentricity than the stationary seal element tilt (this is intuitive because the seal response is dominated by the synchronous component). Still, the stationary element tilt clearly indicates each impact via a commensurate increase in instantaneous frequency.

These observations are corroborated in the chaotic response at a shaft speed of 370 rad/s (see Fig. 10.27). The steady-state waveform and time energy frequency spectrum are given in Figs. 10.31 and 10.32 for the rotor eccentricity and the stationary seal element tilt, respectively. Once again, the rotor eccentricity displays prominent and sudden increases in instantaneous frequency at each occurrence of contact. In contrast to the period-1 response, other IMFs appear in the response corresponding to subharmonic vibrations. For the chaotic response, the time-energy-frequency spectrum of the stationary seal element tilt contains sudden increases in instantaneous frequency due to contact which are less defined than in the eccentric rotor response. More generally, the stationary seal element tilt is defined by prominent scattering of the energy caused by contact.

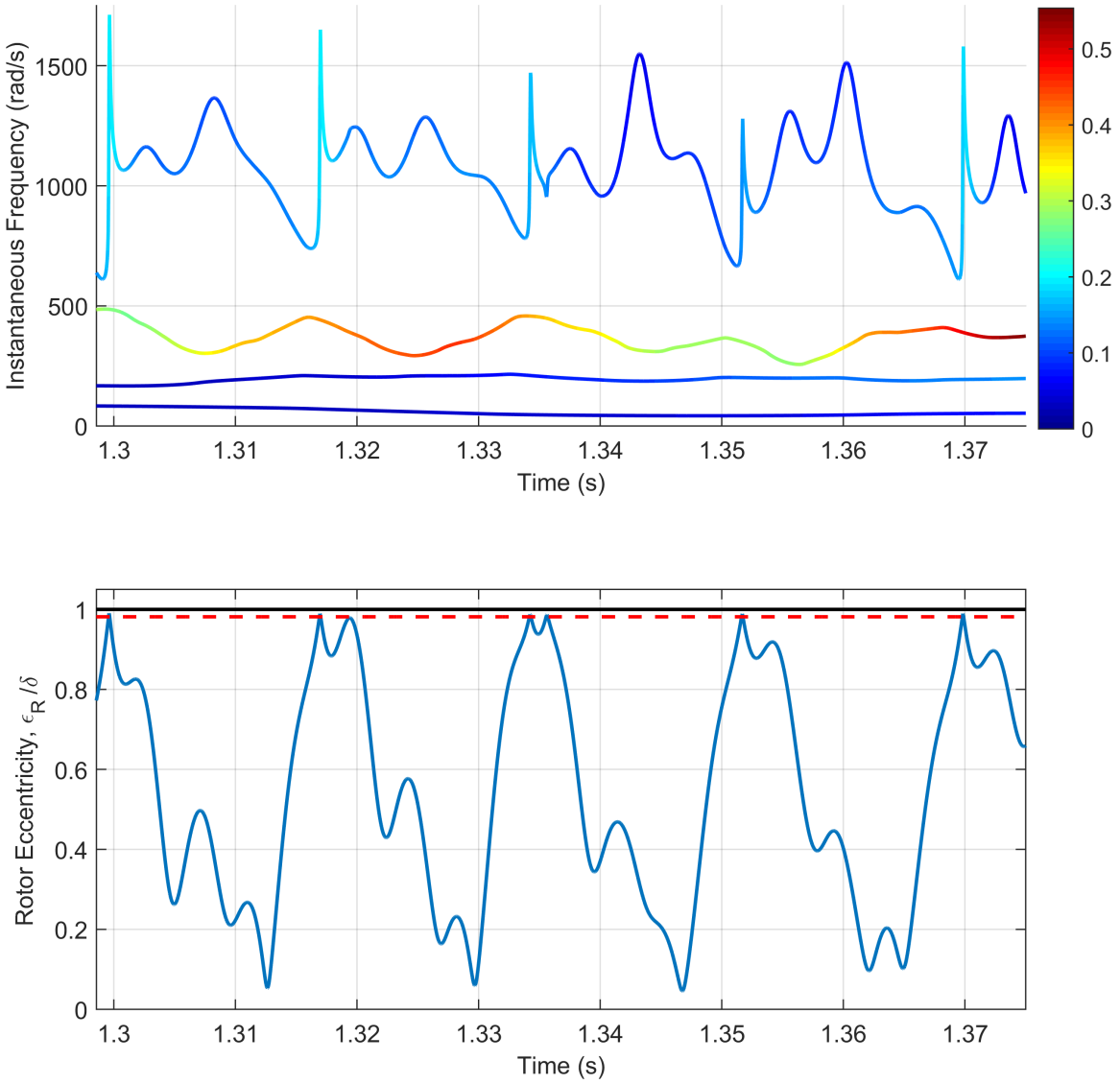

Figure 10.31: HHT: Rotor eccentric response ϵ_R corresponding to a chaotic response ($\omega_r = 370$ rad/s).

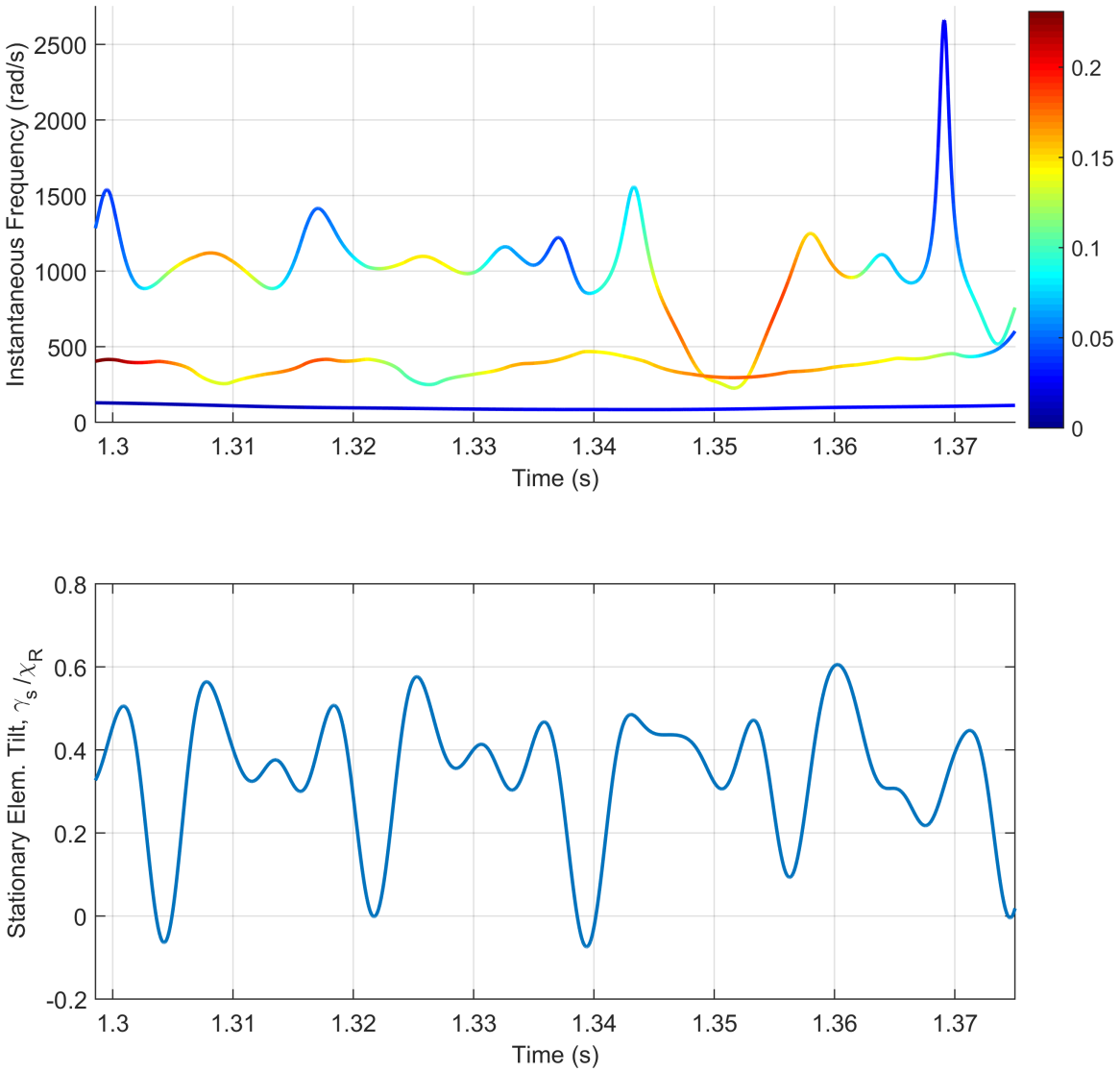

Figure 10.32: HHT: Stationary seal element tilt response γ_s corresponding to a chaotic response ($\omega_r = 370$ rad/s).

10.7 Summary

The results presented in this chapter clearly elucidate that contact is defined by events that occur on vastly different scales. In the time domain, each impact event is characterized by a short-duration rebound that occurs on the dimension of the composite surface roughness. In the time-energy-frequency domain, this phenomenon manifests as a sudden increase in instantaneous frequency over the duration of the contact. More specifically, the results from the simulations presented in this chapter are summarized as the following:

1. Rotor-stator rub is strongly nonlinear and displays a rich variety of responses, including periodic, quasiperiodic, and chaotic motion.

2. The RSCM causes different rotordynamic responses than the classic LECM; thus, accurately predicting the rotor response requires realistic contact models.

3. Rotor-stator rub in the FMSR-ER system manifests prominently in the stationary seal element tilt. Consequently, a monitoring system designed to measure the stationary seal element tilt can also be used to detect rotor-housing contact.

4. In the time-energy-frequency spectrum, contact is defined by (a) large and sudden increases in instantaneous frequencies, (b) broadband scattering of the signal energy, and (c) prominent subharmonic energy bands.

Also, severe seal face contact was shown to occur for poorly-designed seals with insufficient fluid film stiffness and an axial set-point clearance comparable to the surface roughness. Thus, it is important to emphasize that using the seal as a surrogate vibration monitor is predicated on healthy seal operation (though some light face contact may be acceptable regarding rotor fault detection).

CHAPTER XI

RESULTS: MULTIPLE SIMULTANEOUS FAULTS

Shaft fatigue cracks and rotor-stator contact typically instigate from either primary incipient machine faults (e.g., misalignment or imbalance) or sudden catastrophic damage (e.g., blade loss). These severe rotor faults can then precipitate additional rotor faults via increased vibration, fatigue, or cumulative damage. For example, prolonged rotor bow can eventually originate a rotor fatigue crack, which in turn could generate rotor-housing contact. Thus, embryonic rotor faults significantly increase the likelihood of a multiple fault scenario.

Previous chapters have studied the FMSR-ER response to two separate faults: a breathing shaft crack and intermittent rotor-housing contact. The dynamic signatures correlated to these faults are concomitant to the physical nature of each fault. The breathing crack mechanism considered here is defined by a predetermined periodic function. Consequently, the system dynamics are linear time-periodic because the crack is always present and breathes according to a known periodic function. This type of breathing crack therefore only generates integer shaft harmonics, which are present regardless of the shaft speed. On the other hand, intermittent rotor-housing contact is essentially a piecewise-smooth nonlinearity because contact forces are only engendered when the local clearance is commensurate to the surface roughness. This fault only appears when the rotor vibration exceeds certain allowable limits; once it does appear, rotor-housing contact causes a rich variety of nonlinear motions such as periodic, quasiperiodic, and chaotic responses.

The objective of this chapter is to characterize the FMSR-ER response when

multiple simultaneous faults exist in the system; i.e., a breathing shaft crack and intermittent contact. Specifically, trends and characteristics in the response are sought to elucidate unique vibration signatures caused by these coexisting faults. A variety of rotor responses are analyzed using bifurcation diagrams, frequency spectra, orbit diagrams, and the HHT.

11.1 Summary of Individual Fault Signatures

This section summarizes previously-discussed vibration signatures of a gaping crack, a breathing crack, and rotor-housing contact, and serves as a precursor to analyzing the more complex multiple fault scenario. These hallmark fault vibration signatures arise from the physical nature of each fault, and thus, are anticipated to also appear in the multiple fault scenario.

Gaping Fatigue Crack: (linear time-periodic) A gaping fatigue crack is a localized stiffness reduction which is invariant in a shaft-fixed frame. In the inertial frame, the rotor stiffness varies twice per revolution. Thus, a constant radial force such as gravity causes the rotor response to vary twice per revolution. This 2X variation produces a sub-synchronous critical speed when the rotor rotation speed is one-half of a system whirl frequency (i.e., the 1/2 critical speed).

Time Domain: In the time domain, the rotor deflection and tilt vary smoothly and periodically according to a period-1 motion. Imbalance and angular misalignments interact with the crack-induced 2X harmonic to generate orbits with a single prominent inflection.

Frequency Domain: The frequency response contains only a 1X harmonic caused by synchronous excitation and a 2X harmonic caused by the crack.

Time-Energy-Frequency Domain: The HHT is composed of two intrinsic mode functions (IMFs) whose instantaneous amplitude and frequency vary smoothly and periodically. One IMF is centered near the synchronous frequency, and one IMF is centered near the 2X harmonic.

Breathing Fatigue Crack: (linear time-periodic) In this work, the breathing crack compliance varies according to a known periodic expression; thus, the crack compliance varies periodically even in a shaft-fixed reference frame. The periodic crack breathing results in a multitude of shaft speed harmonics and associated sub-synchronous critical speeds.

Time Domain: The FMSR-ER response is period-1, and varies smoothly and periodically. The orbit shapes are dictated by the dominant shaft speed harmonic.

Frequency Domain: The frequency domain contains numerous integer shaft speed harmonics (primarily, the 1X, 2X, and 3X harmonics).

Time-Energy-Frequency Domain: The HHT results in two IMFs whose instantaneous amplitude and frequency vary smoothly and periodically. One IMF is centered near the synchronous speed, while the other is centered at the dominant shaft harmonic.

Intermittent Rotor-Housing Contact: (piecewise-smooth nonlinearity) Rotor - housing contact only occurs when the rotor deflection exceeds the allowable clearances, and is characterized by features occuring on disparate scales (e.g., the contact duration is short compared to the rotor period). Consequently,

the system dynamics are characterized by a rich diversity of motions, including periodic, quasiperiodic, and chaotic responses.

Time Domain: The rotor waveforms display prominent features caused by impact and rebound. The rotor orbits likewise demonstrate significant complexity not observed in the cracked rotor response, such as higher periodic, quasiperiodic, and chaotic responses. Furthermore, the rotor response shows rich bifurcation structure with variations in shaft speed (and other system parameters).

Frequency Domain: The frequency domain contains integer and fractional shaft speed harmonics. Quasiperiodic response results in the appearance of incommensurate frequencies, while chaotic vibration causes broadband frequency content that may be modulated by various dominant shaft speed harmonics.

Time-Energy-Frequency Domain: Another defining feature of rotor-housing contact is sudden increases in instantaneous frequency in the IMFs. These sudden increases are directly correlated to each rotor-housing impact. The instantaneous frequency displayed in these IMFs can be significantly larger than the synchronous frequency.

These observations are summarized according to the specific nature of each fault: a crack always exists in the system, whereas rotor-housing contact is ephemeral, occurring only when the rotor contacts the housing. Thus, methods for distinguishing coexisting disparate faults should focus on the temporal consistency of the fault signatures.

Table 11.1: Properties of the FMSR-ER system used in the multiple fault simulation.

Parameter	**Value**
Rotor imbalance, ε_{RG}	8 μm
Rotating seal element imbalance, ε_{rG}	5 μm
Rotor dynamic angular misalignment, χ_R	1 mrad
Rotating seal element dynamic angular misalignment, χ	0.1 mrad
Rotating seal element static angular misalignment, χ_s	0.5 mrad
Rotor external viscous damping ratio, $\zeta_\epsilon = \zeta_\gamma$	0.01
Rotor radius, R_r	100 mm
Rotor width, B_r	10 mm
Rotor-housing dry friction coefficient, μ_f	0.1
Rotor-housing clearance, δ	80 μm

11.2 Solution Method

The FMSR-ER system is simulated by solving the equations of motion numerically according to the variable-step procedures discussed in Section 9.3.2. The FMSR-ER and rotor equations of motion (Eqs. 3.104 and 4.2, respectively) are solved commensurately by coupling the equations of motion in the state space. This method allows the rotor and seal dynamics to be extracted at identical simulation time steps. An alternative approach could be to solve the rotor response independent from the seal response, and then send the rotordynamics to the seal dynamics simulation. However, the variable-step solver would then require many interpolations of the rotor response at each time step in the seal dynamics simulation, since the variable step sizes are unknown *a priori*. The cracked rotor stiffness matrix is obtained in the inertial frame using the crack-closure line approach described in Section 6.2.2, where each crack compliance is reconstructed prior to the simulation using the Fourier transform. The rotor-housing contact forces are derived using the RSCM and implemented in the equations of motion using Eqs. 7.26 - 7.31.

The FMSR-E equations of motion are then reduced to the steady-state case without inertial maneuver loads, as described in Chapter 5 (see Eqs. 5.48 - 5.57). The steady-state response is extracted by retaining a fixed number of periods following the exodus of simulation transients. The steady-state response of the undamaged rotor is used to provide the initial conditions (see Eq. 9.3), while the stationary seal element initial conditions are commensurate to the element's static deflection. The rotor and seal parameters used here are provided in Tables 8.1, 8.2 and 9.1. Other dynamic parameters used in the simulation are specified in Table 11.1. The results given here are for a thin seal and thin rotor ($I_{pr} = 8(10)^{-4}$ kg·m^2 and $I_{pR} = 0.4$ kg·m^2); similar results are obtained for the thick rotor and are omitted here for brevity. It is also important to note that this chapter is not meant to be a treatise concerning parametric studies of the FMSR-ER system; such a study is left to future works. To reiterate, the purpose here is to identify hallmark characteristics of the FMSR-ER response to multiple simultaneous faults.

11.3 Multiple Fault Results

The FMSR-ER equations of motion, including a breathing shaft crack and intermittent rotor-housing contact, are solved to obtain the steady-state response over a range of shaft speeds and crack depths. The results are summarized using bifurcation diagrams of the rotor eccentricity and stationary seal element tilt, and are provided in Figs. 11.1 - 11.4 for crack depths of 0%, 20%, 30%, and 40%, respectively. In all cases, the set-point clearance δ between the rotor and housing is assumed to be 80 μm. The bifurcation study with only a crack and no rotor-housing contact is omitted because the response is strictly period-1 (and, the rotor-housing clearance is a fundamental system attribute, and should be included for consistent comparison). In all cases shown here, the shaft speed is restricted to values beneath the first critical speed to ensure that the crack breathing model remains valid. The results presented

here are grouped by type to elicit comparison (e.g., the bifurcation diagrams are given consecutively for increasing crack depths).

Shaft speed bifurcations for the uncracked rotor are shown in Fig. 11.1 for the rotor eccentric deflection and the stationary seal element tilt. The corresponding frequency spectra are shown in Fig. 11.5, and the integer higher harmonics are extracted and plotted versus shaft speed in Fig. 11.8. These figures indicate that rotor-housing contact first appears near a shaft speed of approximately 145 rad/s. Though indiscernible on the bifurcation diagrams, the frequency domain and higher harmonics clearly indicate the sudden onset of contact once the rotor deflection exceeds the allowable clearance. Following the onset of contact, the period-1 motion persists until a shaft speed of approximately 185 rad/s, at which point the rotor bifurcates into period-2 motion. This bifurcation also manifests in the frequency domain, where fractional shaft speed harmonics appear throughout the duration of the period-2 motion. The rotor briefly returns to period-1 motion before a grazing bifurcation results in chaotic response near $\omega_r = 215$ rad/s. The chaotic region is defined by both a scattering of the Poincaré return points and broadband frequency content. The orbits and Poincaré sections at specific shaft speeds also provide useful information for understanding the fault vibration signatures. The Poincaré sections for the rotor eccentric response are shown for the uncracked rotor at several representative shaft speeds in Fig. 11.11, while the angular orbits for the stationary seal element are given at the same shaft speeds in Fig. 11.12. The Poincaré sections corroborate previous observations regarding the type of system response (e.g., period-2 motion is seen at $\omega_r = 184$ rad/s). The stationary seal element angular orbit displays obvious deviations from the circular synchronous orbit once contact occurs between the rotor and housing.

These fault signatures for the uncracked rotor provide a baseline vibration signature for comparison with the multiple fault results. Without a crack, the defining

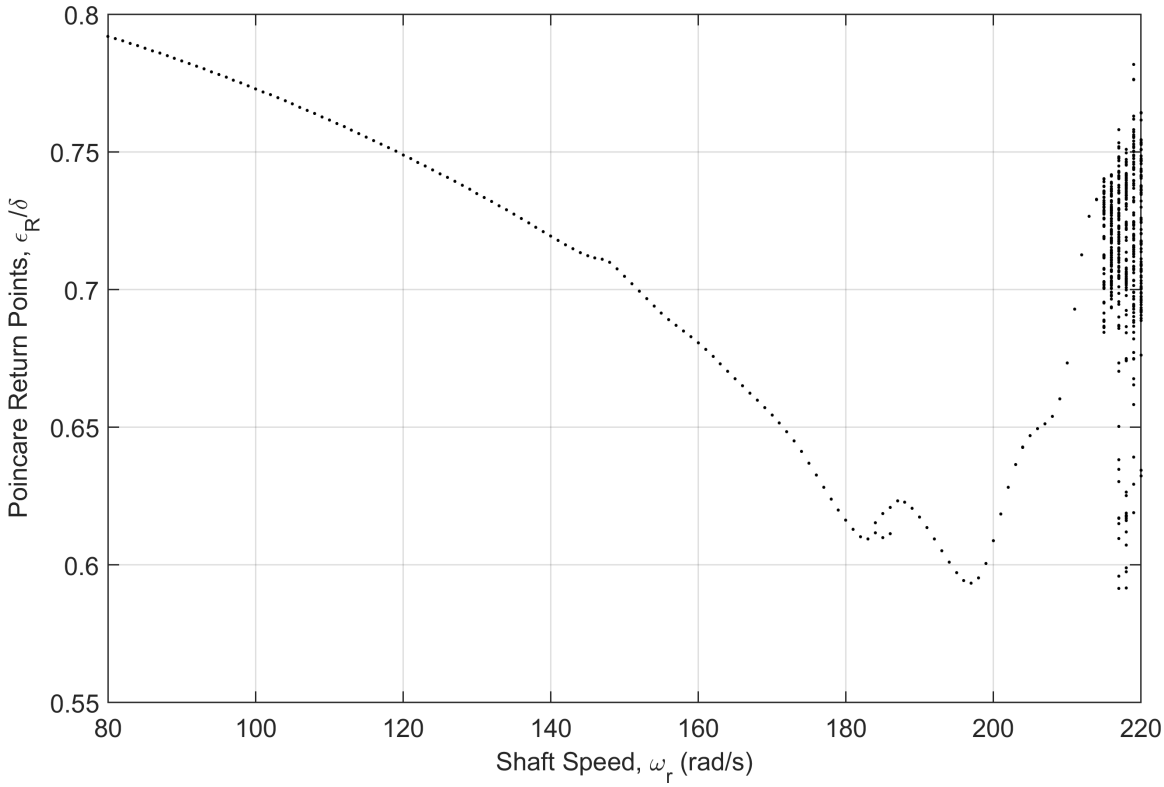

(a) Rotor eccentricity

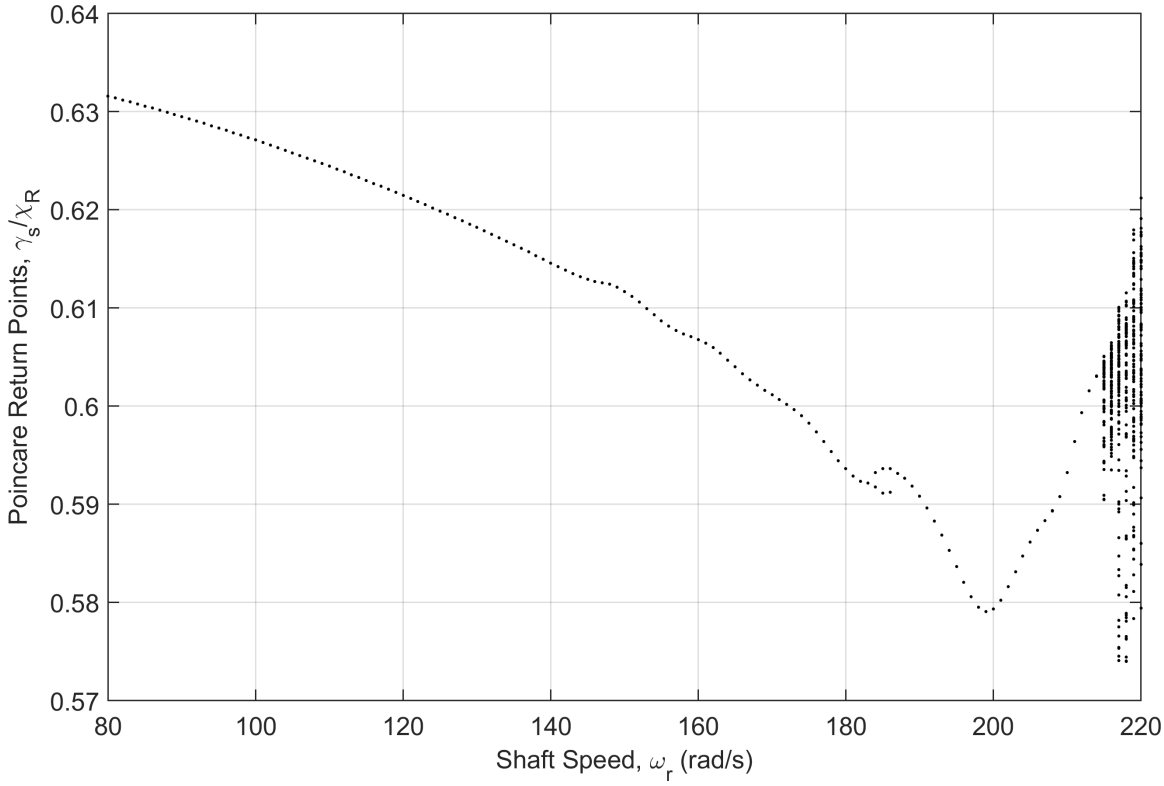

(b) Stationary seal element tilt

Figure 11.1: Shaft speed bifurcations of the FMSR-ER system with an uncracked rotor (a = 0%, $\delta = 80$ μm).

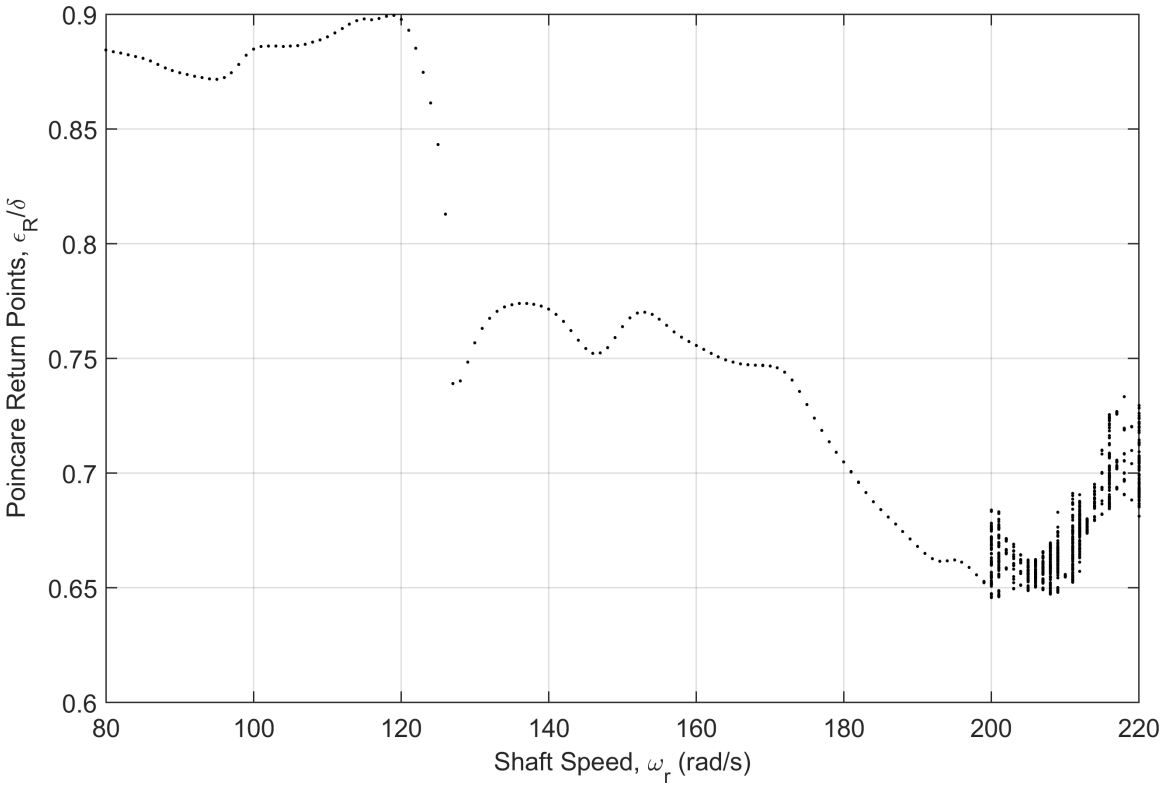

(a) Rotor eccentricity

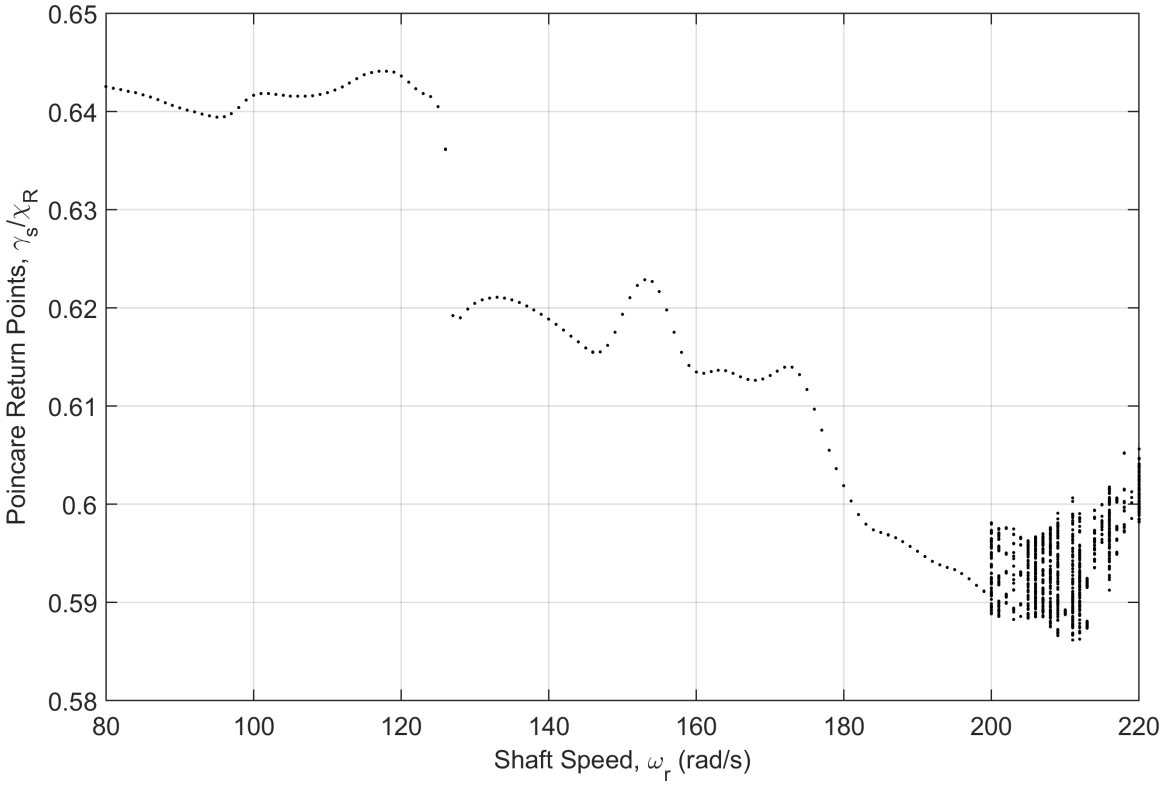

(b) Stationary seal element tilt

Figure 11.2: Shaft speed bifurcations of the FMSR-ER system with a 20% shaft crack (a = 20%, $\delta = 80$ μm).

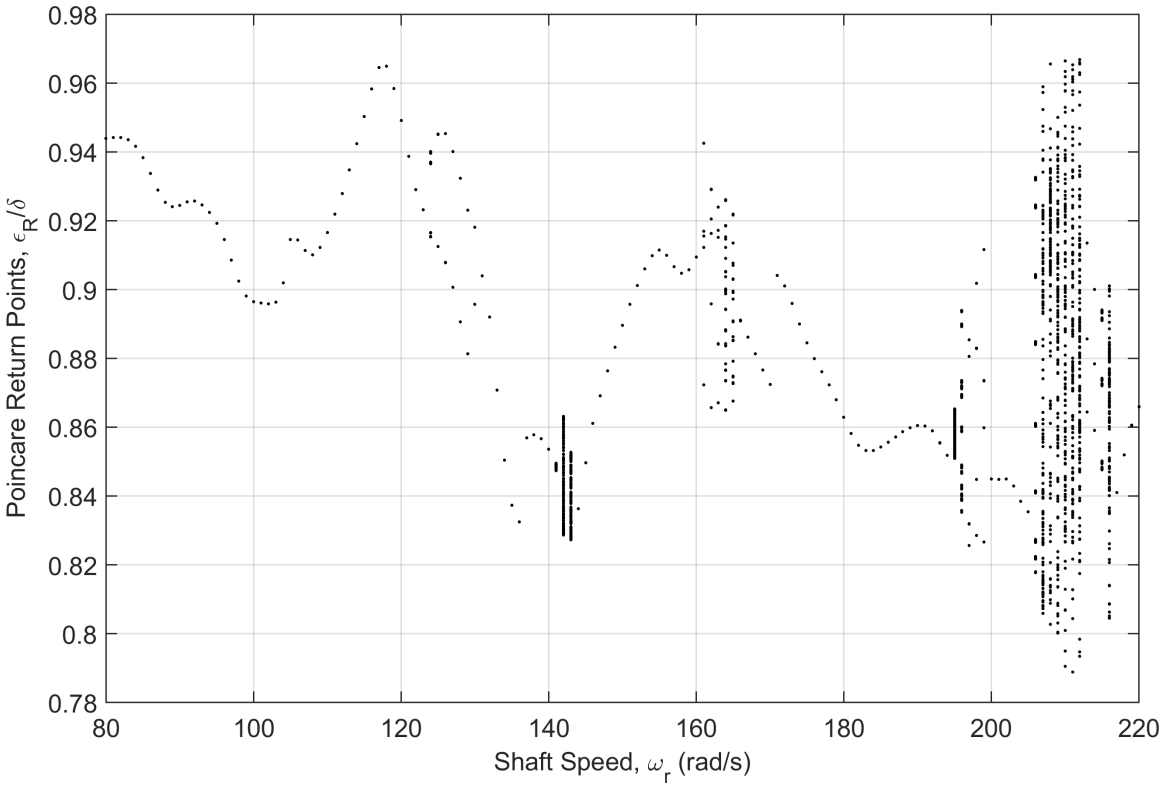

(a) Rotor eccentricity

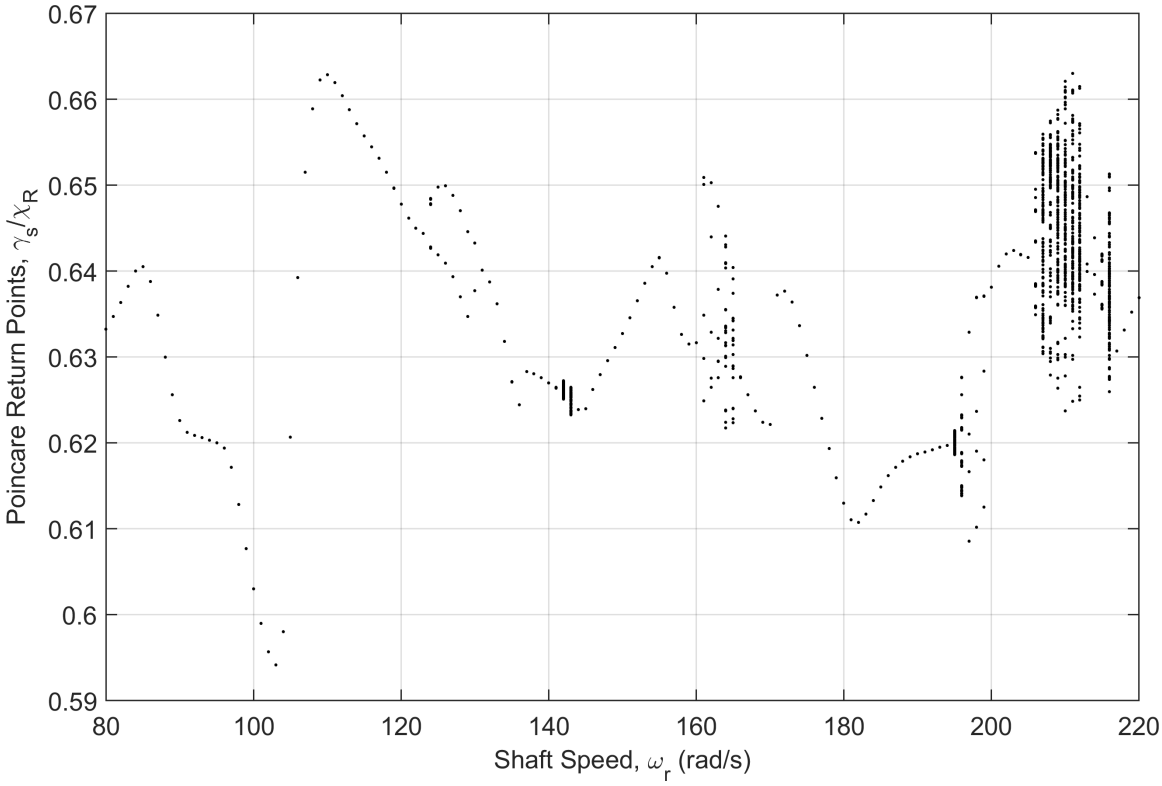

(b) Stationary seal element tilt

Figure 11.3: Shaft speed bifurcations of the FMSR-ER system with a 30% shaft crack (a = 30%, $\delta = 80$ μm).

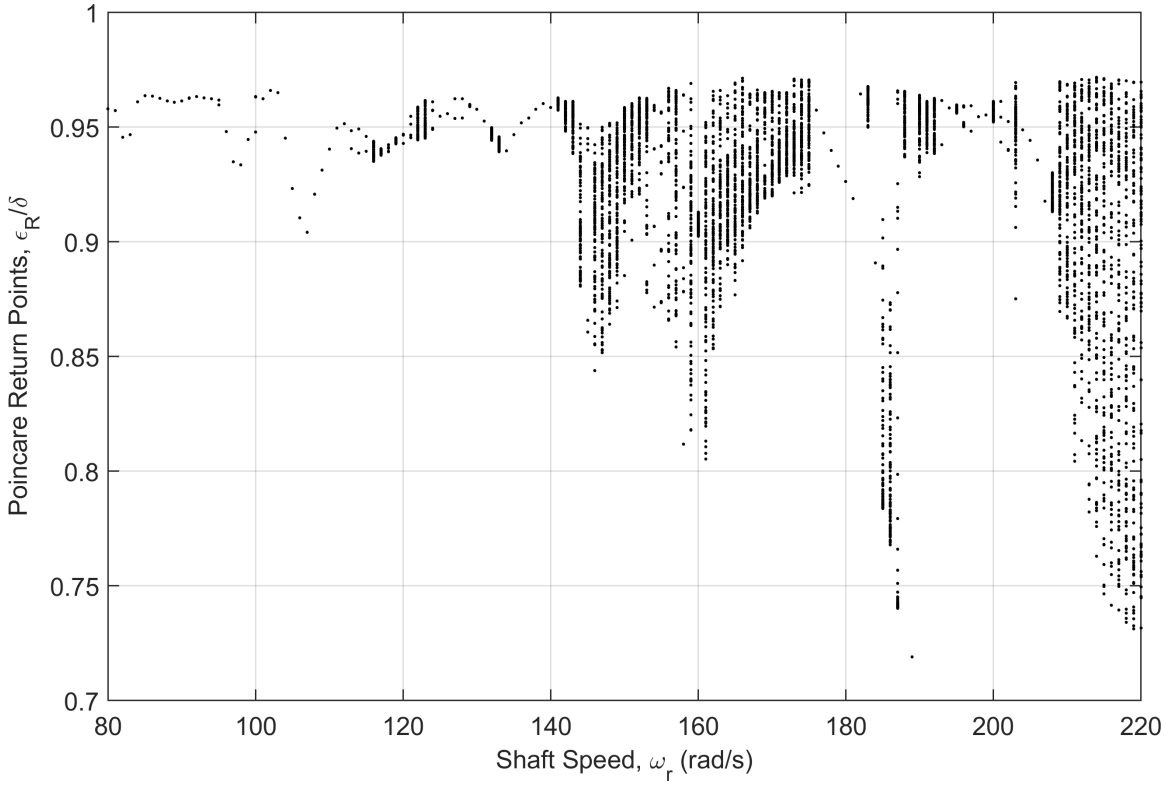

(a) Rotor eccentricity

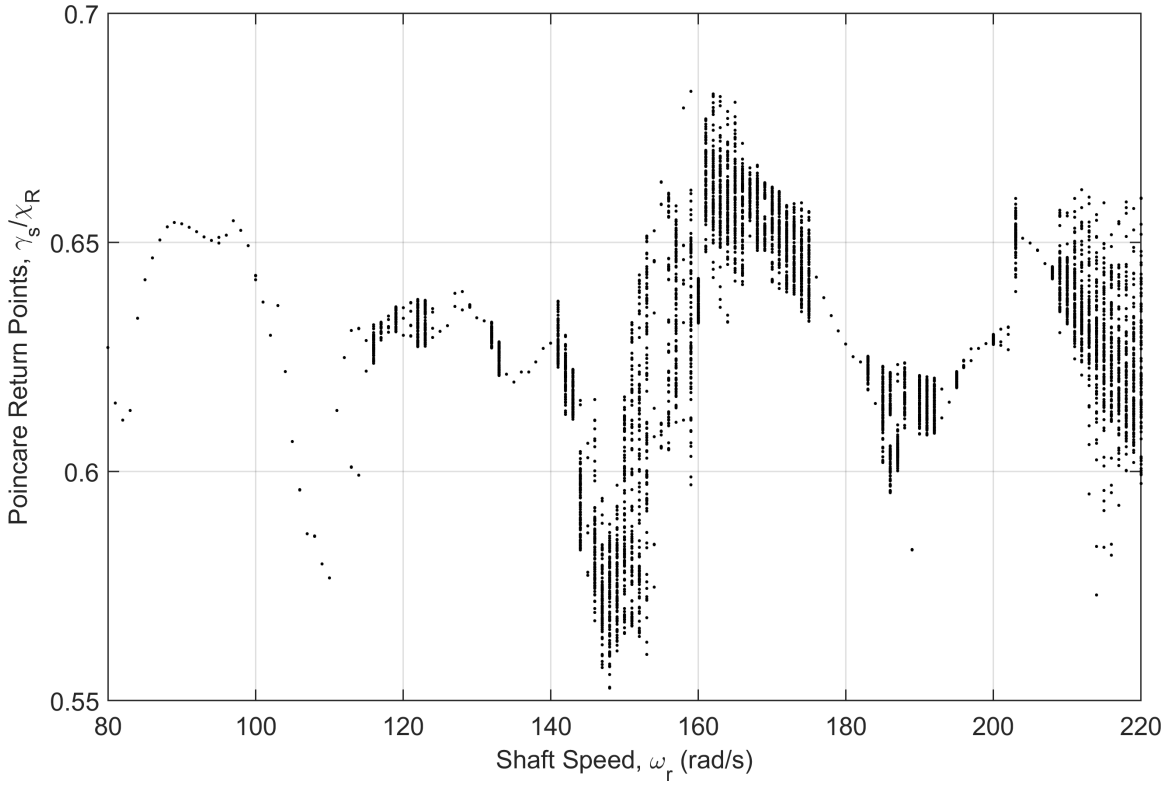

(b) Stationary seal element tilt

Figure 11.4: Shaft speed bifurcations of the FMSR-ER system with a 40% shaft crack (a = 40%, $\delta = 80$ μm).

feature of rotor-housing contact is the sudden appearance of integer shaft speed harmonics in the FMSR-ER response at the onset of contact. Also, it is once again important to emphasize that these fault signatures appear in the stationary seal element tilt, thus reinforcing the efficacy of using the stationary seal element as a surrogate rotordynamic vibration monitor.

The FMSR-ER dynamic response changes significantly when a crack of 20% depth is included in the system. The bifurcation diagrams shown in Fig. 11.2 display a pronounced change near approximately $\omega_r = 125$ rad/s when the rotor begins to contact the housing. Also, chaotic motion appears earlier in the response profile ($\omega_r = 200$ rad/s) when compared to the uncracked rotor ($\omega_r = 220$ rad/s). These distinctions are also observed in the frequency spectrum provided in Fig. 11.6 (the corresponding shaft speed harmonics are extracted and displayed in Fig. 11.9). When the breathing crack is included in the system, the integer shaft speed harmonics are always present, irrespective of shaft speed. In addition, these crack-induced harmonics generate sub-synchronous critical speeds in the system response. As expected, the rotor orbit prior to the onset of rotor-housing contact is dictated by the cracked rotor response, as shown in Figs. 11.13 and 11.14 (the Poincaré section is provided separately for comparison). Prior to rotor-housing contact, the rotor eccentric orbit is defined by a smoothly-varying orbit with several prominent lobes caused by the crack higher harmonic oscillations. Once contact occurs ($\omega_r = 150$ rad/s), the rotor orbit clearly shows sharp transitions caused by rebound from the housing. Likewise, the stationary seal element angular orbit again shows significant deviations from the synchronous orbit.

In this case (a = 20%), the breathing crack and rotor-housing contact are distinguished by the permanency of their respective vibration signatures. The crack-induced harmonics are always present in the response, regardless of the shaft speed. Still, the crack only generates integer shaft speed harmonics; once the shaft speed is

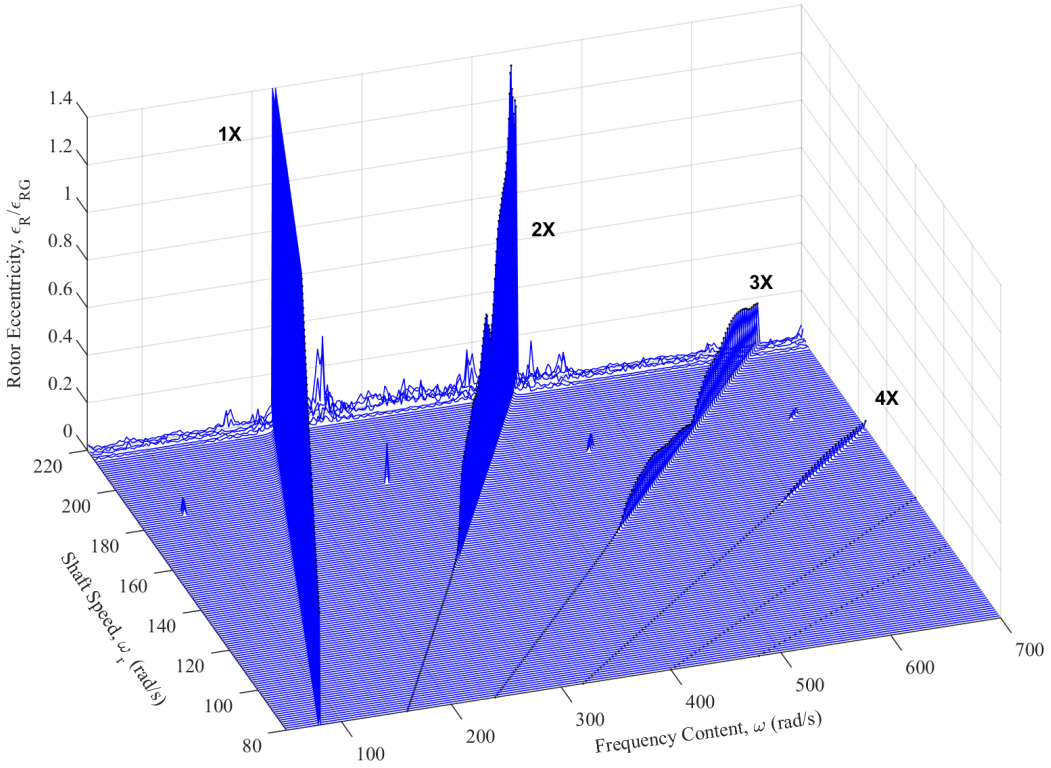

(a) Normalized rotor eccentric response

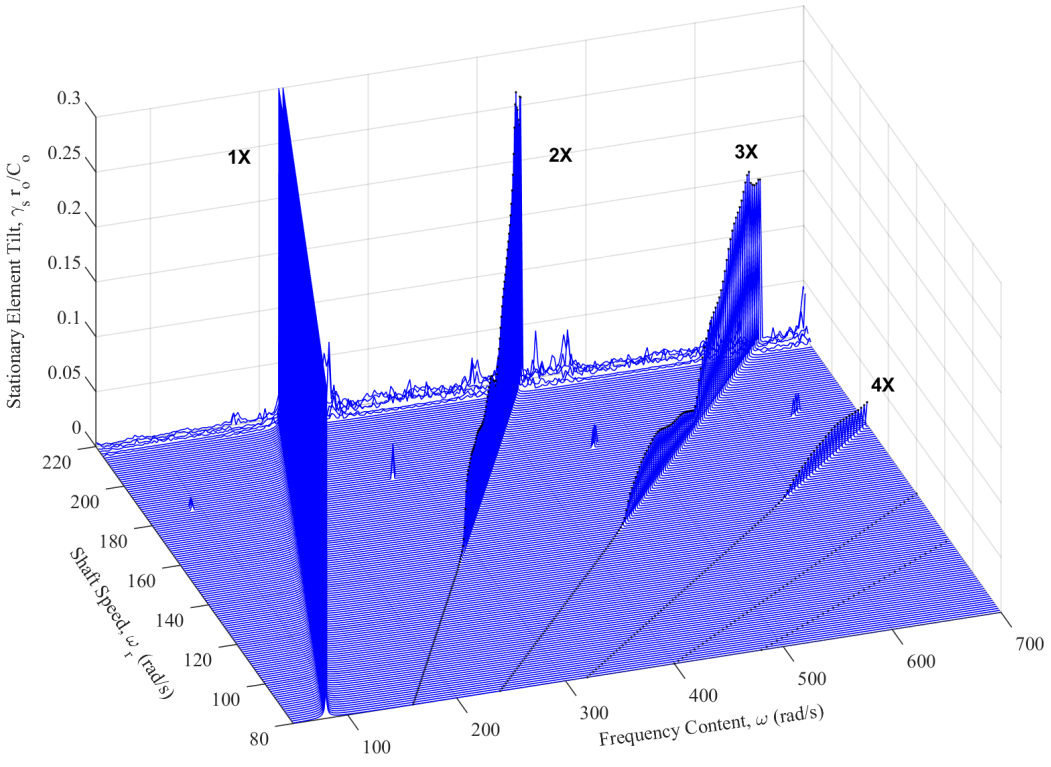

(b) Normalized stationary seal element tilt

Figure 11.5: Frequency spectrum: Rotor-housing contact in the uncracked rotor (i.e., a = 0%).

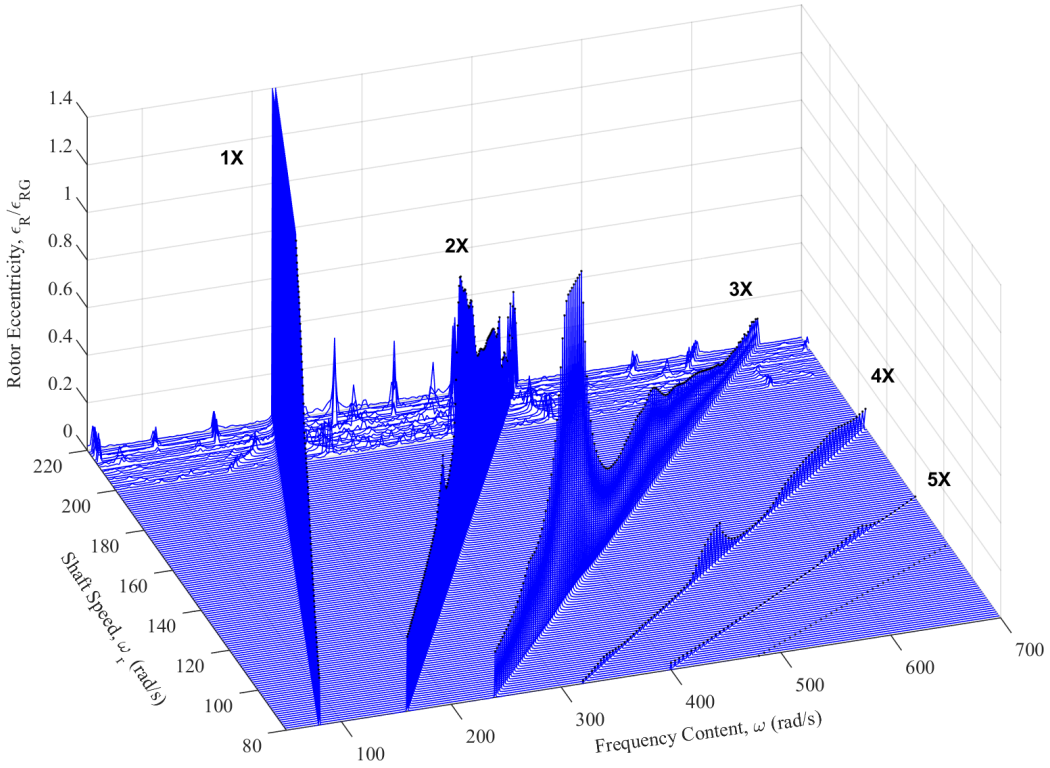

(a) Normalized rotor eccentric response

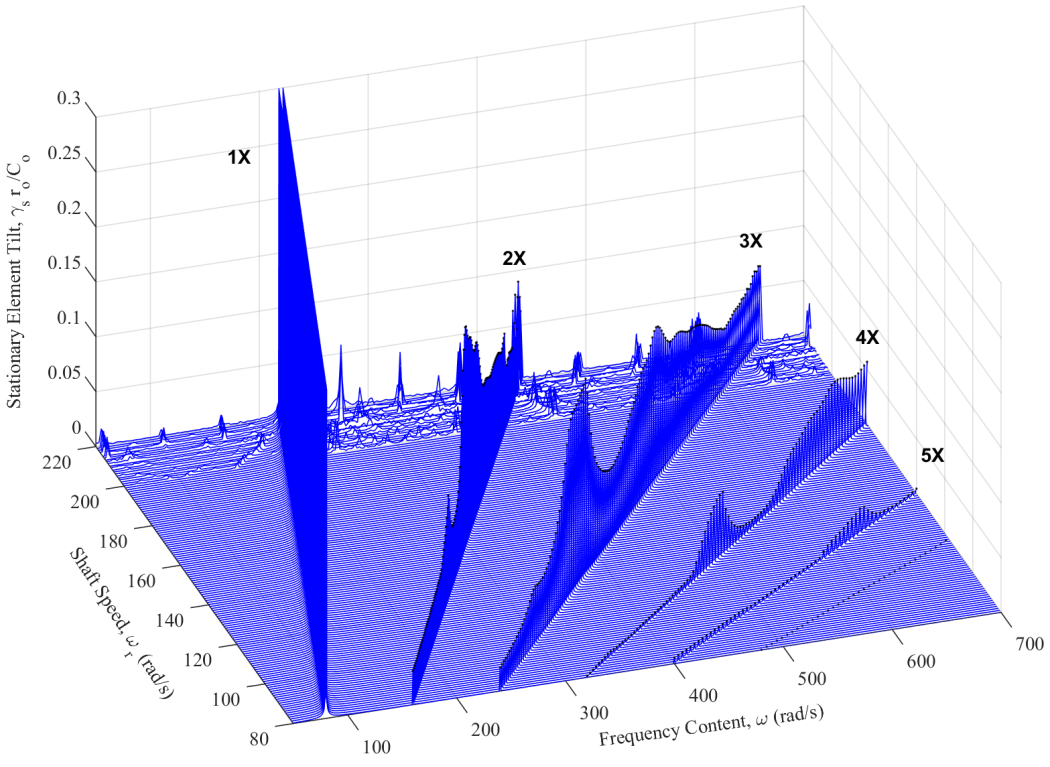

(b) Normalized stationary seal element tilt

Figure 11.6: Frequency spectrum: 20% breathing crack and rotor-housing contact.

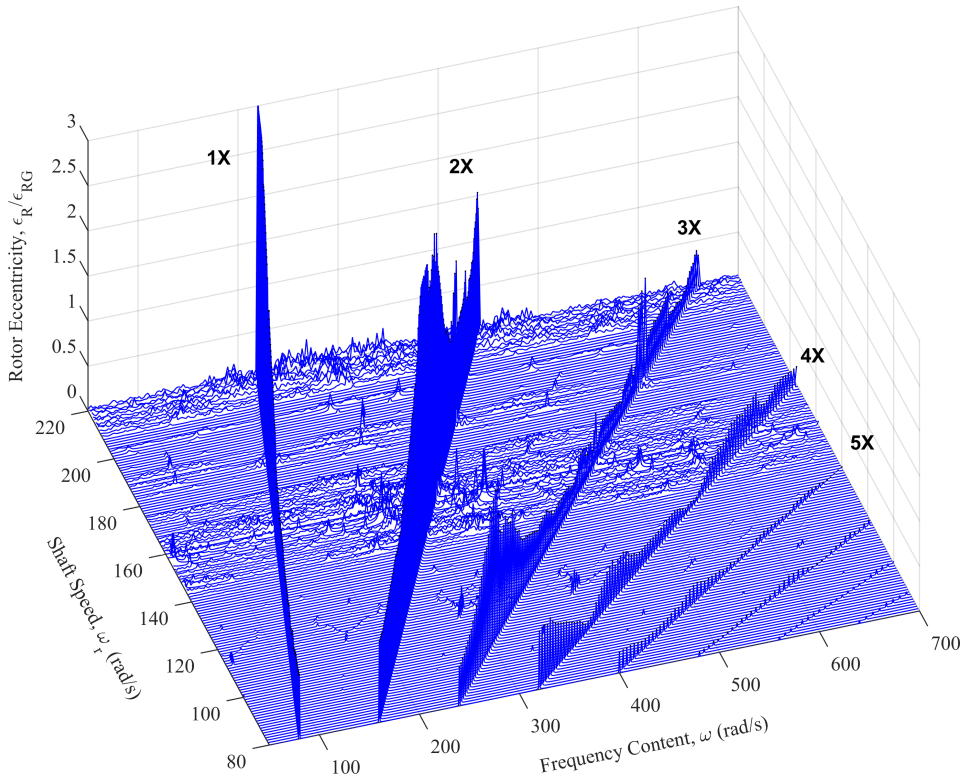

(a) Normalized rotor eccentric response

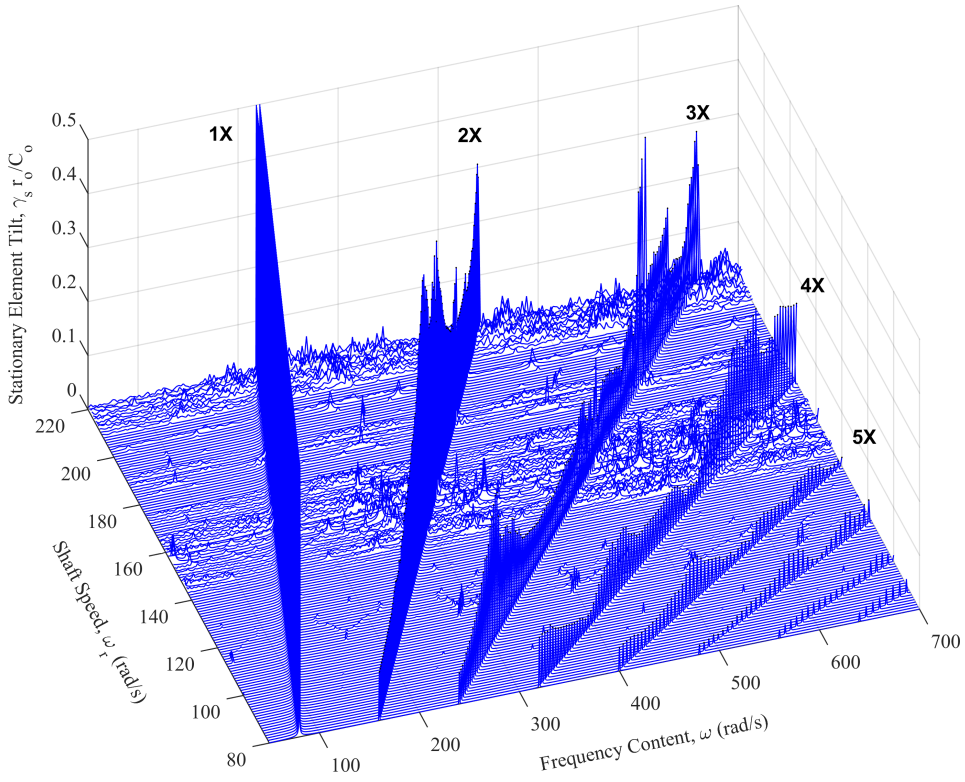

(b) Normalized stationary seal element tilt

Figure 11.7: Frequency spectrum: 40% breathing crack and rotor-housing contact.

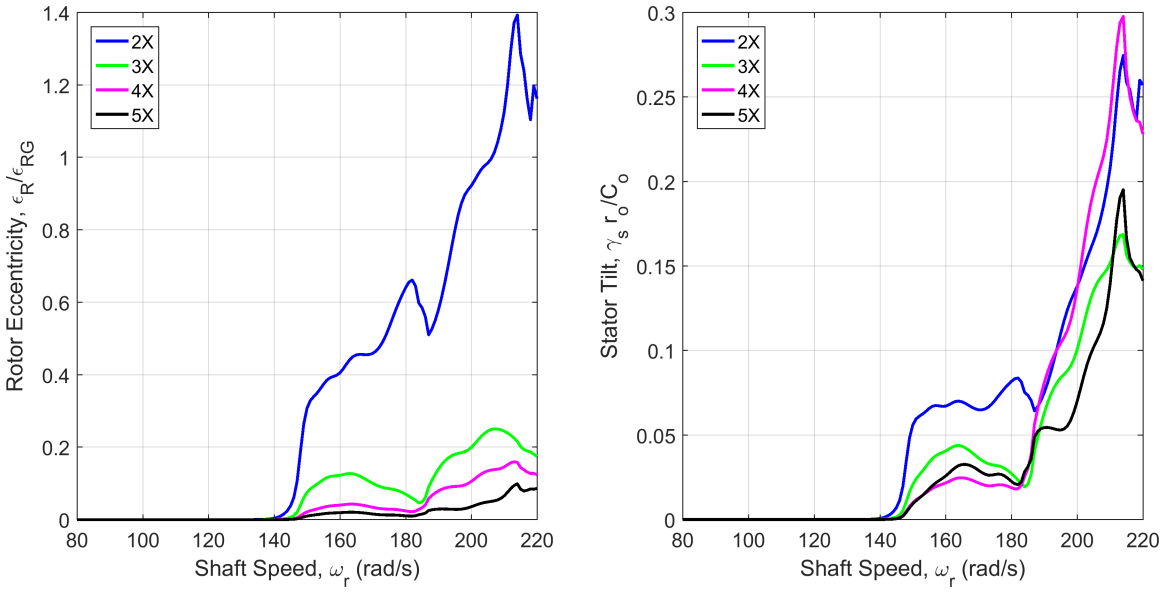

Figure 11.8: Uncracked Rotor: Magnitudes of the shaft speed harmonics in the rotor eccentric response and the stationary seal element tilt.

increased, the appearance of more complex dynamic responses highlights the simultaneous appearance of rotor-housing contact.

Similar conclusions are also reached for the case where the rotor crack reaches 30% and 40% depth. Bifurcation diagrams for these crack depths are given in Figs. 11.3 and 11.4, respectively. In both cases, the bifurcation diagrams show a prominent increase in complexity when compared to the baseline bifurcation diagram for the uncracked rotor. The bifurcation diagrams indicate that chaotic and quasiperiodic responses occur for much lower shaft speeds when compared to the uncracked rotor. The crack causes a significant reduction in rotor stiffness, and thus, precipitates contact at lower shaft speeds. The frequency domain and associated shaft speed harmonics are shown for the 40% depth crack in Figs. 11.7 and 11.10 (similar results for the 30% depth crack are omitted for brevity). The frequency domain again shows prominent integer shaft speed harmonics, sub-synchronous critical speeds, and broadband frequency content. Once again, Figs. 11.16 and 11.17 highlight the appearance of periodic, quasiperiodic, and chaotic responses in the rotor and seal dynamics.

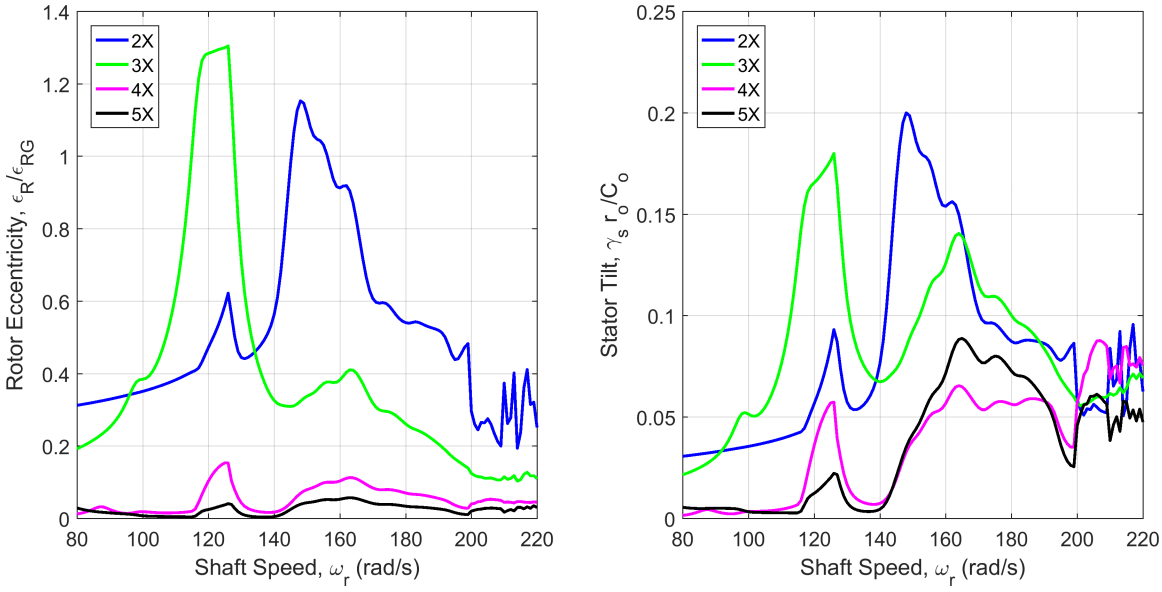

Figure 11.9: 20% Crack: Magnitudes of the shaft speed harmonics in the rotor eccentric response and the stationary seal element tilt.

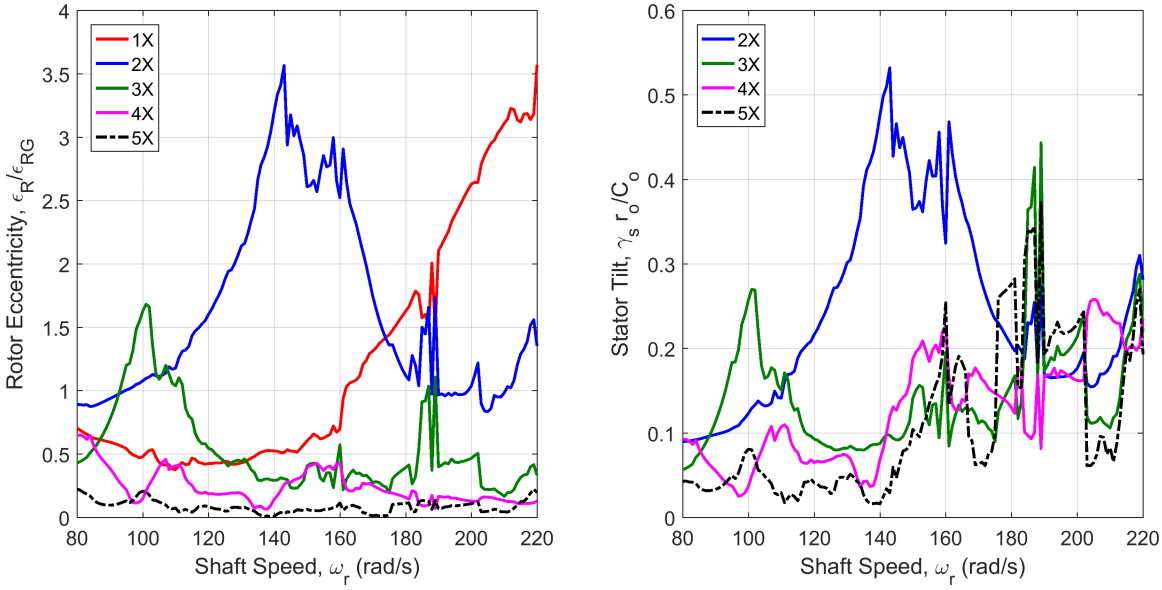

Figure 11.10: 40% Crack: Magnitudes of the shaft speed harmonics in the rotor eccentric response and the stationary seal element tilt.

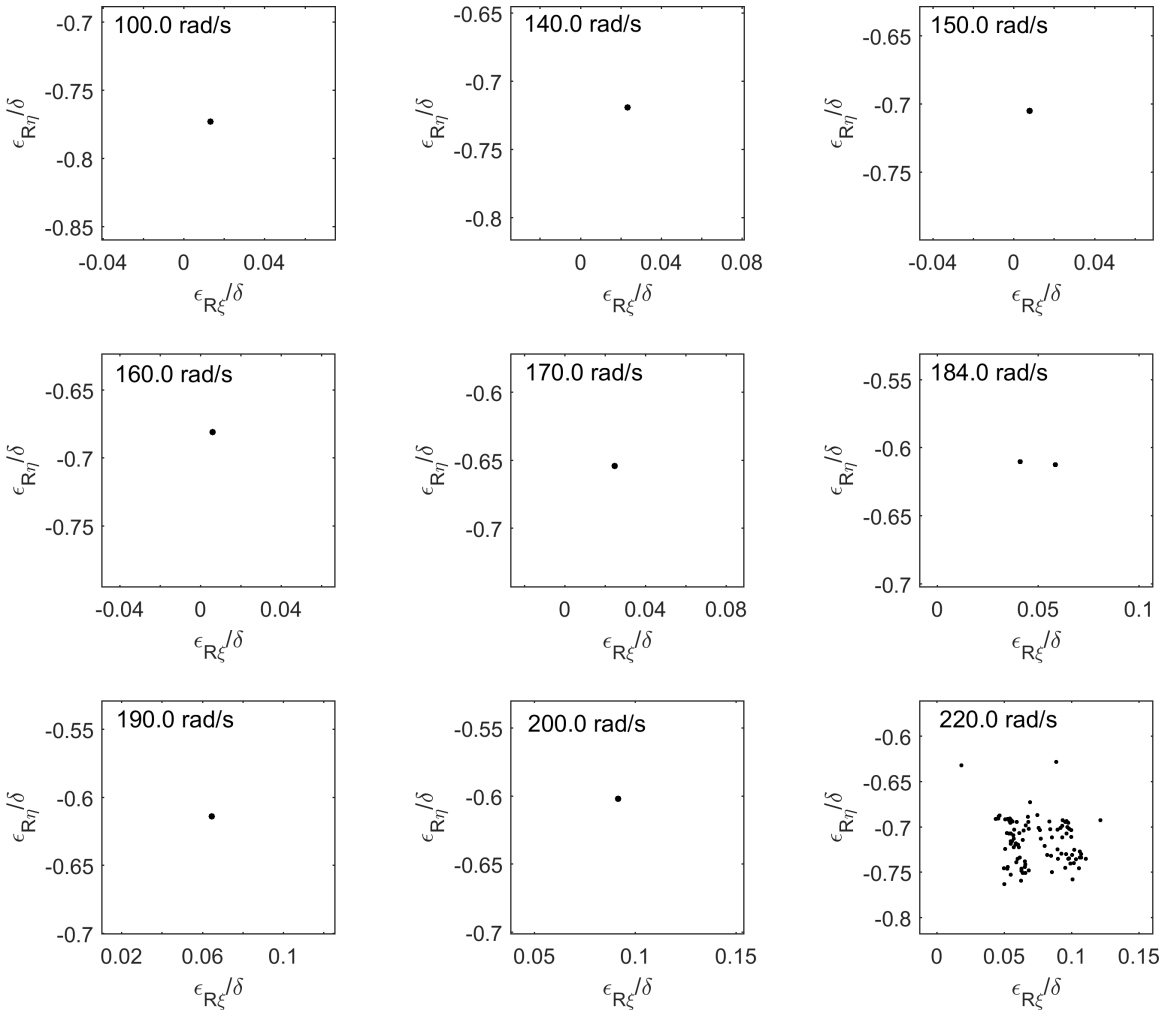

Figure 11.11: Poincare Section: Rotor eccentric response corresponding to the uncracked rotor (a = 0%).

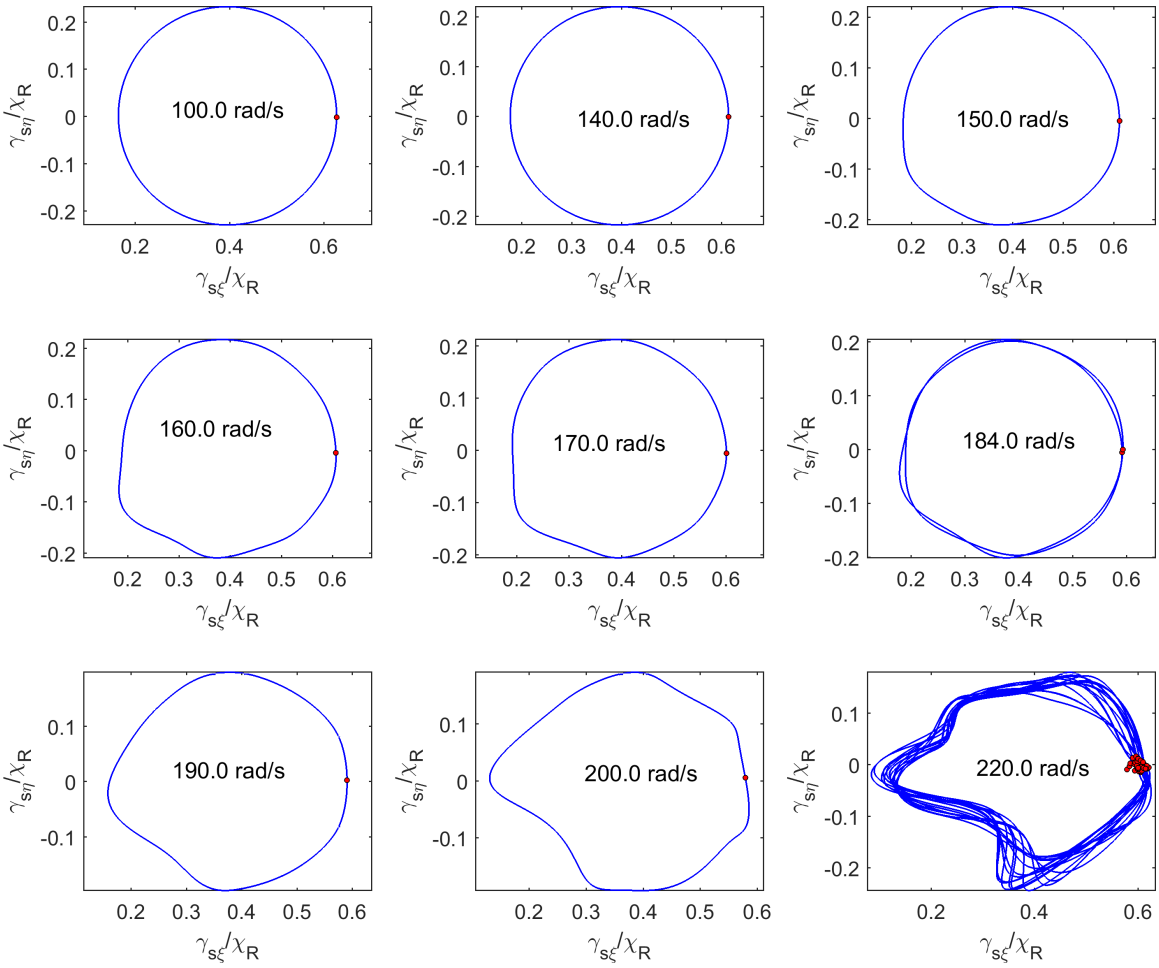

Figure 11.12: Stationary seal element angular orbits corresponding to the uncracked rotor (a = 0%).

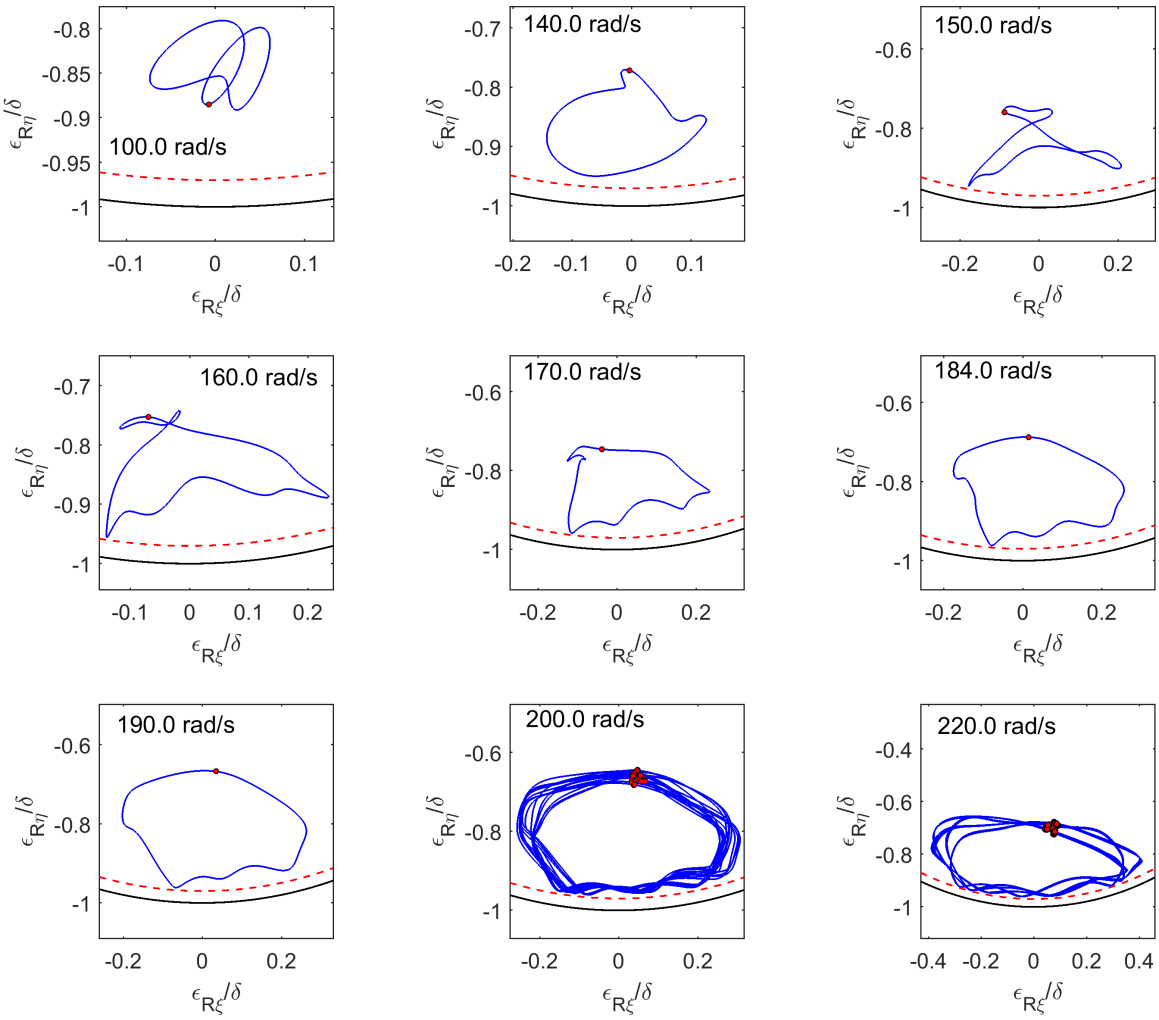

Figure 11.13: Rotor eccentric orbits (a = 20%).

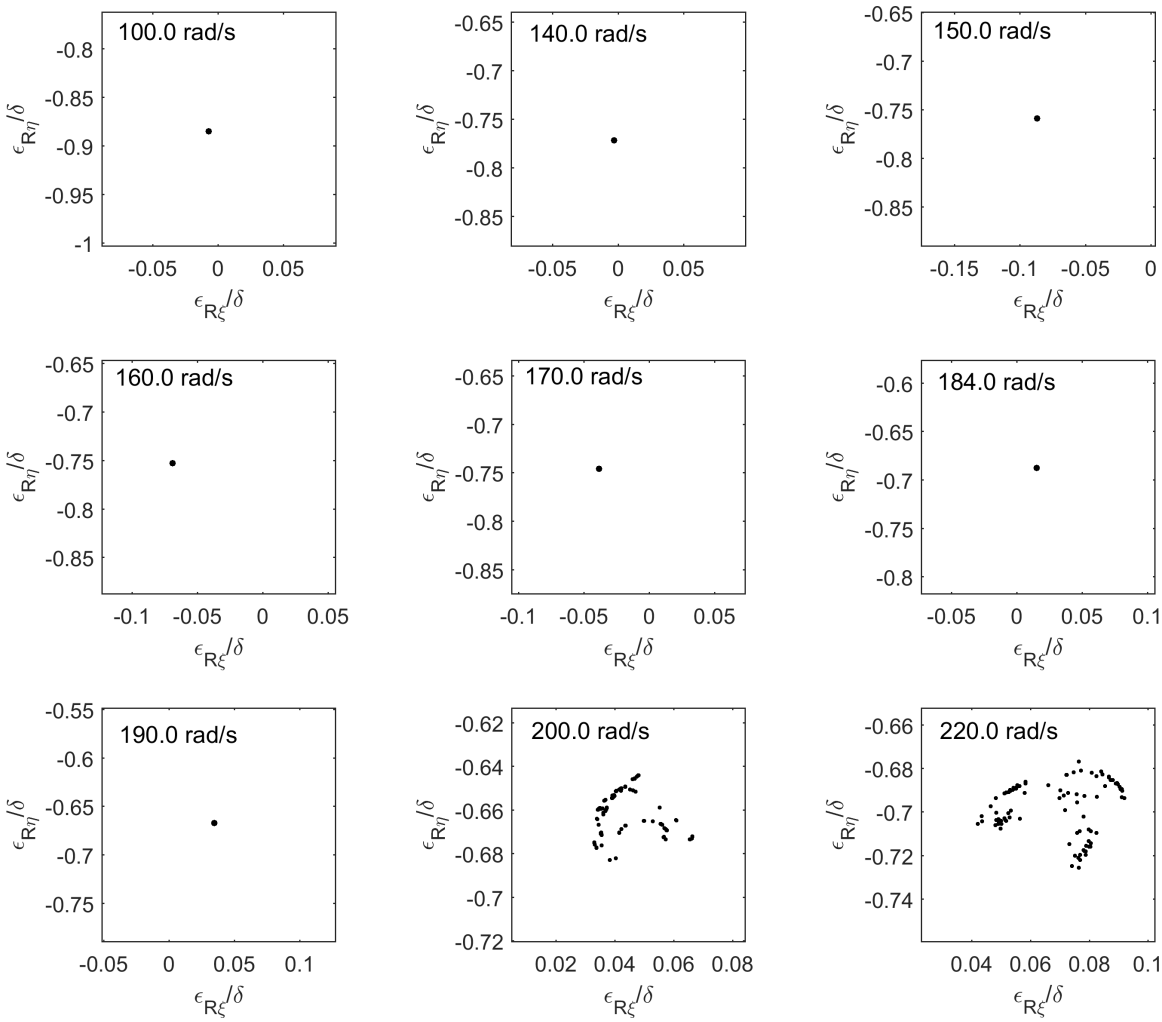

Figure 11.14: Poincare Section: Rotor eccentric response (a = 20%).

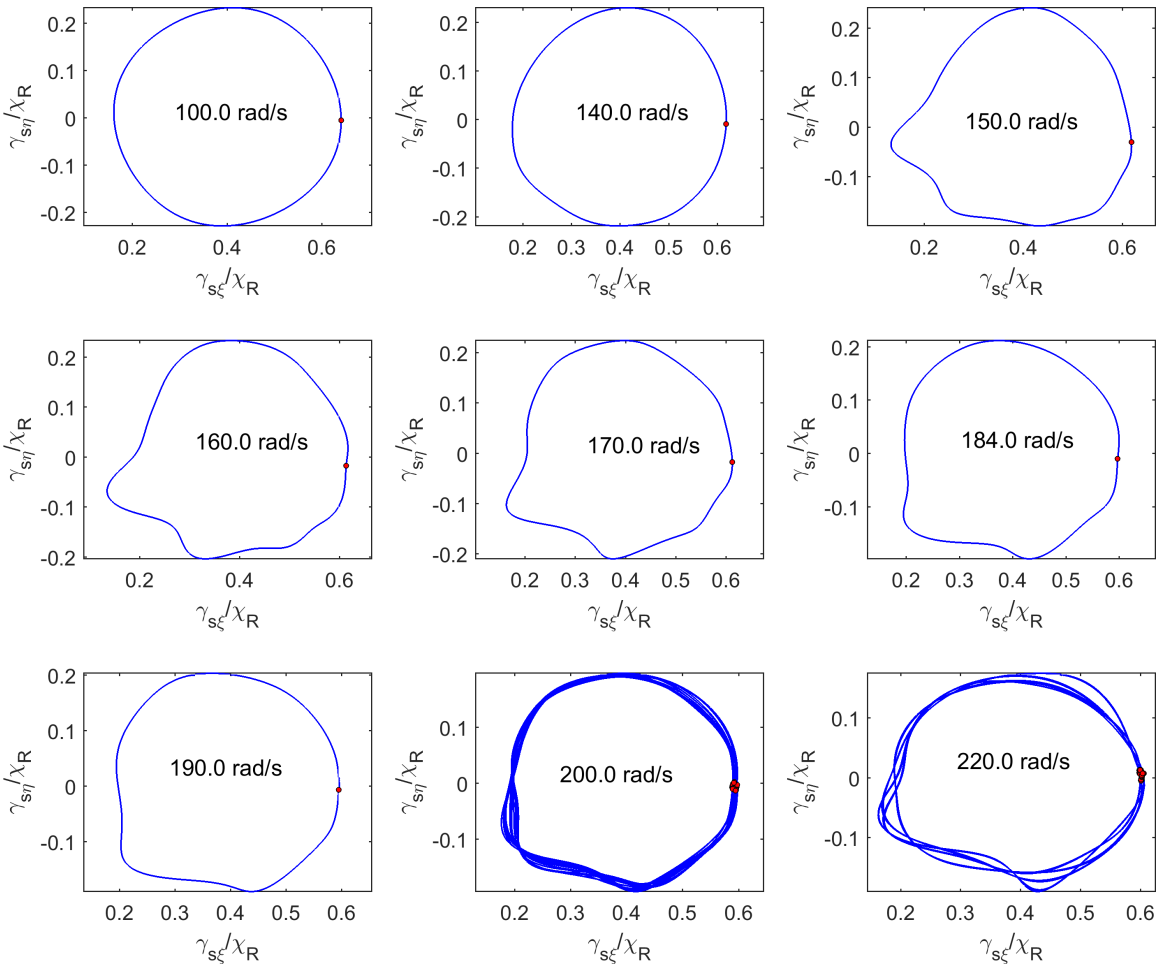

Figure 11.15: Stationary seal element angular orbits (a = 20%).

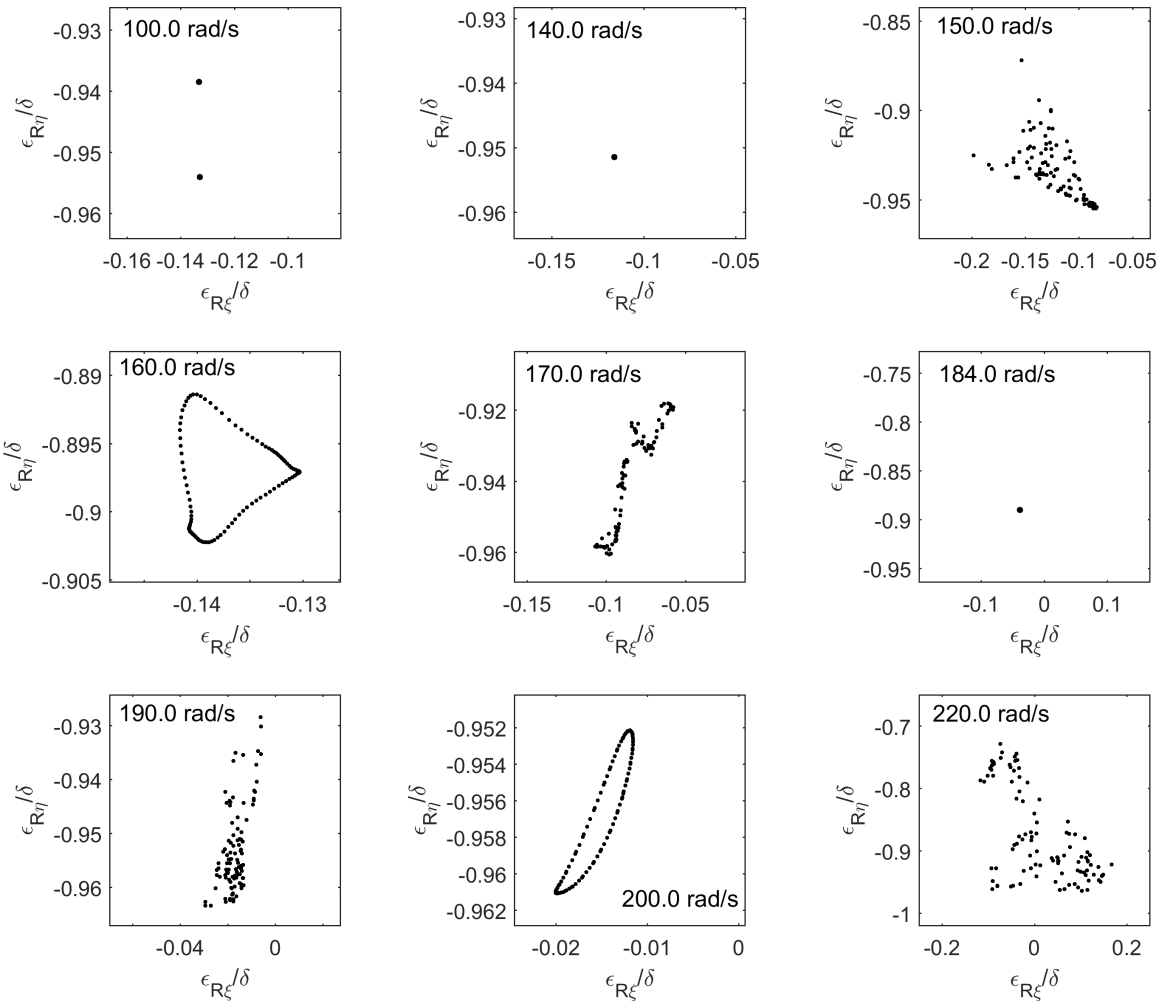

Figure 11.16: Poincare Section: Rotor eccentric response (a = 40%).

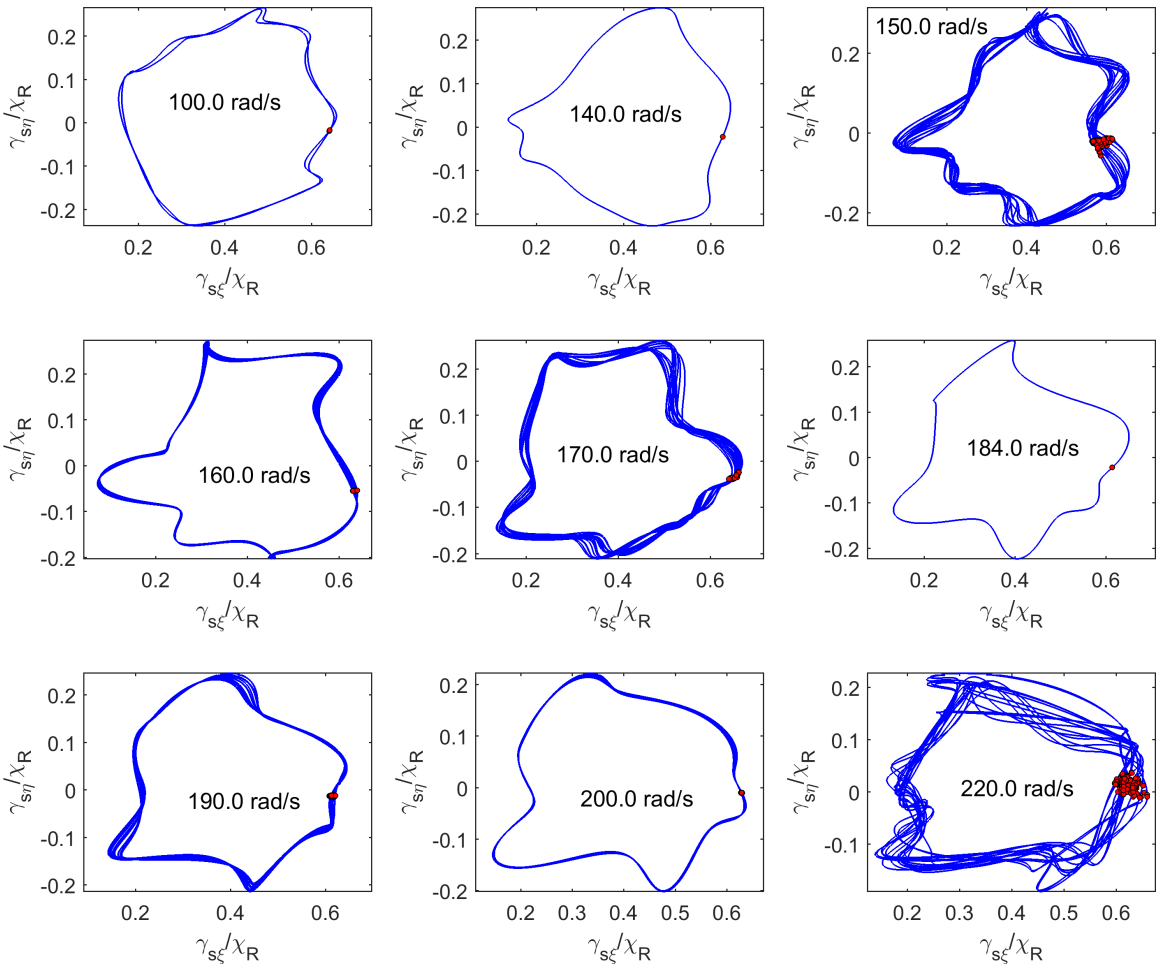

Figure 11.17: Stationary seal element angular orbits (a = 40%).

11.4 Time-Energy-Frequency Domain

The FMSR-ER response is now analyzed using the HHT to obtain the time-energy-frequency spectra associated with various multiple fault scenarios. The HHT is first calculated for the uncracked rotor at a shaft speed that gives chaotic response via rotor-housing contact (ω_r = 220 rad/s). The rotor eccentric response is shown in Fig. 11.18, and the stationary seal element angular response is provided in Fig. 11.19. As expected from similar results presented in Chapter 10, the rotor eccentric response is primarily characterized by two different contributions. The first contribution represents a concentration of energy near the synchronous frequency, and is characterized by nearly-constant instantaneous frequency and amplitude. The second contribution is directly related to rotor-housing impact, and is characterized by sudden increases in instantaneous frequency at each occurrence of rotor-housing impact. The stationary seal element angular response is defined by a dominant component whose instantaneous frequency fluctuates between half and twice the shaft speed.

Including a relatively shallow rotor breathing crack (a = 20%) results in little change in the time-energy-frequency spectrum. The results for this case are shown in Figs. 11.20 and 11.21 for the rotor eccentric response and stationary seal element angular response, respectively. Again, the rotor eccentric response is primarily composed of a synchronous component with nearly constant instantaneous amplitude and frequency. The rotor eccentric response time-energy-frequency spectrum appears to indicate a small increase in energy near the 2X harmonic because of the crack, though the difference is small when compared to the uncracked case shown in Fig. 11.18. The stationary seal element angular response is nearly indistinguishable from the uncracked case (see Fig. 11.19).

The time-energy-frequency spectrum displays significant differences from the reference case when the crack depth is increased to 40%, for both the rotor eccentric

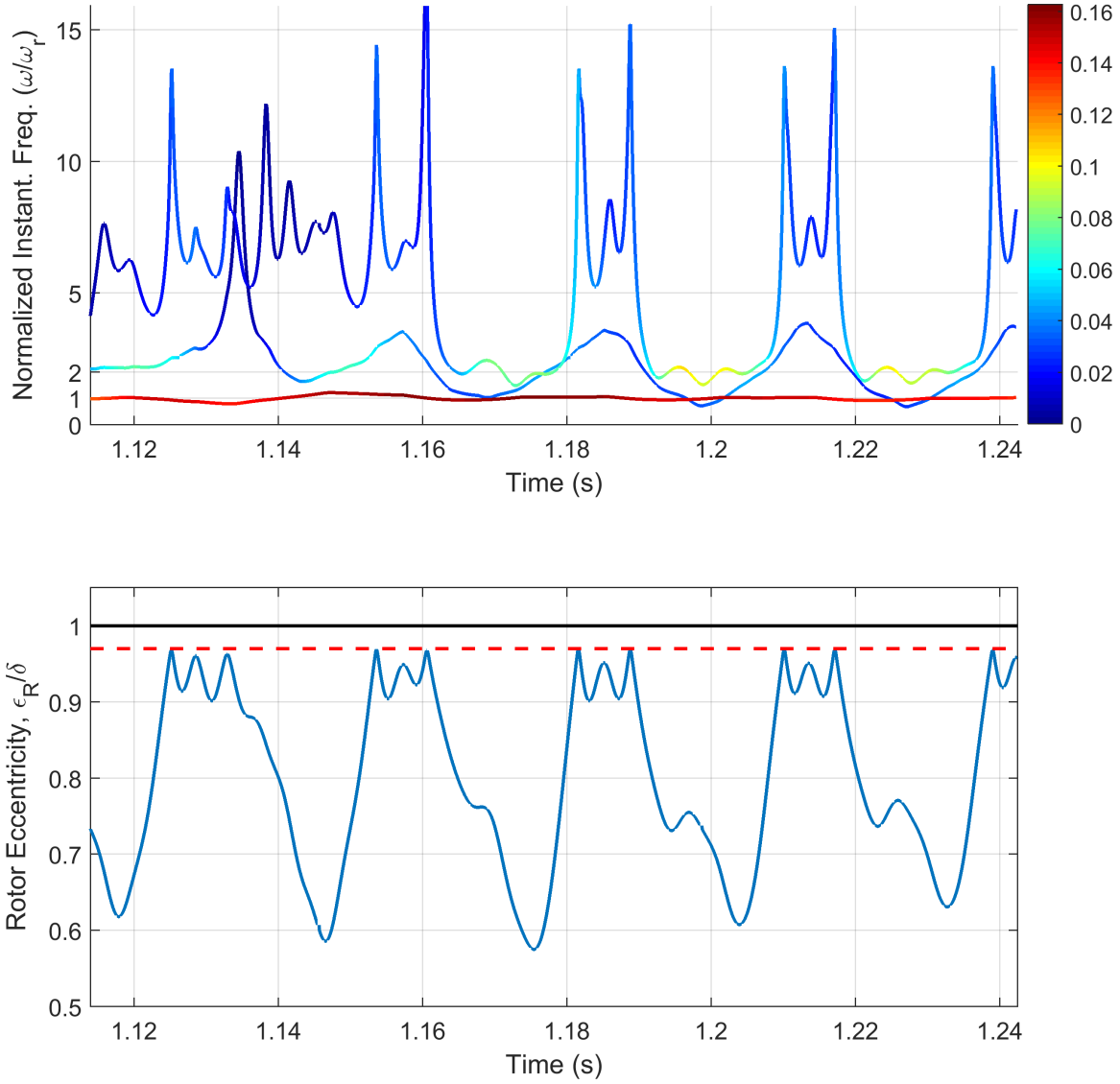

Figure 11.18: Rotor eccentricity time-frequency-energy spectrum: Uncracked rotor with lateral rotor-housing contact ($\delta = 80\mu$m, a = 0%, $\omega_r = 220$ rad/s).

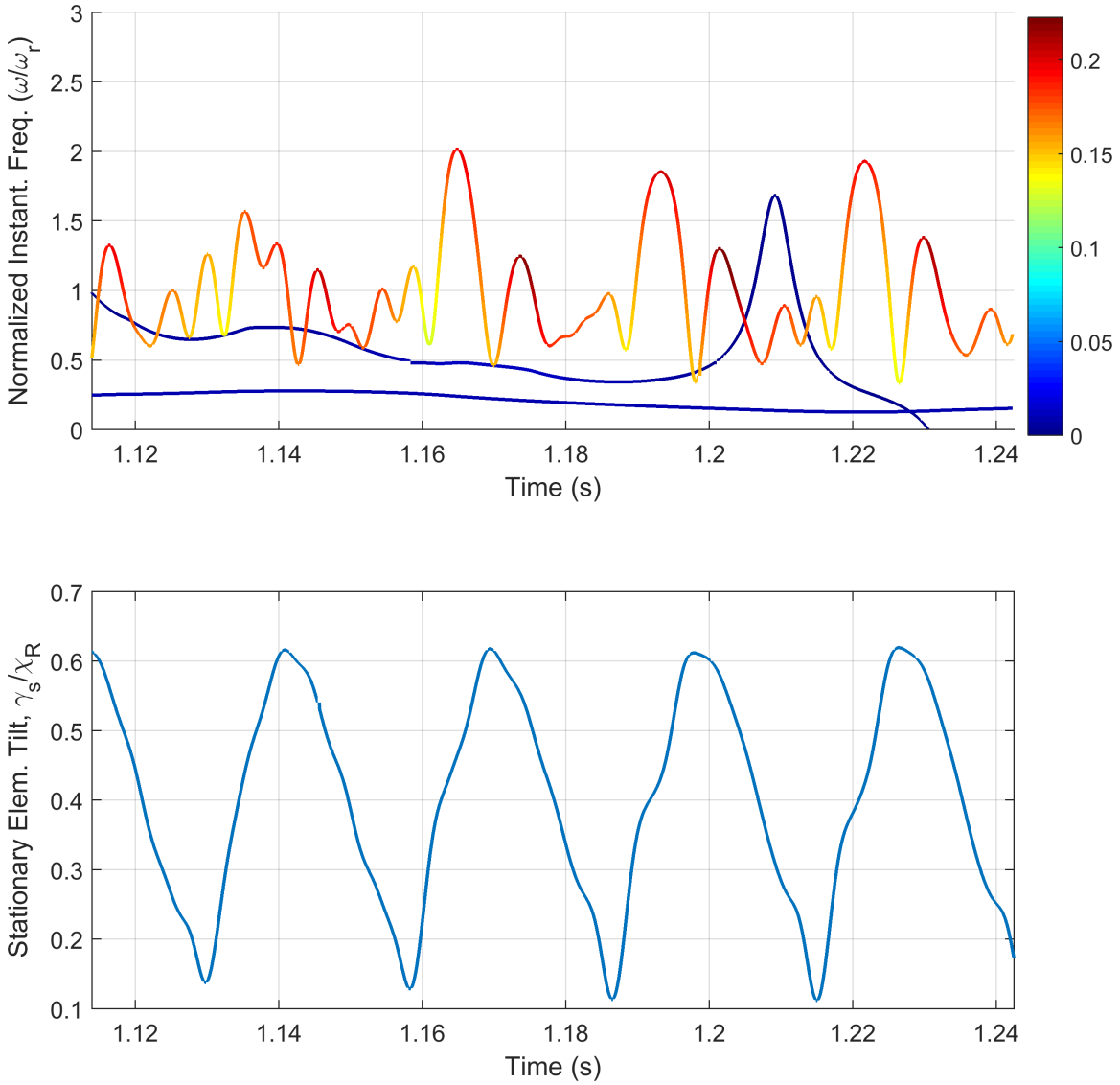

Figure 11.19: Stationary seal element time-frequency-energy spectrum: Uncracked rotor with lateral rotor-housing contact ($\delta = 80\mu$m, a = 0%, $\omega_r = 220$ rad/s).

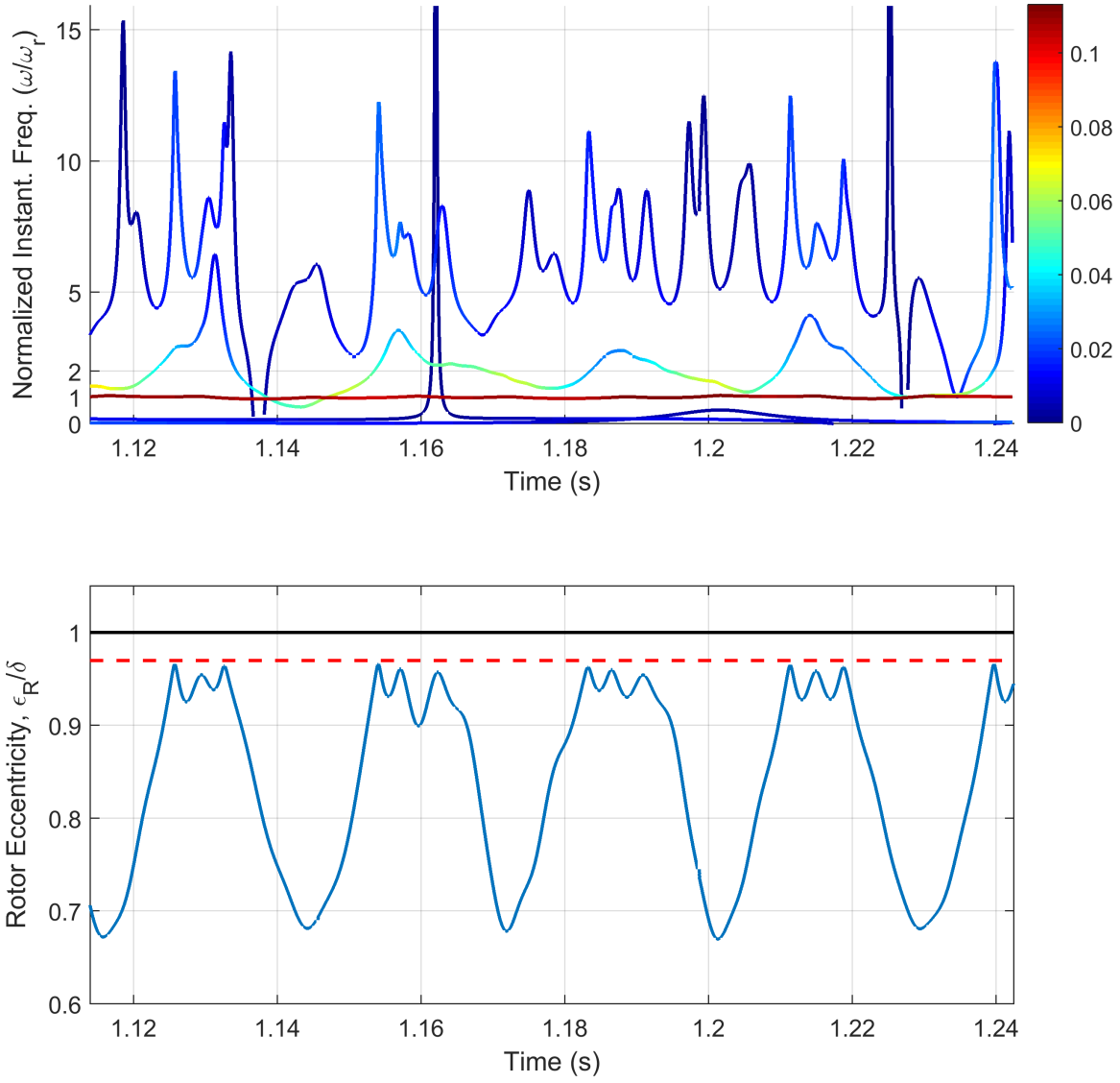

Figure 11.20: Rotor eccentricity time-frequency-energy spectrum: Cracked rotor with lateral rotor-housing contact ($\delta = 80\mu$m, a = 20%, $\omega_r = 220$ rad/s).

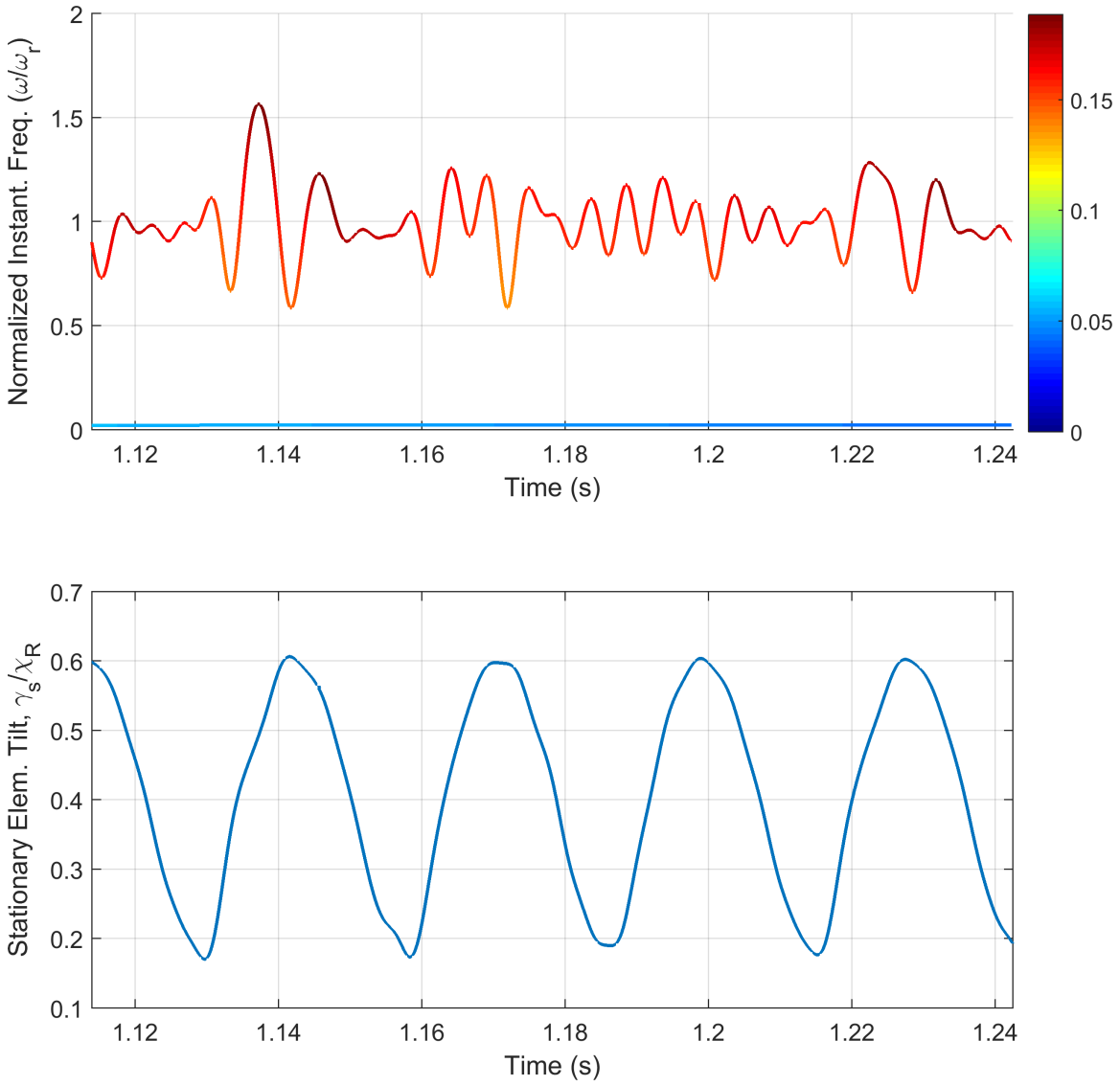

Figure 11.21: Stationary seal element time-frequency-energy spectrum: Cracked rotor with lateral rotor-housing contact ($\delta = 80\mu$m, a = 20%, $\omega_r = 220$ rad/s).

response and stationary seal element angular response (Figs. 11.22 and 11.23, respectively). The rotor eccentric response is no longer dominated by the synchronous component, and instead contains a significant increase in energy near the 2X harmonic (while still retaining the hallmark characteristic of rotor-housing impact, the sudden increases in instantaneous frequency). The increased severity of rotor-housing impact caused by the crack also causes the stationary seal element response to accrue an additional component beyond the synchronous frequency. This additional component is directly attributable to rotor-housing impact occurrences (i.e., it displays sudden increases in instantaneous frequency at each instance of contact).

Similar responses are also provided for a shaft speed in the vicinity of the 1/2 critical speed corresponding to a rotor crack with 40% depth ($\omega_r = 160$ rad/s). The reference uncracked response is shown first in Figs. 11.24 and 11.25, for the rotor eccentric response and stationary seal element angular response, respectively. The time-energy-frequency spectrum for both responses is dominated again by the synchronous frequency, though the rotor eccentric response contains local increases in instantaneous frequency caused by rotor-housing impact. When the 40% crack is included in the simulation (Figs. 11.26 and 11.27), the energy in the rotor eccentric response shifts primarily to a region near the 2X and 3X frequencies. However, the stationary seal element response is still primarily dictated by the synchronous component, with a small contribution from rotor-housing impact.

The results from the HHT analysis indicate several conclusions regarding multiple fault detection using non-stationary signal processing techniques. First, the breathing shaft crack is nearly indistinguishable from rotor-housing contact for shallow cracks when only a single shaft speed is considered. As the crack depth increases, a prominent shift in the signal energy occurs, resulting in larger instantaneous amplitudes (i.e., energy) near the 2X and 3X frequencies. The second conclusion that can be

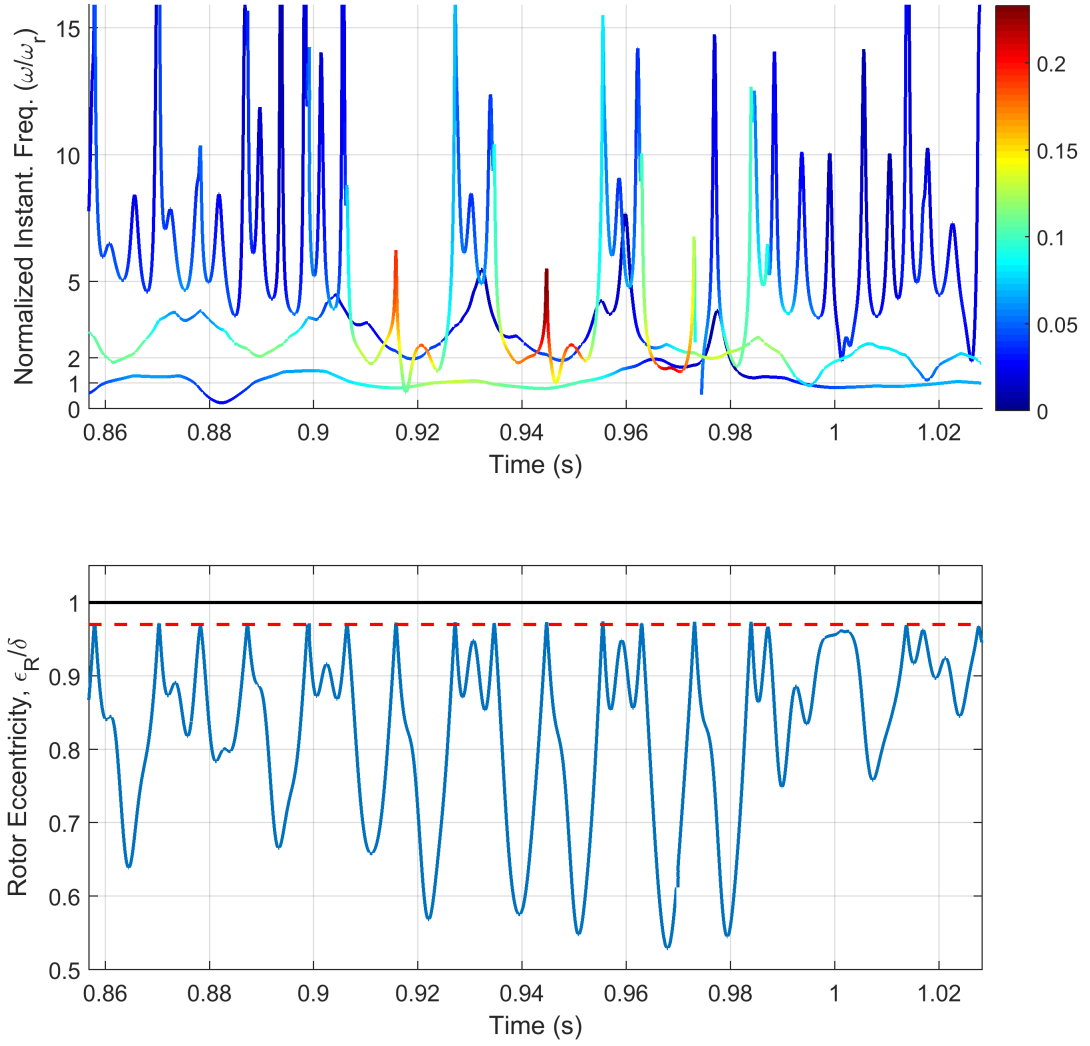

Figure 11.22: Rotor eccentric response time-frequency-energy spectrum: Cracked rotor with lateral rotor-housing contact ($\delta = 80$ μm, a = 40%, $\omega_r = 220$ rad/s).

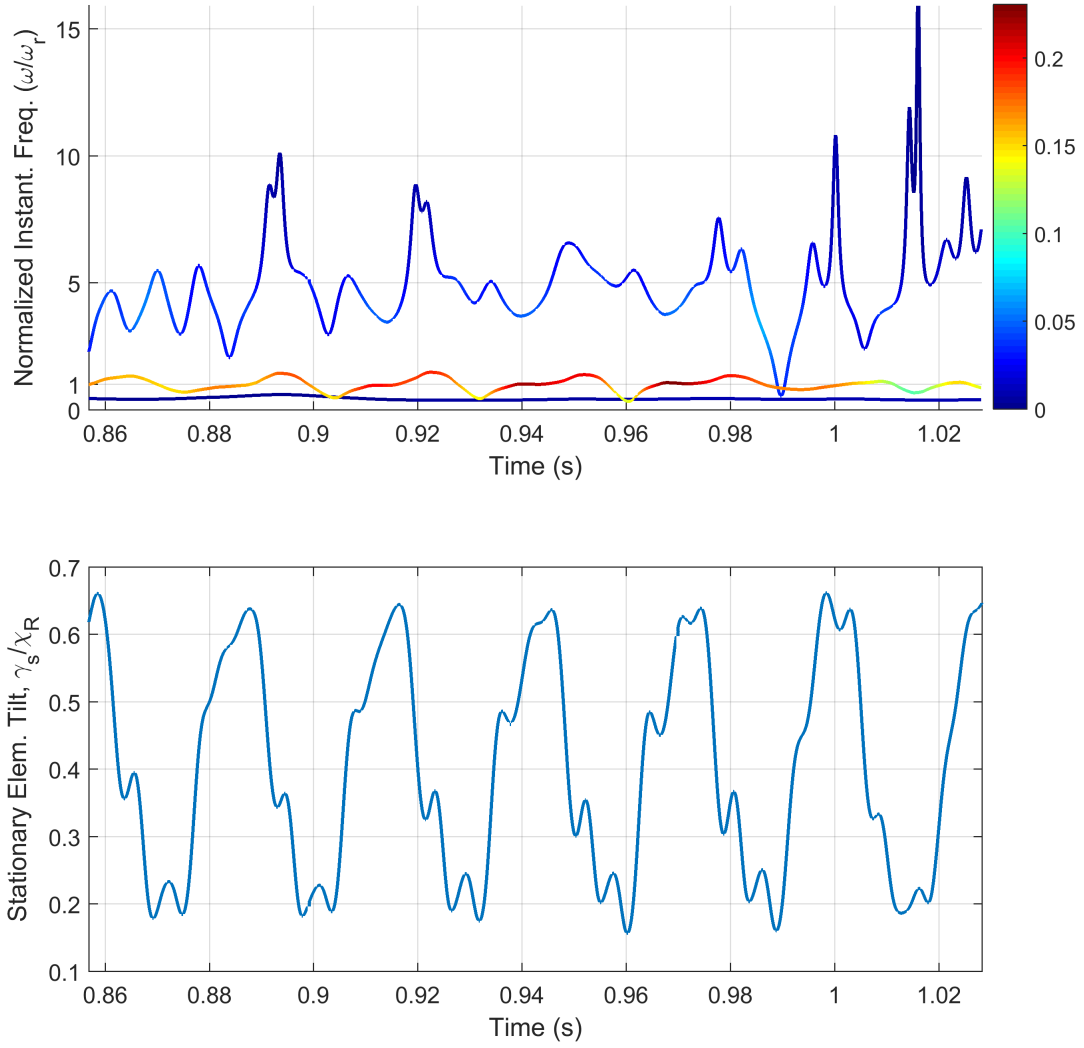

Figure 11.23: Stationary seal element tilt response time-frequency-energy spectrum: Cracked rotor with lateral rotor-housing contact (δ = 80 μm, a = 40%, ω_r = 220 rad/s).

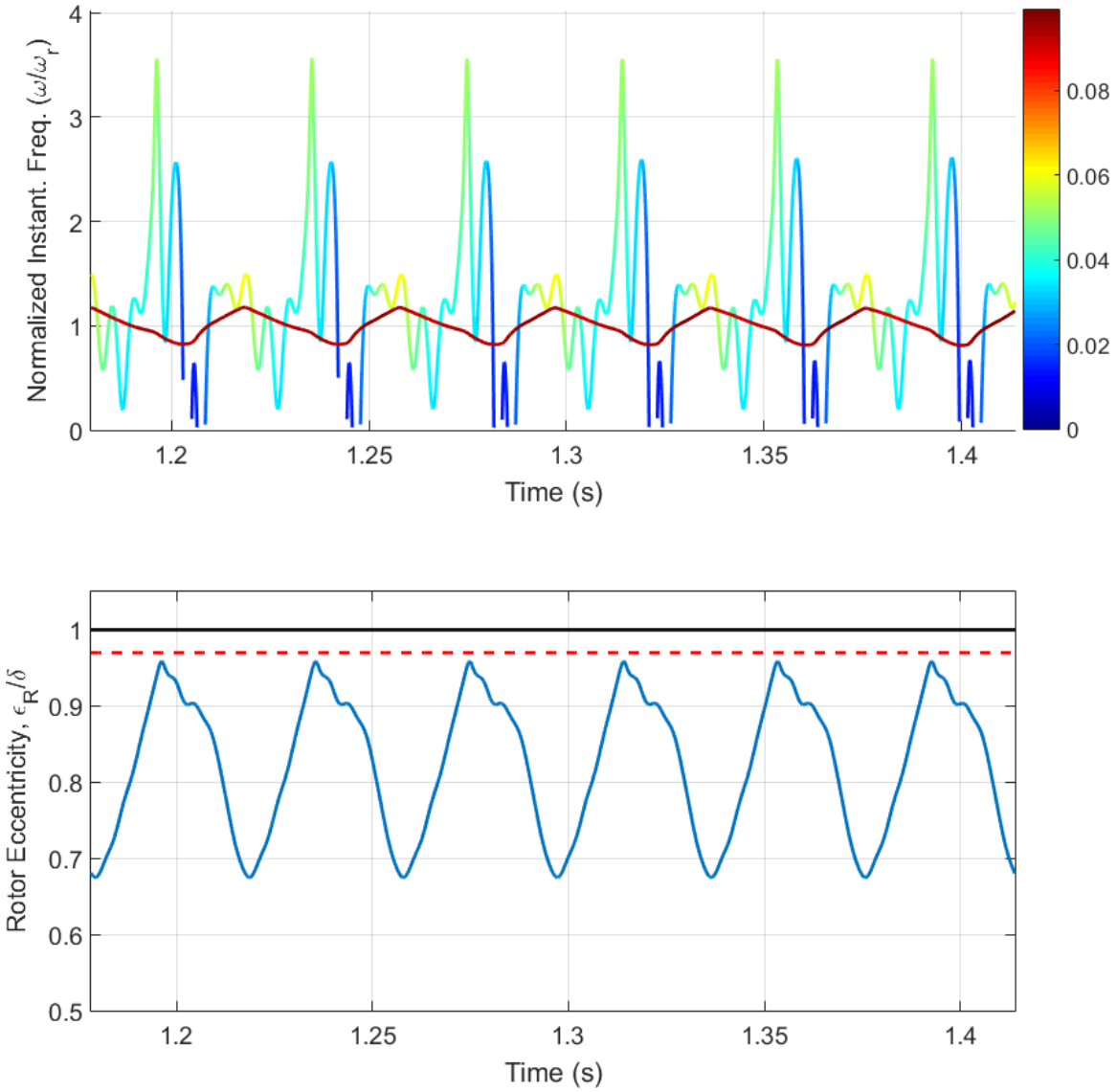

Figure 11.24: Rotor eccentric response time-frequency-energy spectrum: Uncracked rotor with lateral rotor-housing contact ($\delta = 80$ μm, a = 0%, $\omega_r = 160$ rad/s).

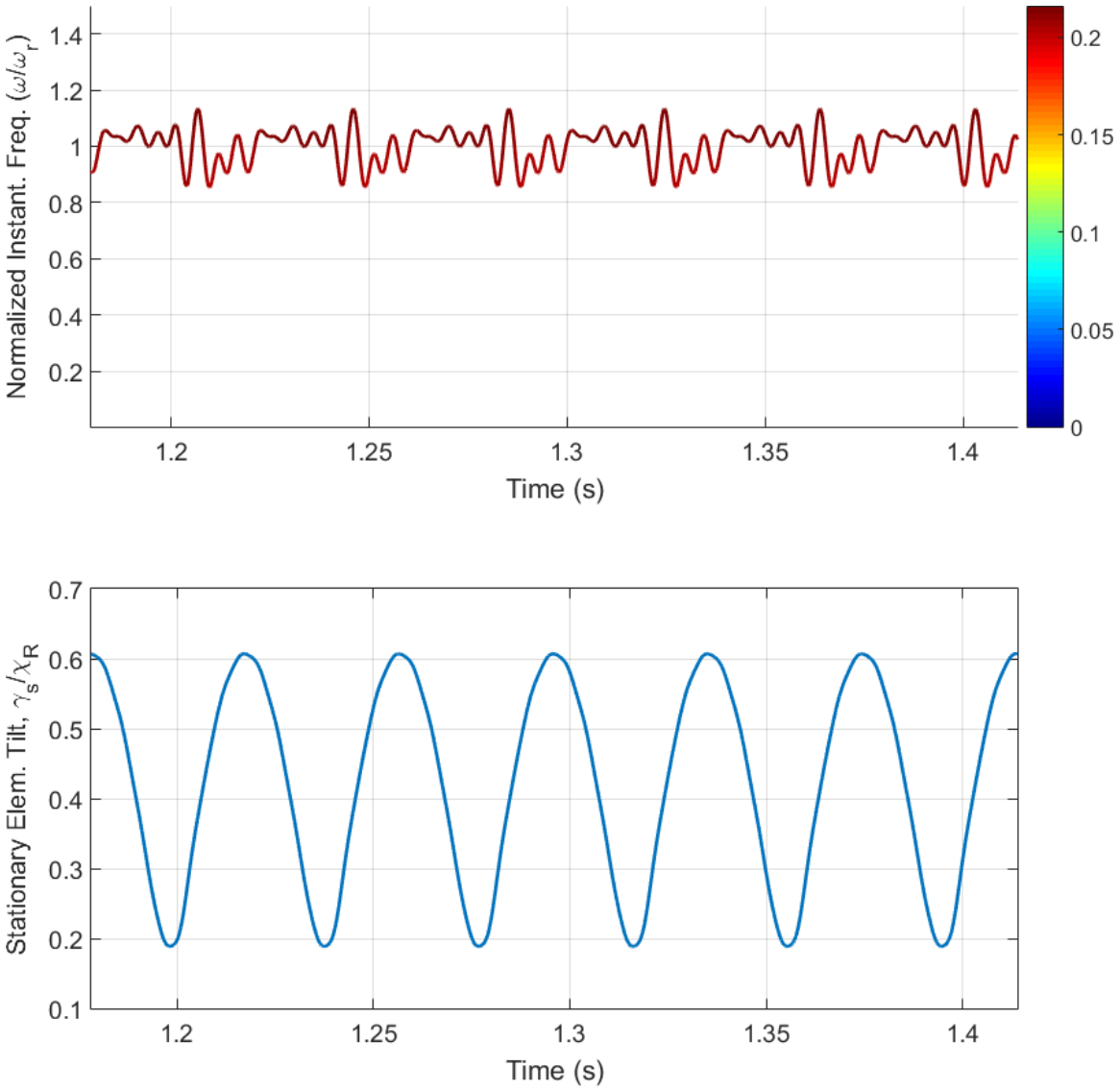

Figure 11.25: Stationary seal element tilt response time-frequency-energy spectrum: Uncracked rotor with lateral rotor-housing contact ($\delta = 80$ μm, a = 0%, $\omega_r = 160$ rad/s).

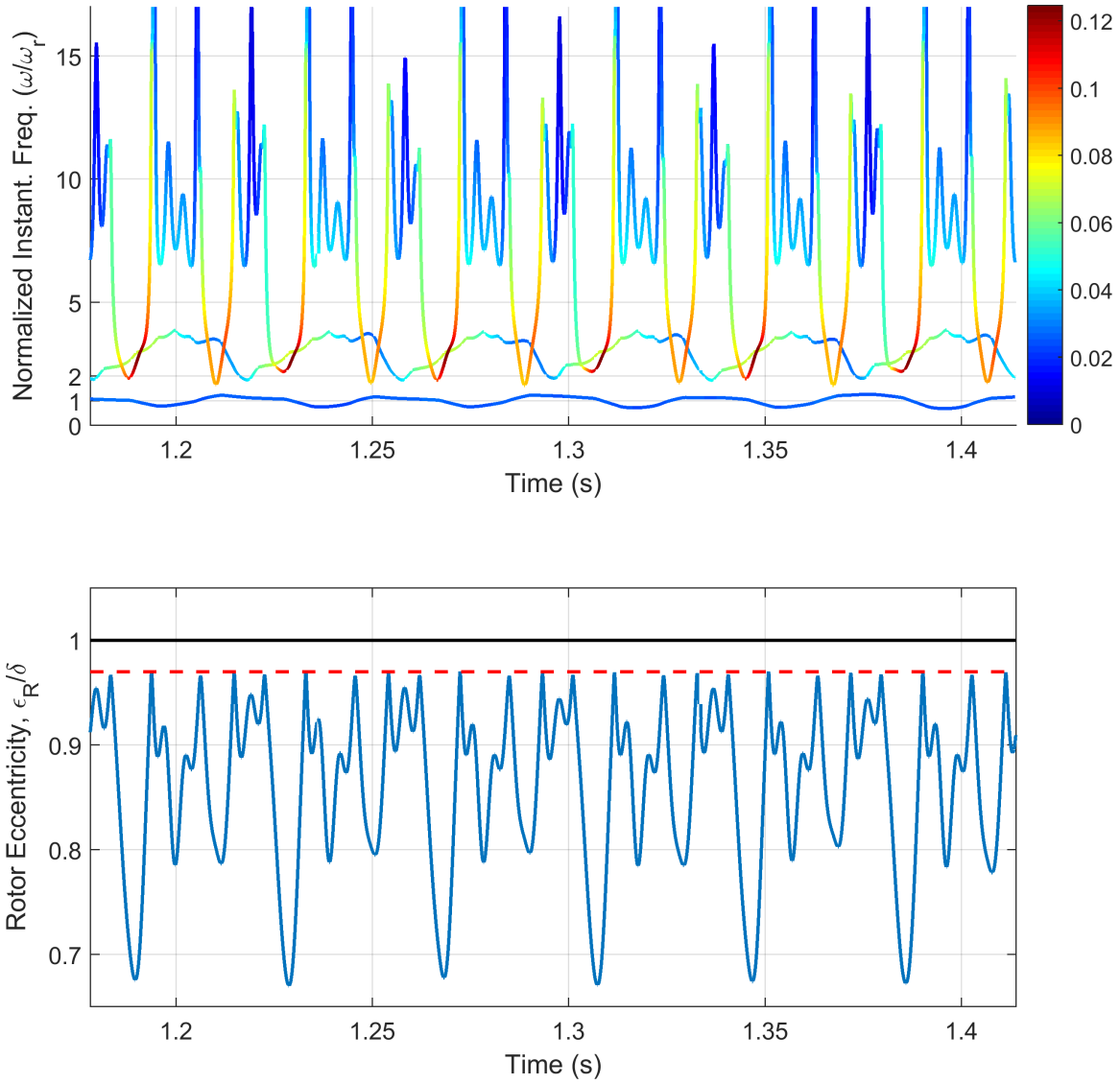

Figure 11.26: Rotor eccentric response time-frequency-energy spectrum: Cracked rotor with lateral rotor-housing contact ($\delta = 80$ μm, a = 40%, $\omega_r = 160$ rad/s).

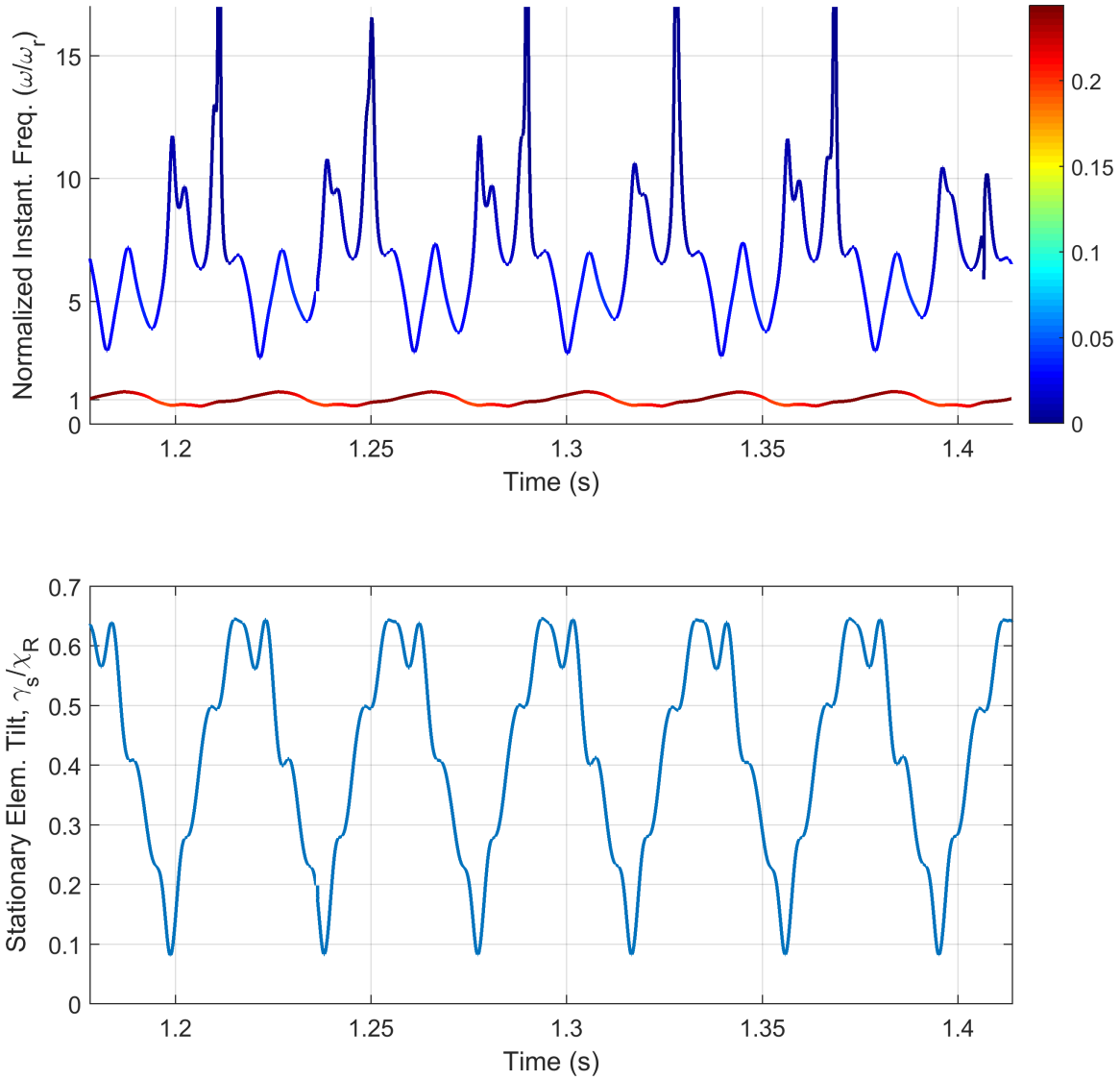

Figure 11.27: Stationary seal element tilt response time-frequency-energy spectrum: Cracked rotor with lateral rotor-housing contact ($\delta = 80$ μm, a = 40%, $\omega_r = 160$ rad/s).

drawn from these results is that the rotor eccentric response is more adept at distinguishing coexisting faults than the stationary seal element response. This conclusion is intuitive because the rotor response represents the unadulterated fault vibration signatures (i.e., the faults considered here are faults associated with the rotor).

11.5 Summary

These steady-state results provide sufficient information for qualitatively distinguishing a breathing rotor crack from rotor-housing contact. Specifically, the simultaneous faults can be distinguished using the following characteristics:

1. When the rotor contains a crack, the onset of chaotic and/or quasiperiodic motion occurs at much lower shaft speeds. This phenomenon becomes particularly pronounced for more severe cracks.

2. Regardless of the shaft speed, the rotor crack always results in only integer shaft speed harmonics. On the other hand, rotor-housing contact is defined by the sudden appearance of additional frequencies as the shaft speed is varied.

3. The rotor crack induces prominent sub-synchronous critical speeds. As the crack propagates (i.e., becomes deeper), the corresponding loss of stiffness causes these resonances to occur at lower shaft speeds (e.g., compare the 1/3 critical speed in Figs. 11.9 and 11.10).

4. The HHT displays a prominent shift in energy to a region near the 2X and 3X frequencies due to the crack, along with sudden increases in instantaneous frequency generated by rotor-housing contact.

Thus, the operator should consider a range of shaft speeds beneath the first critical speed if multiple simultaneous faults are suspected in the rotor. In either case, single or multiple faults, each fault is primarily defined by the appearance of shaft speed harmonics; these frequencies exist in contrast to the undamaged operation, where the

response is entirely synchronous. Thus, even if the specific fault type is unknown, the operator should still recognize that any significant deviation from the undamaged synchronous response is likely caused by a rotor (or seal) fault.

It is also important to contextualize the results presented in this chapter. These results are provided to give a deeper understanding of multiple fault vibration signatures in realistic rotor systems. This work is not intended to provide an algorithm or diagnostic procedure for quantifying the fault severity or fault parameters, but rather, to provide an adaptable tool and basic understanding from which a quantitative diagnostic procedure could be derived. For example, Varney and Green [110] develop a model-based diagnostic approach for identifying crack location and depth using the 1/2 critical speed and associated resonant response amplitude. Similar approaches could be developed using the tools and models presented herein. Still, it is our belief that the most robust diagnostic paradigms involve machine learning algorithms rather than exhaustive model-based simulation. This concept is discussed further in the next chapter.

The objective of this work is to use the stationary seal element response to identify dynamic characteristics of rotor faults. However, the results presented in this chapter indicate the superiority of using the rotor eccentric response to distinguish multiple coexisting rotor faults. On the other hand, the stationary seal element response is advantageous because it is relatively easy to measure. To address this discrepancy, the following chapter will suggest a method for predicting the rotor response directly from the stationary seal element response using an artificial neural network trained from system simulation data.

CHAPTER XII

CONCLUSIONS AND FUTURE WORK

12.1 Summary

The objective of this work was to examine the efficacy of using mechanical face seal vibration to characterize rotor faults. A comprehensive mechanical face seal dynamic model has been presented that incorporates features fundamental to this task:

- Eccentric, angular, and axial degrees-of-freedom for both seal elements (stationary and rotating).
- Dynamic coupling between the rotordynamics and the seal dynamics.
- Realistic operating conditions, including static and dynamic angular misalignment of both seal elements and rotating seal element imbalance.
- Transient operation terms in the equations of motion.

Developing a seal model that accounts for realistic rotordynamic effects is a principal and novel contribution of this work. In addition, the FMSR-ER seal model developed here includes terms resulting from inertial maneuver loads and thermoelastic deformations of the seal elements, though these aspects of system operation were not simulated in this work. Accompanying the FMSR-ER seal model in this work is a lumped parameter rotordynamic model accounting for eccentric and angular degrees-of-freedom. The rotor model includes a generally time-dependent stiffness matrix, gyroscopic effects, rotating internal damping, and external viscous damping. Once again, the model is developed to account for realistic operating conditions, and as such, includes synchronous excitations resulting from dynamic angular misalignment, imbalance, and rotor bow.

12.1.1 Summary: Rotor-Seal Coupling

Analysis of the simpler FMS-R system proves that the rotordynamics are not influenced by the seal dynamics when the rotor inertia is much larger than the seal inertia. This conclusion is important for two reasons. First, it indicates that the rotordynamics can be simulated independently and sent to the seal dynamics as an exogenous input. Secondly, it implies that the rotor fault signatures are unadulterated by the seal (i.e., the seal does not change the fault-induced rotor vibration). The undamaged FMSR-ER system is then simulated by numerically integrating the system equations of motion. The most important conclusion gleaned from the undamaged FMSR-ER simulation is that the rotordynamics prominently influence the seal dynamics, thus validating the use of the stationary seal element dynamics as a surrogate rotordynamic vibration monitor. This conclusion is not surprising because the seal elements are inextricably coupled to the rotor via the elastomer support and the fluid film.

In particular, the fluid film between the seal faces is significantly more adept at transferring angular tilts between the seal faces than it is at transferring eccentric deflections. This conclusion is intuitive because the non-contacting mechanical face seal is designed to minimize relative angular misalignments between the elements. Thus, the angular deflection of the stationary seal element is specifically identified as a potential target for a surrogate rotordynamic condition monitoring system.

12.1.2 Summary: FMSR-ER Response to a Cracked Rotor

Modeling: This work assumes that the rotor static deflection dominates the crack breathing such that the rotor stiffness can be expressed using a known periodic function. This function has been obtained using the strain energy release rate, where the stress intensity factors are evaluated along the crack edge to determine the open and closed crack regions. The rotor compliances are found over one revolution and analytically reconstructed in the frequency domain.

Results: The principle vibration signature of the breathing crack in the FMSR-ER system is integer shaft speed harmonics (e.g., 1X, 2X, 3X, etc.). Accompanying each harmonic is a sub-synchronous critical speed that occurs when the shaft speed corresponds to the inverse of the harmonic (e.g., the 2X creates a 1/2 critical speed when the shaft speed is one-half of a system whirl frequency). The rotor and seal orbits are also useful for detecting the crack, and particularly so near the sub-synchronous critical speeds. The time-energy-frequency spectrum obtained via the HHT indicates that the response is defined by two primary components centered near the synchronous speed and the dominant harmonic (e.g., the 2X). The instantaneous energy and frequency associated with each component vary periodically and smoothly.

12.1.3 Summary: Intermittent Contact

Modeling: A novel model for rotor-stator contact has been developed herein using the conceptual framework of rough surface contact. This approach is a significant improvement over previous rotor-stator contact models because it approximates the contact force using real physical principles rather than heuristic approximation. In addition, the model maintains positive clearances, which allows the fluid film pressure to be calculated between the contacting bodies. Specifically, the elasto-plastic Jackson-Green rough surface contact model is used to predict the contact pressure between two rough surfaces as a function of clearance. Because the model is quasi-static, an exponential curve-fit is used to approximate the pressure-clearance relationship, thus permitting significant improvements in computational efficiency. Most fundamentally, the contact forces represent a piecewise-smooth nonlinearity in the system dynamics. The dynamics of impact, spatial and temporal, occur on a scale very different from the rotordynamics (i.e., the impact duration is much shorter than the rotation period, and the impact scale is much smaller than the nominal clearance between the bodies).

Results: The hallmark characteristic of intermittent impact in rotating systems is the appearance of diverse system dynamics, including periodic, chaotic, and quasi-periodic responses (along with rich bifurcation structure). These characteristics are observed for every contact scenario investigated here: lateral contact in the Jeffcott rotor, face contact in the FMS seal, and eccentric contact between the rotor and housing. Frequency domain analysis indicates the possible appearance of integer shaft speed harmonics, fractional harmonics of the shaft speed, incommensurate frequencies, and/or broadband frequency content, depending on the specific response. The time-energy-frequency spectrum, obtained via the HHT, is defined by sudden increases in the instantaneous frequency at each instance of impact.

12.1.4 Summary: Characterizing Multiple Faults

Multiple coexisting rotor faults can be distinguished by characterizing the rotor and seal vibration versus shaft speed. Intermittent rotor-housing contact is defined by the sudden appearance of complex dynamic motion observed when the rotor exceeds the allowable clearance in the system. On the other hand, the symptoms of a breathing fatigue crack are present in the response irrespective of shaft speed. When taken in tandem, the stiffness reduction caused by the crack induces rotor-housing impact at lower shaft speeds when compared to the uncracked rotor. As the crack propagates, the severity of the impact increases, and the onset shaft speed at which rotor-housing contact first occurs decreases. Furthermore, the crack causes sub-synchronous critical speeds which decrease in frequency as the crack propagates.

12.2 Future Work

A principal contribution of this work is an adaptable tool for simulating the dynamics of a non-contacting mechanical face seal in a variety of realistic operation conditions. Still, the specific objective here was to use this model to assess the efficacy of using the mechanical face seal vibration as a suitable surrogate rotordynamic condition

monitor. Consequently, a significant amount of work remains towards improving the system model, simulating other operating conditions, and proving the validity of this work with experimentation.

12.2.1 Modeling

Mechanical Face Seal Modeling: Many practical non-contacting mechanical face seals employ gas lubrication instead of incompressible liquid lubrication. For example, the oil used to lubricate the bearings in a modern turbofan engine is contained via a suite of gas lubricated seals. A liquid-lubricated seal was assumed in this work because an analytic expression can be found for the resulting fluid pressure between the seal faces. A significant advancement in mechanical face seal modeling could be realized by expanding the fluid model to account for gas lubrication, while still allowing angular, axial, and eccentric seal dynamics.

Rub Modeling: The rub model used here assumed a quasi-static force-displacement relationship between the interacting surfaces. In reality, hysteresis and plastic deformation result in a force-displacement relationship that depends on the loading-unloading cycle of the surfaces. Furthermore, the rough surface contact model used here neglects bulk substrate deformation. The rough surface contact model should be expanded to account for both of these realistic phenomena. In addition, most rotor-housing designs deviate significantly from the ideal disk-annulus configuration assumed here (e.g., the rotor-housing clearance in the turbine and compressor depends on the complicated clearance between the rotating blades and the stationary vanes). More realistic predictions for rotor-housing rub vibrations could be gleaned by investigating more realistic contact geometries.

Crack Modeling: An important aspect of a rotordynamic crack is coupling between the lateral, axial, and torsional rotor vibrations [134]. Thus, the rotor model and crack compliance matrix should be expanded to include axial and torsional vibrations.

In addition, a more robust approach for crack breathing should be developed that permits response-dependent crack breathing (i.e., a model where the crack breathing depends on the instantaneous load acting on the crack cross-section).

12.2.2 Simulation

The following operating conditions should be investigated in future works regarding mechanical face seal performance and rotordynamic fault diagnostics:

1. The influence of inertial maneuver loads on mechanical face seal performance should be studied to improve the robustness of modern seal designs.

2. The transient performance of the FMSR-ER system in start-up and shut-down operation should be thoroughly investigated to improve the seal design with regard to transient thermal deformations of the seal faces and/or non-ideal rotor start conditions (e.g., rotor bow).

3. Transient start-up and shut-down rotor vibrations should be used to more accurately identify rotor faults. Specifically, shaft-speed dependent phenomena such as sub-critical resonance and the onset of contact could be identified from a single start-up test.

In addition, computation time could be improved when simulating the FMSR-ER system model by reducing the fluid film forces and moments to equivalent stiffness and damping coefficients (this approach is possible if the seal is operating as-intended, i.e., with small relative angular misalignment between the faces).

12.2.3 Experimental Validation

Finally, the validity of the model and results presented here must be validated experimentally; the importance of this step in future work cannot be understated. A test rig for a FMSR-ER seal system should be constructed and equipped with a modern suite

of vibration monitoring equipment, and should be capable of measuring both the rotordynamic response and the seal dynamic response. Furthermore, the experimental validation regarding fault detection will be predicated on the ability to manufacture and control the desired rotor faults. A procedure should be developed to manufacture real rotordynamic fatigue cracks in a manner commensurate with reality.

12.2.4 Diagnostics Using Machine Learning

This work has provided an adaptable tool for predicting rotordynamic fault signatures resulting from breathing fatigue cracks and intermittent rotor-housing contact. Even still, the complex model presented here is significantly less complicated than the actual rotors employed in modern high-performance turbomachines. For this reason, it is our belief that diagnostics founded only on model-based algorithms will remain insufficient for precisely diagnosing complicated rotor fault scenarios. An attractive alternative to model-based diagnostics is machine learning algorithms, which can be trained using realistic system models and then refined using real test data. Future works should use the concepts elaborated in this work as the basis for precise fault diagnostics using advanced machine learning algorithms.

12.2.5 Rotor Response Prediction using Artificial Neural Networks

An important conclusion from this work is that the stationary seal element vibration is useful for detecting rotor faults. However, the stationary seal element vibration was seen to be less successful at distinguishing coexisting disparate rotor faults at a single shaft speed. In that case, the rotor eccentric response displayed the best fidelity in exposing hallmark vibration signatures of each fault. An intriguing avenue for future work is applying artificial neural networks to predict the eccentric rotor response using the stationary seal response. Thus, the advantage of the seal-fixed monitoring system is retained (i.e., ease of use, feasibility, etc.) while still incurring the advantages of using the rotor eccentric response to detect the rotor fault(s).

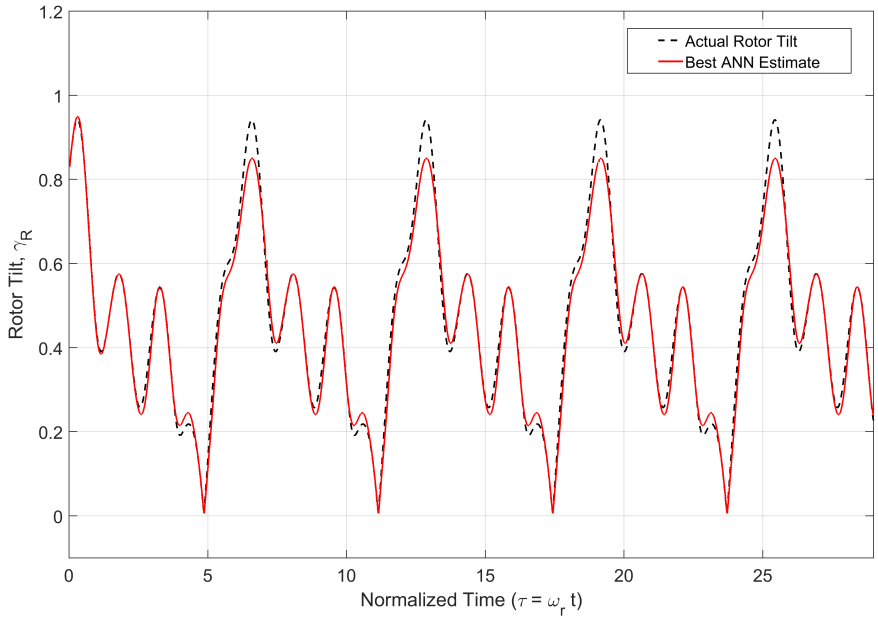

Figure 12.1: The rotor tilt response predicted from the corresponding stationary seal element tilt using the NARX network.

One particular approach for accomplishing this task is the nonlinear autoregressive neural network with exogenous input (i.e., the NARX network). The objective of this method is to predict one waveform using another waveform, without requiring knowledge of the process connecting the two waveforms. Thus, the value of the target waveform $y(t)$ at time t is a function of previous values of that waveform in addition to previous values of the exogenous waveform $u(t)$:

$$y(t) = f\big(y(t-1), y(t-2), ..., y(t-n_y), u(t-1), u(t-2), ..., u(t-n_u)\big) \qquad (12.1)$$

where n_y and n_u represent the desired number of delay points used to predict the current response. The NARX network is first trained on known and available waveforms (i.e., the simulation results of the FMSR-ER system) to obtain the appropriate weights in the artificial neural network. The resulting network is then used to predict an unknown signal $y(t)$ using only a known (i.e., measurable) signal $u(t)$.

An advantage of this particular approach is the availability of validated subroutines in MATLAB to perform the NARX network construction. To demonstrate the concept, a NARX network is trained in MATLAB using simulation data corresponding to a period-1 rub response in the FMSR-ER system. The network is designed to use four delays in the stationary seal element tilt (i.e., the exogenous input) and four delays in the rotor tilt. Specifically, this means that the network uses the previous four data points in both time series to predict the next data point in the desired output, which in this case is the rotor tilt. This process is performed for both orthogonal tilts to ensure that the final resultant tilt is always greater than zero. For each tilt, one hundred different networks are trained, and the best network in each case is selected using a least-squares error performance metric.

The result from the prediction is shown in Fig. 12.1 for a period-1 motion caused by rotor-housing contact. The trained network is clearly capable of predicting the rotor response given only the stationary seal element response. It should also be noted that the method used here is only provided as a proof-of-concept. Future works should identify ideal NARX network parameters (number of delays, number of hidden layers in the artificial neural network, etc.), and use the resulting approach to predict the rotor eccentric response (only the tilt response is predicted in Fig. 12.1).

The estimated rotor response represents the completely unadulterated fault signature, and can be used to specifically classify and identify rotor faults. Quantifiable fault vibration signatures could be extracted from the predicted rotor response (i.e., the energy density within prescribed regions of the time-energy-frequency spectrum) and then used as inputs to a classification machine learning algorithm (trained using system simulation data). This classification algorithm could potentially be a tool for robustly identifying complicated rotor fault scenarios (e.g., multiple faults).

12.3 Final Summary

A deeper understanding the dynamic interplay between non-contacting mechanical face seals and the rotor is important for not only improving seal designs, but also for using the seal vibration to detect rotor faults. This work has significantly advanced the state-of-the-art by providing a comprehensive and novel mechanical face seal dynamic model that accounts for numerous realistic operating conditions. Most notably, the model presented here incorporates the complete rotordynamic response into the seal equations of motion, thus permitting a more complete understanding of seal performance. A novel approach is also given for predicting contact forces between the rotating and stationary machine elements.

The FMSR-ER model was simulated for several scenarios: an undamaged rotor, a cracked rotor, intermittent rotor-housing contact, and a multiple fault case where both a crack and rub exist simultaneously in the system. Vibration symptoms indicative of each fault were identified using stationary and non-stationary signal processing techniques, thus allowing the operator to detect individual faults and distinguish coexisting faults. Simulation results from these dynamic models indicated that the rotordynamic response is inseparable from the seal dynamics; the rotor vibration is definitively transferred to the seal elements, and the character of the vibration is preserved along the transference path. Consequently, this work concludes that the stationary seal element angular response is an appropriate tool for detecting individual faults in the rotor and distinguishing multiple coexisting rotor faults.

APPENDIX A

THE REYNOLDS EQUATION

The fluid film forces and moments create seal face separation and, along with element support flexibility, minimize relative misalignments between the seal faces. Since the fluid film is thin, the pressure distribution within the sealing dam is governed by the Reynolds equation. The Reynolds equation is derived herein according to the definitions and parameters used in this work, and is then used to obtain the fluid film forces and moments.

A.1 Deriving the Reynolds Equation

The seal geometry is cylindrical, and consequently, it will be convenient to provide the Reynolds equation in polar coordinates. The sealing apparatus is generically described as two translating and/or rotating disks, as shown in Fig. A.1, where the film thickness $h(r, \theta)$ is shown greatly exaggerated in comparison to the seal dimensions (i.e., inner and outer radii). The central axes of the disks are not necessarily co-linear because of eccentric deflections of both elements. Importantly, it is assumed that the stationary seal element is much larger than the rotating seal element, and thus, the sealing dam is always contained within the bounds of the rotating seal element geometry.

The fluid pressure will be found relative to an inertial polar coordinate system $r\theta$ centered on the rotating seal element, designated element 1. The inertial $\xi\eta\zeta$ frame is shown in Fig. A.1 for reference, and is attached to the undeflected center of element 1 without any loss of generality. The circumferential coordinate θ is referenced as positive from ξ. The absolute surface velocity of point (r, θ) on element j is expressed in the polar coordinate system and then decomposed into radial, circumferential, and

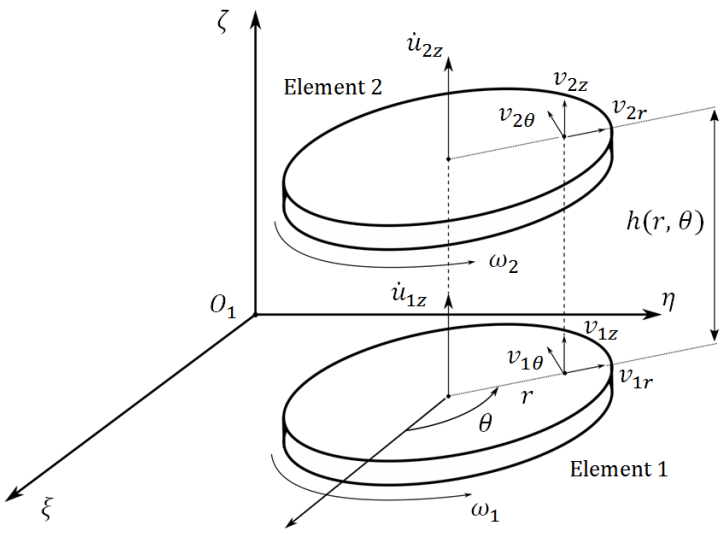

Figure A.1: Kinematics of two translating and rotating disks used to derive the Reynolds Equation

axial components (V_{jr}, $V_{j\theta}$, and V_{jz}, respectively). The rotation rate of element j is denoted ω_j.

The Navier-Stokes equations in polar coordinates, neglecting body forces, are [28]:

$$\rho\frac{Dv_r}{Dt} = -\frac{\partial P}{\partial r} + \mu\left[\nabla^2 v_r - \frac{v_r}{r^2} - \frac{2}{r^2}\frac{\partial v_\theta}{\partial \theta}\right] \tag{A.1}$$

$$\rho\frac{Dv_\theta}{Dt} = -\frac{1}{r}\frac{\partial P}{\partial \theta} + \mu\left[\nabla^2 v_\theta - \frac{v_\theta}{r^2} - \frac{2}{r^2}\frac{\partial v_r}{\partial \theta}\right] \tag{A.2}$$

$$\rho\frac{Dv_\zeta}{Dt} = -\frac{\partial P}{\partial \zeta} + \mu\nabla^2 v_\zeta \tag{A.3}$$

where the fluid density is ρ and the viscosity is μ. The velocity field within the fluid is denoted (v_r, v_θ, v_ζ). Continuity is expressed as

$$\frac{\partial \rho}{\partial t} + \frac{1}{r}\frac{\partial}{\partial r}\left(\rho r v_r\right) + \frac{1}{r}\frac{\partial}{\partial \theta}\left(\rho v_\theta\right) + \frac{\partial}{\partial \zeta}\left(\rho v_\zeta\right) = 0 \tag{A.4}$$

The following assumptions are made regarding the fluid film:

1. The film thickness $h(r,\theta)$ is small (i.e., thin) compared to seal dimensions in the r and θ directions. Consequently:

   (a) Viscous forces overwhelm inertial forces since the film thickness is small.

(b) The Reynolds number is small, indicating laminar flow.

(c) Fluid pressure is not a function of ζ, and thus, $\partial P/\partial \zeta = 0$.

(d) Velocity gradients in the ζ direction are much larger than those in the r and θ directions.

2. No-slip conditions exist on the seal surfaces.

These assumptions reduce Eqs. A.1 - A.3 to the following form:

$$0 = -\frac{\partial P}{\partial r} + \mu \frac{\partial^2 v_r}{\partial \zeta^2} \tag{A.5}$$

$$0 = -\frac{1}{r}\frac{\partial P}{\partial \theta} + \mu \frac{\partial^2 v_\theta}{\partial \zeta^2} \tag{A.6}$$

$$0 = \frac{\partial^2 v_\zeta}{\partial \zeta^2} \tag{A.7}$$

This set of differential equations governs the velocity field within the fluid as a function of position and pressure. The velocity boundary conditions are the surface velocities of the seal elements:

$$v_r(z=0) = V_{1r} \quad , \quad v_r(z=h) = V_{2r} \tag{A.8}$$

$$v_\theta(z=0) = V_{1\theta} \quad , \quad v_\theta(z=h) = V_{2\theta} \tag{A.9}$$

$$v_\zeta(z=0) = V_{1\zeta} \quad , \quad v_\zeta(z=h) = V_{2\zeta} \tag{A.10}$$

Using these boundary conditions, the reduced Navier-Stokes equations are integrated along ζ to provide the velocity fields within the fluid. As will be seen, the fluid velocity field is important for deriving the Reynolds equation and finding eccentric viscous fluid forces. Performing the integration yields:

$$v_r(r,\theta) = \frac{1}{2\mu}\frac{\partial P}{\partial r} z^2 + \left(\frac{V_{1r} - V_{2r}}{h} - \frac{1}{2\mu}\frac{\partial P}{\partial r} h \right) z + V_{2r} \tag{A.11}$$

$$v_\theta(r,\theta) = \frac{1}{2r\mu}\frac{\partial P}{\partial \theta} z^2 + \left(\frac{V_{1\theta} - V_{2\theta}}{h} - \frac{1}{2r\mu}\frac{\partial P}{\partial \theta} h \right) z + V_{2\theta} \tag{A.12}$$

Finally, these velocity profiles are inserted into the continuity expression and integrated across the film thickness to give the general Reynolds equation governing the

fluid pressure between two translating and rotating disks:

$$\frac{\partial}{\partial r}\left(h^3\frac{\rho r}{12\mu}\frac{\partial P}{\partial r}\right)+\frac{\partial}{\partial \theta}\left(h^3\frac{\rho}{12r\mu}\frac{\partial P}{\partial \theta}\right)=r\rho(V_{2\zeta}-V_{1\zeta})+\frac{\partial}{\partial r}\left(\rho r h\frac{V_{2r}+V_{1r}}{2}\right)$$
$$+\frac{\partial}{\partial \theta}\left(\rho h\frac{V_{1\theta}+V_{2\theta}}{2}\right)-\rho r V_{2r}\frac{\partial h}{\partial r}-\rho r V_{2\theta}\frac{\partial h}{\partial \theta}+rh\frac{\partial \rho}{\partial t} \qquad \text{(A.13)}$$

This expression is reduced further by recognizing that practical seals are narrow rings where the inner and outer radii are close in magnitude (i.e., the sealing dam is narrow). The consequences of this are that circumferential pressure gradients and seal curvature can be neglected with little loss in accuracy [29]. Recognizing these assumptions, and assuming isoviscous and incompressible flow, Eq. A.13 reduces to the following final form:

$$\frac{\partial}{\partial r}\left(h^3\frac{\partial P}{\partial r}\right)=6\mu\left[2\frac{\partial h}{\partial t}+(V_{1r}-V_{2r})\frac{\partial h}{\partial r}+\frac{(V_{1\theta}-V_{2\theta})}{r}\frac{\partial h}{\partial \theta}\right.$$
$$\left.+h\frac{\partial}{\partial r}\big(V_{1r}+V_{2r}\big)+\frac{h}{r}\frac{\partial}{\partial \theta}\big(V_{1\theta}+V_{2\theta}\big)+\frac{h}{r}\big(V_{1r}+V_{2r}\big)\right] \qquad \text{(A.14)}$$

where

$$\frac{\partial h}{\partial t}=V_{2\zeta}-V_{1\zeta} \qquad \text{(A.15)}$$

When lateral deflections are ignored, Eq. A.14 reduces to the Reynolds equation for either the FMS [40] or FMR [46] seal, depending on which element rotation is constrained.

A.2 Solving the Reynolds Equation

Since Eq. A.14 is linear, the principle of superposition applies and the total fluid pressure is obtained by summing the homogeneous and non-homogeneous solutions (i.e., the static and dynamic pressures). The static pressure profile is governed by the following boundary value problem (BVP):

$$\frac{d}{dr}\left(h^3\frac{dP_s}{dr}\right)=0 \qquad \text{(A.16)}$$

$$P_s(r_i,\theta)=P_i \quad , \quad P_s(r_o,\theta)=P_o \qquad \text{(A.17)}$$

This BVP has been previously solved by Etsion and Sharoni [30] to give:

$$P_s(r,\theta) = P_o - (P_o - P_i)\frac{h_i^2}{h_o^2 - h_i^2}\left[\left(\frac{h_o}{h}\right)^2 - 1\right] \tag{A.18}$$

where i and o denote functions evaluated along the inner and outer boundaries. The dynamic pressure is likewise obtained by solving the following BVP, where the homogeneous boundary conditions are used since the non-homogeneous boundary conditions were included in the static solution:

$$\frac{\partial}{\partial r}\left(h^3\frac{\partial P_d}{\partial r}\right) = R.H.S. \tag{A.19}$$

$$P_d(r_i,\theta) = 0 \quad , \quad P_d(r_o,\theta) = 0 \tag{A.20}$$

The forcing function on the right-hand side of Eq. A.14 is denoted 'R.H.S.' for brevity, and includes hydrodynamic contributions from seal velocities in the radial, tangential, and axial directions. As expected, the solution to Eq. A.19 depends wholly on the seal apparatus kinematics and the lubricant properties. Even though the kinematics considered here represent a specific case, BVPs analogous to Eqs. A.19 and A.20 have been solved previously by other researchers for various seal configurations [46, 52, 56]. A closed-form expression is possible if variations in r are assumed to be small enough so that $r \cong r_m$, where r_m is the mean seal radius. This assumption is reasonable since the seal is narrow. The total solution is found by following the integration process described by Wileman and Green [52]:

$$P_d(r,\theta) = -3\mu(R.H.S)|_{r=r_m}\frac{(r_o - r)(r - r_i)}{h_m h^2} \tag{A.21}$$

The total fluid pressure $P_f(r,\theta)$ is the sum of the hydrostatic and hydrodynamic components:

$$P_f(r,\theta) = P_s(r,\theta) + P_d(r,\theta) \tag{A.22}$$

The expressions for the static and dynamic fluid pressures are left general to avoid restricting the solution to a particular function of geometry (i.e., film thickness).

Practical application of the fluid pressure profile will necessitate a specific form for $h(r, \theta)$, the imposition of which will cause Eqs. A.18 and A.21 to depend on the seal degrees-of-freedom.

APPENDIX B

BALANCING THE FMSR SEAL

Non-contacting mechanical face seals are designed to operate at a constant set-point centerline clearance C_o. This clearance is attained by balancing the axial forces acting on each seal element, stationary and rotating, in the absence of tilt. The FMSR seal geometry is shown in Fig. B.1, which is used to intuitively understand the opening and closing forces on each element. Figure B.1 reflects the previous assumption that the inner and outer stationary element radii, r_{os} and r_{is}, must be larger than those of the rotating element, r_o and r_i, to maintain a consistent sealing dam when subject to eccentric deflections.

B.1 Opening Force

The opening force is generated solely by fluid pressure within the sealing dam. In the absence of tilt, the fluid pressure in the sealing dam consists entirely of the static pressure, $P_s(r,\theta)$, which is found from the Reynolds equation using the narrow seal approximation [29] (see Appendix A). The opening force is found by integrating the total pressure profile across each element:

$$F_{o,s} = \int_{r_i}^{r_o} \int_0^{2\pi} P_s(r,\theta) r \; dr d\theta + \pi P_o(r_{os}^2 - r_o^2) + \pi P_i(r_i^2 - r_{is}^2) \tag{B.1}$$

$$F_{o,r} = \int_{r_i}^{r_o} \int_0^{2\pi} P_s(r,\theta) r \; dr d\theta \tag{B.2}$$

The stationary seal element (or, more generally, the larger seal element) accrues additional opening force contributions from the inner and outer pressure reservoirs. These pressure forces are shown graphically on the free body diagram provided in Fig. B.2.

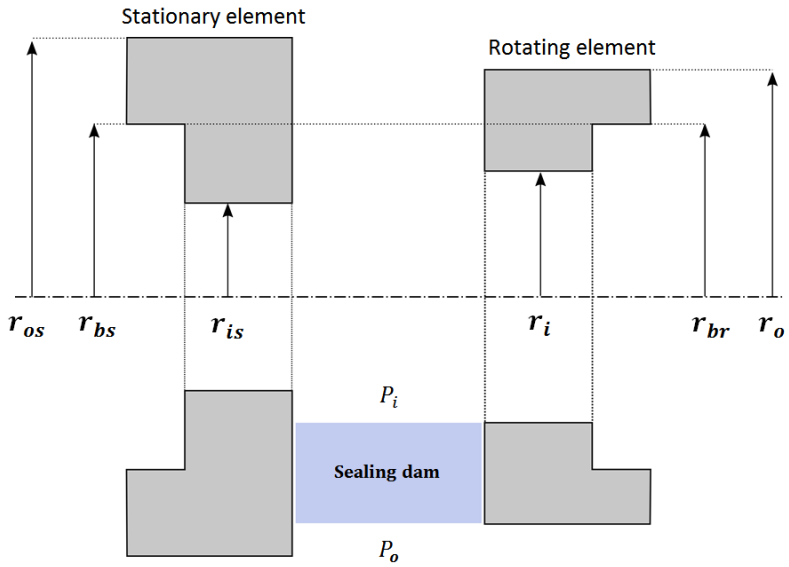

Figure B.1: FMSR seal geometry.

B.2 Closing Forces

Each seal element is flexibly-mounted using an elastomeric O-ring and a pre-loaded axial support spring. The elastomeric O-ring also functions as a secondary seal; in this work, the secondary seal is assumed to be ideal (i.e., no leakage on the seal backside). In this work, the support springs attached to each element are assumed to have the same pre-load force, F_{spr}. The spring force is also assumed to be constant ($F_{spr} \neq f(u_z)$), since the axial deflections contribute only a small deviation from the pre-load.

The total closing force is found by summing the support spring force, F_{spr} and the pressure forces acting on the element's backside.

$$F_{cls,s} = F_{spr,s} + \pi \left[P_o(r_{os}^2 - r_{bs}^2) + P_i(r_{bs}^2 - r_{is}^2) \right] \tag{B.3}$$

$$F_{cls,r} = F_{spr,r} + \pi \left[P_o(r_o^2 - r_{br}^2) + P_i(r_{br}^2 - r_i^2) \right] \tag{B.4}$$

Balancing the seal apparatus amounts to identifying balance radii r_{bs} and r_{br} for the stationary and rotating seal element that yield the desired set-point clearance

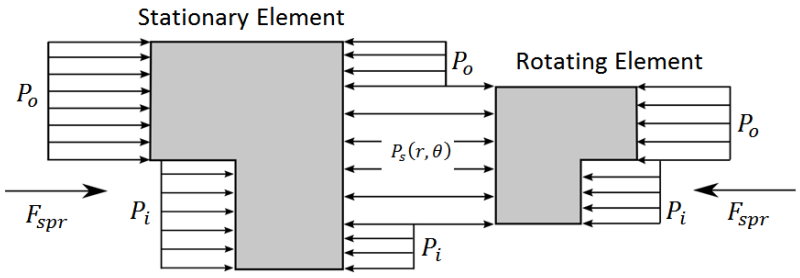

Figure B.2: Balancing the opening and closing forces on the FMSR seal apparatus.

C_o. Physically, the balance radius represents the radial location at which the O-ring secondary seal is attached.

B.3 Balancing the Seal

The opening and closing forces on both elements are then required to be statically-balanced:

$$F_{cls,s} - F_{o,s} = 0 \quad , \quad F_{cls,r} - F_{o,r} = 0 \tag{B.5}$$

Performing this operation indicates that the balance radii for each element must be equivalent if the support spring force is the same on each element ($r_{br} = r_{bs} = r_b$). Any contribution of the fluid reservoir to the opening force on the rotating seal element is negated by an equal and opposite contribution to the closing force. This conclusion is intuitive because the same resultant opening force acts on each element; thus, each element must also be subject to the same closing force. The balance radius is then found by iteratively varying r_b until static equilibrium is obtained.

APPENDIX C

THE HILBERT-HUANG TRANSFORM

Conventional signal processing methods, e.g., Fourier analysis, assume that the target signal is generated by a stationary process. For the purposes of this work, stationarity is defined as such if the underlying model remains unchanged (e.g., the synchronous response of an imbalanced rotor where the model remains consistent and does not change with time). On the other hand, intermittent rotor-housing contact is fundamentally nonstationary: the system dynamics (i.e., the model) fundamentally changes when the rotor contacts the housing. Consequently, the frequency content contained in a non-stationary signal changes with time (whereas the Fourier transform assumes that all frequencies are present at all times, which is only definitively true if the signal is generated by a stationary process).

Non-stationary signals must therefore be analyzed using processing techniques that localize frequency content in the time domain. As will be discussed further, one such technique is the Hilbert Huang transform (HHT), which uses an adaptive algorithm to decompose signals into components which are well-conditioned for Hilbert analysis. The output of the HHT is therefore the time-energy-frequency spectrum of the signal. Other non-stationary signal processing methods have been developed to extract the time-frequency-energy spectrum of a signal, but these additional processing methods are not considered in this work (e.g., the short-time Fourier transform, wavelet analysis, the Wigner-Ville distribution, etc.).

C.1 Empirical Mode Decomposition

The first step in the HHT is to decompose a given signal into a set of intrinsic mode functions (IMFs) using the empirical mode decomposition (EMD) algorithm. The IMFs are nearly-orthogonal signal components which must meet the following criteria:

1. The number of extrema (maximums and minimums) and the number of zero-crossings must be equal or differ at most by one.

2. At every point in the IMF, the mean value of an envelope connecting the local maximums and an envelope connecting the local minimums must be zero.

These criteria redefine the concept of an oscillatory signal by generalizing the notions of amplitude and frequency. Fourier analysis decomposes a given signal into a sum of complex exponentials whose amplitude and frequency is constant with time. The EMD algorithm, on the other hand, decomposes a signal into a set of oscillatory components (IMFs) whose amplitude and frequency is free to vary so long as the IMF obeys the above criteria. In general, the objective is to decompose a signal $y(t)$ into a set of N IMFs $c_i(t)$ such that:

$$y(t) = \sum_{i=1}^{N} c_i(t) + r_I \tag{C.1}$$

where the number of IMFs N is typically unknown until the conclusion of the EMD algorithm. The residue r_I is a monotonic component with no more than two extrema (i.e., the extrema of r_I are the end points of r_I).

The EMD algorithm is a sifting technique that progressively removes extraneous components until the remaining signal obeys the definition of an IMF set forth in the above criteria. Then, the IMF is subtracted from the signal and the process is repeated on the residual signal. This iteration is repeated until the residual signal is monotonic (and thus, the remaining component is identified as r_I). Sequentially, the EMD algorithm is described according to the following steps [78]:

1. Initialize $r_0 = y(t)$ $(i = 1)$.

2. Extract the ith IMF, $c_i(t)$:

   (a) Initialize the intermediary signal $h_{i(k-1)} = r_{(i-1)}$ (k = 1).

   (b) Identify the local extrema of $h_{i(k-1)}$.

   (c) Obtain the lower envelope of $h_{i(k-1)}$ by interpolating the local minima using cubic splines.

   (d) Obtain the upper envelope of $h_{i(k-1)}$ by interpolating the local maxima using cubic splines.

   (e) Average the upper and lower envelopes to obtain the local mean $m_{i(k-1)}$.

   (f) Now, calculate h_{ik} such that $h_{ik} = h_{i(k-1)} - m_{i(k-1)}$.

   (g) If h_{ik} is an IMF, set $c_i = h_{ik}$. Otherwise, iterate $k = k + 1$ and repeat the process beginning with step (b).

3. Calculate the remaining signal such that $r_{i+1} = r_i - c_i$.

4. If r_i contains more than 2 extrema, iterate $i = i + 1$ and repeat the sifting process beginning at step (2). Otherwise, the sifting process is complete and the remainder r_i is the signal residue r_I.

The EMD algorithm is shown graphically in Fig. C.1. This algorithm is well-suited for analyzing non-stationary signals precisely because it is adaptive. No presumptions are made concerning the signal to be analyzed, and the analysis does not depend on the *a priori* choice of a basis function (e.g., as is the case with wavelet analysis).

C.2 The Hilbert Transform

The Hilbert transform converts a real-valued function $x(t)$ into an analytic representation $z(t)$ by projecting $x(t)$ into the complex plane (such that the projection $\tilde{x}(t)$

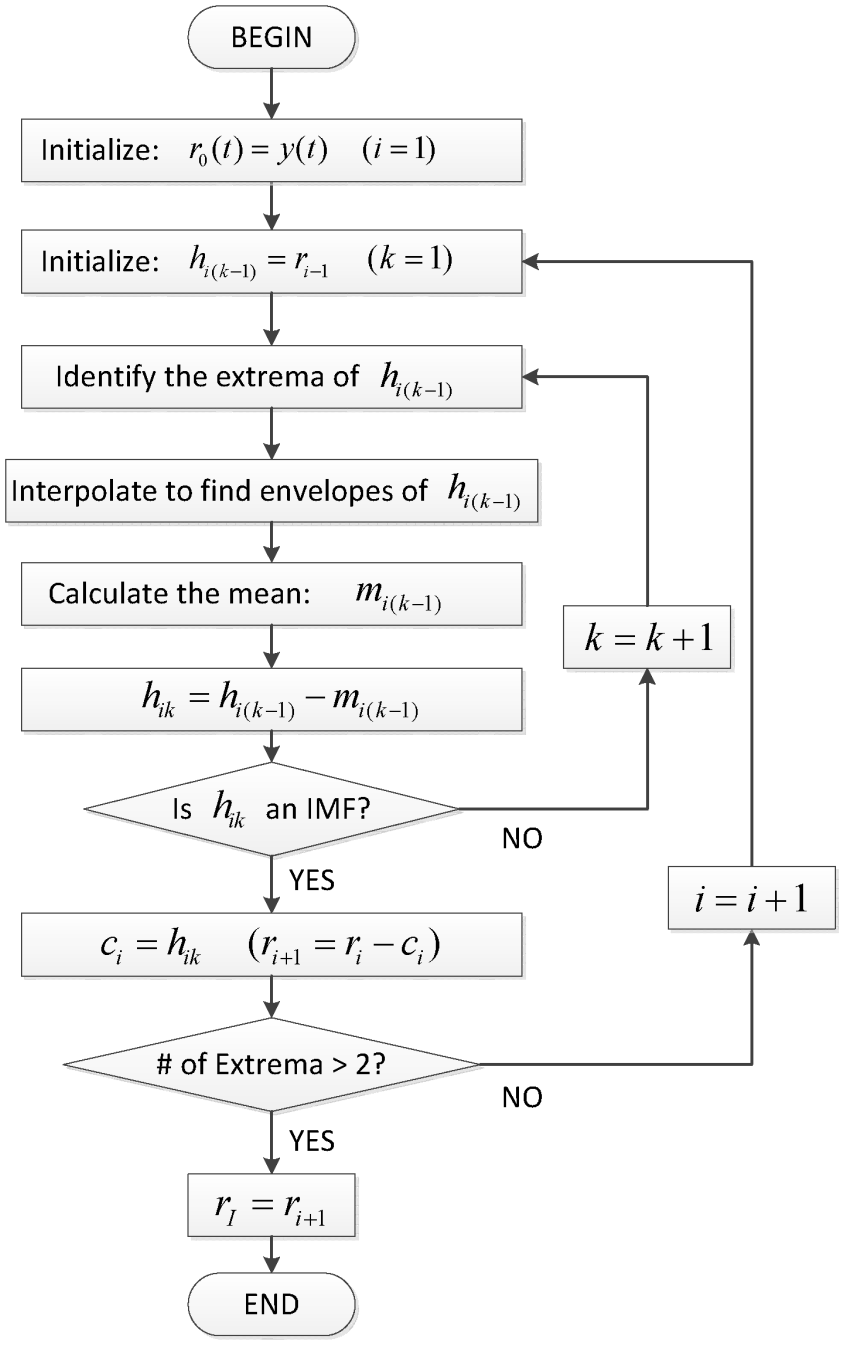

Figure C.1: EMD sifting algorithm used to obtain the IMFs $c_i(t)$ of a signal $y(t)$.

satisfies the Cauchy-Riemann equations). Mathematically, the Hilbert transform is defined as

$$H[x(t)] = \tilde{x}(t) = \pi^{-1} \int_{-\infty}^{\infty} \frac{x(\tau)}{t-\tau} d\tau \tag{C.2}$$

The transform results in a signal comprised of the real-valued function $x(t)$ and its complex-valued counterpart $\tilde{x}(t)$

$$z(t) = x(t) + i\tilde{x}(t) = a(t)e^{i\theta(t)} \tag{C.3}$$

Thus, the Hilbert transform provides a local approximation of the signal's instantaneous amplitude $a(t)$ and phase $\theta(t)$. These instantaneous quantities are calculated according to the following:

$$a(t) = \sqrt{x(t)^2 + \tilde{x}(t)^2} \tag{C.4}$$

$$\theta(t) = \arctan\left(\frac{\tilde{x}(t)}{x(t)}\right) \tag{C.5}$$

The instantaneous frequency $\omega(t)$ is then obtained by differentiating the instantaneous phase:

$$\omega(t) = \frac{d\theta}{dt} \tag{C.6}$$

The final step of the HHT then amounts to performing the Hilbert transform on each IMF $c_i(t)$ obtained via the EMD sifting algorithm. The EMD algorithm ensures that each IMF is well-conditioned for analysis with the Hilbert transform (i.e., the local mean being zero and an alternating appearance of positive maximums and negative minimums). The output of the HHT is therefore a set of IMFs along with the instantaneous amplitude and frequency of each IMF.

REFERENCES

[1] Acker, F., 2011. "Fatal Failures". *Engineering and Technology,* ***6***(7), August, pp. 66 – 69.

[2] Bently, D., and Muszynska, A., 1986. "Early Detection of Shaft Cracks on Fluid-Handling Machines". In Proceedings of ASME International Symposium on Fluid Machinery Trouble Shooting, Vol. 7, pp. 287 – 296.

[3] Sabnavis, G., Kirk, R. G., Kasarda, M., and Quinn, D., 2004. "Cracked Shaft Detection and Diagnostics: A Literature Review". *The Shock and Vibration Digest,* ***36***(4), pp. 287 – 296.

[4] Bartha, A. R., 2000. "Dry Friction Backward Whirl of Rotors". PhD thesis, Swiss Federal Institute of Technology Zurich.

[5] Chupp, R. E., Hendricks, R. C., Lattime, S. B., and Steinetz, B. M., 2006. Sealing in Turbomachinery. Tech. Rep. 2006-214341, NASA.

[6] Ek, M. C., 1980. "Solving Subsynchronous Whirl in the High-Pressure Hydrogen Turbomachinery of the SSME". *Journal of Spacecraft and Rockets,* ***17***(3), pp. 208 – 218.

[7] Childs, D. W., 1978. "The Space Shuttle Main Engine High Pressure Fuel Turbopump Rotordynamic Instability Problem". *Journal of Engineering for Gas Turbines and Power,* ***100***(1), pp. 48 – 57.

[8] Batailly, A., Legrand, M., Millecamps, A., and Garcin, F., 2012. "Numerical-Experimental Comparison in the Simulation of Rotor/Stator Interaction Through Blade-Tip/Abradable Coating Contact". *Journal of Engineering for Gas Turbines and Power,* ***134***(8), pp. 082504: 1 – 11.

[9] Draskovich, B. S., Frani, N. E., Joseph, S. S., and Narasimhan, D., 1996. Patent US5704759 A: Abrasive tip/abradable shroud system and method for gas turbine compressor clearance control.

[10] ISO7919-4: Mechanical vibration - Evaluation of machine vibration by measurements on rotating shafts - Part 4: Gas turbine sets with fluid-film bearings, 2009.

[11] Wild, T., and Kroes, M., 2013. *Aircraft Powerplants.* McGraw-Hill Education.

[12] Steinetz, B. M., Hendricks, R. C., and Munson, J., 1998. Advanced seal technology role in meeting next generation turbine engine goals. Tech. rep., National Aeronautics and Space Administration, Lewis Research Center.

[13] Buck, G. S., 1980. "A Methodology for Design and Application of Mechanical Seals". *ASLE Transactions,* ***23***(3), pp. 244 – 252.

[14] Will, T. P., 1982. "Experimental Observation of a Face-Contact Mechanical Shaft Seal Operation on Water". *Lubrication Engineering,* ***38***(12), pp. 767 – 772.

[15] Burton, R. A., 1980. "Thermal Deformation in Frictionally Heated Contact". *Wear,* ***59***(1), pp. 1 – 20.

[16] Kennedy, F. E., and Hussaini, S. Z., 1987. "Thermo-Mechanical Analysis of Dry Sliding Systems". *Computers and Structures,* ***26***(1), pp. 345 – 355.

[17] Etsion, I., 1982. "A Review of Mechanical Face Seal Dynamics". *The Shock and Vibration Digest,* ***14***(3), pp. 9 – 14.

[18] Lebeck, A. O., 1991. *Principles and Design of Mechanical Face Seals.* Wiley Interscience.

[19] Green, I., and Etsion, I., 1986. "A Kinematic Model for Mechanical Seals with Antirotation Locks or Positive Drive Devices". *Journal of Tribology,* ***108***(1), pp. 42 – 45.

[20] Green, I., 2008. "On the Kinematic and Kinetics of Mechanical Seals, Rotors, and Wobbling Bodies". *Mechanism and Machine Theory,* ***43***(7), pp. 909–917.

[21] Lee, A. S., and Green, I., 1994. "Rotordynamics of a Mechanical Face Seal Riding on a Flexible Shaft". *Journal of Tribology,* ***116***(2), pp. 345 – 351.

[22] Lee, A. S., and Green, I., 1995. "An Experimental Investigation of the Steady-State Response of a Noncontacting Flexibly Mounted Rotor Mechanical Face Seal". *Journal of Tribology,* ***117***(1), pp. 153 – 159.

[23] Zou, M., Dayan, J., and Green, I., 2000. "Feasibility of Contact Elimination of a Mechanical Face Seal Through Clearance Adjustment". *Journal of Engineering for Gas Turbines and Power,* ***122***(2), pp. 478 – 484.

[24] Zou, M., Dayan, J., and Green, I., 2000. "Dynamic Simulation and Monitoring of a Non-Contacting Flexibly Mounted Rotor Mechanical Face Seal". In Proceedings of the Institution of Mechanical Engineers, Part C: Journal of Mechanical Engineering Science, Vol. 214, pp. 1195 – 1206.

[25] Varney, P., and Green, I., 2016. "Impact Phenomena in a Non-Contacting Mechanical Face Seal". *Journal of Tribology,* ***139***, pp. 022201: 1 – 8.

[26] Etsion, I., 1985. "Mechanical Face Seal Dynamics Update". *Shock and Vibration Digest,* ***17***(4), pp. 11 – 16.

[27] Etsion, I., 1991. "Mechanical Face Seal Dynamics 1985 - 1989". *Shock and Vibration Digest,* ***23***(4), pp. 3 – 7.

[28] Hamrock, B. J., 1994. *Fundamentals of Fluid Film Lubrication.* McGraw Hill.

[29] Etsion, I., 1980. "The Accuracy of the Narrow Seal Approximation in Analyzing Radial Face Seals". *ASLE Transactions,* ***22***(2), pp. 208 – 216.

[30] Etsion, I., and Sharoni, A., 1980. "Performance of End-Face Seals with Diametral Tilt and Coning - Hydrostatic Effects". *ASLE Transactions,* ***23***(3), pp. 279 – 288.

[31] Sharoni, A., and Etsion, I., 1980. "Performance of End-Face Seals with Diametral Tilt and Coning - Hydrodynamic Effects". *ASLE Transactions,* ***24***(1), pp. 61 – 70.

[32] Etsion, I., 1980. "Squeeze Effects in Radial Face Seals". *Journal of Lubrication Technology,* ***102***(2), pp. 145 – 151.

[33] Kligerman, Y., and Etsion, I., 2001. "Analysis of the Hydrodynamic Effects in a Surface Textured Circumferential Gas Seal". *Tribology Transactions,* ***44***(3), pp. 472–478.

[34] Etsion, I., and Halperin, G., 2002. "A Laser Surface Textured Hydrostatic Mechanical Seal". *Tribology Transactions,* ***45***(3), pp. 430 –434.

[35] Etsion, I., 2005. "State of the Art in Laser Surface Texturing". *Journal of Tribology,* ***127***(1), pp. 248–253.

[36] Bai, S., Peng, X., Li, Y., and Sheng, S., 2010. "A Hydrodynamic Laser Surface-Textured Gas Mechanical Face Seal". *Tribology Letters,* ***38***(2), pp. 187–194.

[37] Miller, B. A., and Green, I., 2001. "Numerical Formulation for the Dynamic Analysis of Spiral-Grooved Gas Face Seals". *Journal of Tribology,* ***123***(2), pp. 395 – 403.

[38] Green, I., and Etsion, I., 1986. "Pressure and Squeeze Effects on the Dynamic Characteristics of Elastomer O-Rings Under Small Reciprocating Motion". *Journal of Tribology,* ***108***(3), pp. 439 – 444.

[39] Green, I., and Etsion, I., 1986. "Nonlinear Dynamic Analysis of Noncontacting Coned-Face Mechanical Seals". *ASLE Transactions,* ***29***(3), pp. 383 – 393.

[40] Green, I., and Etsion, I., 1983. "Fluid Film Dynamic Coefficients in Mechanical Face Seals". *Journal of Lubrication Technology,* ***105***(2), pp. 297 – 302.

[41] Harp, S. R., and Salant, R. F., 1998. "Analysis of Mechanical Seal Behavior During Transient Operation". *Journal of Tribology,* ***120***(2), pp. 191 – 197.

[42] Green, I., 2002. "A Transient Dynamic Analysis of Mechanical Seals Including Asperity Contact and Face Deformation". *Tribology Transactions,* ***45***(3), pp. 284 – 293.

[43] Chang, W. R., Etsion, I., and Bogy, D. B., 1987. "An Elastic-Plastic Model for the Contact of Rough Surfaces". *Journal of Tribology,* ***109***(2), pp. 257 – 263.

[44] Gao, B. C., Meng, X. K., Shen, M. X., and Peng, X. D., 2016. "Transient Thermal-Mechanical Coupling Behavior Analysis of Mechanical Seals During Start-up Operation". In IOP Cinf. Series: Materials Science and Engineering.

[45] Salant, R. F., and Cao, B., 2005. "Unsteady Analysis of a Mechanical Seal Using Duhamel's Method". *Journal of Tribology,* ***127***(3), pp. 623 – 631.

[46] Green, I., 1987. "The Rotor Dynamic Coefficients of Coned-Face Mechanical Seals with Inward or Outward Flow". *Journal of Tribology,* ***109***(1), pp. 129 – 135.

[47] Green, I., 1989. "Gyroscopic and Support Effects on the Steady-State Response of a Noncontacting Flexibly-Mounted Rotor Mechanical Face Seal". *Journal of Tribology,* ***111***(2), pp. 200 – 208.

[48] Green, I., 1990. "Gyroscopic and Damping Effects on the Stability of a Noncontacting Flexibly-Mounted Rotor Mechanical Face Seal". In Dynamics of Rotating Machinery, pp. 153 – 157.

[49] Lee, A. S., and Green, I., 1994. "Higher Harmonic Oscillations in a Non-contacting FMR Mechanical Face Seal Test Rig". *Journal of Vibration and Acoustics,* ***116***(2), pp. 161 – 167.

[50] Lee, A. S., and Green, I., 1995. "Physical Modeling and Data Analysis of the Dynamic Response of a Flexibly Mounted Rotor Mechanical Seal". *Journal of Tribology,* ***117***(1), pp. 130 – 135.

[51] Wileman, J. M., 1994. "Dynamic Analysis of Eccentric Mechanical Face Seals". PhD thesis, Georgia Institute of Technology.

[52] Wileman, J., and Green, I., 1991. "The Rotordynamic Coefficients of Mechanical Seals Having Two Flexibly Mounted Rotors". *Journal of Tribology,* ***113***(4), pp. 795 – 804.

[53] Wileman, J., and Green, I., 1998. "Stability Analysis of Mechanical Seals with Two Flexibly Mounted Rotors". *Journal of Tribology,* ***120***(2), pp. 145 – 151.

[54] Wileman, J., and Green, I., 1999. "Parametric Investigation of the Steady-State Response of a Mechanical Seal with Two Flexibly Mounted Rotors". *Journal of Tribology,* ***121***(1), pp. 69 – 76.

[55] Etsion, I., and Sharoni, A., 1980. "The Effect of Coning on Radial Forces in Misaligned Radial Face Seals". *Journal of Lubrication Technology,* ***102***(2), pp. 139 – 144.

[56] Wileman, J., and Green, I., 1996. "The Rotor Dynamic Coefficients of Eccentric Mechanical Face Seals". *Journal of Tribology,* ***118***(1), pp. 215 – 224.

[57] Wileman, J., 2004. "Dynamic Response of Eccentric Face Seals to Synchronous Shaft Whirl". *Journal of Tribology,* ***126***(2), pp. 301 – 309.

[58] Etsion, I., and Constantinescu, I., 1984. "Experimental Observation ofthe Dynamic Behavior of Noncontacting Coned-Face Mechanical Seals". *ASLE Transactions,* ***27***(3), pp. 263 – 270.

[59] Huang, W., Lin, Y., Liu, Y., Liu, X., Gao, Z., and Wang, Y., 2013. "Face Rub-Impact Monitoring of a Dry Gas Seal Using Acoustic Emission". *Tribology Letters,* ***52***(2), pp. 253 – 259.

[60] Anderson, W. B., Jarzynski, J., and Salant, R. F., 2001. "A Condition Monitor for Liquid Lubricated Mechanical Seals". *Tribology Transactions,* ***44***(3), pp. 479 – 483.

[61] Goilkar, S. S., and Hirani, H., 2009. "Design and Development of a Test Setup for Online Wear Monitoring of Mechanical Face Seals Using a Torque Sensor". *Tribology Transactions,* ***52***(1), pp. 47 – 58.

[62] Gupta, L. A., and Peroulis, D., 2012. "Wireless Temperature Sensor for Condition Monitoring of Mechanical Seals". In Proceedings of the 42nd European Microwave Conference, pp. 424 – 427.

[63] Zou, M., and Green, I., 1999. "Clearance Control of a Mechanical Face Seal". *Tribology Transactions,* ***42***(3), pp. 535 – 540.

[64] Dayan, J., Zou, M., and Green, I., 1999. "Contact Elimination in Mechanical Face Seals Using Active Control". In Proceedings of the 7th IEEE Mediterranean Conference on Control and Automation.

[65] Yelma, S. S., Miller, B. A., and Landers, R. G., 2006. "Clearance Regulation of Mechanical Gas Face Seals: Part II - Analysis and Control". *Tribology Transactions,* ***49***(3), pp. 373 – 386.

[66] Zhang, H., Landers, R. G., and Miller, B. A., 2010. "Adaptive Control of Mechanical Gas Face Seals with Rotor Runout and Static Stator Misalignment". *Journal of Dynamic Systems, Measurement, and Control,* ***132***(4), pp. 041009.1 – 10.

[67] Minet, C., Brunetiere, N., and Tournerie, B., 2011. "A Deterministic Mixed Lubrication Model for Mechanical Seals". *Journal of Tribology,* ***133***(4), pp. 042203.1–11.

[68] Ruan, B., 2002. "Numerical Modeling of Dynamic Sealing Behaviors of Sprial Groove Gas Face Seals". *Journal of Tribology,* ***124***(1), pp. 186 – 195.

[69] Goldman, P., and Muszynska, A., 1999. "Application of Full Spectrum to Rotating Machinery Diagnostics". *Bentley Nevada Orbit,* ***1***(1), pp. 17 – 21.

[70] Muszynska, A., 2005. *Rotordynamics.* CRC Taylor and Francis Group, Boca Raton, FL.

[71] Fengqi, W., and Meng, G., 2006. "Compound Rub Malfunctions Feature Extraction Based on Full-Spectrum Cascade Analysis and SVM". *Mechanical Systems and Signal Processing,* ***20***(8), pp. 2007 – 2021.

[72] Patel, T. H., and Darpe, A. K., 2008. "Vibration Response of a Cracked Rotor in Presence of Rotor-Stator Rub". *Journal of Sound and Vibration,* ***317***(3), pp. 841 – 865.

[73] Patel, T. H., Zuo, M. J., and Darpe, A. K., 2011. "Vibration Response of Coupled Rotor Systems with Crack and Misalignment". In Proceedings of the Institution of Mechanical Engineers, Part C: Journal of Mechanical Engineering Science, Vol. 225, pp. 700 – 713.

[74] Patel, T. H., and Darpe, A. K., 2011. "Application of Full Spectrum Analysis for Rotor Fault Diagnosis". In IUTAM Symposium on Emerging Trends in Rotor Dynamics, Springer Netherlands, pp. 535 – 545.

[75] Cohen, L., 1995. *Time-Frequency Analysis.* Prentice Hall.

[76] Mallat, S., 1999. *A Wavelet Tour of Signal Processing.* Academic Press.

[77] Peng, Z. K., Jackson, M. R., Rongong, J. A., Chu, F. L., and Parkin, R. M., 2009. "On the Energy Leakage of Discrete Wavelet Transform". *Mechanical Systems and Signal Processing,* ***23***(2), pp. 330 – 343.

[78] Lei, Y., Lin, J., He, Z., and Zuo, M. J., 2013. "A Review on Empirical Mode Decomposition in Fault Diagnosis of Rotating Machinery". *Mechanical Systems and Signal Processing,* ***35***(1), pp. 108 – 126.

[79] Huang, N. E., Shen, Z., and Long, S. R., 1998. "The Empirical Mode Decomposition and the Hilbert Spectrum for Nonlinear and Non-stationary Time Series Analysis". *Proceedings of the Royal Society of London,* ***454***(1971), pp. 903 – 995.

[80] Lei, Y., He, Z., and Zi, Y., 2009. "Application of the EEMD Method to Rotor Fault Diagnosis of Rotating Machinery". *Mechanical Systems and Signal Processing,* ***23***(4), pp. 1327 – 1338.

[81] Wu, F., and Qu, L., 2008. "An Improved Method for Restraining the End Effect in Empirical Mode Decomposition and its Applications to the Fault Diagnosis of Large Rotating Machinery". *Journal of Sound and Vibration,* ***314***(3), pp. 586–602.

[82] Dimarogonas, A. D., and Paipetis, S., 1983. *Analytical Methods in Rotor Dynamics.* Applied Science Publishers.

[83] Papadopoulos, C. A., 2008. "The Strain Energy Release Rate Approach for Modeling Cracks in Rotors: A State-of-the-Art Review". *Mechanical Systems and Signal Processing,* ***22***(4), pp. 763 – 789.

[84] Green, I., and Casey, C., 2005. "Crack Detection in a Rotor Dynamic System by Vibration Monitoring - Part I: Analysis". *Journal of Engineering for Gas Turbines and Power,* ***127***(2), pp. 425 – 436.

[85] Varney, P., and Green, I., 2012. "Crack Detection in a Rotordynamic System by Vibration Monitoring - Part II: Extended Analysis and Experimental Results". *Journal of Engineering for Gas Turbines and Power,* ***134***(11), pp. 112501.1 – 112501.10.

[86] Mayes, I., and Davies, W. G. R., 1984. "Analysis of the Response of a Multi-Rotor-Bearing System Containing a Transverse Crack in a Rotor". *Journal of Vibration, Acoustics, Stress and Reliability,* ***106***(1), pp. 139 – 145.

[87] Han, Q., and Chu, F., 2013. "Dynamic response of cracked rotor-bearing system under time-dependent base movements". *Journal of Sound and Vibration,* ***332***(25), pp. 6847 – 6870.

[88] Ebrahimi, A., Heydari, M., and Behzad, M., 2014. "A Continuous Vibration Theory for Rotors with an Open Edge Crack". *Journal of Sound and Vibration,* ***333***(15), pp. 3522–3535.

[89] Xiang, L., Gao, X., and Hu, A., 2016. "Nonlinear dynamics of an asymmetric rotor-bearing system with coupling faults of crack and rub-impact under oil-film forces". *Nonlinear Dynamics,* ***86***(2), pp. 1057–1067.

[90] Guo, C., Yan, J., and Yang, W., 2017. "Crack Detection for a Jeffcott Rotor with a Transverse Crack: An Experimental Investigation". *Mechanical Systems and Signal Processing,* ***83***, pp. 260–271.

[91] Dimarogonas, A. D., and Massouros, G., 1981. "Torsional Vibration of a Shaft With a Circumferential Crack". *Engineering Fracture Mechanics,* ***15***(3), pp. 439 – 444.

[92] Papadopoulos, C. A., and Dimarogonas, A. D., 1987. "Coupled Longitudinal and Bending Vibrations of a Rotating Shaft with an Open Crack". *Journal of Sound and Vibration,* ***117***(1), pp. 81 – 93.

[93] Varney, P., 2013. "Transverse Fatigue Crack Diagnosis in a Rotordynamic System Using Vibration Monitoring". Master's thesis, Georgia Institute of Technology.

[94] Andrieux, S., and Vare, C., 2002. "A 3D Cracked Beam Model with Unilateral Contact: Application to Rotors". *European Journal of Mechanics - A/Solids,* ***21***(5), pp. 793–810.

[95] Bachschmid, N., and Tanzi, E., 2003. "Deflections and Strains in Cracked Shafts Due to Rotating Loads: A Numerical And Experimental Analysis". *International Journal of Rotating Machinery,* ***9***(4), pp. 303 – 311.

[96] Zapica-Valle, J. L., Rodriguez, E., Garcia-Dieguez, M., and Cortizo, J., 2014. "Rotor Crack Identification Based on Neural Networks and Modal Data". *Meccanica,* ***49***(2), pp. 305–324.

[97] Giannopoulos, G. I., Georgantzions, S., and Anifantis, N., 2015. "Coupled Vibration Response of a Shaft with a Breathing Crack". *Journal of Sound and Vibration,* ***336***(1), pp. 191–206.

[98] Al-Shudeifat, M. A., and Butcher, E. A., 2011. "New Breathing Functions for the Transverse Breathing Crack of the Cracked Rotor System: Approach for the Critical and Subcritical Harmonic Analysis". *Journal of Sound and Vibration,* ***330***(3), pp. 526 – 544.

[99] Silva, J., and Gomez, A., 1990. "Experimental Dynamic Analysis of Cracked Free-Free Beams". *Experimental Mechanics,* ***30***(1), pp. 20 – 25.

[100] Gomez, A., and Silva, J., 1991. "Theoretical and Experimental Data on Crack Depth effects in the Dynamic Behavior of Free-Free Beams". In 9th International Modal Analysis Conference, Vol. 1, pp. 274 – 283.

[101] Dimarogonas, A., and Papadopoulos, C. A., 1983. "Vibration of Cracked Shafts in Bending". *Journal of Sound and Vibration,* ***91***(4), pp. 583 – 593.

[102] Papadopoulos, C. A., and Dimarogonas, A. D., 1988. "Coupled Longitudinal and Bending Vibrations of a Cracked Shaft". *Journal of Vibration, Acoustics, Stress, and Reliability in Design,* ***110***(1), pp. 1 – 8.

[103] Arem, S., and Maitournam, H., 2008. "A Cracked Beam Finite Element for Rotating Shaft Dynamics and Stability Analysis". *Journal of Mechanics of Materials and Structures,* ***3***(5), pp. 893–910.

[104] Arem, S. E., and Nguyen, Q. S., 2012. "Nonlinear Dynamics of a Rotating Shaft with a Breathing Crack". *Annuals of Solid Strucures Mechanics,* ***3***(1), pp. 1 – 14.

[105] Ishida, Y., 2008. "Cracked Rotors: Industrial Machine Case Histories and Nonlinear Effects Shown by Simple Jeffcott Rotor". *Mechanical Systems and Signal Processing,* ***22***(4), pp. 805 – 817.

[106] Gounaris, G. D., and Papadopoulos, C. A., 2002. "Crack Identification in Rotating Shafts by Coupled Response Measurements". *Engineering Fracture Mechanics,* ***69***(3), pp. 339 – 352.

[107] Al-Shudeifat, M. A., 2013. "On the Finite Element Modeling of the Asymmetric Cracked Rotor". *Journal of Sound and Vibration,* ***332***(11), pp. 2795 – 2807.

[108] Liu, C., and Jiang, D., 2013. "Experimental Study on Lateral and Torsional Vibration of Cracked Rotor with Torsional Excitation". In ASME Turbo Expo.

[109] Sawicki, J. T., Sen, A. K., and Litak, G., 2009. "Multiresolution Wavelet Analysis of the Dynamics of a Cracked Rotor". *International Journal of Rotating Machinery*, pp. 1 –8.

[110] Varney, P., and Green, I., 2013. "Rotordynamic Crack Diagnosis: Distinguishing Crack Location and Depth". *Journal of Engineering for Gas Turbines and Power,* ***135***(11), pp. 112101.1–8.

[111] Mayes, I. W., and Davies, W. G. R., 1976. "The Vibration Behaviour of a Rotating Shaft System Containing a Transverse Crack". In Vibrations in Rotating Machinery, IMechE, pp. 53 – 64.

[112] Inagaki, T., Kanki, H., and Shiraki, K., 1982. "Transverse Vibrations of a General Cracked-Rotor Bearing System". *Journal of Mechanical Design,* ***104***(2), pp. 345 – 355.

[113] Sinou, J., 2009. "An Experimental Investigation of Condition Monitoring for Notched Rotors Through Transient Signals and Wavelet Transform". *Experimental Mechanics,* ***49***(5), pp. 683–695.

[114] Dimarogonas, A. D., 1996. "Vibration of Cracked Structures: A State-of-the-art Review". *Engineering Fracture Mechanics,* ***55***(5), pp. 831 – 857.

[115] Inagaki, T., Kanki, H., and Shiraki, K., 1980. "Response Analysis of a General Asymmetric Rotor-Bearing System". *Journal of Mechanical Design,* ***102***(1), pp. 147 – 157.

[116] Casey, C., 2000. "Crack Detection in a Rotordynamic System by Vibration Monitoring". Master's thesis, Georgia Institute of Technology.

[117] Hsieh, S., Chen, J., and Lee, A., 2008. "A Modified Transfer Matrix Method for the Coupled Lateral and Torsional Vibrations of Asymmetric Rotor-Bearing Systems". *Journal of Sound and Vibration,* ***312***(4), pp. 563–571.

[118] Gounaris, G. D., Papadopoulos, C. A., and Dimarogonas, A. D., 1996. "Crack Identification in Beams by Coupled Response Measurement". *Computers and Structures,* ***58***(2), pp. 299 – 305.

[119] Sekhar, A. S., Mohanty, A. R., and Prabhakar, S., 2005. "Vibrations of Cracked Rotor System: Transverse Crack versus Slant Crack". *Journal of Sound and Vibration,* ***279***(3), pp. 1203 – 1217.

[120] Karthikeyan, M., Tiwari, R., and Talukdar, S., 2008. "Development of a Novel Algorithm for a Crack Detection, Localization, and Sizing in a Beam Based on Forced Response Measurements". *Journal of Vibration and Acoustics,* ***130***(2), pp. 021002: 1 – 14.

[121] Grabowski, B., 1980. "The Vibration Behavior of a Turbine Rotor Containing a Transverse Shaft Crack". *Journal of Mechanical Design,* ***102***(1), pp. 140 – 146.

[122] Wauer, J., 1990. "Modelling and Formulation of Equations of Motion for Cracked Rotating Shafts". *International Journal of Solids Structures,* ***26***(8), pp. 901 – 914.

[123] Ge-Qun, S., 1999. "Torsional-Flexural Coupled Vibrations of Continuous Shaft with its Weight". In International Modal Analysis Conference, Society for Experimental Mechanics.

[124] Chasalevris, A. C., and Papadopoulos, C. A., 2009. "A Continuous Model Approach for Cross-Coupled Bending Vibrations of a Rotor-Bearing System with Transverse Breathing Crack". *Mechanism and Machine Theory,* ***44***(6), pp. 1176 – 1191.

[125] Jun, O. S., Eun, H. J., Earmee, Y. Y., and Lee, C. W., 1992. "Modelling and Vibration Analysis of a Simple Rotor with a Breathing Crack". *Journal of Sound and Vibration,* ***155***(2), pp. 273 – 290.

[126] Papadopoulos, C. A., and Dimarogonas, A. D., 1992. "Coupled Vibration of Cracked Shafts". *Journal of Vibration and Acoustics,* ***114***(4), pp. 461 – 467.

[127] Gasch, R., 1976. "Dynamic Behavior of a Simple Rotor with a Cross-sectional Crack". In Vibration in Rotating Machinery, IMechE, pp. 123–128.

[128] Davies, W. G. R., and Mayes, I. W., 1984. "The Vibrational Behavior of a Multi-Shaft, Multi-Bearing System in the Presence of a Propagating Transverse Crack". *Journal of Vibration, Acoustics, Stress and Reliability,* ***106***(1), pp. 146 – 153.

[129] Guo, D., and Peng, Z. K., 2007. "Vibration Analysis of a Cracked Rotor using Hilbert Huang Transform". *Mechanical Systems and Signal Processing,* ***21***(8), pp. 3030 – 3041.

[130] Guo, C., Al-Shudeifat, M. A., Yan, J., Bergman, L. A., McFarland, D. M., and Butcher, E. A., 2013. "Application of Empirical Mode Decomposition to a Jeffcott Rotor with a Breathing Crack". *Journal of Sound and Vibration,* ***332***(16), pp. 3881 – 3892.

[131] Zou, J., and Chen, J., 2004. "A Comparative Study on Time-Frequency Feature of Cracked Rotor by Wigner-Ville Distribution and Wavelet Transform". *Journal of Sound and Vibration,* ***276***(1), pp. 1 – 11.

[132] Babu, T. R., Srikanth, S., and Sekhar, A. A., 2008. "Hilbert-Huang Transform for Detection and Monitoring of Crack in a Transient Rotor". *Mechanical Systems and Signal Processing,* ***22***(4), pp. 905 – 914.

[133] Wang, K. S., Guo, D., and Heyns, P. S., 2012. "The Application of Order Tracking for Vibration Analysis of a Varying Speed Rotor with a Propagating Transverse Crack". *Engineering Failure Analysis,* ***21***(1), pp. 91 – 101.

[134] Darpe, A., Gupta, K., and Chawla, A., 2004. "Coupled Bending, Longitudinal, and Torsional Vibrations of a Cracked Rotor". *Journal of Sound and Vibration,* ***269***(1), pp. 33 – 60.

[135] Darpe, A. K., Gupta, K., and Chawla, A., 2004. "Transient Response and Breathing Behavior of a Cracked Jeffcott Rotor". *Journal of Sound and Vibration,* ***272***(1), pp. 207 – 242.

[136] Patel, T. H., and Darpe, A. K., 2008. "Influence of Crack Breathing Model on Nonlinear Dynamics of a Cracked Rotor". *Journal of Sound and Vibration,* ***311***(3), pp. 953 – 972.

[137] Ferfecki, P., 2007. "Study of Coupling between Bending and Torsional Vibrations of Cracked Rotor System Supported by Radial Active Magnetic Bearings". *Applied and Computational Mechanics,* ***1***, pp. 427 – 436.

[138] Liong, R., and Proppe, C., 2013. "Finite Element Multibody Simulation of a Breathing Crack in a Rotor with a Cohesive Zone Model". *ISRN Mechanical Engineering*, pp. 1–10.

[139] Chu, X., and Wang, F., 2014. "Analysis of Vibration Characteristics of a Cracked Rotor". *Applied Mechanics and Materials,* ***620***, pp. 296–299.

[140] Gasch, R., 2008. "Dynamic Behavior of the Laval Rotor with a Transverse Crack". *Mechanical Systems and Signal Processing,* ***22***(4), pp. 790 – 804.

[141] Yang, Y., Ren, X., and Qin, W., 2013. "Nonlinear Response Prediction of Cracked Rotor Based on EMD". In 54th AIAA/ASME/ASCE/AHS/ASC Structures, Structural Dynamics, and Materials Conference, American Institute of Aeronautics and Astronautics.

[142] Szolc, T., Tauzowski, P., Knabel, J., and Stocki, R., 2009. "Nonlinear and Parametric Coupled Vibrations of the Rotor-Shaft System as Fault Identification Symptom using Stochastic Methods". *Nonlinear Dynamics,* ***57***(4), pp. 533 – 557.

[143] Imam, I., Azzaro, S., Bankert, R., and Scheibel, J., 1989. "Development of an Online Rotor Crack Detection and Monitoring System". *Journal of Vibration, Acoustics, Stress, and Reliability in Design,* ***111***(3), pp. 241 – 250.

[144] Saridakis, K. M., C., A., Chasalevris, Papadopoulos, C. A., and Dentsoras, A. J., 2008. "Applying Neural Networks, Genetic Algorithms and Fuzzy Logic for the Identification of Cracks in Shafts by Using Coupled Response Measurements". *Computers and Structures,* ***86***(11), pp. 1318 – 1338.

[145] Bachschmid, N., Pennacchi, P., Tanzi, E., and Vania, A., 2000. "Identification of Transverse Crack Position and Depth in Rotor Systems". *Meccanica,* ***35***(6), pp. 563 – 582.

[146] Darpe, A. K., Gupta, K., and Chawla, A., 2006. "Dynamics of a Bowed Rotor with a Transverse Surface Crack". *Journal of Sound and Vibration,* ***296***(4), pp. 888 – 907.

[147] Wu, X., and Meagher, J., 2008. "A Two-Disk Extended Jeffcott Rotor Model Distinguishing a Shaft Crack from Other Rotating Asymmetries". *International Journal of Rotating Machinery*, pp. 1 – 11.

[148] Darpe, A. K., 2007. "A Novel Way to Detect Transverse Surface Crack in a Rotating Shaft". *Journal of Sound and Vibration,* ***305***(1), pp. 151 – 171.

[149] Sekhar, A., 2004. "Crack Identification in a Rotor System: A Model-Based Approach". *Journal of Sound and Vibration,* ***270***(4), pp. 887–902.

[150] Adewusi, S. A., and Al-Bedoor, B. O., 2001. "Wavelet Analysis of Vibration Signals of an Overhang Rotor with a Propagating Transverse Crack". *Journal of Sound and Vibration,* ***246***(5), pp. 777 – 793.

[151] Yang, B., and Suh, C. S., 2004. "Interpretation of Crack-Induced Rotor Non-Linear Response Using Instantaneous Frequency". *Mechanical Systems and Signal Processing,* ***18***(3), pp. 491 – 513.

[152] di Bernardo, M., Budd, C. J., Champneys, A. R., and Kowalczyk, P., 2008. *Piecewise-Smooth Dynamical Systems: Theory and Applications*. Springer.

[153] Varney, P., and Green, I., 2015. "Nonlinear Phenomena, Bifurcations, and Routes to Chaos in an Asymmetrically Supported Rotor-Stator Contact System". *Journal of Sound and Vibration,* ***336***(2), pp. 207 – 226.

[154] Beatty, R. F., 1985. "Differentiating Rotor Response Due to Radial Rubbing". *Journal of Vibration, Acoustics, Stress, and Reliability in Design,* ***107***(2), pp. 151 – 160.

[155] Kim, Y. B., and Noah, S. T., 1990. "Bifurcation Analysis for a Modified Jeffcott Rotor with Bearing Clearances". *Nonlinear Dynamics,* ***1***(3), pp. 221 – 241.

[156] Chu, F., and Zhang, Z., 1997. "Bifurcation and Chaos in a Rub-Impact Jeffcott Rotor System". *Journal of Sound and Vibration,* ***210***(1), pp. 1 – 18.

[157] Sawicki, J. T., Padovan, J., and Al-Khatib, R., 1999. "The Dynamics of Rotor with Rubbing". *International Journal of Rotating Machinery,* ***5***(4), pp. 295 – 304.

[158] Edwards, S., Lees, A. W., and Friswell, M. I., 1999. "The Influence of Torsion on Rotor/Stator Contact in Rotating Machinery". *Journal of Sound and Vibration,* ***225***(4), pp. 767 – 778.

[159] Lin, F., Schoen, M. P., and Korde, U. A., 2001. "Numerical Investigation with Rub-Related Vibration in Rotating Machinery". *Journal of Vibration and Control,* ***7***(6), pp. 833 – 848.

[160] Karpenko, E. V., Wiercigroch, M., and Cartmell, M. P., 2002. "Regular and Chaotic Dynamics of a Discontinuously Nonlinear Rotor System". *Chaos, Solitions, and Fractals,* ***13***(6), pp. 1231 – 1242.

[161] Qin, W., Chen, G., and Meng, G., 2004. "Nonlinear Responses of a Rub-Impact Overhung Rotor". *Chaos, Solitions, and Fractals,* ***19***(5), pp. 1161 – 1172.

[162] Peng, Z. K., Chu, F. L., and Tse, P. W., 2005. "Detection of the Rubbing-Caused Impacts for Rotor-Stator Fault Diagnosis Using Reassigned Scalogram". *Mechanical Systems and Signal Processing,* ***19***(2), pp. 391 – 409.

[163] Zhang, W. M., and Meng, G., 2006. "Stability, Bifurcation and Chaos of a High-Speed Rub-Impact Rotor System in MEMS". *Sensors and Actuators,* ***127***(1), pp. 163 – 178.

[164] Chang-Jian, C. W., and Chen, C. K., 2009. "Chaos of Rub-Impact Rotor Supported by Bearings with Nonlinear Suspension". *Tribology International,* ***42***(3), pp. 426 – 439.

[165] Inayat-Hussain, J. I., 2010. "Bifurcations in the Response of a Jeffcott Rotor with Rotor-to-Stator Rub". In ASME 2010 Biennial Conference on Engineering Systems Design and Analysis.

[166] Cao, J., Ma, C., Jiang, Z., and Liu, S., 2011. "Nonlinear Dynamic Analysis of Fractional Order Rub-Impact Rotor System". *Communications in Nonlinear Science and Numerical Simulation,* ***16***(3), pp. 1443 – 1463.

[167] Abu-Mahfouz, I., and Banerjee, A., 2013. "On the Investigation of Nonlinear Dynamics of a Rotor with Rub-Impact Using Numerical Analysis and Evolutionary Algorithms". *Procedia Computer Science,* ***20***, pp. 140 – 147.

[168] Choy, F. K., and Padovan, J., 1987. "Nonlinear Transient Analysis of Rotor-Casing Rub Events". *Journal of Sound and Vibration,* ***113***(3), pp. 529 – 545.

[169] Al-Bedoor, B. O., 2000. "Transient Torsional and Lateral Vibrations of Unbalanced Rotors with Rotor-to-Stator Rubbing". *Journal of Sound and Vibration,* ***229***(3), pp. 627 – 645.

[170] Popprath, S., and Ecker, H., 2007. "Nonlinear Dynamics of a Rotor Contacting an Elastically Suspended Stator". *Journal of Sound and Vibration,* ***308***(3), pp. 767 – 784.

[171] Dai, X., Jin, Z., and Zhang, X., 2002. "Dynamic Behavior of the Full Rotor/Stop Rubbing: Numerical Simulation and Experimental Verification". *Journal of Sound and Vibration,* ***251***(5), pp. 807 – 822.

[172] Chang-Jian, C. W., and Chen, C. K., 2007. "Chaos and Bifurcation of a Flexible Rub-Impact Rotor Supported by Oil Film Bearings with Nonlinear Suspension". *Mechanism and Machine Theory,* ***42***(3), pp. 312 – 333.

[173] Groll, G. V., and Ewins, D. J., 2002. "A Mechanism of Low Subharmonic Response in Rotor/Stator Contact Measurements and Simulation". *Journal of Vibration and Acoustics,* ***124***(3), pp. 350 – 358.

[174] Abu-Mahfouz, I., 1993. "Routes to Chaos in Rotor Dynamics". PhD thesis, Case Western Reserve University.

[175] Chu, F., and Zhang, Z., 1997. "Periodic, Quasi-Periodic and Chaotic Vibrations of a Rub-Impact Rotor System Supported on Oil Film Bearings". *International Journal of Engineering Science,* ***35***(9), pp. 963 – 973.

[176] Smyth, P. A., Varney, P. A., and Green, I., 2016. "A Fractional Calculus Model of Viscoelastic Stator Supports Coupled with Elastic Rotor-Stator Rub". *Journal of Tribology,* ***138***(4), pp. 041101: 1 – 8.

[177] Qin, W., Su, H., and Yang, Y., 2008. "Grazing Bifurcation and Chaos in Response of Rubbing Rotor". *Chaos, Solitons, and Fractals,* ***37***(1), pp. 166 – 174.

[178] Yuan, Z., Chu, F., and Hao, R., 2007. "Simulation of Rotor's Axial Rub-Impact in Full Degrees of Freedom". *Mechanism and Machine Theory,* ***42***(7), pp. 763 – 775.

[179] Yu, J. J., 2013. "Rub Diagnostics Based on Vibration Data". In ASME Turbo Expo 2013: Turbine Technical Conference and Exposition.

[180] Patel, T. H., and Darpe, A. K., 2009. "Study of Coast-up Vibration Response for Rub Detection". *Mechanism and Machine Theory,* ***44***(8), pp. 1570–1579.

[181] Qi, K., He, Z., and Zi, Y., 2007. "Cosine Window-Based Boundary Processing Method for EMD and its Application in Rubbing Fault Diagnosis". *Mechanical Systems and Signal Processing,* ***21***(7), pp. 2750 – 2760.

[182] Cheng, J., Yu, D., Tang, J., and Yang, Y., 2009. "Local Rub-Impact Fault Diagnosis of the Rotor Systems Based on EMD". *Mechanism and Machine Theory,* ***44***(4), pp. 784–791.

[183] Patel, T. H., and Darpe, A. K., 2009. "Coupled Bending-Torsional Vibration Analysis of Rotor with Rub and Crack". *Journal of Sound and Vibration,* ***326***(3), pp. 740 – 752.

[184] Wan, F., Xu, Q., and Li, S., 2004. "Vibration Analysis of Cracked Rotor Sliding Bearing System with Rotor-Stator Rubbing by Harmonic Wavelet Transform". *Journal of Sound and Vibration,* ***271***(3), pp. 507–518.

[185] Huang, Z., Zhou, J., Yang, M., and Zhang, Y., 2011. "Vibration Characteristics of a Hydraulic Generator Unit Rotor System with Parallel Misalignment and Rub-Impact". *Archive of Applied Mechanics,* ***81***(7), pp. 829 – 838.

[186] Shen, X., Jia, J., and Zhao, M., 2008. "Nonlinear Analysis of a Rub-Impact Rotor-Bearing System with Initial Permanent Rotor Bow". *Archive of Applied Mechanics,* ***78***(3), pp. 225 – 240.

[187] Chen, J., Jiang, D., and Liu, C., 2013. "Identification of Multi-Concurrent Fault in a Steam Turbine Rotor System Using Model-Based Method". In ASME Turbo Expo 2013: Turbine Technical Conference and Exposition.

[188] Prabhakar, S., and Sekhar, A. S., 2002. "Crack versus Coupling Misalignment in a Transient Rotor System". *Journal of Sound and Vibration,* ***256***(4), pp. 773 – 786.

[189] Markert, R., Platz, R., and Seidler, M., 2001. "Model Based Fault Identification in Rotor Systems by Least Squares Fitting". *International Journal of Rotating Machinery,* ***7***(5), pp. 311 – 321.

[190] Genta, G., 2005. *Dynamics of Rotating Systems.* Mechanical Engineering Series. Springer Science and Business Media, Inc., New York, NY.

[191] Rao, J. S., 1996. *Rotor Dynamics*, 3 ed. New Age International, New Delhi.

[192] Sandberg, H., Mollerstedt, E., and Bernhardsson, B., 2005. "Frequency-Domain Analysis of Linear Time-Periodic Systems". *IEEE Transactions on Automatic Control,* ***50***(12), pp. 1971 – 1983.

[193] Nayfeh, A. H., and Balachandran, B., 2004. *Applied Nonlinear Dynamics: Analytical, Computational, and Experimental Methods.* Wiley-VCH.

[194] Guilhen, P. M., Berthier, P., Ferraris, G., and Lalanne, M., 1988. "Instability and Unbalance Response of Dissymmetric Rotor-Bearing Systems". *Journal of Vibration and Acoustics,* ***110***(3), pp. 288–294.

[195] Anderson, T., 2005. *Fracture Mechanics: Fundamentals and Applications.* CRC.

[196] Papadopoulos, C. A., 2004. "Some Comments on the Calculation of the Local Flexibility of Cracked Shafts". *Journal of Sound and Vibration,* ***278***(4), pp. 1205 – 1211.

[197] Strogatz, S. H., 1998. *Nonlinear Dynamics and Chaos.* Perseus Books, Reading, Massachusetts.

[198] Greenwood, J. A., and Williamson, J. B., 1966. "Contact of Nominally Flat Surfaces". *Proceedings of the Royal Society of London A,* ***295***(1442), pp. 300 – 319.

[199] Varney, P., and Green, I., 2015. "Rough Surface Contact of Curved Conformal Surfaces: An Application to Rotor-Stator Rub". *Journal of Tribology,* ***138***(4), pp. 041401: 1 – 7.

[200] Jackson, R. L., and Green, I., 2006. "A Statistical Model of Elasto-Plastic Asperity Contact Between Rough Surfaces". *Tribology International,* ***39***(9), pp. 906 – 914.

[201] Jackson, R. L., and Green, I., 2005. "A Finite Element Study of Elasto-Plastic Hemispherical Contact". *Journal of Tribology,* ***127***(2), pp. 343 – 354.

[202] Green, I., 2005. "Poisson Ratio Effects and Critical Values in Spherical and Cylindrical Hertzian Contact". *International Journal of Applied Mechanics and Engineering,* ***10***(3), pp. 451 – 462.

[203] Wileman, J., and Green, I., 1997. "Steady-State Analysis of Mechanical Seals With Two Flexibly Mounted Rotors". *Journal of Tribology,* ***119***(1), pp. 200 – 204.

[204] English, C., 1989. "Stiffness Determination of Elastomeric O-Rings Using the Finite Element Method". Master's thesis, Georgia Institute of Technology.

[205] Hale, J. K., 1963. *Oscillations in Nonlinear Systems.* McGraw-Hill, New York.

[206] Urabe, M., 1974. "Quasiperiodic Solutions of Ordinary Differential Equations". *Nonlinear Vibration Problems,* ***18***, pp. 85 – 93.

[207] Thota, P., and Dankowicz, H., 2008. "TC-HAT: A Novel Toolbox for the Continuation of Periodic Trajectories in Hybrid Dynamical Systems". *SIAM Journal of Applied Dynamical Systems,* ***7***(4), pp. 1283 – 1322.

[208] Chavez, J. P., and Wiercigroch, M., 2013. "Bifurcation Analysis of Periodic Orbits of a Non-Smooth Jeffcott Rotor Model". *Communications in Nonlinear Science and Numerical Simulation,* ***18***(9), pp. 2571 – 2580.

[209] Varney, P., and Green, I., 2014. "Rotor/Stator Rubbing Contact in an Overhung Rotordynamic System". In STLE Annual Meeting, Orlando, FL.

[210] Etsion, I., 1982. "Dynamic Analysis of Noncontacting Face Seals". *Journal of Tribology,* ***104***(4), pp. 460 – 468.